Mechanics of Advanced Materials and Structures

ICMAMS 2026

5th International Conference on Mechanics of Advanced Materials and Structures (ICMAMS 2026), 1–3 July 2026, Institut Clément Ader (ICA), Toulouse, France



Edited by

Riccardo Augello

Giovanna Carrera

MRF

Mechanics of Advanced Materials and Structures ICMAMS 2026

5th International Conference on Mechanics of Advanced Materials and Structures (ICMAMS 2026) took place from 1–3 July 2026 at Institut Clément Ader (ICA) in Toulouse, France

Editors
Riccardo Augello and Giovanna Carrera

Department of Mechanical and Aerospace Engineering, Politecnico di Torino, Italy

Organised by Institut Clément Ader and AIDAA
Hosted at INSA Toulouse







Peer review statement

All papers published in this volume of "Materials Research Proceedings" have been peer reviewed. The process of peer review was initiated and overseen by the above proceedings editors. All reviews were conducted by expert referees in accordance to Materials Research Forum LLC high standards.

Copyright © 2026 by authors

Content from this work may be used under the terms of the Creative Commons Attribution 3.0 license. Any further distribution of this work must maintain attribution to the author(s) and the title of the work, journal citation and DOI.

Published under License by **Materials Research Forum LLC**
Millersville, PA 17551, USA

Published as part of the proceedings series
Materials Research Proceedings
Volume 73 (2026)

ISSN 2474-3941 (Print)
ISSN 2474-395X (Online)

ISBN 978-1-64490-444-2 (Print)
ISBN 978-1-64490-445-9 (eBook)

This book contains information obtained from authentic and highly regarded sources. Reasonable efforts have been made to publish reliable data and information, but the author and publisher cannot assume responsibility for the validity of all materials or the consequences of their use. The authors and publishers have attempted to trace the copyright holders of all material reproduced in this publication and apologize to copyright holders if permission to publish in this form has not been obtained. If any copyright material has not been acknowledged please write and let us know so we may rectify in any future reprint.

Distributed worldwide by

Materials Research Forum LLC
105 Springdale Lane
Millersville, PA 17551
USA
https://mrforum.com

Manufactured in the United States of America
10 9 8 7 6 5 4 3 2 1

Table of Contents

Preface
Committees
Effect of Tool-Temperature Compensation on the Mechanical Behavior of AFP-Manufactured CF/LM-PAEK Laminates
Dieudonné IRAGUHA, Wiyao AZOTI, Bruno CASTANIE, Philippe OLIVIER 1
Component-Wise Free Vibration Analysis of Sandwich Metamaterials by Carrera Unified Formulation
Erasmo Carrera, Riccardo Augello, Ningning Liu 7
Experimental Determination of Length Scale Parameter: A Comparison of Static and Dynamic Responses
Hareem JAWAID, Mikko SUOMINEN 13
Enhanced Dielectric and Conductive Properties of ZnO via Transition Metal Doping a Computational Study for Advanced Materials
Rasool Akhtar Alias OSAMA, Hannah LEVENE, Graham WOOD, Peter LOMAX, Rebecca CHEUNG 18
3D Micromechanical Modeling of Compressive Failure in Unidirectional CFRP
Doha KASHOUA, Samuel RIVALLANT, Pierre RAHME, Christophe BOUVET 23
Multiscale Numerical Modeling of Vitrimer-Based Woven Face Sheets used in Sandwich Structure Applications
Georgios KOTSINIS, Festus Ifeanyi ANAGWU, Oussema KACHOURI, Gaston RAUCHS, Levent KIRKAYAK, Lucas BINSFELD, Gaetano GIUNTA 27
Finite Element Modeling of Frictional Stick–Slip Behavior in Structural Systems within the CUF Framework
Shabnam KIASAT, Matteo FILIPPI, Alfonso PAGANI, Erasmo CARRERA 31
Experimental and Numerical Analysis of Compression and Shear Wrinkling in Sandwich Beams under Three-Point Bending
Befekadu GASHE, Abdulmaliq ALAWODE, Samuel RIVALLANT, Bruno CASTANIE 37
Low-velocity/Low-energy Impact Response of Khaya (Khaya ivorensis) for Sustainable Mobility Applications
Riccardo HOUNGBEGNON, Bruno CASTANIÉ, Valery DOKO, José XAVIER, Rostand MOUTOU PITTI 43
Composite Reinforced Railway Modelling as a Step to Help in Design and Conception
Jean-Emmanuel CHAMBE, Hamza BENYAHIA, Léo SUDRIÈS, Joël SERRA, Wiyao-Leleng AZOTI, Bruno CASTANIÉ 47
Heat-Treatment Control of δ Phase in HIPed L-PBF Alloy 718: Microstructural Baseline for Creep and Dwell-Fatigue Assessment
Rana ELSAYED, Johan MOVERARE, Emil ERIKSSON 51
Coupled Isogeometric Phase-Field Modeling and Embedded Distributed Fiber Optic Strain Sensing for Degradation Analysis of Complex Structures
Ha-Thanh PHAN, Aghiad KHADOUR 56

Fatigue Crack Analysis Using a Coupled 2D CUF–3D Peridynamics Framework
Qiang ZHANG, Alfonso PAGANI, Xiang LIU, Wei ZHOU, Erasmo CARRERA 62

Indentation on Anisotropic Magneto-Electro-Viscoelastic Layer-Substrate using a Semi-Analytical Approach
Do Duc DO, Nguyen Dinh DUC, Van Thuong NGUYEN 66

Design to Manufacturing Process Calibration and Simulation of LPBF Structures
Ijaz AKBAR, Djamel ABOU MAAMAR, Mohamed El IBRAHIMI, Kevin Nocentini 72

Phase Holographic Imaging based on Acoustic Metasurfaces
Xiao Guo, Yifan Zhu, Hui Zhang, Haiyan Fan 78

Static and Modal Response of Curved Honeycomb Metastructure Panels
Riccardo AUGELLO, Erasmo CARRERA 85

Influence of Printing Parameters and Testing Temperature on the Tensile Behaviour of 3D-Printed Hemp/PLA
Matthieu CARENTON, Fabienne TOUCHARD, Laurence CHOCINSKI-ARNAULT, Damien MARCHAND 91

Physics-Constrained Surrogate Modeling for Microscale Elastic Homogenization of Additively Manufactured Continuous Carbon Fiber Composites
Tongwha KIM, Kamran BEHDINAN 95

Multidisciplinary Optimization of Passively-Insulated Liquid Hydrogen Tanks for Aircraft Applications
Sergio BAGARELLO, Alberto MILAZZO, Ali ELHAM, Ivano BENEDETTI 100

Modeling Hygrothermal-Induced Degradation in Polymer Adhesive Joints for Composite-Metal Assemblies
Touati Benali Abdelaziz, Habib Achache, Mohammed Benyettou, Alberto García-Peñas 105

Low-Velocity Impact on Composite Stiffened Panels Using a Component-Wise Approach
Marco PETROLO, Chiara FRANCESCHINI, Matteo FILIPPI, Erasmo CARRERA 109

Lattice Structures: From Computed Tomography to Simplified Models
Davide Lorenzo CAPPA, Riccardo VESCOVINI, Alessandro LEVATI, Stefano FOLETTI 114

Space-Frequency PGD Formulation with Refined Sinusoidal Kinematics for Forced Vibration Analysis of Composite and Sandwich Beams
M. NDIAYE, P. VIDAL, G. DI CARA, L. GALLIMARD, O. POLIT 118

Free Vibration and Electromechanical Response Analysis of Piezoelectric Beams using the Dynamic Stiffness Method and the Carrera Unified Formulation
Yu WANG, Alfonso PAGANI, Erasmo CARRERA, Xiang LIU 124

Pull-Out Energy Dissipation and Fracture Toughness of Plasma-Modified Para-Aramid Soft Material
Erman BILISIK, Havva Esra BAKBAK, Mahmut KORKMAZ, Gülhan ERDOGAN, Kadir BILISIK 130

Element-Free Galerkin Method for Cantilever Nano-Beam Based on the Modified Kernel Integral Non-Local Elasticity Model
S.L. AKHIL, I.R. PRAVEEN KRISHNA 136

Innovative Viscous Damper Design for Stay Cable Control: The Hysteretic Maxwell Model
Selsebil SOLTANE, Othman BEN MEKKI 142

Geometrical Nonlinear Analysis of Beams by Hierarchical Legendre Expansion CUF Models
Alfonso PAGANI, Piero CHIAIA, Erasmo CARRERA 147

Finite Strain Ductile Phase-Field Modelling under Chemo Thermo-Mechanical Coupling: Application to Viscoplastic Silicon Anode Particles
Armel TENE TESSE, Seydou HEBIE, Emmanuelle LANCELLE BELTRAN, Habibou MAITOURNAM, Ziad MOUMNI 151

A Mixed Formulation for Geometrically Exact Beams based on the Concept of Discrete Curvature
Alexander HUMER, Ivo STEINBRECHER, Astrid PECHSTEIN 156

Fatigue Limit Evaluation of Hybrid Fibre Reinforced Polymer-Matrix Composites (PMC) Using Self-Heating Tests and Embedded Piezoelectric Transducers
Ones GAMMOUDI, Walid HARIZI, Jamal NAJD, Enrico ZAPPINO, Erasmo CARRERA 160

Novel Glass Fibre Z-Pins to Improve the Delamination Bridging Performance of Laminated Composite Materials
Romain RUTAR, Luiz KAWASHITA, Eduardo SANTANA DE VEGA, Christophe BOUVET, Bruno CASTANIÉ, Stephen R HALLETT 166

Development of ZnO Nanoparticle-Based Voltage Sensor using Copper Oxide Nanofluids via Large-Area Printing Technology
K.R.V. Subramanian, Niranjan Murthy, Bharath V. 170

Multi-Fidelity Reliability-Based Design Optimization of Advanced Composite Structures
Dario ZAMANI, Alfonso PAGANI, Marco PETROLO, Erasmo CARRERA 177

An Effective Methodology for Strength Prediction of Fusion-Welded Thermoplastic Composite Repairs
A. Viste, B. Castanié, L. Crouzeix, D. Espinassou, C. Briançon 183

Evaluation of Best Theories using Neural Networks and Adaptive Sampling
Marco PETROLO, Giulio CANDITA, Alfonso PAGANI, Erasmo CARRERA 190

Effect of Geometric Parameters on the Failure Index of Composite Deployable Booms
Riccardo AUGELLO, Erasmo CARRERA, Francesco LATINI, Marco PETROLO 195

Mode Change and Evolution of Thin Deployable Space Structures in Small and Large Displacement Regimes
Erasmo CARRERA, Riccardo AUGELLO, Andrea SERINO 200

Numerical Simulation of the Water-Air-Abrasive Mixture within a Cutting Head for Water Jet Machining
Amene ALLAL, Pascal FEDE, Laurent CROUZEIX, Patrick GILLES 206

Dynamic Mechanical Analysis of Mechanical Anomalies at Spin-State Transitions in Powder Samples
Maryam NASIMSOBHAN, Nagham MAWASSY, Baptiste MARTIN, Ruben TURO-CORTES, Carlos BARTUAL-MURGUI, José Antonio REAL, Malcolm HALCROW, Gábor MOLNÁR, Azzedine BOUSSEKSOU 211

Buckling and Post-Buckling of Multi-Material Metastructure Panels
Riccardo AUGELLO, Erasmo CARRERA 217

Investigating the Dynamic Behavior of FGM Structures using the Carrera Unified Formulation
Munise Didem DEMİRBAS, Riccardo AUGELLO, Erasmo CARRERA 223

Tailoring Interfacial Strategies to Enhance Mechanical Properties of Bi-Layered LSR-Based Polymer Composite Radiation Shields
Pramod A.C., Ambika, Subramanian K.R.V., Niranjan Murthy, Roopa, Nagaiah N., Sherry Shajan Kuttukaran 229

Lamb Wave Propagation in Damaged Sandwich Structures using High Order Finite Plate Elements
Myka ABAQUIN, Alfonso PAGANI, Matteo FILIPPI 235

Advances in Design and Fabrication of Fiber-Reinforced Polymer Composite Bottles for Aerospace Applications
Girish V Kulkarni, Prakrathi S., Bijayalakshmi Das 239

Numerical Analysis of Composite Shells with Curved Fibers via Curvilinear 2|3D Finite Elements
Piero CHIAIA, Maria CINEFRA 245

Impact of Blades Icing on Wind Turbine Aeroelastic Fragility
Carmelo Rosario Vindigni, Giuseppe Mantegna, Antonio Esposito, Calogero Orlando, Andrea Alaimo, Djamel Rezgui, Raffaele De Risi 249

Effect of Cumulative Impact Energy on Damage Accumulation in Glass–Carbon Hybrid Composite Laminates
Shilpa R.S., Jyothilakshmi R., Mohandas K.N. 253

Hierarchical Anisotropic-Order Finite Elements for the Analysis of Incompressible Materials
Piero CHIAIA, Alexander HUMER, Alfonso PAGANI 262

Comparative Analysis of FGM Euler - Bernoulli and Timoshenko - Ehrenfest Beam Theories for Bending Response of Sea Ice
Giacomo STIRPE, Mikko SUOMINEN 266

Deep Learning Prediction of Crack Propagation in Ductile Materials using Surface Displacements Fields
Lahouari BENABOU 270

Dynamic Stiffness Method and CUF-based Component-Wise Theories Applied to Free Vibration Analysis of Composite, Thin-Walled, and Viscoelastic Sandwich Structures
Xiao LIU, Alfonso PAGANI, Erasmo CARRERA, Xiang LIU 274

Design of Sandwich Panels for Lightweight Vibroacoustic Performance
Nuno R. COSTA, José F. AGUILAR MADEIRA, Aurélio ARAÚJO, Girolamo DI CARA, Michele D'OTTAVIO, Olivier POLIT 280

Dynamic Stiffness Method for Free Vibration of Beams and Frameworks with Cutouts
J. Ranjan BANERJEE, David KENNEDY 284

Shell Finite Elements with Arbitrary Fields Along the Thickness by using RMVT
Erasmo CARRERA, Daniele SCANO 290

Dynamic Analysis of Bolted Rotor Systems using CUF-Based Beam Models and Interface Friction Modelling
Rodolfo AZZARA, Yulian JIANG, Matteo FILIPPI, Chaofeng LI, Erasmo CARRERA 294

Numerical Modeling of a Bistable Composite Piezoelectric Energy Harvester with Four-Corner Simply Supported Boundary Conditions
Danish BASHIR, P.M. ANILKUMAR, S. SCHEFFLER, A. HALDAR, B.N. RAO, R. ROLFES 298

Damage Localization Beyond Modal Curvature Methods
Giada FARACO, Andrea Vincenzo DE NUNZIO, Nicola Ivan GIANNOCCARO, Arcangelo MESSINA 302

Beam Finite Elements with Arbitrary Shape Functions
Erasmo CARRERA, Daniele SCANO 307

Economical and Global Warming Potential Evaluation of Thermoplastic Pultruded Materials
Léo SUDRIÈS, Joël SERRA, Wiyao AZOTI, Bruno CASTANIÉ 311

Interfacial Management via Dynamic Pore-Formation for High-Energy-Density Grid-Scale Aqueous Zn–MnO_2 Storage
J.V. Alamelu, K.R.V. Subramanian, Sharath Ramesh, Gaurav Manoj Bhangale, K.S. Vignesh, Mohamed Tanveer M. 315

Keyword Index

Preface

This volume brings together contributions from the Fifth International Conference on Mechanics of Advanced Materials and Structures (ICMAMS 5), held in Toulouse, France, from 1 to 3 July 2026. Organised by the Institut Clément Ader and hosted at INSA Toulouse, the conference provided a meeting place for researchers working on the mechanical behaviour, modelling and design of advanced materials and structures. The proceedings extend these exchanges beyond the meeting, making the work presented available to the wider mechanics community.

ICMAMS is the conference of the journal Mechanics of Advanced Materials and Structures (MAMS), published by Taylor & Francis. Under the chairmanship of Professor Erasmo Carrera, the series has developed alongside the journal as a forum for discussion across theoretical, computational and experimental mechanics. Its history began in Torino, Italy, in June 2018, followed by Nanjing, China, in October 2019; College Station, Texas, USA, in August 2023; and Bangalore, India, in December 2024. The fifth edition brought the conference to France, continuing a sequence of meetings that has connected research communities across Europe, Asia and North America.

The Toulouse edition benefited from the involvement of Professor Carrera, Editor-in-Chief of MAMS, Professor Bruno Castanié of the Institut Clément Ader, and Professor J. N. Reddy, the journal's founding Editor-in-Chief. Their participation embodied the connection between the conference, its host institution and the journal. The international Scientific Committee and the Organising Committee supported the meeting, with the local team providing the practical coordination and hospitality on which a successful conference depends.



Figure 1. Erasmo Carrera, Bruno Castanié and J. N. Reddy at ICMAMS 5.

The Institut Clément Ader's research in structural mechanics and composite materials provided a fitting setting. Toulouse's close relationship with aeronautical engineering also gave particular relevance to discussions connecting material behaviour and structural analysis with manufacturing and engineering practice.

The three-day scientific programme combined nine plenary lectures with 109 scheduled contributions in parallel sessions. Five parallel rooms accommodated 25 session blocks, chaired by 18 different researchers, and seven special-session themes provided a focus for coordinated discussions. The plenary speakers were J. N. Reddy, Laurent Risse, Christian Hellmich, Carlos G. Dávila, Weiqiu Chen, Davide Bigoni, Kun Zhou, Rostand Moutou Pitti and Christophe Bouvet. Their lectures ranged from composite mechanics and aircraft structures to fatigue,

contact mechanics, structural instability, additive manufacturing, geomaterials and wood-based materials.

The special sessions brought together work on virtual testing and digital manufacturing, numerical and analytical methods for composites and multiphysics, topology and anisotropy optimisation, reinforced panels and architected metastructures, lightweight sandwich structures, natural wood materials, and the interface between biomechanics and geomechanics. Alongside these themes, the wider programme addressed damage and fracture, structural dynamics, smart materials, monitoring and data-driven modelling. This breadth offered opportunities to compare methods developed in different areas and to consider how advances in modelling could be supported by experiments and applied to structural design.

A special occasion during the conference was the presentation of the J. N. Reddy Medals for 2025 and 2026. Established by MAMS in 2018, the medal honours Professor Reddy's contributions to mechanics as a researcher, educator and author. Its inaugural presentation took place at the first ICMAMS in Torino. The award remains a close link between the conference community and the scientific and educational tradition represented by the journal.

The 2025 medal recognised Professor Davide Bigoni of the University of Trento for his contributions to instabilities, metamaterials, plasticity, porous media, soil mechanics and fracture. The 2026 medal recognised Professor Kun Zhou of Nanyang Technological University, Singapore, for his work on contact in heterogeneous materials and on the relationship between mechanics and additive manufacturing. Honouring both recipients in Toulouse brought two distinct and influential directions of research into the shared setting of the conference.



Figure 2. J. N. Reddy Medal presentations to Davide Bigoni (2025, left) and Kun Zhou (2026, right), with Erasmo Carrera and J. N. Reddy.

Before the gala dinner, participants gathered for an outdoor aperitif beneath the Concorde at the Aeroscopia aerospace museum in Blagnac. The aircraft provided a striking setting for informal conversation, while the museum's collection, including the Airbus Beluga, offered a close encounter with the aeronautical heritage of Toulouse. The dinner that followed brought colleagues together in this distinctive museum setting, creating a memorable occasion to celebrate the conference and the engineering achievements surrounding them.

The social programme extended the discussions beyond the lecture rooms. An Airbus visit and the gathering at the Aeroscopia aerospace museum connected the meeting with the engineering heritage of Toulouse. The museum visit, aperitif and gala dinner offered time for colleagues to

meet informally, renew existing collaborations and begin new conversations. The medal ceremony formed part of this shared evening, placing the recognition of scientific achievement within the wider life of the conference community.



Figure 3. Participants enjoying the pre-dinner aperitif beneath the Concorde at Aeroscopia (left). The Airbus Beluga at Aeroscopia, the museum that hosted the gala evening (right)

We are grateful to all authors and speakers for sharing their research, and to the participants whose questions and discussions gave the meeting its substance. We thank the Scientific Committee, the special-session organisers and the session chairs for their contribution to the scientific programme. Particular thanks are due to Bruno Castanié and the local Organising Committee at the Institut Clément Ader, to INSA Toulouse for hosting the conference, and to the staff and students who supported its daily activities. We also gratefully acknowledge the support of the MAMS community and the conference partners.



Figure 4. Participants gathered at INSA Toulouse during ICMAMS 5.

The purpose of these proceedings is to preserve and share the research associated with the Toulouse meeting. We hope that readers will find results and methods relevant to their own work, as well as questions that invite further investigation. Above all, we hope that this volume will sustain the exchanges begun at ICMAMS 5 and contribute to the continuing development of the mechanics of advanced materials and structures.

The Editors

Riccardo Augello and Giovanna Carrera

Committees

Honorary Chair

J. N. Reddy — Texas A&M University, USA

Conference Chairs

Erasmo Carrera — Politecnico di Torino, Italy
Bruno Castanié — Institut Clément Ader, France

Organizing Committee

Erasmo Carrera, EiC MAMS, Professor at Politecnico di Torino
Bruno Castanié, Professor at Clément Ader Institute
Philippe Olivier, Professor at Clément Ader Institute
Christophe Bouvet, Professor at Clément Ader Institute
Steven Marguet, Professor at Clément Ader Institute
Philippe Margueres, Assistant Professor at Clément Ader Institute
Pablo Navarro, Assistant Professor at Clément Ader Institute
Wiyao Azoti, Assistant Professor at Clément Ader Institute
Laurent Crouzeix, Assistant Professor at Clément Ader Institute
Anthony Viste, PhD student at Clément Ader Institute
Léo Sudriès, University of KwaZulu-Natal, PhD student at Clément Ader Institute
Romain Rutar, PhD student at Clément Ader Institute
Dieudonné Iraguha, PhD student at Clément Ader Institute
Jean-Emmanuel Chambe, Post-doc at Clément Ader Institute
Atef Sawalmeh, PhD student at Clément Ader Institute
Sara Marie Delcourte, Erasmus Mundus FRP++ Student
Youssef Ait Lamine, Erasmus Mundus FRP++ Student
Jawad Naciri, PhD student at Clément Ader Institute
Eloise Gavard, PhD student at Clément Ader Institute
Riccardo Houngbegnon, PhD student at Clément Ader Institute
Eduard Marenic, Assistant Professor at Clément Ader Institute
Valérie Monnerie, Secretary at Clément Ader Institute
Giovanna Carrera, Managing Editor MAMS
Riccardo Augello, Assistant Professor at Politecnico di Torino

Scientific Committee

Weiqiu Chen, Ph.D. – Zhejiang University, China
Maenghyo Cho – Seoul National University, Korea
Arun R. Srinivasa – West Texas A&M University, USA
Vinu U. Unnikrishnan, Ph.D. – West Texas A&M University, USA
Xiangyang Xu – Soochow University, Suzhou, China
Sarp Adali, University of KwaZulu-Natal, Durban, South Africa
Adegbola Akinola, Obafemi Awolowo University, Ile-Ife, Nigeria

Olivier Allix, Ecole Normale Supérieure de Cachan, France
Marco Amabili, McGill University, Montreal, Canada
Aurélio Lima Araújo, Tecnico Lisboa, Portugal
Ferdinando Auricchio, University of Pavia, Italy
Sara Bagassi, Università di Bologna, Italy
Ever J Barbero, West Virginia University, USA
Ayech Benjeddou, Supmeca, Saint Ouen, France
Davide Bigoni, University of Trento, Italy
Chiara Bisagni, Politecnico di Milano, Italy
Bruno Castanié, INSA, Toulouse, France
Francisco Chinesta, Ecole Centrale de Nantes, France
Carlos Alberto Cimini, DEES-UFMG, Belo Horizonte, Brazil
El Mostafa Daya, University of Lorraine, France
Mohsen Botshekanan Dehkordi, Shahr-e-kord University, Iran
Faramarz Djavanroodi, Prince Mohammad Bin Fahd University, the Kingdom of Saudi Arabia
Michele D'Ottavio, Université Paris Nanterre, France
Prof. Xin Fang, National University of Defense Technology, China
Fiorenzo Fazzolari, University of Liverpool, UK
Xi-Qiao Feng, Tsinghua University, Beijing, China
Matteo Filippi, Politecnico di Torino, Italy
Cun-Fa Gao, Nanjing University, China
Gaetano Giunta, LIST, Luxembourg
Yuantong Gu, Queensland University of Technology, Australia
Michele Guida, Università Federico II, Naples, Italy
Christian Hellmich, TU Wien, Austria
Heng Hu, Wuhan University, China
Dr. Ibrahim Kaleel, NASA Glenn, USA
Liao-Liang Ke, Beijing Jiaotong University, China
Jun-Sik Kim, Kumoh National Institute of Technology, Korea
Gennady Kulikov, Tambov State University, Russia
R. Krishna Kumar, Indian Institute of Technology Madras, India
Bo Li, Tsinghua University, Beijing, China
Prof. Xiangyu Li, Southwest Jiaotong University, China
C.W. Lim, City University of Hong Kong, Hong Kong
Chaofeng Lü, Zhejiang University, China
Raimondo Luciano, Università di Cassino, Italy
Erdogan Madenci, The University of Arizona, Tucson, USA
Josè Luis Mantari Laureano, UTEC, Lima, Perù
Marianna Maiuarù, University of Massachusetts, Lowell, USA
Jose Daniel Diniz Melo, Federal University of Rio Grande do Norte, Brazil
Arcangelo Messina, University of Salento, Italy
Alberto Milazzo, University of Palermo, Italy
Antonio Miravete, University of Zaragoza, Spain
Filipa Moleiro, Instituto Superior Tecnico, Portugal
Marco Montemurro, ENSAM, Bordeaux, France
Carlos A. Mota Soares, Tecnico Lisboa, Portugal
Manish Nagaraj, University of Massachusetts Lowell, USA

Yoshi Narita, Hokkaido University, Japan
Dr. Ana M.A. Neves, Universidade do Porto, Portugal
Alfonso Pagani, Politecnico di Torino, Italy
Marco Paggi, IMT, Institute for Advanced Studies, Lucca, Italy
Glaucio Paulino, Georgia Institute of Technology, USA
Marco Petrolo, Politecnico di Torino, Italy
Evan J. Pineda, NASA Glenn Research Center, Cleveland, USA
Olivier Polit, Université Paris Nanterre, France
M. Ramulu, University of Washington, Seattle, USA
Prof. Xin Ren, Nanjing Tech University, China
Sebastien Roth, Université de Technologie Belfort-Montbéliard, France
Samit Roy, University of Alabama, USA
Elio Sacco, Università Federico II, Naples, Italy
Fabrizio Scarpa, University of Bristol, UK
Huishen Shen, Shanghai Jiao Tong University, China
Marina V Shitikova, Voronezh State Technical University, Voronezh, Russia
K. P. Soldatos, The University of Nottingham, UK
Dr. Yipin Su, Politecnico di Milano, Italy
Karan Surana, University of Kansas, USA
Liqun Tang, South China University of Technology, China
Prakash Thamburaja, UKM, Malaysia
Uday Vaidya, University of Tennessee, USA
Janis Varna, Lulea University of Technology, Sweden
Philippe Vidal, Université Paris Nanterre, France
Tony Waas, University of Washington, Seattle, USA
Thomas Wallmersperger, University of Dresden, Germany
Wolfgang A. Wall, Technical University of Munich, Germany
Ji Wang, Ningbo University, China
George J. Weng, Rutgers University, USA
Bin Wu, National University of Ireland, Galway, Ireland
Jie Yang, RMIT, Australia
Wenbin Yu, Purdue University, West Lafayette, USA
Gun Jin Yun, Seoul National University, Korea
Enrico Zappino, Politecnico di Torino, Italy
Ashraf Zenkour, King Abdulaziz University, Jeddah, Saudi Arabia
Prof. Weijian Zhou, Harbin Institute of Technology Shenzhen, China
Kun Zhou, Nanyang Technological University, Singapore

Materials Research Proceedings 73 (2026) 1-6 https://doi.org/10.21741/9781644904459-1

Effect of Tool-Temperature Compensation on the Mechanical Behavior of AFP-Manufactured CF/LM-PAEK Laminates

Dieudonné IRAGUHA[1,a], Wiyao AZOTI[1,b*], Bruno CASTANIE[1,c], Philippe OLIVIER[1,d]

[1]Institut Clément Ader (ICA), Université de Toulouse, CNRS UMR 5312, INSA, ISAE-Supaéro, IMT Mines Albi, 3 Rue Caroline Aigle 31400 Toulouse, France

[a]iraguha@insa-toulouse.fr, [b]azoti@insa-toulouse.fr, [c]castanie@insa-toulouse.fr, [d]philippe.olivier@iut-tlse3.fr

Keywords: Laser-assisted Automated Fibre Placement, Thermoplastic Composites, In-situ Consolidation, Interlaminar Shear Strength, Digital Image Correlation

Abstract. This study investigates tool-temperature compensation (TTC) technique, a strategy aimed at optimizing the use of heated tooling during in-situ consolidation of thermoplastics in automated fibre placement (ICT-AFP). Rather than maintaining the tool at a fixed temperature to promote crystallization and reduce residual stresses, in TTC the tool temperature is dynamically increased during deposition to improve through-thickness crystallinity uniformity. Although this strategy has been shown to reduce warpage and void content, its influence on mechanical performance has not yet been established, which constitutes the main objective of this paper. The performance of laminates manufactured via TTC is assessed through interlaminar behaviour, as determined by short-beam shear (SBS) tests, and through correlation with crystallinity, void content, and morphology. Indeed, employing TTC through varying the tool temperature between 150-200°C resulted in laminate layers of homogenous crystallinity with 18% crystallinity difference, compared with 41.4% for laminates manufactured using a fixed tool temperature of 150°C. This homogeneous crystallinity was also reflected in the mechanical response, as TTC specimens exhibited 20.72% higher shear modulus than their counterparts manufactured using a fixed tool temperature.

1. Introduction

In aircraft industry, although high-performance composites are typically manufactured through hand-layup techniques with subsequent autoclave processing, these methods remain highly-labour intensive and time-consuming. Given Airbus's forecast of a 4.3% annual increase in air-transport demand from 2019 to 2038 [1], a corresponding large-scale increase in the need for advanced composite materials is expected. Such high demand necessitates employing processing methods that are faster, repeatable, and capable of producing large monolithic parts in order to reduce weight [2]. To meet these technological needs, automated fibre placement (AFP) has emerged as an attractive manufacturing route, particularly for thermoplastic prepregs, as it offers high productivity, greater architectural flexibility, and rapid consolidation during deposition, thereby enabling the so-called in-situ consolidation of thermoplastics by AFP (ICT-AFP) [2]. Combined with the sustainability advantages of thermoplastics [3], including recyclability and repairability, as well as the potential to eliminate secondary post-consolidation steps such as autoclave processing, ICT-AFP is a highly attractive manufacturing concept. Nevertheless, achieving laminates with good mechanical properties comparable to those obtained by benchmark consolidation routes (e.g., hot pressing) remains challenging, which continues to limit widespread industrial acceptance. The consolidation time scales involved in ICT-AFP provide a first indication of the underlying difficulty: in comparison to other established thermoplastic consolidation processes, in-situ consolidation AFP occurs for a very short duration [4]. In addition, the high

Content from this work may be used under the terms of the Creative Commons Attribution 3.0 license. Any further distribution of this work must maintain attribution to the author(s) and the title of the work, journal citation and DOI. Published under license by Materials Research Forum LLC.

Materials Research Proceedings 73 (2026) 1-6 https://doi.org/10.21741/9781644904459-1

processing temperatures associated with thermoplastics promote the development of thermal residual stresses, which can drive warpage and contribute to defect formation during cooling [5].

Among thermoplastic matrices, although AFP with PEEK has been the mostly studied, its inherent high melt viscosity limits the deposition rates, resulting in a small processing window [6]. This limitation has recently been addressed through the introduction of low-melt polyaryletherketone (LM-PAEK) thermoplastic, which exhibits lower viscosity and can therefore improve intimate contact and bonding kinetics during deposition [6]. Nevertheless, issues of high void content, warpage deformation, and poor consolidation persist in AFP-manufactured CF-LMPAEK laminates [7]. Such drawbacks have spurred numerous studies coupling ICT-AFP along with a second step of post-processing or low-temperature annealing methods to improve crystallinity and interlaminar bonding [8]. Heated tooling tuned to cold or hot crystalline temperatures is the simplest in-process annealing method commonly used in AFP. The study by Mössinger et al., [8] focusing on the effect of heated tooling, attributed it to 69.5% of warpage reduction in comparison to unheated tooling performance. However, using a hot tool is not without flaws. Despite using a heated tool, the warpage found was still significantly larger than that obtained with a hot-press. Wang et al. [9] conducted an investigation aimed at reducing the significant warpage deformations in AFP on heated tool. It also pointed out that the tool temperature (T_{tool}) benefits mostly tool-side layers, which shield the temperature to reach to top layers. This resulted in top layers exhibiting relatively low crystallinity, which in turn led to high crystallinity difference in the laminate, hence large warpage deformations. Ultimately, a novel tool temperature compensation isothermal consolidation technology (TTC-IC) was proposed and successfully established as way to dynamically increase T_{tool} throughout deposition to achieve high crystallinity, low warpage, and low voids.

However, the effect of TTC-IC on mechanical performance has not yet been established. Besides, to this date obtaining optimum part quality with ICT-AFP alone remains challenging and highly depends on process parameters. This necessitates examining and understanding influence of every new parameters in order to accelerate progress toward laminates with improved consolidation quality. In addition, although the original tool-temperature adjustment [9] was based on exact measured thermocouple data, this approach may restrict the rapid adoption of the technique in practical AFP manufacturing. Since TTC-IC is based on the clear physical concept of compensating the non-uniform thermal distribution through the laminate thickness, a simplified implementation may still provide significant benefits. Hence such implementation is proposed and examined in the present study alongside through-thickness thermal characterization, surface void measurement, and mechanical testing through SBS tests.

2. Experimentation

Laminates were manufactured using an in-house Coriolis AFP machine “Pico” from CF/LM-PAEK prepreg tapes supplied by Victrex, with nominal dimensions of 6.35 mm × 0.192 mm. Three 150 mm × 150 mm panels were produced: ICT-TT20°C, ICT-TT150°C, and ICT-TTC150_200°C, corresponding respectively to a cold-tool condition, a fixed heated-tool condition at 150 °C, and a tool-temperature-compensated condition between 150 and 200 °C. The selected TTC range was chosen to replicate the conditions investigated in a previous study [9], while being implemented here through a simplified approach in which the 50 °C tool temperature difference was evenly distributed across the laminate thickness, as shown in Fig. 2.2(a). The tool-temperature ramps between ply groups were defined based on the thermocouple-measured heating rate of the tool, approximately 8°C/min. Each panel consisted of 16 plies with a quasi-isotropic $[45°/90°/-45°/0°]_{2s}$ stacking sequence. The ICT-AFP process parameters were kept constant, with a layup speed of 50 mm/s, a nip-point temperature of 350°C, and a consolidation force of 50 N.

Materials Research Proceedings 73 (2026) 1-6 https://doi.org/10.21741/9781644904459-1

2.1 Differential Scanning Calorimetry (DSC) and Void Content

The degree of crystallinity (DOC) was determined using a DSC 250 from TA instruments. Specimens weighing between 12-15 mg were systematically extracted from each panel at the bottom, middle, and top layers for the through-thickness thermal characterization. A temperature cycle of 10ºC/min from the ambient temperature till 380ºC, followed by a 5min isothermal dwell was used. Based on the fibre mass fraction of w_f=66% and a crystallization enthalpy of H_{ref}=130J/g, the degree of crystallinity of specimens was computed and reported in Fig. 2.1. Results indicate glass transition at 150ºC, notably pronounced for ICT-TT20ºC samples. The cold crystallization and endothermal melting peaks are found to be around 182-187ºC and 305-310ºC, respectively. It is noteworthy that long-term exposure to heated tooling across the three manufacturing conditions led to a drastic reduction in the cold-crystallization exotherm, indicating that heated tooling promoted crystallization of initially amorphous regions after ICT-AFP. This was reflected in DOC values that were 131% higher in ICT-TT150°C layers than in ICT-TT20°C layers. However, in the ICT-TT150°C panel, the top layers, being less influenced by the heated tool, exhibited the lowest DOC, resulting in a laminate crystallinity difference of 41.4%. In contrast, the ICT-TTC150_200°C panel showed a much more uniform crystallinity profile, with a difference of 18%. This improved through-thickness homogeneity suggests more consistent bonding conditions across the laminate and highlights the potential of TTC for enhancing thermal uniformity during ICT-AFP.

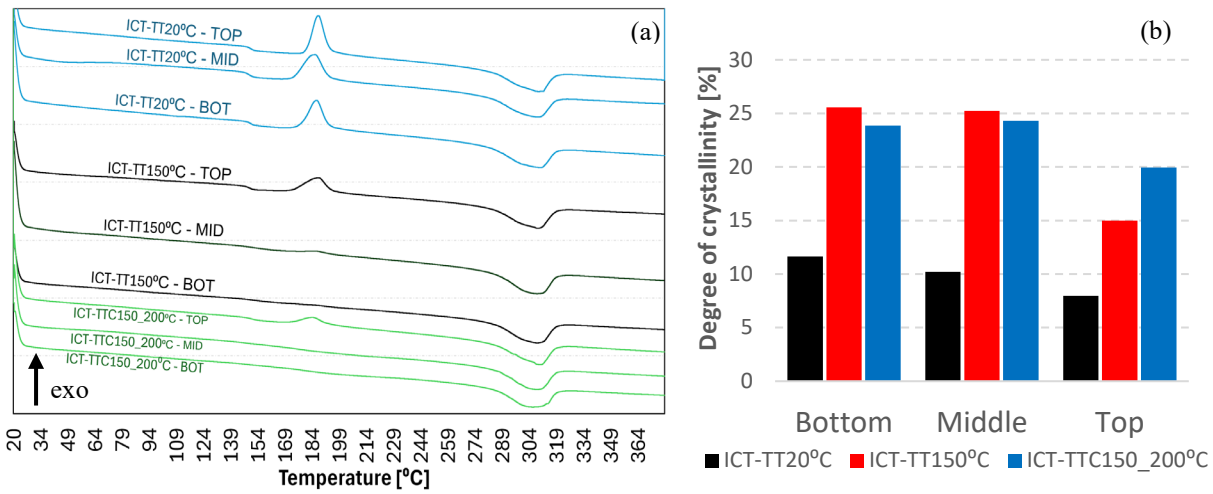

Figure 2.1: *(a) DSC measurements of ICT-TT20ºC, ICT-TT150ºC, and ICT-TTC150_200ºC specimens (b) Through-thickness crystallinity distribution of all three configurations*

To calculate the void content, 2 specimens of 20 mm x 20 mm dimension were waterjet-cut from each panel and polished for optical observation under Keyence VHX700 digital microscope. The sample images were further analysed using Image J software by setting them to an 8-bit greyscale. ICT-TT20ºC, ICT-TT150ºC, ICT-TTC150_200ºC samples respectively resulted in porosity of 3.82%, 1.98%, and 0.99%, further highlighting TTC benefits to void suppression.

2.2 Mechanical Testing

SBS tests were performed in accordance with EN 2563 using a three-point bending configuration to evaluate the apparent interlaminar shear strength. Specimens measuring 30 mm × 15 mm were tested after applying a black-on-white speckle pattern to enable digital image correlation (DIC) monitoring of strain localization, crack initiation, and crack growth. The measured SBS strengths and DIC-identified crack initiation points are reported in Fig. 2.2(c) and Fig. 2.3(a). Since crack initiation criteria are essential inputs for cohesive-zone modelling in finite element simulations

Materials Research Proceedings 73 (2026) 1-6 https://doi.org/10.21741/9781644904459-1

[10], crack onset was evaluated using an elbow-point method based on the shear-strain-rate evolution obtained from DIC measurements. As shown in Fig. 2.3, fibre placement on a heated tool turned out to be beneficial as ICT-TT150°C specimens reached an average ultimate SBS strength of 28 MPa, representing a 24% increase relative to ICT-TT20°C specimens. This improvement was even more pronounced at crack initiation strengths, with a 32.17% increase, highlighting the role of heated tooling in delaying crack formation.

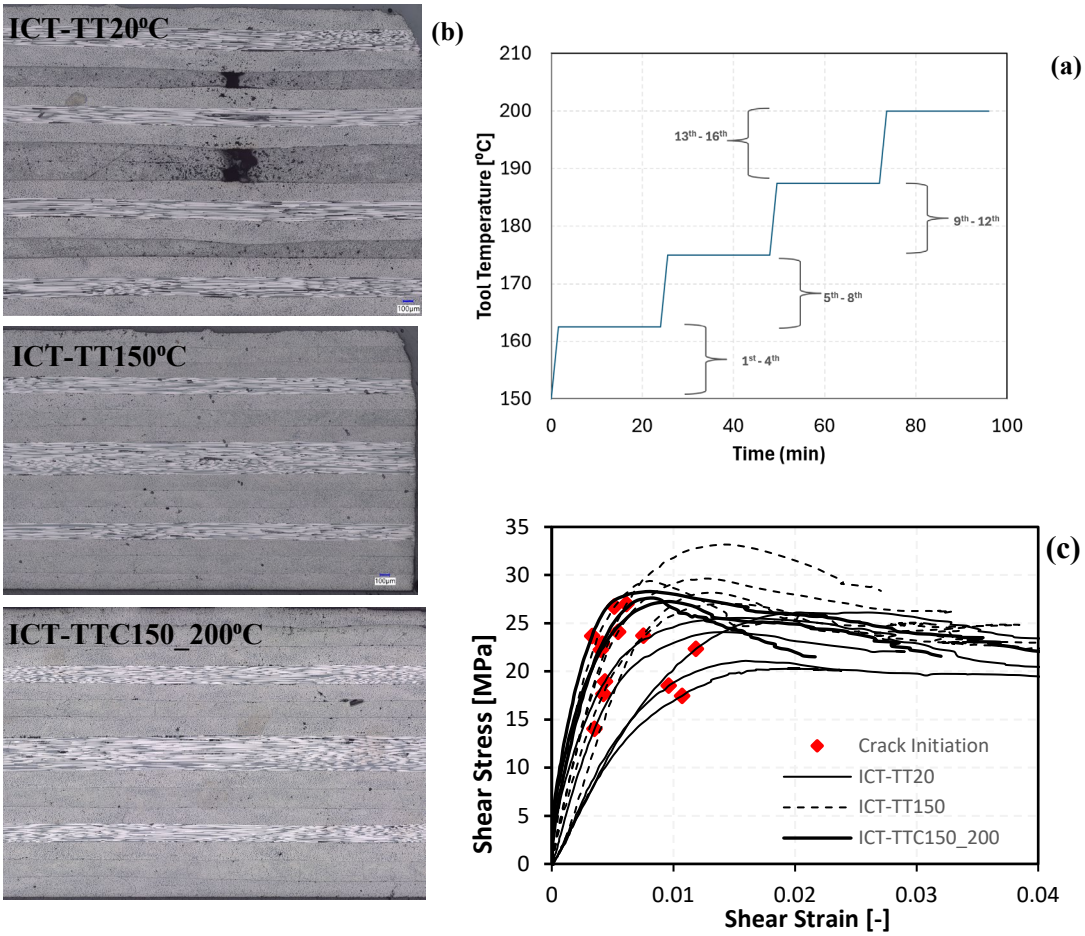

Figure 2.2: *(a) T_{tool} adjustment used in production of ICT-TTC150_200°C panel, (b) Greyscale porosity analysis results: scale of 100µm, (c) Shear stress-strain curves of SBS specimens*

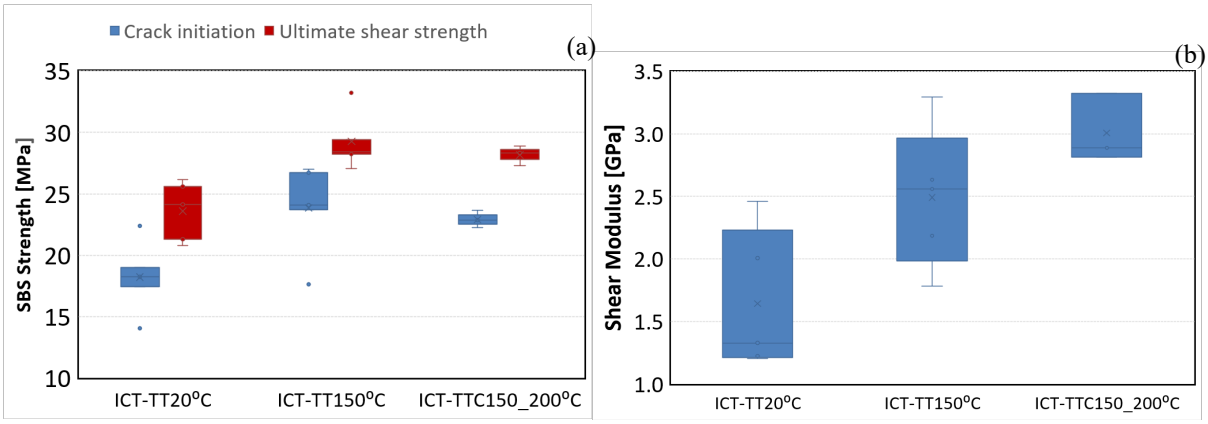

Figure 2.3: *(a) Interlaminar shear strength results (b) Shear modulus achieved in SBS specimens*

Although Fig. 2.3(a) indicates that TTC did not produce a significant improvement in ultimate interlaminar shear strength, which is expected given the limited 50°C tool-temperature increase, the chord shear modulus calculated up to 4000μ strain, shown in Fig. 2.3(b), reveals a different trend. With a compensated T_{tool} ICT-TTC150_200°C specimens exhibited an apparent shear modulus of 3 GPa, representing a 20.72% increase compared with specimens manufactured at a fixed T_{tool} of 150°C. This increase is consistent with the more homogeneous through-thickness crystallinity measured for the TTC panel, suggesting that improved crystallinity uniformity contributes to enhanced apparent interlaminar stiffness.

Conclusion

This study assessed the effect of a simplified tool-temperature compensation strategy on the through-thickness crystallinity and interlaminar response of ICT-AFP performed on CF/LM-PAEK laminates. Compared with fixed-temperature heated tooling, TTC substantially improved crystallinity uniformity, reducing the through-thickness crystallinity difference from 41.4% to 18%. Although this improved thermal homogeneity did not lead to a significant increase in ultimate short-beam shear strength over the fixed T_{tool} 150°C condition, it resulted in a 20.72% increase in apparent shear modulus, indicating enhanced interlaminar stiffness. These findings suggest that TTC is a promising and practical in-process strategy for improving laminate homogeneity and stiffness in ICT-AFP.

References

[1] ‘Airbus SAS. "Global Market Forecast 2019-2038

[2] B. Castanie *et al.*, ‘Review of monolithic composite laminate and stiffened structures in aeronautic applications’, *Compos. Part C Open Access*, vol. 17, p. 100585, Jul. 2025. https://doi.org/10.1016/j.jcomc.2025.100585

[3] M. Arowolo, W. Azoti, and B. Castanié, ‘Comparative study of the thermomechanical properties of natural fiber reinforced thermoplastic composites: A structural application for quadcopter design’, *Mech. Adv. Mater. Struct.*, vol. 32, no. 7, pp. 1425–1446, Apr. 2025. https://doi.org/10.1080/15376494.2024.2364067

[4] M. J. Donough, Shafaq, N. A. St John, A. W. Philips, and B. Gangadhara Prusty, ‘Process modelling of In-situ consolidated thermoplastic composite by automated fibre placement – A review’, *Compos. Part Appl. Sci. Manuf.*, vol. 163, p. 107179, Dec. 2022. https://doi.org/10.1016/j.compositesa.2022.107179

[5] S. Van Hoa, M. Duc Hoang, and J. Simpson, ‘Manufacturing procedure to make flat thermoplastic composite laminates by automated fibre placement and their mechanical properties’, *J. Thermoplast. Compos. Mater.*, vol. 30, no. 12, pp. 1693–1712, Dec. 2017. https://doi.org/10.1177/0892705716662516

[6] L. Raps, A. R. Chadwick, I. Schiel, and I. Schmidt, ‘CF/LM-PAEK: Characterisation and sensitivity to critical process parameters for automated fibre placement’, *Compos. Struct.*, vol. 284, p. 115087, Mar. 2022. https://doi.org/10.1016/j.compstruct.2021.115087

[7] T. Yap *et al.*, ‘In-plane properties of an in-situ consolidated automated fiber placement thermoplastic composite’, *Compos. Part Appl. Sci. Manuf.*, vol. 188, p. 108525, Jan. 2025. https://doi.org/10.1016/j.compositesa.2024.108525

[8] I. Mössinger, L. Raps, D. Fricke, J. Freund, M. Löbbecke, and A. R. Chadwick, ‘Characteristics of in-situ automated fiber placement carbon-fiber-reinforced low-melt polyaryl ether ketone laminates part 1: Manufacturing influences’, *J. Compos. Mater.*, vol. 58, no. 15, pp. 1769–1787, Jun. 2024. https://doi.org/10.1177/00219983241244882

[9] Y. Wang *et al.*, 'Through-thickness crystallinity gradient controls warpage reduction in CF/PAEK via in-situ consolidation automated fiber placement', *Compos. Part Appl. Sci. Manuf.*, vol. 200, p. 109310, Jan. 2026. https://doi.org/10.1016/j.compositesa.2025.109310

[10] L. Raps, A. R. Chadwick, I. Mössinger, M. Vinot, T. Behling, and Y. Schaefer, 'Characteristics of in-situ automated fiber placement carbon-fiber-reinforced low-melt polyaryl ether ketone laminates part 2: Effect of prepreg composition', *J. Compos. Mater.*, vol. 58, no. 13, pp. 1523–1535, Jun. 2024. https://doi.org/10.1177/00219983241240585

Materials Research Proceedings 73 (2026) 7-12 https://doi.org/10.21741/9781644904459-2

Component-Wise Free Vibration Analysis of Sandwich Metamaterials by Carrera Unified Formulation

Erasmo Carrera[1,a], Riccardo Augello[1,b*], Ningning Liu[1,c]

[1]mul2 lab, Politecnico di Torino, Italy

[a]erasmo.carrera@polito.it, [b]riccardo.augello@polito.it, [c]ningning.liu@polito.it

Keywords: Carrera Unified Formulation, Component-Wise Modelling, Metamaterials, Free Vibration, Sandwich Structures

Abstract. This work presents a free vibration analysis of honeycomb sandwich metamaterial structures with complex cellular cores using the Carrera Unified Formulation (CUF). Three distinct unit cell geometries are investigated within a component-wise (CW) modelling framework. The CUF-based one-dimensional beam approach enables accurate cross-sectional discretization via high-order Lagrange polynomials, offering an efficient balance between computational cost and geometric fidelity for diverse topologies. Convergence studies regarding axial and cross-sectional mesh refinements are conducted, highlighting the error reduction trends across different core configurations. Results show that the proposed methodology achieves rapid convergence and captures the essential vibrational characteristics of metamaterial panels, validating it as a flexible and robust platform for the hierarchical modelling of architected materials.

Introduction

Lattice-based metamaterials are engineered architectures whose macroscopic behaviour is dictated by geometry rather than chemistry. Built from periodically replicated unit cells (UCs), these structures can achieve targeted properties—from auxetic systems with negative Poisson's ratio[1-3] to pentamodes[4] and programmable or multistable shape-morphing structures[5,6]. However, geometric complexity poses severe challenges to conventional computational tools: fully 3D or shell finite element models require complete remeshing for every new topology, while classical 1D beam theories lack cross-sectional kinematic richness for cellular cores.

This study addresses this gap by employing the CUF within a CW framework. By reorienting the beam axis and discretizing the cross-section via high-order Lagrange polynomials, the same 1D beam model accommodates diverse cellular topologies with tunable fidelity, providing a computationally efficient alternative to high-fidelity 3D models.

Methodology

Carrera Unified Formulation (CUF) provides a unified framework for structural modelling using 1D, 2D, or 3D theories. By adjusting the expansion order and cross-sectional discretization, Equivalent Single Layer (ESL), Layer-Wise (LW), or Component-Wise (CW) theories are recovered within a single mathematical structure. The governing equations are automatically derived from a fundamental nucleus once the polynomial expansion functions and axial interpolation are defined, enabling 3D-like behaviour with 1D beam elements.

The Layer-Wise (LW) theory assigns independent displacement fields to each layer but requires homogenized properties at the layer level, precluding representation of actual cellular geometry.

$$\mathrm{u}(\mathrm{x},\mathrm{y},\mathrm{z}) = \mathrm{F}_\tau(\mathrm{x},\mathrm{z})\mathrm{N}_\mathrm{i}(\mathrm{y})\mathrm{u}_{\tau\mathrm{i}}, \qquad \tau = 1,2,\dots,\mathrm{M}, \quad \mathrm{i} = 1,2,\dots,\mathrm{N}_\mathrm{n} \tag{1}$$

where $F_\tau(x, z)$ denotes the expansion functions in the cross-sectional plane, $N_i(y)$ the shape functions along the beam axis, and $u_{\tau i}$ the nodal unknowns.

Content from this work may be used under the terms of the Creative Commons Attribution 3.0 license. Any further distribution of this work must maintain attribution to the author(s) and the title of the work, journal citation and DOI. Published under license by Materials Research Forum LLC.

Materials Research Proceedings 73 (2026) 7-12 https://doi.org/10.21741/9781644904459-2

Component-Wise (CW) theories achieve the highest modelling detail by treating each structural part as separate subdomains without homogenization. The sandwich panel is modelled using 1D beam elements with the beam axis oriented along the height direction (Fig. 1). Cross-sections of both skins and cellular core are discretized using high-order Lagrange polynomials. Shared Lagrange nodes at interfaces guarantee displacement and strain continuity between face sheets and core.

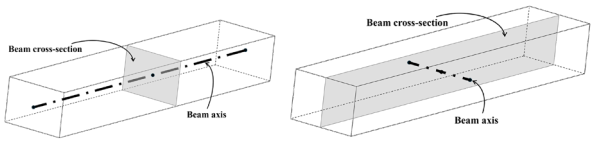

(a) (b)

Figure 1: (a) Canonical beam representation.(b) Novel CUF-based beam representation.

In the CW formulation, the displacement field is defined component-wise:

$$u^{(k)}(x,y,z) = \sum_{\tau=1}^{M^{(k)}} F_{\tau}^{(k)}(x,z) N_i(y) u_{\tau i}^{(k)}, \qquad k = skin_{top}, core, skin_{bottom} \tag{2}$$

where the superscript (k) identifies the structural component. Each component retains its own expansion order M (k) and cross-sectional discretisation, enabling heterogeneous fidelity within the same beam model: the skins may use a low-order expansion whereas the cellular core employs a dense L9 Lagrange mesh to resolve local bending and torsion of the cell walls.

The sandwich panel investigated in this study consists of top and bottom skins (each with thickness (h_1 = 1 mm) and a cellular core (h_2 = 8 mm), resulting in a total panel height of (h = 10 mm). The structure is subjected to four-side simply supported (SSSS) boundary conditions. Three distinct unit cell topologies are considered for the core layer: Geometry 1: Hexagonal core; Geometry 2: Re-entrant (auxetic) core; Geometry 3: Star-shaped core.

For all configurations, both the skins and the cellular core are made of the same aluminum alloy to ensure structural homogeneity at the material level. The material properties are defined as: density ρ=2700kg/m^3, Young's modulus E=70GPa, and Poisson's ratio ν=0.33. The specific geometric parameters for each unit cell are detailed in Table 1, while the 3D schematic and coordinate system, where the y-axis is defined as the beam element axis oriented along the panel height, are illustrated in Fig. 2.

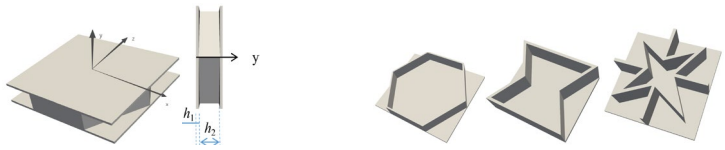

(a) (b)

Figure 2: Sandwich metamaterial geometry: (a) assembled structure and coordinate system; (b) investigated core topologies. (y-axis denotes the beam axis).

Table 1: Geometric parameters (wall thickness t = 1 mm). Units: Length [mm], Volume[mm^3]. Equivalent thickness is calculated as V /A, where A = a × b is the projected area.

		Geo 1		Geo 2		Geo 3
Geometry		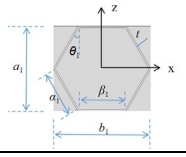		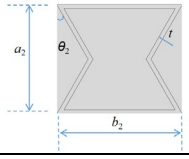		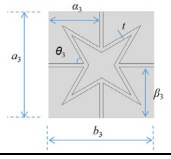
Dimensions	a_1	51.96	a_2	26	a_3	30
	b_1	60	b_2	30	b_3	30
	α_1	30	θ_2	30°	α_3	10
	β_1	30			β_3	10
	θ_1	30°			θ_3	60°
Volume (V)		7650		2470		2850
Eq.Thickness		2.454		3.167		3.167

Numerical Results

Convergence studies with respect to axial and cross-sectional refinements are conducted. The CUF-based axial FE elements achieve rapid convergence: only 5 elements in the axial direction (one per skin and three for the core) are required to achieve errors below 1.5% for the first ten modes (Fig. 3, Table 2). Alternatively, 3 elements are sometimes sufficient with errors below 6%. Table 2 summarises the relative errors for Modes 1, 5, and 10. The convergence rate is mode-dependent: higher-order modes demand finer axial resolution. Notably, the star-shaped core's torsional response is extremely sensitive to axial mesh density, with Mode 9 showing a coarse-mesh error of 5.5% that collapses to 0.3% with 5 elements.

Table 2: Relative errors of natural frequencies (values are given in %). The last column shows reference frequencies.

Mode	Axial elements					Ref.(Hz)
	3	5	10	15	20	30
			Geometry 1 (Cross-section: 461 elements)			
1	0.730	0.276	0.070	0.030	0.012	3387.63
5	1.051	0.614	0.059	0.025	0.010	7036.20
10	0.404	0.765	1.074	0.028	0.011	11640.96
			Geometry 2 (Cross-section: 200 elements)			
1	1.646	0.579	0.147	0.064	0.025	19931.90
5	1.604	0.590	0.153	0.066	0.027	31059.97
10	1.012	0.296	0.079	0.040	0.012	46740.63
			Geometry 3 (Cross-section: 526 elements)			
1	0.689	0.251	0.061	0.027	0.009	21264.27
5	0.524	0.175	0.043	0.020	0.006	38298.16
10	3.108	0.334	0.090	0.046	0.014	59662.02

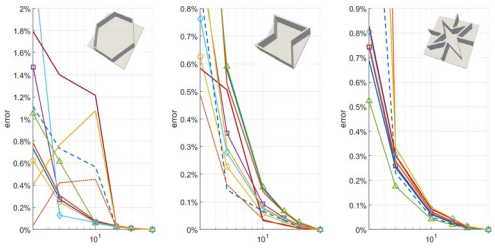

Figure 3: Convergence of the relative errors of natural frequencies with respect to the number of axial elements for the five geometric configurations.

With the number of axial elements fixed, the cross-sectional convergence is investigated by progressively refining the L9 Lagrange mesh (Table. 3). The results indicate that the hexagonal core(Fig. 4) exhibits a distinct three-stage convergence characteristic. The re-entrant core(Fig. 5) demonstrates superior robustness, with errors remaining below 13% even under coarse meshes,

thanks to the smooth displacement fields associated with its stretching-dominated mechanism. Similarly, the star-shaped core(Fig. 6) follows a relatively gradual convergence path without a sharp initial decline. Its error is primarily governed by the torsional modes; the complex star-shaped branches render the torsional response extremely sensitive to mesh density, thereby decelerating the overall convergence rate.

Table 3: Five different cross-sectional geometries with mesh refinements from A (coarsest) to F(finest).

Geometry	A (coarse)	B	C	D	E	F (fine)	Ref
	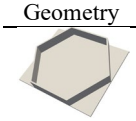	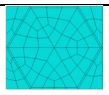	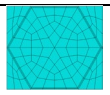	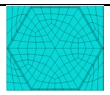	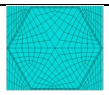	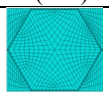	
N_{cs}	42	90	152	237	461	799	2795
DOF	9504	17616	31944	45816	84744	154188	418500
		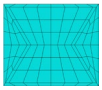	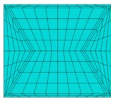	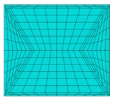	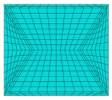	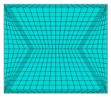	
N_{cs}	56	96	200	284	420	656	2652
DOF	14160	21504	47688	61368	82992	138240	500496
		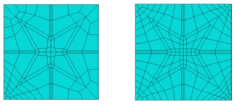	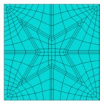	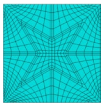	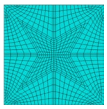		
N_{cs}	116	192	314	526	789	1192	7792
DOF	27348	38532	64188	93780	133116	205476	1098636

Note: N_{cs} denotes the number of cross-sectional elements. DOF denotes degrees of freedom.

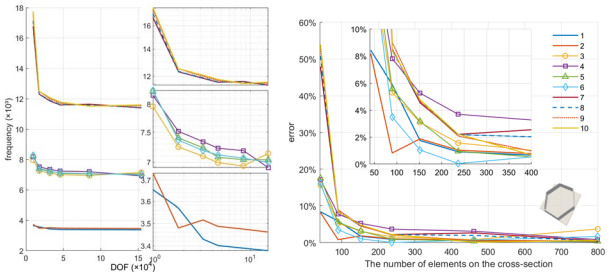

Figure 4: Convergence of natural frequencies with respect to the number of degrees of freedom (DOFs) and cross-sectional discretization for the hexagonal core.

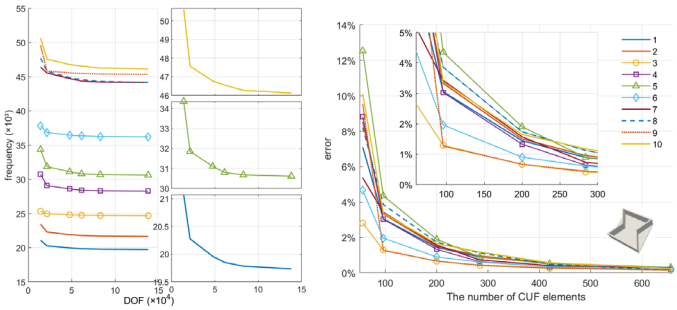

Figure 5: Convergence of natural frequencies with respect to DOFs and cross-sectional discretization for the re-entrant core.

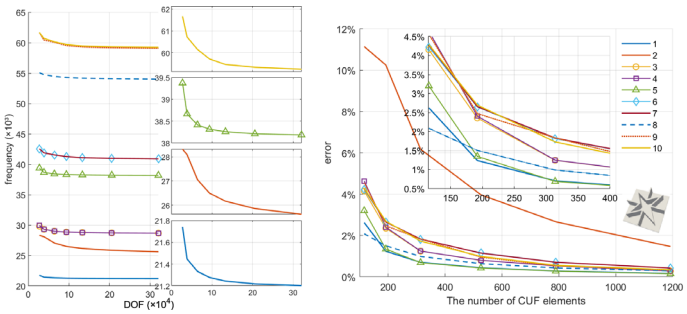

Figure 6: Convergence of natural frequencies with respect to DOFs and cross-sectional discretization for the star-shaped core.

Note: The left figure shows the variation of the first ten natural frequencies, including an overall view and detailed subplots in logarithmic scale, while the right figure presents the corresponding relative errors as functions of the number of cross-sectional elements.

Table 4: Natural frequencies (Hz) and corresponding relative errors (in %, inside parentheses)

Mode	Cross-sectional mesh refinements						Ref.(Hz)
	A	B	C	D	E	F	
				Geometry 1			
1	3654.83	3569.66	3429.68	3401.54	3390.01	3379.14	3370.71
	(8.429)	(5.902)	(1.750)	(0.915)	(0.572)	(0.250)	
5	8240.48	7404.71	7235.69	7080.52	7040.32	7040.45	7013.76
	(17.490)	(5.574)	(3.164)	(0.952)	(0.379)	(0.381)	
10	17747.22	12498.42	12079.33	11784.49	11515.94	11601.72	11528.06
	(53.948)	(8.417)	(4.782)	(2.224)	(0.105)	(0.639)	
				Geometry 2			
1	21074.82	20278.17	19961.22	19852.78	19784.51	19736.16	19677.25
	(7.102)	(3.054)	(1.443)	(0.892)	(0.545)	(0.299)	
5	34355.75	31855.18	31107.35	30800.06	30683.53	30619.14	30526.86
	(12.543)	(4.351)	(1.902)	(0.895)	(0.513)	(0.302)	
10	50670.81	47570.88	46777.69	46560.93	46280.78	46134.73	46018.20
	(10.110)	(3.374)	(1.650)	(1.179)	(0.571)	(0.253)	
				Geometry 3			
1	21740.44	21446.81	21333.24	21277.30	21244.06	21203.60	21184.27
	(2.625)	(1.239)	(0.703)	(0.439)	(0.282)	(0.162)	
5	39373.27	38665.13	38414.12	38314.44	38258.37	38209.37	38151.38
	(3.203)	(1.347)	(0.689)	(0.427)	(0.280)	(0.152)	
10	61666.59	60724.78	60151.93	59715.65	59461.09	59246.05	59129.97
	(4.290)	(2.697)	(1.728)	(0.991)	(0.560)	(0.347)	

for Modes 1, 5, and 10.

Conclusions

This study investigated the free vibration of sandwich metamaterials with three distinct cellular cores using the Carrera Unified Formulation(CUF). The Component-Wise(CW) approach effectively bridges the gap between efficiency and geometric fidelity. The main findings are:

1. The CW-CUF framework successfully models complex ligaments as 1D beam elements with arbitrary cross-sectional refinement, providing a highly flexible platform for architected materials without the cost of 3D solid meshes.
2. Only 5 axial elements are required to reduce the relative errors of the first ten natural frequencies to below 1.5%. In the cross-sectional direction, the convergence behavior exhibits significant topological dependence: the hexagonal core displays a distinct three-stage convergence characteristic, while the convergence rate of the star-shaped core tends to be gradual, governed by the high sensitivity of torsional modes to mesh density. Once the lattice features are adequately resolved, the cross-sectional errors remain within 2%, demonstrating the robustness of the proposed methodology for the structural design of such metamaterials.
3. The vibrational response is highly geometry-dependent. Re-entrant and star-shaped cores exhibit significantly higher fundamental frequencies compared to hexagonal cores, highlighting the potential for targeted frequency tuning through topology.

Future work will extend this framework to include non-linear geometric effects and multi-physics coupling for active metamaterial systems.

References

[1] Katia Bertoldi, Pedro M Reis, Stephen Willshaw, and Tom Mullin. Negative poisson's ratio behavior induced by an elastic instability. Advanced materials, pages 361-366, 2010. https://doi.org/10.1002/adma.200901956

[2] Trishan AM Hewage, Kim L Alderson, Andrew Alderson, and Fabrizio Scarpa. Double-negative mechanical metamaterials displaying simultaneous negative stiffness and negative poisson's ratio properties. Advanced Materials, 28(46):10323-10332, 2016. https://doi.org/10.1002/adma.201603959

[3] L Ai and X-L Gao. Metamaterials with negative poisson's ratio and non-positive thermal expansion. Composite Structures, 162:70-84, 2017. https://doi.org/10.1016/j.compstruct.2016.11.056

[4] Muamer Kadic, Tiemo Bückmann, Nicolas Stenger, Michael Thiel, and Martin Wegener. On the practicability of pentamode mechanical metamaterials. Applied Physics Letters, 100(19), 2012. https://doi.org/10.1063/1.4709436

[5] Bastiaan Florijn, Corentin Coulais, and Martin van Hecke. Programmable mechanical metamaterials. Physical review letters, 113(17):175503, 2014. https://doi.org/10.1103/PhysRevLett.113.175503

[6] Babak Haghpanah, Ladan Salari-Sharif, Peyman Pourrajab, Jonathan Hopkins, and Lorenzo Valdevit. Multistable shape-reconfigurable architected materials. Adv. Mater, 28(36):7915-7920, 2016. https://doi.org/10.1002/adma.201601650

Materials Research Proceedings 73 (2026) 13-17 https://doi.org/10.21741/9781644904459-3

Experimental Determination of Length Scale Parameter: A Comparison of Static and Dynamic Responses

Hareem JAWAID[1,a*], Mikko SUOMINEN[1,b]

[1]Department of Energy and Mechanical Engineering, Aalto University, Espoo, Finland

[a]hareem.jawaid@aalto.fi, [b]mikko.suominen@aalto.fi

Keywords: Static Response, Dynamic Response, Modified Couple Stress Theory, Length Scale Parameter

Abstract. The present study experimentally determines the length scale parameter in a three-point bending foam beam using Modified Couple Stress Theory (MCST). Two approaches are proposed and compared, namely the Static Response Method and the Dynamic Response Method, to accurately capture size effects using the size-dependent Timoshenko beam theory. The effective bending stiffness is obtained experimentally by measuring deflection using the Static Response Method and natural frequency using the Dynamic Response Method. The material length-scale parameter was identified by relating the experimentally determined effective bending stiffness to the corresponding classical theoretical bending stiffness through the MCST formulation for both methods. The results show that both static and dynamic approaches provide consistent length scale parameter values that differ by <3%, indicating that either method can be reliably employed for its determination. The difference can be attributed to small force fluctuations and the neglect of inertial effects in the static response method, unlike the dynamic response method. Both test methods across foams of different stiffness/density indicate strong microstructural influence; the size-dependent model predicts reduced deflection and increased natural frequency.

Introduction

MCST accurately captures the size effects in small-scale materials, showing that an increase in the material length scale ratio results in enhanced beam stiffness [1, 2]. While analytical studies on size-dependent beams are extensive, experimental work is limited. Some notable examples are: bending experiments on SU-8 to identify the scale parameter [3] and vibration based tests to extract length scale parameter showing microstructural-dependent effects [4]. However, a systematic comparison between bending and vibration approaches has not been sufficiently addressed. Therefore, the present study experimentally determines the material length-scale parameter of closed-cell PVC foam beams using both static (bending-based) and dynamic (vibration-based) methods within the framework of the MCST-based Timoshenko beam theory (TBT), and directly compares the values obtained from the two approaches.

Methodology

To study size-dependent effects in PVC foam, two PVC foam grades (PVC-60 and PVC-100 [5]) were tested. For each grade, five rectangular beams of length L, width b, and thickness h (200×60×10mm) were prepared per ASTM D790 Standard, using a vertical band-saw as shown in Fig.1.

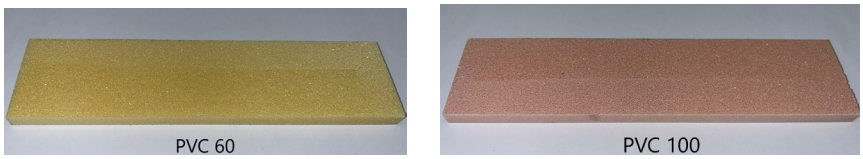

Figure 1 (Foam beams)

Content from this work may be used under the terms of the Creative Commons Attribution 3.0 license. Any further distribution of this work must maintain attribution to the author(s) and the title of the work, journal citation and DOI. Published under license by Materials Research Forum LLC.

Materials Research Proceedings 73 (2026) 13-17 https://doi.org/10.21741/9781644904459-3

To extract and compare the length scale parameter, two methods were used- Static Response Method and Dynamic Response Method. In a **Static Response Method**, a three-point bending test setup applied the load on beam, see Fig. 2 [6] for setup. Digital Image Correlation (DIC) captured the beam's deflection at 80 fps with a 5280 × 4608-pixel camera equipped with a 50 mm lens. The setup was calibrated with a dotted grid calibration target of 0.014 pixel to achieve sub-pixel accuracy, and all specimens were speckle patterned using rollers with 0.033 inches speckle diameter. The analysis was performed using VIC-3D 10 software. The DAQ (Data Acquisition System), in sync with the DIC, recorded the applied displacement, the measured force, and the beam's deflection simultaneously. Flexural Modulus $\boldsymbol{E_f}$ and effective bending stiffness $\mathbf{D_{eff}}$ of all samples were then calculated from the resulting force–deflection curve in accordance with ASTM D790. In **Dynamic Response Method**, the natural frequency of the three point bending beams was measured by exciting beams using a rubber hammer. FFT analyzer of DIC analyzed the dynamic response by taking the images at 800 FPS. First peak in the frequency response spectrum was recorded as the first natural frequency of the beam from which the effective bending stiffness was determined.

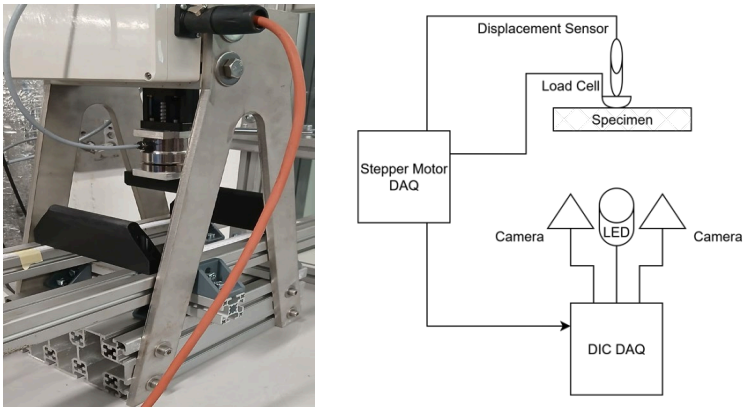

Figure 2 (Experimental Setup)

To validate the presence of size effects, the experimentally measured deflection and natural frequency responses were evaluated using the classical and MCST-based Timoshenko beam theories for a linear, homogeneous beam without thermal loads (see Reddy [2]). The corresponding theoretical responses were obtained numerically using finite element method (FEM) solvers implementing the Timoshenko Beam Theory (TBT). The classical bending rigidity was first calculated as $\boldsymbol{EI}$, where $\boldsymbol{E}$is the Young's modulus and $\boldsymbol{I}$is the second moment of area. The experimentally determined effective bending rigidity, $\boldsymbol{D_{eff}}$, was then related to the theoretical classical rigidity, $\boldsymbol{EI}$, through the MCST expression proposed by Reddy [2] to determine the material length-scale parameter, $\boldsymbol{\ell}$, as given in Eq. 1.

$$D_{\text{eff}} = EI + 4\mu A l^2 \tag{1}$$

where μ = shear modulus, A = cross-sectional area, and l is length scale parameter.

Using the identified length-scale parameter, the MCST-based bending stiffness and the corresponding theoretical deflection and natural frequency responses were subsequently calculated. Finally, the experimental deflection and natural frequency results were compared with the predictions of both the classical and MCST-based Timoshenko beam theories. Since the experimentally determined properties correspond to finite-width beam specimens, whereas the analytical predictions presented in this study are based on a one-dimensional beam formulation, finite-width effects are not explicitly accounted for in the present analysis. The incorporation of finite-width effects into the analytical model is left for future work.

Materials Research Proceedings 73 (2026) 13-17 https://doi.org/10.21741/9781644904459-3

Results and Discussions

The experimental deflection responses of the PVC 60 and PVC 100 foam beams under applied loads of 20 N and 14 N, respectively, are presented in Fig. 3. From the resulting force–deflection curves, the experimental effective bending stiffness, D_{eff}, was determined for both foam beams. The experimentally determined stiffnesses were found to exceed the corresponding classical theoretical bending stiffnesses. The observed difference may include a small contribution from finite-width effects but is primarily attributed to shear deformation and size-dependent effects. The theoretical classical bending stiffness, EI, was calculated as 320 kN·mm^2 for PVC 60 and 535 kN·mm^2 for PVC 100, while the experimentally determined effective bending stiffnesses were 342 kN·mm^2 and 579 kN·mm^2, respectively. The material length-scale parameter was subsequently determined using Equation (1), and the corresponding MCST-based bending stiffness and deflection response were calculated. The experimental results were then compared with the predictions of both the classical Timoshenko beam theory (C.TBT) and the size-dependent Timoshenko beam theory (S.TBT), as shown in Fig. 4 and Table 1. The MCST-based predictions exhibited improved agreement with the experimental response.

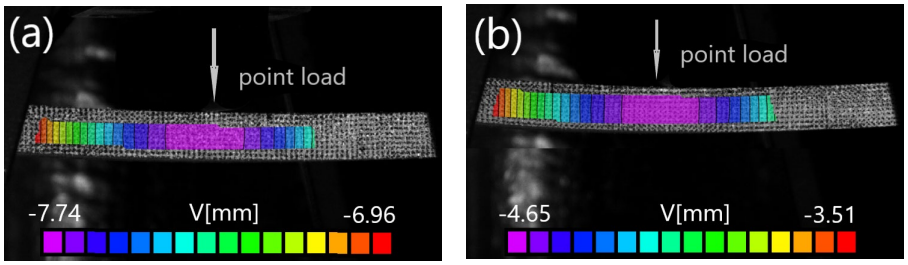

Figure 3 (Transverse Deflections (a) PVC 60 Foam Beam (b) PVC 100 Foam Beam)

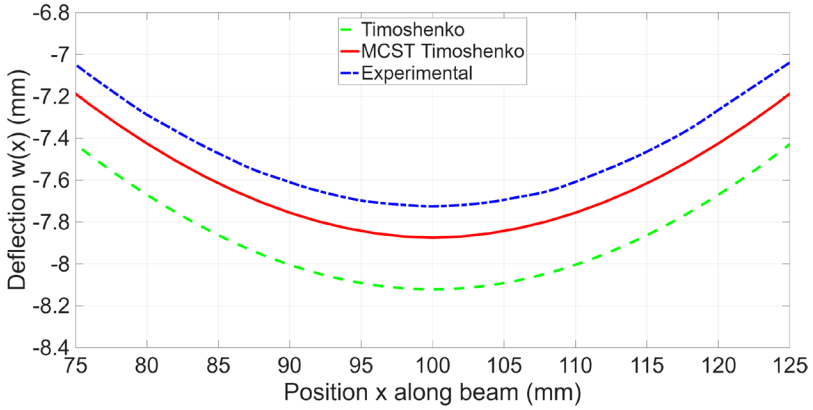

Figure 4 (Deflection of PVC 60 beam)

Similarly, the natural frequencies of all specimens were obtained using VIC-3D DIC as shown in Fig. 5. The first natural frequency for both PVC grades presented in Table 1 exceeded the corresponding classical predictions, further indicating the presence of size effects. The measured frequencies were consistent across repeated tests, confirming increased beam stiffness due to shear deformation and size-dependent effects. From the measured frequencies, the effective bending stiffness was calculated, and length scale parameters were subsequently extracted in a similar manner.

Materials Research Proceedings 73 (2026) 13-17 https://doi.org/10.21741/9781644904459-3

Table 1 (Midspan Deflection and Natural Frequency)

PVC Beams	Midspan Deflection [mm]			Natural Frequency [Hz]		
Grades	C.TBT	S.TBT	Experiment	C.TBT	S. TBT	Experiment
PVC 60	-8.121	-7.874	-7.725	116.71	121.08	121.39
PVC 100	-4.712	-4.614	-4.630	116.90	121.83	122.65

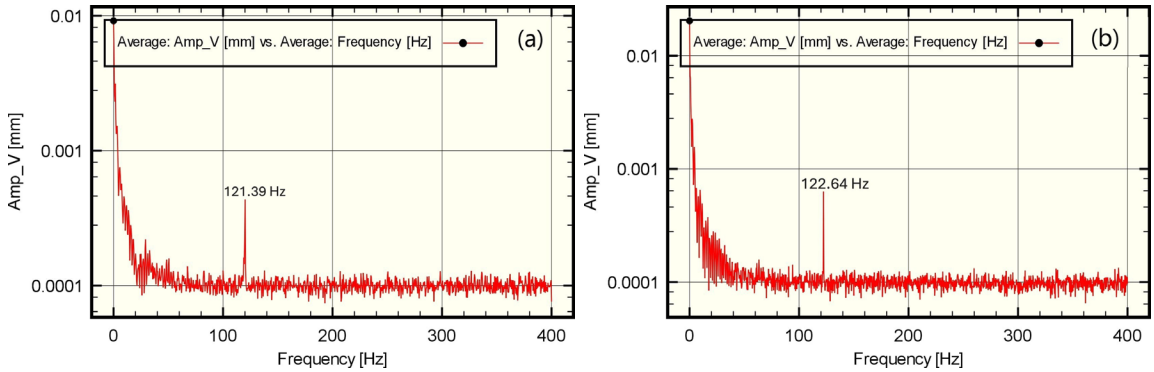

Figure 5 (Dynamic Response (a) PVC 60, (b) PVC 100)

➢ Comparison

The average values obtained from the tests are summarized in Fig. 6 and it shows all specimens with range bars (min–max). The length scale parameter values obtained from both methods differ by <3% likely due to noise in the Static Response Method. The dynamic response method also incorporates inertial effects in the response, yet close agreement between two results indicates that either method can be reliably used. PVC 100 scale parameter is slightly higher than PVC 60 due to higher stiffness, density, and stronger microstructural effects leading to lower deformation. These trends align with Reddy [2] that an increase in the material length scale ratio leads to higher stiffness, reduced displacements, and increased natural frequency.

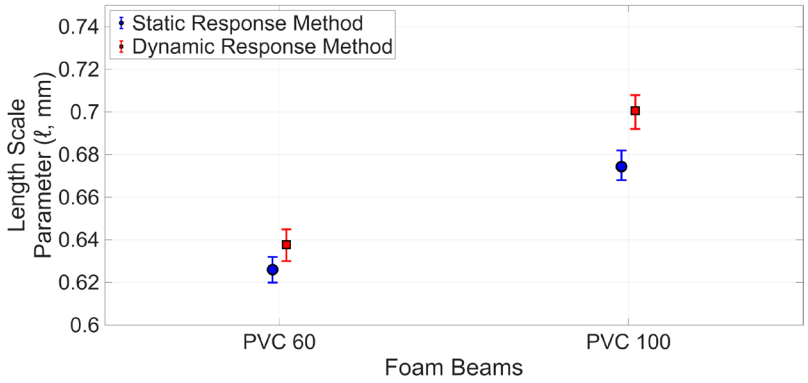

Figure 6 (Comparison)

Conclusions

An experimental size-dependent investigation of closed-cell PVC foam beams was conducted within the framework of Modified Couple Stress Theory (MCST). Two approaches, namely the Static Response Method and the Dynamic Response Method, were proposed for the experimental determination of the material length-scale parameter based on classical and size-dependent beam theories. The length-scale parameters obtained using these two approaches agreed within 3%. The size-dependent TBT model effectively captures shear and size effects in porous beams, whereas

classical beam theory fails to account for these effects. The results indicate that the length scale parameter increases with material stiffness and structural rigidity. It is also influenced by density, where higher-density grades exhibit stronger microstructural effects, resulting in reduced beam deflection and increased natural frequency. The proposed methods are practical and cost-effective for experimentally determining the material length scale parameter in MCST across materials of varying stiffness and density. Future work may extend the present framework by incorporating finite-width effects and higher-order shear deformation theories to further reduce the discrepancy between the experimental and theoretical MCST responses. In addition, fitting the theoretical predictions to the experimental response could enable a more accurate determination of the material length-scale parameter.

References

[1] F. Yang, A. Chong, D. Lam and a. P. Tong, "Couple stress based strain gradient theory for elasticity," International Journal of Solids and Structures, vol. 39, p. 2731-2743, May 2002. https://doi.org/10.1016/S0020-7683(02)00152-X

[2] J. Reddy, "Microstructure-dependent couple stress theories of functionally graded beams," Journal of the Mechanics and Physics of Solids, vol. 59, p. 2382-2399, November 2011. https://doi.org/10.1016/j.jmps.2011.06.008

[3] C. Liebold and W. H. Müller, "Comparison of gradient elasticity models for the bending of micromaterials.," Computational Materials Science, vol. 116, p. 52-61, April 2016. https://doi.org/10.1016/j.commatsci.2015.10.031

[4] L. Jian, H. Yuming, G. Song, L. Zhenkun and L. Dabiao, "Size-dependent vibration of nickel cantilever microbeams: Experiment and gradient elasticity," AIP Advances, vol. 6, Oct 2016. https://doi.org/10.1063/1.4964660

[5] "Gurit PVC STRUCTURAL FOAM CORE," [Online]. Available: https://kevra.fi/wp-content/uploads/Gurit-PVC-foam-v4.pdf.

[6] S. Oksala, P. Lehto and a. J. Tuhkuri, "A practical method to establish the apparent fracture toughness of ice in the field," In Proceedings of the 28th International Conference on Port and OceanEngineering under Arctic Conditions (POAC), vol. 48, p. 1157-1165, 2025.

Materials Research Proceedings 73 (2026) 18-22 https://doi.org/10.21741/9781644904459-4

Enhanced Dielectric and Conductive Properties of ZnO via Transition Metal Doping a Computational Study for Advanced Materials

Rasool Akhtar Alias OSAMA[1,a *], Hannah LEVENE[1,b], Graham WOOD[1,c], Peter LOMAX[1,d] and Rebecca CHEUNG[1,e]

[1]IMNS, School of Engineering, The University of Edinburgh, Edinburgh, UK

[a]Rasool.akhtar@ed.ac.uk, [b]Hannah.Levene@ed.ac.uk, [c]G.S.Wood@ed.ac.uk, [d]Peter.Lomax@ed.ac.uk, [e]R.Cheung@ed.ac.uk

Keywords: Doped ZnO, Band Structure, Optics, Computational Study, XRD Spectra, Elastic Constants

Abstract. The study employs first-principles calculations to investigate the doping of transition metals in the crystal structure of ZnO. The dielectric and conductive properties of the material are enhanced by the addition of these dopants. The changes of properties of ZnO in modeling is carried out by the use of Material Studio and simulation in CASTEP. In this study, the atoms of Manganese (Mn) and Indium (In) are replaced by the atoms of Zinc (Zn). Some of the aspects that we are interested in are the X-ray diffraction spectra, band structure and optical properties, including conductivity and dielectric function. The presented computational study is promising and can be used as an excellent source of information in experimental studies in the future.

Introduction

We are surrounded by various portable electronic devices and sensors that enhance our daily lives. However, these devices require electrical power to run at all times. This raise a challenge, which can be tackled opting the energy resources which are self-sustained. Therefore, the researchers are focused on exploring free accessible energy sources, such as solar, thermal, and piezoelectric options, to fulfill this need [1, 2]. Piezoelectric sensors transform the energy from mechanical to electrical, and the instruments that carry out this process are called piezoelectric nanogenerators (PENGs). Our environment offers a vast amount of freely available mechanical energy that could be utilized to generate electrical energy [3, 4].

Zinc oxide (ZnO) is a very useful semi-conductor compound famous for its wide band-gap, affordability, and bio-compatibility. It has turned out to be an essential substance in many sophisticated technological uses. ZnO is an essential component in the current electronics and sustainable energy systems due to its excellent optoelectronic and piezoelectric properties, environmental stability, and its ubiquitous presence [5-8].

The addition of dopant should enhance the mobility of electrons thus improving conductivity, causing higher transmittance rate at shorter wavelengths. Dopants should be of soluble nature. The literature proposes that the addition of dopants can significantly improve the properties of ZnO, with various types employed to tailor it for specific applications. The band gap diminishes with the inclusion of a transition element, so only a minute energy enables the electrons to transit from the valence band to the conduction band [9, 10].

Computational Models

The computational study conducted before and after the addition of the dopants is compared to the literature. Material Studio facilitates the design and simulation of a ZnO supercell, which is then analyzed using CASTEP. Inside the crystal lattice, Mn and In atoms are introduced and replaces the Zn atoms. Two levels of dopant concentrations of 14.2% and 28.4% are included. The pure and doped ZnO models are shown in Figure 1.

Content from this work may be used under the terms of the Creative Commons Attribution 3.0 license. Any further distribution of this work must maintain attribution to the author(s) and the title of the work, journal citation and DOI. Published under license by Materials Research Forum LLC.

Materials Research Proceedings 73 (2026) 18-22 https://doi.org/10.21741/9781644904459-4

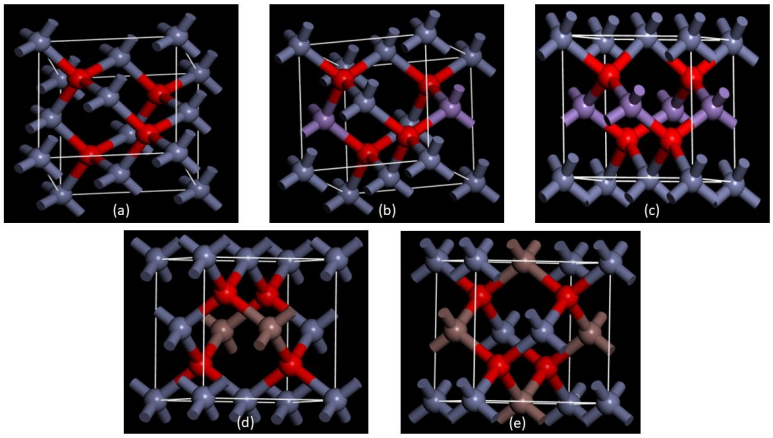

Figure 1. (a) Atomic Model ZnO supercell (Oxygen atoms as red, Zn as dark grey, Mn as purple, and In atoms as brown). (b) Atomic Model 2Mn doped ZnO supercell. (c) Atomic Model 4Mn doped ZnO supercell. (d) Atomic Model 2In doped ZnO supercell. (e) Atomic Model 4In doped ZnO supercell.

Results and Discussions

Results with their analysis are given below:

a. Band Structure of doped ZnO

The study investigates the band structure in both doped and undoped ZnO systems as shown in Figure 2 (a-e). It explores the effects of doping with manganese (Mn) and indium (In) on pure ZnO. The band structures are evaluated after the geometries of models are completely relaxed and fully optimized.

There is a significant change observed in band structure of the structure after doping of 2Mn and 4Mn atoms, it overlaps as shown in Figure 2 (b)-(c). This clearly indicates that the material's conductivity has significantly improved, allowing it to conduct electricity with less energy than pure ZnO.

Similarly, In atoms have been introduced in the crystal structure by replacing Mn atoms and the results show overlapping as well, which are shown in Figure 2 (d)-(e). In doping at both 2In and 4In concentrations results in full band gap closure, confirming a persistent metallic character independent of dopant level.

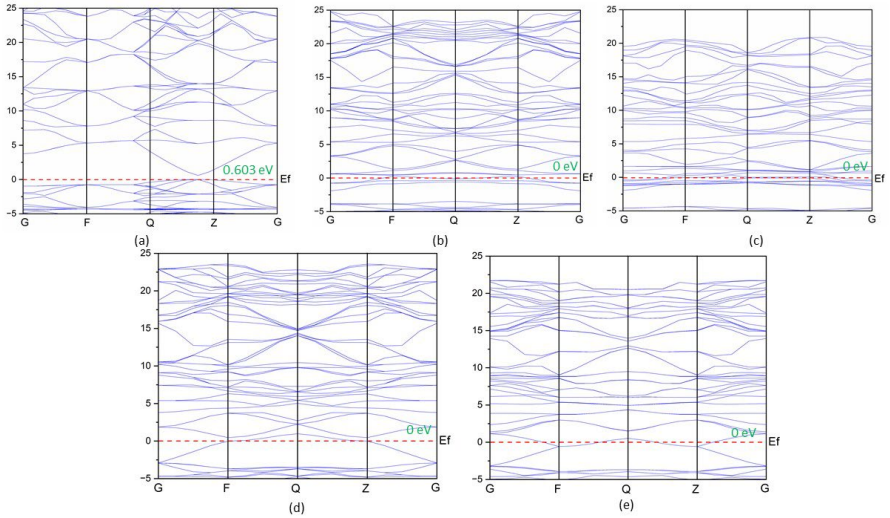

Figure 2. Comparison of Band Structures (a) Pure ZnO, (b) 2Mn doped ZnO system (c) 4Mn doped ZnO system, (d) 2In doped ZnO system and (e) 4In doped ZnO system.

Materials Research Proceedings 73 (2026) 18-22 https://doi.org/10.21741/9781644904459-4

b. Optical Properties

The optical characteristics of both pure and doped ZnO system have been investigated in the literature, the properties studied are conductivity and dielectric function. The basis set is chosen in accordance with the credible literature [11, 12]. PBE approximation is used for the DFT analysis. The Figure 3 (a) illustrates the variation of conductivity of ZnO (Zinc Oxide) to different proportions of Mn (Manganese) and In (Indium) at varying frequencies. Photovoltaic and piezoelectric use has required conductivity, which is quantified by 1/fs. As an example, pure ZnO has a conductivity peak of the order of 1 eV at approximately 0.75 (1/fs). Optimal values with 2Mn and 4Mn are at about 1 eV and about 1.5 eV respectively with conductivity of about 2.25 (1/fs) and 3.75 (1/fs) respectively. Similarly, 2In and 4In doping give peak values of about 3.5 and 4.5 eV respectively with values of about 0.5 and 1.75 respectively (1/fs). These high conductivity values play an important role in photovoltaic applications where they increase the conductivity of the material to the conductivity of the material, which increases the conversion efficiency of sunlight into electrical energy.

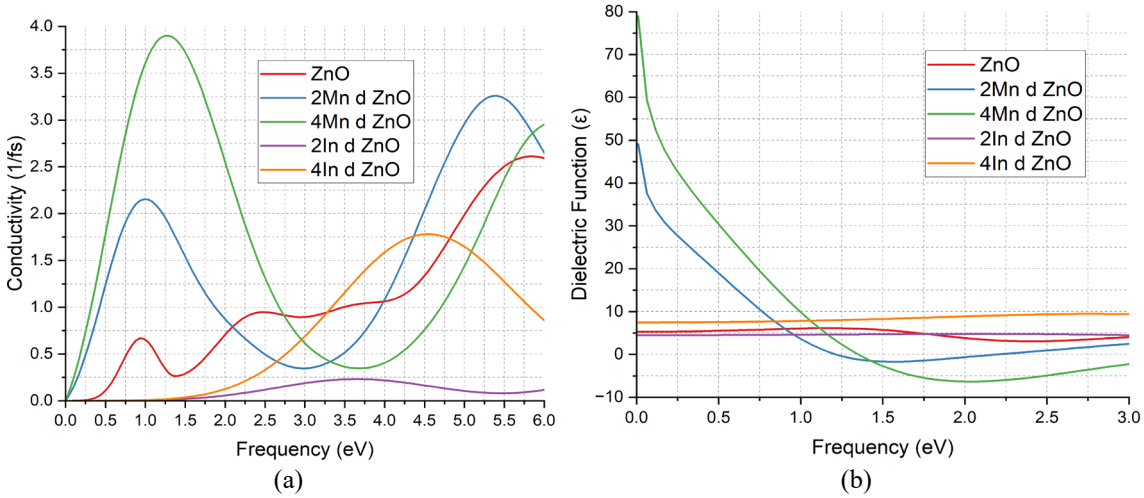

Figure 3. Comparison of (a) Conductivity and (b) Dielectric Function for different ZnO systems.

The Figure 3 (b) shows the variation of dielectric function of ZnO (Zinc Oxide) with various quantities of Mn (Manganese) and In (Indium) at various frequencies. Dielectric function, which is denoted by epsilon, is critical in photovoltaic applications and piezoelectric applications. As an example, the dielectric function of pure ZnO is ranging between approximately 2 to 8 throughout the frequency range. At the addition of the 2Mn, the dielectric function increases to about 2 to 50 and at 4Mn, it increases to 80. Similarly, adding 2In leaves the dielectric constant stays at 4 whereas adding 4In raises the dielectric constant to approximately 8. Addition of Mn and In to ZnO changes these characteristics and can increase the effectiveness and sensitivity of piezoelectric devices.

The advantages of an increased dielectric function are great in applications in capacitors, insulators and other electronics that demand a high dielectric constant. A high dielectric function implies that the material is capable of storing more electrical energy and this results in better performance at the devices which need the dielectric properties.

c. XRD Spectra

Material Studio was used to compute the XRD spectra of different ZnO configurations. JCPDS card number 36-1451 is the standard card of un-doped ZnO [13-16]. Figure 4 (a) indicates the XRD Spectra comparison of the doped and un-doped ZnO. The XRD peaks of the undoped ZnO are sharp and well-defined which indicates a high degree of crystallinity and phase purity.

When ZnO is doped with Mn, the XRD patterns indicate that the similar peaks of un-doped ZnO are also present with slight shifts in the positions of the peaks and variation of the intensity. These alterations and transformations point out that Mn atoms are properly absorbed into the ZnO lattice, causing distortion and changes to the crystal structure and lattice.

Figure 4 (b) presents XRD of ZnO and In-doped ZnO system. The graph shows the XRD Spectra of Zinc Oxide (ZnO) and the patterns of ZnO doped with 2In and 4In. As the doping of ZnO is done with 2In, the peaks do not change their angles but have a bit higher intensity, which indicates increased crystallinity. The peaks become stronger with 4In doping suggesting further crystallinity improvement.

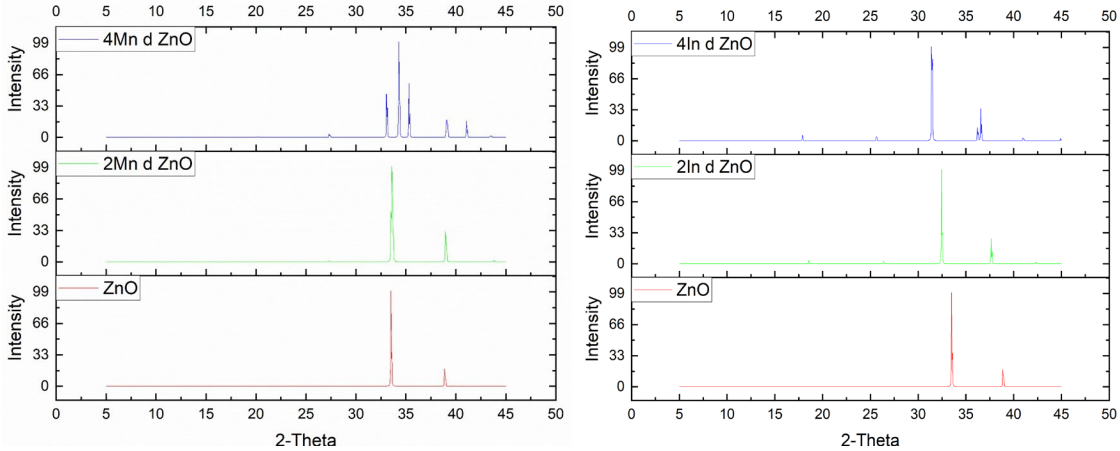

Figure 4. XRD Spectra Comparison of (a) Y doped and (b) In doped ZnO systems.

Conclusion

An in-depth examination of ZnO doped with atoms of Mn and In reveals that the electronic and optical properties have been significantly improved. Band Structures analysis has revealed that doping creates new electronic states moving the conduction band and valence band closer. The transformation improved the mobility of electrons, leading to better conductivity. Improved optical characteristics of doped ZnO are also exhibited. This is useful in photovoltaics and photodetectors applications. The presence of Mn and In atoms into the ZnO lattice are confirmed by X-ray diffraction (XRD) patterns. The small changes in the positions of the peaks, and the changes in the intensity reflect the deformations of the lattice and alteration of the crystalline structure. However, the basic structure of ZnO is hexagonal wurtzite, and the material has not lost its main properties, getting the advantages of doping additions. To sum up, the doping of ZnO with Mn and In leads to significant changes in the electronical and optical properties. Such developments make Mn and In doped ZnO potential possibilities in the state-of-the-art applications in optoelectronics, electronics and materials science. The findings can be compared with the previous studies and support the idea that doped ZnO systems can be used in further technological achievements.

Acknowledgment

This research was conducted with the support of the University of Edinburgh, the CASTEP Developers' Group (CDG), Cambridge Enterprise, and the Higher Education Commission of Pakistan.

References

[1] Osama, R.A.A., et al., Computational study of structural and optical properties of ZnO system through elemental Mn & Y doping using first-principles calculations. Materials Today Communications, 2025. 46. https://doi.org/10.1016/j.mtcomm.2025.112959

[2] Alias Osama, R.A., et al., Tailoring structural and optical properties of ZnO system through elemental Mn Doping through First-principles calculations. Heliyon, 2024. 10(13). https://doi.org/10.1016/j.heliyon.2024.e33443
[3] Osama, R.A.A., et al., Advancing ZnO nanostructures through strategic transition metal doping. Scientific Reports, 2026. https://doi.org/10.1038/s41598-026-37977-y
[4] Rasool Akhtar Alias Osama, D.Z., Rebecca Cheung, Peter Lomax, Nayyar Hussain and Shakir Ali, Tailoring ZnO properties via Mn and V doping: a path toward advanced functional materials. Oxford Open Materials Science, 2025. 5(1). https://doi.org/10.1093/oxfmat/itaf020
[5] Chiang, C.H., et al., Manipulating Ferroelectric Polarization and Spin Polarization of 2D CuInP(2)S(6) Crystals for Photocatalytic CO(2) Reduction. J Am Chem Soc, 2024. 146(33): p. 23278-23288. https://doi.org/10.1021/jacs.4c05798
[6] Shatnawi, M., et al., Influence of Mn doping on the magnetic and optical properties of ZnO nanocrystalline particles. Results in Physics, 2016. 6: p. 1064-1071. https://doi.org/10.1016/j.rinp.2016.11.041
[7] Zhang, X., et al., Characterizing and Optimizing Piezoelectric Response of ZnO Nanowire/PMMA Composite-Based Sensor. Nanomaterials (Basel), 2021. 11(7). https://doi.org/10.3390/nano11071712
[8] Mrabet, S., et al., Structural, optical, and magnetic properties of V-doped ZnO nanoparticles and the onset of ferromagnetic order. Journal of Alloys and Compounds, 2022. 920. https://doi.org/10.1016/j.jallcom.2022.165920
[9] Rahaman, M.Z., H. Tanaka, and A.K.M. Akther Hossain, An experimental and theoretical insights into the dielectric properties of (Li, Nd) co-doped ZnO ceramics. Journal of Materials Science: Materials in Electronics, 2020. 31(22): p. 20113-20128. https://doi.org/10.1007/s10854-020-04533-x
[10] Saadi, H., et al., Enhancing the electrical conductivity and the dielectric features of ZnO nanoparticles through Co doping effect for energy storage applications. Journal of Materials Science: Materials in Electronics, 2023. 34(2). https://doi.org/10.1007/s10854-022-09470-5
[11] Muhammad, R., Y. Shuai, and H.-P. Tan, A first-principles study on alkaline earth metal atom substituted monolayer boron nitride (BN). Journal of Materials Chemistry C, 2017. 5(32): p. 8112-8127. https://doi.org/10.1039/C7TC02894F
[12] Muhammad, R., Y. Shuai, and H.-P. Tan, First-principles study on hydrogen adsorption on nitrogen doped graphene. Physica E: Low-dimensional Systems and Nanostructures, 2017. 88: p. 115-124. https://doi.org/10.1016/j.physe.2016.12.012
[13] Wang, P., et al., The electronic structures and optical properties of yttrium-doped zinc oxide with zinc interstitial defects calculated by first-principles. Materials Science in Semiconductor Processing, 2015. 36: p. 36-42. https://doi.org/10.1016/j.mssp.2015.03.022
[14] Yu, H., et al., Modulating Electronic Properties of Carbon for Selective Electrochemical Reduction of CO2 to Methanol on Cu3P@C. ACS Catalysis, 2024. 14(17): p. 12783-12791. https://doi.org/10.1021/acscatal.4c02465
[15] Pérez-Rodríguez, S., et al., Single atom Cu-N-C catalysts for the electro-reduction of CO2 to CO assessed by rotating ring-disc electrode. Journal of Energy Chemistry, 2024. 88: p. 169-182. https://doi.org/10.1016/j.jechem.2023.09.005
[16] Guo, L., et al., Electronic Structure Design of Transition Metal-Based Catalysts for Electrochemical Carbon Dioxide Reduction. ACS Nano, 2024. 18(14): p. 9823-9851. https://doi.org/10.1021/acsnano.4c01456

Materials Research Proceedings 73 (2026) 23-26 https://doi.org/10.21741/9781644904459-5

3D Micromechanical Modeling of Compressive Failure in Unidirectional CFRP

Doha KASHOUA[1,2,a], Samuel RIVALLANT[1,b*], Pierre RAHME[2,c *], Christophe BOUVET[1,d]

[1]Univ Toulouse, IMT Mines Albi, INSA Toulouse, ISAE-SUPAERO, CNRS, ICA, Toulouse, France

[2]Department of Industrial and Mechanical Engineering, Lebanese American University, Lebanon

[a]doha.kashoua@isae-supaero.fr, [b]samuel.rivallant@isae-supaero.fr, [c]pierre.rahme@lau.edu.lb, [d]christophe.bouvet@isae-supaero.fr

Keywords: Micromechanics, Kink-Band, Compressive Failure, CFRP Composites

Abstract. To address the limitations of current design safety factors in aerospace structures, accurate simulation models predicting the compressive failure of unidirectional CFRP composites are required. These materials are limited by localized shear instabilities, or kink-bands, which are sensitive to unavoidable fiber misalignment. This study develops a 3D explicit micromechanical model in Abaqus to investigate the morphology of the kink-band failure and explain its scenario. It addresses the existing limitations of imposing the right input parameters and boundary conditions that can produce a kink-band. The simulation successfully captures kink-band formation initiated by matrix shear, fiber rotation and fiber breakage.

Introduction

The compressive strength of unidirectional (UD) Carbon Fiber Reinforced Polymer (CFRP) composites is significantly lower than their tensile strength, primarily due to the phenomenon of fiber micro-buckling and subsequent kink-band formation. Fiber misalignment, a manufacturing induced defect, is the primary trigger for these localized shear instabilities [1]. In this paper, a numerical framework is conducted to observe the failure scenario of the kink band formation and its morphology through micromechanical modeling.

Methodology

The model is based on a Representative Volume Element (RVE) featuring a hexagonal fiber distribution with a fiber volume fraction of approximately 60% (Figure 1). The geometry and meshing of the elementary layer section are generated using a mesh Fortran file with one row of RVE in thickness direction, 48 in the width and 260 across the length to induce the in-plane kink band failure and introduces a specific fiber misalignment angle (θ) using a sinusoidal function (Figure 2).

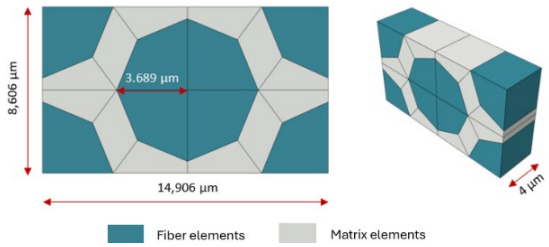

Figure 1 *The geometry of the composite unit cell*

Content from this work may be used under the terms of the Creative Commons Attribution 3.0 license. Any further distribution of this work must maintain attribution to the author(s) and the title of the work, journal citation and DOI. Published under license by Materials Research Forum LLC.

Materials Research Proceedings 73 (2026) 23-26 https://doi.org/10.21741/9781644904459-5

The constituent behaviors of materials are implemented via a user-defined VUMAT subroutine:

- Matrix (Epoxy 914): governed by a Drucker-Prager plasticity model featuring a pressure-dependent yield surface. This accounts for hydrostatic pressure sensitivity, which is critical for capturing the shear localization that precedes kinking. The Drucker-Prager material parameters β=39.43, d=73.12 MPa and K=0.795 for this material are considered [2].
- Fibers (T300): modeled with transversely isotropic properties and a linear brittle law. Fiber failure is triggered when the longitudinal strain reaches the specified limit tensile or compressive strain values.

The explicit solver is utilized to manage the highly non-linear response associated with sudden fiber breakage and localized instability. The compressive loading is applied by imposing a linear ramp of velocity on the longitudinal faces of the RVE. The top and bottom faces of the plate are each tied to a reference point on which the velocity is applied. The face at y=0 is fixed from translating in the y direction, and the reference points are constrained for both the x and y translation, and the y and z rotation.

To address existing limitations in micromechanical modeling, the model uses elastic non-damageable zones longitudinally where the velocity is applied to eliminate artificial edge effects (Figure 2, blue area), in addition to the boundaries between the plastic zone (Figure 2, red area) and the equivalent material on the sides to ensure no edge effects of the tie between the two zones is interfering with the kink band formation. The equivalent material elements are constructed laterally on the sides of the plate section to overcome the free edge problem (Figure 2, green area) [3]. These 3D elements represent the composite at the macroscopic scale as they carry the composite's homogenized properties.

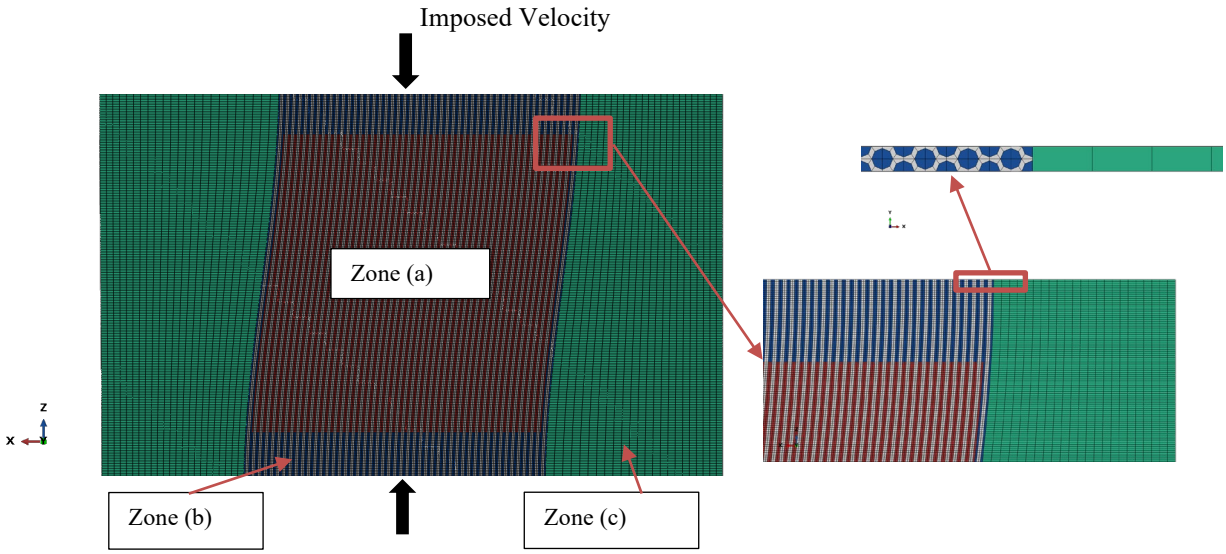

Figure 2 *Plate structure with the three main sections: the middle plastic zone of the composite (red area), the elastic caps (blue area) and the zone of the elements with the composite equivalent properties (green area)*

Numerical Results

The simulation provides a detailed insight into the kink-band failure scenario which other 3D micromechanical models fail to obtain [4]. Initially, as the compressive load increases, matrix plasticity is recorded well before the formal initiation of the kink-band. This early plasticity is due

Materials Research Proceedings 73 (2026) 23-26 https://doi.org/10.21741/9781644904459-5

to the occurrence of the shear stresses induced by the initial fiber misalignment and is located where the misalignment is the highest. The matrix eventually loses the stiffness necessary to support the fibers, causing them to bend and rotate in the lateral (shear) direction. This specific morphological evolution, that forms a localized zone where the kink-band will eventually emerge, is clearly captured in the simulation (Figure 3, a). As the loading continues, the transition from localized bending to ultimate failure is marked by a distinct shift in the system's response. The curve of plastic dissipation in the matrix, on Figure 3, exhibits a sharp change in slope, shifting from a marginal increase to a significantly higher rate of dissipation (Figure 4, a). This shift corresponds to the point where the fiber rotation becomes extreme (Figure 3, a and Figure 4, a), leading to fiber rupture as the elements reach their limit strain due to high local curvature (Figure 3, b). At this stage, the plate section fails via a fully developed kink-band, as evidenced by the sudden drop in the stress-strain curve and the rapid accumulation of matrix damage (Figure 3, c and Figure 4, c).

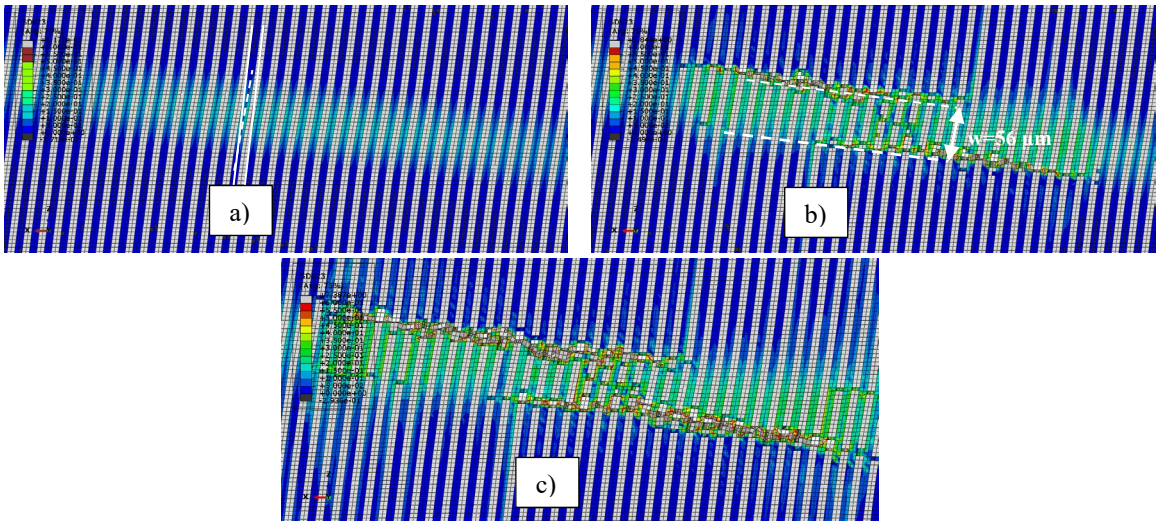

Figure 3 *(a), (b) and (c) represent the three points of Figure 4 at which the fibers reach the maximum bending while the matrix is losing its stiffness, the fibers breaking in kink band, and the kink band at the first load drop, respectively*

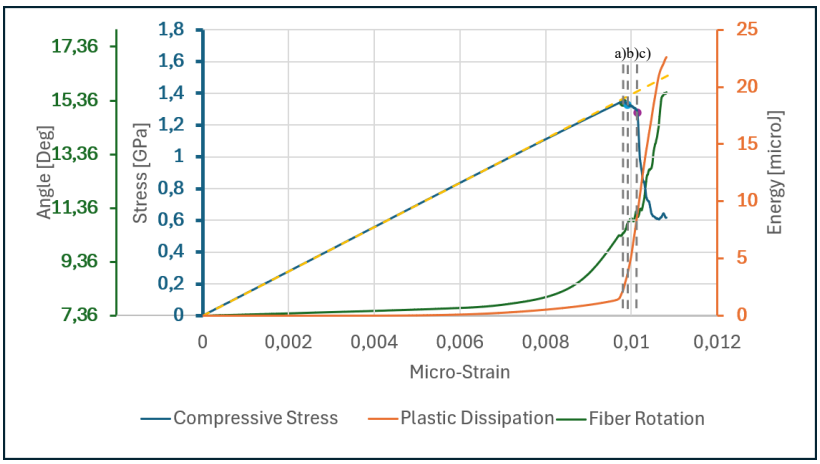

Figure 4 *Stress (in blue), Plastic dissipation (in orange) and fibre rotation angle (in green) against the strain upon compression*

Conclusions

In this paper, a 3D micromechanical model is developed from which we managed to obtain the development of the full sequence of events that lead to the kink band formation. We were able to catch the phenomenon and predict the kink-band morphology, including band angle and width. The model successfully captures the interaction between matrix plasticity and fiber rotation. the predicted kink band morphology generated by this model, including the kink-band width, is in agreement with experimental measurements found in the literature [5]. However, the model has limitations that will direct our future work. The major limitation is that the framework currently imposes an in-plane kink band, whereas the physical microbuckling phenomenon also experiences a part of out-of-plane kink band. Additionally, we will test the model's sensitivity by reducing the initial fiber misalignment angle to evaluate how the failure initiation and propagation adapt to smaller, more realistic defect scales, in addition to simulating for a thicker layer section. Furthermore, fibers in our model fail in compression based on the reached limit compressive strains. Realistically, it is believed that fibers within a kink-band fail due to local tensile strains induced by the high curvature of the fiber during extreme rotation. Adjusting these failure laws with the other mentioned limitations will be the focus for future research to improve the model's physical accuracy.

References

[1] M. R. Wisnom, “The effect of fibre misalignment on the compressive strength of unidirectional carbon fibre/epoxy,” *Composites*, vol. 21, no. 5, Art. no. 5, Sep. 1990. https://doi.org/10.1016/0010-4361(90)90438-3

[2] W. Sun, Z. Guan, Z. Li, M. Zhang, and Y. Huang, “Compressive failure analysis of unidirectional carbon/epoxy composite based on micro-mechanical models,” *Chin. J. Aeronaut.*, vol. 30, no. 6, Art. no. 6, Dec. 2017. https://doi.org/10.1016/j.cja.2017.10.002

[3] M. Bishara, R. Rolfes, and O. Allix, “Revealing complex aspects of compressive failure of polymer composites – Part I: Fiber kinking at microscale,” *Compos. Struct.*, vol. 169, pp. 105–115, Jun. 2017. https://doi.org/10.1016/j.compstruct.2016.10.092

[4] J. Chen, L. Wan, K. Nelms, G. Allegri, and D. Yang, “Failure analysis of unidirectional CFRP composites with the coupled effects of initial fibre waviness and voids under longitudinal compression,” *Compos. Struct.*, vol. 347, p. 118451, Nov. 2024. https://doi.org/10.1016/j.compstruct.2024.118451

[5] A. C. Bergan, S. C. Garcea, and P. J. Withers, “Quantification of damage evolution in cross-ply polymer composites under longitudinal compression by fast computed tomography and semi-automated segmentation,” *Compos. Sci. Technol.*, vol. 241, p. 110128, Aug. 2023. https://doi.org/10.1016/j.compscitech.2023.110128

Materials Research Proceedings 73 (2026) 27-30 https://doi.org/10.21741/9781644904459-6

Multiscale Numerical Modeling of Vitrimer-Based Woven Face Sheets used in Sandwich Structure Applications

Georgios KOTSINIS[1,a*], Festus Ifeanyi ANAGWU[1,b], Oussema KACHOURI[1,c], Gaston RAUCHS[1,d], Levent KIRKAYAK[1,e], Lucas BINSFELD[1,f], Gaetano GIUNTA[1,g]

[1]Luxembourg Institute of Science and Technology (LIST), Sustainable Composite Materials & Manufacturing (SCMM) Innovation Centre, 5, rue Bommel, L-4940 Hautcharage, Luxembourg

[a]georgios.kotsinis@list.lu, [b]festus-ifeanyi.anagwu@list.lu, [c]oussema.kachouri@list.lu, [d]gaston.rauchs@list.lu, [f]levent.kirkayak@list.lu, [g]lucas.binsfeld@list.lu, [h]gaetano.guinta@list.lu

Keywords: Sandwich Structure, Composite Materials, Multiscale Fem Modelling, Vitrimer Composites

Abstract. To enhance the sustainability of high-performance sandwich structures, this research introduces a multiscale numerical framework for vitrimer-based woven composites. Unlike traditional chemistries, vitrimers utilize reversible bonding to enable repair and recycling. The modeling approach, implemented in Finite element software Abaqus, begins with micro-scale constituent homogenization followed by meso-scale FE modeling informed by Micro-Computed Tomography (μCT) for precise yarn geometry. Validated against interlaminar shear and flexural benchmarks, the models were integrated into a comprehensive sandwich structure simulation. This high-fidelity framework reduces reliance on physical testing, accelerating the industrial adoption of recyclable composite structures.

Introduction

Sandwich structures find extensive usage in structural applications due to their superior properties relative to their low weight. The face sheets can consist of different types of materials, while the core can vary in properties, patterns, and geometries [1].

The selection of material is based on the specific requirements of the application. In cases where recyclable and sustainable sandwich structures are desired, vitrimers [2] in combination with woven fabrics provide an ideal solution. Woven fabrics enhance the assembly by providing bi-directional strength and superior impact resistance due to their fiber architecture. This construction also improves delamination resistance and ensures better conformability to complex shapes, resulting in a more durable and high-performance structure.

Multi-scale modeling is a necessary procedure to evaluate the properties of composites, starting from the micro-scale up to the macro-model [3]. This is because the fabrication of the yarn sections and the fiber volume fraction within each yarn play a crucial role in the mechanical properties and the final response of the laminate.

This paper presents a modelling procedure for determining the properties of a woven glass fabric with a vitrimer resin used as a face sheet for a sandwich structure focusing on the elastic region. Numerical results are validated against experimental results at the coupon level. Finally, a preliminary simulation of a sandwich structure under three-point bending is presented.

Methodology

The modeling framework, implemented in Abaqus and Python scripting, utilizes micro-scale constituent homogenization and meso-scale FE modeling based on μCT for precise yarn geometry of a glass fabric. The material was fabricated using a 296 g/m² glass fabric (8H satin weave, aero-

Content from this work may be used under the terms of the Creative Commons Attribution 3.0 license. Any further distribution of this work must maintain attribution to the author(s) and the title of the work, journal citation and DOI. Published under license by Materials Research Forum LLC.

Materials Research Proceedings 73 (2026) 27-30 https://doi.org/10.21741/9781644904459-6

grade, FK 144 finish) with a 100 cm width, combined with a vitrimer resin. All skin-layers constituent properties are detailed in Table 1.

Table 1: Properties of considered fabric and resin constituents.

Constituent	Tensile modulus [GPa]	Poisson's ratio [−]
Fiber	74 ± 2	0.22 ± 0.01
Resin	2.5 ± 0.4	0.45 ± 0.05

The methodology follows a multiscale approach, beginning with the homogenization of the fiber-resin and yarn-resin systems to calculate the homogenized material properties. These properties are then applied to coupon-level models for the skins, which are validated against interlaminar shear and flexural experiments. Finally, these validated models for the skins are integrated into a simulation of the complete sandwich structure to analyze its overall structural performance under flexural bending.

Numerical Results

The first step involved determining the homogenized properties of a yarn. For this, the micromechanical plugin in Abaqus was utilized. The inputs and final mesh parameters, after convergency study, for the Representative Volume Elements (RVE) are detailed in Table 2.

Table 2: Material, geometry and mesh data used for micro scale homogenization.

	Tensile modulus [GPa]	Poisson ratio [-]	Tensile strength [MPa]	Vf [%]	Fiber Radius [µm]	Depth [mm]	Elements in Radius	Elements in Depth
Fiber	74 ± 2	0.22 ± 0.01	-	42.1	3	0.1	12	8
Resin	2.5 ± 0.4	0.45 ± 0.05	44.2 ± 0.6		-			

For the mesoscale modeling, TexGen software was utilized to design the specific 8H satin weave architecture that reflects the physical material as accurately as possible. To achieve this, a µCT (micro-computed tomography) analysis was performed, providing, high-resolution 3D imaging of the internal structure (Fig. 1). This allowed for the precise measurement of the yarn cross-sectional geometry, yarn path (crimp), and the inter-yarn spacing.

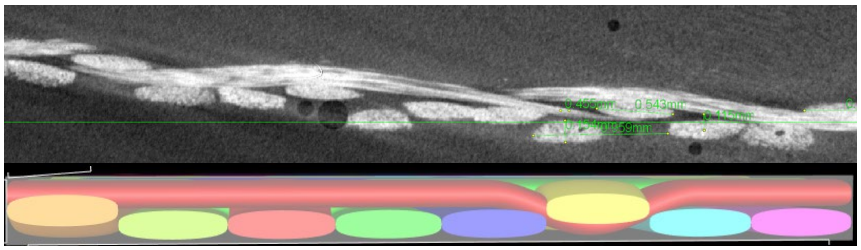

Fig. 1: The cross section of the woven from the mCT (upper) and from the TexGen software (lower).

The final cross section of the yarn used for the analysis features a "Power Ellipse" geometric profile with width 0.57 mm, height 0.15 mm, and a power setting of 0.6, which results in the elongated, slightly pointed ovalis. The properties obtained using the micromechanics plug in are presented in Table 3.

Table 3: Homogenized properties.

Scale	E_{11} [MPa]	$E_{22} = E_{33}$ [MPa]	v_{12} [-]	v_{13} [-]	v_{23} [-]	G_{12} [MPa]	G_{13} [MPa]	G_{23} [MPa]
Micro	32636.4	6850.2	0.34	0.35	0.70	2001.2	2001.2	2016.2
Meso	13852.2	7208.4	0.16	0.61	0.61	1653.8	1557.0	1557.0

To validate the multi-scale procedure, the homogenized properties were used to model the macro-scale behavior of coupons in three-point bending and ILSS tests, which were then compared against some experimental results based on the ASTM D7264 and ASTM D2344 respectively. The numerical model was defined using orthotropic, linear elastic material properties and geometrical non-linearities. To simulate the physical interaction, surface-to-surface contact was implemented between the rollers and the specimen with a friction coefficient of 0.005 and Lagrangian normal behavior. The boundary conditions consisted of fixed bottom supports, with a downward displacement applied to the top roller through a non-linear static step. For discretization, C3D8R reduced-integration brick elements were used for the while R3D4 rigid shell elements were assigned to the loading and support rollers. Flexural test coupons were modeled with a 48 mm span and a test speed of 2 mm/min, using 5 mm radius for all loading edges. For the ILSS tests, the span was 15 mm with a 1 mm/min test speed, a 5 mm loading radius, and 2 mm support radius.

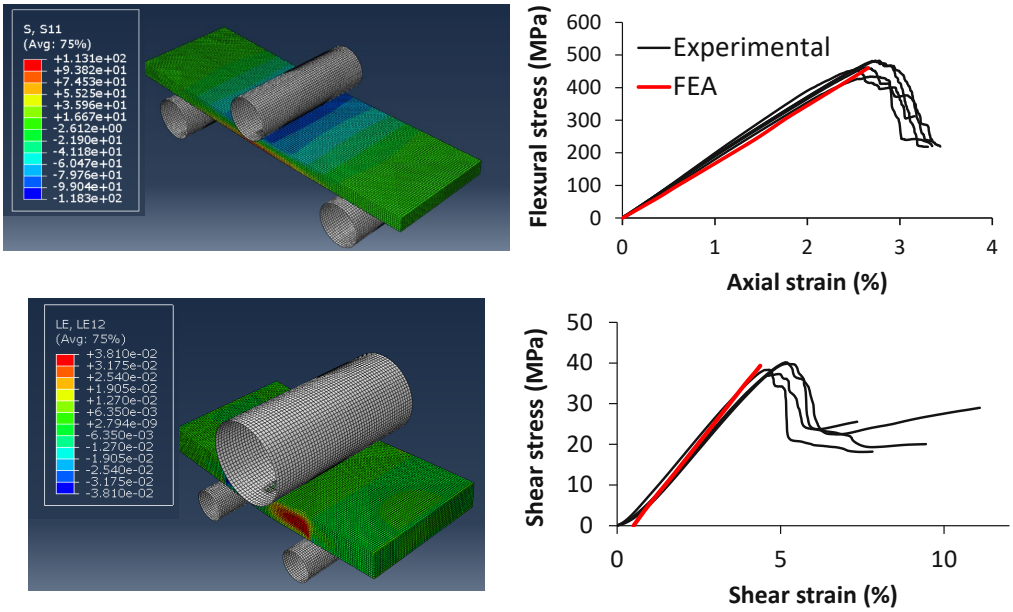

Fig. 2: The FE models along with a contour of the axial stresses for the bending test and the shear strains for the ILSS (left). Comparison of the FEA and experimental results for the two tests (right)

As presented in Fig. 2, the numerical simulations accurately capture the linear response of the specimens prior to damage initiation. This high level of correlation demonstrates that the homogenized properties obtained through this procedure are reliable and representative of the physical woven-vitrimer composite.

A NOMEX® ECA 3.2-64 honeycomb core with 12.7 mm wall thickness was modeled in detail as an elastoplastic material for the flexural sandwich simulation. The Nomex properties used are $E = 3$ GPa and $v = 0.2$. The assembly included a cohesive material layer between the skins and

the core to capture interfacial behavior. Using an explicit solver, to avoid convergency problems, the core was represented by 2D shell S4R elements and the skins by continuum shell SC8R elements, while the rollers were modeled as rigid surfaces (R3D4 elements used). In Fig. 3 some preliminary results are presented.

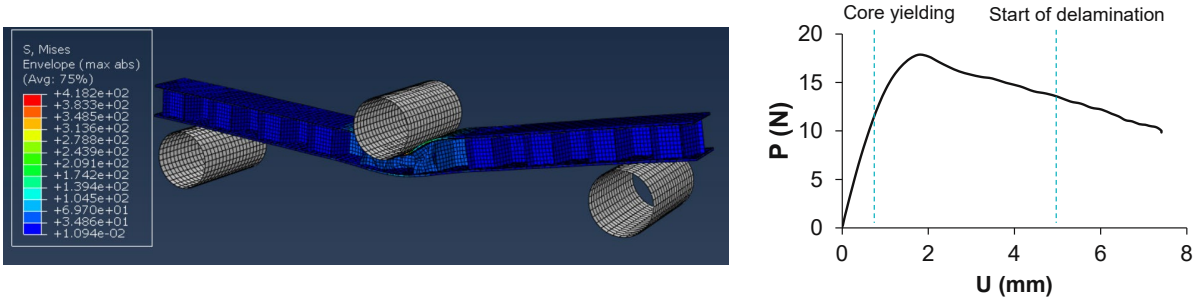

Fig. 3: Bending of the sandwich structure (left), force-displacement curve (right)

Conclusions

Multiscale optimization provided accurate macro-scale properties for modeling the linear response of the vitrimer/woven glass fiber configuration under bending and ILSS conditions. A key finding was the significant impact of yarn geometry on overall performance. These properties, combined with a Nomex honeycomb core, were used to simulate the 3PB response of the sandwich structure for future comparison with experimental results.

Acknowledgment

The project benefits from the support of the European Regional Development Fund under convention No. 2023-01-21 "Sustainable Composite Materials and Manufacturing (SCMM)" and by the Luxembourg Government - Ministry of the Economy under the SC2M convention.

References

[1] Birman, V., & Kardomateas, G. A. (2018). Review of current trends in research and applications of sandwich structures. Composites Part B: Engineering, 142, 221-240. https://doi.org/10.1016/j.compositesb.2018.01.027

[2] Montarnal, D., Capelot, M., Tournilhac, F., & Leibler, L. (2011). Silica-like malleable materials from permanent organic networks. Science, 334(6058), 965–968. https://doi.org/10.1126/science.1212648

[3] Aranda-Iglesias, D., Giunta, G., Peronnet-Paquin, A., Sportelli, F., Keniray, D., & Belouettar, S. (2021). Multiscale modelling of the mechanical response of 3D multi-axial knitted 3D spacer composites. Composite Structures, 257, 113139. https://doi.org/10.1016/j.compstruct.2020.113139.

Materials Research Proceedings 73 (2026) 31-36 https://doi.org/10.21741/9781644904459-7

Finite Element Modeling of Frictional Stick–Slip Behavior in Structural Systems within the CUF Framework

Shabnam KIASAT[1,a *], Matteo FILIPPI[1,b], Alfonso PAGANI[1,c], Erasmo CARRERA[1,d]

[1]MUL[2] Lab, Department of Mechanical and Aerospace Engineering, Politecnico di Torino, Turin, Italy

[a]shabnam.kiasat@polito.it, [b]matteo.filippi@polito.it, [c]alfonso.pagani@polito.it, [d]erasmo.carrera@polito.it

Keywords: Boundary Condition Nonlinearities, Friction, Carrera Unified Formulation, Jenkins

Abstract. Frictional interfaces can influence the nonlinear response of engineering structures because local stick–slip mechanisms affect stiffness, energy dissipation, and overall dynamic behavior. Because interfacial slip is difficult to characterize experimentally, particularly under dynamic loading, numerical models help study friction under controlled conditions. This work investigates integrating a reduced-order frictional element within the Carrera Unified Formulation (CUF). The interface behavior is described by a force–slip law suitable for finite element assembly. The frictional state is updated through a return-mapping procedure, based on the analogy between friction and rate-independent plasticity. The resulting formulation allows localized stick–slip effects in CUF-based structural models while maintaining a direct link between the interface law and the global finite element equations. It may be useful for studying interface effects in jointed structures, composite interfaces, and other systems where local slip plays a relevant role.

Introduction

Frictional interactions are inherent in many engineering structures, particularly at interfaces where relative motion may occur. In aerospace systems, they commonly occur in bolted and riveted joints, lap connections, and panel interfaces, where even small-amplitude slip can modify effective interface stiffness, redistribute vibrational energy, and introduce amplitude-dependent damping [1, 2, 3]. In advanced composite structures, frictional effects arise at ply interfaces and in partially bonded or delaminated regions, where local sliding and intermittent contact can dissipate energy, alter the laminate's apparent stiffness, and promote progressive interface degradation [4]. Similarly, in mechanical assemblies, contact interfaces and jointed components often exhibit friction-induced nonlinear behavior, so that the dynamic response may change with excitation amplitude through stiffness softening, hysteretic energy loss, and resonance frequency shifts [5]. These examples highlight how localized stick–slip mechanisms at interfaces can propagate from small-scale contact regions to affect the global structural response. As a result, accounting for frictional effects is important for improving the prediction of structural systems involving interface nonlinearities.

Direct experimental characterization of interfacial frictional slip remains difficult, especially under dynamic loading. Frictional motion often occurs at buried or confined interfaces, where direct observation requires dedicated measurement techniques and is subject to considerable uncertainty, particularly at high oscillation rates and when contact stiffness and interface state evolve during the test. Moreover, separating actual frictional sliding from the accompanying elastic deformation of the interface is not straightforward. In composite structures, another challenge is distinguishing friction-induced dissipation from other damping sources, such as

Content from this work may be used under the terms of the Creative Commons Attribution 3.0 license. Any further distribution of this work must maintain attribution to the author(s) and the title of the work, journal citation and DOI. Published under license by Materials Research Forum LLC.

Materials Research Proceedings 73 (2026) 31-36 https://doi.org/10.21741/9781644904459-7

viscoelastic losses in the resin. These limitations motivate the use of numerical models to support prediction and to isolate frictional mechanisms under reproducible conditions.

However, the very mechanisms that make numerical modeling necessary also make it difficult. This difficulty is not limited to detecting the transition between sticking and slipping, but also lies in capturing how this transition changes the nature of the structural response. Frictional interfaces are governed by path-dependent and non-smooth transitions between sticking and slipping states. Once a local slip occurs, the interface stiffness is no longer constant; the response depends on loading history and excitation amplitude, and the principle of superposition no longer applies. As a result, increasing the excitation level does not simply scale the response; it may change how energy is distributed within the system. Frictional nonlinearities can transfer energy from the fundamental excitation frequency to higher-order harmonic components, leading to response patterns that linear finite element models cannot predict. Capturing these mechanisms is particularly demanding in large-scale simulations, where localized stick–slip events must be represented while maintaining compatibility with the global finite element solution procedure.

Existing approaches to numerically modeling frictional interfaces generally follow two main directions. On one hand, contact-based formulations provide a general framework for simulating frictional interactions, allowing for a detailed description of contact conditions and slip behavior. However, this level of generality often comes at a high computational cost and may lead to convergence difficulties, particularly in large-scale or dynamic simulations involving multiple interfaces. In contrast, reduced-order models, such as Jenkins- or Iwan-type elements, provide a compact representation of friction-induced hysteresis through simplified force–slip relations [6]. Despite their usefulness, these models are often used in simplified settings, and integrating them into advanced structural formulations remains non-trivial.

In this context, the Carrera Unified Formulation (CUF) provides a general framework for structural analysis, in which different levels of kinematic refinement can be introduced within the same finite element formalism [7]. This hierarchical nature allows CUF-based models to incorporate additional element-level or interface-related contributions while remaining compatible with the global finite element assembly. Within such a framework, the local frictional interaction can be expressed via an interface law compatible with the adopted kinematic description and implemented as a nodal interface contribution. Building on this idea, the present work explores integrating a Jenkins-type frictional element into the CUF framework as a reduced-order strategy to represent localized stick–slip behavior at structural interfaces. We adopt the Jenkins model because it reduces the local stick–slip mechanism to a force–slip relation suitable for element-level implementation. By exploiting the analogy between frictional slip and rate-independent plasticity, the formulation provides a structured return-mapping procedure to update the frictional state while preserving a clear physical interpretation of stick–slip transitions. In this way, localized interface effects can be included in a global CUF-based structural model while maintaining a direct link between the interface law and the finite element formulation.

CUF kinematics and relative slip integration

The structural model is formulated within the Carrera Unified Formulation (CUF). In this framework, the three-dimensional displacement field is expressed as a generalized expansion over the cross-section. For a beam-like structure, the displacement vector can be written as Eq. (1).

$$u(x,y,z) = \sum_{\tau=1}^{M} F_{\tau}(x,z)u_{\tau}(y) \tag{1}$$

In Eq. (1), $\mathbf{u} = \{u_x, u_y, u_z\}^T$ is the three-dimensional displacement vector, $F_\tau(x,z)$ are the cross-sectional expansion functions, M is the number of expansion terms, and $\mathbf{u}_\tau(y,t)$ is the vector

Materials Research Proceedings 73 (2026) 31-36 https://doi.org/10.21741/9781644904459-7

of generalized displacement variables associated with the τ-th expansion term. The beam axis is denoted by y, while $x$and z are the cross-sectional coordinates. The generalized displacement variables are interpolated along the beam axis using standard one-dimensional finite element shape functions as in Eq. (2).

$$u_\tau(y) = \sum_{i=1}^{n_e} N_i(y) q_{\tau i} \tag{2}$$

Where $N_i(y)$ are the finite element shape functions, n_e is the number of nodes of the one-dimensional element, and $\mathbf{q}_{\tau i}(t)$ are the nodal degrees of freedom associated with the τ-th CUF expansion term. Substitution of Eq. (2) into Eq. (1) gives the element-level CUF approximation, as in Eq. (3).

$$u(x,y,z) = \sum_{\tau=1}^{M} \sum_{i=1}^{n_e} F_\tau(x,z) N_i(y) q_{\tau i} \tag{3}$$

Frictional effects are introduced through localized reduced-order elements connecting two paired points of the structural model. These paired points may belong to different components, different regions of the same structure, or opposite sides of a contact or jointed interface. For each frictional connection, the relative tangential displacement is obtained from the displacement jump between the two paired points. Denoting the displacement vectors at the two points by $\mathbf{u}^{(1)}$ and $\mathbf{u}^{(2)}$, the relative slip is defined as Eq. (4).

$$w_{\text{rel}} = \mathbf{t}^T (\mathbf{u}^{(1)} - \mathbf{u}^{(2)}) \tag{4}$$

Where $\mathbf{t}$ is the unit vector along the local tangential direction of the frictional interaction. Since the displacement at each paired point is obtained from the CUF approximation, the relative slip can be expressed directly in terms of the element nodal unknowns. Introducing the CUF interpolation matrices $\mathrm{H}^{(1)}$ and $\mathrm{H}^{(2)}$, which evaluate the displacement field at the two paired points, Eq. (4) can be written as Eq. (5).

$$\begin{aligned} w_{\text{rel}} &= \mathrm{t}^T \left(\mathrm{H}^{(1)} - \mathrm{H}^{(2)}\right) \mathrm{q}_e = \mathrm{B}_f \mathrm{q}_e \\ \mathrm{B}_f &= \mathrm{t}^T \left(\mathrm{H}^{(1)} - \mathrm{H}^{(2)}\right) \end{aligned} \tag{5}$$

In Eq. (5) q_e is the vector of CUF nodal degrees of freedom associated with the paired points, and B_f is the frictional kinematic operator. This operator maps the CUF nodal unknowns to the relative tangential slip that drives the local friction law; see Fig. (1).

Materials Research Proceedings 73 (2026) 31-36 https://doi.org/10.21741/9781644904459-7

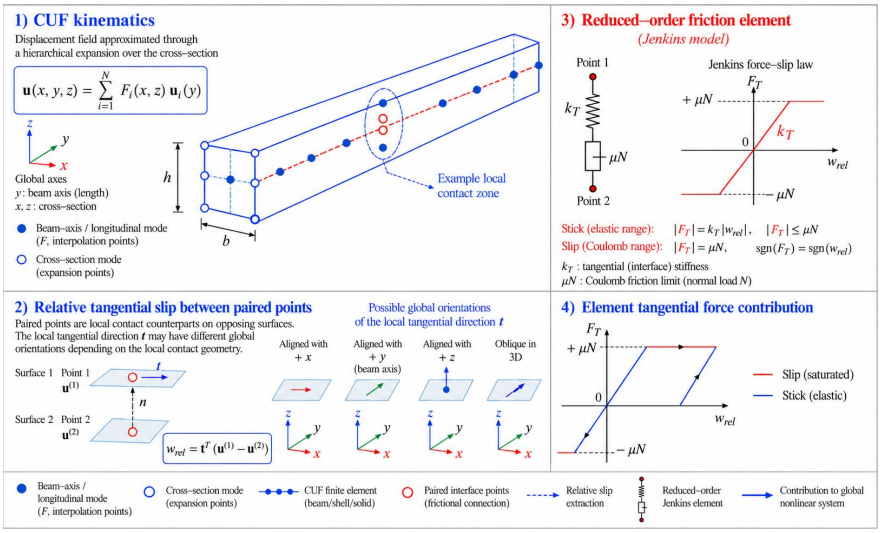

Figure 1. Schematic overview of the CUF–Jenkins coupling strategy

This definition establishes the kinematic link between the CUF structural description and the reduced-order Jenkins friction model. The CUF approximation provides the displacement field at the selected interface points, while the Jenkins element uses the resulting relative slip as its scalar driving variable. Consequently, the frictional force and its tangent contribution can be expressed in terms of the CUF nodal variables and assembled at the element level into the global residual vector and tangent matrix.

Preliminary behavioural verification of the full-slip branch

The preliminary verification is focused on the full-stick branch of the reference analytical model. In that model, the frictional clamp is represented by an equivalent boundary moment, and the response is reported in terms of the clamp/root rotation ($\boldsymbol{\phi_A}$). The full-stick branch corresponds to a frictional moment proportional to this rotation, whereas the full-slip branch is reached when the frictional moment attains the Coulomb limit. In the present CUF-based finite element model, the clamp/contact region is not represented by a single rotational spring at the root. Instead, the frictional constraint is distributed over the interface through several Jenkins-type connections. Therefore, the analytical quantity ($\boldsymbol{\phi_A}$) is approximated here by a locally fitted rotation extracted from a monitored region near the clamp edge, as schematically shown in Fig. 2. The comparison is consequently intended as a behavioural verification of the full-stick mechanism, rather than a one-to-one quantitative reproduction of the analytical curve.

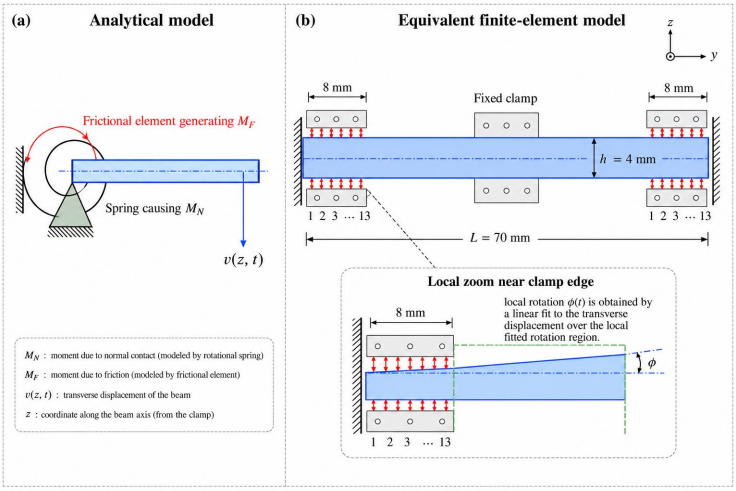

Figure 2. Analytical clamp representation and equivalent CUF–Jenkins FE model. The inset shows the monitored region used to extract the local fitted rotation.

The Jenkins parameters were transferred from the reference model by matching the equivalent rotational stiffness and the limiting friction moment. For ($N_{JK} = 26$) Jenkins connections and an effective arm (r=0.002) m, the tangential stiffness of each Jenkins element was selected as while the limiting force was defined from the Coulomb moment as follows:

$$k_t = \frac{k_F}{N_{JK} r^2} = 9.615 \times 10^9 (N/m)$$

$$F_y = \frac{\mu F_N h}{N_{JK} r} = 0.615\ (N)$$

$$M_{lim} = N_{JK} F_y r \simeq 0.03198\ (N.m)$$

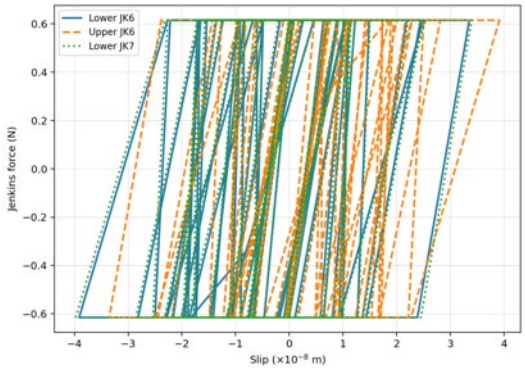

Figure 3. Local Jenkins force–slip response

Which is consistent with the theoretical value ($\boldsymbol{\mu F_N h = 0.032\ N\ m}$). The local hysteretic response is used as the main verification indicator. In the full-slip regime, the Jenkins force must saturate at ($\boldsymbol{F_{jk} \simeq \pm F_y}$), and the equivalent frictional moment must remain close to the Coulomb limit. In Fig. (3), the hysteretic outputs confirm this behaviour. The Jenkins force reaches the prescribed saturation value, the parallel linear contribution is zero, and the inferred slip state remains close to full-slip. This confirms that the local frictional elements operate in the intended regime. Figure (4) indicates the full stick behaviour predicted by the analytical and the FE models.

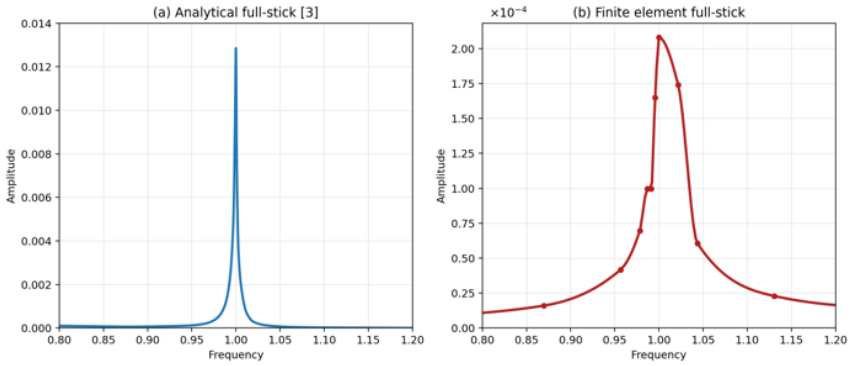

Fig. 4. (a) Approximate replotted analytical full-stick curve from Ref. [3]. (b) Full-stick response predicted by the present FE model.

Conclusion

The present work establishes the basis for incorporating localized reduced-friction elements into CUF-based finite element models and provides a preliminary behavioural verification of the stick-slip response. Future work will focus on obtaining amplitude-dependent frequency response due to the friction nonlinear effects and validating the results qualitatively against the analytical trends and quantitatively against a commercial finite element model.

References

[1] S. Kiasat, M. Filippi, A. S. Nobari, and E. Carrera, "A study of frictional contact effects on modal dissipation characteristics in a debonded structure," International Journal of Non-Linear Mechanics, 2026. https://doi.org/10.1016/j.ijnonlinmec.2026.105389.

[2] S. Kiasat, "Novel approach to damage detection in laminated structures: modal damping as a damage indicator," Materials Research Proceedings, vol. 42, pp. 31–37, 2024. https://doi.org/10.21741/9781644903193-8.

[3] S. Kiasat, A. S. Nobari, and M. Filippi, "Time-domain analysis of delaminated sandwich structures: Viscoelastic and frictional damping effects," Mechanics of Advanced Materials and Structures, vol. 33, no. 1, 2026. https://doi.org/10.1080/15376494.2025.2535741.

[4] K. Asadi, H. Ahmadian, and H. Jalali, "Micro/macro-slip damping in beams with frictional contact interface," Journal of Sound and Vibration, vol. 331, no. 21, pp. 4704–4712, 2012. https://doi.org/10.1016/j.jsv.2012.05.026

[5] M. Tüfekci, J. P. Dear, and L. Salles, "Forced vibration analysis of beams with frictional clamps," Applied Mathematical Modelling, vol. 128, pp. 450–469, 2024. https://doi.org/10.1016/j.apm.2024.01.031

[6] W. D. Iwan, "On a class of models for the yielding behavior of continuous and composite systems," Journal of Applied Mechanics, vol. 34, no. 3, pp. 612–617, 1967. https://doi.org/10.1115/1.3607751

[7] E. Carrera, M. Cinefra, M. Petrolo, and E. Zappino, Finite Element Analysis of Structures through Unified Formulation. Hoboken, NJ, USA: Wiley, 2014. https://doi.org/10.1002/9781118536643

Materials Research Proceedings 73 (2026) 37-42 https://doi.org/10.21741/9781644904459-8

Experimental and Numerical Analysis of Compression and Shear Wrinkling in Sandwich Beams under Three-Point Bending

Befekadu GASHE[1,2,a*], Abdulmaliq ALAWODE[1,3,b], Samuel RIVALLANT[1,c], and Bruno CASTANIE[1,d]

[1]Institut Clement Ader (ICA), CNRS UMR 5312, ISAE-SUPAERO, INSA, IMT Mines Albi, University of Toulouse, 31400 Toulouse, France

[2]Department of Structures for Engineering and Architecture, University of Naples Federico II, Via Claudio 21,80125 Naples, Italy

[3]Department of Civil Construction, and Environmental Engineering, The University of Alabama, Tuscaloosa, AL 35487, USA

[a]befekaduchalew.gashe@unina.it, [b]alawodeabdulmaliq@gmail.com, [c]samuel.rivallant@isae-supaero.fr, [d]bruno.castanie@insa-toulouse.fr

Keywords: Sandwich, Three-Point Bending, Compression, Wrinkling, Shear Wrinkling, Finite Element Analysis, Digital Image Correlation

Abstract. Wrinkling is a local instability that can greatly reduce the load-carrying capacity of lightweight sandwich structures. This paper presents an experimental and numerical study of the wrinkling response of sandwich beams tested under three-point bending, with particular attention to the difference between compression-driven and shear-driven wrinkling. The specimens were made of glass fiber-epoxy skins bonded to a PMI ROHACELL® foam core. Two different stacking configurations were selected so that one specimen was more likely to develop compression wrinkling, while the other was intended to promote shear wrinkling. The experimental campaign was carried out to capture both the overall structural response and the local deformation patterns associated with the onset of instability. Force and displacement were recorded throughout the tests, and Digital Image Correlation (DIC) was used to monitor the deformation field and follow the development of wrinkling in detail. Alongside the experiments, finite element analyses were performed in ABAQUS, and the numerical results were compared with the test observations as well as with available analytical predictions. The comparison showed a good agreement for the compression-wrinkling case, where the numerical model was able to reproduce the measured behaviour with reasonable accuracy. In contrast, for the shear-wrinkling case, the numerical simulations predicted higher wrinkling loads than those observed experimentally. This difference suggests that shear wrinkling is more sensitive to modelling choices, especially geometric imperfections and mesh discretization. Overall, the results show that combining experiments, numerical simulations, and analytical estimates is a useful approach for better understanding wrinkling mechanisms and improving the prediction of instability-related failure in sandwich structures.

Introduction

Sandwich beams are widely used when high bending stiffness must be achieved with low structural mass, but their efficiency depends on the stability of thin load-carrying skins supported by a much more compliant core [1, 2]. Among the local instability modes of these systems, wrinkling is especially critical because it develops over a short wavelength, rapidly reduces stiffness, and can precipitate skin failure, core damage, or interface failure before global instability becomes dominant [3,4]. Classical wrinkling theory established that the critical state is governed by the coupled stiffness of the face sheet and the core, and it still provides the basis for preliminary sizing

Content from this work may be used under the terms of the Creative Commons Attribution 3.0 license. Any further distribution of this work must maintain attribution to the author(s) and the title of the work, journal citation and DOI. Published under license by Materials Research Forum LLC.

under compressive loading [5,6,7,8]. In practice, however, sandwich components are rarely subjected to pure compression [9]. Bending, shear, laminate anisotropy, and unavoidable manufacturing imperfections can modify both the onset load and the shape of the unstable mode, so predicting compression and shear-driven wrinkling remains more difficult than the idealized classical case suggests [10,11,12]. Against this background, the present paper investigates two independent beam-scale configurations developed to study compression-driven and shear-driven wrinkling under three-point bending. The first configuration is designed to promote local instability of the compressed face sheet, while the second configuration is designed to favor wrinkling of the thin side faces subjected mainly to shear. Although the two tests are analyzed separately, they share the same general beam geometry, material system and loading arrangement, which allows a consistent comparison of the two instability mechanisms. Full-field experimental measurements are combined with finite-element buckling simulations to evaluate the predicted onset load, wrinkle shape and location of instability. Attention is given to the difference between the compression case, where the numerical prediction is relatively stable and close to the experimental response, and the shear case, where the results are more sensitive to mesh refinement, geometric imperfections and local modelling assumptions [13]. The objective of this paper is therefore to present a concise experimental–numerical comparison of these two wrinkling configurations and to identify the current limitations of the numerical approach for shear-dominated wrinkling.

Methodology

Two sandwich-beam families were manufactured to trigger different local instability modes within the same three-point-bending configuration as shown in Fig. 1(a,b). All specimens had nominal overall dimensions of 500 mm × 50 mm × 50 mm and consisted of glass/epoxy skins bonded to a 50 mm-thick PMI foam core (ROHACELL 51 WF) as the mechanical properties for the skin and the foam are depicted on Table 1 and Table 2 respectively. Plywood inserts were embedded at the loading and support regions to reduce local foam crushing with the dimension of 50×50×15 mm as illustrated on Table 3. For the shear-wrinkling configuration, the upper and lower skins were kept relatively stiff, while the side faces were reduced to a single ±45 fabric ply so that instability would preferentially develop in the shear-loaded faces. The corresponding layups on the top five 0° UD plies + two 45° fabric plies $[0_5/[+45/-45]_2]$, bottom five 0° UD plies + one 45° fabric ply $[0_5/\pm45]$, and side faces one 45° fabric ply [±45]. For the compression-wrinkling configuration, the lower skin was intentionally thinned so that bending-induced compression controlled the first local buckle; the layup on the top is one 0° UD ply + two 45° fabric plies $[0/[+45/-45]_2]$, bottom one 0° UD ply + one 45° fabric ply [0/±45], and side faces one 45° fabric ply [±45]. Specimens were made by hand lay-up with manual impregnation and cured in a mould [13]. Tests were performed on a manually operated three-point-bending rig and are therefore described here as quasi-static. Load was measured with a 10 kN force cell, and vertical displacement with an LVDT mounted on the loading arm: 25 mm range for the shear series and 20 mm for the compression series. Two 5 MP DIC cameras (2462 × 2052 px) monitored the unstable region, viewing the side faces for the shear specimens and the lower face for the compression specimens; the supports were raised in the latter case to maintain optical access. Before loading, DIC was used to map the initial out-of-plane shape; during loading, force, displacement, and full-field images were acquired continuously. Wrinkling onset can be defined compactly as the first localized short-wavelength out-of-plane mode visible in DIC, confirmed by the first load drop or a clear departure from the initial linear load–displacement response. Six specimens were tested in each configuration. Repeatability was good in initial stiffness, but onset loads showed marked scatter, especially in the shear series, consistent with the measured imperfection field: about 0.1 mm maximum lower-face deviation in the compression specimens and up to about 0.8 mm on some shear-test side faces [13].

Materials Research Proceedings 73 (2026) 37-42 https://doi.org/10.21741/9781644904459-8

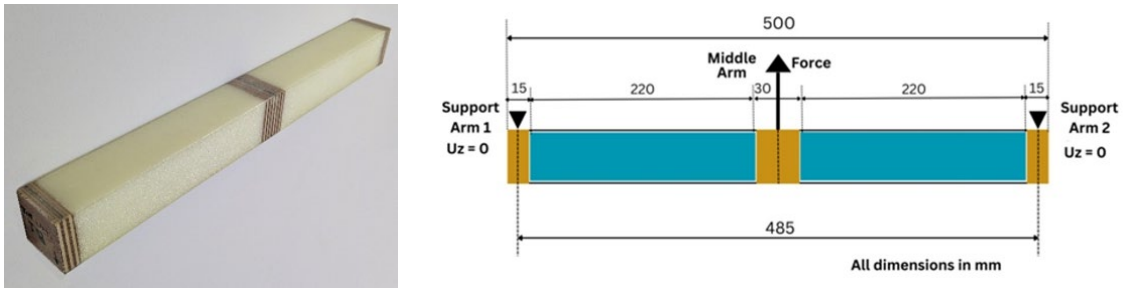

(a) (b)

Fig. 1 Specimen: overall geometry (a), three-point bending test principle and specimen dimension (blue: foam; brown: plywood) (b)

Table 1 Mechanical properties of skin materials

Skin Material	E_1 [MPa]	E_2 [MPa]	ν_{12}	G_{12} [MPa]	G_{13} [MPa]	G_{23} [MPa]	Thickness, ts [mm]
Unidirectional	38,000	10,000	0.25	4000	4000	4000	0.30
Bidirectional [Fibers]	23,000	23,000	0.098	2900	2900	2900	0.16

Table 2 Mechanical properties of isotropic core material

Core Material	E [MPa]	G [MPa]	Density [kg/m^3]	Shear Strength [MPa]	Thickness, tc [mm]
Rohacell 51 WF	75	24	52	0.8	50

Table 3 Mechanical characteristics of plywood material [14]

Plywood Material	E_{11} [MPa]	E_{22} [MPa]	E_{33} [MPa]	G_{12} [MPa]	G_{13} [MPa]	G_{23} [MPa]	ν_{12}	ν_{13}	ν_{23}	Density [kg/m^3]
Poplar	10,900	1,003	469	818	752	120	0.392	0.318	0.329	480
Okoume	9000	828	387	675	621	99	0.392	0.312	0.329	430

Numerical Results

The numerical investigation was carried out using a full-scale finite-element model of the three-point-bending configuration in ABAQUS/Standard 2022 as illustrated on Fig. 2(a,b) [13]. The loading nose and the two supports were modelled as rigid bodies, while the composite skins were represented by S4R shell elements. The foam core and the plywood inserts were modelled using C3D8R reduced-integration solid elements. This modelling strategy allowed the global bending response and the local wrinkling modes to be captured within the same numerical framework. A linear eigenvalue buckling analysis was first used to estimate the critical wrinkling load and the associated mode shape. For the compression-wrinkling configuration, the numerical response showed good mesh convergence.

Materials Research Proceedings 73 (2026) 37-42 https://doi.org/10.21741/9781644904459-8

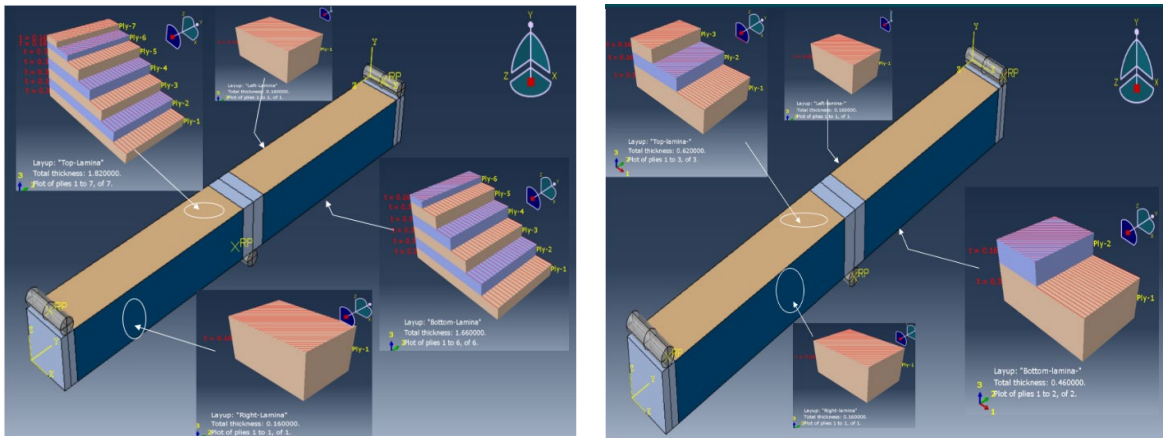

(a) (b)

Fig. 2 Finite elements models with face lay-up definition: shear wrinkling (a) and compression wrinkling (b)

The predicted critical load decreased slightly from 4.20 kN for a 5 mm mesh to 3.94 kN for a refined 0.7 mm mesh, while the corresponding full wavelength changed from approximately 20 mm to 12.7 mm. The predicted wrinkle appeared on the lower compressed skin close to the loading region, in agreement with the experimental observations. The load–displacement comparison shows in Fig. 3(a) that the numerical model reproduces the initial stiffness of the compression specimens well. The predicted buckling load of 3.94 kN is close to the main experimental failure-load group (3.56–3.91 kN), although two specimens failed earlier because of manufacturing scatter or local imperfections [13].

The same modelling approach was then applied to the shear-wrinkling. In this case, the numerical response was much more sensitive to mesh refinement. The first eigenvalue increased from about 8.38 kN for the 0.7 mm mesh to approximately 15.78 kN for the 5 mm mesh, while the predicted full wavelength increased from 3.97 mm to about 11.2 mm. Unlike the compression case, the numerical shear wrinkles tended to localize near the support regions, whereas the experimental wrinkles were mainly observed around the central part of the beam. This discrepancy shows that shear wrinkling is more difficult to predict using a purely linear buckling approach. For the shear specimens as shown on Fig. 3(b), the numerical model also gives a comparable initial stiffness, but it clearly overestimates the failure load. The predicted buckling load of 8.38 kN overestimates the experimental shear-wrinkling loads, which ranged from about 1.44 kN to 4.39 kN [13].

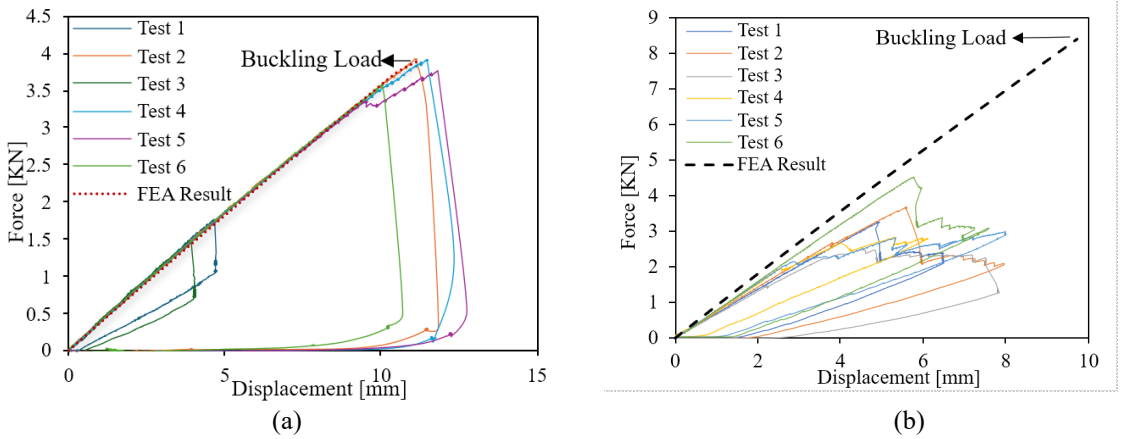

(a) (b)

Fig. 3 Load–displacement relationship graph for experimental and numerical results compression (a) and shear (b)

Conclusions

This study presented a compact experimental and numerical investigation of compression and shear wrinkling in glass/epoxy–PMI foam sandwich beams tested under three-point bending. By modifying the laminate stacking sequence, the same test configuration was used to activate two different local instability mechanisms: compression wrinkling on the lower face sheet and shear wrinkling on the thin side faces. The finite-element model reproduced the compression-wrinkling behaviour with good agreement in terms of initial stiffness, critical load and wrinkle location, showing that linear eigenvalue buckling analysis can provide a useful prediction for compression-dominated instability. In contrast, the shear-wrinkling case was less accurately captured, with numerical predictions overestimating the experimental onset load and showing stronger mesh sensitivity and differences in wrinkle location. It should be possible to use more advanced models incorporating initial imperfections, skin-interface delamination, and foam failure under tension or compression, as described in reference [15,16].

References

[1] A. Petras and M. P. F. Sutcliffe, “Failure mode maps for honeycomb COMPOSITE STRUCTURES sandwich panels,” 1999.

[2] I. M. Daniel, E. E. Gdoutos, I. M. Daniel, R. R. Mccormick, and E. E. Gdoutos, “Failure Modes of Composite Sandwich Beams,” 2009.

[3] L. Léotoing, S. Drapier, and A. Vautrin, “First applications of a novel unified model for global and local buckling of sandwich columns,” 2002.

[4] E. E. Gdoutos, I. M. Daniel, K.-A. Wang, and R. R. Mccormick, “Compression facing wrinkling of composite sandwich structures,” 2002. [Online]. Available: www.elsevier.com/locate/mechmat

[5] N. J. HOFF and S. E. MAUTNER, “Bending and Buckling of Sandwich Beams,” *Journal of the Aeronautical Sciences*, vol. 15, no. 12, pp. 707–720, Dec. 1948. https://doi.org/10.2514/8.11699

[6] S. Yusuff, “Theory of Wrinkling in Sandwich Construction,” *The Journal of the Royal Aeronautical Society*, vol. 59, no. 529, pp. 30–36, Jan. 1955. https://doi.org/10.1017/s0368393100131761

[7] H. G. ALLEN, “WRINKLING AND OTHER FORMS OF LOCAL INSTABILITY,” in *Analysis and Design of Structural Sandwich Panels*, Elsevier, 1969, pp. 156–189. https://doi.org/10.1016/b978-0-08-012870-2.50012-2

[8] G. S. Gough, C. F. Elam, G. H. Tipper, and N. A. De Bruyne, “The Stabilisation of a Thin Sheet by a Continuous Supporting Medium,” *The Journal of the Royal Aeronautical Society*, vol. 44, no. 349, pp. 12–43, Jan. 1940. https://doi.org/10.1017/s036839310010495x

[9] V. Birman and C. W. Bert, “Wrinkling of composite-facing sandwich panels under biaxial loading,” *Journal of Sandwich Structures and Materials*, vol. 6, no. 3, pp. 217–237, May 2004. https://doi.org/10.1177/1099636204033643

[10] M. Ginot, C. Bouvet, B. Castanié, M. D’Ottavio, J. Serra, and N. Mahuet, “Local buckling on large sandwich panels applied to light aviation: Experimental and computation dialogue,” *Int. J. Solids Struct.*, vol. 268, Apr. 2023. https://doi.org/10.1016/j.ijsolstr.2023.112170

[11] L. Fagerberg and D. Zenkert, “Effects of anisotropy and multiaxial loading on the wrinkling of sandwich panels,” *Journal of Sandwich Structures and Materials*, vol. 7, no. 3, pp. 177–194, May 2005. https://doi.org/10.1177/109963205048525

[12] L. Fagerberg and D. Zenkert, “Imperfection-induced wrinkling material failure in sandwich panels,” *Journal of Sandwich Structures and Materials*, vol. 7, no. 3, pp. 195–219, May 2005. https://doi.org/10.1177/1099636205048526

[13] B. Gashe, A. Alawode, S. Rivallant, and B. Castanié, “Shear and Compression Wrinkling Experimental Analysis with a Sandwich Beam Submitted to Three-Point Bending,” *Materials*, vol. 18, no. 18, Sep. 2025. https://doi.org/10.3390/ma18184286

[14] J. Susainathan, F. Eyma, E. DE Luycker, A. Cantarel, and B. Castanie, “Numerical modeling of impact on wood-based sandwich structures,” *Mechanics of Advanced Materials and Structures*, vol. 27, no. 18, pp. 1583–1598, Sep. 2020. https://doi.org/10.1080/15376494.2018.1519619

[15] M. Ginot, C. Bouvet, B. Castanié, J. Serra, and N. Mahuet, “Local buckling on large sandwich panels used in light aviation: Experimental setup and failure scenarios,” *Compos. Struct.*, vol. 304, Jan. 2023. https://doi.org/10.1016/j.compstruct.2022.116439

[16] B. CASTANIE, C. BOUVET, and M. Ginot, “Review of composite sandwich structure in aeronautic applications,” Aug. 01, 2020, *Elsevier B.V.* doi: 10.1016/j.jcomc.2020.100004

Materials Research Proceedings 73 (2026) 43-46 https://doi.org/10.21741/9781644904459-9

Low-velocity/Low-energy Impact Response of Khaya (*Khaya ivorensis*) for Sustainable Mobility Applications

Riccardo HOUNGBEGNON[1,2,a *], Bruno CASTANIÉ[3,b], Valery DOKO[2,c], José XAVIER[4,d], Rostand MOUTOU PITTI[1,5,e]

[1]Université Clermont Auvergne, CNRS, Clermont Auvergne INP, Institut Pascal, Clermont-Ferrand, France

[2]Université d'Abomey-Calavi, Ecole Polytechnique d'Abomey-Calavi, Abomey-Calavi, Bénin

[3]Univ Toulouse, IMT Mines Albi, INSA Toulouse, ISAE-SUPAERO, CNRS, ICA, Toulouse, France

[4]UNIDEMI, Department of Mechanical and Industrial Engineering, Faculdade de Ciências e Tecnologia NOVA FCT, Universidade NOVA de Lisboa, Caparica, Portugal

[5]CENAREST, IRT, Libreville, Gabon

[a]mahugnon_riccardo.houngbegnon@doctorant.uca.fr, [b]bruno.castanie@insa-toulouse.fr, [c]dokovalery@yahoo.fr, [d]jmc.xavier@fct.unl.pt, [e]rostand.moutou_pitti@uca.fr

Keywords: Wood, Mobility, Low-Velocity, Low-Energy Impact, Energy Absorption

Abstract. The growing urgency of environmental protection and the need to reduce greenhouse gas emissions are driving a transition toward more sustainable materials in engineering applications. In the mobility sector, particular attention is being paid to the integration of renewable and low-carbon materials capable of combining structural performance with reduced environmental impact. Among bio-based materials, wood emerges as a promising candidate due to its renewability, low carbon footprint, and favorable mechanical properties. Its high strength-to-weight ratio and natural energy-absorbing capacity make it particularly attractive for applications where impact resistance and lightweight design are critical. This study examines the impact resistance of khaya (*Khaya ivorensis*). This species was selected to assess the potential of a tropical hardwood for advanced engineering applications. Drop-weight impact tests were conducted at low-velocity/low-energy levels, which correspond to common uses of structures and that are critical for innovative structures. At impact energies of 5, 10 and 15 J, *Khaya ivorensis* absorbed on average 3.1, 6.7 and 10.2 J, respectively, showing a stable and predictable response governed by stiffness rather than by extensive deformation.

Introduction

Among recent innovative developments in wood utilization, the Japanese species *Magnolia obovata* has drawn particular attention, notably due to its use in the design of the first wooden satellite, launched in December 2024 as part of the Lignosat project [1]. This project highlighted the exceptional mechanical and durability properties of wood under extreme conditions, thereby opening the way to new possibilities for its use in complex technical contexts. However, due to geographical constraints and issues related to forest exploitation, it has become necessary to identify alternative wood species capable of substituting for *Magnolia obovata*, particularly for applications in environments subjected to severe constraints, such as mobility infrastructures [1, 2]. *Khaya ivorensis*, an African tropical wood species, emerges as a promising candidate for this comparison due to its attractive properties, notably its density, hardness, dimensional stability, highly interlocked grain structure, as well as its availability.

Content from this work may be used under the terms of the Creative Commons Attribution 3.0 license. Any further distribution of this work must maintain attribution to the author(s) and the title of the work, journal citation and DOI. Published under license by Materials Research Forum LLC.

Materials Research Proceedings 73 (2026) 43-46 https://doi.org/10.21741/9781644904459-9

Throughout their service life, all mobility structures may be subjected to various impacts that could weaken them and prove detrimental to their integrity [3]. It is therefore undeniable that impact resistance is an important indicator for the selection of wood species. Impact tests on wood-based materials or wood composites aim to characterize their behavior under loading conditions, whether involving low-, medium-, or high-velocity impacts. This study aims to improve the understanding of the impact resistance behavior of *Khaya ivorensis* through drop-weight impact testing and focuses on low-energy/low-velocity impacts, which correspond to the common service conditions encountered by mobility structures.

Methodology

Khaya ivorensis, also known as African mahogany, is a valuable wood species highly appreciated for its aesthetic and mechanical properties (Fig. 1). Khaya used in this study was sourced from the Upper Ouémé forest, located in southern Benin. At a moisture content of 12%, *Khaya ivorensis* exhibits an average density of 824 kg/m³. As a moderately dense and dimensionally stable tropical species, this species offers high mechanical strength, making it a suitable candidate for the study of wood behavior in mobility-related structural applications [1, 2].

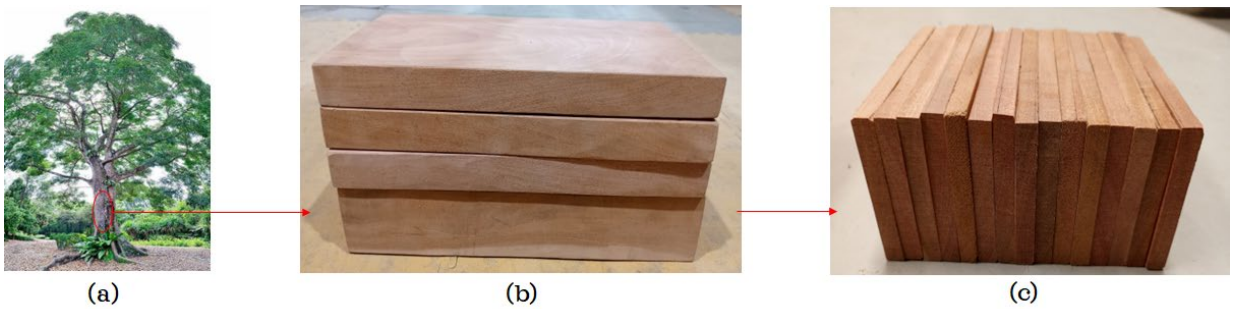

Fig. 1: Khaya ivorensis (a) tree; (b) planks; (c) specimens.

To perform impact tests on *Khaya ivorensis* specimens, we machined plates measuring 150x100x15 mm3 based on the AIRBUS AITM 1-0010 standard, which was defined for composite materials (fiber-resin) similar to wood. After machining, the samples were stored in a climate-controlled room at a temperature of 23°C and a relative humidity of 45%.

The drop-weight impact tests were performed at three energy levels (5J, 10J, and 15J), using a device consisting of an instrumented impactor equipped with a force sensor, a mechanical test bench, a laser velocimeter, a laser displacement sensor positioned beneath the specimen, a Genesis rapid acquisition system, and Perception software. The drop-weight principle consists in dropping an instrumented mass, guided in a tube, onto a sample plate [3]. A mass of 2.08 kg was chosen to reach impact velocities of up to 5m/s and fitted with a hemispherical impactor 16 mm in diameter. Fig. 2 shows the entire experimental setup. The test specimens were tested at an average moisture content of 11%.

Materials Research Proceedings 73 (2026) 43-46 https://doi.org/10.21741/9781644904459-9

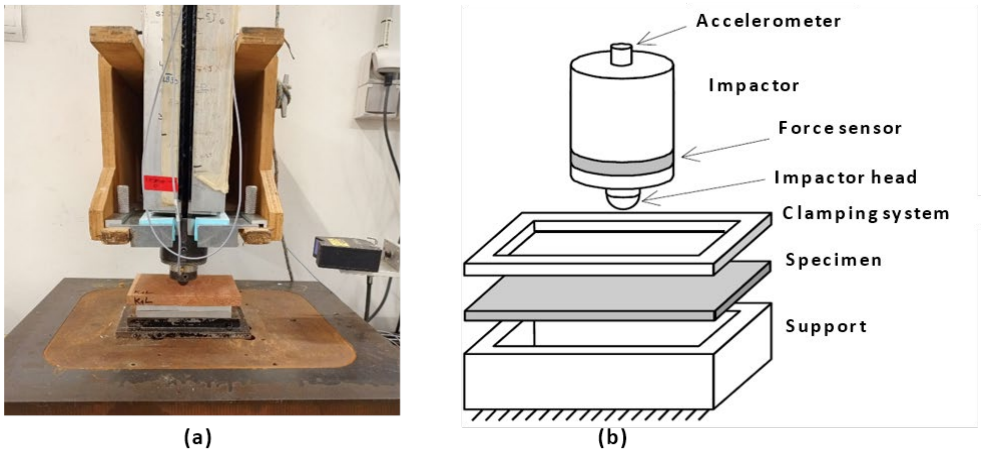

Fig. 2: (a) Experimental setup of drop-weight impact tests; (b) Equipment

Results

Force–displacement curves obtained on Khaya specimens at 5, 10 and 15 J are shown in Fig. 3 (three representative curves per energy level). They show a progressive increase in force followed by pronounced load drops before reaching the peak, indicating progressive damage development under impact. The maximum forces reached are high for all energy levels, reflecting the high density and intrinsic stiffness of this wood species. However, the associated displacements remain moderate compared with those of other hardwoods, indicating an energy absorption capacity that is more governed by strength than by extensive deformation.

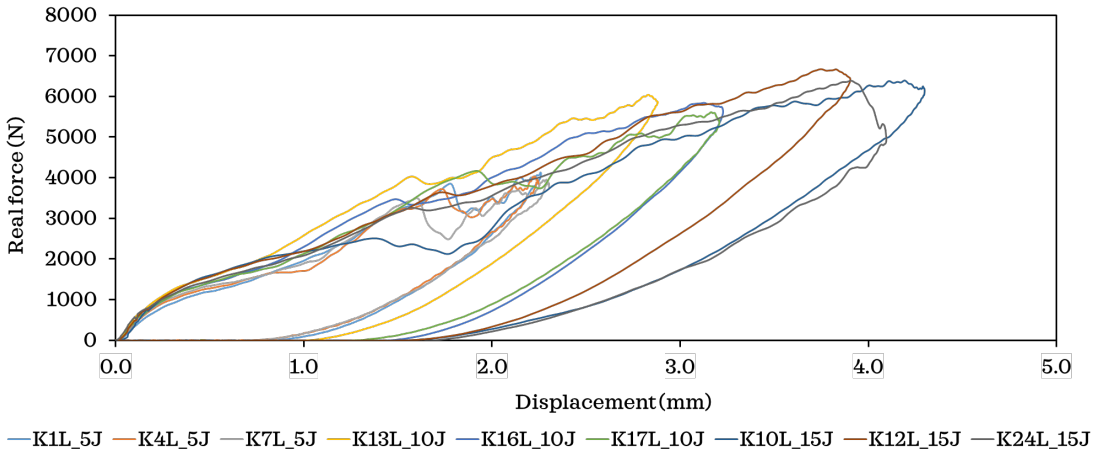

Fig. 3: Force-displacement curves of Khaya ivorensis specimens at 5, 10 and 15J

The impact resistance of Khaya was subsequently calculated numerically by integrating the force–displacement curves [3]. Fig. 4 shows the absorbed energy and specific absorbed energy of Khaya specimens at 5, 10, and 15 J. At these energy levels, Khaya absorbs approximately 3.08 J, 6.68 J, and 10.15 J, respectively, reflecting a progressive increase in dissipated energy with the impact level. The corresponding specific absorbed energies (3.76, 8.50, and 12.56 J·cm³/g) remain moderate but increase steadily, indicating an impact resistance behavior dominated by material stiffness rather than by a high deformation capacity.

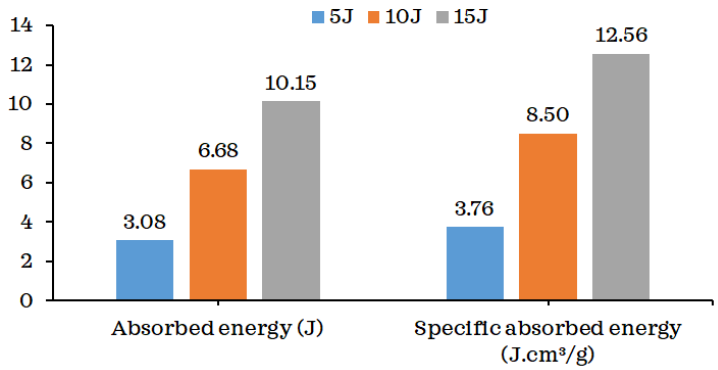

Fig. 4: Energy and specific absorbed energy of Khaya specimens

Conclusion

This paper presents a study of the impact behavior of a tropical African species with potential for use in mobility applications. The results show that Khaya exhibits a progressive increase in absorbed and specific absorbed energy with increasing impact energy, confirming a stable and predictable response under low-velocity/low-energy impact. Although its specific energy absorption remains moderate, the combination of high force levels and limited indentation highlights a behavior governed by structural rigidity rather than extensive deformation, making Khaya a material of interest for sustainable mobility applications where impact tolerance and dimensional stability are required. Future work will include impact testing of Khaya under cryogenic conditions, followed by a systematic investigation of the influence of moisture variations on its impact response.

Acknowledgment

The authors would like to express their gratitude to the French government through the Eiffel Excellence Program and the National Research Agency (ANR) through DIAMWOOD ANR PRCE N◦ 23-CE22-0006-03 project for the support provided for this work. Financial support from national funds through FCT, I.P. – Fundação para a Ciência e a Tecnologia, under the project UID/00667/2025 (https://doi.org/10.54499/UID/00667/2025) (UNIDEMI), is also gratefully acknowledged.

References

[1] B. Castanié, et al., « Wood and plywood as eco-materials for sustainable mobility: A review.» Composite Structures, Vol 329, p 117790, 2024. https://doi.org/10.1016/j.compstruct.2023.117790

[2] R. Houngbegnon et al., « Fracture toughness of Khaya ivorensis and Magnolia obovata for mobility applications », Theoretical and Applied Fracture Mechanics, vol. 141, p. 105209, 2026. https://doi.org/10.1016/j.tafmec.2025.105209

[3] J. Susainathan, F. Eyma, E. De Luycker, A. Cantarel, et B. Castanie, « Experimental investigation of impact behavior of wood-based sandwich structures », Composites Part A: Applied Science and Manufacturing, vol. 109, p. 10-19, 2018. https://doi.org/10.1016/j.compositesa.2018.02.029

Materials Research Proceedings 73 (2026) 47-50 https://doi.org/10.21741/9781644904459-10

Composite Reinforced Railway Modelling as a Step to Help in Design and Conception

Jean-Emmanuel CHAMBE[1,a *], Hamza BENYAHIA[1], Léo SUDRIÈS[1,b], Joël SERRA[1], Wiyao-Leleng AZOTI[1,c], Bruno CASTANIÉ[1,d]

[1]Université de Toulouse, Institut Clément Ader, UMR CNRS 5312, INSA/UPS/ISAE-SUPAERO/IMT-Mines Albi, Toulouse, France

[a]jean-emmanuel.chambe@insa-toulouse.fr, [b]leo.sudries@insa-toulouse.fr, [c]wiyao-leleng.azoti@insa-toulouse.fr, [d]bruno.castanie@insa-toulouse.fr

Keywords: Composite Railway, Finite Element Model, Thermoplastic, Pultrusion

Abstract. In this paper, a numerical Finite Elements Model used to help in the design and conception of a fully composite railway infrastructure is presented. The main objective is to address a cost efficient as well as an ecological cost acceptable solution that meets the structural and mechanical criteria for a lightweight train service. A satisfactory solution has been reached after numerous iterations, in respects to the loads, constraints and geometric restrictions suiting the standards requirement. Only the numerical aspect to craft the preliminary design is presented in this paper.

Introduction

With an objective of reducing financial and environmental costs in the rail transportation sector, while extending, strengthening current infrastructures and deploying a better inter-city connectivity offer, the replacement of conventional iron rails with composite material rails is being studied.

Solutions adapted for light railway infrastructures made with composite materials are studied with having reducing environmental costs in mind in the transport sector. The design of composite rails requires consideration of dimensioning, in particular mechanical and structural strength. To this end, both an experimental study is carried out as well as a numerical model being developed to determine the orthotropic properties of pultruded composite materials made of thermoplastic matrix and glass or carbon or bio-sourced reinforcement fibers. Woven and UD plies are been tested. The stacking is also studied and the thickness evaluated. Only the numerical aspect of the study is presented in this paper. Loads and speeds conditions were calculated based on prototypes of actual lightweight train cars, namely Ecotrain and Draisy [1]. A conceptual design illustration is given Figure 1.



Figure 1: Concept design of a lightweight train car Draisy [1].

Content from this work may be used under the terms of the Creative Commons Attribution 3.0 license. Any further distribution of this work must maintain attribution to the author(s) and the title of the work, journal citation and DOI. Published under license by Materials Research Forum LLC.

Materials Research Proceedings 73 (2026) 47-50 https://doi.org/10.21741/9781644904459-10

The composite rails production is intended to come from the pultrusion process [2] with design constraints provided by the manufacturing partners. The mechanical and structural strength must meet the expected standards requirement in terms of loads, constraints criteria and geometric restrictions suited for a lightweight train. These are given through IN 1895 V2 and IN 2640 Standards for railway maintenance and geometry.

Methodology

Initial calculations and modulizations were based on current specifications and inspired by the actual loads of railway transportation sector. Contacts, input loads, generated forces, reaction stress and global mechanical response in the composite rail beam were expected to be identical as in the iron rail beam, though at different levels and adapted values. A better understanding of the forces induced by a railway wheel on a rail is given in numerous studies [3, 4] and depicted in Figure 2.

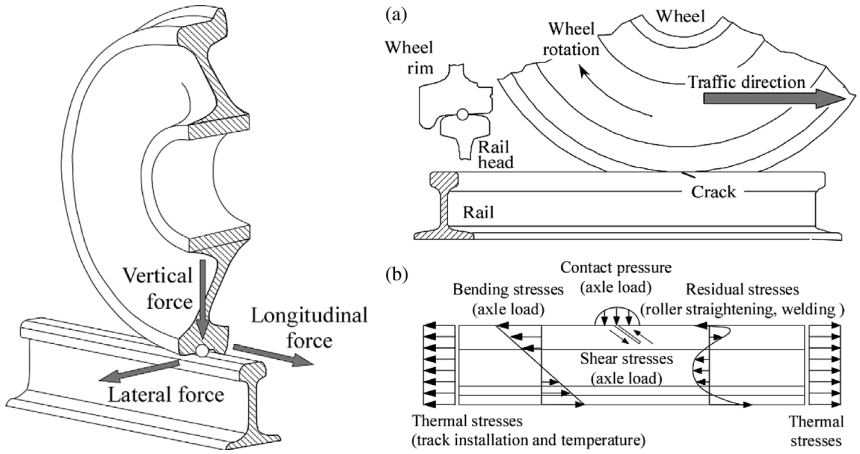

Figure 2: (left) Vertical, Longitudinal and Lateral forces introduced by a railway wheel on a rail, (right) (a) Wheel rolling on a welded rail, (b) Contact and longitudinal stresses components [3].

The contact zone for loads application has been numerically evaluated. This was found to be in accordance with previous studies [4, 5] focused on contact pressure on the wheel–rail interface. A non-symmetric loading is applied on the rail, per standards of the railway transportation usage. The vertical force is applied at an angle of 0° relative to the rail's vertical axis, for a comparison with Hertz's theory, before tilting the rail geometry to an angle of 1/20th (~approximatively 2,86°) to correspond to actual railway installations. Details and focus are depicted in Figure 3 and 4.

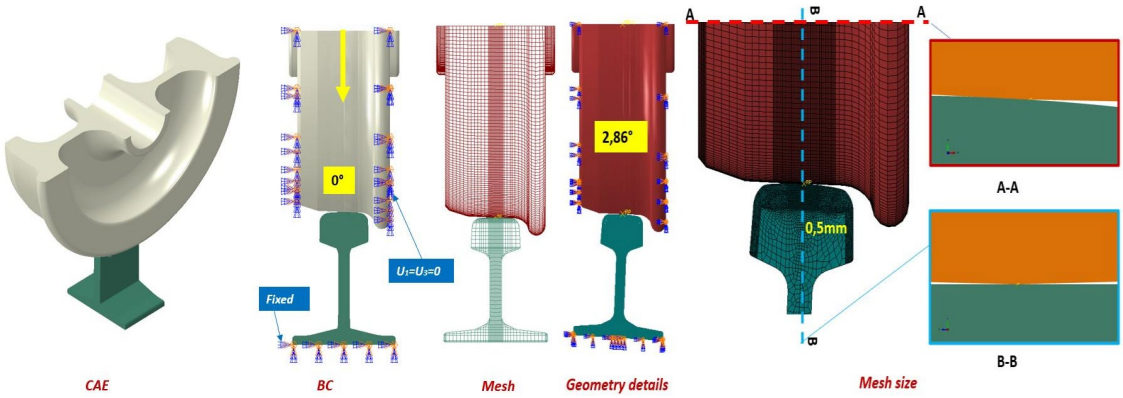

Figure 3: CAE, Boundary Conditions, Geometry details, Contact and Mesh for the wheel/rail.

Materials Research Proceedings 73 (2026) 47-50 https://doi.org/10.21741/9781644904459-10

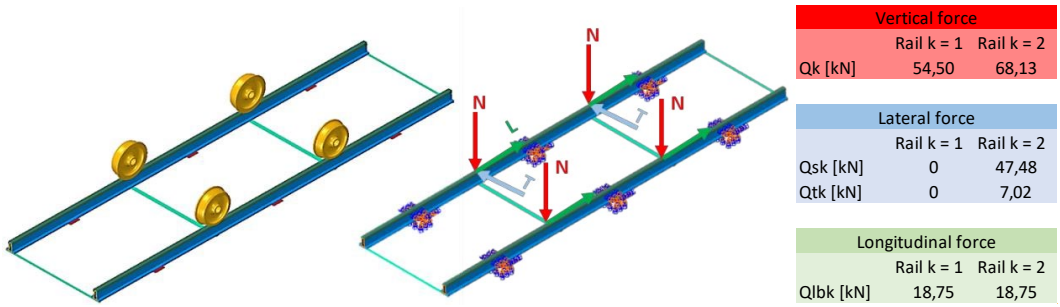

Figure 4: Loads values with directions and Boundary Conditions for the railway model.

Material properties for resin and fibers material used are based on actual characterization testing as well as manufacturers datasheet. Partitions are created and extruded through the entire length of the rail to apply the material properties to the corresponding woven and unidirectional sections. The modelled railway structure is partitioned and meshed using 3D elements, C3D8 and C3D8R, hexahedral volumic elements. Depending on the model length and size and on the refinement of the mesh, the number of elements in the model varies from 200 000 to 2 million.
Numerical simulations are achieved using Abaqus® 2022.

Numerical Results

Based on the static simulation results, it is observed that the contact indentation takes the form of an ellipse, characterized by a depth IC of approximately 2 mm. The IC is determined by the distance between the two axes of the min and max stress concentration points, which represent the in-depth stress in the shear plane τ_{yz}. The elliptic shape and corresponding stress are shown in Figure 5.

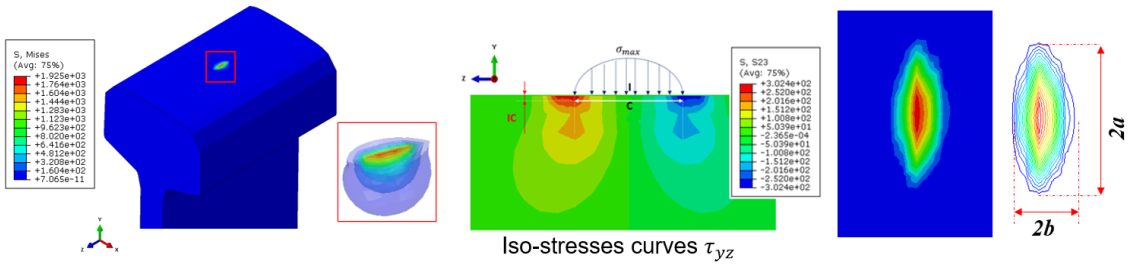

Figure 5: Stress values and wheel-rail contact elliptic shape resulting from numerical simulation.

Since the studied (and modelled) rail is expected to be crafted (through pultrusion) in composite materials, therefore highly anisotropic and fibers orientation dependent [6, 7], all the components of the stress tensor: σ_{11}, σ_{22}, σ_{33}, σ_{12}, σ_{13}, σ_{23} are of interest in the model. They are evaluated and analyzed for each section of the rail beam, consequently for each woven and UD parts, individually.

Stresses components in longitudinal direction, transverse direction, and out of plane, as well as shear stresses, for each ply type, are used as a discriminant parameter. Identically, displacements and maximum deflection are verified and used as validation parameters. Initial results are presented Figure 6, highlighting the rail global displacement (25-scale factor used for visualization purposes). Both the stresses maximum (tension) and minimum (compression) values, and the displacements (deflection) values respected the specifications (70 kN vertical load, -7 mm vertical displacement).

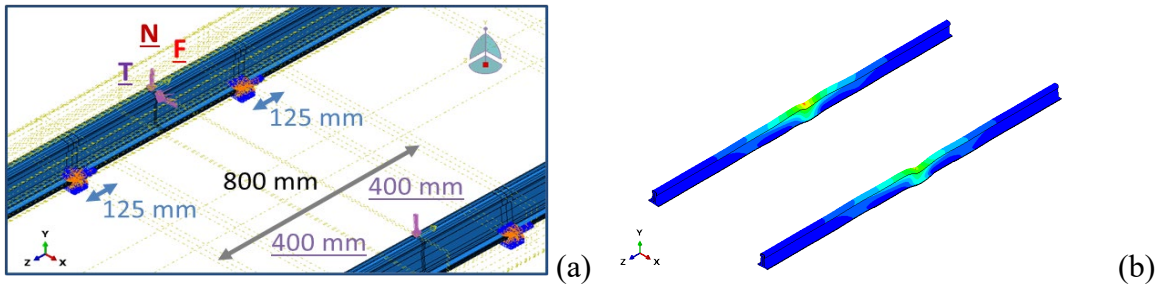

Figure 6: (a) Railroad loading conditions (b) corresponding results highlighting displacement.

Materials include thermoplastic resins and various fibers such as carbon, glass, bio-sourced for reinforcement. Material selection was achieved, reaching low cost PA6 TP resin and glass fibers. Woven and UD plies have been used and the optimum stacking was also determined.

Expected outcomes to reduce the thicknesses and adapt the dimensions (plies, stacking, part size ...), and help the pultruders production that led to an industrial solution have been met. The preliminary composite railway design resulting from this study will be manufactured to create a 200-meter rail track which will be installed and actual-size-tested.

Conclusions

The feasibility of a pultruded composite rail design for lightweight trains has been demonstrated, meeting geometry requirements as well as the loads, constraints and safety criteria of the railway sector, by a safety coefficient of 2.

Acknowledgment

The authors would like to thank the ADEME Agency (French Gov.) for the financing of this project. Thanks are also duly addressed to the CALMIP High Performance Computing platform for the numerical support and the computational power it provided.

References

[1] JEC Group: A lightweight composite train reinventes rural railways. JEC Composites Magazine, N°162, May-June 2025, ISSN: 2678-7024.
[2] L. Sudriès, et al., Selection of pultruded composite materials for new, low-carbon emission, lightweight railways tracks, with a focus on mechanics, economics and sustainability. Materials & Design, Vol. 261, 2026, ISSN 0264-1275. https://doi.org/10.1016/j.matdes.2025.115401
[3] U. Zerbst, R. Lundén, K.O. Edel, R.A. Smith, Introduction to the damage tolerance behaviour of railway rails - a review, Engineering Fracture Mechanics, Vol. 76, 2009, ISSN: 0013-7944. https://doi.org/10.1016/j.engfracmech.2009.09.003
[4] M. Maglio, A. Pieringer, J.C.O. Nielsen, T. Vernersson, Wheel-rail impact loads and axle bending stress simulated for generic distributions and shapes of discrete wheel tread damage, Journal of Sound and Vibration, Vol. 502, 2021, ISSN: 0022-460X. https://doi.org/10.1016/j.jsv.2021.116085
[5] A. Saulot, Analyse tribologique du contact roue-rail Modélisation et expérimentations - Cas de l'usure ondulatoire. Ph.D. Defense Thesis, Engineering Sciences, INSA Lyon, France, 2005, NNT: TEL-01247047.
[6] S. Zhang, C. Caprani, A. Heidarpour, Influence of fibre orientation on pultruded GFRP material properties. Composite Structures, Vol. 204, 2018, ISSN: 0263-8223. https://doi.org/10.1016/j.compstruct.2018.07.104
[7] T.Q. Liu, P. Feng, Y. Wu, S. Liao, X. Meng, Developing an innovative curved-pultruded large-scale GFRP arch beam. Composite Structures, Vol. 256, 2021, ISSN: 0263-8223. https://doi.org/10.1016/j.compstruct.2020.113111

Materials Research Proceedings 73 (2026) 51-55 https://doi.org/10.21741/9781644904459-11

Heat-Treatment Control of δ Phase in HIPed L-PBF Alloy 718: Microstructural Baseline for Creep and Dwell-Fatigue Assessment

Rana ELSAYED[1,a] *, Johan MOVERARE[1,b] and Emil ERIKSSON[2,c]

[1]Division of Engineering Materials, Linköping University, SE-581 83 Linköping, Sweden

[2]GKN Aerospace Sweden AB, SE-461 38 Trollhättan, Sweden

[a]rana.elsayed@liu.se, [b]johan.moverare@liu.se, [c]emil.eriksson@gknaerospace.com

Keywords: Alloy 718, Nickel-Based Superalloy, Laser Powder Bed Fusion, Hot Isostatic Pressing, Heat Treatment, Delta Phase, Vickers Hardness, Creep

Abstract. Alloy 718 is a nickel-based superalloy widely used in fatigue-critical hot-section gas turbine applications because of its high strength at temperatures up to 650 °C, mainly due to γ″ precipitation hardening. While casting and wrought routes are commonly used, additive manufacturing offers on-demand production of complex parts with shorter lead times and reduced waste. However, the high-temperature integrity of laser powder bed fusion (L-PBF) Alloy 718 remains under-characterized, and this material often shows reduced creep ductility, higher dwell-fatigue crack-growth rates, and greater notch sensitivity than wrought or cast alloys. This study investigates the mechanisms behind these limitations and evaluates post-processing strategies to improve microstructural stability and damage tolerance. Microstructural evolution is examined across multiple processing states, and creep and elevated temperature fatigue crack-growth tests are in progress on smooth and notched specimens, with L-PBF material benchmarked against cast and wrought alloys. Preliminary results show similar microstructures in the HIPed and post-HIP conditions, with carbides concentrated near grain boundaries. The standard heat-treated condition shows extensive δ-phase precipitation, while the other heat treatment does not, resulting in a microstructure closer to the post-HIP condition.

Introduction

Alloy 718 is a high-performance nickel-based superalloy widely used in aerospace and power generation because of its excellent creep, tensile, and thermo-mechanical fatigue resistance at temperatures up to about 650 °C [1]. Its strength comes from the γ matrix and strengthening phases such as γ' and γ'', while δ phase and carbides can improve creep resistance [2]. In additively manufactured Alloy 718, rapid solidification can cause Nb segregation and the formation of Laves and δ phases at grain boundaries, which degrade creep performance and promote crack initiation [3,4]. Although Laser Powder Bed Fusion offers high design flexibility and shorter production times, the process also produces non-equilibrium microstructures and defects such as porosity, lack of fusion, residual stress, and segregation [1]. As a result, L-PBF Alloy 718 often shows reduced creep ductility, higher crack growth rates, and greater sensitivity to dwell fatigue [1,3,4]. Therefore, post-processing and heat-treatment strategies are essential to improve damage tolerance and enable safe use in aeroengine applications [8,9]. This study focuses on the key microstructural characteristics and heat treatments required to achieve damage tolerance comparable to cast and forged materials [10], an approach also pursued for other additively manufactured superalloys [3,4,12].

Methods

This study investigates the microstructural behavior of L-PBF Alloy 718 under different processing conditions; As-Built, Stress-Relieved, Hipped. Post-Hipped-treated, and after each heat treatment from Standard, Space, and Modified heat treatments. All material was stress relieved at

Content from this work may be used under the terms of the Creative Commons Attribution 3.0 license. Any further distribution of this work must maintain attribution to the author(s) and the title of the work, journal citation and DOI. Published under license by Materials Research Forum LLC.

Materials Research Proceedings 73 (2026) 51-55 https://doi.org/10.21741/9781644904459-11

1065 °C for 1.5 h, hot isostatically pressed at 1155 °C for 4 h at a minimum pressure of 100 MPa, and given a post-HIP treatment at 1065 °C for 1.5 h, all in vacuum, to GKN specification SDB0063 Issue 02. The three heat treatments were applied to the post-HIP material and are denoted STD, SPC and modified (Table 1). STD is the solution and precipitation treatment of SDB0063 Issue 02. SPC uses a higher solution temperature with the longer 718/621 °C double age. The modified heat treatment replaces the single solution step with a 1030 °C solution, an 840 °C stabilisation and a 930 °C step, before a 760/650 °C double age. Heating to the solution temperature was at 10 °C/min to 870 °C and 5 °C/min thereafter for STD and SPC, and at 7 °C/min to 870 °C and 4 °C/min thereafter for the modified treatment. Cooling from the solution step was at a rate equal to or faster than air cooling to below 550 °C. Furnace charge thermocouple records were obtained for every cycle.

Table 1. Heat-treatment schedules applied to HIPed L-PBF Alloy 718.

Condition	Solution / stabilisation	Ageing	Cycle time [h]
STD	954 °C / 1 h	760 °C / 5 h → 649 °C over 2 h → 649 °C / 1 h	13.5
SPC	1065 °C / 1 h	718 °C / 8 h → 621 °C over 1.25 h → 621 °C / 8 h	23.0
Modified	1030 °C / 1 h + 840 °C / 4 h + 930 °C / 1 h	760 °C / 5 h → 650 °C → 650 °C / 1 h	18.9

All three treatments were applied to material in the stress-relieved, HIPed and post-HIP condition. → denotes controlled cooling to the stated temperature.

Additively manufactured (L-PBF), cast, and forged specimens will be examined, and the effect of Standard HT, Space HT, and Modified HT on the L-PBF material will be evaluated. Smooth and notched specimens will be used in creep, stressrupture, and dwell crack-propagation tests at elevated temperatures. Specimens were sectioned perpendicular to the building direction Z, mounted, ground and polished for the microstructure analysis. Microstructures were imaged in a Hitachi SU-70 field-emission SEM at 15 kV using secondary-electron and backscattered-electron detection. Phase identification in this contribution is based on morphology and BSE contrast only; EDS and EBSD phase mapping are in progress. Vickers hardness was measured with ten indentations distributed over the polished section of each condition, using HV5. Results are reported as the mean of the ten indentations; the full distributions are shown as box plots.

Results and Discussion

Fig. 1 shows the microstructure from the as-built state through HIP to the post-HIP condition. The as-built material is strongly heterogeneous, with melt-pool boundaries and a fine cellular-dendritic substructure. After HIP the cellular substructure is no longer resolved and equiaxed grains with annealing twins are evident, consistent with recrystallisation and with dissolution of the interdendritic Nb-rich constituents during the HIP hold. The post-HIP condition shows a high density of fine bright particles distributed through the matrix and concentrated near grain

Materials Research Proceedings 73 (2026) 51-55 https://doi.org/10.21741/9781644904459-11

boundaries. On BSE contrast and morphology these are consistent with MC-type carbides, but this assignment requires EDS confirmation before it can be stated as a result.

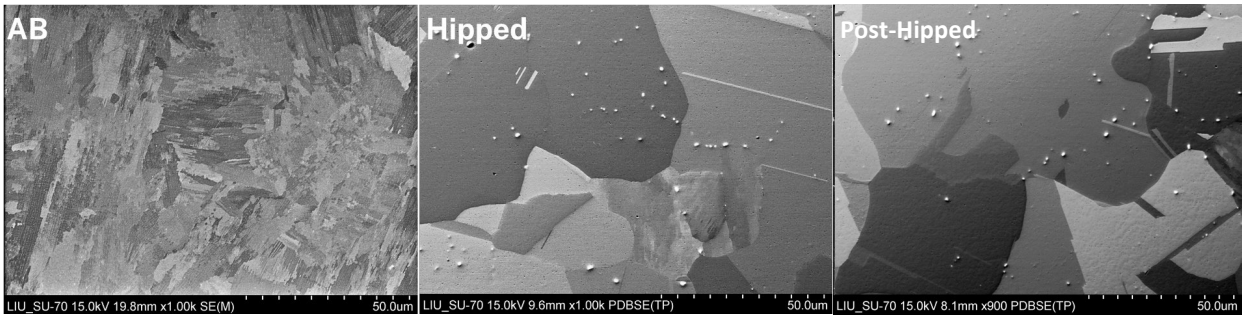

Fig. 1. SEM micrographs of L-PBF Alloy 718 in the as-built (AB), HIPed and post-HIP conditions. Secondary- and backscattered-electron images, Hitachi SU-70, 15 kV. Scale bar 50 µm.

Fig. 2 compares the three heat treatments. The STD condition contains numerous elongated, plate-like precipitates decorating the grain boundaries and extending into the grains, a morphology characteristic of δ phase. No comparable population is resolved in the SPC condition, whose boundaries are comparatively clean; this is consistent with a solution anneal above the δ solvus followed by ageing conditions under which δ does not re-precipitate appreciably. The modified condition is intermediate: plate-like precipitates are present but are shorter and more widely spaced along the boundaries, and are accompanied by a high density of fine, discrete intragranular particles.

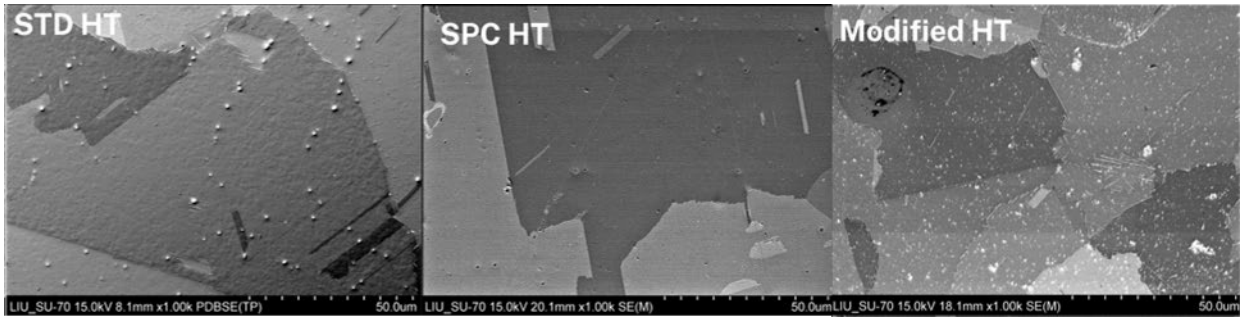

Fig. 2. SEM micrographs of HIPed L-PBF Alloy 718 after the STD, SPC and modified heat treatments. Scale bar 50 µm.

It should be noted that δ phase, η phase and Nb-rich carbides can present similar plate-like morphologies in BSE contrast. The identifications above are therefore reported as consistent with δ phase rather than as confirmed, pending EDS and EBSD phase mapping.

The differences between conditions are modest relative to that skew. A post-build heat treatment applied to already-recrystallised, HIPed material is not expected to refine the grain structure, so the smaller mean measured in the modified condition is more plausibly a consequence of sampling and of the grain-definition convention than of grain refinement by the treatment itself. Fig. 3 shows the Vickers hardness distributions for the three heat treatments. The modified condition gave the highest mean hardness, 444.6 HV, followed by STD at 436.0 HV and SPC at 434.2 HV. The modified condition also shows the narrowest interquartile range. However, the STD and SPC distributions overlap almost completely, and the difference between their means, 1.8 HV, is far smaller than the scatter within either condition. On the present data only the modified condition can be separated from the other two, and that separation is itself modest; the ranking of STD against SPC is not supported.

Materials Research Proceedings 73 (2026) 51-55 https://doi.org/10.21741/9781644904459-11

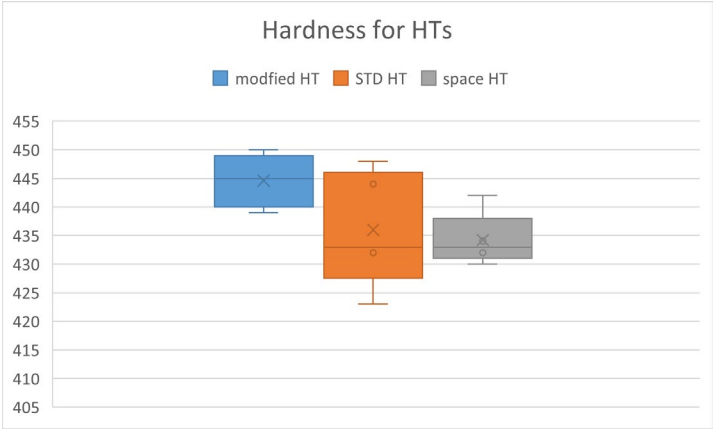

Fig. 3. Vickers hardness of HIPed L-PBF Alloy 718 after the modified, STD and SPC heat treatments (ten indentations per condition).

Fig. 4 compares the three manufacturing routes after the STD and after the modified heat treatment. In both cases the L-PBF material shows the highest median hardness and the forged material the lowest, and the separation between routes is larger after the modified treatment. A higher hardness in the L-PBF condition is consistent with a finer as-built substructure and a higher density of γ″ after ageing. It is emphasised that hardness is an indentation response dominated by precipitate strengthening and says nothing directly about creep or dwell-fatigue crack-growth resistance, which are governed by grain-boundary character, δ and carbide distribution and environmental damage. The hardness ranking reported here is therefore used only as a consistency check on the ageing response, not as a predictor of damage tolerance.

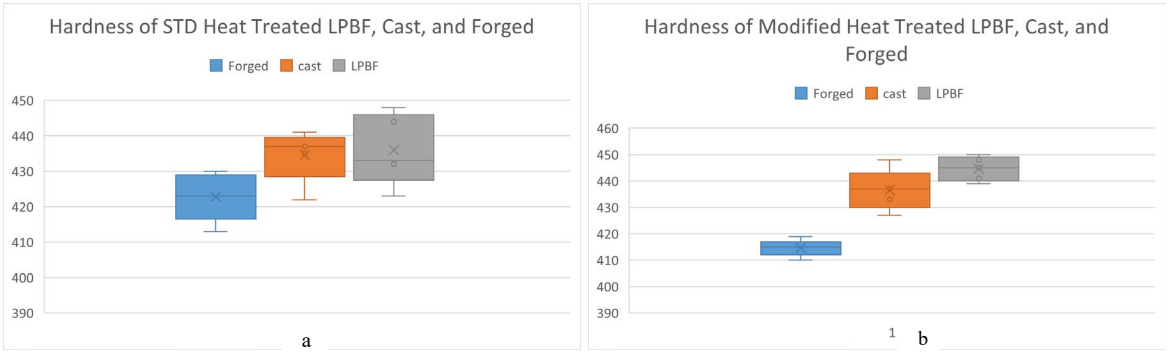

Fig. 4. Vickers hardness of L-PBF, cast and forged Alloy 718 after (a) the STD and (b) the modified heat treatment.

Summary

This project demonstrates that the microstructural stability and mechanical performance of L-PBF Alloy 718 are responsive to post-processing and heat treatment conditions. HIP and post-HIP processing homogenised the microstructure and closed internal porosity, while the applied heat treatment governed the grain-boundary phase distribution and the hardness. The three heat treatments then produced clearly different grain-boundary states: extensive plate-like precipitation consistent with δ phase after the STD treatment, no resolvable equivalent after the SPC treatment, and an intermediate, more discrete distribution together with fine intragranular particles after the modified treatment.

Vickers hardness was highest after the modified treatment, and in all three conditions the L-PBF material was harder than the cast and forged references. Because hardness does not measure damage tolerance, the ranking of these heat treatments for dwell-fatigue and creep resistance

remains open. Creep, stress-rupture and dwell crack-growth testing of smooth and notched specimens at elevated temperature is in progress and will be reported subsequently, together with EDS and EBSD phase identification of the grain-boundary constituents.

References

[1] E. Sadeghi, P. Karimi, R. Esmaeilizadeh, F. Berto, S. Shao, J. Moverare, E. Toyserkani, N. Shamsaei, A state-of-the-art review on fatigue performance of powder bed fusion-built Alloy 718, Prog. Mater. Sci. 133 (2023) 101066. https://doi.org/10.1016/j.pmatsci.2022.101066
[2] G. Bryndza, J. Tchoufang Tchuindjang, F. Chen, A.M. Habraken, H. Sepúlveda, V. Tuninetti, A. Mertens, L. Duchêne, Review of the microstructural impact on creep mechanisms and performance for laser powder bed fusion Inconel 718, Materials 18 (2025) 276. https://doi.org/10.3390/ma18020276
[3] T. Trosch, J. Strößner, R. Völkl, U. Glatzel, Microstructure and mechanical properties of selective laser melted Inconel 718 compared to forging and casting, Mater. Lett. 164 (2016) 428-431. https://doi.org/10.1016/j.matlet.2015.10.136
[4] D. Deng, R.L. Peng, H. Brodin, J. Moverare, Microstructure and mechanical properties of Inconel 718 produced by selective laser melting: sample orientation dependence and effects of post heat treatments, Mater. Sci. Eng. A 713 (2018) 294-306. https://doi.org/10.1016/j.msea.2017.12.043
[5] K. Gruber, P. Szymczyk-Ziółkowska, S. Dziuba, S. Duda, P. Zielonka, S. Seitl, G. Lesiuk, Fatigue crack growth characterization of Inconel 718 after additive manufacturing by laser powder bed fusion and heat treatment, Int. J. Fatigue 166 (2023) 107287. https://doi.org/10.1016/j.ijfatigue.2022.107287
[6] S. Wu, H.Z. Peng, X. Gao, P.D. Hodgson, H.Y. Song, Y.M. Zhu, Y. Tian, A.J. Huang, Improving creep property of additively manufactured Inconel 718 through specifically-designed post heat treatments, Mater. Sci. Eng. A 857 (2022) 144047. https://doi.org/10.1016/j.msea.2022.144047
[7] D. Deng, R.L. Peng, J. Moverare, A comparison study of the dwell-fatigue behaviours of additive and conventional IN718: the role of dislocation substructure on the cracking behaviour, Mater. Sci. Eng. A 797 (2020) 140072. https://doi.org/10.1016/j.msea.2020.140072
[8] S. Zhang, L. Wang, X. Lin, H. Yang, M. Li, L. Lei, W. Huang, Precipitation behavior of δ phase and its effect on stress rupture properties of selective laser-melted Inconel 718 superalloy, Compos. Part B Eng. 224 (2021) 109202. https://doi.org/10.1016/j.compositesb.2021.109202
[9] J.T. Benzing, N. Derimow, O.L. Kafka, N. Hrabe, P. Schumacher, D. Godfrey, C. Beamer, Enhanced strength of additively manufactured Inconel 718 by means of a simplified heat treatment strategy, J. Mater. Process. Technol. 322 (2023) 118197. https://doi.org/10.1016/j.jmatprotec.2023.118197
[10] J. Peng, M. Gao, H. Zhang, X. Geng, X. Liu, H. Pan, Small punch creep test reveals the differences of high-temperature creep behaviours for laser powder bed fusion and rolled Inconel 718 alloys, Mater. Sci. Eng. A 886 (2023) 145698. https://doi.org/10.1016/j.msea.2023.145698
[11] H. Pasiowiec, et al., Effect of creep deformation on the microstructure evolution of Inconel 625 nickel-based superalloy additively manufactured by laser powder bed fusion, Mater. Sci. Eng. A 887 (2023) 145742. https://doi.org/10.1016/j.msea.2023.145742
[12] V. Kalyanasundaram, A. De Luca, R. Wróbel, J. Tang, S.R. Holdsworth, C. Leinenbach, E. Hosseini, Tensile and creep-rupture response of additively manufactured nickel-based superalloy CM247LC, Addit. Manuf. Lett. 5 (2023) 100119. https://doi.org/10.1016/j.addlet.2022.100119

Materials Research Proceedings 73 (2026) 56-61 https://doi.org/10.21741/9781644904459-12

Coupled Isogeometric Phase-Field Modeling and Embedded Distributed Fiber Optic Strain Sensing for Degradation Analysis of Complex Structures

Ha-Thanh PHAN[1,a,*], Aghiad KHADOUR[1,b]

[1]IMSE Lab, COSYS Department, Gustave Eiffel University, France

[a]ha-thanh.phan@univ-eiffel.fr, [b]aghiad.khadour@univ-eiffel.fr

Keywords: Isogeometric Analysis, Modeling, Finite Element, Phase Field Method, Distributed Fiber Optic Strain Sensing, Embedded Fiber Optic Cable, Concrete Deterioration

Abstract. Monitoring degradation in complex structures remains a major challenge, especially when damage initiation and propagation must be inferred from indirect measurements. Distributed fiber optic strain sensing provides valuable strain data along embedded trajectories, but their interpretation requires a robust numerical framework able to capture both complex geometries and evolving fracture processes. In this work, an isogeometric phase-field framework is proposed for modeling degradation in complex structures instrumented with embedded optical fibers. The structural geometry is represented exactly using NURBS-based isogeometric analysis, while crack initiation and propagation are described through a regularized phase-field formulation. The embedded optical fiber is modeled as a parametric curve within the solid, and the strain observable along the fiber is obtained by projecting the strain tensor onto the local fiber tangent direction. The proposed framework establishes a consistent link between internal damage evolution and measurable distributed strain signals. Numerical examples illustrate its ability to capture damaged localization in complex geometries and to reproduce the associated fiber-optic strain response. The results demonstrate the potential of the proposed approach as a predictive and an interpretative tool for structural health monitoring of degrading structures.

1 Introduction

Distributed optical fiber sensors are increasingly used in structural health monitoring because they provide quasi-continuous strain measurements over long distances with limited invasiveness. However, the measured signal is indirect: a local peak may arise from geometry, boundary effects, stress concentration, or actual damage, see for example [1-3]. Numerical modeling is therefore required to relate distributed strain measurements to meaningful structural quantities, [4].

In this context, Isogeometric Analysis (IGA) [5] and phase-field fracture are complementary. IGA uses NURBS functions to describe both geometry and unknown fields, which are attractive for instrumented structures with curved boundaries and embedded sensing paths. Phase-field models, see for example [6], [7] regularize discontinuous cracks through a scalar damage variable and allow crack initiation and propagation without tracking the crack surface explicitly. The objective of this paper is to couple these two problems with an optical-fiber post-processing procedure to compute directly the strain observable measured along the sensing line.

2 Phase field Model for concrete fracture

The phase-field approach regularizes sharp crack discontinuities by introducing a continuous scalar field $d(x) \in [0, 1]$, where $d = 0$ denotes intact material and $d = 1$ a fully broken state. Following the variation framework of Francfort and Marigo [8], the total energy functional reads:

$$\mathcal{E}(u, d, \nabla d) = \int_\Omega g(d)\Psi(\varepsilon(u))d\Omega + G_c \int_\Omega \gamma_d(d, \nabla d)d\Omega \quad (1)$$

Content from this work may be used under the terms of the Creative Commons Attribution 3.0 license. Any further distribution of this work must maintain attribution to the author(s) and the title of the work, journal citation and DOI. Published under license by Materials Research Forum LLC.

Materials Research Proceedings 73 (2026) 56-61 https://doi.org/10.21741/9781644904459-12

where $g(d) = (1-d)^2$ is the quadratic degradation function that reduces the material stiffness as damage grows, $\Psi(\varepsilon(u)) = 1/2\, \varepsilon : \mathbb{C}_0 : \varepsilon$ is the elastic strain energy density with $\mathbb{C}_0$ the undamaged elasticity tensor, and G_c is the critical energy release rate. The crack surface density function is defined as [6-7].

The degraded stress becomes $\sigma = g(d)\partial\psi^+/\partial\varepsilon + \partial\psi^-/\partial\varepsilon$ using the eigenvalue decomposition as in [6-7]. The variation principle yields two coupled governing equations:

The mechanical problem:

$$\begin{cases} \nabla.\sigma + f = 0, & in\ \Omega \\ u = \bar{u}, & on\ \Gamma_u \\ \sigma.n = \bar{t}, & on\ \Gamma_t \end{cases} \tag{2}$$

The phase-field evolution equation:

$$2(1-d)\mathcal{H}\left(\psi^+(\varepsilon)\right) - \frac{G_c}{l_0}(d - l_0^2\nabla d) = 0,\ in\ \Omega \tag{3}$$

where $\mathcal{H}\left(\psi^+(\varepsilon)\right) = \max_{s\in[0,t]} \psi^+\left(\varepsilon(x,s)\right)$ is the history variable enforcing damage irreversibility.

The coupled system is solved by a staggered scheme: at each load step, the displacement sub-problem is solved for frozen d, then the phase-field equation for updated strains, iterating until convergence.

3 Isogeometric formulation

IGA was introduced to unify CAD geometry and numerical analysis by employing spline-based functions as Non-Uniform Rational B-Splines (NURBS) to describe both geometry and the unknown fields, referring to [5] for all details. In the phase field framework, both the displacement field u and phase field d are approximated as in [7].

In this work, the optical fiber is modelled as a parametric curve in 3D, $C(s)$ within the NURBS. where *s* denotes the curvilinear abscissa along the fiber path. For a helix wound on a cylinder of radius *R* at angle α, the fiber trajectory is defined as $\boldsymbol{C}(\boldsymbol{s}) = \left[R\cos\left(\theta(s)\right),\ R\sin\left(\theta(s)\right),\ z(s)\right]$, with $\theta(s) = s\cos(\alpha)/R,\ z(s) = s\sin(\alpha)$

The strain tensor $\boldsymbol{\varepsilon}$ is then evaluated from the isogeometric displacement field, and the measurable axial fiber strain is obtained by projection onto the local tangent, see for example [4]:

$$\varepsilon_f(s) = \boldsymbol{t}^{\boldsymbol{T}}(\boldsymbol{s})\boldsymbol{\varepsilon}\left(\boldsymbol{C}(\boldsymbol{s})\right)\boldsymbol{t}(\boldsymbol{s}) = t_i\varepsilon_{ij}t_j \tag{4}$$

where $\boldsymbol{\varepsilon}\left(\boldsymbol{C}(\boldsymbol{s})\right)$ is is the total strain tensor and the unit tangent vector $\boldsymbol{t}(\boldsymbol{s})$.

This post-processing operation does not alter the governing equations. It provides a physically meaningful observable directly comparable to distributed optical fiber measurements establishing a quantitative link between the internal damage state described by $d(x)$ and the externally measurable strain signal along the fiber.

4 Numerical Results

The framework is illustrated on a cylindrical concrete specimen equipped with an internal helical optical fiber. This experiment was carried out by Aubert et al. [3]. The specimen has a height of 250 mm, an outer diameter of 150 mm, and a thickness of 25 mm, see Fig.1. It is subjected to an internal pressure history applied to both sides of the inner surface by a cylindrical hydraulic machine.

Materials Research Proceedings 73 (2026) 56-61 https://doi.org/10.21741/9781644904459-12

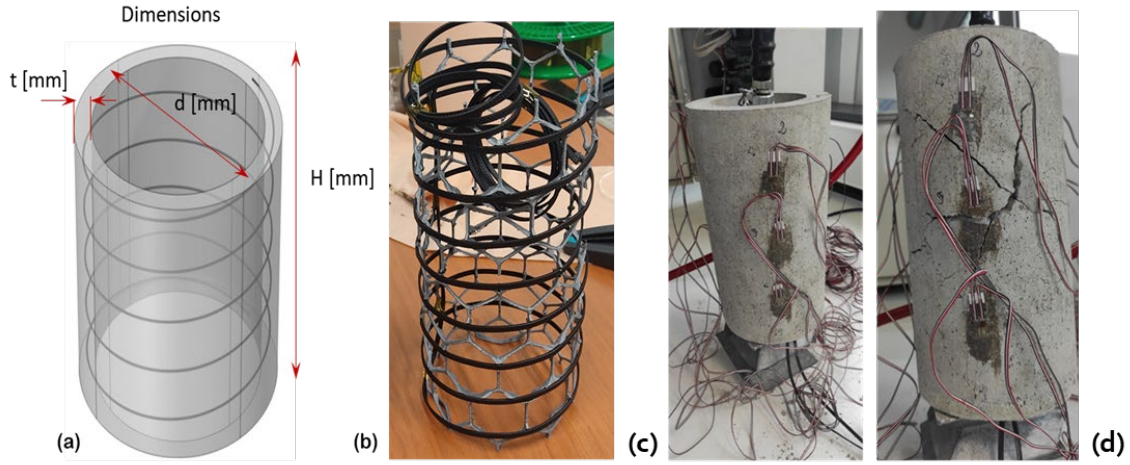

Fig. 1. Pattern of the cylindrical concrete structure with the fiber optic cable embedded (a) and support by the additive printed structure (b), a cylindrical hydraulic machine (c) and the cracks on the surface of the cylinder at the end of test (d).

The material used for these samples was the mortal type CEM I Beffes 52.2 N with a water-to-binder ration w/b = 0.5, sand-to-binder ratio s/b = 2.25, and superplasticizer-to-binder ratio sp/b = 0.0075. The model parameters selected for this simulation are $E_c = 28\ [GPa], \nu = 0.2, G_c = 4\ [N/m], l_c = 1[mm]$. The geometry of the structure and its finite element mesh is constructed based on fundamental NURBS functions as introduced in Section 3, as shown in Fig. 2. The mesh of the structure consists of 3450 spline elements. The boundary conditions prevent rigid body motion by fixing the base plane Z=0.

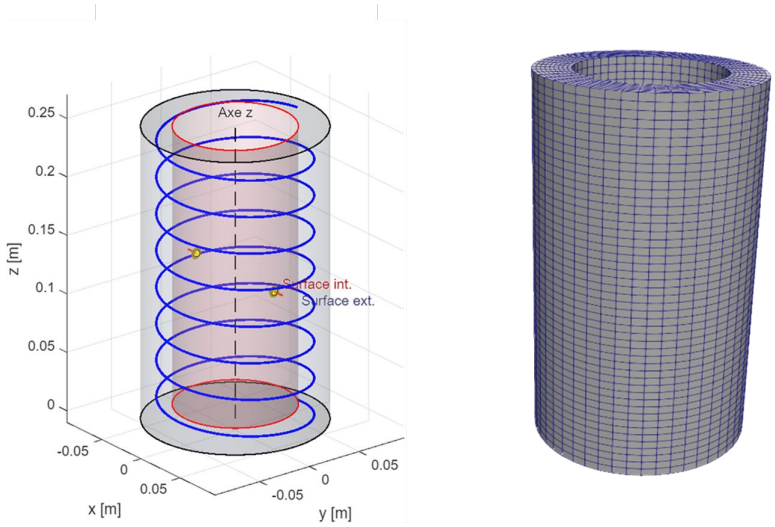

Fig. 2. NURBS-based geometry and IGA discretization of a cylindrical structure.

The phase-field damage variable d at the end of the loading sequence reveals a strongly localized damage zone on the cylinder surface, Fig. 3. This localization appears as a bounded region where d approaches its highest values, while most of the remaining surface remains only weakly damaged. Such a pattern indicates that fracture dissipation is concentrated within a restricted area rather than being distributed uniformly over the structure.

Materials Research Proceedings 73 (2026) 56-61 https://doi.org/10.21741/9781644904459-12

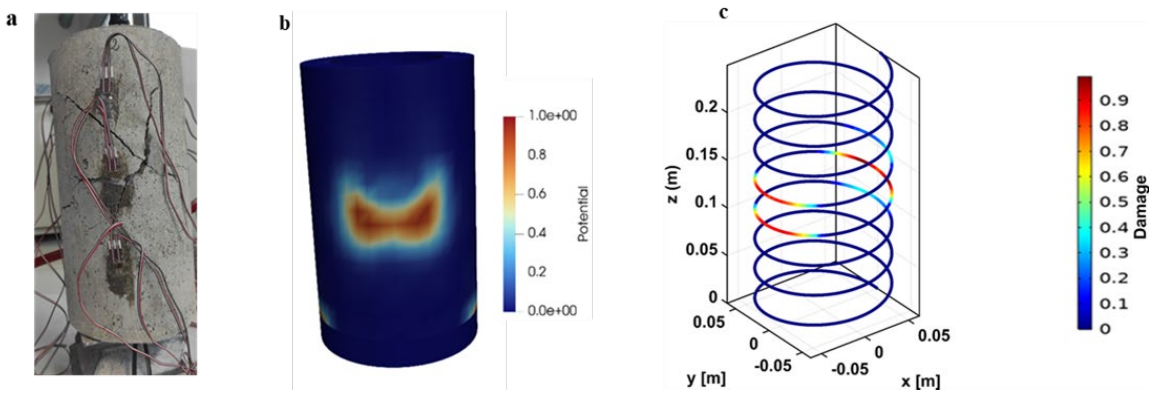

Fig. 3. Phase field damage variable at end of simulation: (a). experimental results, (b)-(c) simulation results.

The local stress-strain curve shows in Fig.4 shows the transition from elastic response to damage initiation. When the peak stress is reached, damage starts. After this point, the local stress decreases, which corresponds to stiffness degradation and softening. This means that even if the hydraulic pressure continues to increase, the local resisting capacity decreases in the damaged zone.

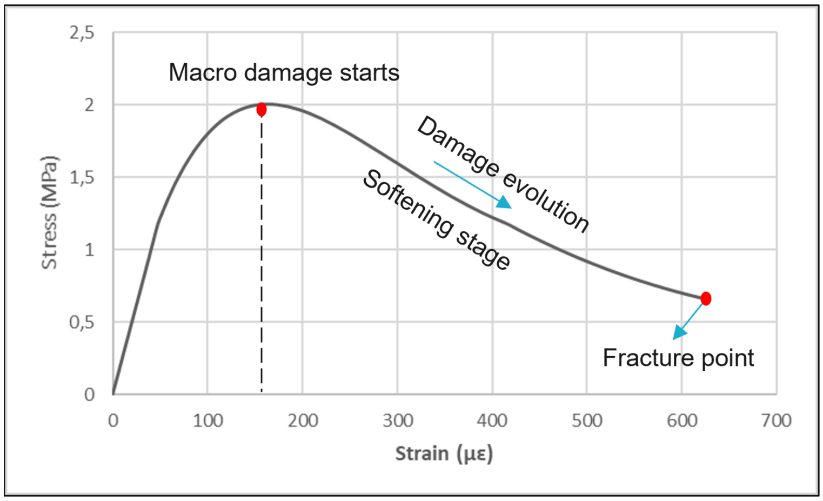

Fig. 4. Stress – strain curve for the softening behavior of structure.

At loading step 6, both experiment and simulation exhibit a localized strain zone with peak values of about 100 με along the helix, see Fig.5a-5b. At the final stage, the fiber-strain profile presents a dominant cluster of peaks around s = 1.6–1.8 m, with a maximum value close to 300 με, see Fig.5c. The numerical response reproduces both the position of the dominant localization zone and its order of magnitude. These results confirm that the proposed model can translate internal degradation into measurable distributed strain signatures.

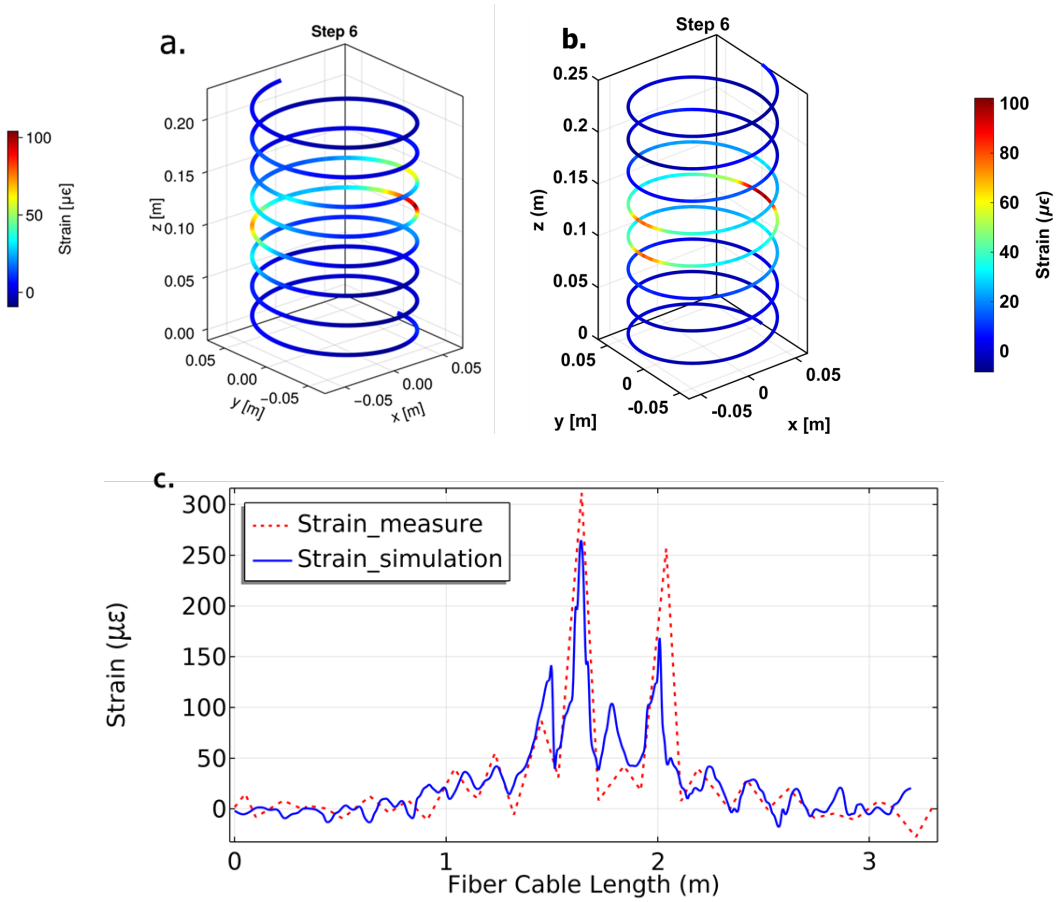

Fig.5. Micro fiber-strain over fiber length at load increment 6: (a) simulation results, (b) measurement results and Micro fiber strains along the fiber length for step 7 of pressure (c).

5 Conclusions

This paper presented a compact framework that couples NURBS-based isogeometric analysis, phase-field fracture, and embedded optical-fiber sensing. The approach can represent complex geometries exactly, simulate damage initiation and propagation without prescribing the crack path, and compute a physically meaningful strain observable along the sensor trajectory. The validation numerical showed that the model captures both damage localization and the main features of the measured distributed strain response. This makes the approach promising for the interpretation of DFOS data in degrading structures. Future work will address parameter identification and extension to coupled thermo-hygro-chemo-mechanical processes.

Acknowledgment

This research project was financially supported by a BPI - PALLAS Project (Plateforme pluridisciplinAire de surveiLLance dans le cadre d'Alternatives au Stockage) 2022-2026.

References

[1] Barrias, A., Casas, J.R., Villalba, S.: A review of distributed optical fiber sensors for civil engineering applications. Sensors 16(5) (2016) https://doi.org/10.3390/s16050748

[2] Waeytens, J., Khadour, A.: Monitoring of concrete structures with optical fiber sensors, pp. 97–121 (2017). https://doi.org/10.1016/B978-0-08-102181-1.00005-8

[3] Aubert, N., Degaugue, S., Pouya, J., Khadour, A.: Additive Printed Structures for Optical Fiber Sensing in Concrete. In: Proc. QNDE 2024, vol. QNDE2024-138489, pp. 001–09002. ASME, Denver, France (2024). https://doi.org/10.1115/QNDE2024-138489

[4] Aung, T.L., Ma, N., Kishida, K., Guzik, A.: Advanced structural health monitoring method by integrated isogeometric analysis and distributed fiber optic sensing. Sensors 21(17) (2021) https://doi.org/10.3390/s21175794

[5] Hughes, T.J.R., Cottrell, J.A., Bazilevs, Y.: Isogeometric analysis: Cad, finite elements, nurbs, exact geometry and mesh refinement. Computer Methods in Applied Mechanics and Engineering 194(39), 4135–4195 (2005) https://doi.org/10.1016/j.cma.2004.10.008

[6] Miehe, C., Welschinger, F., Hofacker, M.: Thermodynamically consistent phase-field models of fracture: Variational principles and multi-field fe implementations. International Journal for Numerical Methods in Engineering 83(10), 1273–1311 (2010) https://doi.org/10.1002/nme.286

[7] Goswami, S., Anitescu, C., Rabczuk, T.: Adaptive fourth-order phase field analysis for brittle fracture. Computer Methods in Applied Mechanics and Engineering 361, 112808 (2020) https://doi.org/10.1016/j.cma.2019.112808

[8] Francfort, G.A., Marigo, J.-J.: Revisiting brittle fracture as an energy minimization problem. Journal of the Mechanics and Physics of Solids 46(8), 1319–1342 (1998) https://doi.org/10.1016/S0022-5096(98)00034-9

Materials Research Proceedings 73 (2026) 62-65 https://doi.org/10.21741/9781644904459-13

Fatigue Crack Analysis Using a Coupled 2D CUF–3D Peridynamics Framework

Qiang ZHANG[1,a], Alfonso PAGANI[2,b *], Xiang LIU[1,c], Wei ZHOU[1,d], and Erasmo CARRERA[2,e]

[1]School of Traffic & Transportation Engineering, Central South University, China

[2]mul2 lab, Politecnico di Torino, Italy

[a]csu_zhangqiang@csu.edu.cn, [b]alfonso.pagani@polito.it, [c]xiangliu@csu.edu.cn, [d]gszx_zhouwei@csu.edu.cn, [e]erasmo.carrera@polito.it

Keywords: Peridynamics, Carrera Unified Formulation, Fatigue Crack Propagation, Hybrid Local–Nonlocal Modelling, High-Order Refined Elements

Abstract. Peridynamics (PD) naturally captures crack initiation and propagation, but fully PD fatigue simulations are computationally demanding. Hybrid CUF–PD approaches address this limitation by confining the 3D PD model to crack-prone regions and using efficient refined finite elements elsewhere. This work represents an initial attempt to extend the 2D CUF–3D PD coupling framework to fatigue crack analysis by incorporating Silling's peridynamic fatigue damage model. The resulting formulation enables efficient prediction of fatigue crack initiation and growth in plate and shell structures while preserving the high-fidelity crack description of 3D PD.

Introduction

Peridynamics (PD) provides an effective framework for fracture and fatigue analysis, as cracks can naturally initiate and propagate through the progressive failure of nonlocal bonds. Peridynamic fatigue models describe bond-level damage accumulation, enabling fatigue crack nucleation and growth without prescribing crack paths. However, fully peridynamic simulations remain computationally expensive, particularly for 3D fatigue problems involving numerous loading cycles and repeated updates of nonlocal interactions.

Hybrid local–nonlocal modelling reduces this cost by limiting the PD discretization to damage-prone regions and using more efficient local structural models elsewhere. In this context, the Carrera Unified Formulation (CUF) provides a hierarchical framework for refined structural modelling with reduced computational cost. Previous studies have shown the effectiveness of coupling 3D PD with CUF-based refined structural models[1], [2], [3]. More recently, a 2D CUF–3D PD framework [4] was developed for fracture analysis of plate- and shell-like structures, combining the efficiency of 2D refined models with the crack description capability of 3D PD. However, to the best of the authors' knowledge, the use of a coupled 2D refined FEM/CUF–3D PD framework for fatigue crack initiation and propagation has not yet been reported.

Building on this framework, the present work incorporates Silling's peridynamic fatigue damage model to extend 2D CUF–3D PD coupling to fatigue crack analysis. The proposed formulation enables fatigue crack initiation and propagation in plate- and shell-like structures under cyclic loading.

Methodology

This work extends the existing 2D CUF–3D PD coupling framework, originally developed for quasi-static fracture analysis, to fatigue cracking analysis. The 3D peridynamic model is used only in the expected damage region, whereas the surrounding elastic domain is represented by refined 2D CUF elements for computational efficiency. In the peridynamic subdomain, material particles

Content from this work may be used under the terms of the Creative Commons Attribution 3.0 license. Any further distribution of this work must maintain attribution to the author(s) and the title of the work, journal citation and DOI. Published under license by Materials Research Forum LLC.

Materials Research Proceedings 73 (2026) 62-65 https://doi.org/10.21741/9781644904459-13

interact with neighboring particles within a finite horizon, and the linearized bond-based equilibrium equation of material point i is written as

$$\sum_{j\in H_i}\mathbf{C}(\boldsymbol{\xi}_{ij})\,(\mathbf{u}_j-\mathbf{u}_i)V_j=\mathbf{f}_i \tag{1}$$

where $\boldsymbol{\xi}_{ij}=\mathbf{x}_j-\mathbf{x}_i$ is the relative position vector, V_j is the volume associated with particle j, and H_i denotes the family of particles within the horizon of particle i. The micromodulus tensor $\mathbf{C}(\boldsymbol{\xi}_{ij})$ defines the bond stiffness. After assembling all pairwise interactions, the discrete peridynamic equilibrium equation is expressed as

$$\mathbf{K}_{\mathrm{PD}}\mathbf{U}_{\mathrm{PD}}=\mathbf{F}_{\mathrm{PD}} \tag{2}$$

The elastic subdomain is represented by 2D CUF plate elements, which reconstruct the 3D displacement field from the x−y reference surface through a thickness-wise expansion:

$$\mathbf{u}(x,y,z)=N_i(x,y)F_\tau(z)\mathbf{u}_{\tau i},\qquad \tau=1,2,\cdots,M,i=1,2,\cdots N \tag{3}$$

where $N_i(x,y)$ are the 2D finite element shape functions defined on the plate reference surface, $F_\tau(z)$ are the CUF expansion functions along the thickness direction, and $\mathbf{u}_{\tau i}$ are the generalized nodal displacement variables. This formulation allows the 2D finite element region to retain a 3D displacement description while using a reduced structural model for the elastic part of the domain.

Substitution of this kinematic approximation into the principle of virtual work gives the discrete equilibrium equation of the CUF plate region:

$$\mathbf{K}_{\mathrm{FE}}\mathbf{U}_{\mathrm{FE}}=\mathbf{F}_{\mathrm{FE}} \tag{4}$$

Here, $\mathbf{K}_{\mathrm{FE}}$ is obtained from the 3D constitutive relations integrated over the plate surface and thickness. Therefore, although the finite element model is 2D in its reference domain, the displacement and stress fields retain a 3D representation through the CUF thickness expansion. This point is essential for distinguishing the present 2D CUF–3D PD framework from previous 1D CUF–3D PD beam formulations.

Displacement compatibility between the 3D peridynamic grid and the 2D CUF plate region is imposed by Lagrange multipliers at the coupling interface. For each interface particle k, the peridynamic displacement is constrained to match the displacement reconstructed from the CUF plate approximation as.

$$\mathbf{u}_k^{\mathrm{PD}}-N_i(x_k,y_k)F_\tau(z_k)\mathbf{u}_{\tau i}=0 \tag{5}$$

where N_i and F_τ are the in-plane finite element shape functions and thickness expansion functions, respectively.

The resulting coupled system is

$$\begin{bmatrix}\mathbf{K} & \mathbf{B}^{\mathbf{T}}\\ \mathbf{B} & 0\end{bmatrix}\begin{bmatrix}\mathbf{U}\\ \boldsymbol{\lambda}\end{bmatrix}=\begin{bmatrix}\mathbf{F}\\ 0\end{bmatrix},\quad \mathbf{K}=\begin{bmatrix}\mathbf{K}_{\mathrm{FE}} & 0\\ 0 & \mathbf{K}_{\mathrm{PD}}\end{bmatrix},\quad \mathbf{U}=\begin{bmatrix}\mathbf{U}_{\mathrm{FE}}\\ \mathbf{U}_{\mathrm{PD}}\end{bmatrix} \tag{6}$$

Materials Research Proceedings 73 (2026) 62-65 https://doi.org/10.21741/9781644904459-13

where $\mathbf{B}$ is the coupling matrix assembled from the displacement compatibility constraints, and $\boldsymbol{\lambda}$ is the vector of Lagrange multipliers. This treatment does not require a one-to-one correspondence between the peridynamic particles and the finite element nodes, which allows the refined 2D CUF mesh and the 3D peridynamic grid to be selected independently according to accuracy and efficiency requirements.

Fatigue damage is introduced into the peridynamic subdomain through a bond-level remaining-life law. Each peridynamic bond is assigned a fatigue life variable $\lambda(\boldsymbol{x},\boldsymbol{\xi},N)$, which evolves with the number of load cycles N as

$$\frac{d\lambda}{dN} = -A\varepsilon^{m}, \qquad \lambda(0)=1, \tag{7}$$

where ε is the cyclic bond strain, and A and m are fatigue parameters calibrated from experimental fatigue data. When the remaining-life variable reaches zero, the corresponding bond is irreversibly broken and removed from the peridynamic interaction list. In this way, fatigue crack initiation and propagation are captured naturally within the nonlocal region without prescribing an external crack path or additional crack-growth criterion.

The fatigue update is embedded into the 2D CUF–3D PD solution procedure. After each coupled equilibrium solution under cyclic loading, the cyclic bond strain is evaluated from the relative displacement of interacting peridynamic particles; the remaining bond life is then updated, and failed bonds are removed from the interaction list. In this way, the existing quasi-static 2D CUF–3D PD fracture framework is extended to fatigue cracking analysis.

Numerical Results

A square plate made of 7075-T651 aluminum alloy and subjected to an in-plane prescribed displacement was used as the first static verification example. The geometry, boundary conditions, and 2D CUF–3D PD coupling strategy are shown in Fig. 1a. The three-dimensional PD region was placed at the center of the plate, while the surrounding domain was discretized using high-order two-dimensional finite elements, with displacement compatibility enforced through the overlapping region. Fig. 1b and 1c also present the Y-direction displacement field and the displacement profile extracted along the plate centerline. The results show a continuous displacement transition across the FE region, PD region, and coupling zone, with no evident interfacial discontinuity, indicating that the proposed coupling method can correctly reproduce the static deformation response of the structure.

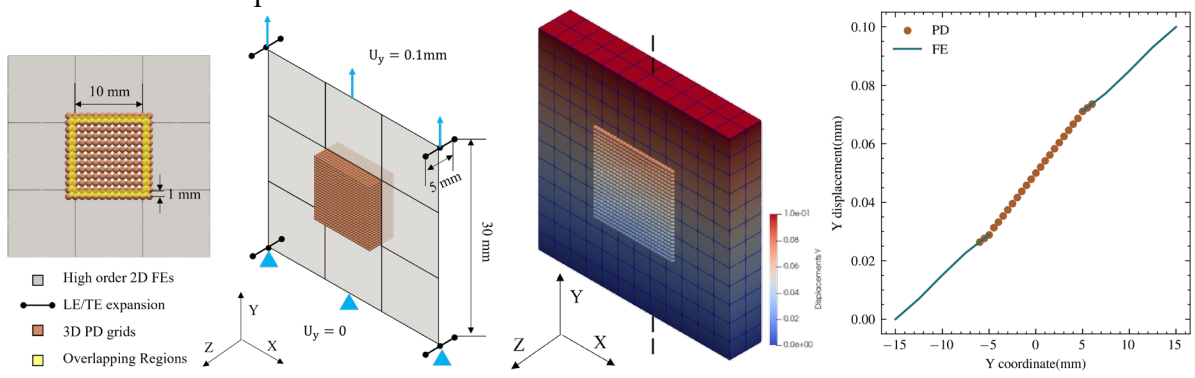

(a) Dimension, BCs and Modeling (b) Y Displacementfield (c) Displacement-coordinated relation in Y axle

Figure 1: Static verification of plate

A pre-crack was further introduced into the same square plate model along the X-direction, with an initial crack length of 1.2 mm, as shown in Fig. 2a. The fatigue parameters were set as

$A_2 = 2857.4$ and $m_2 = 3.0$, with a PD grid spacing of 0.4 mm. Fig 2b and 2c show the damage distributions after N=400 and N=600 loading cycles, respectively. The crack progressively propagates from the initial crack tips under cyclic loading, demonstrating that the proposed model can capture fatigue crack growth without prescribing the crack path in advance.

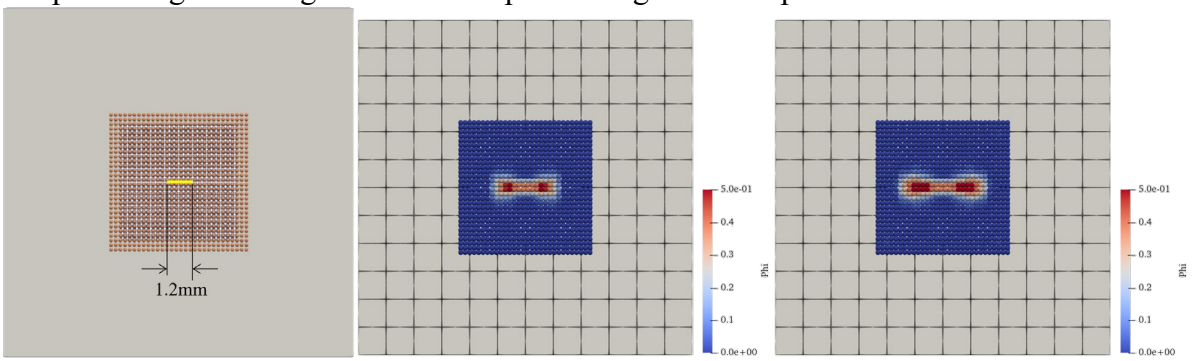

(a) Predefined crack (b) N = 400 (c) N = 600

Figure 2: Fatigue cracking verification of plate

Conclusions

This work extends the existing 2D CUF–3D peridynamics coupling framework to fatigue crack analysis by incorporating a bond-level peridynamic fatigue damage model. The 3D PD model is restricted to the crack-prone region, while the surrounding elastic domain is represented by refined 2D CUF plate elements, allowing local fatigue damage evolution to be captured with reduced computational cost. The static verification example shows a continuous displacement transition across the FE, PD, and coupling regions. The fatigue example further demonstrates that the model can reproduce progressive crack growth from an initial crack without prescribing the crack path. These preliminary results indicate the potential of the proposed framework for efficient fatigue crack analysis of plate-like structures.

Acknowledgment

Qiang Zhang acknowledges the support from the China Scholarship Council (File No. 202406370014)

References

[1] A. Pagani and E. Carrera, “Coupling three-dimensional peridynamics and high-order one-dimensional finite elements based on local elasticity for the linear static analysis of solid beams and thin-walled reinforced structures,” Numerical Meth Engineering, vol. 121, no. 22, pp. 5066–5081, Nov. 2020. https://doi.org/10.1002/nme.6510.

[2] A. Pagani, M. Enea, and E. Carrera, “Quasi-static fracture analysis by coupled three-dimensional peridynamics and high order one-dimensional finite elements based on local elasticity,” Numerical Meth Engineering, vol. 123, no. 4, pp. 1098–1113, Feb. 2022. https://doi.org/10.1002/nme.6890.

[3] F. Scabbia and M. Enea, “An improved coupling of 3D state-based peridynamics with high-order 1D finite elements to reduce spurious effects at interfaces,” Numerical Meth Engineering, vol. 124, no. 17, pp. 3687–3708, Sep. 2023. https://doi.org/10.1002/nme.7297.

[4] J. Zhang et al., “A computational approach to integrate three-dimensional peridynamics and two-dimensional higher-order classical elasticity theory for fracture analysis,” Engineering with Computers, vol. 41, no. 1, pp. 335–351, Feb. 2025. https://doi.org/10.1007/s00366-024-02001-2.

Materials Research Proceedings 73 (2026) 66-71 https://doi.org/10.21741/9781644904459-14

Indentation on Anisotropic Magneto-Electro-Viscoelastic Layer-Substrate using a Semi-Analytical Approach

Do Duc DO[1,a], Nguyen Dinh DUC[1,b], Van Thuong NGUYEN[1,c *]

[1]VNU University of Engineering and Technology, Vietnam National University, Hanoi, Vietnam

[a]22024131@vnu.edu.vn, [b]ducnd@vnu.edu.vn, [c]thuong.nv@vnu.edu.vn

Keywords: Anisotropy, Magneto-Electro-Elasticity, Viscoelasticity, Layer-Substrate

Abstract. By combining the elastic-viscoelastic correspondence principle with a semi-analytical method (SAM), the indentation problem of a magneto-electro-viscoelastic (MEV) layer-substrate structure is solved. A surface Green's function for anisotropic magneto-electro-elastic (MEE) bimaterials is first derived in the Laplace domain, which inherently satisfies interfacial continuity conditions and eliminates the need for interface discretization. Using this Green's function as the kernel, the influence matrices of SAM are evaluated analytically, improving computational accuracy and efficiency. Numerical examples are provided to verify the correctness and applicability of the proposed method for anisotropic MEV layer-substrate structures.

1. Introduction

Magneto-electro-viscoelastic (MEV) materials represent an advanced class of smart materials that combine piezomagnetic, piezoelectric, and viscoelastic behaviors within a unified framework. Owing to their multifunctional coupling effects, these materials have attracted significant attention in a wide range of engineering applications, including aerospace, civil, and mechanical systems [2]. In many practical designs, MEV materials are often implemented in layer-substrate configurations, which are commonly encountered in modern high-performance devices [2,3]. Indentation analysis plays a crucial role in characterizing the local mechanical and multiphysical properties of such materials, particularly at the micro- and nanoscale [4]. Among various techniques, rigid punch indentation has been widely recognized as an effective approach for evaluating material responses under coupled fields [5]. Consequently, studying indentation behavior in anisotropic MEV layer-substrate systems is important for both theoretical investigation and practical applications. In this paper, a semi-analytical method is developed to investigate two-dimensional indentation induced by a rigid indenter acting on an MEV layer bonded to a substrate. The formulation accounts for different electrical and magnetic boundary conditions at the indenter, including both conducting and insulating cases. To demonstrate the accuracy and robustness of the proposed approach, several numerical examples are presented and discussed.

2. Problem descriptions

Consider the contact problems between a flat-ended indenter and an anisotropic MEV layer-substrate, as illustrated in Fig. 1. In the analysis, we align the Cartesian coordinate system (x_1, x_2) with the shared interface between the layer and the substrate, positioning the vertical axis through the center of the indenter. The layer, composed of material 1, occupies the region $0 \le x_2 \le h$, while the substrate, made of material 2, extends over the remaining region $x_2 < 0$. Materials 1 and 2 are both anisotropic magneto-electro-viscoelastic, and their properties and the related physical quantities of the layer and substrate are denoted by superscripts (1) and (2), respectively. The indenter is subjected to a generalized load vector $\mathbf{q}$, which consists of mechanical loads q_i (i = 1,2,3), electric charge e, and magnetic charge m. When the load $\mathbf{q}$ is applied, the indenter contacts the MEV layer-substrate at the contact region Ω_c on the layer's upper surface. This contact generates generalized contact tractions, along with normal electric and magnetic displacements,

Content from this work may be used under the terms of the Creative Commons Attribution 3.0 license. Any further distribution of this work must maintain attribution to the author(s) and the title of the work, journal citation and DOI. Published under license by Materials Research Forum LLC.

Materials Research Proceedings 73 (2026) 66-71 https://doi.org/10.21741/9781644904459-14

on the contact surface. These effects, in turn, lead to surface deformation, electric potential, and magnetic potential beneath the indenter.

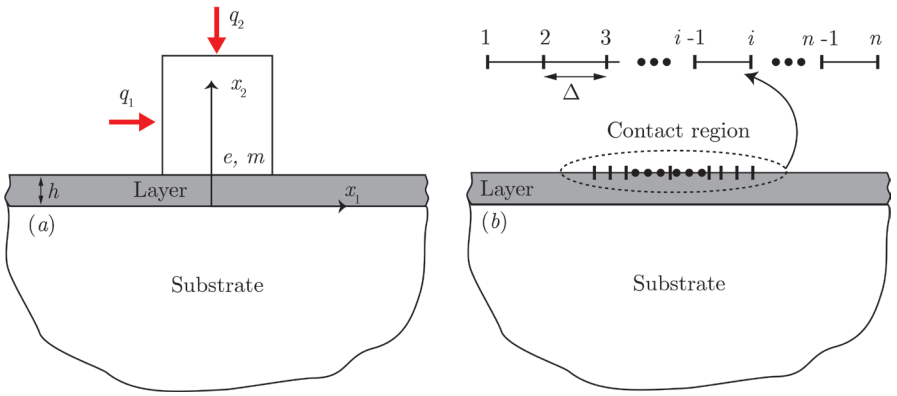

Fig. 1. (a) Indentation on MEE viscoelastic layer-substrate (b) Modeling contact problem by SAM

3. Methodology

3.1. Elastic-viscoelastic correspondence principles

If the body forces are omitted, the small deformation and the static force are considered, the basic equations for anisotropic MEV material at time t can be expressed as [6,7]

$$\begin{cases} \sigma_{ij}(t)=C_{ijkl}(t)*\varepsilon_{kl}(t)-e_{kij}(t)*E_k(t)-q_{kij}(t)*H_k(t) \\ D_j(t)=e_{jkl}(t)*\varepsilon_{kl}(t)+w_{jk}(t)*E_k(t)+m_{jk}(t)*H_k(t), \\ B_j(t)=q_{jkl}(t)*\varepsilon_{kl}(t)+m_{jk}(t)*E_k(t)+\xi_{jk}(t)*H_k(t) \end{cases} \begin{cases} \varepsilon_{ij}(t)=\frac{1}{2}\left(u_{i,j}(t)+u_{j,i}(t)\right) \\ E_j(t)=-u_{4,j}(t) \\ H_j(t)=-u_{5,j}(t) \end{cases}, \begin{cases} \sigma_{ij,j}(t)=0 \\ D_{j,j}(t)=0 \\ B_{j,j}(t)=0 \end{cases} \quad (1)$$

where $i,j,k,l=1,2,3$; u_i, i=1,2,3 are mechanical displacements, and u_4 and u_5 are the electric and magnetic potentials; σ_{ij}, D_j, and B_j denote the mechanical stress, electric displacement, and magnetic induction, respectively; e_{kij} and w_{jk} are piezoelectric stress and dielectric permittivity tensors. q_{kij}, m_{jk} and ξ_{jk} are, respectively, the piezomagnetic stress, magnetoelectric coupling, and magnetic permeability tensors; C_{ijkl} is the elastic stiffness tensor. The operation * stands for the convolution integral, i.e.,

$$a(t)*b(t)=a(t)b(0)+\int_0^t a(t-\tau)\frac{\partial b(\tau)}{\partial \tau}d\tau \quad (2)$$

For simplicity, the properties are assumed to be represented using a Prony series [8-10]

$$a(t)=a_0\left\{\rho+\sum_{p=1}^{N}\rho_p e^{-t/\omega_p}\right\} \quad (3)$$

where a can be C_{ijkl}, e_{kij}, q_{kij}, m_{jk}, w_{jk} and ξ_{jk}; a_0 is the properties at the initial state; ω_p, $p=1,2,...,N$ denotes the relaxation times; ρ and ρ_p, $p=1,2,...,N$ denotes the Prony series coefficient. They can be different for different material constants and satisfy the following relation

$$\rho+\sum_{p=1}^{N}\rho_p=1, \text{ where } 0\le\rho\le 1, \text{ and } 0\le\rho_p\le 1 \quad (4)$$

Taking the Laplace transform of Eq. 1 yields [1]

Materials Research Proceedings 73 (2026) 66-71 https://doi.org/10.21741/9781644904459-14

$$\begin{cases} \breve{\sigma}_{ij} = s\breve{C}_{ijkl}\breve{\varepsilon}_{kl} - s\breve{e}_{kij}E_k - s\breve{q}_{kij}\breve{H}_k \\ \breve{D}_j = s\breve{e}_{jkl}\breve{\varepsilon}_{kl} + s\breve{w}_{jk}\breve{E}_k + s\breve{m}_{jk}\breve{H}_k \\ \breve{B}_j = s\breve{q}_{jkl}\breve{\varepsilon}_{kl} + s\breve{m}_{jk}\breve{E}_k + s\breve{\xi}_{jk}\breve{H}_k \end{cases}, \begin{cases} \breve{\varepsilon}_{ij} = \frac{1}{2}\left(\breve{u}_{i,j} + \breve{u}_{j,i}\right) \\ \breve{E}_j(t) = -\breve{u}_{4,j} \\ \breve{H}_j(t) = -\breve{u}_{5,j} \end{cases}, \begin{cases} \breve{\sigma}_{ij,j} = 0 \\ \breve{D}_{j,j} = 0 \\ \breve{B}_{j,j} = 0 \end{cases} \tag{5}$$

where s is the Laplace transform variable. It can be seen that Eq. 5 is equivalent to the basic equations for MEE materials. In the Laplace domain, the solutions of Eq. 5 can therefore be obtained directly from those of the corresponding MEE solutions. The solutions in the real-time domain can then be obtained by using the Laplace transform [1].

3.2. Semi-analytical method

To obtain the contact solutions, a semi-analytical method will be developed here to solve the indentation problems on the MEV layer-substrate in the Laplace domain. The method starts from the fundamental solution Eq. 6, which expresses the relationship between surface deformation on the contact surface and the distributed contact traction of a bimaterial, i.e., [11, 16]

$$\begin{cases} \breve{\mathbf{u}}^{(1)}\left(x_1\right) = 2\mathrm{Re}\left\{\mathbf{A}_s^{(1)}\left[\mathbf{F}_{0s}^{(1)}\left(x_1\right) + \mathbf{F}_{ps}^{(1)}\left(x_1\right)\right]\right\} \\ \mathbf{F}_{0s}^{(1)}\left(x_1\right) = \int_{\Omega_c} \mathbf{f}_{0s}^{(1)}\left(x_1, \hat{x}_1\right) d\hat{x}_1,\ \mathbf{F}_{ps}^{(1)}\left(x_1\right) = \int_{\Omega_c} \mathbf{f}_{ps}^{(1)}\left(x_1, \hat{x}_1\right) d\hat{x}_1 \end{cases} \tag{6a}$$

where

$$\begin{aligned} \mathbf{f}_{0s}^{(1)}\left(x_1, \hat{x}_1\right) &= \left\langle \ln\left(x_1 - \hat{x}_1\right)\right\rangle \left(\mathbf{B}_s^{(1)}\right)^{-1} \breve{\mathbf{t}}^{(1)} / 2\pi i, \\ \mathbf{f}_{ps}^{(1)}\left(x_1, \hat{x}_1\right) &= \sum_{j=1}^{5} \left\langle \ln\left(x_1 + \left(\mu_\alpha^s\right)^{(1)} h - \hat{x}_1 - \left(\overline{\mu}_j^s\right)^{(1)} h\right)\right\rangle \mathbf{A}_j^{*(1)} \breve{\mathbf{t}}^{(1)} / 2\pi i. \end{aligned} \tag{6b}$$

where <> denotes the 5x5 diagonal matrix whose component varies with subscript α; μ_α^s is the material eigenvalue and $\mathbf{A}_s^{(1)}$ and $\mathbf{B}_s^{(1)}$ are the corresponding material eigenmatrices in the Laplace domain; $\mathbf{A}_j^{*(1)}$ is the matrix which accounts for the layer-substrate interaction [11].

By discretizing the contact region into n contact elements (see Fig. 1) and assuming that the contact traction is constant within each element, integrating Eq. 6 can be further reduced to

$$\breve{\mathbf{u}}^{(1)} = \mathbf{C}^{(1)} \breve{\mathbf{t}}^{(1)} \tag{7}$$

It should be noted that the fundamental solution in Eq. 6b already satisfies the continuity condition at the interface between the layer and the substrate. Only the mesh along the potential contact region is needed. In Eq. 7, $\breve{\mathbf{u}}^{(1)}$ and $\breve{\mathbf{t}}^{(1)}$ are, respectively, global generalized displacement and traction vectors in the Laplace domain, and $\mathbf{C}^{(1)}$ is a global influence matrix. Inside the contact region, both displacement and traction are usually unknown in advance. Eq. 7 thus gives us 5N equations and 10N unknown variables. To obtain unique solutions, 5N additional equations from contact constraint relations are needed. For the indentation problems, the contact constraint relations are

$$\breve{t}_1^{(1)}\left(x_1, h\right) = \pm\eta \breve{t}_2^{(1)}\left(x_1, h\right),\ \breve{u}_2^{(1)}\left(x_1, h\right) = f\left(x_1\right) + \delta,\ \breve{t}_3^{(1)}\left(x_1, h\right) = 0 \tag{8}$$

where η is the friction coefficient, whose sign ahead depends on the sliding direction [6, 11].
In addition to the mechanical condition given in Eq. 8, the electromagnetic boundary conditions on the contact surface must also be considered. Four types of electromagnetic conditions are examined, corresponding to combinations of electric insulating ($\breve{t}_4^{(1)}\left(x_1, h\right)$=0), or electric conducting ($\breve{u}_4^{(1)}\left(x_1, h\right) = \breve{u}_{4p}$), and magnetic insulating ($\breve{t}_5^{(1)}\left(x_1, h\right) = 0$) or magnetic conducting

Materials Research Proceedings 73 (2026) 66-71 https://doi.org/10.21741/9781644904459-14

($\breve{u}_5^{(1)}(x_1,h)=\breve{u}_{5p}$) cases. Here, $\breve{u}_{4p}$ and $\breve{u}_{5p}$ denote the prescribed electric and magnetic potentials of the punch, which are assumed to be constant over the contact region.

By gathering the contact constraints for all nodes within the contact region and using the indenters' equilibrium conditions, we can derive the following equations

$$\mathbf{D}_u\breve{\mathbf{u}}^{(1)}+\mathbf{D}_t\breve{\mathbf{t}}^{(1)}+\mathbf{D}_q\delta=\mathbf{f}_c,\ \mathbf{E}_q\breve{\mathbf{t}}^{(1)}=\mathbf{f}_q \tag{9}$$

Combining Eq. 7 and Eq. 9, we obtain the solvable system of linear equations

$$\begin{bmatrix}\mathbf{I} & -\mathbf{C}^{(1)} & \mathbf{0}\\ \mathbf{D}_u & \mathbf{D}_t & \mathbf{D}_q\\ \mathbf{0} & \mathbf{E}_q & \mathbf{0}\end{bmatrix}\begin{Bmatrix}\breve{\mathbf{u}}^{(1)}\\ \breve{\mathbf{t}}^{(1)}\\ \delta\end{Bmatrix}=\begin{Bmatrix}\mathbf{0}\\ \mathbf{f}_c\\ \mathbf{f}_q\end{Bmatrix} \tag{10}$$

In solving this system of equations, all the contact responses are uniquely determined. After obtaining the solutions in the Laplace domain, their corresponding real-time solutions can be determined by the numerical inversion of the Laplace transform [1].

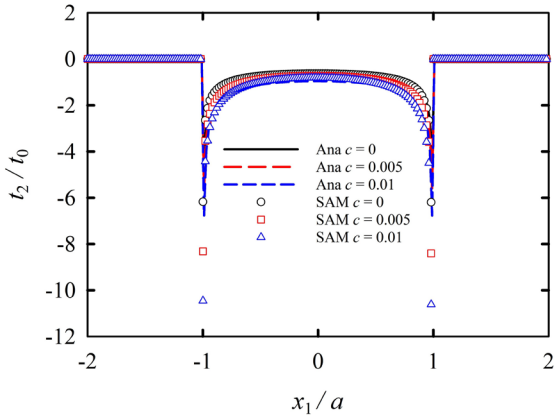

Fig. 2. Contact traction with different loading rates c at t = 50 (s). Here, $t_0 = q_0/2a$.

4. Numerical Results

4.1. Indentation on homogeneous viscoelastic half-plane

Consider the indentation of a homogeneous viscoelastic half-plane. The punch is an electric and magnetic insulator. It has a width $2a$ = 0.02 (m) and is subjected to the load $q_2 = q_0(1+ct)$ (kN/m) ($t \geq 0$), where q_0 = 100 (kN/m) and c is the loading rate, which is varied as c = 0, 0.005, 0.01 (unit: 1/s). To simulate the homogeneous viscoelastic half-plane, the layer thickness is taken as $h/a = 5$, but both layer and substrate are assumed to be made of a high-density cellulose-based composite (HDCBC), whose initial material properties in its principal directions are [13,14]

$$E_{11}^0=12.6999,\ E_{22}^0=9.503,\ E_{33}^0=0.3995,\ G_{12}^0=4.794,\ G_{31}^0=G_{23}^0=0.1989,\ \text{(unit: GPa)},$$
$$\nu_{12}=0.24,\ \nu_{13}=\nu_{23}=0,\ N=5,\ \rho=0.5883,\ \rho_1=0.0941,\ \rho_2=\rho_3=0.0706,\ \rho_4=0.1176, \tag{11}$$
$$\rho_5=0.0588,\ \omega_1=5,\ \omega_2=75,\ \omega_3=1200,\ \omega_4=21000,\ \omega_5=400000\ \text{(unit: s)}$$

To get the numerical result of anisotropic materials, the principal directions are rotated about the x_1, x_2, and x_3 axes by the angles α=60°, β=45° and γ=30°. To simulate a homogeneous viscoelastic material in SAM, the electric and magnetic properties are assumed to be uncoupled from the mechanical properties, i.e., we set e_{kij}=0 and q_{kij}=0, while the other electric and magnetic properties are arbitrary. Fig. 2 presents the contact pressure distribution along the upper surface of the layer for different values of the loading rate c. The results obtained by SAM show good agreement with the analytical solutions reported in [12]. In addition, contact pressure increases with increasing loading rate, consistent with engineering intuition.

Materials Research Proceedings 73 (2026) 66-71 https://doi.org/10.21741/9781644904459-14

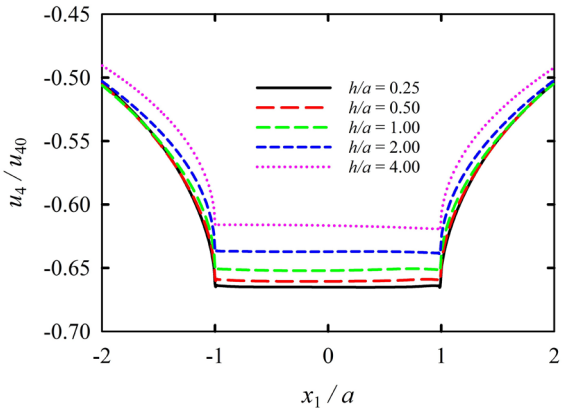

Fig. 3. The variation of the electric potential at the layer's upper surface, u_4, with different layer thicknesses. Here, $u_{40} = 50(\mu\text{V})$

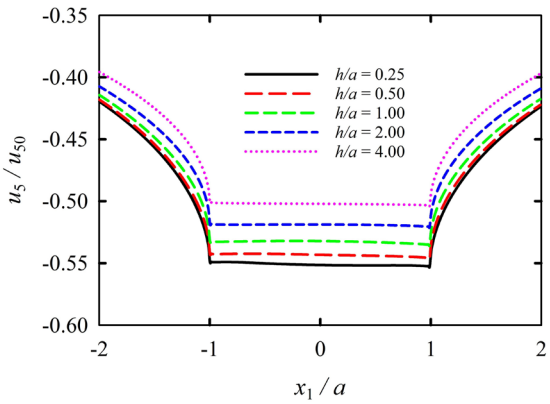

Fig. 4. The variation of the magnetic potential at the layer's upper surface, u_5, with different layer thicknesses. Here, $u_{50} = 50(n\text{A})$

4.2. Indentation on MEV layer-substrate

To illustrate the applicability of SAM to the anisotropic MEV layer-substrate, the layer is now assumed to be $BaTiO_3$-$CoFe_2O_4$ with 50% volume fraction of $BaTiO_3$, i.e., $v_f(BaTiO_3)$ =50%, whose material properties are expressed by the Voigt notation as [15]

$$\begin{aligned}
&C_{11} = C_{22} = 213,\ C_{12} = C_{13} = C_{23} = 113,\ C_{33} = 207,\ C_{44} = C_{55} = 49.9,\ C_{66} = 50,\ \text{(unit: GPa)},\\
&e_{31} = e_{32} = -2.71,\ e_{33} = 8.86,\ e_{24} = e_{15} = 0.15,\ \text{(unit: C/m}^2\text{)},\ w_{11} = w_{22} = 0.24\times10^{-9},\\
&w_{33} = 6.37\times10^{-9},\ \text{(unit: C}^2\text{/Nm}^2\text{)},\ q_{31} = q_{32} = 222,\ q_{33} = 292,\ q_{24} = q_{15} = 185,\\
&\text{(unit: N/Am)},\ m_{11} = m_{22} = -5.23\times10^{-12},\ m_{33} = 2750\times10^{-12},\ \text{(unit: Ns/VC)},\\
&\xi_{11} = \xi_{22} = 2.01\times10^{-4},\ \xi_{33} = 0.893\times10^{-4},\ \text{(unit: Ns}^2\text{/ C}^2\text{)}
\end{aligned} \tag{12}$$

The substrate is assumed to be a mixture of $BaTiO_3$-$CoFe_2O_4$ with $v_f(BaTiO_3)$ =50% and HDCBC. The relaxation time and Prony series coefficient are assumed to be the same as HDCBC, while the material properties a are followed by the mixture rule, i.e., a(substrate)=v_f (HDCBC)a(HDCBC)+ (1-v_f (HDCBC))a($BaTiO_3$-$CoFe_2O_4$). As in the previous example, to simulate a general anisotropic material, the principal directions of all materials are rotated about the x_1, x_2, and x_3 axes by angles α=60°, β=45° and γ=30°. The contact is assumed to be frictionless, and the punch profile is flat-ended with width $2a$ = 0.02m and is an electric and magnetic conductor. The electric charge and magnetic charge are set to be zero, and the punch is subjected to time-independent loading q_2=100(kN/m). The thickness varies as h/a = 0.25, 0.5, 1, 2, and 4. Figs. 3 and 4 show the electric potential and magnetic potential along the upper surface of the layer at the time t = 10 (s). It can be observed that, although the applied loading remains constant, increasing the layer thickness results in higher electric and magnetic potentials.

5. Conclusions

A semi-analytical method has been developed to analyze indentation in anisotropic magneto-electro-viscoelastic layer-substrate systems. The method is based on surface Green's functions tailored for bimaterials, allowing the influence matrices in the SAM to be evaluated analytically. By employing these Green's functions, the interfacial boundary conditions between the layer and substrate are satisfied in closed form, improving accuracy and computational efficiency. The proposed SAM applies to general anisotropic magneto-electro-elastic composites and can handle both conducting and insulating indenters. To verify the accuracy and applicability of the proposed method, numerical examples have been provided.

Acknowledgment
This research is funded by Vietnam National Foundation for Science and Technology Development (NAFOSTED) under grant number 107.02-2025.51.

References

[1] V.T. Nguyen, C. Hwu, Holes, cracks, or inclusions in two-dimensional linear anisotropic viscoelastic solids. Compos. B. Eng. 117 (2017) 111-123. https://doi.org/10.1016/j.compositesb.2017.01.050

[2] V.L. Nguyen, T.K.H. Nguyen, N.D. Duc, V.T. Nguyen, Pin-loaded joint contact in anisotropic viscoelastic plates via a semi-analytical method, Comput. Struct. 317 (2025) 107940. https://doi.org/10.1016/j.compstruc.2025.107940

[3] M. Ajdour, A. Bakkali, L. Azzar, A. El Omri, Modeling and analysis of loaded multilayered magneto-electro-elastic structures composite materials: Applications, Adv. Electromagn. 5 (3) (2016) 92-97. https://doi.org/10.7716/aem.v5i3.426

[4] E. Broitman, Indentation Hardness Measurements at Macro-, Micro-, and Nanoscale: A Critical Overview, Tribol Lett 65 (2017) 23. https://doi.org/10.1007/s11249-016-0805-5

[5] Y. Zhang, H. Ma, J. Yang, S. Ding, Frictionless multifield coupling contact problem for a thermoelectric layer loaded by two rigid punches, Acta Mech. Solida Sin. 36 (2023) 282-292. https://doi.org/10.1007/s10338-022-00355-y

[6] V.T. Nguyen, C. Hwu, Boundary element method for two-dimensional frictional contact problems of anisotropic elastic solids, Eng. Anal. Bound. Elem. 108 (2019) 49-59. https://doi.org/10.1016/j.enganabound.2019.08.010

[7] E. Pan, Exact solution for simply supported and multilayered magneto-electro-elastic plates, J. Appl. Mech 68(4) (2001) 608-618. https://doi.org/10.1115/1.1380385

[8] T. Chen, Determining a Prony series for a viscoelastic material from time varying data, Nasa, 2000.

[9] M. Abouhamzeh, J. Sinke, K.M.B. Jansen, R. Benedictus, Thermo-viscoelastic analysis of GLARE, Compos. B. Eng. 99(15) (2016) 1-8. https://doi.org/10.1016/j.compositesb.2016.05.060

[10] X. Liu, T. Tang, W. Yu, R.B. Pipes, Multiscale modeling of viscoelastic behaviors of textile composites, Int. J. Eng. Sci 130 (2018) 175-86. https://doi.org/10.1016/j.ijengsci.2018.06.003

[11] V.T. Nguyen, V.S. Pham, N.D. Duc, T.Q. Bui, Semi-analytical method for frictional sliding contact of a piezoelectric layer-substrate, Mech. Mater. 213 (2025) 105572. https://doi.org/10.1016/j.mechmat.2025.105572

[12] C. Hwu, Anisotropic Elasticity with Matlab, Springer: New York, 2021.

[13] D. Tjahjanto, O. Girland, S. Östlund, Anisotropic viscoelastic-viscoplastic continuum model for high-density cellulose-based materials, J. Mech. Phys. Solids. 84 (2015) 1-20. https://doi.org/10.1016/j.jmps.2015.07.002

[14] V.T. Nguyen, C. Hwu, Analytical solutions and boundary element analysis for holes and cracks in anisotropic viscoelastic solids via time-stepping method, Mech. Mater. 160 (2021) 103964. https://doi.org/10.1016/j.mechmat.2021.103964

[15] C.X. Xue, E. Pan, On the longitudinal wave along a functionally graded magneto-electro-elastic rod, Int. J. Eng. Sci. 62 (2013) 48-55. https://doi.org/10.1016/j.ijengsci.2012.08.004

[16] C. Hwu, Anisotropic Elastic Plates, Springer: New York, 2010.

Materials Research Proceedings 73 (2026) 72-77 https://doi.org/10.21741/9781644904459-15

Design to Manufacturing Process Calibration and Simulation of LPBF Structures

Ijaz AKBAR[1,a *], Djamel ABOU MAAMAR[1], Mohamed El IBRAHIMI[1,b], Kevin Nocentini[1]

[1]Capgemini Engineering, T&I, Blagnac, France

[a]ijaz.akbar@capgemini.com, [b]mohamed.el-ibrahimi@capgemini.com

Keywords: Design of Thin Walls, Machine Learning, Process Parameters, LPBF Process Simulation

Abstract. In LPBF, printing failures are mainly driven due to thin-wall structures, use of non-calibrated machines and material parameters. Hereof, to pre-identify the design for additive thin walls (DFATW), a macro-design tool is under development that could predict the existence of thin walls below a threshold so the critical zones could be treated to be printable with LPBF process. In addition, an AI4AM approach is developed to predict the combined and individual influence driven by process parameters, especially around melt-pool dimensions, length, width, and height. These dimensions predicted by AI4AM are cross validated following an MAPE of < 6% with FEM so from hundreds of process parameters the best combination could be identified in seconds to better train the LPBF machine. Finally, the process simulation modelling based on AI4AM predictions is performed to investigate further process driven defects. The LPBF simulation results showed that the as produced and heat-treated structures have significant differences in structural distortion and final residual stresses (an approximately 35% reduction).

Introduction

Laser Powder Bed Fusion (LPBF) enables printing of complex metal geometries, but thin-wall and complex features remain highly defect-prone due to process-induced distortion, residual stresses, porosity, and cracking [1]. Part quality is sensitive to uncertainty in machine/material calibration and to the combined selection of key parameters (laser power, scan speed, layer thickness, hatch spacing), leading to variability and limiting defect-sensitive performance such as fatigue [2]. For thin-wall applications (e.g, heat exchangers), manufacturability is further constrained by process instability, thermal stresses, part orientation, and limited studies have validated a wall thickness below ~400 μm [3]. Today, LPBF limitations are often discovered through costly trial-and-error experiments, while available numerical tools are not yet sufficiently reliable to identify complex feature's printability early in design phase [4]. Meanwhile, as-build residual-stress control is challenging because high-fidelity multi-physics models are too slow for engineering loops and simplified thermal models can neglect the solidification effects and geometric complexity [5]. Overall, current approaches rarely support rapid pre-identification of DFATW and real-time exploration of multi-parameter interactions; integrating fast AI models with simulation is therefore needed to pre-qualify the process parameters and reduce defects [6].

This study objective is to identify DFATW configurations that ensure mechanical stability during printing and in service, while meeting manufacturing constraints. In addition, AI4AM is considered a key enabler to determine optimal parameters choice and configure the LPBF machine with calibrated settings to achieve first-time-right printing. To validate the AI4AM predictions, FEM process simulations are used to crosscheck the outputs from selected parameter sets and to evaluate how residual stresses can be reduced through post heat treatments. Overall, the DFATW

Content from this work may be used under the terms of the Creative Commons Attribution 3.0 license. Any further distribution of this work must maintain attribution to the author(s) and the title of the work, journal citation and DOI. Published under license by Materials Research Forum LLC.

Materials Research Proceedings 73 (2026) 72-77 https://doi.org/10.21741/9781644904459-15

and AI4AM results will populate a database that supports simulation model to validate and helps define acceptable thresholds for robust, defect-free printing with additional post treatments.

Methodology

- The methodology is linked to the following research questions to be studied:
- How to pre-design thin walls to avoid premature structural failures?
- Effects of process parameters at fusion zones will be addressed using machine learning (ML) and cross-validation by the finite element (FE) process simulations.
- How does the controlled thermo-mechanical behaviour of parts produced by the LPBF process reduce the level of residual stress and part distortion?

Design for Additive thin walls (DFATW)

Fabrication of thin walls presents major challenges, particularly with respect to buckling and structural distortion. To identify the minimum printable dimensions at an early stage a macro-design tool *"DFATW"* based on a machine-learning is proposed, that can accelerate early risk screening of unseen geometries. Accordingly, several supporting methodologies were reviewed, such as CATIA Wall Thickness Analysis Tool [3], Face-to-Face Distance Measurement[7], Point Cloud / Grid Projection Method[8], Bounding Box–Based Geometric Analysis, Surface Extraction [9], Decomposed Surface Extract Analysis [7], Feature-Based Thickness Retrieval [7], Python/ FreeCAD Normal-Vector and Sphere method [10].

Artificial Intelligence 4 Additive Manufacturing (AI4AM)

A ML model will be employed on fusion characteristics of Ti64 material, where a dataset that includes LPBF process parameters is taken from Ref.[2], however, these 300 data points for each parameter (e.g., laser power and scan speed) are of Inconel 625. After this initial ML testing and validation, the model is adopted to Ti64. The second step is data preprocessing, and finally, feature selection to identify the most relevant variables for predicting process and part-level properties. From various ML models, Gaussian Process Regression (GPR), is chosen due to its advantages of modelling complex, non-linear relationships between process parameters and mechanical properties. The step after is model training, optimization and validation. A Tenfold cross-validation technique is used where the dataset is divided into ten equally sized parts or "folds." one-fold serves as a validation set, while the remaining nine folds are used for training.

LPBF Process Simulation

For process simulation and precise evaluation, the temperature dependent properties of Ti64 are modeled [6]. A Renishaw AM250 LPBF machine is modelled for a lattice and simple rectangular geometry as well as an aerospace bracket for LPBF process simulation. The thermal model is solved using transient heat transfer modes, while capturing the evolution of metallurgical phases. An uncoupled thermo-structural model as demonstrated in Fig. 1 is employed to calculate the thermal profiles in the initial step and then the structural analysis is performed based on the thermal profiles as input. For an uncoupled thermo-structural model, the basic energy equation, constitutive relationships of laser heat source, and structural model equations such as solid phase transformation kinetics could be consulted elsewhere [11].

Numerical Results

A *Macro_Design* tool could automatically detect the critical regions (<0.5 mm) based on geometric characteristics such as wall thickness, height, and width. Among the approaches reviewed, only the bounding-box, sphere and ray methods have been tested so far. The initial output of bounding box was limited to fixed mesh points that did not adapt to the part dimensions, meanwhile, the program was improved (Fig. 2a) to adapt the part dimensions. It can now measure thickness by positioning points over all external surfaces and projecting a segment through the

material. Fig. 2b-c illustrates the valid points (>0.5 mm) in light green and non-valid red points below threshold <0.5mm.

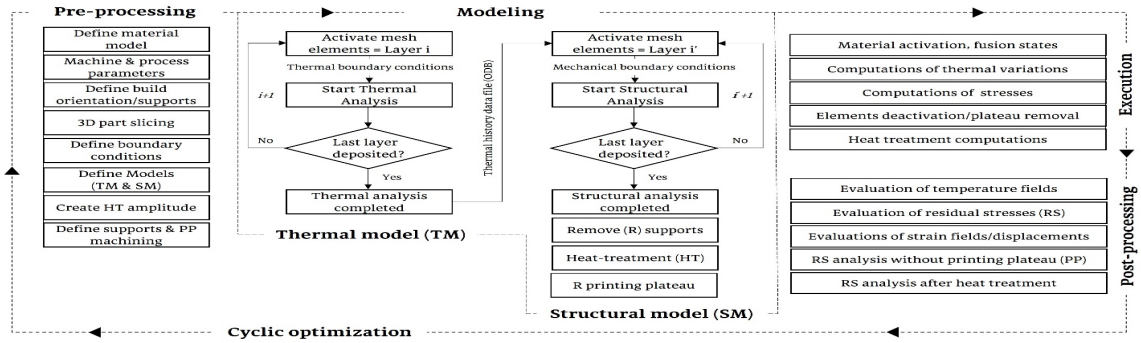

Fig. 1, Framework of multiscale thermo-structural modelling and post treatment analysis.

Finally, how the output is generated and the key values are shown in Fig. 2c. Secondly, the sphere-and-ray method is applied to a similar rectangular geometry (Fig. 2d), the goal is to improve this method until satisfactory results are achieved for sharp, thin, and complex edges. The method worked well, in Fig. 2d red sphere indicates the critical thicknesses (0.4 mm) and green indicates the non-critical zones (0.6 mm). However, currently the sphere size isn't yet automatically adaptable near edges; therefore, those sphere points are counted as anomalies, as illustrated by the red edges (Fig. 2d). Efforts to understand and address this issue are ongoing.

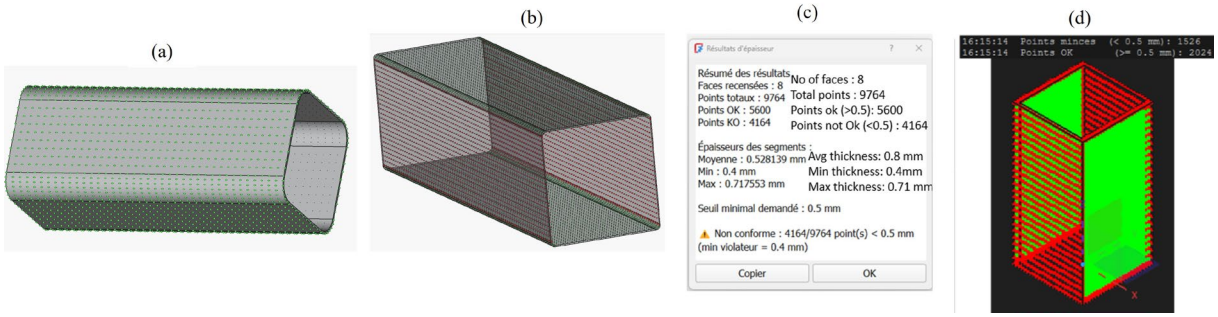

Fig. 2, Creation of mesh points to detect the thickness (a) Improved mesh points to adapt the part dimensions (b) Representation of valid (0.6mm) and non-valid (0.4mm) wall points (c) Output showing list of valid and non-valid points (d) Sphere method, illustration of red thin wall points (Point minces) and representation of green as valid points.

To validate our AI4AM model, Tenfold cross-validation and GPR model showed (Fig. 3abc) strong predictive performance for melt pool length and width, with Mean Absolute Percentage Error (MAPE) of approximately 8.08%, 4.28%, and 18.87%, close to those reported in the literature [2], except pool depth. Afterwards, the model was trained using Ti64 dataset from [12], based on individual parametric influence rates (Fig. 4D) the input variables have been reduced to four parameters: laser power, scan speed, preheat temperature, and hatch spacing. The improved ML model predicted the melt pool characteristics with MAPE of 2.24%, 2.76%, and 5.75% for length, width, and depth, as illustrated in Fig. 3def. These results demonstrate the robustness of the GPR model used in this study, with a high precision MAPE of less than 10% for all dimensions. Finally, the individual parametric effects are predicted with the Random Forest and the Sobol method. The analysis revealed that laser power and scan speed are the primary factors significantly affecting (85%, 14%) melt pool characteristics compared to preheat temperature and hatch spacing (Fig. 4AD).

Materials Research Proceedings 73 (2026) 72-77 https://doi.org/10.21741/9781644904459-15

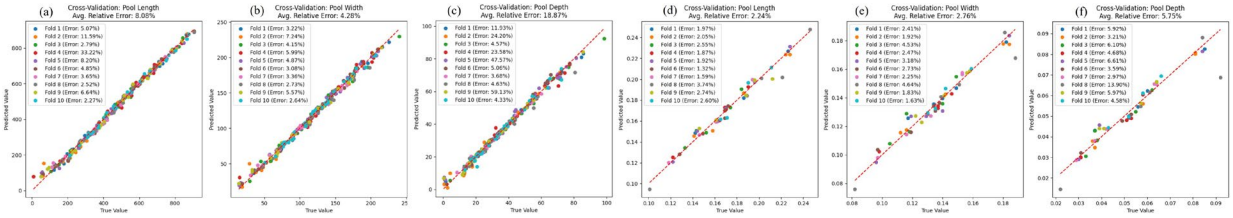

Fig. 3, (abc) Predictions of melt pool characteristics by ML model of Inconel625 (def) Final prediction by ML model adapted for "Ti64".

Due to negligible influence, the last two parameters were fixed for the rest of analysis. Fig. 4BC illustrates the effects of varying laser power and scan speed on three melt pool variables. An increase in laser power leads to an increase in the melt pool size, in contrast, an increase in scan speed results in a decrease in the melt pool dimensions. This inverse relationship depicts the effect of reduced laser-powder interaction time: as scan speed increases. Hence, the ML model predicted the optimal parameters to be 95 W laser power and 305 mm/s scan speed, resulting in an uncertainty level of less than 5%, while other two parameters were fixed: preheat temperature at 110°C and hatch spacing at 0.075 mm. The combination of laser power and scan speed are physically realistic for LPBF of Ti64 to produce a continuous melt pool as analyzed in Eq.1. According to linear energy density (LED), a value of 0.2-0.4J/mm is best compromise as cited elsewhere [13].

$$\boldsymbol{LED = \frac{P}{v} = \frac{95}{305} = 0.312\, J/mm} \quad (1)$$

To cross validate with ML predictions a FE based thermal analysis related to melt pool characteristics is studied. For that, a set of parameters predicted by ML approach is used in FE analysis to trigger the thermal profiles directly associated to melt pool zones. Melt pool zones of a solid geometry shown in Fig. 4A exhibits an excellent shape formation. Due to the complexity of the melt pool shape, only the length and depth were measured from simulation environment, as shown in Fig. 4A. For a solid geometry, the ML predictions for melt pool length and depth (≈162 µm, 43.14 µm) are comparable to the FE based observations of 166 µm and 47 µm, with a MAPE as quite low, with a value of 5.7%. This precise correlation provides a high level of confidence on ML model's ability to predict and optimize melt pool characteristics for MAM processes. Meanwhile, FE analysis of lattice structure (Fig. 5a) predicts significantly larger dimensions (≈412 µm length, 246 µm depth) compared to ML model estimates (≈162 µm, 43.14 µm), highlighting a substantial discrepancy to cross-validate. It might be due to non-uniform lattice geometry leading to uneven energy absorption and distribution, causing distinct melting behaviour compared to solid uniform structures. A comparative residual stress analysis was conducted between the as-built and heat-treated LPBF parts (Fig. 5b-c). The as-built part exhibited a residual stress of 765 MPa (Fig. 5b) lower than the >800 MPa reported elsewhere [14]. Annealing was simulated at 10°C/min with a constant hold, and trial analyses identified an optimal duration of ~2 h instead of 11 h. Heat treatment reduced residual stress by ~35%, from 765 MPa to 495 MPa (Fig. 5c) thereby minimizing distortion. It also enhances mechanical performance, including elongation, fatigue strength, and surface quality [15].

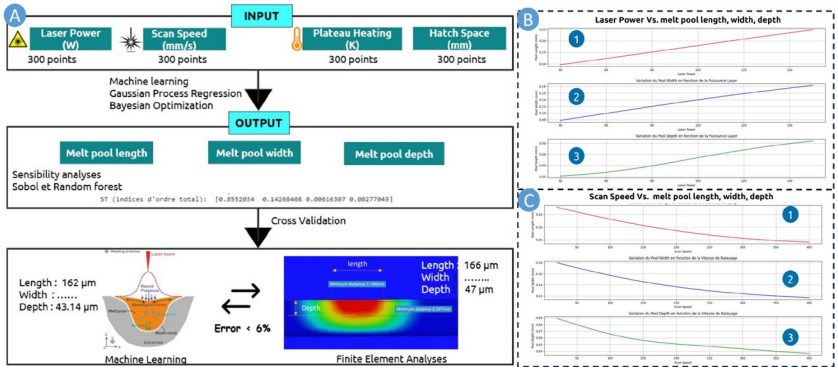

D

Outputs	Length	Width	Depth
Laser Power (W)	83.72	73.13	77.07
Scan speed (mm)	13.27	24.18	21.35
Preheat temperature (°C)	1.86	1.3	1.17
Hatch spacing (mm)	1.15	1.39	0.41

Fig. 4, (A) Overview of ML model and cross-validation with a solid geometry (B) Influence of varying laser powers in watts (C) Influence of varying scan speed in mm (D) Individual influence of printing parameters in % on the potential outputs.

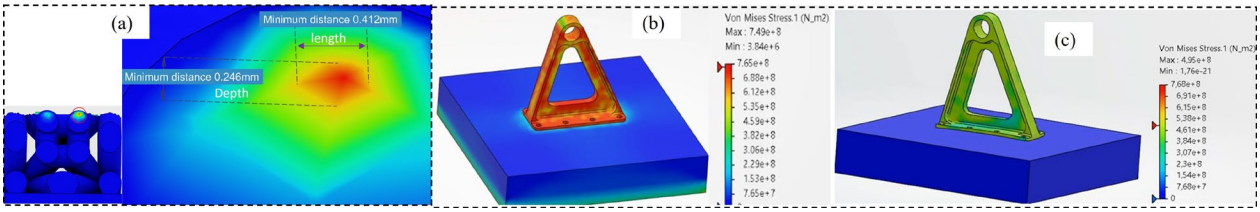

Fig. 5. (a) LPBF process simulation and highlighted pool dimensions of a lattice (b) Correlation of as build residual stresses (c) and after heat treatment annealing.

Conclusions

From the DFATW perspective, pre-design validation of thin walls governed by thickness-to-height ratios is indispensable. The initially adopted approaches (bounding-box, sphere, and ray) demonstrated high accuracy, with further improvements currently in progress. Second, the AI4AM/ML model was applied to quantify the influence of individual and combined parameters and found that laser power and scan speed have the greatest impact on melt pool characteristics. The current ML model is tested for both solid and lattice structures; however, the closer predictions, with an MAPE of < 6%, obtained through cross-validation with FE analyses are linked to a solid uniform geometry. The ML approach can potentially reduce (in part) the need for FE analysis while still providing reliable results for solid structures. Finally, AI4AM parametric predictions are used for thermo-structural and heat treatment simulations. The simulation results suggest that as-built and heat-treated components exhibit markedly different behavior in terms of residual stress, deformation, and mechanical response. The future objective is to develop a program/plugin that analyzes the part in greater detail and can adapt the mesh, sphere size, and checking procedure to the geometry; this will soon be in practice. AI4AM will be further developed to generalize predictions to complex structures; notably, a Physics-Informed ML model could be an ideal solution. The present analysis demonstrates the added value of post-treatment operations for as-built LPBF structures and supports the adoption of these best practices for a first-time right MAM.

References

[1] G. Weil, G., Analytical and numerical analyses of neo-Hookean thin-wall composite spheres, Mathematics and Mechanics of Solids 24 (2019) 1800–1820. https://doi.org/10.1177/1081286518807257

[2] Z. Wang, C. Jiang, P. Liu, W. Yang, Y. Zhao, M.F. Horstemeyer, L.Q. Chen, Z. Hu, L. Chen, Uncertainty quantification and reduction in metal additive manufacturing, NPJ Comput. Mater. 6 (2020). https://doi.org/10.1038/s41524-020-00444-x

[3] Z. Wu, S.P. Narra, A. Rollett, Exploring the fabrication limits of thin-wall structures in a laser powder bed fusion process, (2020). https://doi.org/10.1007/s00170-020-05827-4/

[4] G. Vastola, W.J. Sin, C.N. Sun, N. Sridhar, Design guidelines for suppressing distortion and buckling in metallic thin-wall structures built by powder-bed fusion additive manufacturing, Mater. Des. 215 (2022). https://doi.org/10.1016/j.matdes.2022.110489

[5] D. Wang, H. Fang, R. Xue, S. Li, Numerical study on the axial collapse of thin-walled columns, Sci. Rep. 14 (2024). https://doi.org/10.1038/s41598-024-56558-5

[6] J. Zhou, R.A. Barrett, S.B. Leen, Three-dimensional finite element modelling for additive manufacturing of Ti-6Al-4V components: Effect of scanning strategies on temperature history and residual stress, Journal of Advanced Joining Processes 5 (2022). https://doi.org/10.1016/j.jajp.2022.100106

[7] M.T. Khan, W. Feng, L. Chen, Y.H. Ng, N. Yew, J. Tan, S.K. Moon, DETC2024-XXXXX Automatic Feature Recognition and Dimensional Attributes Extraction from CAD Models for Hybrid Additive-Subtractive Manufacturing, n.d.

[8] Z. Wu, S.P. Narra, A. Rollett, Exploring the fabrication limits of thin-wall structures in a laser powder bed fusion process, (n.d.). https://doi.org/10.1007/s00170-020-05827-4/

[9] W. Shen, X. Zhang, X. Jiang, L.H. Yeh, Z. Zhang, Q. Li, B. Li, H. Qin, Surface extraction from micro-computed tomography data for additive manufacturing, in: Procedia Manuf., Elsevier B.V., 2021: pp. 568–575. https://doi.org/10.1016/j.promfg.2021.06.057

[10] M. Inui, N. Umezu, K. Wakasaki, S. Sato, Thickness and clearance visualization based on distance field of 3D objects, J. Comput. Des. Eng. 2 (2015) 183–194. https://doi.org/10.1016/j.jcde.2015.04.001

[11] P. Tan, F. Shen, B. Li, K. Zhou, A thermo-metallurgical-mechanical model for selective laser melting of Ti6Al4V, Mater. Des. 168 (2019). https://doi.org/10.1016/j.matdes.2019.107642

[12] J.R. Zhuang, Y.T. Lee, W.H. Hsieh, A.S. Yang, Determination of melt pool dimensions using DOE-FEM and RSM with process window during SLM of Ti6Al4V powder, Opt. Laser Technol. 103 (2018) 59–76. https://doi.org/10.1016/j.optlastec.2018.01.013

[13] H.L.W. a, J.S.Z. a, T.M. a, J.W.E. b, J.O.M. c, A.M.B. a, A.W.-H. a, A.D. d, W.Z. e T. DebRoy a, Additive manufacturing of metallic components – Process, structure and properties, Prog. Mater. Sci. (2018).

[14] N. Ahmed, I. Barsoum, R.K. Abu Al-Rub, Numerical investigation of residual stresses in thin-walled additively manufactured structures from selective laser melting, Heliyon 9 (2023). https://doi.org/10.1016/j.heliyon.2023.e19385

[15] S. Önder, N. Saklakoğlu, A. Sever, Selective laser melting of Ti6Al4V alloy: Effect of post-processing on fatigue life, residual stress, microstructure, microhardness and surface roughness, Mater. Charact. 196 (2023). https://doi.org/10.1016/j.matchar.2022.112571

Materials Research Proceedings 73 (2026) 78-84 https://doi.org/10.21741/9781644904459-16

Phase Holographic Imaging based on Acoustic Metasurfaces

Xiao Guo[1,a], Yifan Zhu[1,2,b *], Hui Zhang[1,2,c *]and Haiyan Fan[1,2,d]

[1]School of Mechanical Engineering, Southeast University, Nanjing, 211189, China.

[2]Key Laboratory of Underwater Acoustic Signal Processing (Southeast University), Ministry of Education, Nanjing, 210096, China

[a]xiaoguoseu@163.com, [b]yifanzhu@seu.edu.cn, [c]seuzhanghui@seu.edu.cn, [d]haiyan.fan@seu.edu.cn

Keywords: Phase Holographic Imaging, Amplitude-Phase Coupling Modulation, Acoustic Hologram, Acoustic Metamaterial

Abstract. Traditional amplitude-based acoustic holography methods suffer from limited capabilities in suppressing energy attenuation and resisting interference due to the influence of sound wave diffraction effects. Phase, a physical parameter often overlooked, offers higher energy utilization efficiency, stronger resistance to attenuation, and superior anti-interference performance compared to amplitude. However, the inherent periodic entanglement characteristics of phase limit its application in acoustic holography, while the coupling effect between amplitude and phase also remains one of the key challenges in phase research. Based on the exceptional imaging potential of phase-based techniques, this study employs spatial folding and periodic transformation methods to eliminate phase-period entanglement. First, the phase entanglement distributed within the period [-π, π] is folded into an independent, non-overlapping distribution within the range [0, π]. Subsequently, a cosine transformation maps this phase to a uniform distribution in the continuous space [-1, 1], thereby overcoming phase periodic entanglement and achieving uniform, non-overlapping phase holographic imaging performance. Due to the coupling effect between phase and amplitude in sound waves, image quality is not a simple superposition of amplitude and phase. To address this, we further investigate the amplitude-phase coupling mechanism in phase holography. By leveraging the differential properties of sound pressure, we reveal the physical essence of amplitude-phase coupling, derive the dynamic equations describing the amplitude-phase coupling relationship, and subsequently derive the acoustic energy conservation constraint term governing amplitude-phase coupling. Under the constraint of this conservation term, the coupling amplitude compensation distribution required for inverting the target phase image was obtained. Using this amplitude-phase coupling modulation method, a high-quality phase hologram with amplitude enhancement effects was achieved. To further validate the advantages of phase parameters in resisting energy attenuation and anti-interference capabilities, we evaluated the far-field imaging performance of phase holograms in information transmission. We ultimately demonstrated that the proposed phase holographic imaging method exhibits higher energy utilization efficiency compared to conventional methods.

Introduction

Acoustic holography is a crucial technology for reconstructing target sound fields through the coordinated modulation of wavefront phase and amplitude[1-4]. Its core lies in achieving active control of acoustic wave propagation and high-resolution imaging by precisely reconstructing the acoustic pressure field distribution near the diffraction limit. In recent years, driven by the advancement of acoustic metamaterials and computational acoustics, acoustic holography has demonstrated immense application potential in cutting-edge fields, including biomedicine[5,6], acoustic printing[7], virtual reality sound field reconstruction[8], information encryption[9-11], and acoustic imaging[12-14].

Content from this work may be used under the terms of the Creative Commons Attribution 3.0 license. Any further distribution of this work must maintain attribution to the author(s) and the title of the work, journal citation and DOI. Published under license by Materials Research Forum LLC.

Materials Research Proceedings 73 (2026) 78-84 https://doi.org/10.21741/9781644904459-16

In sound field manipulation, conventional phase-only modulation (PM) suffers from limited reconstruction accuracy without coordinated amplitude optimization[2], whereas amplitude-phase modulation (APM) utilizes lossy metamaterials for independent control to achieve high-fidelity reconstructions[15]. Although amplitude-based holography is well-established, it struggles with energy attenuation caused by acoustic diffraction. In contrast, phase parameters offer superior energy efficiency, attenuation resistance, and anti-interference capabilities. However, the exploration of phase holograms remains limited. Previous studies often oversimplified designs by constraining phases to discrete values (0 or π) or prescribing identical amplitude-phase images. These approaches ignore the clarity-degrading phase wrapping phenomenon and the inherent amplitude-phase coupling, severely restricting the practical performance of phase holograms.

Motivated by this, we propose a high-quality phase holographic imaging method utilizing acoustic metasurfaces. To eliminate phase wrapping, we introduce a spatial folding and period conversion technique. This approach folds the wrapped phase from a [-π,π] period into an independent [0,π] distribution, subsequently mapping it into a continuous [-1,1] space via cosine transformation. To resolve the critical challenge of amplitude-phase coupling, we elucidate its physical essence using acoustic pressure differential properties. We derive the governing dynamic equation and establish an acoustic energy conservation constraint. Under this constraint, we combine the Horned Lizard Optimization Algorithm[16] with the time-reversal method to inversely determine the optimal coupled amplitude compensation distribution for the target phase image. This strategy yields high-quality, amplitude-enhanced phase holograms. Finally, evaluations of far-field information transmission confirm that the proposed method demonstrates superior energy efficiency and robustness against attenuation compared to traditional techniques.

Methodology

The reconstruction of a holographic acoustic field fundamentally relies on the time-reversal principle. By designating the desired acoustic field at each pixel on the target image plane as a secondary wave source and back-propagating these waves to the holographic plane for coherent superposition, the requisite complex sound pressure distribution is achieved. Its expression is formulated as:

$$p_j = \sum_{l=1}^{N} \frac{A_{0l}}{r_l} \exp[i(k_0 r_l + \phi_{0l})] \equiv A_j \exp(i\phi_j) \tag{1}$$

where N signifies the total pixel count within the image. The variables A_{0l} and ϕ_{0l} represent the target amplitude and initial phase at the l-th pixel on the image plane, respectively, with k_0 denoting the wavenumber. The Euclidean spatial distance r_l between the j-th pixel on the holographic plane and the l-th pixel on the image plane is defined as:

$$r_l = \sqrt{(x_j - x_l)^2 + (y_j - y_l)^2 + (z_j - z_l)^2} \tag{2}$$

Within the scope of sound field manipulation, the intrinsic coupling between amplitude and phase emerges as a primary physical barrier that limits the quality of holographic imaging. To comprehensively elucidate this underlying coupling mechanism, a one-dimensional complex acoustic pressure wave equation is introduced to parse the wavefront evolution. By substituting the complex pressure form into the governing wave equation, a unified differential expression depicting the wavefront propagation can be derived:

$$\frac{d^2A(x)}{dx^2} + 2i\frac{dA(x)}{dx}\frac{d\phi(x)}{dx} + iA(x)\frac{d^2\phi(x)}{dx^2} - A(x)\left(\frac{d\phi(x)}{dx}\right)^2 + k^2A(x) = 0 \tag{3}$$

Materials Research Proceedings 73 (2026) 78-84 https://doi.org/10.21741/9781644904459-16

Leveraging the differential properties of acoustic pressure helps expose the physical essence of this amplitude-phase interaction. Specifically, the wave equation for complex acoustic pressure can be decoupled into a real-part equation that dictates the spatial evolution of the amplitude, and an imaginary-part equation that characterizes their dynamic coupling:

$$\begin{cases} \frac{d^2A(x)}{dx^2} = A(x)\left(\left(\frac{d\phi(x)}{dx}\right)^2 - k^2\right) \\ \frac{d^2\phi(x)}{dx^2} = -\frac{2}{A(x)}\frac{dA(x)}{dx}\frac{d\phi(x)}{dx} \end{cases} \tag{4}$$

Further analysis reveals that the imaginary-part equation inherently reflects the physical constraints governing acoustic energy transmission. Under ideal plane-wave excitation, acoustic waves propagate with a uniform amplitude (i.e., $A(x) = A_0$). Consequently, the real part of the wave equation governing the amplitude-phase evolution simplifies to a constant. Concurrently, the phase exhibits a linear spatial gradient (i.e., $\phi(x) = kx + \phi_0$). In such cases, the imaginary-part equation dictates the dynamic coupling behavior, and the conservation of acoustic energy flux is naturally satisfied. This theoretical framework demonstrates that during holographic imaging, any non-linear spatial modulation applied to the phase inevitably forces a spatial redistribution of the amplitude.

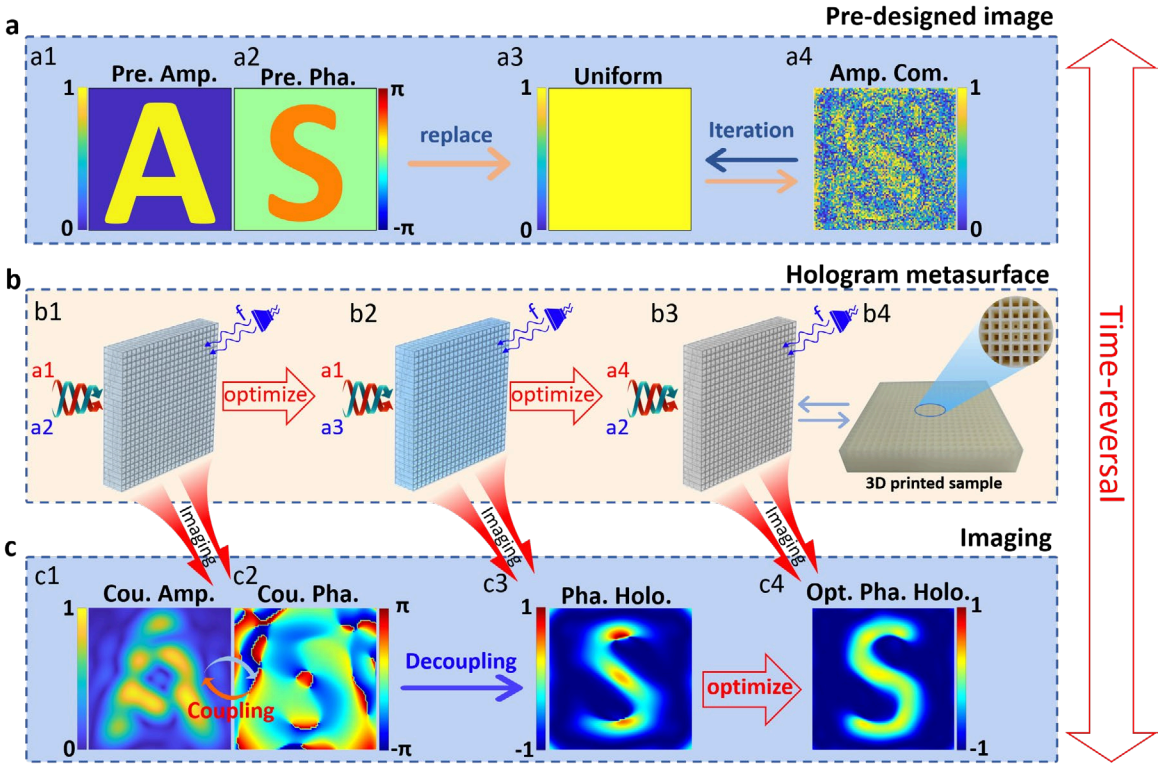

Figure 1. Amplitude-phase coupling effect and the phase hologram optimization process. (a) Preset target field distributions. (a1) target amplitude distribution (letter "A"). (a2) target phase distribution (letter "S"). (a3) uniform amplitude distribution; (a4) amplitude compensation distribution after iterative optimization. (b) Physical model of the holographic metasurface. (c) Holographic reconstruction results. (c1) coupled amplitude distribution. (c2) coupled phase distribution. (c3) phase holographic reconstruction under the uniform amplitude condition. (c4) optimal phase holographic distribution upon introducing amplitude compensation.

Materials Research Proceedings 73 (2026) 78-84 https://doi.org/10.21741/9781644904459-16

In phase holography, the intrinsic 2π periodicity inevitably causes phase wrapping across the $-\pi$ to π boundary, introducing severe diffraction artifacts. To suppress this, a non-linear mapping constrains the effective target phase within $[0,\pi]$ (preset to $\pi/2$). Designating $-\cos(\phi)$ as the objective function folds the wrapped phase into a continuous $[-1,1]$ space, achieving continuization and fundamentally eliminating reconstruction instability from phase truncation.

To intuitively verify amplitude-phase coupling during acoustic spatial evolution, orthogonal dual-target fields were designed with target amplitude and phase set to "A" (Figure 1(a1)) and "S" (Figure 1(a2)), respectively. The holographic inversion reveals that both the reconstructed amplitude (Figure 1(c1)) and phase (Figure 1(c2)) fields exhibit heavily aliased contours, generating pronounced modal crosstalk. This directly demonstrates the strong coupling between amplitude evolution and phase gradients, preventing completely independent modulation. Forcibly disregarding this mechanism by assuming a spatially uniform amplitude (Figure 1(a3)) causes severe distortion and information loss in the reconstructed phase hologram (Figure 1(c3)).

To address these coupling and periodicity limitations, this paper proposes a joint inversion strategy combining time-reversal with the HLOA. A time-reversal model first acquires the initial complex sound pressure. Subsequently, constrained strictly by acoustic energy flux conservation, the HLOA iteratively compensates for amplitude errors induced by wave propagation coupling. This resolves the optimal amplitude compensation precisely matching the target phase (Figure 1(a4)), generating a high-fidelity, robust phase hologram (Figure 1(c4)). The loss function based on phase cosine mapping is defined as:

$$Loss = \frac{1}{N}\sum_{x,y}[1 - cos(\phi_d(x,y) - \phi_a(x,y))] \tag{5}$$

Here $\phi_d(x,y)$ is the pre-designed phase distribution, $\phi_a(x,y)$ is the phase distribution after amplitude compensation, and N is the total number of pixels in the image plane. Ultimately, we obtain phase holograms with optimal coupled amplitude compensation, as shown in Figure 3(a4).

Numerical Results

To validate spatial transmission performance, numerical simulations utilizing the target "E" evaluated far-field capabilities of conventional amplitude versus optimized phase holography. Figures 2(a)-(c) present the prescribed phase, the inversely derived amplitude compensation, and the resulting optimal phase hologram.

Figures 2(d)-(e) extract the axial acoustic pressure evolution (10-50 cm). Comparatively, conventional amplitude holography undergoes rapid diffusion and drastic fidelity degradation over distance, whereas the amplitude-compensated phase hologram distinctly preserves the "E" contour. Phase holography demonstrates substantially superior spatial correlation and exceptional transmission stability throughout the observation range.

These observations elucidate the fundamental discrepancies in the physical evolution of distinct acoustic parameters during spatial propagation, amplitude rapidly dissipates driven by energy divergence and diffraction broadening, while phase exhibits robust resilience against cumulative diffraction. Consequently, adequately compensated phase-dominated holography possesses an intrinsic physical advantage in long-distance acoustic information transmission.

Materials Research Proceedings 73 (2026) 78-84 https://doi.org/10.21741/9781644904459-16

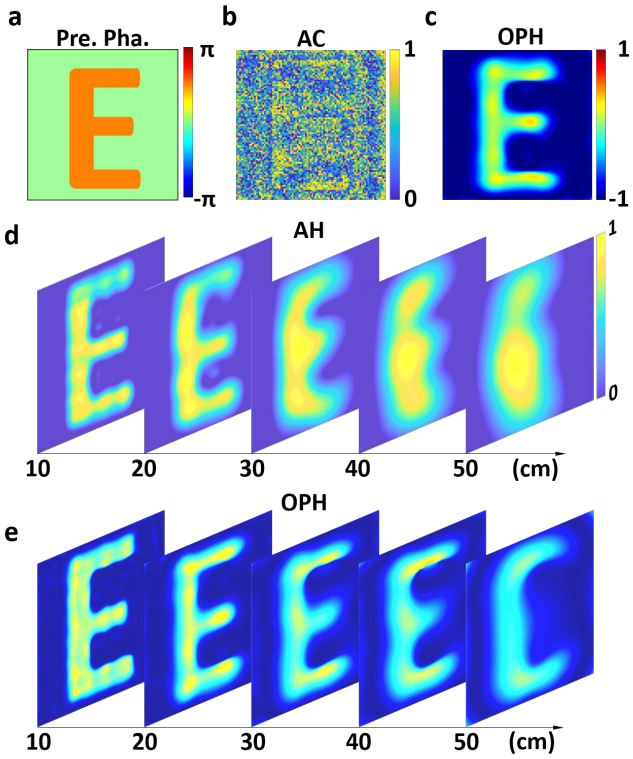

Figure 2. Information transmission capabilities of phase and amplitude holograms. (a) Prescribed target phase distribution (letter "E"). (b) Inversely derived amplitude compensation distribution based on amplitude-phase coupling. (c) Optimal amplitude-compensated phase hologram. (d) and (e) Acoustic field spatial evolution over a 10–50 cm transmission distance for conventional amplitude holography and optimized phase holography, respectively.

Conclusions

This study highlights the intrinsic physical superiority of the phase parameter over conventional amplitude parameters in mitigating energy dissipation during acoustic field manipulation. In response to the inevitable amplitude-phase coupling effects encountered during acoustic wave propagation, we elucidate the physical nature of this interaction utilizing the differential properties of spatial complex sound pressure. Consequently, the coupled differential equations dictating the dynamic evolution of the wavefront are derived, leading to the establishment of a theoretical model based on acoustic energy flux conservation that governs the spatial amplitude-phase evolution. To resolve the inherent periodic wrapping of the phase variable, a nonlinear cosine mapping technique is proposed to continuize the spatial phase, thereby fundamentally eradicating phase-truncation step artifacts. By incorporating the Horned Lizard Optimization Algorithm (HLOA) bounded by the acoustic energy conservation constraint, the optimal amplitude compensation distribution strictly required for the target phase holographic field is precisely reconstructed. This inversion strategy successfully yields high-fidelity phase holograms that feature adaptive amplitude enhancement. Ultimately, comprehensive quantitative comparisons of far-field information transmission capabilities in free space confirm the exceptional performance of the phase parameter in resisting energy attenuation and sustaining transmission stability compared to traditional amplitude holography.

Acknowledgment
This work was supported by the National Natural Science Foundation of China (no. 52272433), the Natural Science Foundation of Jiangsu Province (grant no. BK20220798), and Southeast University Interdisciplinary Research Program for Young Scholars (2024FGC1003).

References

[1] K. Melde, A. G. Mark, T. Qiu, P. Fischer, Holograms for acoustics. Nature 537, 518–522 (2016). https://doi.org/10.1038/nature19755

[2] A. Marzo, S. A. Seah, B. W. Drinkwater, D. R. Sahoo, B. Long, S. Subramanian, Holographic acoustic elements for manipulation of levitated objects. Nat Commun 6, 8661 (2015). https://doi.org/10.1038/ncomms9661

[3] Y. Xie, C. Shen, W. Wang, J. Li, D. Suo, B.-I. Popa, Y. Jing, S. A. Cummer, Acoustic Holographic Rendering with Two-dimensional Metamaterial-based Passive Phased Array. Sci Rep 6, 35437 (2016). https://doi.org/10.1038/srep35437

[4] A. Marzo, S. A. Seah, B. W. Drinkwater, D. R. Sahoo, B. Long, S. Subramanian, Holographic acoustic elements for manipulation of levitated objects. Nat Commun 6, 8661 (2015). https://doi.org/10.1038/ncomms9661

[5] Z. Ma, A. W. Holle, K. Melde, T. Qiu, K. Poeppel, V. M. Kadiri, P. Fischer, Acoustic Holographic Cell Patterning in a Biocompatible Hydrogel. Advanced Materials 32, 1904181 (2020). https://doi.org/10.1002/adma.201904181

[6] J. Kim, S. Kasoji, P. G. Durham, P. A. Dayton, Acoustic holograms for directing arbitrary cavitation patterns. Applied Physics Letters 118, 051902 (2021). https://doi.org/10.1063/5.0035298

[7] K. Wu, J.-J. Liu, Y. Ding, W. Wang, B. Liang, J.-C. Cheng, Metamaterial-based real-time communication with high information density by multipath twisting of acoustic wave. Nat Commun 13, 5171 (2022). https://doi.org/10.1038/s41467-022-32778-z

[8] M. Derayatifar, M. Habibi, R. Bhat, M. Packirisamy, Holographic direct sound printing. Nat Commun 15, 6691 (2024). https://doi.org/10.1038/s41467-024-50923-8

[9] P. Zheng, Q. Dai, Z. Li, Z. Ye, J. Xiong, H.-C. Liu, G. Zheng, S. Zhang, Metasurface-based key for computational imaging encryption. Sci. Adv. 7, eabg0363 (2021). https://www.science.org/doi/full/10.1126/sciadv.abg0363

[10] H. Zeng, Z. He, Y. Wu, S. Gao, F. Mao, H. Fan, X. Fan, W. Kan, Y. Zhu, H. Zhang, B. Assouar, Amplitude-Phase Dual-Channel Encrypted Acoustic Meta-Holograms. Adv Funct Materials 34, 2405132 (2024). https://doi.org/10.1002/adfm.202405132

[11] K. Wu, J.-J. Liu, Y. Ding, W. Wang, B. Liang, J.-C. Cheng, Metamaterial-based real-time communication with high information density by multipath twisting of acoustic wave. Nat Commun 13, 5171 (2022). https://doi.org/10.1038/s41467-022-32778-z

[12] X. Guo, H. Zeng, X. Hu, Y. Mo, X. Wang, X. Liang, Y. Wu, T. Li, H. Fan, Y. Zhu, H. Zhang, B. Assouar, Phase Hologram by Acoustic Metasurfaces. Small Structures, e202500354 (2025). https://doi.org/10.1002/sstr.202500354

[13] K. Melde, H. Kremer, M. Shi, S. Seneca, C. Frey, I. Platzman, C. Degel, D. Schmitt, B. Schölkopf, P. Fischer, Compact holographic sound fields enable rapid one-step assembly of matter in 3D. Sci. Adv. 9, eadf6182 (2023). https://www.science.org/doi/full/10.1126/sciadv.adf6182

[14] X. Guo, X. Wang, G. Tang, H. Zeng, S. Fan, X. Hu, Y. Mo, Z. He, T. Li, H. Xu, J. Shen, H. Fan, X. Gao, Y. Zhu, H. Zhang, B. Assouar, Super-Resolution and High-Data-Density Acoustic Meta-Hologram via Amplitude and Phase Coupling. Advanced Science, e76251 (2026). https://doi.org/10.1002/advs.76251

[15] Y. Zhu, J. Hu, X. Fan, J. Yang, B. Liang, X. Zhu, J. Cheng, Fine manipulation of sound via lossy metamaterials with independent and arbitrary reflection amplitude and phase. Nat Commun 9, 1632 (2018). https://doi.org/10.1038/s41467-018-04103-0

[16] H. Peraza-Vázquez, A. Peña-Delgado, M. Merino-Treviño, A. B. Morales-Cepeda, N. Sinha, A novel metaheuristic inspired by horned lizard defense tactics. Artif Intell Rev 57, 59 (2024). https://doi.org/10.1007/s10462-023-10653-7

Materials Research Proceedings 73 (2026) 85-90 https://doi.org/10.21741/9781644904459-17

Static and Modal Response of Curved Honeycomb Metastructure Panels

Riccardo AUGELLO[1,a *] and Erasmo CARRERA[1,b]

[1]MUL2 Lab, Politecnico di Torino, Italy

[a]riccardo.augello@polito.it, [b]erasmo.carrera@polito.it

Keywords: Curved Panels, Honeycomb Metastructures, Static Analysis, Free Vibration, Carrera Unified Formulation

Abstract. The response of a metastucure panel depends on how its internal architecture interacts with the overall geometry. This work examines the effect of initial curvature on a honeycomb sandwich panel using a refined two-dimensional finite element model based on the Carrera Unified Formulation. The skins and cellular walls are represented within a common kinematic description, with Lagrange expansions resolving displacement variations through their local thickness. Three configurations are compared while keeping the nominal dimensions, constituent material, honeycomb topology and support conditions unchanged. The static assessment considers an imposed transverse displacement, whereas the dynamic assessment compares the natural frequencies and mode shapes of panels clamped along one edge. A shallow curvature of 10^{-4} mm^{-1} produces frequency differences below 0.2% relative to the flat panel. Increasing the curvature to 10^{-3} mm^{-1} gives a nonuniform change in the reported spectrum: the third frequency increases by 4.82%, while the fourth decreases by 14.29%. The displacement and stress fields also reveal changes in the static response. These results identify curvature as a mode-dependent design variable and illustrate a unified modeling route for resolving the interaction between cellular walls and facesheets.

Introduction

Architected cellular solids provide a means of modifying structural behavior through geometry. Their response depends on the arrangement and connectivity of internal members as well as on the constituent material, allowing stiffness, deformation and dynamic properties to be adjusted within a common structural concept [1,2]. In panel applications, the cellular region must work together with the external skins. The resulting component therefore combines deformation at the scale of the whole panel with bending and distortion of individual walls and facesheet regions.

Curvature introduces a further geometric variable into this interaction. An initially curved panel can develop a different balance of membrane, bending and transverse deformation from an otherwise comparable flat panel. Studies of curved locally resonant panels have shown that this geometric effect is relevant to wave propagation [3]. For a finite honeycomb component, a necessary first step is to establish how curvature changes its static fields and vibration modes before drawing conclusions about frequency-selective attenuation.

The present study addresses this step for one honeycomb topology and different curvature levels. The objective is to distinguish responses that remain close to the flat reference from those that change appreciably as the panel becomes shell-like. Particular attention is given to the different sensitivity of the reported frequencies and to the local deformation visible in the corresponding mode shapes.

Methodology

The structural model uses the Carrera Unified Formulation (CUF), in which the displacement approximation through the thickness can be refined independently of the discretization over the

Content from this work may be used under the terms of the Creative Commons Attribution 3.0 license. Any further distribution of this work must maintain attribution to the author(s) and the title of the work, journal citation and DOI. Published under license by Materials Research Forum LLC.

Materials Research Proceedings 73 (2026) 85-90 https://doi.org/10.21741/9781644904459-17

reference surface [4]. Related variable-kinematic shell elements have been developed for laminated and sandwich components [5], and refined thickness expansions have also been used to represent plates with straight and curved stiffeners [6]. Here, the same modeling principle is applied to the skins and walls of a honeycomb panel.

Let α and β denote coordinates on the reference surface, and let z measure position through the local thickness, as shown in Fig. 1. The three displacement components are collected in the vector u. The approximation combines thickness functions F_τ with surface finite element functions N_i:

$$u(\alpha, \beta, z) = F_\tau(z)\, N_i(\alpha, \beta)\, q_{\tau i} \quad (1)$$

The summation extends over the retained thickness terms and element nodes, and $q_{\tau i}$ contains the three associated displacement unknowns. Lagrange polynomials are used for the thickness expansion. Their interpolation points can be located at the facesheet surfaces, at the skin–core interfaces and within the height of a cellular wall. Increasing the number of points enriches the local displacement field without replacing the two-dimensional element family.

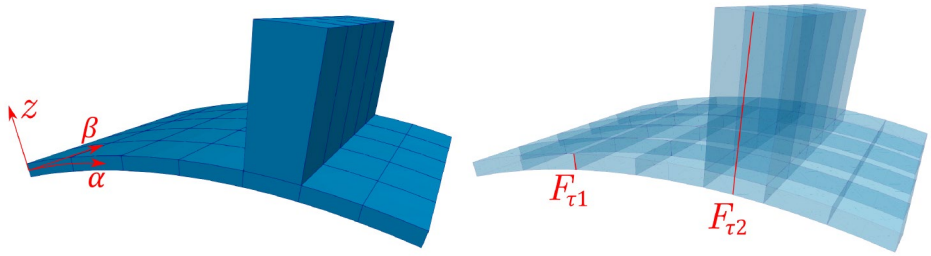

Fig. 1. Refined representation of a reinforced region using surface elements and local thickness expansions.

The support of each thickness expansion follows the actual solid region. A skin domain spans the facesheet thickness, whereas a wall domain includes the height of the reinforcement. The voids of the honeycomb remain unoccupied. Displacement continuity is imposed by sharing unknowns at coincident Lagrange points on adjoining components. In this way, the facesheets and core walls belong to one compatible model, without separate beam-to-shell ties. Figure 1 illustrates this construction for flat and curved reinforced regions.

For linear elasticity, the strains and stresses follow from the interpolated displacement field through ε = Bq and σ = Cε. The matrix B includes the surface and thickness derivatives together with the metric terms of the curved geometry, while C contains the elastic properties. Integration over the occupied material volume and assembly give the stiffness matrix K and consistent mass matrix M. The same kinematics therefore governs both the static and modal descriptions.

$$Kq = f, \qquad (K - \omega^2 M)\varphi = 0 \quad (2)$$

In the modal problem, ω and φ are the natural circular frequency and eigenvector, with f = ω/(2π).

This formulation retains local deformation of the cellular architecture explicitly. CUF-based free-vibration analyses of periodic plates [7] and nonlinear dynamic studies of thin-walled metastructures [8] provide related applications of refined structural kinematics.

Numerical results

The panel has nominal dimensions a × b = 850 mm × 470 mm and an overall thickness of 120 mm. Two 3 mm facesheets enclose a 114 mm honeycomb core. The three geometries are shown in Fig. 2. Case C1 is flat, C2 has curvature $\kappa = 10^{-4}$ mm^{-1} and C3 has curvature $\kappa = 10^{-3}$ mm^{-1}. The corresponding radii are infinite, 10,000 mm and 1,000 mm. All cases retain the same cellular topology and nominal thicknesses.

The material is aluminum and it is held fixed across the comparison. Consequently, the changes discussed below concern the effect of the initial curvature.

Materials Research Proceedings 73 (2026) 85-90 https://doi.org/10.21741/9781644904459-17

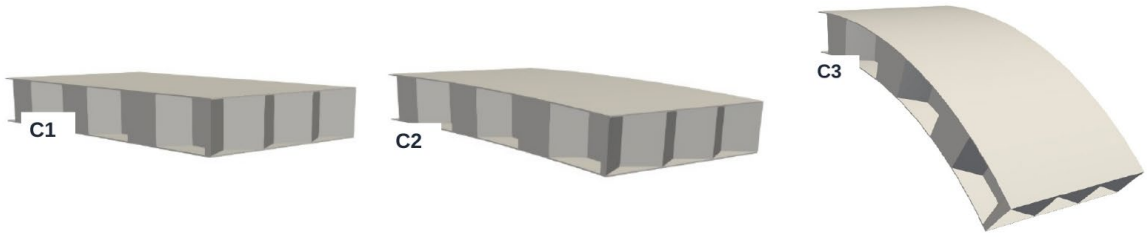

Fig. 2. Honeycomb configurations C1, C2 and C3 in order of increasing curvature.

Static response under prescribed transverse displacement

Each configuration is subjected to the same prescribed transverse displacement with clamped support conditions. Figure 3 compares the transverse displacement field and the normal stress component σ_{xx} .

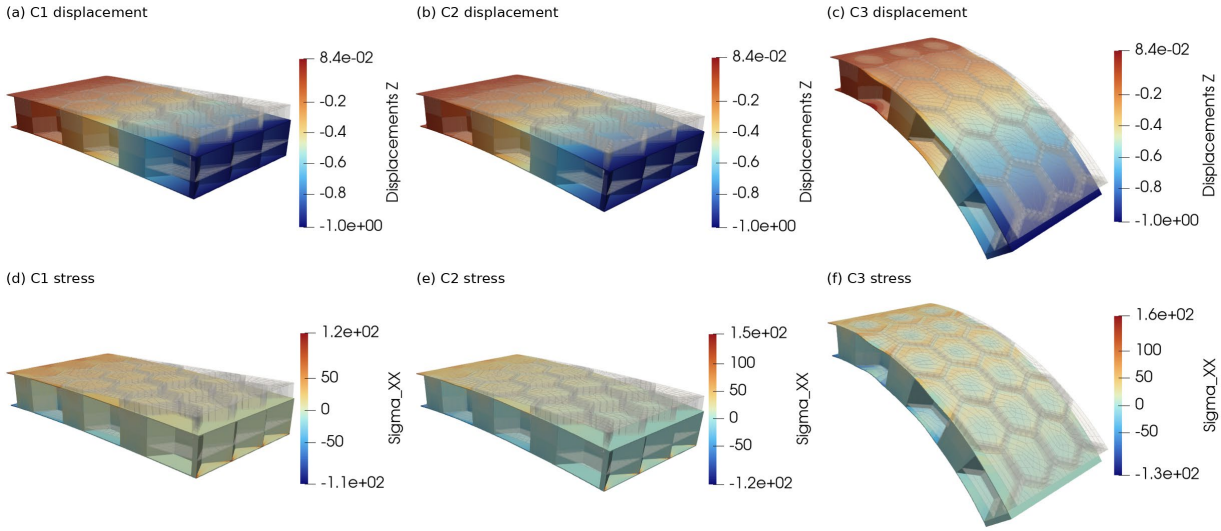

Fig. 3. Transverse displacement (top) and σ_{xx} stress (bottom) for C1, C2 and C3. Original contour scales are retained; stress scales differ between cases.

The flat and shallow-curvature panels display similar overall displacement patterns. In C3, the displacement field follows the pronounced initial arch, and the stress distribution across the skin–core assembly is visibly modified. The plots show a combination of smooth panel-scale deformation and local variations associated with the underlying cellular walls. Thus, even when the imposed transverse displacement is identical, the internal deformation field is sensitive to the reference geometry.

Natural frequencies

The free-vibration calculations use the same boundary conditions, one side is clamped and the other sides are free. Table 1 collects the five frequencies reported for each configuration. The percentage changes are calculated relative to the corresponding frequency of C1 as

$$\Delta f_j(\%) = 100\,[f_j(Ck) / f_j(C1) - 1], \quad k = 2,3 \qquad (3)$$

Materials Research Proceedings 73 (2026) 85-90 https://doi.org/10.21741/9781644904459-17

Table 1. Reported natural frequencies and changes relative to the flat configuration.

Index j	C1 [Hz]	C2 [Hz]	C3 [Hz]	Δf C2 [%]	Δf C3 [%]
1	114.2	114.1	110.6	-0.09	-3.15
2	234.6	234.3	211.5	-0.13	-9.85
3	361.3	361.6	378.7	+0.08	+4.82
4	600.5	599.3	514.7	-0.20	-14.29
5	849.8	850.7	824.5	+0.11	-2.98

For C2, the changes range from −0.20% to +0.11%. The first frequency differs by only 0.1 Hz, and the largest absolute difference is 1.2 Hz for the fourth reported frequency. This near coincidence is consistent with the similar deformation patterns of C1 and C2. Figure 4 shows a representative pair of modes with local facesheet undulations, which remain visually similar at this shallow curvature.

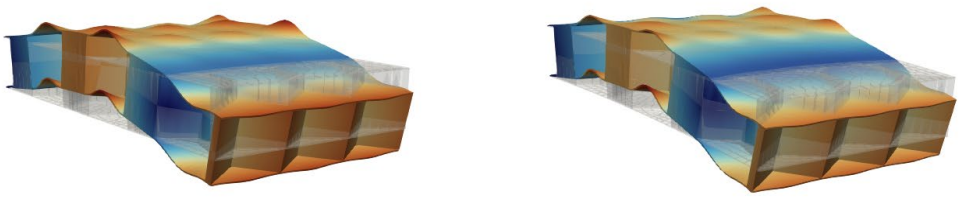

Fig. 4. Representative modes of C1 and C2 at 600.5 Hz and 599.3 Hz, respectively.

The similar shapes in Fig. 4 support the close relation between the illustrated C1 and C2 modes, while stronger geometric changes require more care when interpreting mode correspondence.

Effect of pronounced curvature on the vibration modes

Case C3 exhibits substantially larger and mode-dependent shifts. The first two reported frequencies decrease by 3.15% and 9.85%, respectively, while the third increases by 4.82%. The fourth decreases from 600.5 Hz to 514.7 Hz, a change of −14.29%, and the fifth decreases by 2.98%. These different signs and magnitudes show that the effect of curvature cannot be represented by applying one stiffness correction to the entire spectrum.

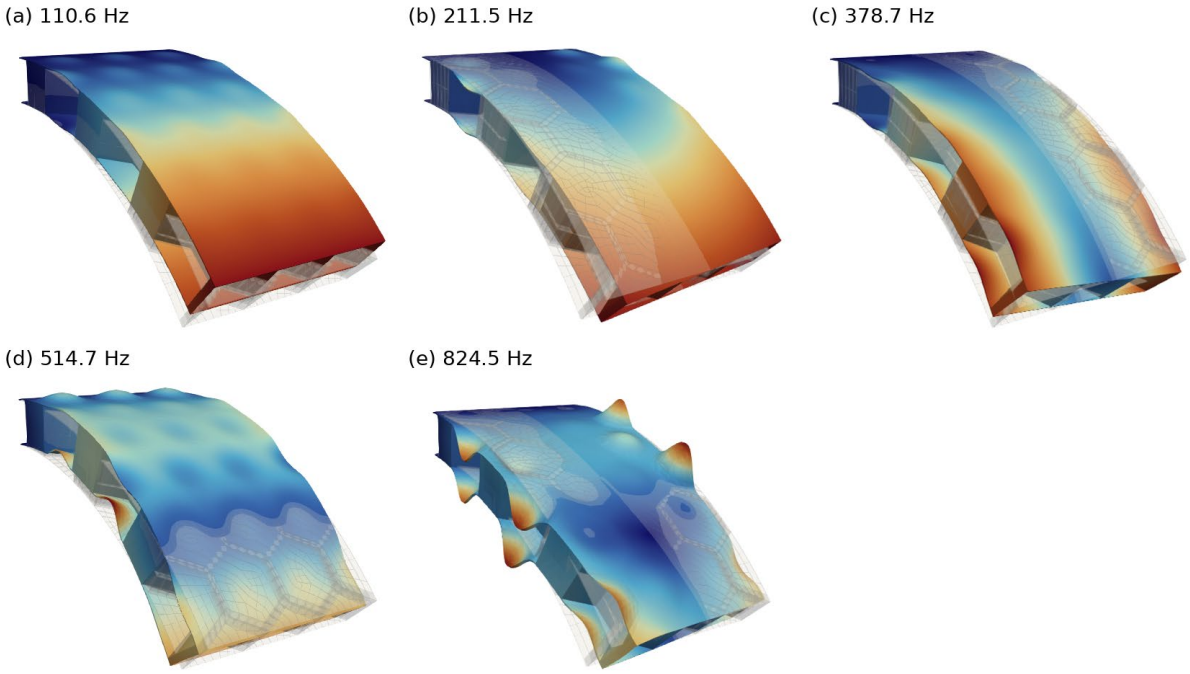

Fig. 5. Mode shapes reported for C3 at 110.6, 211.5, 378.7, 514.7 and 824.5 Hz.

The first two shapes in Fig. 5 show deformation distributed over a large part of the panel. The shapes at 514.7 Hz and 824.5 Hz exhibit additional spatial variations and local facesheet undulations. These features emphasize the coexistence of global deformation and shorter-scale mechanisms associated with the cellular support of the skins.

The refined two-dimensional description is useful because it represents the facesheets and cellular walls in a common displacement field. This avoids introducing separate structural idealizations at each skin–core junction and allows local kinematic refinement where required.

Conclusions

A CUF-based model has been used to examine the static and modal response of honeycomb panels with three initial curvatures. Surface finite elements and Lagrange thickness expansions describe the skins and cellular walls within a compatible structural formulation. The comparison retains one honeycomb topology and isolates the response changes associated with the flat, shallow and more strongly curved configurations.

The shallow case differs from the flat panel by no more than 0.20% in the reported natural frequencies. At $\kappa = 10^{-3}$ mm^{-1}, the changes become selective: the third reported frequency increases by 4.82%, whereas the fourth decreases by 14.29%. The static and modal fields reveal how the global geometry interacts with local skin and wall deformation. These findings support the use of curvature as a design variable for tailoring the spectrum of cellular panels.

References

[1] J. U. Surjadi, L. Gao, H. Du, X. Li, X. Xiong, N. X. Fang, and Y. Lu, "Mechanical metamaterials and their engineering applications," Advanced Engineering Materials, 21(3), 1800864, 2019. https://doi.org/10.1002/adem.201800864

[2] E. Barchiesi, M. Spagnuolo, and L. Placidi, "Mechanical metamaterials: a state of the art," Mathematics and Mechanics of Solids, 24(1), 212-234, 2019. https://doi.org/10.1177/1081286517735695

[3] A. Nateghi, L. Van Belle, C. Claeys, E. Deckers, B. Pluymers, and W. Desmet, "Wave propagation in locally resonant cylindrically curved metamaterial panels," International Journal of Mechanical Sciences, 127, 73-90, 2017. https://doi.org/10.1016/j.ijmecsci.2016.07.003

[4] E. Carrera, M. Cinefra, M. Petrolo, and E. Zappino, Finite Element Analysis of Structures through Unified Formulation. Wiley, 2014. https://doi.org/10.1002/9781118536643

[5] A. Pagani, E. Carrera, D. Scano, and R. Augello, 2023. Finite elements based on Jacobi shape functions for the analysis of beams, plates and shells. International Journal for Numerical Methods in Engineering, 124(20), pp.4490-4519. https://doi.org/10.1002/nme.7316

[6] R. Augello and E. Carrera, "Analysis of plate reinforced by straight and curved stiffeners by using novel plate elements with refined through-the-thickness expansion," Mechanics of Advanced Materials and Structures, 31(1), 13-21, 2024. https://doi.org/10.1080/15376494.2023.2270794

[7] M. Cinefra, A. G. de Miguel, M. Filippi, C. Houriet, A. Pagani, and E. Carrera, "Homogenization and free-vibration analysis of elastic metamaterial plates by Carrera Unified Formulation finite elements," Mechanics of Advanced Materials and Structures, 28(5), 476-485, 2021. https://doi.org/10.1080/15376494.2019.1578005

[8] R. Augello and E. Carrera, "Nonlinear dynamics and band gap evolution of thin-walled metamaterial-like structures," Journal of Sound and Vibration, 578, 118329, 2024. https://doi.org/10.1016/j.jsv.2024.118329

Materials Research Proceedings 73 (2026) 91-94+ https://doi.org/10.21741/9781644904459-18

Influence of Printing Parameters and Testing Temperature on the Tensile Behaviour of 3D-Printed Hemp/PLA

Matthieu CARENTON[1,a *], Fabienne TOUCHARD[1,b], Laurence CHOCINSKI-ARNAULT[1,c], Damien MARCHAND[1,d]

[1]Département Physique et Mécanique des Matériaux, Institut Pprime, CNRS-ISAE-ENSMA-Université de Poitiers, UPR 3346, 1 avenue Clément Ader, 86961 Futuroscope, France

[a]matthieu.carenton@ensma.fr, [b]fabienne.touchard@ensma.fr, [c]laurence.chocinski@ensma.fr, [d]damien.marchand@ensma.fr

Keywords: Additive Manufacturing, Natural Fibres, Biocomposites, Process Parameters, Thermo-Mechanical Behaviour

Abstract. Fused Filament Fabrication (FFF) is a 3D printing process in which a heated thermoplastic filament is deposited layer by layer through a nozzle to manufacture parts. This work focuses on a fully bio-based short hemp-fibers/PLA-matrix composite. Printing parameters were optimised through thermal characterisation, temperature monitoring during printing and tensile testing. The printing parameters investigated included nozzle temperature, printing speed, the presence of walls and infill line connections, and cooling at the nozzle exit. Tensile tests were then conducted on 3D-printed hemp/PLA samples at ambient temperature for three different raster angles (0°, ±45°, and 90°), and the Classical Laminate Theory was verified. Finally, tensile tests were performed at different testing temperatures from ambient to 110°C and the mechanical behaviour was examined as a function of temperature.

Introduction

Additive manufacturing, also known as 3D printing, consists in producing three-dimensional objects through the deposition of a material layer by layer. Compared to the others, this manufacturing method can reduce production costs and offer greater design freedom for complex geometries and customised prototypes [1]. Among the various 3D printing methods, Fused Filament Fabrication (FFF) relies on the extrusion of a filament of thermoplastic polymer heated to its molten state through a nozzle. The molten material is then deposited onto a heated build platform to form the final layered structure [2].

Among the thermoplastic polymers available for FFF, polylactic acid (PLA) is widely considered a suitable material when easy processing, low environmental impact [3], and satisfactory mechanical properties are required [4]. In this study, short hemp fibres were added into a PLA matrix to produce a fully bio-based composite. One important issue for biocomposites is their behaviour under temperature variations, both for temperature-dependent applications and for thermomechanical modelling.

First, the printing parameters were optimised using in-situ thermal measurements during printing, micro-CT scans, DSC and TGA analyses, and tensile tests with marker tracking. Then, the influence of temperature on the tensile behaviour of the biocomposite was investigated. Post-failure observations were finally carried out using SEM.

Methodology

Manufacturing of the biocomposite specimens was done using an Ultimaker S5+ Pro printer and models were sliced with the Ultimaker slicing software CURA. Before 3D printing, spools were dried in an oven at 40°C during 24h and stored in the printer's humidity-controlled material station.

Content from this work may be used under the terms of the Creative Commons Attribution 3.0 license. Any further distribution of this work must maintain attribution to the author(s) and the title of the work, journal citation and DOI. Published under license by Materials Research Forum LLC.

Materials Research Proceedings 73 (2026) 91-94 https://doi.org/10.21741/9781644904459-18

After manufacturing, samples were stored in light-protected boxes containing desiccant to maintain dry atmosphere until testing.

Rectangular samples were manufactured following the standard test method for tensile properties of polymer matrix composite materials ASTM D3039/3039M. Their dimensions were 150 × 20 × 2 mm3. Samples were printed without bottom/top layers, the infill pattern was chosen as lines with 100% density. A brim adhesion type was used to keep the specimen stuck to the 60°C bed during 40mm/s speed printing. Three raster angles were studied: 0°, with filaments aligned with the longitudinal direction of the specimen; 90°, with filaments oriented perpendicular to this direction; and ±45°, consisting of alternating layers oriented at ±45° with respect to the longitudinal direction. For some specimens, an infrared camera (Variocam HD Head from InfraTec) was placed above the printer to measure their temperature during printing (Fig. 1). The resulting data were treated using Irbis 3 software.

The characteristic temperatures and the crystallinity ratio of the material studied were measured by Differential Scanning Calorimetry (DSC) with a Q20 machine from TA Instruments. The degradation temperatures were obtained by Thermogravimetric Analysis (TGA) using a SETSYS Evolution machine from SETARAM Instrumentation. Tensile tests were carried out on an INSTRON 5982 machine equipped with a climatic chamber at a crosshead displacement rate of 0.5 mm/min. Strain was measured using optical marker tracking on MANTA Mg 1236 camera from Allied Vision. Fracture surfaces were examined using a Scanning Electron Microscope (SEM) VEGA3 from TESCAN company. Micro-CT observations were also performed using an UltraTom CT scanner manufactured by RX Solutions (France).

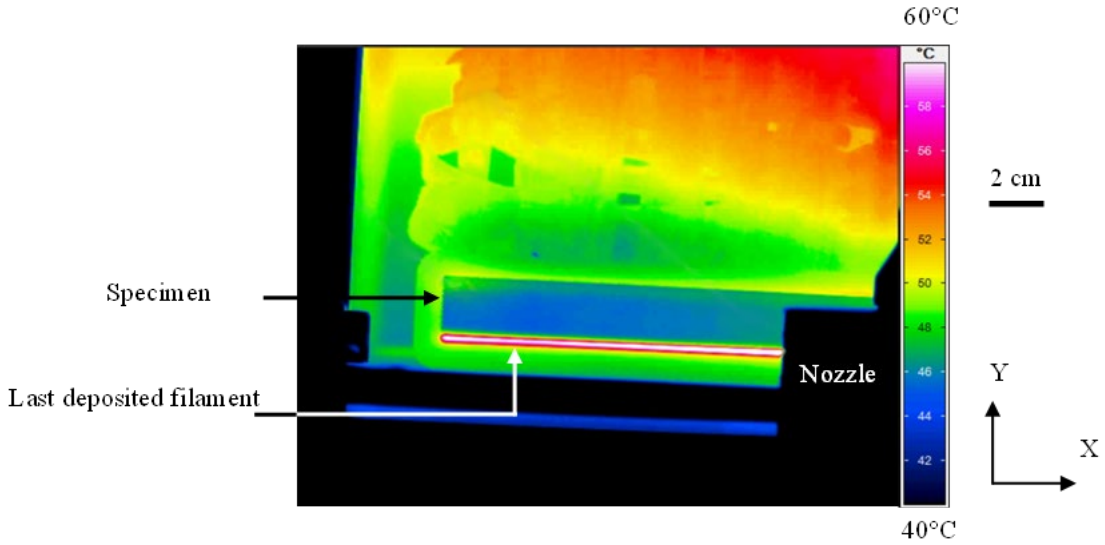

Fig. 1. Temperature measurement by infrared camera of a hemp/PLA specimen during printing

Results and discussion

Various printing parameters were tested to determine the optimal process conditions for minimizing porosity and maximizing tensile behaviour of the specimens. For example, Fig. 2 compares micro-CT scans of hemp/PLA specimens printed at two different temperatures: 190°C (Fig. 2a) and 210°C (Fig. 2b). The results clearly show that a printing temperature of 210°C significantly reduces porosity in the specimen.

Materials Research Proceedings 73 (2026) 91-94 https://doi.org/10.21741/9781644904459-18

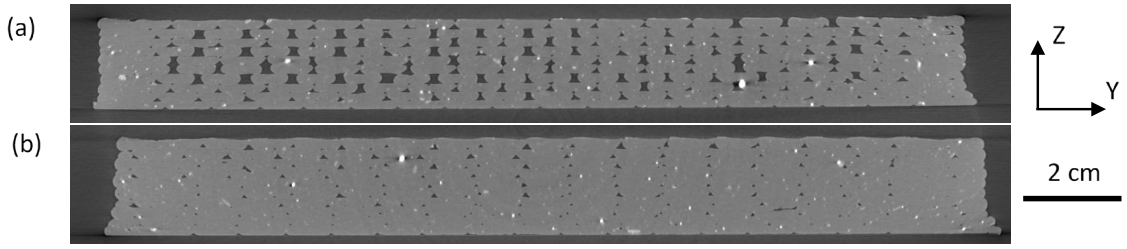

Fig. 2. Micro-CT scans of hemp/PLA specimens for two printing temperatures: (a) 190°C; (b) 210°C

After optimisation, the layer height and the deposited filament width were set to respectively 0.2mm and 0.8mm. Moreover, specimens were chosen to be printed without infill lines connections or walls, at a nozzle temperature of 210°C and with the nozzle cooling fan activated.

A thermomechanical characterisation of the specimens was then performed for three different raster angles (0°, ±45°, 90°), using a tensile testing machine equipped with a climatic chamber. The tensile curves of the specimens for all three orientations show that temperature has a direct influence on mechanical behaviour, as observed for the 0° orientation in Fig. 3. Indeed, as the glass transition temperature (Tg) is reached at around 60°C, the specimens' Young's modulus and strength sharply decrease, transitioning from a glassy to a rubbery state. The cold crystallisation of PLA around 90°C then causes a stiffening of the microstructure, which is visible in the tensile curves, as some of the polymer chains reorganise into crystallite groups.

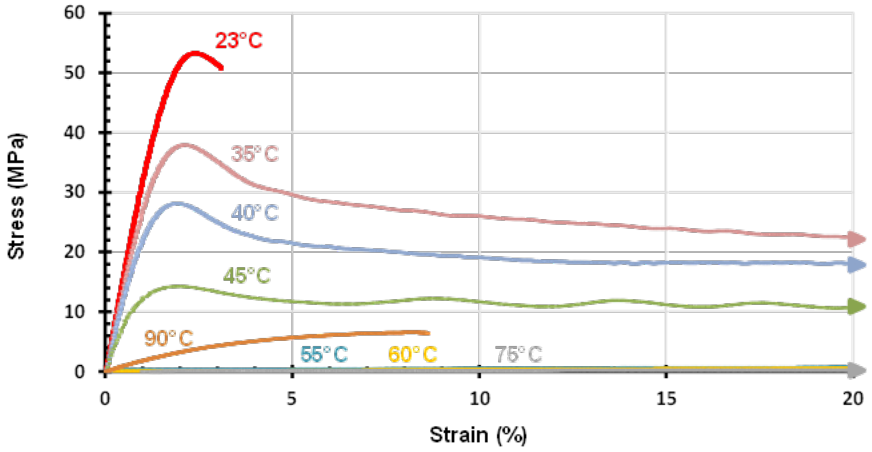

Fig. 3. Influence of testing temperature on tensile curves of 0° hemp/PLA specimens.

Conclusions

In this paper, the influence of printing parameters and tensile testing temperature on the behaviour of 3D printed hemp/PLA specimens was investigated. Firstly, five selected printing parameters have been optimised through thermal characterisation (DSC, TGA, DMA), in-situ thermal measurements during 3D printing, tensile tests and micro-CT observations.

Secondly, tensile tests on the three raster angles (0°, ±45°, 90°) were done at different testing temperatures from ambient to 110°C and the tensile properties obtained were examined as a function of temperature. The rubbery state above the glass transition temperature was observed,

and cold crystallisation stiffened the tested specimens, in accordance with the thermal characterisation.

This study provides a robust database for better understanding and modelling the thermomechanical behaviour of 3D printed hemp/PLA composites.

Acknowledgment

This work was partially founded by the French Government program “Investissements d’Avenir” (EQUIPEX GAP, reference ANR-11-EQPX-0018) and by the CPER FEDER project of Région Nouvelle Aquitaine. It pertains to the French Government program “Investissements d’Avenir” (EUR INTREE, reference ANR-18-EURE-0010). The authors also thank Chanvre Mellois, Futuramat and CANOE for the manufacture of the local hemp/PLA composite.

References

[1] Rajan K, Samykano M, Kadirgama K, Wan Harun WS, Rahman MM (2022). Fused deposition modeling: process, materials, parameters, properties, and applications. Int J Adv Manuf Technol 120:1531–1570. https://doi.org/10.1007/s00170-022-08860-7

[2] Zotti A, Paduano T, Napolitano F, Zuppolini S, Zarrelli M, Borriello A (2025). Fused Deposition Modeling of Polymer Composites: Development, Properties and Applications. Polym 17(8): 1054. https://doi.org/10.3390/polym17081054

[3] Borda F, Conte R, Ambrogio G, Gagliardi F (2026). Environmental performance of PET and biopolymers: a comparative LCA of end-of-life scenarios. Int J Adv Manuf Technol 142: 2599-2613. https://doi.org/10.1007/s00170-025-17057-7

[4] Wickramasinghe S, Do T, Tran P (2020). FDM-Based 3D Printing of Polymer and Associated Composite: A Review on Mechanical Properties, Defects and Treatments. Polym 12(7):1529. https://doi.org/10.3390/polym12071529

Materials Research Proceedings 73 (2026) 95-99 https://doi.org/10.21741/9781644904459-19

Physics-Constrained Surrogate Modeling for Microscale Elastic Homogenization of Additively Manufactured Continuous Carbon Fiber Composites

Tongwha KIM[1,a *] and Kamran BEHDINAN[1,b]

[1]Department of Mechanical & Industrial Engineering, University of Toronto, Toronto, ON M5S 3G8, Canada

[a]tongwha.kim@mail.utoronto.ca, [b]behdinan@mie.utoronto.ca

Keywords: Surrogate Modeling, Physics-constrained, Machine Learning, Additive Manufacturing, Continuous Carbon Fiber Composites

Abstract. In this paper, a physics-constrained surrogate model is presented for the microscale elastic homogenization of additively manufactured continuous carbon fiber reinforced polymer (CCFRP) composites. Stochastic representative volume elements (RVE) of the CCFRP filament cross-section are generated across four domain sizes, and homogenized stiffness tensors are extracted from periodic finite element analyses. The surrogate model maps scalar RVE descriptors to five effective elastic constants; Voigt-Reuss bounds and thermodynamic consistency conditions are enforced as analytical hinge penalties during training. The model achieves $R2 \geq 0.93$ and MAPE < 1.3% across all outputs on the held-out test set, demonstrating both predictive accuracy and physical admissibility. The proposed framework provides a computationally efficient alternative to direct finite element homogenization, supporting future integration into multiscale process-structure-property frameworks.

Introduction

Additively manufactured continuous carbon fiber reinforced polymer composites (CCFRP) offer high specific stiffness for lightweight structural applications [1], yet the extrusion-based fabrication process introduces stochastic microstructural features, including non-uniform packing and fiber radius scatter, that govern effective elastic properties and must be quantified across statistically representative volume elements (RVE). RVE-based finite element (FE) homogenization accurately predicts effective elastic properties by resolving stochastic fiber arrangements within the filament cross-section, but the computational cost of repeated solves across large ensembles is prohibitive for inference, uncertainty quantification and design. This motivates the development of an efficient physics-constrained surrogate model that directly maps microstructure descriptors to homogenized elastic properties.

Machine learning surrogates have been applied to composite homogenization with substantial reductions in computational cost relative to direct FE analysis [2, 3]. Physics-informed and physics-constrained approaches improve predictive robustness by enforcing admissible constitutive behavior and material consistency conditions [4, 5]. Descriptor-based representations offer a more computationally tractable alternative to image or voxel inputs, which introduce resolution dependence and high dimensionality that complicate efficient learning of stochastic microstructures [2, 6].

This work presents a physics-constrained multilayer perceptron (MLP) surrogate for the microscale elastic homogenization of stochastic CCFRP filament RVEs. Fiber distributions are generated via a random sequential expansion algorithm with particle swarm optimization (RSE-PSO) [7] across four domain sizes, and homogenized stiffness tensors are extracted from periodic FE analyses of the resulting RVEs. The MLP maps scalar RVE descriptors to effective elastic

Content from this work may be used under the terms of the Creative Commons Attribution 3.0 license. Any further distribution of this work must maintain attribution to the author(s) and the title of the work, journal citation and DOI. Published under license by Materials Research Forum LLC.

Materials Research Proceedings 73 (2026) 95-99 https://doi.org/10.21741/9781644904459-19

properties; Voigt-Reuss bounds and thermodynamic consistency are enforced as analytical loss penalties, constraining predictions to physically admissible regions of the parameter space. The proposed framework achieves close agreement with the FE homogenization results and provides physically consistent elastic property predictions, supporting future applications into multiscale process-structure-property pipelines for CCFRPs.

Methods

Stochastic RVE Generation. RVEs of the CCFRP filament cross-section are generated using the RSE-PSO algorithm [7], which optimizes fiber placement spacing parameters to mitigate matrix-rich corners and biased central regions of dense fiber while targeting fiber volume fractions (V_f) of 60%. Fiber radii are sampled from a Gaussian distribution with nominal radius of 3.5μm and a coefficient of variation of 5%, consistent with Anisoprint CCF manufacturing tolerances. Four domain sizes are considered: 50, 75, 120, and 200 μm. A total of 4000 realizations is generated, with achieved volume fractions of 50.5-61.5% across domain sizes due to finite-domain packing constraints (Fig. 1).

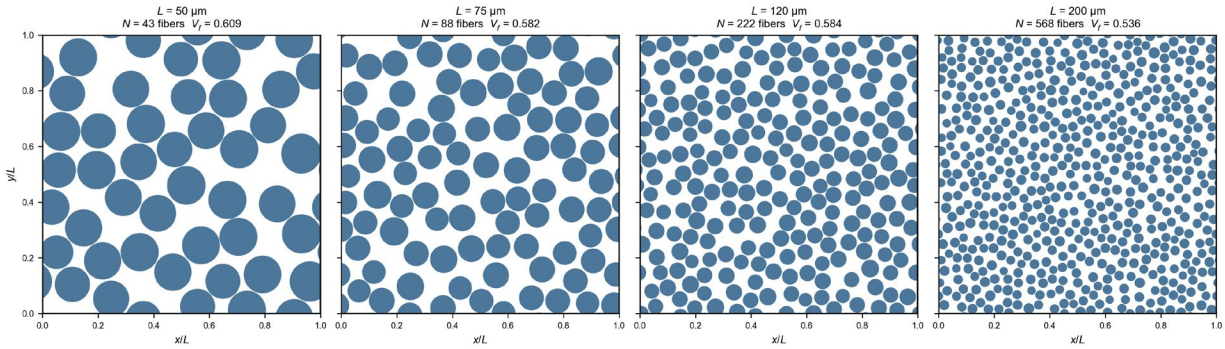

Figure 1. Realizations of stochastic fiber distributions across four domain sizes.

Periodic Finite Element Homogenization. Periodic FE homogenization is performed in COMSOL Multiphysics® [8], with each RVE discretized as a 3D unit cell comprising continuous fibers extruded along the axial direction. Six Voigt load cases are applied via prescribed macroscopic strain states and resulting stress fields are volume-averaged to obtain the homogenized stiffness tensor. The constituent material properties for the transversely isotropic CCFRP composite filament are summarized in Table 1.

Table 1. Summary of constituent material properties.

	E_1 [GPa]	E_2 [GPa]	G_{12} [GPa]	G_{23} [GPa]	υ_{12}	υ_{23}
Carbon Fiber	230	15	15	7	0.2	0.07
Epoxy	3.35	-	1.24	-	0.35	-

Physics-constrained Surrogate Model. The surrogate model was implemented as a fully-connected MLP mapping six RVE descriptors – domain size, fiber volume fraction, and first- and second-order fiber geometry and nearest neighbor spacing statistics – to five homogenized elastic constants: axial modulus (E_1), transverse modulus (E_2), in-plane shear modulus (G_{12}), major Poisson ratio (υ_{12}) and transverse Poisson ratio (υ_{23}). Four hidden layers of width (64, 128, 128, 64) used batch normalization, tanh activation, and dropout (p=0.05) with Xavier uniform weight initialization. Targets were log-transformed prior to standardization; the dataset was split into 60/20/20 by stratified sampling within each domain size. The total loss combined mean-squared error with a physics penalty ($\lambda_p = 0.1$) comprising ten hinge terms: Voigt-Reuss bounds on E_1, E_2, G_{12}, a Voigt bound on υ_{12}, positivity and upper bounds on υ_{21}, and a positive-definiteness condition on the transverse stiffness submatrix; each contributing only when violated. Training used the

Materials Research Proceedings 73 (2026) 95-99 https://doi.org/10.21741/9781644904459-19

Adam optimizer (learning rate=0.001, weight decay=0.0001) with cosine annealing warm restarts for up to 2000 epochs with early stopping on validation loss.

Results

The model is evaluated on the held-out test set across all domain sizes (n=800), with performance summarized in Table 2. The model achieves $R^2 \geq 0.97$ and mean absolute percentage error (MAPE) less than 0.5% for E_1 and E_2, with slightly reduced performance on G_{12}, υ_{12}, and υ_{23}.

Table 2. Predictive performance of the physics-constrained MLP surrogate on the test set across all domain sizes.

	E_1	E_2	G_{12}	υ_{12}	υ_{23}
R^2	0.9936	0.9783	0.9591	0.9660	0.9308
MAPE [%]	0.4110	0.4549	1.2512	0.2689	0.7881
RMSE [GPa]	0.5766	0.0520	0.0817	0.0010	0.0040

Training convergence is shown in Fig. 2. The data loss converges over approximately 850 epochs with no evidence of overfitting. The validation loss remains below the training loss, likely reflecting the distribution of lower-variance microstructure descriptors into the validation split rather than data leakage. The physics constraint loss reduces by three orders of magnitude from initialization (~10^1 to 10^{-2}), confirming that the hinge penalties are actively minimized during training. The periodic spikes in the data loss correspond to learning rate restarts under cosine annealing warm restarts and do not reflect training instability.

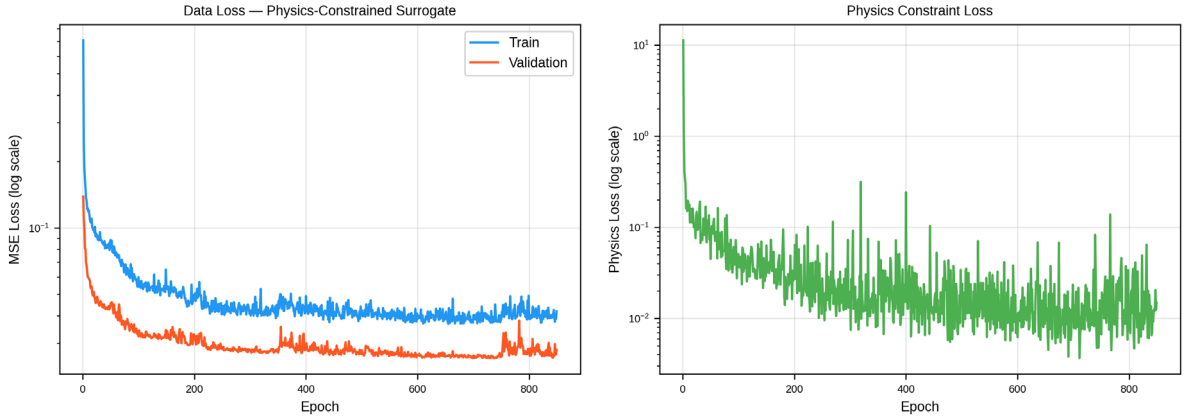

Figure 2. Training convergence of the physics-constrained surrogate: data loss (left) and physics constraint loss (right) over 850 epochs. Periodic spikes correspond to cosine annealing warm restarts.

Figure 3 shows the predicted elastic moduli against the Voigt-Reuss bounds as a function of the fiber volume fraction. All test predictions lie within the physically admissible region, confirming zero bound violations across the full volume fraction range. For E_1, predictions track closely to the upper bound, consistent with the fiber-dominated axial response of continuous fibers. For E_2 and G_{12}, predictions occupy the lower region, reflecting matrix-influenced transverse and shear response.

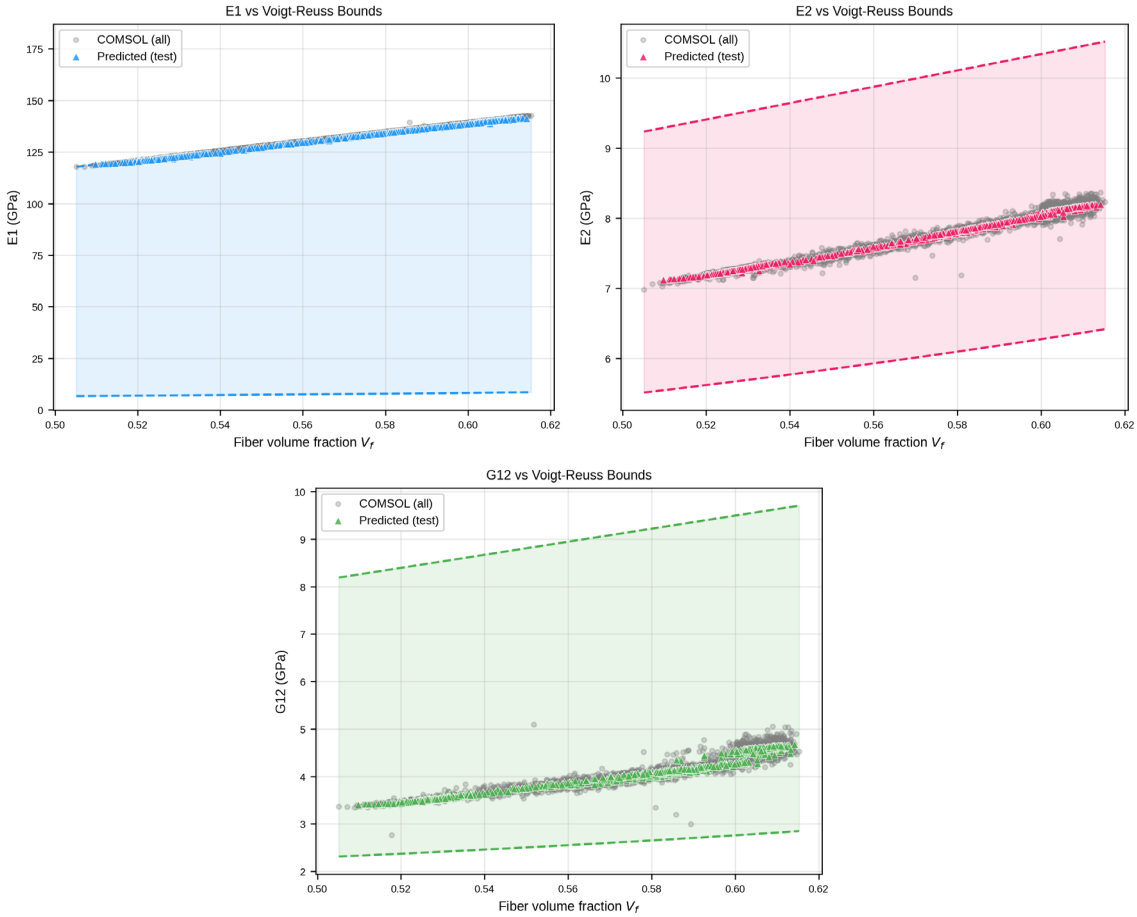

Figure 3. Predicted test set values for axial, transverse, and shear modulus relative to Voigt-Reuss bounds (-- line) across the achieved fiber volume fraction range.

Conclusions

A physics-constrained MLP surrogate was developed for microscale elastic homogenization of stochastic CCFRP filament RVEs, mapping scalar microstructural descriptors to five homogenized elastic properties as a computationally efficient alternative to direct FE analysis. Trained on 4000 RVE realizations across four domain sizes, the surrogate achieves $R2 \geq 0.93$ and MAPE < 1.3% across all targets with zero Voigt-Reuss bound violations, confirming both predictive accuracy and physical admissibility. Future work includes extending the architecture to encode explicit stochastic fiber distributions and integrating the surrogate within a multiscale process-structure-property framework for 3D-printed CCFRP components.

References

[1] Y. Zhang, W. Zheng, Y. Wang, K. Ma, X. Feng, Q. Ji, W. Guo, and B. Lu, "A review of 3D printing continuous carbon fiber reinforced thermoplastic polymers: Materials, processes, performance enhancement, and failure analysis," Polymer Composites, vol. 46, no. 14, pp. 12619-12649, 2025, doi: https://doi.org/10.1002/pc.29895

[2] R. Nakka, D. Harursampath, and S. A. Ponnusami, "A generalised deep learning-based surrogate model for homogenisation utilising material property encoding and physics-based bounds," Scientific Reports, vol. 13, no. 1, p. 9079, 2023, doi: 10.1038/s41598-023-34823-3

[3] Y. Yamanaka, S. Matsubara, N. Hirayama, S. Moriguchi, and K. Terada, "Surrogate modeling for the homogenization of elastoplastic composites based on RBF interpolation," Computer

Methods in Applied Mechanics and Engineering, vol. 415, p. 116282, 2023, doi: https://doi.org/10.1016/j.cma.2023.116282

[4] J. N. Fuhg and N. Bouklas, "On physics-informed data-driven isotropic and anisotropic constitutive models through probabilistic machine learning and space-filling sampling," Computer Methods in Applied Mechanics and Engineering, vol. 394, p. 114915, 2022, doi: https://doi.org/10.1016/j.cma.2022.114915

[5] J. Jiang, J. Wu, Q. Chen, G. Chatzigeorgiou, and F. Meraghni, "Physically informed deep homogenization neural network for unidirectional multiphase/multi-inclusion thermoconductive composites," Computer Methods in Applied Mechanics and Engineering, vol. 409, p. 115972, 2023, doi: https://doi.org/10.1016/j.cma.2023.115972

[6] E. Pitz and K. Pochiraju, "A neural network transformer model for composite microstructure homogenization," Engineering Applications of Artificial Intelligence, vol. 134, p. 108622, 2024, doi: https://doi.org/10.1016/j.engappai.2024.108622

[7] H. Maher Saad Hayder, H. Afrasiab, and M. Gholami, "Efficient generation of random fiber distribution by combining random sequential expansion and particle swarm optimization algorithms," Composites Part A: Applied Science and Manufacturing, vol. 173, p. 107649, 2023, doi: https://doi.org/10.1016/j.compositesa.2023.107649

[8] COMSOL Multiphysics®. COMSOL AB, Stockholm, Sweden.

Materials Research Proceedings 73 (2026) 100-104 https://doi.org/10.21741/9781644904459-20

Multidisciplinary Optimization of Passively-Insulated Liquid Hydrogen Tanks for Aircraft Applications

Sergio BAGARELLO[1,a], Alberto MILAZZO[1,b], Ali ELHAM[2,c], Ivano BENEDETTI[1,d *]

[1]Department of Engineering, University of Palermo, Italy

[2]Department of Aeronautics and Astronautics, University of Southampton, UK

[a]sergio.bagarello@unipa.it, [d]alberto.milazzo@unipa.it, [c]a.elham@soton.ac.uk, [d]ivano.benedetti@unipa.it

Keywords: Hydrogen Tank Optimization, Composite Pressure Vessel, Sustainable Aviation

Abstract. A finite-element-based multidisciplinary optimization framework is developed for passively insulated sandwich-composite liquid-hydrogen pressure vessels. Coupled steady-state thermo-elastic analyses are combined with nonlinear constrained optimization, where layer thicknesses are sized under stress, Hashin criterion, and boil-off-rate constraints. Realistic tank features, including non-spherical domes, refueling cutouts, thermal bridges, anti-sloshing baffles, and airframe-integration constraints, are progressively introduced. The results show that all-metal configurations are strongly penalized, with gravimetric efficiency below 30%, whereas composite-based vessels remain close to 50% even with the inclusion of representative integration features.

Introduction

Hydrogen is attracting increasing interest as an aviation energy carrier because it has the potential to eliminate direct carbon-dioxide emissions, offers high gravimetric energy density [1], and may also improve energy resilience. Unlike fossil fuels, whose supply chains are exposed to geopolitical instability and maritime chokepoints, hydrogen can in principle be produced from diversified domestic or regional energy sources, including renewable electricity. Its use in aircraft, however, remains limited by onboard storage [2]. Compared with kerosene stored at ambient conditions, in fact, hydrogen requires specialized systems, with penalties in both mass and volume. For medium- and long-range missions, liquid hydrogen (LH_2) is generally more attractive than compressed gaseous hydrogen because of its higher storage density, although it must be maintained at cryogenic conditions.

Methodology

The performance of an LH_2 vessel is governed by two conflicting requirements. First, the tank must achieve high gravimetric efficiency:

$$\eta_{\text{tank}} = \frac{W_{\text{H}_2}}{W_{\text{H}_2} + W_{\text{tank}} + W_{\text{subsystems}}},$$

where W_{H2} is the weight of the hydrogen the tank can store at design conditions, W_{tank} represents the structural weight of the tank itself and $W_{\text{subsystems}}$ quantifies the weight of the subsystems necessary for tank operation, which is assumed as 0 in the case of passive components.

Heat ingress must be sufficiently limited to keep the boil-off rate within acceptable operational limits, being defined as:

$$\text{BOR} = \frac{Q}{\rho_{\text{LH}_2} V_{\text{LH}_2} \lambda_{v_{\text{LH}_2}}},$$

Content from this work may be used under the terms of the Creative Commons Attribution 3.0 license. Any further distribution of this work must maintain attribution to the author(s) and the title of the work, journal citation and DOI. Published under license by Materials Research Forum LLC.

Materials Research Proceedings 73 (2026) 100-104 https://doi.org/10.21741/9781644904459-20

where Q represents the total heat from the exterior environment to the tank inner cavity, ρ_{LH2} is the density of the liquid fuel, V_{LH2} is the volume of LH_2 inside the tank and $\lambda_{v_{LH2}}$ denotes the latent heat of vaporization for liquid hydrogen.

A thermo-mechanical finite-element tank model is developed, with the liner and outer structural shell discretized by thermally coupled shell elements, while the foam insulation is represented by coupled three-dimensional solid elements because its thickness is much larger than that of the external layers. The steady-state analysis assumes a fuselage environment at 283 K, a tank inner wall at 20 K, natural convection on the outer surface, a 1.7 bar pressure differential, hydrostatic loading, and support constraints representative of tank-airframe mounting [3]. Material failure is assessed with layer-specific criteria. Metals and foam are constrained by safety-factor-adjusted von Mises stress limits, whereas the composite shell is constrained through Hashin damage initiation indices. The optimization problem is stated in:

$$\begin{aligned}
&\texttt{minimize} && m_{\text{tank}}(t_j) \\
&\texttt{with respect to} && t_j^{\text{lb}} \le t_j = [t_{\text{Al}}, t_{\text{PUR}}, t_{\text{Ti}}, t_{\text{CFRP}}] \le t_j^{\text{ub}} \\
&\texttt{subject to} && g_i = \begin{cases} \dfrac{\sigma_{\text{Al}}}{\bar{\sigma}_{\text{SF}}^{\text{Al}}} - 1 \le 0 \\ \dfrac{\sigma_{\text{PUR}}}{\bar{\sigma}_{\text{SF}}^{\text{PUR}}} - 1 \le 0 \\ \dfrac{\sigma_{\text{Ti}}}{\bar{\sigma}_{\text{SF}}^{\text{Ti}}} - 1 \le 0 \\ \text{HSNCRT}_{\text{SF}} - 0.667 \le 0 \\ \text{BOR} - \text{BOR}_{\text{allowable}} \le 0 \end{cases}
\end{aligned}$$

Minimizes tank mass with respect to the layer thicknesses, subject to structural constraints and a daily BOR limit of 2.50% of the stored LH_2 mass.

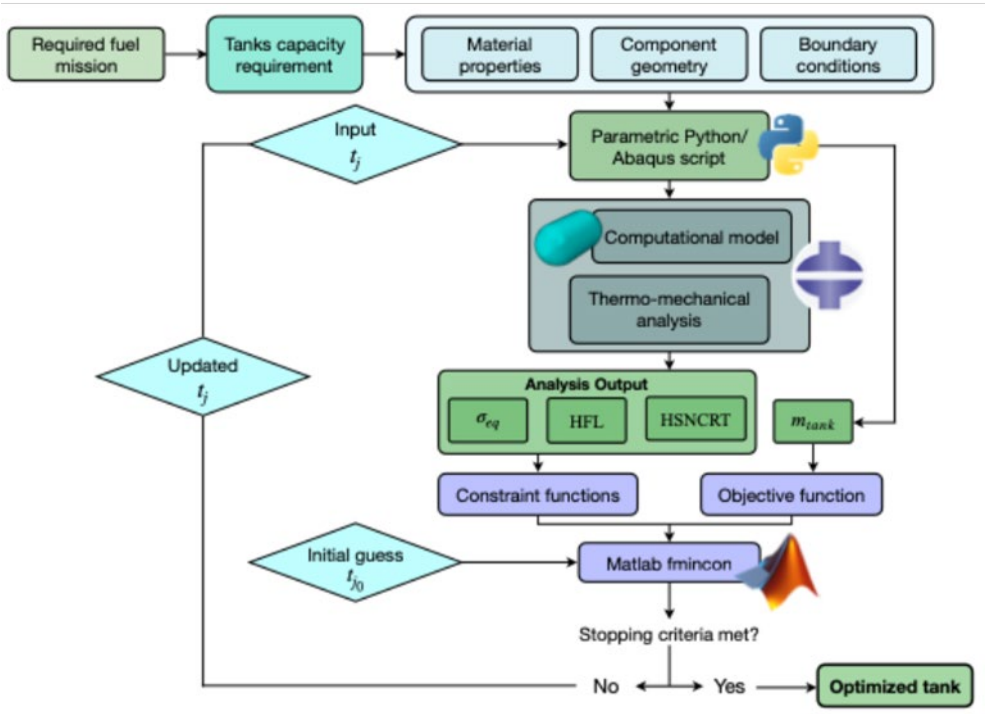

Figure 1 - Optimization workflow scheme. Adapted from Ref.[5].

Materials Research Proceedings 73 (2026) 100-104 https://doi.org/10.21741/9781644904459-20

The FE model is coupled with MATLAB fmincon, as reported in Fig.(1), using an interior-point algorithm, finite-difference gradients, a BFGS Hessian update, and KS aggregation to manage the large number of local constraints [4, 5].

Numerical Results

Six configurations are analysed to isolate the effects of material choice, dome geometry, and integration features. *Tank I* is the metallic baseline with a Ti-6Al-4V outer shell and hemispherical domes. *Tank II* replaces titanium with CFRP. *Tank III* introduces hemi-ellipsoidal domes. *Tank IV* adds refuelling cutouts and a thermal-bridge correction. *Tank V* adds anti-sloshing baffles. *Tank VI* combines ellipsoidal domes, cutouts, and baffles and is therefore the most representative architecture. Each tank has the same internal capacity and is subject to the same boundary conditions. Comparison of optimized tank mass is provided in Fig.(2).

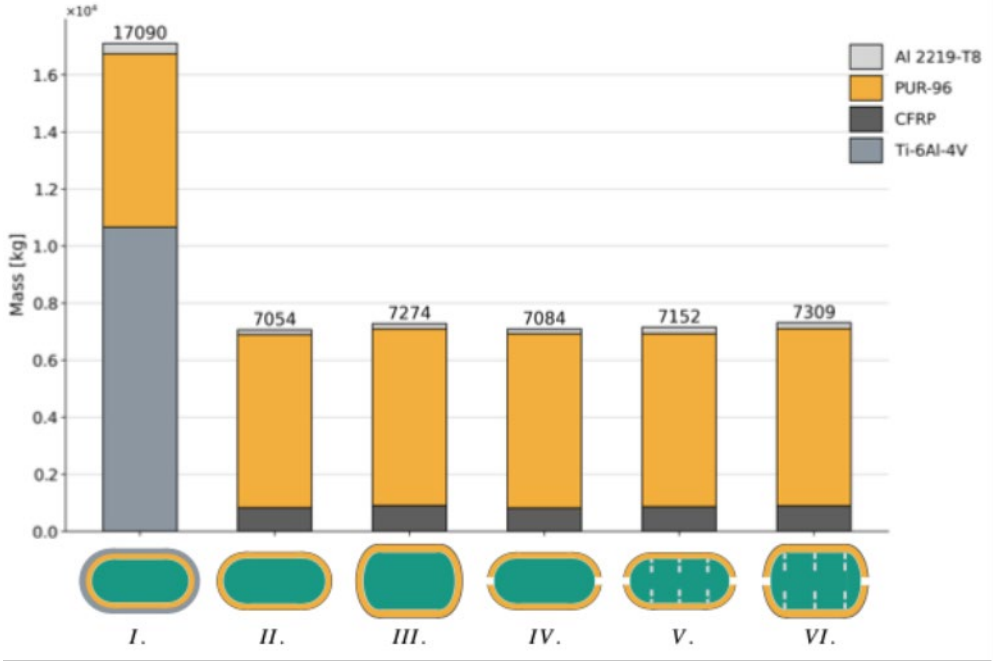

Figure 2 - Comparison of minimum achievable mass for each tank configuration. Adapted from Ref.[5].

The results highlight the mass penalty associated with metallic construction. Even with titanium as the outer shell, the metallic baseline reaches only 29.31% gravimetric efficiency. Replacing titanium with CFRP reduces the optimized tank mass from 17090 kg to 7054 kg and increases $\boldsymbol{\eta_{tank}}$ to 50.11%, indicating that composite construction is necessary to approach competitive storage performance.

The progressive introduction of practical aircraft features produces moderate but non-negligible penalties. Hemi-ellipsoidal domes increase the surface-to-volume ratio and therefore insulation demand. Refuelling cutouts reduce local thermal performance through thermal bridges. Anti-sloshing baffles increase liner mass, although the overall penalty remains limited. The complete *Tank VI* configuration reaches $\boldsymbol{\eta_{tank}}$ = 49.22%, despite the inclusion of all the pragmatic features considered.

A laminate comparison for the most representative tank indicates that the quasi-isotropic *[0/90/45/-45]s* lay-up provides the lowest mass among the feasible sequences tested. This reflects the coupled nature of the structural response, which depends on the interaction among laminate stiffness, foam stress limits, liner deformation, supports, and thermal contraction.

Materials Research Proceedings 73 (2026) 100-104 https://doi.org/10.21741/9781644904459-20

The most representative vessel is also scaled and integrated within a next-generation ultra-high-aspect-ratio strut-braced-wing aircraft concept (UHARW) [6], Fig.(3). The resulting forward and aft tanks show slightly lower gravimetric efficiency than the 100 m³ reference case because smaller tanks have higher surface-to-volume ratios. Field analyses indicate that stresses are governed primarily by thermally induced deformation rather than by pressure loading. The PUR insulation becomes the limiting layer near supports and baffle interfaces, whereas the CFRP shell remains below the Hashin thresholds.

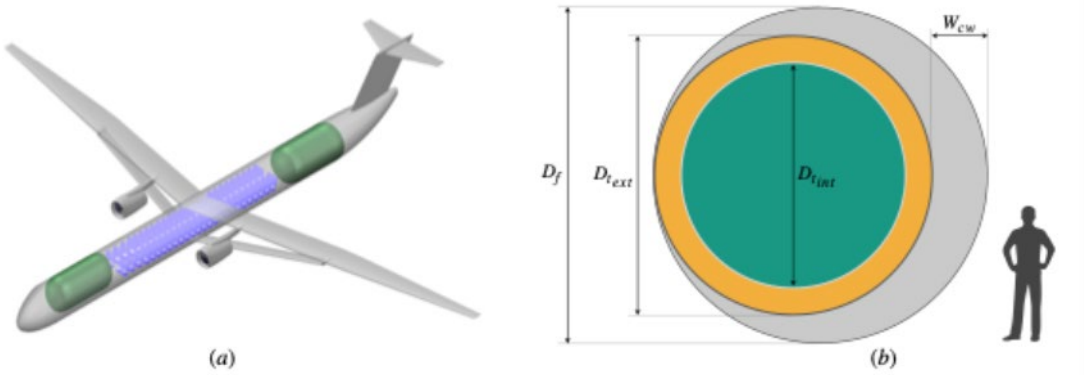

Figure 3 - a) isometric view of the UHARW aircraft; b)sectional view of the forward fuselage with tank integration. Adapted from Ref.[5].

Conclusions

A multidisciplinary optimization framework has been summarized for passively insulated LH_2 pressure vessels intended for aircraft applications. The approach couples finite-element thermo-mechanical analysis with constrained optimization and enables the systematic assessment of material selection, layer thicknesses, dome geometry, cutouts, baffles, and airframe-integration constraints under a common boil-off requirement. The study confirms that all-metal architectures impose severe mass penalties, whereas CFRP outer shells allow gravimetric efficiencies close to 50%. Realistic integration features reduce performance only moderately, while highlighting the importance of local stress concentrations, thermal bridges, and support-induced constraints. Future work should address transient boil-off, more detailed interface modelling, buckling and reliability constraints, and refined patch-wise or conformal thickness tailoring.

Acknowledgment

S.B. and I.B. acknowledge the support by the European Union - NextGenerationEU - National Sustainable Mobility Center CN00000023, Italian Ministry of University and Research Decree n. 1033-17/06/2022, Spoke 12, CUP B73C22000760001.

References

[1] Bagarello S., Campagna D., Benedetti I. A survey on hydrogen tanks for sustainable aviation. Green Energy and Intelligent Transportation, 2024. https://doi.org/10.1016/j.geits.2024.100224

[2] Adler E.J., Martins J.R.R.A. Liquid hydrogen tank boil-off model for design and optimization. Journal of Thermophysics and Heat Transfer, 2024. https://doi.org/10.2514/1.T7005

[3] Bagarello S., Campagna D., Benedetti I. Computational thermo-mechanical modelling and design-space exploration of cryogenic hydrogen tanks for aviation. Aerospace Science and Technology, 2026. https://doi.org/10.1016/j.ast.2025.110755

[4] Poon N., Martins J. An Adaptive Approach to Constraint Aggregation Using Adjoint Sensitivity Analysis. Structural and Multidisciplinary Optimization, 2007. https://doi.org/10.1007/s00158-006-0061-7

[5] Bagarello S., Elham A., Benedetti I. Design, optimization, and integration of passively-insulated liquid hydrogen tanks for sustainable aviation. International Journal of Hydrogen Energy, 2026. https://doi.org/10.1016/j.ijhydene.2025.153042

[6] Wahler N.F.M., Ma Y., Elham A. Conceptual design and aerostructural trade-offs in hydrogen-powered strut-braced wing aircraft. Aerospace, 2025. https://doi.org/10.3390/aerospace12020077

Materials Research Proceedings 73 (2026) 105-108 https://doi.org/10.21741/9781644904459-21

Modeling Hygrothermal-Induced Degradation in Polymer Adhesive Joints for Composite-Metal Assemblies

Touati Benali Abdelaziz[1,a *], Habib Achache[2,b], Mohammed Benyettou[3,c], Alberto García-Peñas[4,d]

[1]Production engineering and industrial maintenance laboratory,IMSI/ University of Oran2 Mohamed Ben Ahmed, 31000 Oran, Algeria

[2]LMPM,IMSI/ University of Oran2 Mohamed Ben Ahmed, 31000 Oran, Algeria

[3]Laboratory of Mechanics of Structures and Solids, LMSS, Mechanical Engineering Department, Djilali Liabes University of Sidi-Bel-Abbes, BP 89 Sidi Bel Abbes, 22000, Algeria

[4]Department of Materials Science and Engineering: uc3m, Madrid, Spain

[a]touatibenali.abdelaziz@univ-oran2.dz, [b]achachehabib@yahoo.fr, [c]mohammed.benyettou97@gmail.com, [d]alberto.garcia.penas@uc3m.es

Keywords: Adhesive Joints, Hygrothermal Ageing, Stress Distribution, Composite Materials

Abstract. The durability of adhesively bonded structures under environmental conditions remains a critical challenge in advanced engineering applications. This study examines the effect of hygrothermal aging on the mechanical response of bonded joints through the investigation of aluminum–carbon/epoxy composite assemblies. The configuration is modeled as a single-lap joint with a defined geometry and bonded using the structural adhesive Adekit A140 to ensure consistency in the analysis. Accelerated aging was performed under 100% relative humidity at three temperatures (20 °C, 40 °C, and 60 °C) for exposure durations of 4, 10, and 24 weeks. A three-dimensional finite element model was developed in Abaqus, incorporating degradation of material properties based on experimental data reported in the literature. The numerical results indicate that the equivalent Von Mises stresses are highly localized at the overlap ends, confirming these regions as critical zones for stress concentration and damage initiation. Furthermore, the combined effect of temperature and exposure time has a significant impact on the adhesive layer's load transfer capability. This study enhances our understanding of the relationship between material properties and hygrothermal conditions, supporting the identification of more durable bonded configurations for long-term structural applications.

Introduction

Structural adhesive joints are widely used in aerospace, automotive, and civil engineering due to their lightweight nature, uniform stress distribution, and ability to bond dissimilar materials. However, hygrothermal aging caused by moisture absorption at elevated temperatures significantly affects adhesive microstructure and mechanical performance.

Previous studies have shown that moisture exposure reduces fatigue life and mechanical strength of bonded joints. Rushforth et al. [1] reported a decrease in fatigue life of aluminum joints near saturation, while Jiang et al. [2] observed significant reductions in tensile and shear strengths after prolonged immersion. El Sallah et al. [3] highlighted that degradation of Adekit A140 stiffness is associated with increased plasticity, which may improve stress redistribution. Similarly, Robert et al. [4] demonstrated that prolonged hygrothermal exposure leads to severe degradation in composite materials, particularly for natural fiber systems.

Finite element investigations by Medjdoub et al. [5] showed that geometric optimization can significantly reduce stress concentrations, although aging reduces adhesive stiffness and increases

Content from this work may be used under the terms of the Creative Commons Attribution 3.0 license. Any further distribution of this work must maintain attribution to the author(s) and the title of the work, journal citation and DOI. Published under license by Materials Research Forum LLC.

joint vulnerability. Moreover, Venkatappagari et al. [6] emphasized the critical role of environmental conditions and design parameters in the durability of adhesive bonded joints.

In this context, the present study examines the effect of hygrothermal ageing on bonded joints by analysing aluminium–carbon/epoxy assemblies using Adekit A140 adhesive. The influence of material degradation on stress distribution is evaluated using a 3D finite element model developed in Abaqus, under accelerated aging conditions of 100% humidity, 20, 40 and 60 °C, and 4, 10 and 24 weeks.

Methodology

A bonded joint configuration was examined in this study to assess the mechanical behavior under hygrothermal ageing. The configuration corresponds to a metal-to-composite hybrid joint, comprising an aluminium plate and a carbon–epoxy composite laminate. The joint was modelled as a single-lap configuration with the following defined dimensions: length L = 100 mm, width W = 25 mm, . The adhesive used is ADEKIT A-140 with the dimensions: length Lc = 25 mm, width w = 25 mm, and thickness t = 0.2 mm, axially loaded along the X-axis by an imposed displacement of 5 mm. The adhesive joint is for a single lap joint of the two aluminium plates (see Fig.1).

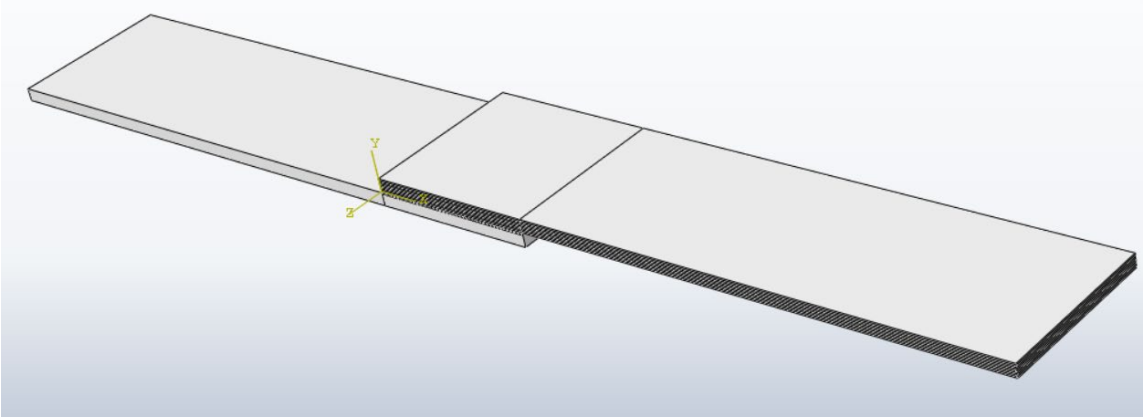

Fig. 1: Geometric configurations of SLJ models

Table 1. Mechanical properties of the aluminum alloy 2024-T3 and Adekit A-140 adhesive.

Materials	Aluminium 2024-T3	Adekit A-140
Young's modulus (GPa)	72.8	2.7
Poisson's ratio υ	0.3	0.3

Table 2. Mechanical properties of the composite material.

Materiel	***E*$_1$ *(GPa***	***E*$_2$**	***E*$_3$**	***G*$_{12}$**	***G*$_{13}$**	***G*$_{23}$**	***ν*$_{12}$**	***ν*$_{13}$**	***ν*$_{23}$**
Carbon-epoxy	110	8.819	8.819	4.315	4.315	3.2	0.342	0.342	0.38

Materials Research Proceedings 73 (2026) 105-108 https://doi.org/10.21741/9781644904459-21

Numerical Results

This section presents the numerical results obtained for the carbon/epoxy–aluminum joint, focusing on the effect of hygrothermal aging on stress distribution. The unaged is compared with aged conditions at 20, 40, and 60 °C (RH = 100%) for exposure durations of 4, 10, and 24 weeks.

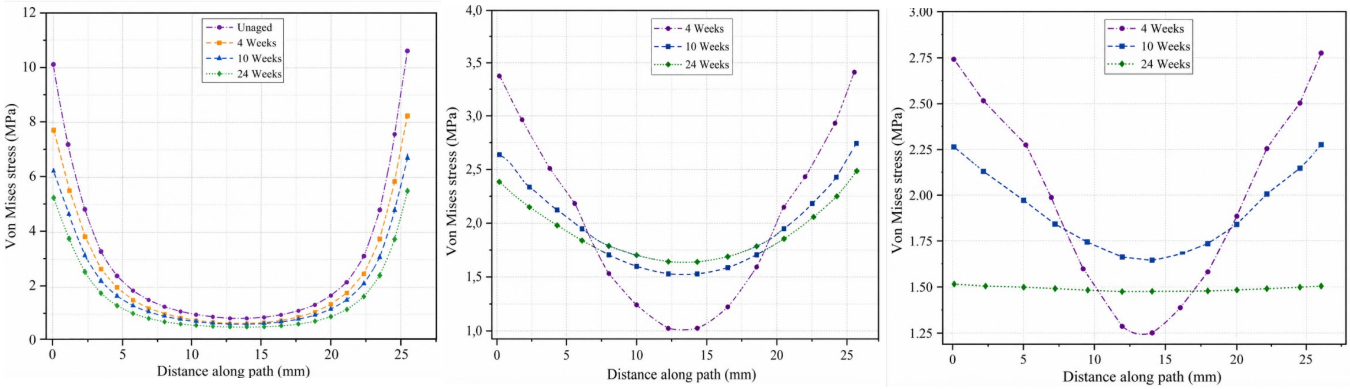

(a) Ageing at 20 °C (b) Ageing at 40 ° (c) Ageing at 60 °

Fig 2. Distribution of Von Mises stress in the adhesive layer for carbon/epoxy–aluminum joint under different aging temperatures: (a) 20 °C, (b) 40 °C, (c) 60 °C.

At 20 °C, the maximum Von Mises stress decreases from 10.88 MPa (unaged) to 8.33, 6.75, and 5.78 MPa after 4, 10, and 24 weeks, corresponding to a reduction of approximately 46.7%, indicating progressive adhesive plasticisation and moderate stiffness degradation. At 40 °C, the degradation becomes significantly more pronounced, with the peak stress dropping to 3.44 MPa after 4 weeks and reaching nearly 76.8% reduction after 24 weeks, highlighting the accelerating effect of temperature on moisture-induced damage mechanisms.

Under the most severe condition (60 °C), the stress levels further decrease to 2.79, 2.29, and 1.50 MPa after 4, 10, and 24 weeks, respectively, corresponding to an overall reduction of about 86%.. Overall, the combined effect of temperature and exposure time leads to a critical loss of stiffness and load transfer capability, confirming that the adhesive layer governs the durability of the bonded joint under hygrothermal conditions.

Comparative ageing response

Figure 3 highlights a clear temperature-dependent degradation of the adhesive behavior, with the maximum Von Mises stress decreasing over time under all conditions. This reduction becomes significantly more pronounced as temperature increases, indicating the combined influence of moisture diffusion and thermal effects. After 24 weeks, higher stress levels are maintained at 20 °C compared to 40 °C and 60 °C, confirming that temperature governs the severity of degradation. Quantitatively, the strength loss increases from about 47% at 20 °C to nearly 86% at 60 °C, showing that the effect of exposure time is strongly amplified at elevated temperatures due to accelerated plasticisation and material deterioration.

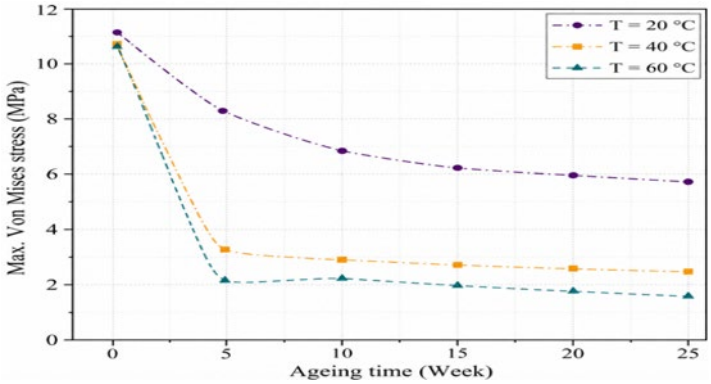

Fig. 3: Maximum Von Mises stress evolution in the adhesive layer versus ageing time (4, 10, 24 weeks) under hygrothermal conditions (100% RH) at 20, 40, and 60 °C

Conclusions

The results show that hygrothermal aging significantly degrades the mechanical performance of the adhesive joint, with temperature and exposure time acting as key factors. Although stress concentrations decrease, this reflects adhesive softening and reduced stiffness rather than improved behavior. The degradation becomes more severe with temperature, with strength loss increasing from about 47% at 20 °C to nearly 86% at 60 °C. This evolution indicates a transition toward less efficient load transfer and confirms the dominant role of the adhesive layer in joint durability.

References

[1] Rushforth MW, Bowen P, Mcalpine E. The effect of surface pretreatment and moisture on the fatigue performance of adhesively-bonded aluminium. J Mater Process Technol 2004;153–154(1):359–65. Compos Struct 2015;125:687–97. https://doi.org/10.1016/j.jmatprotec.2004.04.319

[2] Jiang X, Qiang X, Kolstein MH, et al. Experimental investigation on mechanical behavior of FRP-to-steel adhesively-bonded joint under combined loading – Part 2: after hygrothermal ageing

[3] El Sallah, Z. M., Abdelmadjid, M., Ali, B., Kouider, M., & Rachid, Z. (2024). Influence of hygrothermal aging on the mechanical strength of an Aluminum/Aluminum bonded assembly. Advances in materials research: AMR, 13(6), 527-546.

[4] Chlela, R., Zombré, W., Quiertant, M., Curtil, L., & Benzarti, K. (2019, July). Influence du vieillissement hygrothermique sur le comportement mécanique de composites conventionnels ou biosourcés destinés au renforcement de structures. In 21ème Journées Nationales sur les Composites.

[5] Medjdoub, S. M., Madani, K., Rezgani, L., Mallarino, S., Touzain, S., & Campilho, R. D. S. G. (2022). Numerical analysis of the combined aging and fillet effect of the adhesive on the mechanical behavior of a single lap joint of type Aluminum/Aluminum.

[6] Venkatappagari, S., Mutra, R. R., & Reddy, D. M. (2025). State-of-the-art in adhesive joint technology: A comprehensive review of recent progress. Journal of Materials Research and Technology, 37, 2593-2615. https://doi.org/10.1016/j.jmrt.2025.06.166

Materials Research Proceedings 73 (2026) 109-113 https://doi.org/10.21741/9781644904459-22

Low-Velocity Impact on Composite Stiffened Panels Using a Component-Wise Approach

Marco PETROLO[1,a *], Chiara FRANCESCHINI[1,b], Matteo FILIPPI[1,c], Erasmo CARRERA[1,d]

[1]MUL2 lab, Department of Mechanical and Aerospace Engineering, Politecnico di Torino, Italy

[a]marco.petrolo@polito.it, [b]chiara.franceschini@polito.it, [c]matteo.filippi@polito.it, [d]erasmo.carrera@polito.it

Keywords: Low-Velocity Impact, Stiffened Panels, CUF

Abstract. Composite stiffened panels, widely used in the aerospace sector, are exposed to low-velocity impacts (LVI) during operation, maintenance, and transport. Computational methods help predict deformation and the extent of damage under dynamic loading, reducing the need for an extensive testing campaign. In this work, structural theories based on the Carrera Unified Formulation (CUF) are proposed for the analysis of low-velocity impacts on stiffened composite panels. The dynamic response of both the skin and the stiffeners is described through refined 1D elements with higher-order kinematic expansions, enabling an accurate evaluation of local deformation effects and stress concentrations, especially at the skin-stiffener interface. A progressive intralaminar damage model is adopted to account for material nonlinearities. The proposed approach is assessed on representative composite stiffened panels subjected to LVI. The results are compared with those obtained from commercial finite element models based on full 3D discretization. The comparison shows that the CUF-based models provide accurate predictions of the structural response while reducing the computational cost in terms of Degrees of Freedom (DOFs). These features make the proposed methodology an efficient alternative to conventional 3D modelling strategies for the design and analysis of lightweight composite stiffened structures.

Introduction

Composite stiffened panels are extensively employed in aerospace structures because they combine low structural weight with high bending stiffness, buckling resistance, and load-carrying capability. Nevertheless, their damage tolerance under low-velocity impact remains a major design concern. Impact events may produce barely visible impact damage, involving matrix cracking, fibre failure, and delamination, with a potentially significant reduction in residual structural performance [1]. The continuing interest in this problem is demonstrated by recent experimental and numerical studies addressing multiple impacts and compression-after-impact behaviour of thin CFRP laminates [2], the influence of impact energy, laminate thickness, and stacking sequence [3], and the response of hybrid carbon-fibre/metal laminates [4]. In stiffened panels, stiffeners introduce discontinuities in stiffness and stress concentration points because the load is redistributed over the complex geometry of the structure. Impact damage on reinforced composite plates has been studied by Li et al. [5] and by Rahman et al. [6]. Generally, the analyses are computationally demanding because these detailed models usually require fine 3D discretization and dedicated material subroutines. An alternative modelling strategy is offered by the Carrera Unified Formulation (CUF), which enables the systematic derivation of refined one- and two-dimensional structural theories using arbitrary-order kinematic expansions [7]. Within this framework, higher-order layer-wise models have been developed for the progressive damage and low-velocity impact analysis of composite laminates [8,9]. The accurate three-dimensional stress fields provided by these models have also been combined with failure criteria and continuum damage formulations for the analysis of tensile and compressive failure [10,11]. More recently,

Content from this work may be used under the terms of the Creative Commons Attribution 3.0 license. Any further distribution of this work must maintain attribution to the author(s) and the title of the work, journal citation and DOI. Published under license by Materials Research Forum LLC.

Materials Research Proceedings 73 (2026) 109-113 https://doi.org/10.21741/9781644904459-22

the framework has been applied to LVI on unstiffened composite plates using 2D layer-wise theories, the 3D Hashin criterion, and cohesive interfaces [12]. These studies demonstrated the capability of refined structural theories to predict local stress and damage fields without requiring conventional solid-element discretization. The present work extends the CUF-based impact framework to 1D component-wise models of composite stiffened panels. Higher-order expansions describe the displacement field over complex skin–stiffener cross-section. The implementation is first verified on an unstiffened composite plate and is subsequently applied to the impact and intralaminar damage analysis of a stiffened panel.

Methodology

The structural theories adopted in this work are developed within the Carrera Unified Formulation (CUF), which enables the systematic derivation of refined one- and two-dimensional models through compact notation. For the one-dimensional formulation, the three-dimensional displacement field is expressed as

$$\mathrm{u}(\mathrm{x},\mathrm{y},\mathrm{z}) = \mathrm{F}_{\tau}(\mathrm{x},\mathrm{z})\mathrm{N}_{\mathrm{i}}(\mathrm{y})\mathrm{u}_{\tau\mathrm{i}} \quad \tau = 1,\dots,\mathrm{M}; \quad \mathrm{i} = 1,\dots,\mathrm{N}. \tag{1}$$

where $N_i(y)$are the finite element shape functions along the beam axis, $F_\tau(x,z)$ are arbitrary expansion functions defined over the cross-section, and $u_{\tau i}$contains the generalized displacement variables. The type and order of the expansion can be selected without modifying the general formulation. Higher-order Lagrange polynomial expansions are employed to discretize the cross-section. In the adopted layer-wise approach, each composite layer is represented as an independent subdomain and different expansions can be assigned to different regions of the cross-section, providing an accurate evaluation of the three-dimensional stress state even for complex stacking sequences. This feature is particularly advantageous for stiffened panels. In 1D CUF models, the skin and the stiffener can be represented directly within the cross-sectional discretization, allowing complex shape stiffener to be modelled while retaining a 1D finite element mesh along the longitudinal direction. An accurate stress prediction is essential because it may affect both damage initiation and propagation. An explicit time-integration procedure based on the Central Difference Scheme is used as solver. Node-to-surface contact, previously only available for 2D elements, has been extended to 1D elements by creating an artificial contact surface. The reliability of the new implementation was verified by comparing the results of 1D and 2D models on an unstiffened plate.

Intralaminar damage initiation is evaluated using the Hashin 3D criterion, which distinguishes fibre and matrix failure under tensile and compressive loading. When one of the four failure indices reaches unity, the corresponding damage evolution is described through a linear law that reduces the material stiffness up to final failure. Interlaminar damage can be represented within the proposed framework through cohesive interface elements. However, cohesive delamination is not activated in the numerical results presented in this work, which focus on the validation of the one-dimensional contact formulation and on the prediction of intralaminar damage in stiffened composite panels.

Numerical Results

The first case reproduces the benchmark presented in [12] to validate the node-to-surface formulation developed for CUF-1D models. A 16 mm spherical impactor strikes at 5 m/s a fully clamped 100×100 mm composite plate. The 2 mm thick quasi-isotropic laminate has stacking sequence $[90/45/0/-45]_{2s}$. The CUF-1D results are compared with CUF-2D and three-dimensional ABAQUS solutions, see Table 1 for models' details. Different cross-sectional refinements provide converged displacement and force histories, confirming the robustness of the contact formulation, see Fig. 1. The 1D models used 320 L9 elements across the cross-section but with different refinements in the contact zone (CZ). The in-plane stress components at (x,y) = (48

Materials Research Proceedings 73 (2026) 109-113 https://doi.org/10.21741/9781644904459-22

mm, 48 mm) and interlaminar shear stresses at (x,y) = (40 mm, 40 mm) show good agreement with the Abaqus solution, see Fig. 2.

Table 1: Model discretization and numbers of degrees of freedom of the unstiffened plate.

Model	Discretisation	DOF
CUF-2D (1 LE1/ply)	400 Q9 (1 LE1/ply)	85'731
CUF-2D (1 LE2/ply)	400 Q9 (1 LE2/ply)	166'419
CUF-2D (1 LE3/ply)	400 Q9 (1 LE3/ply)	247'107
CUF-1D	320 L9 – 20 B4	247'599
ABQ-3D (5 elem/ply)	512000 C3D83 (5 el/ply)	1'594'323

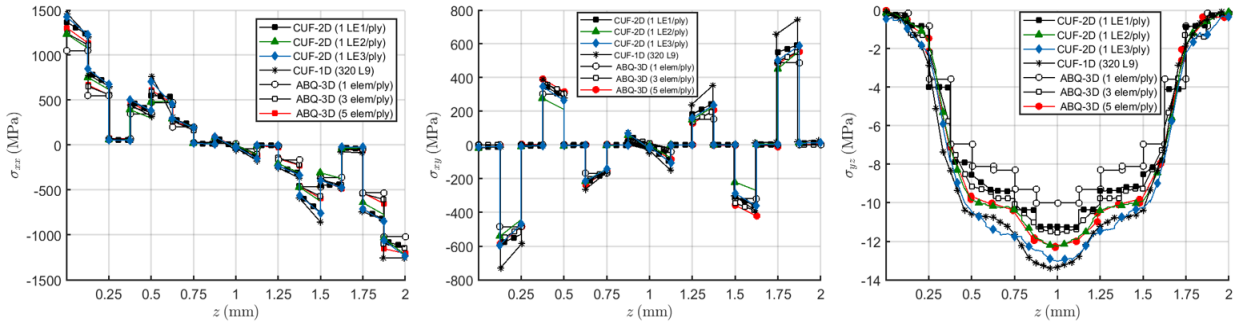

Figure 1: Through-thickness stress distribution of the unstiffened plate. CUF-1D (320 L9) refers to the 8L9 in the contact zone CZ.

The second case considers a fully clamped 200 × 200 mm composite plate reinforced by two I-shaped parallel stiffeners, subjected to central impacts at 20, 30, and 40 m/s. The skin laminate has stacking sequence [0/90/0/90/0]and a total thickness of 2.69mm. The unidirectional [0] stiffeners have a reference height of 7 mm. The structure is made of T300/934 graphite/epoxy taken from [5] and is impacted by a rigid spherical impactor with a radius of 6 mm. Both the skin and stiffeners are represented using CUF-1D elements, with a total of 77 L9 and 12 B4 and 39'183 DOFs. Good agreement with the reference solution [5] is obtained during the initial loading stage and for the first contact-force peak, see Fig. 3. The late-stage differences may be attributed to the different contact formulations: the reference model uses Hertzian indentation, whereas the present model evaluates contact reactions through Lagrange multipliers. The 3D Hashin criterion reproduces the initiation and early evolution of matrix damage near the impact region, see Fig. 4. Larger differences are observed at later stages. Since delamination is not included, the present results should be regarded as a preliminary assessment of intralaminar damage.

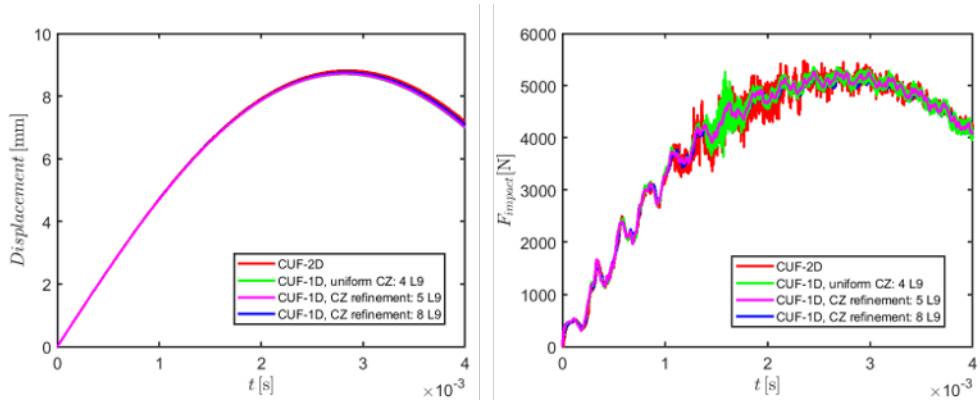

Figure 2: Mid-point displacement and impact force histories of the stiffened plate.

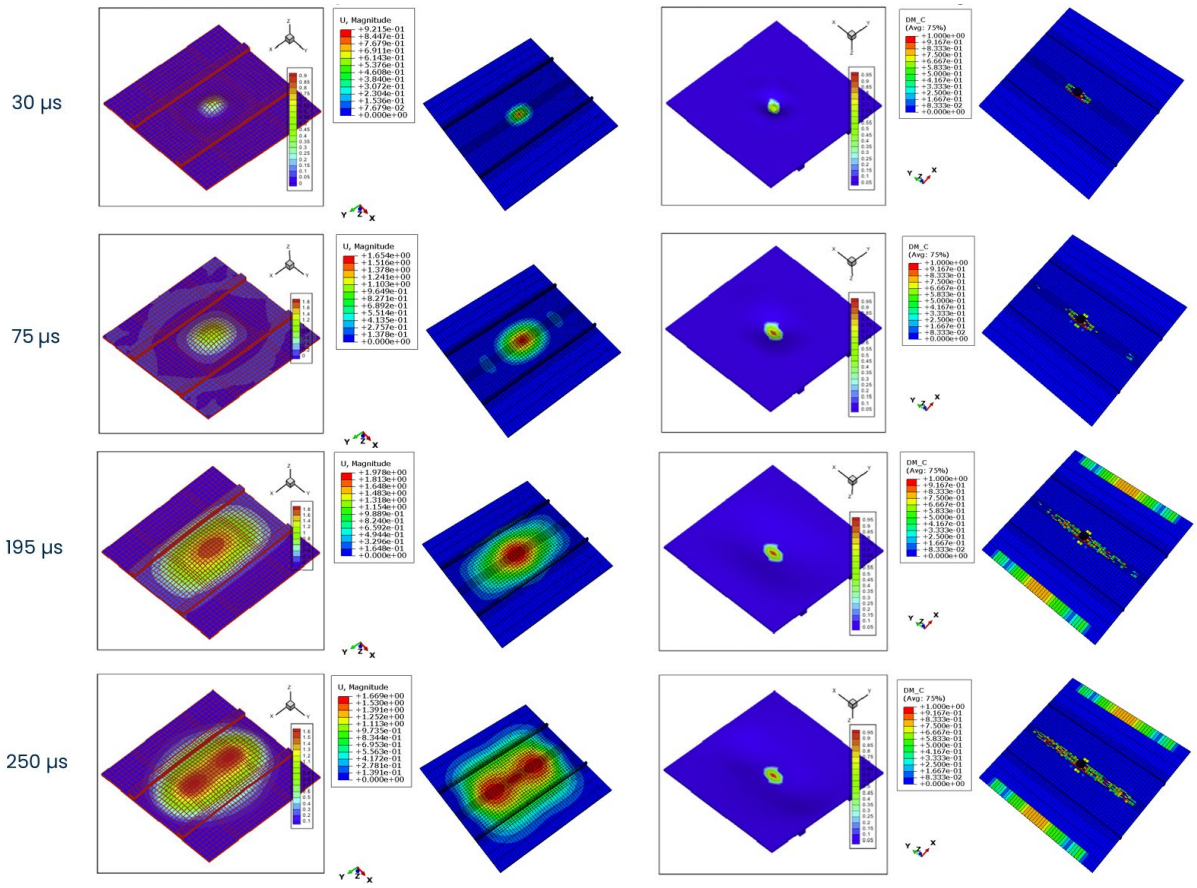

Figure 3: Displacement and matrix-damage contours at selected times for an initial velocity of $V_0 = 20\ m/s$ of the stiffened plate. Boxed panels show the reference solution from [5].

Conclusions

A node-to-surface contact formulation was successfully extended to CUF-1D models through the reconstruction of an artificial contact surface. The unstiffened plate benchmark shows good agreement with CUF-2D and full 3D solutions while using only about 15% of the DOFs of the three-dimensional model. The formulation was then applied to a stiffened composite plate, accurately capturing the initial impact response and the onset of intralaminar damage. Future developments will include cohesive delamination modelling and element deletion beyond a critical damage threshold.

Acknowledgment

This study was carried out within the Space It Up! project funded by the Italian Space Agency, ASI, and the Ministry of University and Research, MUR, under contract n. 2024-5-E.0 - CUP n. I53D24000060005.

References

[1] E. Greenhalgh, M. Hiley. “The assessment of novel materials and processes for the impact tolerant design of stiffened composite aerospace structures”. Composites Part A: Applied Science and Manufacturing, vol. 34, no. 2, pp. 151–161, 2003.

[2] Y. Gao, Y. Gong, X. Li, Z. Li, M. Shan, J. Zhang, L. Zhao, N. Hu, “Multiple low-velocity impact induced damage evolution and compressive performance of thin cross-ply CFRP laminates”. Construction and Building Materials, vol. 517, 2026, https://doi.org/10.1016/j.conbuildmat.2026.145738

[3] S. Adhityan, B. Razim Ahamed, D. M. Reddy, R. R. Mutra, J. Naveen, and R. Rzadkowski, “Modeling and Analysis of Low Velocity Impact Damage in Carbon Fiber Laminates”. Polymer Composites 47, no. S2 (2026): S275–S287, https://doi.org/10.1002/pc.70932.

[4] M. İ. Özsoy, E. C. Yakar, S. Fidan, S. Ürgün, and M. Ö. Bora, “ Progressive Damage and Impact Behavior of Carbon Fiber/Epoxy-Aluminum 2024-T3 CARALL Composites: Experimental Investigation and Hybrid Finite Element Modeling Approach,” Polymer Composites (2026): 1–15, https://doi.org/10.1002/pc.71474.

[5] D.H. Li, Y. Liu, X. Zhang. “Low-velocity impact responses of the stiffened composite laminated plates based on the progressive failure model and the layerwise/solid-elements method”. Composite Structures 110 (2014) 249–275.

[6] M. Rahman, E. Maravilla, S. Devaru, S. Lin, A. Waas, V. Ranatunga. “A Computational Method for Predicting the Damage and Failure Due to Impact of Double Hat Stiffened Aircraft Skin Panels”. Aerotecnica Missili & Spazio, 2026. https://doi.org/10.1007/s42496-025-00301-4

[7] E. Carrera, M. Cinefra, E. Zappino and M. Petrolo, “Finite Element Analysis of Structures through Unified Formulation”. Hoboken, NJ, USA: Wiley, 2014. https://doi.org/10.1002/9781118536643

[8] M.H. Nagaraj, E. Carrera and M. Petrolo, “Progressive damage analysis of composite laminates subjected to low-velocity impact using 2D layer-wise structural models”. Int. J. Non-Linear Mech. 127, 2020. https://doi.org/10.1016/j.ijnonlinmec.2020.103591

[9] M.H. Nagaraj, “Higher-order layer-wise models for the progressive damage and impact analysis of composite structures”. PhD thesis, Politecnico di Torino, 2021. Doctoral Dissertation, Doctoral Program in Mechanical Engineering (33rd Cycle), January 2021

[10] M. Petrolo, E. Tortorelli and S. Saputo, “Compressive damage of composite structures using 3D Failure criteria and 2D higher order structural theories”. Mechanics of Advanced Materials and Structures, pages 1–11, 2025. https://doi.org/10.1080/15376494.2025.2489138

[11] M. Petrolo, E. Tortorelli, S. Saputo and E. Carrera, “Tensile damage analysis of composite structures based on 3D Hashin failure criteria and 2D higher-order structural theories”. Comp. Commun. 56, 102395, 2025. https://doi.org/10.1016/j.coco.2025.102395

[12] M. Petrolo, M. Filippi, E. Carrera, C. Franceschini and E. Tortorelli, “Low-velocity Impact in Composite Plates Using the Hashin 3D Criterion and 2D Layer-Wise Theories”. Aerotecnica Missili & Spazio, 2026, https://doi.org/10.1007/s42496-026-00320-9.

Materials Research Proceedings 73 (2026) 114-117 https://doi.org/10.21741/9781644904459-23

Lattice Structures: From Computed Tomography to Simplified Models

Davide Lorenzo CAPPA[1,a *], Riccardo VESCOVINI[1,b], Alessandro LEVATI[2,c], Stefano FOLETTI[2,d]

[1]Dipartimento di Scienze e Tecnologie Aerospaziali, Politecnico di Milano, Milano, Italy

[2]Dipartimento di Meccanica, Politecnico di Milano, Milano, Italy

[a]davidelorenzo.cappa@polimi.it, [b]riccardo.vescovini@polimi.it, [c]alessandro.levati@polimi.it, [d]stefano.foletti@polimi.it

Keywords: Lattice Structures, Additive Manufacturing, Simplified Models

Abstract. Additive manufacturing of lattice structures introduces geometrical imperfections that significantly affect their mechanical response. In this work, CT scans are used to reconstruct imperfect struts through a statistical description of their geometry. The reconstructed struts are employed to derive nonlinear tensile and bending responses, which are embedded into a reduced-order beam formulation in Abaqus. Results show that the simplified beam model captures the initial stiffness, yielding behavior, and orthotropic response of the CT-based models while significantly reducing the computational cost.

Introduction

All Lattice structures are increasingly appealing for the aerospace sector as they offer high structural efficiency and high adaptability. Their production is made possible by additive manufacturing, which inevitably introduces geometrical and material imperfections, such as waviness, surface defects and porosity [1]. The modelling of defects is crucial for the design of lattice structures, several studies are dedicated to this topic, with imperfect beams [2], spheres-based models [3], finite element models with scan data [4].

Although the literature on this subject is extensive, modelling of imperfections is frequently reliant on computationally expensive analyses, making it impractical for early-stage evaluations. Consequently, there is a clear need for efficient modelling approaches to simplify and accelerate the preliminary design phase while enabling a more effective use of these structures.

In this paper, finite element models of lattice structures are developed using computed tomography (CT) images of AlSi10Mg T6 specimens produced by laser powder bed fusion (LPBF). Starting from CT scans, struts are geometrically reconstructed and used to generate models with realistic imperfections, following the approach in [5]. These struts are modelled using three-dimensional finite elements and subjected to tensile and bending loads to derive a constitutive model. This model is then implemented in simplified one-dimensional beam elements, enabling the inclusion of imperfection effects with reduced computational cost.

Strut Modelling From CT Scans

CT images are acquired from an 8×8×8 octahedral cells specimen with 20% relative volumetric density and a cell dimension of 2 mm. Individual struts are then isolated through an ImageJ–Strut Surface pipeline, and their cross-sections are mapped along the principal axis using best-fit ellipses. This procedure enables the representation of the main geometric imperfections of the struts: the ellipses capture the cross-sectional asymmetry that follows the building direction, waviness is described by tracking the centroids of the sections, and dimensional inaccuracies are reflected in the ellipse semi-axes.

Content from this work may be used under the terms of the Creative Commons Attribution 3.0 license. Any further distribution of this work must maintain attribution to the author(s) and the title of the work, journal citation and DOI. Published under license by Materials Research Forum LLC.

Materials Research Proceedings 73 (2026) 114-117 https://doi.org/10.21741/9781644904459-23

The octahedral cell is formed by four horizontal struts and eight struts inclined at 45° with respect to the building direction. Cross-sections are extracted from both horizontal and diagonal struts to account for orientation-dependent differences.

The parameters describing each cross-section, namely the semi-axes a and b, the centroid coordinates y_c and z_c, and the tilting angle ϕ, are statistically characterized by their mean values and standard deviations, computed on their absolute values. In addition, for each parameter, the standard deviation of the difference between consecutive sections is evaluated. The resulting values are reported in Table 1 for the horizontal struts and in Table 2 for the diagonal struts.

Table 1: Section parameters for horizontal struts.

parameter	a	b	y_c	z_c	ϕ
Mean	0.267	0.177	0.0	0.0	0.015
Standard deviation	0.037	0.026	0.031	0.011	0.218
Std. dev. of increments	0.015	0.011	0.010	0.009	0.140

Table 2: Section parameters for diagonal struts.

parameter	a	b	y_c	z_c	ϕ
Mean	0.298	0.177	0.0	0.0	0.264
Standard deviation	0.047	0.026	0.046	0.010	0.204
Std. dev. of increments	0.014	0.011	0.013	0.009	0.184

This dataset enables the generation of random struts based on the observed distributions. For each cross-sectional parameter, a sequence is generated by balancing a normal distribution with the deviation between consecutive values, according to the following formulation:

$$\begin{cases} p_1 = \mathcal{N}(p_{mean}, p_{dev}) \\ p_{k+1} = p_k + \alpha(p_{mean} - p_k) + \mathcal{N}(0, \Delta p_{dev}) \end{cases} \quad (1)$$

Where $\mathcal{N}(\mu, \sigma)$ denotes a random variable drawn from a normal distribution with mean μ and standard deviation σ, $\alpha \in [0,1]$ is a parameter controlling the balance between regression toward the mean value and local variability between consecutive sections. In the present work, α is set to 0.2. An example of a generated strut is shown in Fig. 1.

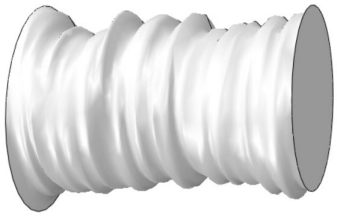

Figure 1: Generated strut

Simplified Model

The previously described 3D models offer a detailed representation of manufacturing-induced imperfections. However, the associated high number of degrees of freedom limits their practical use. To address this, a reduced-order modelling approach based on 1D beam elements is introduced to capture the initial stiffness, yield, and post-yield response of the structure under compression.

Materials Research Proceedings 73 (2026) 114-117 https://doi.org/10.21741/9781644904459-23

The simplified model is built by embedding the non-linear response of the imperfect strut in the constitutive law of the beam element using the Python scripting interface in Abaqus. Each generated 3D strut is meshed using C3D4 elements and tested under tensile load and bending load in both axes. The material is modeled with a bilinear curve having Young's modulus E = 70000 MPa, yield strain ε = 0.002, Poisson's ratio ν = 0.33 and plastic modulus Ep = E/50. The tensile load-displacement curve and the bending moment-curvature curves are embedded in the beam elements using the *BEAM GENERAL SECTION keyword.

To consider the material accumulation near the nodes, which can result in an increased local stiffness at strut intersections, the Young's modulus in these regions is increased by a factor of 1000, as proposed in [6]. In this work the stiffened node region is defined at both ends of a strut with a length equal to the nominal radius.

Numerical Results

The framework is tested on a 2×2×2 octahedral cell configuration with a cell dimension of 2 mm for four different cases: the ideal geometry with the as-designed relative density of 20%; the ideal geometry with the measured relative density of 29.5%; the geometry reconstructed from CT scans and meshed with solid elements; and the simplified model based on nonlinear beam elements with elliptical cross-sections. All configurations are shown in Fig. 2.

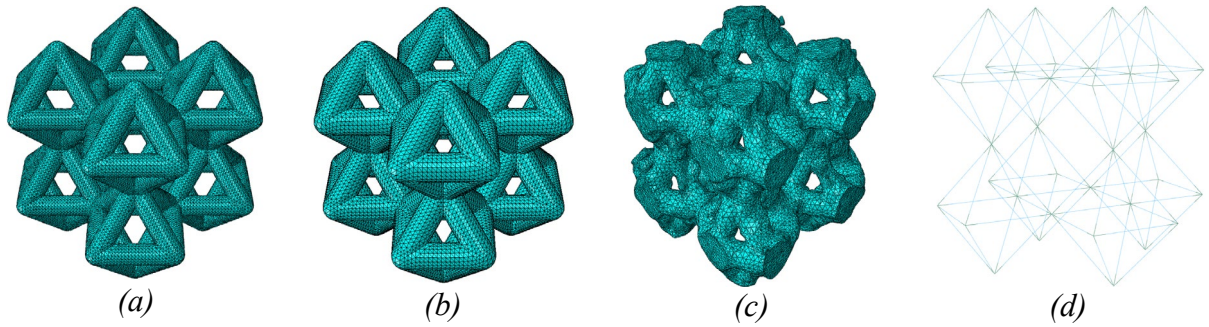

Figure 2: 2×2×2 octahedral cell configurations: (a) ideal geometry with the as-designed relative density of 20%; (b) ideal geometry with the measured relative density of 29.5%; (c) geometry reconstructed from CT scan data; and (d) beam model.

Each configuration is tested under compressive loading along two directions: parallel and perpendicular to the building direction, using a quasi-static analysis. Periodic boundary conditions are applied to the structure. For the beam model, the nonlinear constitutive responses derived from 10 generated horizontal struts and 10 generated diagonal struts are randomly assigned to the 96 struts of the structure.

Results are shown in Fig. 3. The reaction force predicted by the ideal model with the as-designed relative density is significantly lower than that obtained from the CT-based model, due to the large discrepancy between the nominal and manufactured geometries. The ideal model with adjusted density shows close agreement with the CT model results; however, it does not capture the orthotropic behavior induced by the building direction. In particular, the yielding response is accurately reproduced for compression along the building direction, while it is overestimated for compression perpendicular to the building direction.

The beam model, despite reducing the number of elements by a factor of 1000, accurately captures the initial stiffness, yielding behavior, and orthotropic response of the structure. However, it fails to reproduce the post-yield stiffness observed in the CT model.

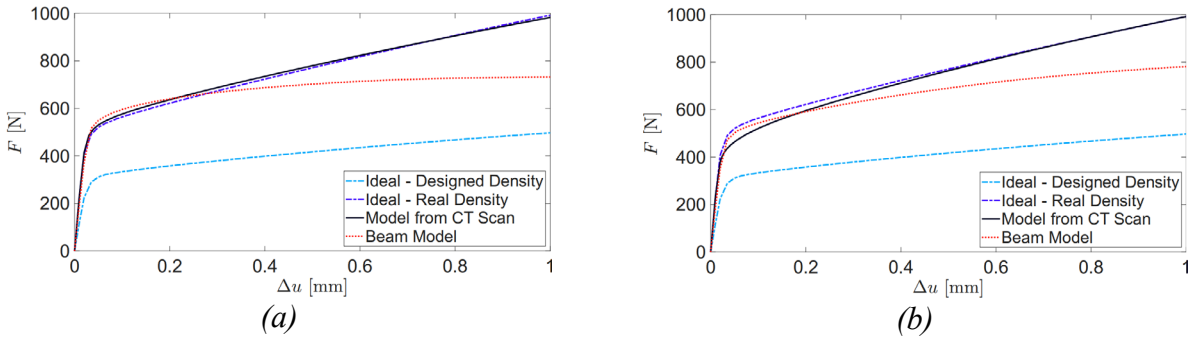

Figure 3: Compression of the 2x2x2 octahedral cell configurations: (a) compression parallel to the building direction; (b) compression perpendicular to the building direction.

Conclusions

In this work, a methodology for the generation and simplified modelling of lattice structures based on CT scan data was presented.

The results showed that ideal models based on nominal geometry may fail to reproduce the mechanical response of the manufactured structure, although the ideal model with corrected density provided a reasonable estimation of global stiffness.

The beam model successfully reproduced the initial stiffness, yielding behavior, and directional dependence of the CT-based model, while reducing the number of elements by approximately three orders of magnitude.

Overall, the proposed framework represents an efficient strategy for incorporating realistic manufacturing imperfections into lattice structure simulations.

Acknowledgments

This work was carried out within the Space It Up! project funded by the Italian Space Agency (ASI) and the Italian Ministry of University and Research (MUR) under contract No. 2024-5-E.0, CUP No. I53D24000060005.

References

[1] I. Echeta, X. Feng, B. Dutton, R. Leach and S. Piano, Review of defects in lattice structures manufactured by powder bed fusion, The International Journal of Advanced Manufacturing Technology 106 (2020) 2649-2668. https://doi.org/10.1007/s00170-019-04753-4

[2] M. Smith, Z. Guan and W.J. Cantwell, Finite element modelling of the compressive response of lattice structures manufactured using the selective laser melting technique, International Journal of Mechanical Sciences 67 (2013) 28-41. https://doi.org/10.1016/j.ijmecsci.2012.12.004

[3] M.R. Karamooz Ravari and M.A. Kadkhodaei, Computationally Efficient Modeling Approach for Predicting Mechanical Behavior of Cellular Lattice Structures, Journal of Materials Engineering and Performance 24 (2015) 245-252. https://doi.org/10.1007/s11665-014-1281-4

[4] H.D. Carlton, N.A. Volkoff-Shoemaker, M.C. Messner, N.R. Barton and M. Kumar, Incorporating defects into model predictions of metal lattice-structured materials, Materials Science and Engineering: A 832 (2022) 142427. https://doi.org/10.1016/j.msea.2021.142427

Materials Research Proceedings 73 (2026) 118-123 https://doi.org/10.21741/9781644904459-24

Space-Frequency PGD Formulation with Refined Sinusoidal Kinematics for Forced Vibration Analysis of Composite and Sandwich Beams

M. NDIAYE[1,a *], P. VIDAL[1,b], G. DI CARA[1,c], L. GALLIMARD[1,d] and O. POLIT[1,e]

[1]LEME, Univ Paris Nanterre, 50 rue de Sèvres, 92410 Ville d'Avray, France

[a]mndiaye@parisnanterre.fr, [b]pvidal@parisnanterre.fr, [c]dicarag@parisnanterre.fr, [d]lgallima@parisnanterre.fr, [e]opolit@parisnanterre.fr

Keywords: Composite, Sandwich, Beam, Proper Generalized Decomposition, Space-Frequency Separation, Refined Sinus Model, Frequency Response Function

Abstract. Composite and sandwich beam structures are widely used in weight-sensitive industrial applications for their high stiffness-to-mass ratio. Their vibrational behavior, however, involves through-thickness effects that classical beam theories capture poorly, while full three-dimensional finite element analyses remain computationally expensive when repeated frequency sweeps are required. A reduced-order strategy is presented, combining a refined sinus kinematics (SinRef-7p) with a Proper Generalized Decomposition (PGD) separating the displacement field between the two-dimensional cross-section domain and the load frequency. The resulting nonlinear problem is solved through a greedy enrichment algorithm, whose robustness is further enhanced by a simultaneous update of all frequency functions once the spatial basis is complete. This step is shown to be essential when, even in the presence of a corrective pair, an accurate prediction of the frequency response cannot be fully restored. It then enables further correction of the solution until convergence is achieved. The approach is validated on symmetric, antisymmetric and sandwich laminated beams for slenderness ratios from 2 to 20, showing that the PGD reduction preserves the accuracy of the underlying SinRef-7p model.

Introduction

Composite and sandwich beams are extensively used in aeronautical, naval and automotive structures for their excellent stiffness-to-weight ratio. Predicting their dynamic behavior accurately requires capturing transverse shear and through-thickness effects that classical Euler-Bernoulli or Timoshenko theories cannot represent, especially for thick or sandwich configurations. Full three-dimensional finite element (FE) models provide reliable results but at a prohibitive computational cost when a wide frequency range must be explored.

Reduced-order models offer an attractive alternative. Among them, the Proper Generalized Decomposition (PGD) [1] builds the solution as a finite sum of separable functions, treating the load frequency as an extra-coordinate and avoiding the repeated resolution of the problem at each excitation frequency. The PGD has already been combined with a Layerwise approach for composite plate structures [2], and Infantes et al. [3] pioneered a space-frequency separation for composite beams through a three-variable separation between the two in-plane/thickness spatial coordinates and the frequency, requiring two independent finite element meshes.

The present work performs the separation directly between the full two-dimensional domain and the frequency domain, combined with the refined sinus SinRef-7p kinematics [4], which reduces the resolution to two coupled sub-problems instead of three and aims at taking advantages of an accurate enriched beam model. The robustness of the greedy PGD algorithm is further enhanced by a simultaneous update of the frequency functions, introduced here to correct the sub-optimal frequency content distribution inherent to the classical sequential enrichment.

Content from this work may be used under the terms of the Creative Commons Attribution 3.0 license. Any further distribution of this work must maintain attribution to the author(s) and the title of the work, journal citation and DOI. Published under license by Materials Research Forum LLC.

Materials Research Proceedings 73 (2026) 118-123 https://doi.org/10.21741/9781644904459-24

PGD formulation with refined sinus kinematics

In the PGD framework, the displacement field $u(x,z,\omega)$ is sought as a finite sum of separable space-frequency products:

$$\boldsymbol{u}(x,z,\omega) \approx \sum_{i=1}^{N} f^i(\omega)\ \boldsymbol{v^i}(x,z) \quad (1)$$

where $f^i(\omega)$ are scalar frequency functions and $v^i(x,z)$ are two-dimensional spatial modes carrying the through-thickness kinematic description. The SinRef-7p model [4] is adopted for v^i: it combines a global sinusoidal warping function with a layerwise zig-zag correction built from Legendre polynomials, reduced through interlaminar continuity and free-surface conditions to only 7 generalized unknowns, independently of the number of layers NC. The two components of the field read

$$\begin{cases} v_1(x,z) = u(x) + z\theta_y(x) + f(z)\left[\omega_3(x) + w_{0,1}(x)\right] + \sum_{k=1}^{NC} \Gamma^{(k)}(x,z)\Delta H(k,k+1) \\ v_3(x,z) = w_0(x) + z\, w_1(x) + z^2\, w_2(x), \end{cases} \quad (2)$$

where $f(z) = \frac{h}{2} sin\left(\frac{\pi z}{h}\right)$ is the sinusoidal warping function common to the whole cross-section. In this field, u is the axial displacement, θ_y is the bending rotation, w_0, w_1 and w_2 are the constant, linear and quadratic coefficients of the transverse displacement, ω_3 is the global shear rotation associated with f(z), and Γ(x,z) is the layer-by-layer zig-zag correction built from Legendre polynomials of the local reduced coordinate in each layer. Enforcing displacement and transverse shear stress continuity at the interfaces, together with the free-surface conditions at z = ±h/2, expresses every local unknown as a linear combination of only seven generalized variables, independently of NC.

The nonlinear coupled problem to find $\boldsymbol{v^i}(x,z)$ and $f^i(\omega)$ is solved by a fixed-point alternating algorithm: at each enrichment step n, a spatial linear problem (mesh in x only, thickness treated analytically layer by layer) and a frequency linear problem are solved successively until convergence, yielding a new pair(v^n, f^n).

In the classical greedy algorithm, each frequency function $f^i(\omega)$ is computed once and frozen, even when subsequent pairs enrich the spatial basis, which can lead to a sub-optimal distribution of the frequency content. To correct this limitation, once the final spatial basis $\{v^i\}_{i=1,\dots,N}$ is fixed, all frequency functions are recomputed simultaneously by solving the coupled system

$$A(\omega)f(\omega) = b(\omega) \quad (3)$$

where $A(\omega)$ is a full NxN matrix projecting the stiffness and mass operators onto the retained spatial modes, with off-diagonal terms expressing the coupling between distinct modes introduced by this update. This step optimally redistributes the frequency content over the whole basis, correcting the successive approximations accumulated during the sequential construction.

Numerical results

Three simply supported cross-ply beam configurations are considered: a symmetric (0/90/0) laminate, an antisymmetric (0/90) laminate, and a sandwich beam, subjected to a harmonic concentrated load applied at $x = \frac{L}{10}$ on the upper face of the beam. Results are compared against a refined 2D ANSYS plane-stress reference (PLANE183 element with a full resolution strategy) and, for the PGD solution, against the three-variable reference of [3]. Two relative errors are reported: SinRef-7p model vs the present approach PGD_SinRef-7p (fidelity of the PGD reduction) denoted Err SinRef-7p/PGD, and Ansys solution vs PGD_SinRef-7p (accuracy of the underlying model), denoted Err Ansys/PGD.

Symmetric lay-up (0/90/0). The material properties, common to both the symmetric and antisymmetric laminates, follow Kapuria et al. [5]: $E_L = 181\,\text{GPa}, E_T = 10.3\,\text{GPa}, G_{LT} =$

Materials Research Proceedings 73 (2026) 118-123 https://doi.org/10.21741/9781644904459-24

$7.17\,\mathrm{GPa}, G_{TT} = 2.87\,\mathrm{GPa}, \nu_{LT} = 0.25, \nu_{TT} = 0.33, \rho = \rho_f = 1578\,\mathrm{kg/m^3}$. Results are presented for the slenderness ratio $S = 5$, in dimensionless form $\bar{\omega} = \omega\, L\, S \sqrt{\frac{\rho_f}{E_T}}$.

Table 1 reports the natural frequencies for $S = 5$ for the SinRef-7p model, the present work and the reference Ansys computation. The nature of the mode is also given (bend for bending, thick for thickness and sh for shear modes, respectively). The SinRef-7p/PGD error remains below 0.2% for all modes, confirming that the PGD reduction faithfully reproduces the reference modal solution. The Ansys/PGD error stays below 0.7% except for the thickness mode (9.42%), a local limitation of the SinRef-7p kinematics rather than of the PGD strategy.

Table 1. Non-dimensional natural frequencies of the symmetric lay-up (0/90/0), S = 5.

S=5	Mode	SinRef-7p	Ansys	PGD_SinRef-7p	Err SinRef-7p/PGD (%)	Err Ansys/PGD (%)
	bend	6.81	6.81	6.81	**0.00**	**0.00**
	bend	16.53	16.52	16.53	**0.00**	**0.06**
	bend	26.72	26.72	26.71	**0.04**	**0.04**
	bend	37.31	37.33	37.28	**0.08**	**0.13**
	thic	47.87	43.75	47.87	**0.00**	**9.42**
	sh	43.79	43.80	43.79	**0.00**	**0.02**
	bend	48.18	48.18	48.10	**0.17**	**0.17**

Figure 1 illustrates the role of the sixth PGD pair, which acts as a residual, quasi-static correction. Without it (5 pairs, panel a), both the classical 5-mode truncated modal superposition (SM-5) and the PGD-5 solution correctly locate the five resonance peaks but deviate markedly from ANSYS between them. Including the sixth pair (panel b) brings the PGD-6 curve into near-perfect agreement with ANSYS over the entire range. In contrast, the 7-mode modal superposition SM-7, built from all seven physical eigenmodes tabulated in Table 1, still fails to converge between resonances: even with one more mode than the PGD basis, a classical superposition contributes only the resonant term of each mode, not the quasi-static residual contribution of the higher modes it represents. This confirms that the improvement is not merely due to one additional term, but specifically to the residual, quasi-static correction naturally embedded in the PGD pair.

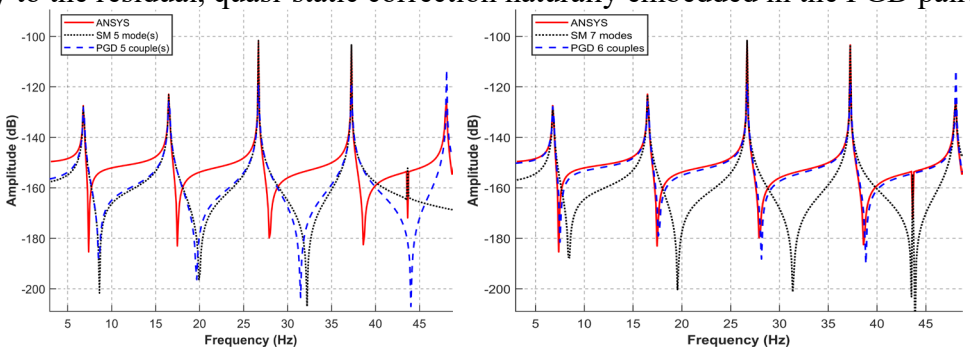

Fig. 1. FRF at the load application point for the symmetric beam, S = 5: (a) without the corrector pair (5 PGD pairs, left) and (b) with the corrector pair (6 PGD pairs, right). ANSYS (red), truncated modal superposition SM (black), PGD (blue).

Figure 2 shows the spatial shape of the sixth PGD pair. Unlike the first five pairs, which reproduce classical bending mode shapes associated with the five natural modes of Table 1, this pair can be considered as a local correction.

Materials Research Proceedings 73 (2026) 118-123 https://doi.org/10.21741/9781644904459-24

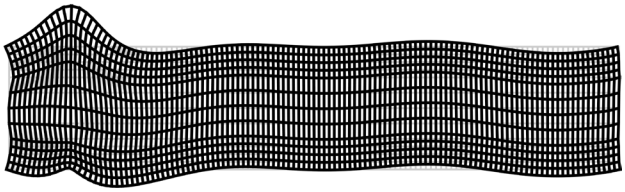

Fig. 2. Sixth spatial function (local thickness correction) obtained by the PGD method for the symmetric beam, S = 5, NC = 3.

Antisymmetric lay-up (0/90). Table 2 ($S = 5$) summarize the same results as Table 1 for the present test cas. It shows that SinRef-7p/PGD error is below 0.1% for all six first eigenmodes, while the Ansys/PGD error remains below 1.5%, showing that the PGD process does not affect the accuracy of the refined model.

Table 2. Non-dimensional natural frequencies of the antisymmetric lay-up (0/90), S = 5.

S=5	Mode	SinRef-7p	Ansys	PGD_SinRef-7p	Err SinRef-7p/PGD (%)	Err Ansys/PGD (%)
	bend	4.78	4.78	4.78	**0.00**	**0.00**
	bend	14.67	14.64	14.67	**0.00**	**0.20**
	bend	25.65	25.46	25.63	**0.08**	**0.67**
	t/c	35.45	35.38	35.45	**0.00**	**0.20**
	bend	36.63	36.12	36.64	**0.03**	**1.44**
	sh	48.51	48.28	48.52	**0.02**	**0.50**

For this beam, the fifth PGD pair plays the same residual, quasi-static corrector role identified for the symmetric case, and already restores excellent agreement with ANSYS for both displacements, transverse u_z and axial u_x, at 5 pairs. The sixth pair, however, captures a genuine physical thickness mode (the fourth such mode in ascending order), and its direct inclusion in the classical sequential PGD basis degrades the solution: a spurious anti-resonance appears near 11 Hz on u_x, and a persistent amplitude offset develops over the 10-35 Hz range (Fig. 3, dashed blue). Applying the simultaneous update of Eq. (3) to this last pair restores an excellent agreement with the ANSYS reference over the entire frequency range for both displacements (Fig. 3, dash-dot green), confirming that this step is essential whenever a genuine physical mode is enriched after a residual corrector pair.

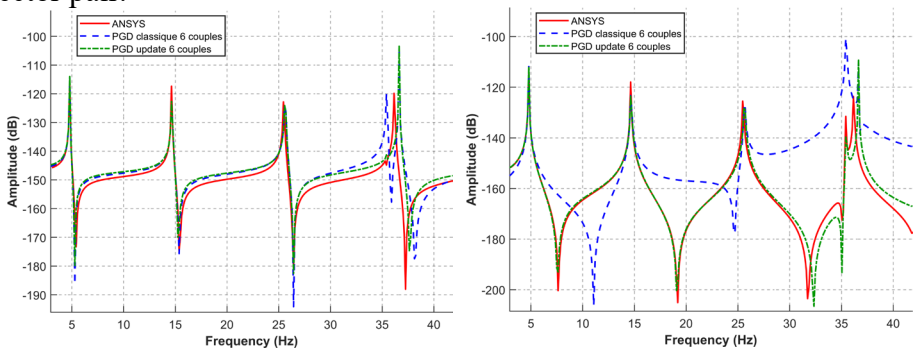

Fig. 3. FRF for the antisymmetric beam, S = 5, 6 PGD pairs: transverse displacement u_z (left) and axial displacement u_x (right) - ANSYS (red), classical PGD (blue dashed), PGD with simultaneous update (green dash-dot).

Sandwich beam. The sandwich beam consists of three layers with relative thicknesses 0.1h/0.8h/0.1h: two graphite-epoxy face sheets, with $E_{1f} = 131.1GPa, E_{2f} = E_{3f} = 6.9GPa, G_{12f} = 3.588GPa, G_{13f} = 3.088GPa, G_{23f} = 2.332GPa, \nu_{12f} = \nu_{13f} = 0.32, \nu_{23f} =$

Materials Research Proceedings 73 (2026) 118-123 https://doi.org/10.21741/9781644904459-24

$0.49\rho_f = 1000kg/m^3$and a soft foam core, with $E_{1c} = 0.2208MPa, E_{2c} = 0.2001MPa, E_{3c} = 2760MPa, G_{12c} = 16.56MPa, G_{13c} = 545.1MPa, G_{23c} = 455.4MPa, \nu_{12c} = 0.99, \nu_{13c} = \nu_{23c} = 3 \times 10^{-5}, \rho_c = 70kg/m^3$.

Natural frequencies are expressed in dimensionless form as $\bar{\omega} = \omega L S \sqrt{\frac{\rho_f}{Y_0}}$, $Y_0 = 6.9$~GPa.

Table 3 reports the results for $S = 10$: the SinRef-7p/PGD error remains negligible for all modes, while the Ansys/PGD error stays below 0.15%, confirming that the PGD reduction preserves the accuracy of the underlying model even for this more heterogeneous configuration.

Table 3. Non-dimensional natural frequencies of the sandwich beam, S = 10.

S	Mode	SinRef-7p	Ansys	PGD_SinRef-7p	Err SinRef-7p/PGD (%)	Err Ansys/PGD (%)
	bend	12.24	12.23	12.24	**0.00**	**0.08**
	bend	31.30	31.30	31.30	**0.00**	**0.00**
	bend	50.25	50.26	50.25	**0.00**	**0.02**
	bend	69.18	69.21	69.18	**0.00**	**0.04**
	bend	88.34	88.41	88.34	**0.00**	**0.08**
	bend	107.87	108.02	107.87	**0.00**	**0.14**

As in the symmetric case, the sixth pair identified acts as a residual corrector rather than a genuine physical mode: Fig. 4 shows that the classical sequential PGD with 6 pairs already matches the ANSYS reference over the whole frequency range, without requiring the simultaneous update.

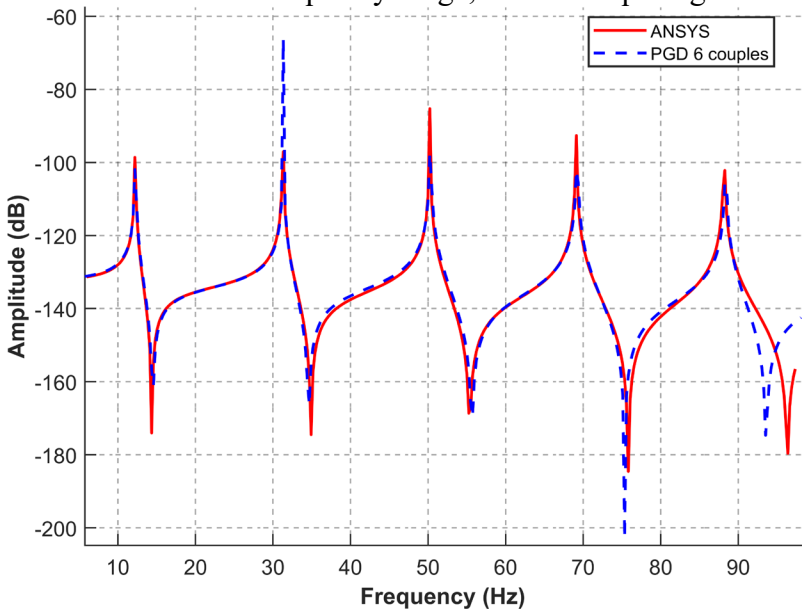

Fig. 4. FRF of the transverse displacement u_z for the sandwich beam, S = 10, 6 PGD pairs (blue dashed) vs. ANSYS (red).

Conclusions

A space-frequency PGD formulation combined with the refined sinus SinRef-7p kinematics has been presented for the forced vibration analysis of laminated and sandwich composite beams. Key findings are:

• The PGD reduction preserves the accuracy of the underlying SinRef-7p model with negligible additional error (below 0.7% in most cases).

• Discrepancies with the ANSYS reference, most significant for thick sandwich configurations, originate from the SinRef-7p kinematic assumptions rather than from the PGD strategy itself.

• The simultaneous update of the frequency functions is essential whenever the last enriched pair captures an additional physical mode: it restores accurate frequency response predictions where the classical sequential construction locally degrades, as shown for the antisymmetric beam.

References

[1] P. Ladeveze, Nonlinear Computational Structural Mechanics: New Approaches and Non-Incremental Methods of Calculation, Springer, New York, 1999. https://doi.org/10.1007/978-1-4612-1432-8

[2] P. Vidal, L. Gallimard, O. Polit, Proper Generalized Decomposition and layer-wise approach for the modeling of composite plate structures, International Journal of Solids and Structures 50(14-15) (2013) 2239-2250. https://doi.org/10.1016/j.ijsolstr.2013.03.034

[3] M. Infantes, P. Vidal, R. Castro-Triguero, L. Gallimard, E. Garcia-Macias, O. Polit, Forced vibration analysis of composite beams based on the variable separation method, Mechanics of Advanced Materials and Structures 28(6) (2019) 618-634. https://doi.org/10.1080/15376494.2019.1578015

[4] P. Vidal, O. Polit, Vibration of multilayered beams using sinus finite elements with transverse normal stress, Composite Structures 92(6) (2010) 1524-1534. https://doi.org/10.1016/j.compstruct.2009.10.009

[5] S. Kapuria, P.C. Dumir, N.K. Jain, Assessment of zigzag theory for static loading, buckling, free and forced response of composite and sandwich beams, Composite Structures 64(3-4) (2004) 317-327. https://doi.org/10.1016/j.compstruct.2003.08.013

Materials Research Proceedings 73 (2026) 124-129 https://doi.org/10.21741/9781644904459-25

Free Vibration and Electromechanical Response Analysis of Piezoelectric Beams using the Dynamic Stiffness Method and the Carrera Unified Formulation

Yu WANG[1,2,a], Alfonso PAGANI[2,b], Erasmo CARRERA[2,c] and Xiang LIU[1,d *]

[1]School of Traffic & Transportation Engineering, Central South University, China

[2]Mul2 lab, Politecnico di Torino, Italy

[a]yuw031299@gmail.com, [b]alfonso.pagani@polito.it, [c]erasmo.carrera@polito.it, [d]xiangliu06@gmail.com

Keywords: Dynamic Stiffness Method, Carrera Unified Formulation, Piezoelectric Laminated Beams, Wittrick-Williams Algorithm, Electromechanical Coupling Response

Abstract. This paper presents a Carrera Unified Formulation (CUF)-based dynamic stiffness method (DSM) for the free vibration and electromechanical response analysis of piezoelectric laminated beams. The displacement field and electric potential are described by Lagrange expansion (LE) over the beam cross-section, so that layer-wise material changes and local electromechanical coupling can be represented within a one-dimensional framework. The governing equations are derived from the principle of virtual displacements and the linear piezoelectric constitutive equations. Exact frequency-domain solutions are then used to build the dynamic stiffness matrix, and the Wittrick-Williams (WW) algorithm is employed to solve the resulting transcendental eigenvalue problem. Two cantilever configurations are studied: a classic bimorph PZT-5H/aluminum beam and a bimorph piezoelectric beam with a composite laminate substrate. For the benchmark bimorph configuration, the computed natural frequencies and mode shapes agree well with COMSOL finite element results. Load-resistance studies also show clear energy-harvesting behavior, with optimal resistances of 1.7783×10^{4} Ω and 199.53 Ω for the two cases, giving maximum average powers of 4.6657×10^{-2} W and 1.495×10^{-2} W, respectively. The results demonstrate that the proposed CUF-DSM framework can provide accurate modal and electromechanical predictions with fewer degrees of freedom.

Introduction

Piezoelectric laminated beams are key components in smart structures because mechanical deformation and electrical response are directly coupled. This property enables vibration sensing, actuation, structural health monitoring, and energy harvesting. In these applications, the response is often controlled by resonant behavior; therefore, accurate prediction of natural frequencies, mode shapes, output voltage, and output power is important for reliable design. Modern piezoelectric beams often contain bonded PZT patches, multilayer substrates, and composite materials, which makes the through-thickness field more complex than that of a classical homogeneous beam.

Three-dimensional finite element models can describe such structures in detail, but they usually require refined meshes and many degrees of freedom (DoFs), especially for frequency sweeps and load-resistance studies. In contrast, analytical and lower-order beam models are efficient, but may lose accuracy when layer-wise fields, electric potential variation, and material interfaces are important. The Carrera Unified Formulation (CUF) [1–2] provides a systematic way to build refined beam theories, while the dynamic stiffness method (DSM) [3–4] gives exact frequency-domain solutions for vibration problems. However, the integrated use of CUF and DSM for

Content from this work may be used under the terms of the Creative Commons Attribution 3.0 license. Any further distribution of this work must maintain attribution to the author(s) and the title of the work, journal citation and DOI. Published under license by Materials Research Forum LLC.

Materials Research Proceedings 73 (2026) 124-129 https://doi.org/10.21741/9781644904459-25

piezoelectric laminated beams, especially including electromechanical output prediction, still needs further study.

This work develops a CUF(LE)-DSM framework for the free vibration and electromechanical response analysis of piezoelectric laminated beams. The formulation is first applied to modal analysis and is then coupled with an external resistive circuit to evaluate voltage and average output power. Two cantilever configurations are considered: a classical PZT-5H/aluminum bimorph and a piezoelectric beam with an epoxy/aluminum/steel multilayer substrate. The two cases are used to examine the modal and load-dependent response capabilities of the proposed formulation.

Methodology

Consider a piezoelectric beam of length L and cross-section Ω, with the beam axis aligned with the y-axis. The generalized displacement vector is defined as

$$\mathbf{q}(x,y,z;t)=\{u_x,u_y,u_z,\phi\}^T. \tag{1}$$

Accordingly, the electric field vector is obtained from the electric potential as:

$$\mathbf{E}=\{E_x,E_y,E_z\}=-\nabla\phi=-\left\{\frac{\partial}{\partial x},\frac{\partial}{\partial y},\frac{\partial}{\partial z}\right\}^T\phi. \tag{2}$$

For linear piezoelectric materials, the coupled constitutive equations can be written as:

$$\boldsymbol{\sigma}=\mathbf{C}\boldsymbol{\varepsilon}-\mathbf{e}^T\mathbf{E},\quad \mathbf{D}_e=\mathbf{e}\boldsymbol{\varepsilon}+\boldsymbol{\chi}^T\mathbf{E}. \tag{3}$$

where $\boldsymbol{\sigma}$ and $\boldsymbol{\varepsilon}$ are the stress and strain vectors, De is the electric displacement vector, $\mathbf{C}$ is the elastic stiffness matrix, $\mathbf{e}$ is the piezoelectric coupling matrix, and $\boldsymbol{\chi}$ is the dielectric permittivity matrix. The generalized displacement field is expressed as an expansion of cross-sectional functions:

$$\mathbf{q}(x,y,z;t)=F_\tau(x,z)\mathbf{q}_\tau(y;t),\quad \tau=1,2,...,M. \tag{4}$$

where F_τ are the cross-sectional functions, q_τ are the generalized displacement unknowns, and M is the number of expansion terms. The repeated subscript τ implies summation according to Einstein's convention. In this work, a Lagrange expansion with 4-node quadrilateral elements is adopted to discretize the beam cross-section. The governing differential equations and natural boundary conditions (NBCs) are derived from the principle of virtual displacements as:

$$\delta L_{\text{int}}=\int_V \delta\overline{\boldsymbol{\varepsilon}}^T\overline{\boldsymbol{\sigma}}\,\mathrm{d}V=\delta L_{\text{ext}}-\delta L_{\text{inertia}}. \tag{5}$$

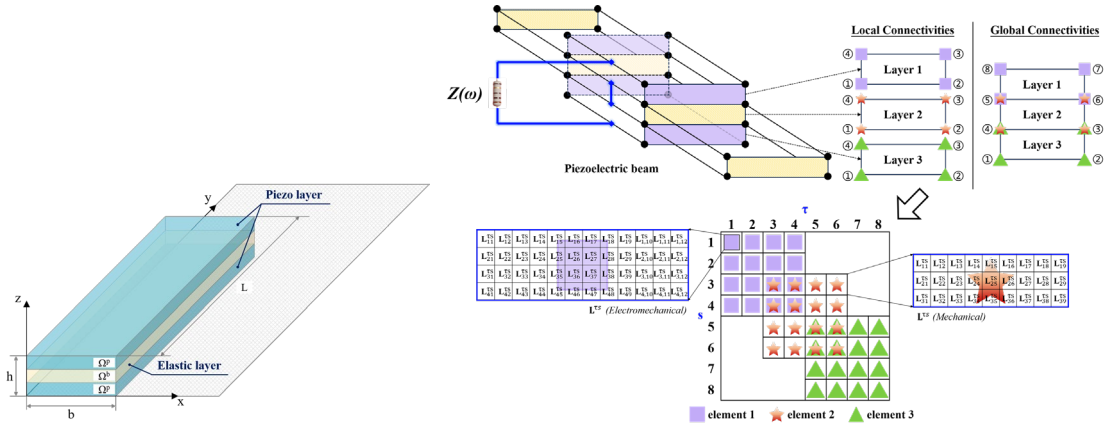

Figure 1. *(a) Geometry and coordinate system of the beam; (b) Global dynamic stiffness matrix assembly.*

Materials Research Proceedings 73 (2026) 124-129 https://doi.org/10.21741/9781644904459-25

Substituting Eq. (4) and Eq. (3) into Eq. (5), and integrating over Ω, yields after integration by parts:

$$\delta L_{\text{int}} = \int_L \delta \mathbf{q}_\tau^T \mathbf{K}^{\tau s} \mathbf{q}_s \mathrm{d}y + \left[\delta \mathbf{q}_\tau^T \mathbf{\Pi}^{\tau s} \mathbf{q}_s \right]_{y=0}^{y=L}. \tag{6}$$

where $\mathbf{K}^{\tau s}$ and $\mathbf{\Pi}^{\tau s}$ are 4×4 fundamental nuclei (FN) representing the differential stiffness matrix and the NBCs matrix, respectively. The compact FN formulation is independent of the beam theory order and the choice of F_τ, enabling automatic implementation for any desired expansion order. For harmonic motion at circular frequency ω, the generalized displacements are expressed as:

$$\mathbf{q}_s(y;t) = \mathbf{Q}_s(y) e^{i\omega t}. \tag{7}$$

Substituting Eq. (7) into the governing equations reduces the system to a set of ordinary differential equations (ODEs). By introducing a state vector $\mathbf{Z}(y)$ containing the displacement unknowns and their first derivatives, the second-order ODEs are transformed into a first-order system:

$$\mathbf{Z}_{,y}(y) = \mathbf{S}(\omega)\mathbf{Z}(y). \tag{8}$$

where $\mathbf{S}(\omega)$ is a frequency-dependent matrix. The general solution is:

$$\mathbf{Z}(y) = \Delta \mathbf{C} e^{\lambda y}. \tag{9}$$

where $\mathbf{\Delta}$ is the eigenvector matrix and $\mathbf{C}$ is the vector of integration constants. Applying boundary conditions yields the relationship between nodal displacements $\overline{\mathbf{U}}$ and nodal forces $\overline{\mathbf{P}}$:

$$\overline{\mathbf{U}} = \mathbf{A}\mathbf{C}, \quad \overline{\mathbf{P}} = \mathbf{R}\mathbf{C}. \tag{10}$$

Eliminating $\mathbf{C}$ gives the exact dynamic stiffness matrix $\mathbf{K}_{\text{DS}}$:

$$\overline{\mathbf{P}} = \mathbf{K}_{DS}(\omega)\overline{\mathbf{U}} \tag{11}$$

For a bimorph piezoelectric beam, the global DS matrix is assembled from individual layers, as illustrated in Figure 1. The free vibration analysis leads to a transcendental eigenvalue problem:

$$\mathbf{K}_{DS}(\omega)\overline{\mathbf{U}} = \mathbf{0} \tag{12}$$

The Wittrick-Williams (WW) algorithm is employed to solve this problem. For a trial frequency ω^*, the number of natural frequencies below ω^* is:

$$J(\omega^*) = J_0(\omega^*) + s\left\{\mathbf{K}_{DS}(\omega^*)\right\} \tag{13}$$

where J_0 is the number of natural frequencies of the clamped beam below ω^*, and $s\{\mathbf{K}_{\text{DS}}\}$ is the sign count. Using the bisection method, natural frequencies can be determined to arbitrary precision.

After obtaining the dynamic stiffness matrix, the electromechanical coupling response is evaluated by coupling the circuit equation, where the current is derived from the generated charge on the electrodes. Assuming harmonic response, the output voltage is expressed as

$$V(\omega) = Zi(\omega) = G(\omega)\int_0^L w''(x)dx = G(\omega)\left(\theta_L - \theta_0\right), \tag{14}$$

where $G(\omega)$ is a complex coefficient determined by the circuit parameters [4]. The coupled system is then solved to directly obtain the tip displacement and voltage frequency response functions.

Numerical Results

Two cantilever piezoelectric laminated beams are considered to examine the proposed CUF-DSM formulation. Case 1 is a classical bimorph beam consisting of two PZT-5H layers bonded to an aluminum substrate. Case 2 retains the bimorph layout but introduces a multilayer substrate composed of epoxy, aluminum, and steel. For both cases, the beam length and width are L=2000 mm and b=100 mm, respectively, and the total thickness is 60 mm. In Case 1, the two PZT-5H layers and the aluminum substrate are each 20 mm thick. In Case 2, the layers from top to bottom

Materials Research Proceedings 73 (2026) 124-129 https://doi.org/10.21741/9781644904459-25

are PZT-5H, epoxy, aluminum, steel, and PZT-5H, with thicknesses of 10, 10, 20, 10, and 10 mm, respectively. Both beams are clamped at the left end and free at the right end. Keeping the same overall beam dimensions allows the influence of the internal laminate layout on the dynamic and electromechanical responses to be examined more clearly.

Table 1. *Table 1. Comparison of the first five natural frequencies and mode shapes obtained by CUF-DSM and COMSOL for Case 1.*

Mode No.	1st	2nd	3rd	4th	5th
CUF-DSM	8.17 Hz	51.01 Hz	141.95 Hz	275.72 Hz	450.76 Hz
	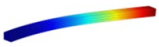	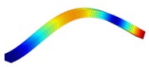	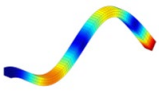	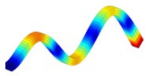	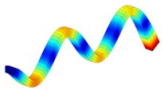
COMSOL	8.75 Hz	52.68 Hz	144.74 Hz	279.98 Hz	456.41 Hz
					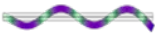

Table 1 compares the first five natural frequencies and corresponding mode shapes of Case 1 obtained from CUF-DSM and COMSOL. The predicted frequencies are 8.17, 51.01, 141.95, 275.72, and 450.76 Hz, while the corresponding COMSOL results are 8.75, 52.68, 144.74, 279.98, and 456.41 Hz. The relative differences are approximately 6.63%, 3.17%, 1.93%, 1.52%, and 1.24%, respectively, with an average difference of about 2.90% over the first five modes. The difference decreases with increasing mode number in the frequency range considered here. More importantly, the deformation patterns predicted by the two methods are consistent for all five modes. The first mode shows the expected fundamental bending shape, while the higher modes contain an increasing number of bending waves along the beam axis. These results indicate that the CUF-DSM model captures both the natural frequencies and the main modal characteristics of the benchmark bimorph beam. Since the present paper focuses mainly on the extension toward circuit-coupled response analysis, the modal comparison is shown for Case 1 as the benchmark configuration.

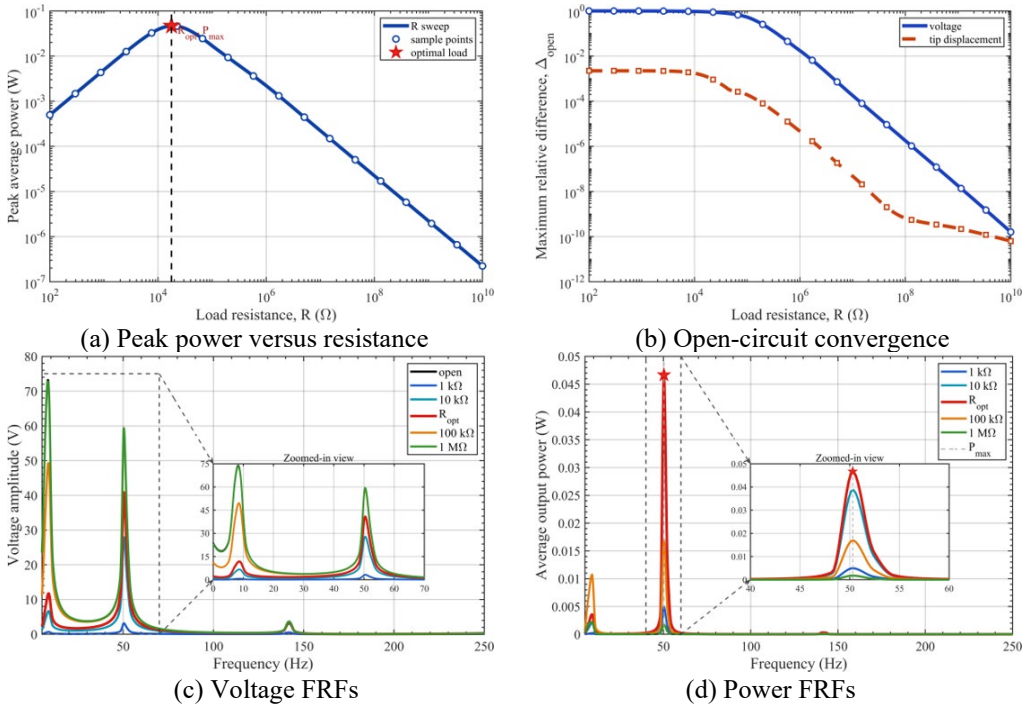

(a) Peak power versus resistance (b) Open-circuit convergence

(c) Voltage FRFs (d) Power FRFs

Figure 2. *Electromechanical and energy-harvesting responses of the classic bimorph piezoelectric beam under different resistive loads.*

Figure 2 presents the electromechanical and energy-harvesting responses of Case 1 under different resistive loads. Figure 2(a) shows the maximum average output power obtained at each resistance. The power does not vary monotonically with the load. Instead, it increases over the low-resistance range, reaches a clear maximum, and then decreases as the resistance continues to increase. The optimum resistance is R_{opt}=1.7783×10^4 Ω, at which the maximum average output power reaches P_{max}=4.6657×10^{-2} W at 50.294 Hz. This frequency is close to the second natural frequency listed in Table 1, showing that the dominant harvesting response in this case is associated with the second bending mode. Figure 2(b) further examines the approach to the open-circuit condition. As the resistance increases, the relative differences in both voltage and tip displacement decrease steadily, confirming that the finite-resistance solution tends toward the open-circuit response for sufficiently large values of (R).

The voltage and power frequency-response functions provide a more direct view of the load effect. As shown in Fig. 2(c), increasing the resistance generally increases the voltage amplitude and gradually moves the response toward the open-circuit curve. The strongest voltage peaks occur near the structural resonances, where the mechanical deformation and the resulting electrical response are amplified. The behavior of the output power is different, as shown in Fig. 2(d). A larger voltage does not necessarily result in a larger harvested power because the electrical resistance also enters the power expression. Consequently, the largest power is obtained at an intermediate resistance rather than in the open-circuit limit. At R_{opt}, the second resonance produces the dominant peak, whereas both lower and higher resistance values give smaller power levels. This result illustrates the need to consider the mechanical resonance and the electrical load together when evaluating the harvesting performance of a piezoelectric beam.

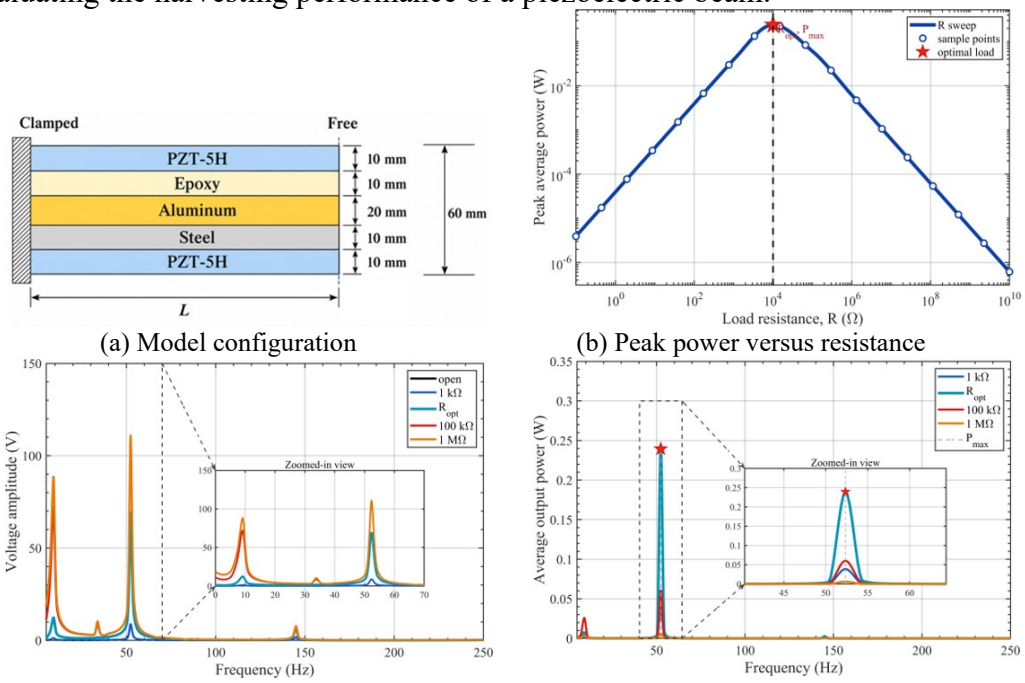

(a) Model configuration (b) Peak power versus resistance

(c) Voltage FRFs (d) Power FRFs

Figure 3. *Electromechanical and energy-harvesting responses of the composite-laminate piezoelectric beam.*

Figure 3 gives the results for Case 2. Compared with the classic bimorph beam, the composite laminate substrate changes the stiffness distribution and produces a more complex electromechanical response. The load-resistance sweep again shows that the maximum harvested power is obtained at an intermediate resistance rather than at the open-circuit limit. For this case, the optimal resistance is R_{opt} = 199.53 Ω, and the maximum average output power is P_{max} =

1.495×10^{-2} W at f = 93.53 Hz. The voltage response approaches the open-circuit response with increasing resistance, while the output power FRFs clearly identify the dominant energy-harvesting peak near 93.53 Hz. These two examples demonstrate that the proposed CUF-DSM framework can be used not only for modal analysis but also for load-dependent electromechanical performance evaluation.

Conclusions

A CUF(LE)-DSM formulation has been developed for the free vibration and electromechanical response analysis of piezoelectric laminated beams. By using Lagrange expansion in the cross-section, the method can describe layer-wise mechanical and electrical variables in a compact one-dimensional form. The exact dynamic stiffness matrix is built from closed-form frequency-domain solutions, and the Wittrick-Williams algorithm is used to solve the transcendental eigenvalue problem without missing modes. Numerical comparisons with COMSOL show good agreement for the natural frequencies and mode shapes of the benchmark bimorph configuration.

The load-resistance studies further show that the proposed method can predict voltage and average output power in energy-harvesting analysis. For the classic bimorph beam, the maximum average power is 4.6657×10^{-2} W at an optimal resistance of $1.7783\times10^{4}\Omega$. For the composite laminate beam, the maximum average power is 1.495×10^{-2} W at an optimal resistance of 199.53 Ω. In both cases, the maximum power occurs at an intermediate electrical load, while the voltage response tends to the open-circuit limit as the resistance increases. The present results indicate that CUF-DSM is an accurate and efficient tool for the analysis and design of piezoelectric laminated beam structures. Future work will consider more general multilayer circuits, damping effects, and experimental validation.

Acknowledgment

The authors gratefully acknowledge the financial support from the China Scholarship Council (Grant No. 202406370341), which made this research possible.

References

[1] Carrera E. Theories and finite elements for multilayered, anisotropic, composite plates and shells. Archives of computational methods in engineering, 2002, 9(2): 87-140. https://doi.org/10.1007/BF02736649

[2] Liu X, Pagani A, Carrera E, Liu X. Free vibration analysis of composite beams and laminated reinforced panels by refined dynamic stiffness method and CUF-based component-wise theory. Composite Structures, 2024, 337: 118058. https://doi.org/10.1016/j.compstruct.2024.118058

[3] Banerjee J R. Free vibration of centrifugally stiffened uniform and tapered beams using the dynamic stiffness method. Journal of Sound and Vibration, 2000, 233(5): 857-875. https://doi.org/10.1006/jsvi.1999.2855

[4] Liu X, Wang Y, Adhikari S, Zhou W. Exact energy harvesting analysis of multimodal piezoelectric beams using the dynamic stiffness method. Computers & Structures, 2025, 313: 107746. https://doi.org/10.1016/j.compstruc.2025.107746

Materials Research Proceedings 73 (2026) 130-135 https://doi.org/10.21741/9781644904459-26

Pull-Out Energy Dissipation and Fracture Toughness of Plasma-Modified Para-Aramid Soft Material

Erman BILISIK[1,2], Havva Esra BAKBAK[3], Mahmut KORKMAZ[4], Gülhan ERDOGAN[5], Kadir BILISIK[1,5,a *]

[1]Nanotechnology Application and Research Centre (ERNAM), Erciyes University, 38039 Talas, Kayseri, Turkey

[2]Department of Nanoscience and Nanotechnology, Graduate School of Natural and Applied Sciences, Erciyes University, 38039 Talas, Kayseri, Turkey

[3]Department of Electrical and Electronic Engineering, Ege University, 35040 Bornova, Izmir, Turkey

[4]Mustafa Cikrikcioglu MYO, Kayseri University, 38280 Talas, Kayseri, Turkey

[5]Nano/Microfiber Preform Design and Composite Laboratory, Department of Textile Engineering, Faculty of Engineering, Erciyes University, 38039 Talas, Kayseri, Turkey

[a]kadirbilisik@gmail.com, kbilisik@erciyes.edu.tr

Keywords: Plasma Treatment, Pull-Out Energy, Fracture Toughness, Para-Aramid Fabric

Abstract. The pull-out behavior, energy dissipation, and fracture toughness of para-aramid fabric structure modified by low-temperature plasma-enhanced chemical vapor deposition (LT-PECVD) were investigated. Results show that pull-out response is governed by a transition from structure-dominated to friction-dominated mechanisms. Fracture toughness decreases with increasing fabric opening length and shows a near-linear correlation with pull-out force. Overall, plasma modification reduces initial structural resistance but improves frictional stability and energy dissipation efficiency, providing a mechanistic basis for optimizing energy-absorbing textile systems.

Introduction

High-performance para-aramid fibers are widely used in both flexible and rigid composite systems for impact-critical applications [1-3]. Yarn pull-out analyses show that targeted structural modifications can enhance inter-yarn friction without compromising flexibility or introducing significant weight penalties [4-6]. Experimental investigations on para-aramid fabrics indicate that both peak pull-out force and total energy dissipation increase with specimen length and applied transverse tension [7-9]. Plasma-assisted vapor deposition has been shown to increase both static and dynamic friction in para-aramid fiber-based materials by introducing particulate features and polar functional groups, while preserving tensile properties and thus ballistic performance [2,10]. Despite numerous studies on plasma-modified fibers and fabrics, this study aims to elucidate the role of plasma-induced surface modification on the friction-controlled pull-out behavior and fracture toughness of para-aramid fabric structure.

Material and Methods

Materials treatment under low-temperature plasma-enhanced chemical vapor deposition (LT-PECVD)

A plain-woven Twaron® para-aramid fabric (CT® 747, Teijin Inc., Japan) was employed. Mechanically, the fibers provided a tensile strength of 3200 MPa, an elastic modulus of 115 GPa,

Content from this work may be used under the terms of the Creative Commons Attribution 3.0 license. Any further distribution of this work must maintain attribution to the author(s) and the title of the work, journal citation and DOI. Published under license by Materials Research Forum LLC.

Materials Research Proceedings 73 (2026) 130-135 https://doi.org/10.21741/9781644904459-26

and an elongation at break of 2.9%. Thermal degradation initiated at approximately 500 °C. Plasma-treated and untreated fabrics were designated as PPO and KPO, respectively. The Low-temperature plasma-enhanced chemical vapor deposition (LT-PECVD) process was employed to modify filament surfaces within the yarn (tow) structure by introducing controlled micro-scale roughness, thereby increasing effective contact area and inter-yarn friction. A detailed description of the experimental methodology and associated procedures has been presented in our previous publication [10] and is therefore not repeated here.

Pull-out testing

Yarn pull-out experiments were conducted on plain-woven para-aramid fabrics to quantify inter-yarn friction using single-, double-, and triple-yarn extractions. The LT-PECVD-treated specimens (50 × 200 mm) with a 100 mm frayed region were tested along the warp direction using a universal testing machine (Instron 4411, 5 kN) at a crosshead speed of 100 mm/min, as illustrated in Fig. 1(a–b). Force–displacement responses were recorded for each extraction sequence to capture progressive frictional interactions (Fig. 1(c)). Single yarn pull-out demonstrates a distinct, slight non-linear escalation approaching the maximum pull-out force as the crimp extension region, the interlacement rupture force and the stick-slip (translation) zone.

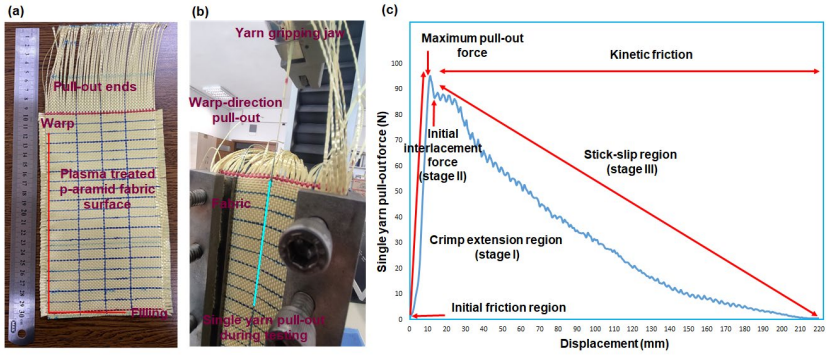

Fig. 1. Pull-out test configurations for plasma-treated p-aramid fabric. (a) Experimental image of plasma-modified fabric during single yarn pull-out testing, (b) experimental image of multiple yarn pull-out testing and (c) representative characterization of pull-out force–displacement behavior for plasma-modified p-aramid fabric (single yarn).

Pull-out energy analysis

Pull-out energy (J) was determined from the area under the force-displacement (F-δ) curves, representing energy dissipation during crimp straightening, interlacement failure, and subsequent stick-slip sliding. Numerical integration was carried out using Python-based scientific tools to ensure high computational accuracy. The pull-out energy response was divided into three distinct stages: Stage I energy (crimp extension), Stage II energy (initial interlacement rupture), and Stage III energy (stick-slip sliding) as shown in Figure 2.

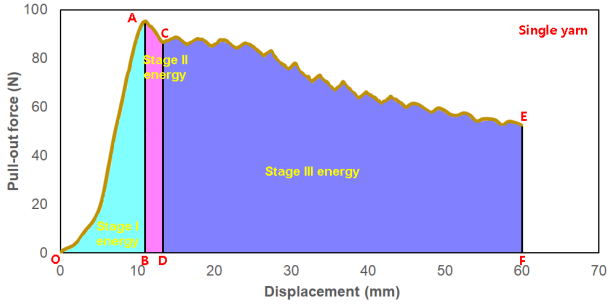

Fig. 2. Pull-out representative energy regions from the pull-out-displacement graph of the plasme treated p-aramid fabric.

Materials Research Proceedings 73 (2026) 130-135 https://doi.org/10.21741/9781644904459-26

Pull-out fracture toughness

Pull-out fracture toughness (G_{pf}) was defined as the energy dissipated per unit area during yarn extraction, specifically within the stick-slip regime of the force-displacement (F-δ) response. This parameter characterizes the resistance of warp-weft interlacements against yarn mobility and is therefore a direct measure of interfacial integrity in plasma-modified fabric systems. To ensure accurate displacement tracking, specimens were marked at 10 mm intervals along the extraction direction, and the effective yarn displacement was determined by incorporating crimp extension at peak load. The fracture toughness was evaluated based on a mode-I energy approach, consistent with ASTM D5528-01, as expressed in Eq. (1) [11], where G_{pf} (J/m²) is the pull-out fracture toughness, F_i is the force at a given displacement increment (N), δ_i is the corresponding displacement including crimp contribution (mm), b is the specimen width (mm), and a_i represents the effective yarn extraction (raveling) length (mm).

$$G_{pf} = \frac{F_i \times \delta_i}{b \times a_i} \quad (1)$$

Results and Discussion

Pull-out force- displacement result

During the first pull-out (Fig. 3a), both pristine (KPO) and plasma-modified (PPO) systems exhibit a pronounced nonlinear increase in maximum pull-out force (F_{max}) with increasing yarn number; however, the scaling behavior is markedly system-dependent. The KPO structure demonstrates a strong superlinear amplification (from 25.24 N to 267.88 N for single to three yarns), significantly exceeding linear scaling, which is attributed to enhanced transverse compaction, increased inter-yarn contact pressure, and frictional locking at intact interlacement nodes. This is further supported by the substantial increase in initial interlacement rupture force (F_{ir}), reaching 180.19 N for three yarns. In contrast, the PPO system shows a more moderate increase in F_{max} (24.43 N to 98.83 N) and a limited rise in F_{ir}, indicating earlier disruption of interlacement junctions and reduced capacity for stress accumulation under multi-yarn loading.

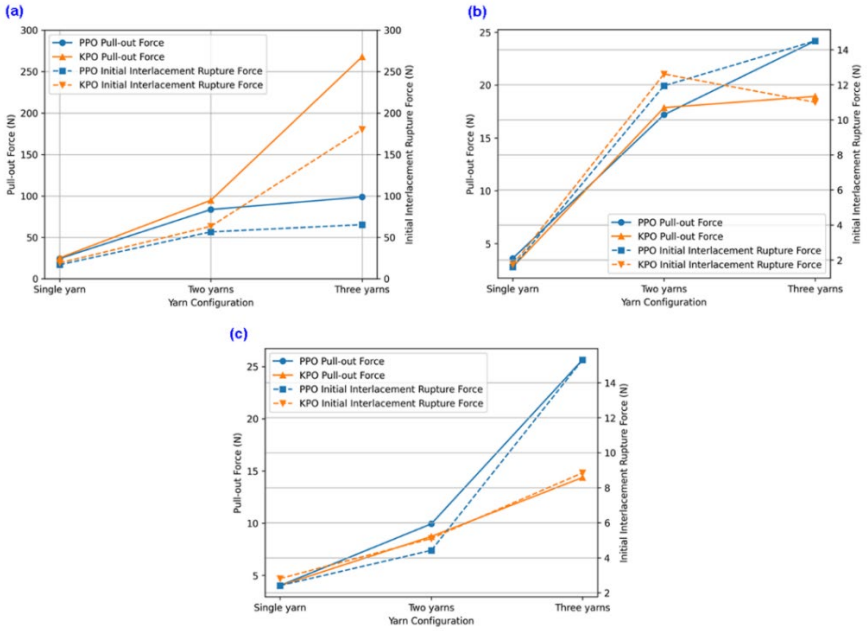

Fig. 3. Consecutive single- and multiple-ultimate pull-out force versus initial interlacement rupture force responses of p-aramid fabrics in pristine (KPO) and plasma-modified (PPO) conditions. (a) First yarn pull-out behavior, (b) second pull-out, and (c) third pull-out extraction responses.

Following the first extraction, the second pull-out (Figure 3b) is characterized by a significant reduction in force levels and a convergence of PPO and KPO responses. This behavior reflects the partial loss of structural confinement due to crimp relaxation and interlacement damage, leading to a transition from structure-dominated to interface-controlled mechanics. In the third pull-out stage (Figure 3c), the system reaches a fully developed friction-dominated regime, where structural interlocking becomes negligible and the response is controlled by fiber-fiber interactions. Notably, PPO exhibits superior performance at higher yarn counts (25.64 N vs. 14.37 N for three yarns), indicating that plasma-induced surface modification enhances interfacial friction and sustains higher residual resistance under repeated extraction.

Pull-out energy result

In the first pull-out stage, total energy increases markedly with yarn number for both systems, with KPO exhibiting significantly higher values at higher yarn multiplicity. For the three-yarn configuration, KPO reaches 11.34 J, compared to 5.73 J for PPO, corresponding to an increase of approximately 98%. This difference is primarily driven by the stick-slip component, which constitutes 91-92% of the total energy in both systems (e.g., 10.35 J / 11.34 J ≈ 91% for KPO31 and 5.22 J / 5.73 J ≈ 91% for PPO31). In the second pull-out stage, total energy decreases substantially for both systems, reflecting the degradation of interlacement structure after the first extraction. In the third pull-out stage, a clear shift toward friction-dominated behavior is observed, with PPO exhibiting comparable or slightly improved energy performance relative to KPO. This behavior highlights that plasma modification primarily enhances the efficiency and stability of frictional energy dissipation, rather than simply increasing total energy magnitude.

Pull-out fracture toughness result

Fig. 4(a-b) presents the variation of single- and multi-yarn pull-out fracture toughness (J/m²) as a function of fabric opening length (mm) for plasma-treated (PPO) and pristine (KPO) para-aramid fabrics.

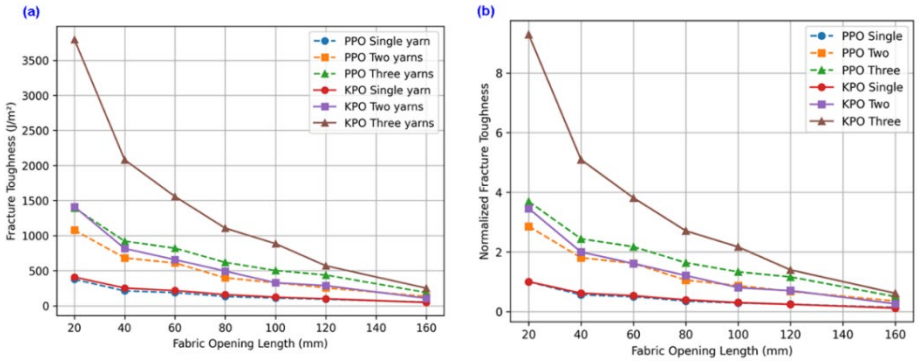

Fig. 4. Fracture toughness of plasma-modified and control para-aramid fabric structures. (a) Fracture toughness versus fabric opening and (b) normalized fracture toughness versus fabric opening length for PPO and KPO fabric structures [10].

As shown in Fig. 4(a-b), in all cases, fracture toughness decreases monotonically with increasing opening length, indicating that the resistance to pull-out-induced fracture is progressively reduced as the free sliding length increases. This behavior suggests that shorter opening lengths promote stronger yarn confinement, higher interlacement constraint, and more effective frictional engagement, thereby enabling greater energy dissipation during extraction. By contrast, as the opening length increases, the structural constraint imposed by the woven architecture becomes weaker, reducing the capacity of the system to store and dissipate energy prior to yarn release. Therefore, Figure 4 collectively indicates that fracture toughness is governed by a competition between geometric constraint and interfacial sliding, with KPO benefiting more

strongly from architecture-assisted toughening, particularly at low opening lengths and higher yarn counts. Notably, the fracture toughness of fabric structures under pull-out loading is governed by a multitude of structural parameters, including the interlacement architecture, directional yarn density, and the yarn linear density [4].

Conclusion

This study investigated the influence of low-temperature plasma-enhanced chemical vapor deposition (LT-PECVD) on the pull-out behavior, energy dissipation mechanisms, and fracture toughness of woven para-aramid fabric structures under sequential single- and multi-yarn extraction conditions. The results consistently demonstrated that pull-out response is governed by a transition from structure-dominated to friction-dominated mechanisms, which is strongly influenced by yarn multiplicity and surface modification. Energy analysis revealed that stick-slip energy constitutes the dominant portion of total pull-out energy across all configurations, confirming that frictional sliding governs the overall dissipation process. Furthermore, fracture toughness showed a strong dependence on pull-out force and fabric opening length, with a near-linear correlation between toughness and force, highlighting the force-controlled nature of the pull-out fracture mechanism. Overall, the results demonstrate that while pristine structures benefit from higher initial structural resistance, plasma-modified fabrics provide enhanced stability and efficiency in friction-dominated regimes. This study establishes a unified mechanistic framework linking structure, friction, and energy dissipation, and provides critical insights for optimizing surface-engineered textile systems for impact-resistant and energy-absorbing applications.

References

[1] B.A. Cheeseman, T.A. Bogetti, Ballistic impact into fabric and compliant composite laminates, Compos. Struct., vol. 61, no. 1-2, pp. 161-178, 2003. https://doi.org/10.1016/S0263-8223(03)00029-1

[2] K. Bilisik, M. Seyduzzaman, G. Erdogan, M. Korkmaz, Advances in ballistic protection, in: S. Maity, K. Singha, P. Pandit (Eds.), Functional and Technical Textiles, Woodhead Publishing, Elsevier Ltd., Cambridge, MA, pp. 71-123, USA, 2023. ISBN 9780323915939.

[3] M.G. Prakash, K. Balasubramanian, Functionalized aramid fibers and composites for protective applications: A review, Ind. Eng. Chem. Res., vol. 57, no. 49, pp. 16537-16563, 2018. https://doi.org/10.1021/acs.iecr.8b04903

[4] Y. Zhou, M. Ali, X. Guo, D. Yang, An overview of yarn pull-out behavior of woven fabrics, Text. Res. J., vol. 89, no. 2, pp. 223-234, 2019. https://doi.org/10.1177/0040517517741156

[5] M. Bajya, A. Majumdar, S.B. Bhupendra, A review on current status and development possibilities of soft armour panel assembly, J. Mater. Sci., vol. 58, pp. 14997-15020, 2023. https://doi.org/10.1007/s10853-023-08961-y

[6] K. Bilisik, Two dimensional (2D) fabrics and three dimensional (3D) preforms for ballistic and stabbing protection: A review, Text. Res. J., vol. 87, no. 18, pp. 2275-2304, 2017. https://doi.org/10.1177/0040517516669075

[7] J.R. Brown, P.J.C. Chappell, Z. Mathys, Plasma surface modification of advanced organic fibres: Part I - Effects on the mechanical, fracture and ballistic properties of aramid/epoxy composites, J. Mater. Sci., vol. 26, pp. 4172-4178, 1991. https://doi.org/10.1007/BF02402964

[8] F.H. Zhang, R.G. Wang, X.D. He, C. Wang, L.N. Ren, Interfacial shearing strength and reinforcing mechanisms of an epoxy composite reinforced using a carbon nanotube/carbon fiber hybrid, J. Mater. Sci., vol. 44, pp. 3574-3577, 2009. https://doi.org/10.1007/s10853-009-3484-x

[9] S.S. Wicks, R.G. Villoria, B.L. Wardle, Interlaminar and intralaminar reinforcement of composite laminates with aligned carbon nanotubes, Compos. Sci. Technol., vol. 70, no. 1, pp. 20-28, 2010. https://doi.org/10.1016/j.compscitech.2009.09.001

[10] E. Bilisik, M. Korkmaz, K. Bilisik, Effects of radio frequency (RF) plasma activation on the pull-out, friction, and fracture toughness performance of para-aramid fabrics, Surfaces and Interfaces, Vol. 86, Article no. 108695, 2026, pp. 1-21. https://doi.org/10.1016/j.surfin.2026.108695

[11] ASTM D5528-01, Standard test method for mode I interlaminar fracture toughness of unidirectional fiber-reinforced polymer matrix composites, ASTM International, West Conshohocken, PA, 2002.

Materials Research Proceedings 73 (2026) 136-141 https://doi.org/10.21741/9781644904459-27

Element-Free Galerkin Method for Cantilever Nano-Beam Based on the Modified Kernel Integral Non-Local Elasticity Model

S.L. AKHIL[1,a,*], I.R. PRAVEEN KRISHNA[1,b]

[1]Indian Institute of Space Science and Technology, Thiruvananthapuram, India, 695547

[a]slakhilofficial@gmail.com, [b]praveenkrishna@iist.ac.in

Keywords: Element-Free Galerkin Method, Nonlocal Elasticity, Strain-Driven Model

Abstract. Nonlocal elasticity models are widely used to capture small-scale effects in nano-scale structures. The original integral nonlocal model proposed by Eringen often fails to satisfy the essential boundary conditions, and the differential model fails to capture scale effects properly. This limitation was attributed to the ill-posedness of the formulation for certain structural problems and to the inability of the bi-exponential kernel to satisfy the natural boundary conditions. To address these issues, recent studies have proposed kernel modification strategies. The modified kernel is obtained by incorporating the physical boundary conditions into the kernel. The present study uses the mesh-free formulation developed for the integral nonlocal model to assess key deformation characteristics. The mesh-free method presented here can be utilized for the deformation studies of other kernel modification attempts. The results show that the modified kernel with constitutive boundary conditions also failed to capture size effects for the cantilever nanobeam with tip load.

Introduction

The theory of nonlocal elasticity, introduced by Kroner [1] and advanced by Eringen and Edelen [2], provides a framework to incorporate long-range interactions. The kernel function, known as the attenuation function or error kernel, introduces an internal length-scale parameter that controls the range of nonlocal interactions. This integral formulation has attracted considerable interest in the analysis of nano-devices, composite materials, and other systems where microstructural effects dominate. However, when applied to structural members, the conflicting boundary conditions and equilibrium requirements lead to paradoxical results. To address this issue, Nobili and Pramanik [3] recently proposed the kernel modification approach. In this approach, the nonlocal kernel is modified by adding a suitable homogeneous solution of the governing differential equation. This ensures that the constitutive boundary conditions embedded in the modified kernel coincide with natural boundary conditions.

In the present work, the EFG formulation [4] is used for the static bending analysis of cantilever nano-beams within the modified kernel nonlocal elasticity framework of Nobili and Pramanik [3]. The modified Helmholtz kernel, which incorporates the natural boundary conditions of the cantilever beam, replaces the standard difference kernel in the nonlocal constitutive relation. The governing integro-differential equation is converted to a weak form suitable for EFG discretization, and the resulting system is solved numerically. Results are compared against analytical solutions of Eringen's integral model and against the classical local theory.

Methodology

Nonlocal Constitutive Model. Following Eringen's nonlocal elasticity theory, the stress at a point depends on the strain field over the entire domain,

$$\sigma(x) = \int_{\Omega} K(x - \bar{x}, \kappa) E(\bar{x}) \epsilon(\bar{x}) \mathrm{d} \quad (1)$$

Content from this work may be used under the terms of the Creative Commons Attribution 3.0 license. Any further distribution of this work must maintain attribution to the author(s) and the title of the work, journal citation and DOI. Published under license by Materials Research Forum LLC.

Materials Research Proceedings 73 (2026) 136-141 https://doi.org/10.21741/9781644904459-27

where $K(x-\bar{x},\kappa)$ is the attenuation kernel and $\kappa = e_0 a$ is the nonlocal parameter, with e_0 a material constant and a the internal length scale. The Helmholtz (exponential) kernel is adopted,

$$K(|x-\bar{x}|,\kappa) = \frac{1}{2\kappa}\exp\left(-\frac{|x-\bar{x}|}{\kappa}\right) \tag{2}$$

Kernel Modification.

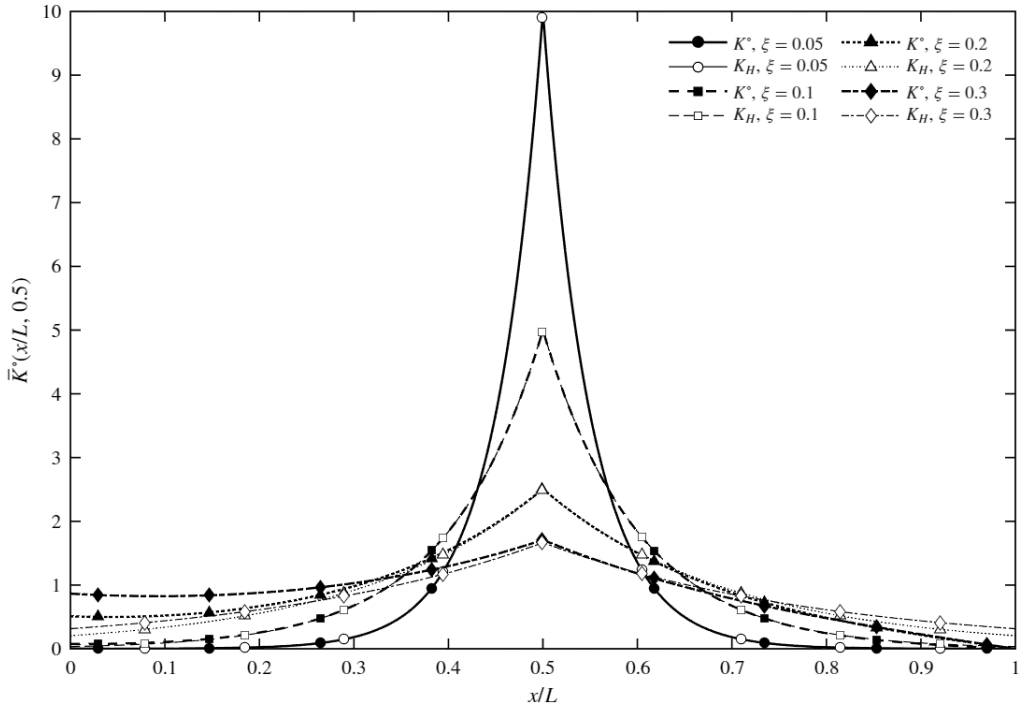

Fig 1: *Comparison of Helmholtz and Modified Kernel*

The kernel in Eq. (2), defined for an infinite domain, embeds constitutive boundary conditions (CBCs) that generally conflict with the natural boundary conditions (BCs) of a finite beam, rendering the integral problem ill-posed [3]. To restore well-posedness, the kernel is modified. For a cantilever beam, the modified kernel is [3],

$$K^\circ(x,\bar{x}) = \begin{cases} \dfrac{\left(e^{2L/\kappa} - e^{2\bar{x}/\kappa}\right)\left(Le^{2x/\kappa} + L - \kappa e^{2x/\kappa} + \kappa\right)e^{-(x+\bar{x})/\kappa}}{2\kappa(Le^{2L/\kappa} - \kappa e^{2L/\kappa} + L + \kappa)} & x < \bar{x} \\ \dfrac{\left(Le^{2\bar{x}/\kappa} + L - \kappa e^{2\bar{x}/\kappa} + \kappa\right)\left(e^{2L/\kappa} - e^{2x/\kappa}\right)e^{-(x+\bar{x})/\kappa}}{2\kappa(Le^{2L/\kappa} - \kappa e^{2L/\kappa} + L + \kappa)} & x > \bar{x} \end{cases} \tag{3}$$

Fig 1 compares the modified kernel with the Helmholtz kernel for different nonlocal parameter values. For the current position x both kernels coincide and deviate towards the boundary.

Element-Free Galerkin Method. In the EFG method, the displacement field $u^h(x)$ is approximated using moving least squares (MLS) as,

$$u^h(x) = p^{\mathrm{T}}(x)a(x) \tag{4}$$

where $\boldsymbol{p}(\boldsymbol{x}) = [\boldsymbol{p_1}, \boldsymbol{p_2}, \ldots, \boldsymbol{p_m}]^{\mathrm{T}}$ is the polynomial basis vector, and *a(x)* contains the unknown coefficients. These coefficients are determined by minimizing the weighted *L_2* norm,

$$J = \sum_{i=1}^{n} w(x-x_i)[\boldsymbol{p^T}(x_i)\boldsymbol{a}(x) - \hat{u}_i]^2 \tag{5}$$

Materials Research Proceedings 73 (2026) 136-141 https://doi.org/10.21741/9781644904459-27

over a local support domain. The cubic spline weight function is adopted,

$$w(r) = \begin{cases} \frac{2}{3} - 4r^2 + 4r^3 & r \le \frac{1}{2} \\ \frac{4}{3} - 4r + 4r^2 - \frac{4}{3}r^3 & \frac{1}{2} < r \le 1 \\ 0 & r > 1 \end{cases} \quad (6)$$

where $r = d_i/d_mi$ is the normalized distance from the node to the point of interest. Minimization yields the system $\boldsymbol{A}(\boldsymbol{x})\boldsymbol{a}(\boldsymbol{x}) = \boldsymbol{C}(\boldsymbol{x})\boldsymbol{đ}$, with $\boldsymbol{A} = \boldsymbol{WPP}^{\mathrm{T}}$ and $\boldsymbol{C} = \boldsymbol{WP}$. Substituting back gives the MLS approximation,

$$\boldsymbol{\phi}^{\boldsymbol{T}}(x) = \boldsymbol{p}^{\boldsymbol{T}}(x)\boldsymbol{A}^{-\boldsymbol{1}}(x)\boldsymbol{C}(x) \quad (7)$$

Since MLS shape functions do not satisfy the Kronecker delta property, essential and constitutive boundary conditions cannot be imposed directly. The scaled transformation method, combined with Lagrange multipliers, is used here: the approximation is rescaled so that it recovers nodal values at essential boundary nodes, while Lagrange multipliers enforce the remaining constraints [5], [6].

Integral Nonlocal Model. For the integral nonlocal model, we start with the total potential and apply the principle of minimum potential energy. The formulation is identical to the finite element method given in [4]. According to this, in equilibrium, a system or structure attains a state of minimum total potential energy. The elastic structure is discretized into N nodes. The displacement field associated with these nodes can be determined using the relation,

$$\frac{\partial \Pi}{\partial u_i} = 0, \quad i = 1,2,\dots,N \quad (8)$$

The total potential energy functional of the structure is given by,

$$\Pi[u] = \sum_{i=1}^{N} \Pi[u_i] \quad (9)$$

Subscripts 1, 2, ...N represent the node number, and u refers to the nodal displacement. In nonlocal elasticity, the terms $\partial \Pi_1/\partial u_2, \partial \Pi_1/\partial u_3, \dots, \partial \Pi_1/\partial u_N$ in these derivatives persist. For simple beam bending, the total potential energy of the system takes the following form,

$$\Pi = U + W \quad (10)$$

Using Eq. (10), total elastic strain energy takes the form,

$$U = \frac{1}{2}\int_V \epsilon_{ij}(x)\ \sigma_{ij}(x)\,\mathrm{d}V = \frac{1}{2}\int_V \epsilon_{ij}(x) \int_V k(|x - \bar{x}|, \kappa)\ C_{ijkl}(\bar{x})\,\epsilon_{kl}(\bar{x})\,\mathrm{d}V(\bar{x})\,\mathrm{d}V(x) \quad (11)$$

By using Eq. (11) and Eq. (9), the total potential for a uniform Euler–Bernoulli beam can be written as,

$$\Pi[w(x)] = \frac{EI}{2}\int_0^L \int_0^L k(|x - \bar{x}|, \kappa)\ w''(x)\,w''(\bar{x})\,\mathrm{d}\bar{x}\,\mathrm{d}x - \int_0^L w(x)\ q(x)\,\mathrm{d}x - \sum_{i=1}^{N} F_i\ w(x_i) + \sum_{i=1}^{N} C_i\ w'(x_i) \quad (12)$$

Where $\int_A z^2 dA = I$ is the second moment of the cross-sectional area of the beam, *q(x)* is the transverse distributed load, F_i is the transverse concentrated load, and C_i is the concentrated bending moment. A background discretization is used for numerical integration. Force vector F_i takes the form $Q_I = F_1, -C_1, F_2, -C_2, \dots, -C_N{}^{\mathrm{T}}$. Differentiating Eq. (12) with respect to each nodal parameter yields,

Materials Research Proceedings 73 (2026) 136-141 https://doi.org/10.21741/9781644904459-27

$$Q_I = \{F_1,\ -C_1,\ F_2,\ -C_2,\ \ldots,\ -C_N\}^{\mathrm{T}} \tag{13}$$

Unlike FEM, the effect of the ith node on itself and the influence of other nodes on the ith node are captured by the single term.

$$\frac{\partial \Pi}{\partial d_i} = EI\left[\int_0^L \int_0^L k(|x-\bar{x}|,\kappa)\ \phi_i''(x)\,\phi_i''(\bar{x})\,\mathrm{d}\bar{x}\,\mathrm{d}x\right] d_i - \int_0^L \phi^{\mathrm{T}}(x)\ q(x)\,\mathrm{d}x - Q_i = 0 \tag{14}$$

$$K_{ij} = EI\int_0^L \int_0^L k(|x-\bar{x}|,\kappa)\ \phi_i''(x)\,\phi_j''(\bar{x})\,\mathrm{d}\bar{x}\,\mathrm{d}x \tag{15}$$

The force vector corresponding to node i is given by the expression,

$$F_i = \int_0^L \phi^{\mathrm{T}}(x)\ q(x)\,\mathrm{d}x - Q_i \tag{16}$$

Gauss quadrature is used to carry out numerical integration.

Numerical Results

In this section, the numerical results for the meshless formulation developed for the modified kernel nonlocal model are presented. Uniform node distribution is used for simplicity. Corresponding results are non-dimensionalized using classical maximum values. The beam properties used in the numerical results are taken from a recent paper [6]: length of the beam $L = 10$ nm, width and height $w = h = 1$ nm, Young's modulus $E = 5500$ nN/nm², and the nonlocal parameter $\kappa = 1.25$. Results are compared with analytical solutions of the differential and integral model [7].

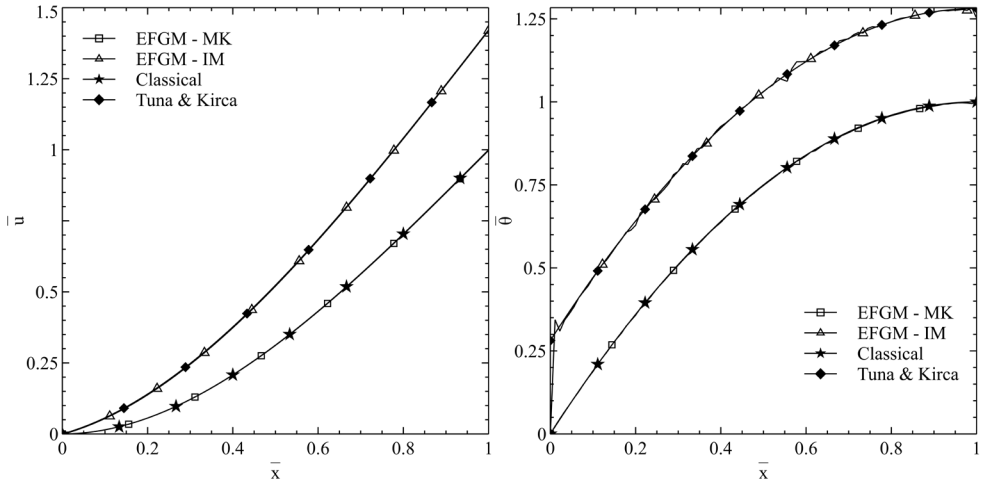

Fig 2 : Normalized (a) displacements (b) slopes for a cantilever nanobeam along the beam axis. MK = modified kernel, IM = Integral model

Materials Research Proceedings 73 (2026) 136-141 https://doi.org/10.21741/9781644904459-27

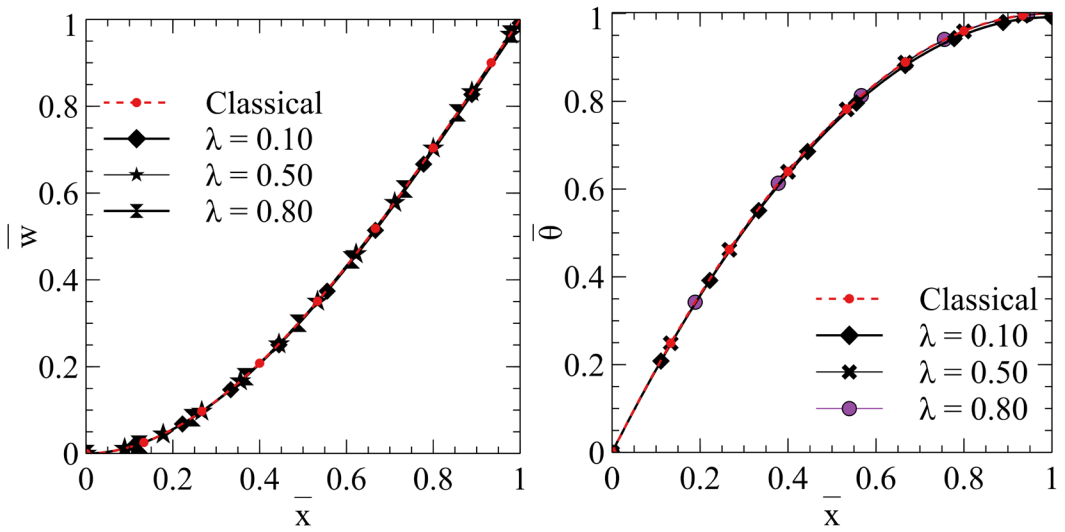

Fig 3 : *(a) Displacement and (b) slopes for different nonlocal parameters λ*

Fig. 2 (a) shows the normalized displacement along the beam axis and (b), the slopes along the non-dimensional beam axis. All models predict zero displacement at the fixed end. This confirms that the essential boundary condition is satisfied. The classical solution gives the lowest displacement. The EFGM with the integral model (EFGM-IM) gives slightly higher displacements. The Tuna & Kirca analytical solution agrees closely with EFGM-IM. The EFGM with the modified kernel (EFGM-MK) matches the classical model and does not reproduce the expected size-dependent stiffening or softening. Parallel observations are obtained for slopes. The slope is zero at the fixed end for all models. This also confirms that the rotational boundary condition is satisfied. The classical model gives the lowest rotation values. The EFGM-IM and Tuna & Kirca results are in close agreement. The integral model shows a sudden spike in rotation at the fixed end. This violates the essential boundary condition. In contrast, the modified kernel predicts zero rotation at the fixed end. This confirms that the modified kernel effectively incorporates the physical boundary conditions into the formulation at the expense of size effects. Fig. 2 (a) shows the normalized displacement and rotation along the beam axis for different nonlocal parameters. For all nonlocal parameters considered, the modified kernel failed to capture the size effects but satisfied the physical boundary conditions. Failure to predict the size effects in a small-scale beam shows that the modified kernel from [3] cannot be used to model small-scale cantilever structures.

Conclusions

This work presents an EFG formulation for the integral nonlocal model. The formulation can be used to quickly assess the behavior of various kernel modification strategies. Various kernel modifications are being proposed to address the well-posedness of Eringen's nonlocal model. The integro-differential form of the governing equation makes it hard to obtain closed-form solutions. Numerical methods, such as the EFG method outlined in this study, provide a better starting point. The numerical analysis of the cantilever nanobeam shows that the given modified kernel fails to capture size effects while satisfying the boundary conditions.

References

[1] K. E, "Elasticity theory of materials with long range cohesive forces," *International Journal of Solids and Structures,* vol. 5, no. 5, pp. 731--742, 1967. https://doi.org/10.1016/0020-7683(67)90049-2

[2] A. C. Eringen and D. Edelen, "On nonlocal elasticity," *International journal of engineering science,* vol. 10, pp. 233-248, 1972. https://doi.org/10.1016/0020-7225(72)90039-0

[3] A. Nobili and D. Pramanik, "A well-posed theory of linear non-local elasticity," *International Journal of Engineering Science,* vol. 215, p. 104314, 2025. https://doi.org/10.1016/j.ijengsci.2025.104314

[4] S. Akhil, I. P. Krishna and M. Aswathy, "Effect of non-dimensional length scale in element free Galerkin method for classical and strain driven nonlocal elasto-static problems," *Computers & Structures,* vol. 312, p. 107724, 2025. https://doi.org/10.1016/j.compstruc.2025.107724

[5] S. Akhil, K. I. Praveen and G. K. Khanra, "Element-free Galerkin method for static analysis of nonlocal elastic solids using differential and integral straindriven models," in *Mechanics of Advanced Materials and Structures*, N. Naidu, K. R. V. Subramanian and G. N. A. K. Nagaraju Kottam, Eds., CRC Press, 2025, pp. 33--40. https://doi.org/10.1201/9781003770442-5

[6] M. Aswathy and C. Arun, "Stochastic analysis of thin beams and plates incorporating von-Kármán nonlinear strains using meshless method," *Thin-Walled Structures,* vol. 196, p. 111478, 2024. https://doi.org/10.1016/j.tws.2023.111478

[7] M. Tuna and M. Kirca, "Bending, buckling and free vibration analysis of Euler-Bernoulli nanobeams using Eringen's nonlocal integral model via finite element method," *Composite Structures,* vol. 179, pp. 269-284, 2017. https://doi.org/10.1016/j.compstruct.2017.07.019

Materials Research Proceedings 73 (2026) 142-146 https://doi.org/10.21741/9781644904459-28

Innovative Viscous Damper Design for Stay Cable Control: The Hysteretic Maxwell Model

Selsebil SOLTANE[1,a *], Othman BEN MEKKI[1,b]

[1]Université de Tunis El Manar, Ecole Nationale d'Ingénieurs de Tunis, LGC, Tunisia

[a]selsebil.soltane@enit.utm.tn, [b]othman.benmekki@enit.utm.tn

Keywords: Viscous Damper, Hysteretic Maxwell Model, Stay Cable Vibration Control

Abstract. This study develops an optimized Hysteretic Maxwell model to capture the nonlinear behavior of viscous dampers while maintaining a limited number of parameters. Following experimental calibration across various frequencies, the model's performance is validated through numerical simulations of the longest stay cable on the Rades-La Goulette bridge. Results show that the proposed model significantly outperforms the standard Maxwell formulation in mitigating both free and forced vibrations, directly enhancing aerodynamic stability. Furthermore, a comparative assessment demonstrates that this optimized viscous damper provides superior modal damping compared to magnetorheological (MR) systems, offering a highly efficient alternative that bypasses the need for complex external power supplies.

Introduction

While high-performance materials allow for flexible designs, they make long stay cables vulnerable to vibrations [1], requiring diverse mitigation strategies. Among these, viscous dampers are widely used; however, their actual performance often deviates from standard linear predictions due to inherent nonlinearities and hysteresis [2].

To capture these dynamics, various mathematical frameworks have been developed. The Maxwell model (spring and dashpot in series) and the Kelvin-Voigt model (in parallel) are widely used to represent elastic and dissipative components [3]. However, these classical models often fail to account for the frequency-dependent behavior of damper polymers. While fractional derivative models offer high precision in describing such frequency dependency [4], their mathematical complexity often limits practical application. Consequently, the simplified Maxwell model incorporating a damping exponent has emerged as a highly efficient alternative, providing an accurate depiction of nonlinear behavior and superior displacement reduction compared to linear models [5].

Building on this framework, the present study proposes a parametric nonlinear model based on the simplified Maxwell approach. The model parameters are identified using experimental data fitting across three characteristic frequencies [6]. The effectiveness of the proposed model is then validated by simulating the free and forced vibration responses of a stay cable from the Rades-La Goulette bridge. Finally, a comprehensive sensitivity analysis evaluates the influence of key parameters on energy dissipation and compares the results with magnetorheological (MR) damper performances.

The proposed model for viscous damper

The simplified Maxwell model captures both the linear and nonlinear behaviors of a viscous damper using the following equation:

$$F_d^M = C\,\mathrm{sgn}(v_d)\,|v_d|^a \quad (0 < a \leq 1) \tag{1}$$

Content from this work may be used under the terms of the Creative Commons Attribution 3.0 license. Any further distribution of this work must maintain attribution to the author(s) and the title of the work, journal citation and DOI. Published under license by Materials Research Forum LLC.

Materials Research Proceedings 73 (2026) 142-146 https://doi.org/10.21741/9781644904459-28

A viscous damper's force F_d^M depends on piston velocity v_d, a damping coefficient C, and a damping exponent a. While a = 1 defines linear behavior, other values dictate nonlinear behavior (Fig. 1), prompting a mathematical transformation to fully model the damper's hysteretic loop across piston velocity $v_d \in [-v_h, v_h]$ by:

$$F_d^{HM} = \begin{cases} C\ \mathrm{sgn}(v_d - v_0)\left[1 - \exp\left(-\mathrm{sgn}(v_d - v_0)\frac{v_d - v_0}{n}\right)\right]|(v_d - v_0)|^a & \text{for } \dot{v}_d < 0 \\ C\ \mathrm{sgn}(v_d + v_0)\left[1 - \exp\left(-\mathrm{sgn}(v_d + v_0)\frac{v_d + v_0}{n}\right)\right]|(v_d + v_0)|^a & \text{for } \dot{v}_d > 0 \end{cases} \quad (2)$$

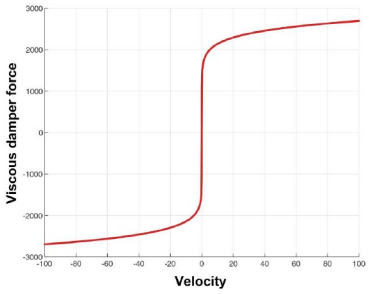

Fig. 1: Simplified Maxwell model.

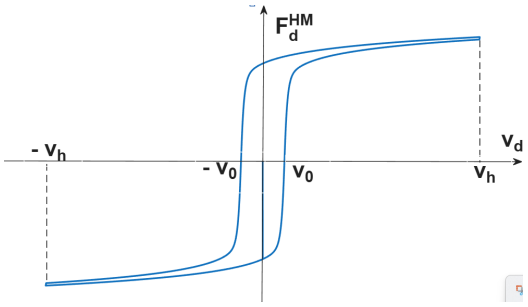

Fig. 2: The hysteretic Maxwell model.

This model uses three key velocity-dimensioned parameters: a scale factor v_0 that determines the overall width of the loop, the maximum reached piston velocity v_h, and a regularization parameter n that dictates the exponential growth of the damping force. The resulting hysteresis loop (Fig. 2) is characterized by an upper curve, which represents the damping force as the piston's velocity decreases, and a lower curve, which shows the force as the velocity increases.

Experimental identification of model parameters

The five parameters (C, v_0, v_h, n, a) of the Hysteretic Maxwell model (Table 1) are identified via least-squares optimization using experimental data from a rotatable-blade viscous damper [6]. Simulated responses under various sinusoidal excitations (frequencies of 0.6–1.8 Hz, amplitudes of 2–15 mm) closely match the experiments, validating the model's accuracy (Fig. 3).

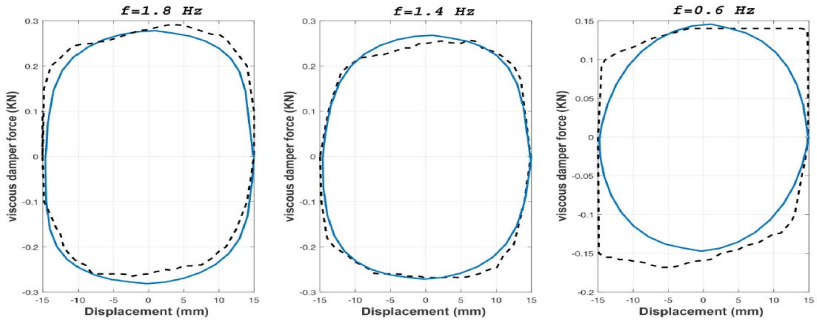

Fig. 3: Validation of model predictions (solid line) against experimental measurements (dashed line).

Table 1. Calibrated parameters for the Hysteretic Maxwell

f	C [N.s/m]	v_0 [m/s]	n [m/s]	a	v_h [m/s]
1.8	1000	0.05	0.01	0.5	0.22
1.4	970	0.05	0.02	0.5	0.22
0.6	550	0.05	0.1	0.3	0.22

Materials Research Proceedings 73 (2026) 142-146 https://doi.org/10.21741/9781644904459-28

Vibration Control of a Stay Cable Using a Viscous Damper

To analyze the dynamics of the inclined stay cable equipped with a viscous damper (Fig. 4), the system's motion is simplified into a single-degree-of-freedom model using the Galerkin method. By focusing specifically on the fundamental mode with the sinusoidal shape function $\phi_i = \sin\left(\frac{i\,\pi\,x}{L}\right)$, the partial differential equation governing the transverse vibrations is reduced to the following discretized ordinary differential equation:

$$m_1\,\ddot{\alpha}_1(t) + \left(k_1 + \lambda^2 m_1\right)\alpha_1(t) = F_1 - F_d(t)\,\phi_1(x_d) \tag{3}$$

Where the system and modal parameters are defined as follows: $\alpha_1(t)$: non-dimensional modal participation factor, $m_1 = m_c\frac{L}{2}$: Equivalent modal mass (m_c: mass per unit length), L: cable length, $k_1 = \frac{T\pi^2}{2L}$: Equivalent modal stiffness (T: static tension), $\lambda^2 = \frac{E_c\,A_c}{L}\left(\frac{m_c\,g\cos\theta}{T}\right)^2$: cable characteristic parameter (E_c: Young's modulus,A_c: the cross-sectional area, , and θ :inclination angle), $F_1 = \int_0^L F_{ext,y}\,\phi_1(x)\,dx$: Generalized modal force ($F_{ext,y}$: external transverse forces), $F_d(t)$: External control force provided by the viscous damper, as defined in Eq.2 , $\phi_1(x_d) = \sin\left(\frac{\pi x_d}{L}\right)$: fundamental mode shape evaluated at the damper's location x_d. The damper's efficacy is evaluated on the Rades-La Goulette bridge's longest cable, S16 (properties in Table 2).

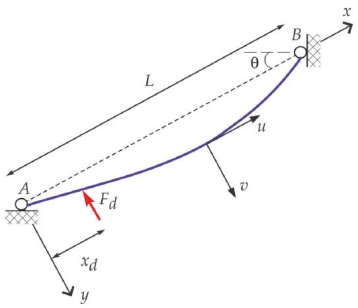

Fig. 4: Stay cable and viscous damper system.

Table 2. Properties of stay cable (S16)

L [m]	θ [°]	T [KN]	E_c [*Gpa*]	A_c [cm^2]	m_c [Kg/m]
55.4	16.5	4313.5	190	55.5	44

Numerical Results

Fig. 5 compares the first-mode dynamic responses at 1.8 Hz. The proposed Hysteretic Maxwell model outperforms the standard version by significantly accelerating vibration decay and reducing peak amplitudes to approximately 74.3%. These numerical results for free vibrations extend to forced excitations. Specifically, for an external force $F_{ext,y}(t) = 1.5\cos\left(\sqrt{\frac{k_1}{m_1}}\,t\right)$ the damper's hysteresis significantly enhances the cable's (S16) damping capacity. Detailed graphical evidence of this forced response was previously established in [7].

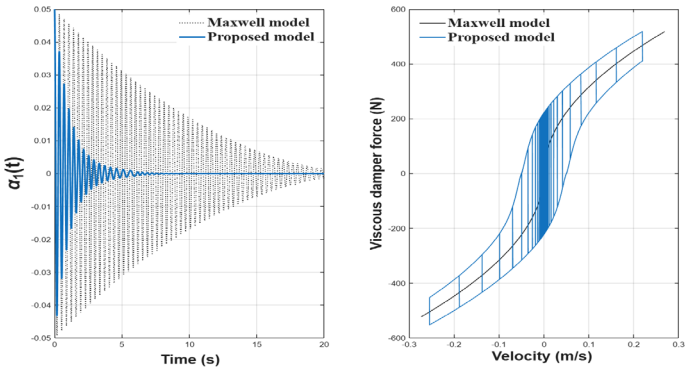

Fig. 5: Free vibration control comparison: standard Maxwell vs. proposed model.

Parametric analysis (Fig. 6) shows that optimizing a, n, and C to expand the hysteresis loop directly maximizes energy dissipation. Notably, increasing the damping coefficient can reduce the maximum vibration amplitude by 89.5% within the first five seconds.

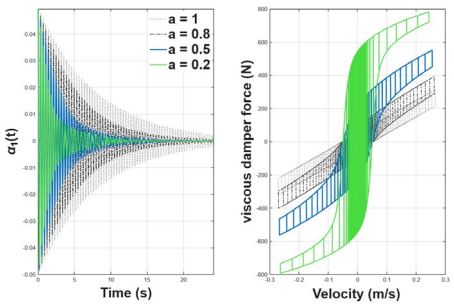

(a) n = 0.01 m/s, v_0= 0.05 m/s, C = 1000 N.s/m

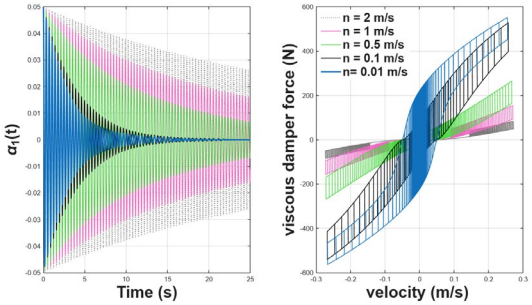

(b) a = 0.5, v_0= 0.05m/s, C = 1000 N.s/m

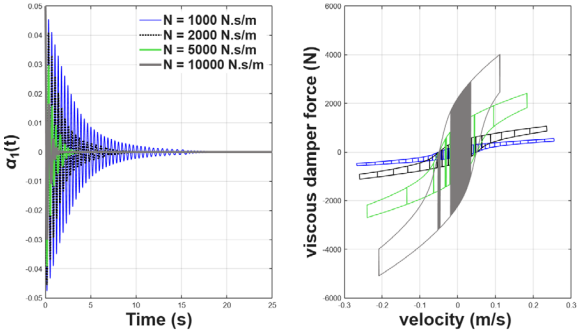

(c) a = 0.5, v_0= 0.05 m/s, n = 0.01 m/s

Fig. 6: Hysteretic parameter effects on the first-mode vibration of the stay cable.

Performance is compared against a Magneto-rheological (MR) damper, characterized by the standard Bingham model. The optimized Hysteretic Maxwell model outperforms the MR damper, achieving faster decay and a 70% amplitude reduction, as illustrated by the comparative curves provided in [7].

Conclusions

In summary, this study develops and optimizes a hysteretic Maxwell model for viscous dampers to enhance the aerodynamic stability of cable-stayed bridges. Applied to the Rades-La Goulette bridge, this model significantly outperforms the simplified Maxwell model in mitigating both free and forced vibrations. Furthermore, a comparative analysis demonstrates that this viscous damper

offers superior performance compared to MR dampe. This highlights the viscous damper's practical superiority: delivering enhanced energy dissipation without an external power source.

References

[1] Y. Hikami, N. Shiraishi, Rain wind induced vibrations of cables in cable stayed bridges, J. Wind Eng. Ind. Aerodyn. 29 (1988) 409-418. https://doi.org/10.1016/0167-6105(88)90179-1

[2] A. Gupta, S. Panda, R. Reddy, Passive control of parametric instability of layered beams using graphite particle filled viscoelastic damping layers, J. Mech. Adv. Mater. Struct. 29 (2021) 3982-3996. https://doi.org/10.1080/15376494.2021.1931993

[3] T. Hatada, T. Kobori, M. Ishida, N. Niwa, Dynamic analysis of structures with Maxwell model, Earthquake Eng. Struct. Dyn. 29 (2000) 159-176. https://doi.org/10.1002/(SICI)1096-9845(200002)29:2<159::AID-EQE902>3.0.CO;2-3

[4] A. Schmidt, L. Gaul, Finite element formulation of viscoelastic constitutive equations using fractional time derivatives, Nonlinear Dyn. 29 (2002) 37-55. https://doi.org/10.1023/A:1016552504657

[5] N. Makris, M. Constantinou, G. Dargush, Analytical model of viscoelastic fluid dampers, J. Struct. Eng. 119 (1993) 3310-3325. https://doi.org/10.1061/(ASCE)0733-9445(1993)119:11(3310)

[6] C. Qu, Z. Cong, T. Sun, Investigation of the mechanical characteristics of a novel viscous damper with rotatable blades, Sustainability 14 (2022) 1-11. https://doi.org/10.3390/su141912053

[7] S. Soltane, O. Ben Mekki, A proposed model to investigate the dynamic response of stay cables with viscous damper, Mech. Adv. Mater. Struct. 32 (2024) 1837-1852. https://doi.org/10.1080/15376494.2023.2281812

Materials Research Proceedings 73 (2026) 147-150 https://doi.org/10.21741/9781644904459-29

Geometrical Nonlinear Analysis of Beams by Hierarchical Legendre Expansion CUF Models

Alfonso PAGANI[1,a], Piero CHIAIA[2,b *] and Erasmo CARRERA[1,c]

[1]MUL2 Lab, Department of Mechanical and Aerospace Engineering, Politecnico di Torino, Corso Duca degli Abruzzi 24, 10129, Torino, Italy

[2]Department of Mechanics, Mathematics and Management, Politecnico di Bari, Via Edoardo Orabona, 4, 70126, Bari, Italy

[a]alfonso.pagani@polito.it, [b]piero.chiaia@poliba.it, [c]erasmo.carrera@polito.it

Keywords: P-refinement, Higher-Order Beam Models, Carrera Unified Formulation, Nonlinear Analysis, Hierarchical Legendre Expansion

Abstract. A 1D Hierarchical Legendre Expansion model is proposed for the geometrically nonlinear analysis of compact and slender, thin-walled beam structures. Developed within the Carrera Unified Formulation framework, the model employs Legendre polynomial expansions to describe higher-order cross-sectional kinematics and enable efficient p-refinement. By increasing the polynomial approximation order, the formulation improves accuracy without requiring excessive mesh refinement. The hierarchical nature of the approach allows the governing equations to be derived in a compact and theory-independent manner through CUF. This makes the method a powerful alternative for generating refined finite element beam models capable of capturing complex three-dimensional deformation effects, particularly under large displacements and rotations. The proposed methodology is validated through nonlinear benchmark problems involving cross-sectional twisting and warping.

Introduction

Accurate analysis of nonlinear instability phenomena, such as localized buckling, critical points, and bifurcations, requires refined numerical models. While accuracy is commonly improved through h-refinement, by increasing mesh density, p-refinement offers an efficient alternative by raising the polynomial order of the approximation functions [1,2]. This strategy enables high-fidelity modelling without excessively refined meshes and is particularly effective for capturing complex three-dimensional effects such as warping, twisting, and localized cross-sectional deformations [3]. This work investigates a higher-order beam model based on p-refinement for geometrically nonlinear analysis. In particular, it extends the Hierarchical Legendre Expansion (HLE) model to large-displacement problems involving compact and thin-walled isotropic and composite structures [4]. The formulation is developed within the Carrera Unified Formulation (CUF) framework, where the governing equations are written through theory-independent Fundamental Nuclei (FNs), the elementary blocks of the present approach.

Numerical examples demonstrate the accuracy and reliability of the proposed method in predicting displacement and stress fields, while also showing its computational efficiency in terms of degrees of freedom compared with classical higher-order models and full three-dimensional solutions.

Methodology

In the present work, high order unified 1D beam models for the geometrically nonlinear analysis of structures are presented in the well-established CUF framework. In this pure displacement-based finite element (FE) model, the displacement field is expressed by a recursive polynomial

Content from this work may be used under the terms of the Creative Commons Attribution 3.0 license. Any further distribution of this work must maintain attribution to the author(s) and the title of the work, journal citation and DOI. Published under license by Materials Research Forum LLC.

Materials Research Proceedings 73 (2026) 147-150 https://doi.org/10.21741/9781644904459-29

expansion of kinematic models along the beam axis and expansion functions along the cross-section direction:

$$\boldsymbol{u}(x,y,z) = F_\tau(x,z)N_i(y)\mathbf{q}_{\tau i} \quad i = 1,2,..,N_n, \quad \tau = 1,2,\ldots,M \tag{1}$$

where $F_\tau(x,z)$ is the cross-section polynomial expansion, $N_i(y)$ are the 1D shape functions involved in the FE definition, M is related to the order of the structural theory employed and q_τi are the final generalized unknowns of the problem. In the present framework, the governing equations are rewritten in matrix form, exploiting the definition of the Fundamental Nuclei (FN), the key aspect of the present modeling approach and the basic elementary blocks of the FE matrices, which are defined regardless of the chosen displacement field expansion model. The theoretical basis of the Legendre expansion model is provided by Szabó et al. [5], where the set of Legendre polynomials for the construction of finite element spaces is introduced. For the sake of brevity, the one-dimensional Legendre polynomials are here reported under the recurrent definition, introducing the generic one-dimensional $L_k(\xi)$ polynomial. By means of the tensor product, the set of interpolating 2D Legendre shape functions can be naturally considered:

$$L_0(\xi) = 1; \;\; L_1(\xi) = \xi; \;\; L_k(\xi) = \frac{2k-1}{k}\xi L_{k-1}(\xi) - \frac{k-1}{k}L_{k-2}(\xi), \quad k = 2,3,\ldots,M \tag{2}$$

The structural modeling based on such features has already been validated in the literature [4] and here extended for the first time to the geometrically nonlinear analysis of structures. The nonlinear governing equation for the quasi-static analysis are carried out through the Principle of Virtual Displacements (PVD):

$$\delta\mathcal{L}_{int} = \delta\mathcal{L}_{ext} \tag{3}$$

where $\boldsymbol{\delta}$ denotes the virtual variation, $\boldsymbol{\mathcal{L}_{int}}$ is the internal work, and $\boldsymbol{\mathcal{L}_{ext}}$ is the work done by inertia external forces, respectively. Adopting the recursive index formalism introduced for the displacement field, the FNs of FE matrices are stemming from the equilibrium equations, rewritten in compact form as:

$$\delta\boldsymbol{q}_{sj}^T\mathbf{K}_S^{\tau sij}(\boldsymbol{q})\boldsymbol{q}_{\tau i} = \delta\boldsymbol{q}_{sj}^T\mathbf{F}_{ext}^{sj} \tag{4}$$

The FNs of the secant stiffness matrix $\mathbf{K}_S^{\tau sij}(\boldsymbol{q})$ and external force vector $\mathbf{F}_{ext}^{sj}$ are independent of the kinematic model adopted and the theory of structure approximation considered; thus, Eq. (3) is the final governing equation in a hierarchical form, where the global FE matrices are obtained exploiting the summation over the recursive indices expansion. For a quasi-static nonlinear analysis, the numerical scheme employed is a Newton-Raphson method coupled with an arc-length constraint [6]. Linearizing the equilibrium equation, the FN of the tangent stiffness matrix is defined, and the global incremental equation is then obtained:

$$\mathbf{K}_T\Delta\boldsymbol{q} = -\boldsymbol{\varphi}_{res}(\boldsymbol{q}_0, \ddot{\boldsymbol{q}}_0, \mathbf{f}_0) + \mathbf{I}\Delta\boldsymbol{\lambda}\mathbf{f}^{rif} \tag{4}$$

Afterwards, in the neighborhood of a non-trivial equilibrium state computed by solving iteratively this last incremental equation until convergence is reached. The complete derivation of the tangent stiffness matrix in terms of FN and the numerical scheme adopted in the present approach can be extensively found in [6].

Numerical results

A Z cross-section cantilever beam is considered as a reference case study to assess the capabilities of the present code updating. A beam of a total length L=1000 mm and cross-section dimensions t=10 mm, a=100 mm, and b = 200 mm is considered clamped at one end and subjected to a single concentrated load at the upper-right vertex of the free cross-section. To assess the capabilities of

Materials Research Proceedings 73 (2026) 147-150 https://doi.org/10.21741/9781644904459-29

the present higher-order HLEm, a convergent FE discretization with 20 cubic elements along the axis has been considered, using different cross-section expansion models to compare the capabilities of LEm and HLEm. In this case, to assess the effects of the p-refinement technique, a five-domain discretization is used, implementing either classical Lagrange-expansion models (Lem) adopting 5 L4, 5 L9, 5 L16, and 5 HLE subdomains. Figure 1 shows the geometrical features of the considered beam, the boundary conditions, and the discretization subdomains adopted in the cross-section modeling.

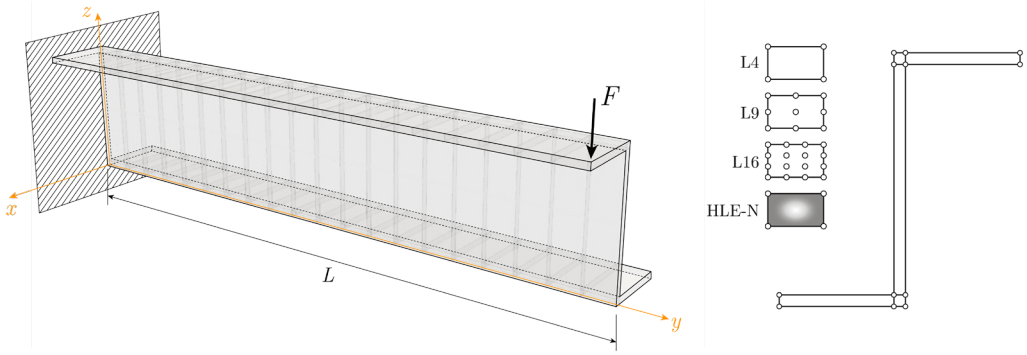

Figure 1 - Cantilever Z-cross section beam: geometrical features, boundary conditions and cross-section modeling

The effects of the discretization model and the theory of structure approximation is investigated in the following, comparing the results obtained via higher-order HLE CUF models, higher-order 3D solutions obtained via anisotropic-order elements implemented in NGSolve [7] with respect to a reference 3D elasticity solution obtained via ABAQUS commercial software. Figure 2 shows the global equilibrium path computed with each considered cross-section expansion model.

References

The analyses confirm the effectiveness of the HLEm for the geometrically nonlinear modelling of compact and thin-walled structures. The proposed approach achieves accurate results by increasing the polynomial expansion order, avoiding excessive mesh refinement, by tuning the accuracy of the model by increasing the polynomial order, capturing complex three-dimensional effects, such as warping, twisting, and localized cross-sectional deformations. The integration within the CUF framework provides a compact and theory-independent derivation of the governing equations. The results demonstrate reliable predictions of displacement and stress fields, even under large displacements and rotations. In addition, an extension of the present modeling approach is intended, including the analysis of curved structures through an independent description of the geometry by means of the blending function method, already implemented in Pagani et al. [8].

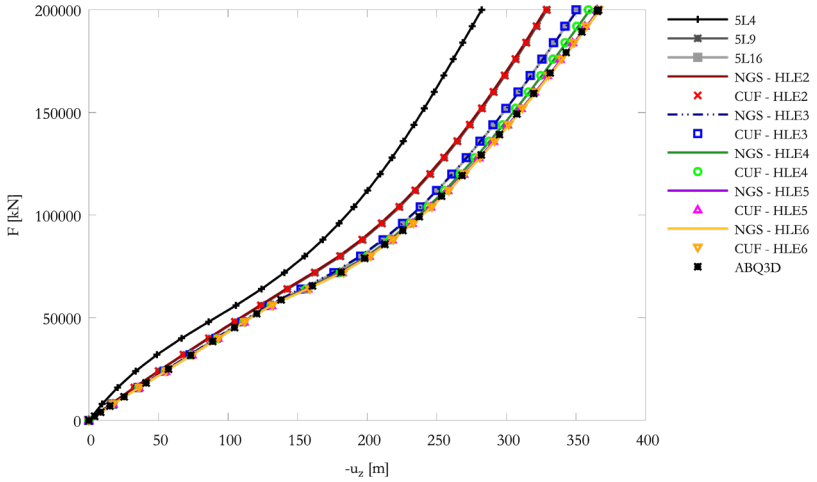

Figure 2 - Cantilever Z-cross section beam: equilibrium paths

Acknowledgment

P. Chiaia acknowledge support by the Space It Up! project funded by the Italian Space Agency, ASI, and the Ministry of University and Research, MUR, under contract CUP n. D93C23001190006.

References

[1] Babuska I, Szabo B.A. and Katz, I. N. "The p-Version of the Finite Element Method". SIAM Journal on Numerical Analysis, Vol 18, n.3, pp. 515-545, 1981. https://doi.org/10.1137/0718033

[2] Surana K.S., Petti S.R., Ahmadi A.R. and Reddy J.N. "On the p-version hierarchical interpolation functions for higher-order continuity finite element models". International Journal of Computational Engineering Science, Vol 02, n.04, pp. 653-673, 2001. https://doi.org/10.1142/S1465876301000507

[3] Carrera E., Pagani A. and Augello R. "Large deflection of composite beams by finite elements with node-dependent kinematics", Computational Mechanics, Vol. 69, pp. 1481-1500, 2022. https://doi.org/10.1007/s00466-022-02151-4

[4] Pagani A., de Miguel A.G., Petrolo M. and Carrera E. "Analysis of laminated beams via Unified Formulation and Legendre polynomial expansions". Composite Structures, Vol. 156, pp. 78-92, 2016. https://doi.org/10.1016/j.compstruct.2016.01.095

[5] Szabo B.A., Duster A. and Rank E. "The p-Version of the Finite Element Method". Encyclopedia of Computational Mechanics, John Wiley & Sons, Ltd, 2004. https://doi.org/10.1002/0470091355.ecm003g

[6] Pagani A. and Carrera E. "Unified formulation of geometrically nonlinear refined beam theories", Mechanics of Advanced Materials and Structures, Vol 25, n. 1, pp. 15-31, 2018. https://doi.org/10.1080/15376494.2016.1232458

[7] Netgen/NGSolve, high performance multiphysics finite element software: https://ngsolve.org;

[8] Pagani A., De Miguel A.G. and Carrera E. "Cross-sectional mapping for refined beam elements with applications to shell-like structures", Computational Mechanics, Vol. 59, pp. 1031–1048, 2017. https://doi.org/10.1007/s00466-017-1390-7

Materials Research Proceedings 73 (2026) 151-155 https://doi.org/10.21741/9781644904459-30

Finite Strain Ductile Phase-Field Modelling under Chemo Thermo-Mechanical Coupling: Application to Viscoplastic Silicon Anode Particles

Armel TENE TESSE[1,2,a *], Seydou HEBIE[1,b], Emmanuelle LANCELLE BELTRAN[1,c], Habibou MAITOURNAM[2,d], Ziad MOUMNI[3,e]

[1]STELLANTIS AUTO-SAS, Tech Research Expertise Center, 212 Bd Pelletier 78955 Carrières-Sous-Poissy, France

[2]IMSIA, CNRS, EDF, ENSTA, Institut Polytechnique de Paris, 91120 Palaiseau, France

[3]LMI, CNRS, EDF, ENSTA, Institut Polytechnique de Paris, 91120 Palaiseau, France

[a]armel.tenetesse@stellantis.com, [b]seydou.hebie@stellantis.com, [c]emmanuelle.lancellebeltran@stellantis.com, [d]habibou.maitournam@ensta.fr, [e]zied.moumni@sjtu.edu.cn

Keywords: Lithium-Ion Battery, Ductile Damage, Silicon Anode, Chemo-Thermo-Mechanical Coupling, Finite-Strain

Abstract. The urgent need to reduce CO_2 emissions is driving the development of low-carbon transportation technologies, including lithium-ion batteries for electric vehicles, where energy density is one of several key performance considerations. Silicon-based composite anodes are promising candidates due to their high lithium storage capacity. However, their large volumetric expansion during lithiation induces severe mechanical degradation. In this work, a finite-strain ductile phase-field framework coupled with viscoplasticity and diffusion-driven chemical expansion is developed to model damage evolution in silicon composite materials. Damage growth is driven by elastic and viscoplastic energy contributions, within a consistent thermodynamic chemo-thermo-mechanical framework, with a particular focus here on chemo-mechanical effects. The model is first used to investigate the influence of lithium diffusion on ductile crack propagation, considering diffusion-induced chemical expansion while neglecting mechanical feedback on transport. It is then applied to simulate continuous damage evolution in a silicon particle using a fully coupled chemo-thermo-mechanical formulation under electrochemically consistent loading conditions. Numerical results demonstrate the influence of viscoplastic dissipation, transport kinetics, and operating rate on damage accumulation. The proposed framework provides a robust multiphysics tool for analysing chemo-mechanically driven degradation in silicon-based anodes and establishes a solid basis for future fatigue and lifetime investigations.

Introduction

The transition toward electrified transportation is a key strategy for reducing the environmental impact of fossil-fuel consumption and is driving the demand for high-performance lithium-ion batteries with increased energy density and durability. While graphite remains the dominant anode material, its limited lithium-storage capacity motivates the development of disruptive materials. Among them, silicon-based composite anodes are particularly attractive due to their high theoretical capacity (~3579 mAh/g) compared to graphite (~372 mAh/g) [1].

However, the practical implementation of silicon anodes is hindered by severe mechanical degradation [1,3], resulting from their large volumetric expansion during lithiation, which induces high stresses, inelastic deformation, and progressive damage accumulation upon cycling. These

Content from this work may be used under the terms of the Creative Commons Attribution 3.0 license. Any further distribution of this work must maintain attribution to the author(s) and the title of the work, journal citation and DOI. Published under license by Materials Research Forum LLC.

Materials Research Proceedings 73 (2026) 151-155 https://doi.org/10.21741/9781644904459-30

mechanisms lead to ductile cracking at the particle scale and rapid capacity fading. Capturing such degradation phenomena remains a major challenge for predictive battery ageing modelling.

The behaviour of silicon anodes is inherently multiphysical [4], involving strong coupling between lithium diffusion, chemically induced swelling, large-deformation viscoplasticity [3], and damage evolution. Many existing modelling approaches rely on small-strain assumptions or brittle fracture descriptions [5], which are inadequate for representing ductile failure mechanisms under large deformation conditions.

In this work, a finite-strain ductile phase-field framework coupled with viscoplasticity and diffusion-driven chemical expansion is proposed to model damage evolution in silicon composite anodes. The framework is first employed to investigate the influence of lithium diffusion on ductile crack propagation by accounting solely for diffusion-induced chemical expansion. It is then applied to simulate continuous damage evolution in a silicon particle using a fully coupled chemo-mechanical formulation under electrochemically consistent boundary conditions.

Methodology

The degradation of silicon composite anodes is modelled using a finite-strain chemo-thermo-mechanical framework coupled with a ductile phase-field formulation. The total deformation gradient is multiplicatively decomposed into elastic, thermal, chemical, and viscoplastic contributions,

$$\underline{\underline{F}} = \underline{\underline{F}}^{e}\,\underline{\underline{F}}^{th}\,\underline{\underline{F}}^{c}\,\underline{\underline{F}}^{vp} \tag{1}$$

where the chemical $\underline{\underline{F}}^{c}$ and thermal $\underline{\underline{F}}^{th}$ deformation gradients account for isotropic volumetric expansions J^{c} and J^{th}($J^{c} = 1 + \Omega C_s$, $J^{th} = exp\left(3\alpha_{th}(\Theta - \Theta_0)\right)$, $J^{i} = det\underline{\underline{F}}^{i}$ with C_s the lithium concentration, Θ and Θ_0 the temperature and its reference value, respectively, Ω the partial molar volume and α_{th} the thermal expansion coefficient), and $\underline{\underline{F}}^{e}$ the elastic deformation gradient. The combined chemo-thermal volumetric contribution is defined as J^{cth}=$J^{c}J^{th}$. Large-deformation viscoplasticity $\underline{\underline{F}}^{vp}$ is introduced to represent irreversible deformation and stress relaxation in silicon during cycling, as observed experimentally [6].

Material degradation is described using an energy-based ductile phase-field approach [2] based on the Ambrosio–Tortorelli AT2 formulation. A scalar phase-field variable $\phi \in [0,1]$ is introduced, where $\phi = 0$ denotes intact material and $\phi = 1$ a fully developed crack. The total free energy density is defined as

$$\psi = g(\phi)\left(J^{cth}\psi_e(\underline{\underline{E}}^{e}) + \psi_{vp}(p)\right) + \psi_{ch}(C_s, \Theta) + \psi_{th}(\Theta) + \psi_f(\phi, Grad\phi) \tag{2}$$

where $\psi_e, \psi_{vp}, \psi_{ch}, \psi_{th}$ and ψ_f denote the elastic, viscoplastic, chemical, thermal and fracture contributions, respectively, and $g(\phi)$ is the degradation function. Here, $\underline{\underline{E}}^{e}$ denotes the elastic Green strain tensor and p is the cumulative viscoplastic strain. The phase-field fracture contribution is defined as

$$\psi_f = \frac{G_c}{2\,l_c}(\phi^2 + l_c^2|\mathrm{Grad}\phi\,|^2) \tag{3}$$

with G_c the fracture toughness and l_c the characteristic length controlling damage regularization. Damage evolution is driven by elastic and viscoplastic energy contributions according to

$$\phi - l_c^2\mathrm{Div}(\mathrm{Grad}\phi) = -\frac{l_c}{G_c}\frac{\partial g}{\partial \phi}H_d,\ H_d = \left(J^{cth}\psi_e(\underline{\underline{E}}^{e}) + \psi_{vp}(p)\right) \tag{4}$$

Materials Research Proceedings 73 (2026) 151-155 https://doi.org/10.21741/9781644904459-30

This formulation is derived in a thermodynamically consistent manner using the micro-force balance framework proposed by Zhen et al. [7], assuming non-dissipative damage evolution. Lithium transport is governed by a diffusion equation derived from chemical potential μ_{ch} as follows

$$\dot{C}_s + \mathrm{Div}\, \underline{J_s} = 0, \underline{J_s} = -\frac{D_s C_s}{R_b \Theta} \det(\underline{\underline{F}})\, \underline{\underline{C}}^{-1} \mathrm{Grad}\mu_{ch},\ \mu_{ch} = \frac{\partial \psi}{\partial C_s} - \frac{\Omega}{3} J^{th}\, \underline{\underline{M}}^e : \underline{\underline{1}} \tag{5}$$

Where D_s is the Diffusion coefficient, R_b the gas constant, $\underline{\underline{C}}$ the right Cauchy tensor, and $\underline{\underline{M}}^e$ the elastic Mandel stress.

Electrochemically consistent boundary conditions are imposed at the particle surface through Butler–Volmer kinetics [8], with the overpotential obtained from a Pseudo two Dimensional (P2D) electrochemical model. Finally, incorporating the chemical free energy contribution into the damage driving force is proposed as a possible extension. In this formulation, chemically driven diffusion would be attenuated in damaged regions without being fully suppressed. Thermal effects are introduced through isotropic thermal expansion. The associated heat balance equations are part of the general formulation but are not presented here to focus on the chemo-mechanical aspects.

Numerical Results

Numerical simulations, performed using COMSOL Multiphysics, illustrate the ability of the framework to capture diffusion-driven ductile fracture and progressive damage. The model is applied to a silicon particle under lithiation. The results are presented in three steps. First, the influence of diffusion on ductile crack propagation is investigated; second, the role of viscoplasticity is analysed; and third, the effect of length scale and C-rate on continuum damage evolution is assessed. Fig. 1(a–b) compares crack evolution without and with diffusion-induced chemical expansion. In both cases, cracks propagate along similar trajectories, but diffusion accelerates crack growth due to additional stresses induced by concentration gradients. This acceleration is attributed to additional stresses induced by lithium concentration gradients, which enhance local plastic deformation and increase the damage driving force, even in the absence of mechanical feedback on transport.

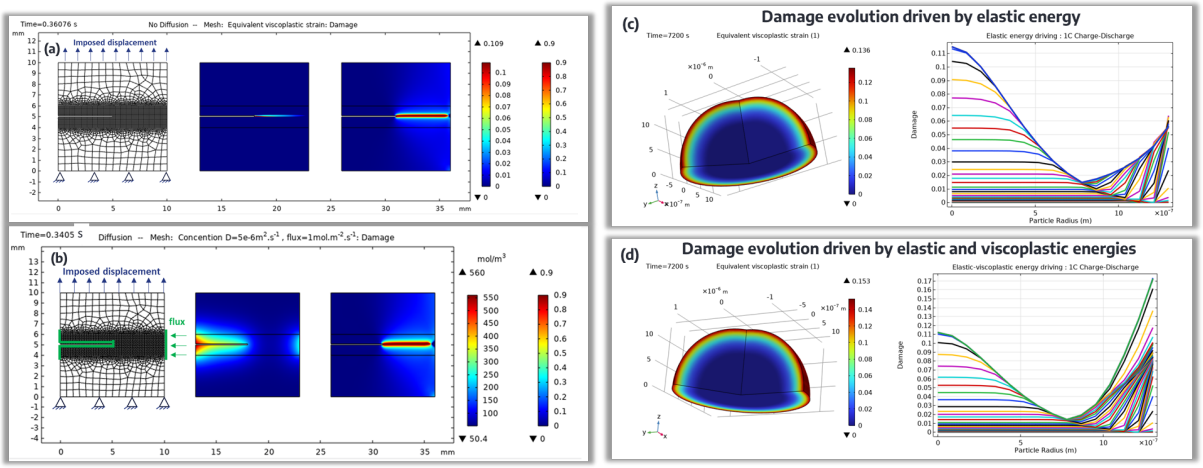

Figure 1: Crack propagation (a) without diffusion and (b) with diffusion-induced chemical expansion. Damage evolution in a silicon particle using a reduced characteristic length $10^{-2} * l_c$*: (c) elastic-energy-driven damage and (d) elastic–viscoplastic-energy-driven damage.*

The model is subsequently applied to simulate the lithiation of a single silicon particle using a fully coupled chemo-mechanical formulation. Fig. 1(c–d) shows the evolution of the damage field for two different damage driving mechanisms. When damage is driven solely by elastic energy, damage initiates at the particle surface and progressively propagates toward the center during

Materials Research Proceedings 73 (2026) 151-155 https://doi.org/10.21741/9781644904459-30

lithiation. Once the center is reached, damage becomes more pronounced in the core due to elastic energy accumulation in the constrained region. In contrast, when viscoplastic dissipation is included in the driving force, damage localizes predominantly at the particle surface, where viscoplastic deformation is dominant, and remains higher at the surface throughout the loading process.

The influence of the characteristic length and C-rate is summarized in Fig. 2. Using $l_c = \sqrt{\left(D_s * \frac{3600[s]}{C_{rate}}\right)}$ together with a fracture energy $G_c = 8J * m^{-2}$ derived from Density Functional Theory (DFT) calculations results in complete particle damage in less than 300 s, which is unsuitable for modelling progressive degradation or fatigue over multiple cycles (Fig. 2-a). A more progressive damage evolution is obtained by reducing the characteristic length by a factor of 10^2 which is equivalent to increasing $G_c$to approximately $800J * m^{-2}$. Increasing the current rate systematically accelerates damage accumulation due to steeper concentration gradients and enhanced viscoplastic deformation as shown in Fig. 2-b.

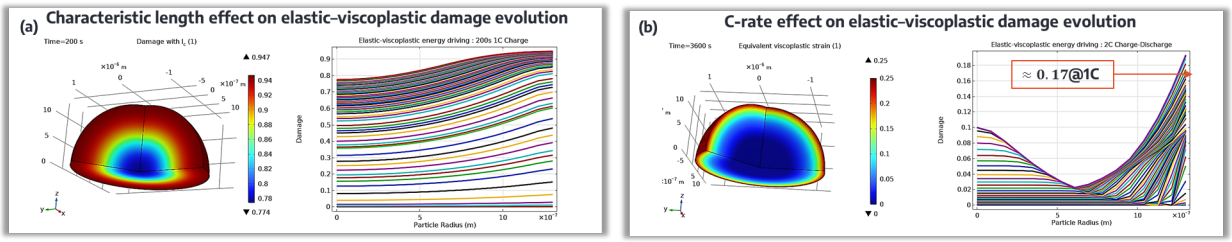

Figure 2: Influence of model parameters on damage evolution: (a) effect of the characteristic length using the reference value l_c, and (b) effect of the current rate (C-rate) using a reduced characteristic length $10^{-2}l_c$.

Conclusions

A finite-strain ductile phase-field framework has been proposed to analyze chemo-mechanically driven damage in silicon composite anodes. The results show that lithium diffusion accelerates ductile crack propagation under identical mechanical loading through chemically induced stress redistribution. At the particle scale, the simulations highlight the critical role of viscoplastic dissipation in controlling damage localization, leading to surface-dominated degradation during lithiation. The strong sensitivity of damage evolution to the characteristic length, fracture energy, and current rate underlines the importance of consistent parameter identification across scales. Overall, the proposed framework provides a solid basis for investigating degradation, fatigue, and lifetime of silicon-based anodes, as it can qualitatively reproduce key damage evolution trends reported in literature.

Acknowledgment

This work was carried out within a CIFRE Ph.D. program funded by the French National Association for Research and Technology (ANRT), in partnership with STELLANTIS. The authors gratefully acknowledge the financial support provided by the ANRT and the industrial partner.

References

[1] M.T. McDowell, S.W. Lee, W.D. Nix, Y. Cui, 25th Anniversary Article: Understanding the Lithiation of Silicon and Other Alloying Anodes for Lithium-Ion Batteries, Adv. Mater. 25 (2013) 4966–4985. https://doi.org/10.1002/adma.201301795

[2] T. Hu, B. Talamini, A.J. Stershic, M.R. Tupek, J.E. Dolbow, A variational phase-field model for ductile fracture with coalescence dissipation, Comput. Mech. 68 (2021) 311–335. https://doi.org/10.1007/s00466-021-02033-1

[3] C.V. Di Leo, E. Rejovitzky, L. Anand, Diffusion–deformation theory for amorphous silicon anodes: The role of plastic deformation on electrochemical performance, Int. J. Solids Struct. 67–68 (2015) 283–296. https://doi.org/10.1016/j.ijsolstr.2015.04.028

[4] S.R. Shah, L.S. de Vasconcelos, K. Zhao, Computational Modeling of Electrochemomechanics of High-Capacity Composite Electrodes in Li-Ion Batteries, J. Appl. Mech. 89 (2022) 081005. https://doi.org/10.1115/1.4054759

[5] J. Yang, W. Tan, Fully coupled multiphysics modelling of fracture behaviour in silicon particles during lithiation–delithiation using the phase-field method, Engineering with Computers 42 (2026) 7. https://doi.org/10.1007/s00366-025-02233-w

[6] V.A. Sethuraman, M.J. Chon, M. Shimshak, V. Srinivasan, P.R. Guduru, In situ measurements of stress evolution in silicon thin films during electrochemical lithiation and delithiation, J. Power Sources 195 (2010) 5062–5066. https://doi.org/10.1016/j.jpowsour.2010.02.013

[7] Y. Zhen, K. Wu, Y. Lu, M. Liu, L. He, Y. Ni, A thermodynamically-consistent non-isothermal phase-field model for probing evolution of crack propagation and phase transformation, Int. J. Mech. Sci. 270 (2024) 109122. https://doi.org/10.1016/j.ijmecsci.2024.109122

[8] M. Masmoudi, Z. Moumni, F. Bidault, Analysis of the Thermo-Mechanical-Chemical Coupled Response of a Lithium-Ion Battery Particle during a Charge-Discharge Cycle, J. Electrochem. Soc. 166 (2019) A5445–A5461. https://doi.org/10.1149/2.0631903jes

Materials Research Proceedings 73 (2026) 156-159 https://doi.org/10.21741/9781644904459-31

A Mixed Formulation for Geometrically Exact Beams based on the Concept of Discrete Curvature

Alexander HUMER[1,a *], Ivo STEINBRECHER[2,b] and Astrid PECHSTEIN[1,c]

[1]Institute of Technical Mechanics, Johannes Kepler University Linz, Austria

[2]Institute for Mathematics and Computer-Based Simulation, University of the Bundeswehr Munich, Germany

[a]alexander.humer@jku.at, [b]ivo.steinbrecher@unibw.de, [c]astrid.pechstein@jku.at

Keywords: Geometrically Exact Beams, Mixed Formulation, High-Order Interpolation, Discrete Curvature, Finite Elements

Abstract. We present a mixed finite element for geometrically exact (Simo–Reissner) beams that introduces the moment vector as an independent field and permits element-local, discontinuous rotations for a simple, efficient discretization; discrete curvature treats rotation jumps consistently. Objectivity is retained via interpolation of relative rotations, and the total Lagrangian setting ensures path-independence. Benchmarks show optimal convergence and accuracy across slenderness and approximation orders. The lowest-order element uses element-constant rotations, avoiding interpolation.

Introduction

It is safe to say that beam theories and corresponding finite-element formulations have come a long way, especially when it comes to problems involving finite spatial deformations. The theoretical framework traces back to the work of Reissner [1], Antman [2], and Simo [3,4], who extended Timoshenko's theory for shear-deformable beams to large-deformation (geometrically exact) regimes. Simo and Vu-Quoc introduced arguably the first successful finite-element formulation [3,4], which remains influential in the numerical analysis of beams to this day. Ever since, numerous finite-element formulations (see the seminal paper by Meier et al. [5] for an overview) have been proposed, all of which mainly address one or more of the following key challenges: parameterization of large spatial rotations, objectivity of strain measures, path independence, and locking phenomena in highly slender structures.

We present a novel finite-element formulation [6] for geometrically exact beams that handles these challenges in a way that is both simple and effective. Within a mixed framework, the (material) moment vector is introduced as an independent field. The proposed concept of discrete curvature allows discontinuous interpolation of moments and rotations, which, along with reduced integration, eliminates locking. Objectivity of curvature measures is ensured by interpolating element-local relative rotations resulting from a multiplicative split of rotations into elementwise constant and higher-order relative contributions, realized at the shape-function level.

Methodology

In the proposed mixed formulation, the moment vector is introduced as an independent field. With the moment vector as additional field, we can shift the continuous approximation from the rotations to the moment vector. In other words, the rotation vector is defined element-local, without need for continuity at mesh nodes. Instead, continuity is enforced in weak sense through the (extended) principle of virtual work. For this purpose, a Legendre transform of the energy density associated with twist and curvature of the beam's axis is adopted, which, in case of linear constitutive relations, can be computed explicitly.

Content from this work may be used under the terms of the Creative Commons Attribution 3.0 license. Any further distribution of this work must maintain attribution to the author(s) and the title of the work, journal citation and DOI. Published under license by Materials Research Forum LLC.

Materials Research Proceedings 73 (2026) 156-159 https://doi.org/10.21741/9781644904459-31

For the work integral to be well-defined, rotations need to be at least weakly differentiable. We introduce the concept of discrete curvature in order to consistently evaluate the weak form at the element interfaces (i.e., vertices), where rotations lack continuity.

In our beam element, we additionally include nodal rotations as unknowns in the sense of hybridization, which allows us to directly impose boundary conditions on rotations.

Summarizing, the proposed beam element uses the following unknown fields:

- Positions interpolated by continuous, piecewise polynomial functions of order k,
- Element-local moments interpolated by discontinuous, piecewise polynomial functions of order k,
- Nodal incremental rotation vectors, single-valued at mesh nodes (no interpolation in element interior)
- Element-local rotations multiplicatively split into a constant part and higher-order contributions with zero mean of order $k - 1$.

The proposed beam element allows for arbitrary orders. When combined with reduced integration in the strain energy associated with force strain, all locking effects are eliminated irrespective of the beam's slenderness. Remarkably, the proposed formulation admits a locking-free lowest-order ($k = 1$) element that uses elementwise constant rotations, thereby avoiding any interpolation of rotations.

Numerical Results

As a first example, we study the classical benchmark of an octant of a circle subjected to an out-of-plane force proposed by Bathe and Bolourchi [7] (see Fig. 1). Irrespective of the beam's slenderness, we obtain optimal rates of convergence (see Fig. 2).

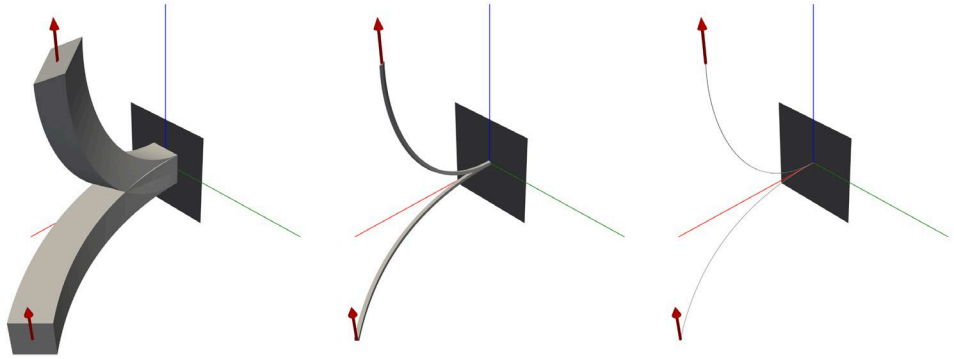

Figure 1: Arc-segment under out-of-plane force: undeformed and deformed configurations for slenderness $\rho = 10$ (left), $\rho = 100$ (center), and $\rho = 1000$ (right).

Materials Research Proceedings 73 (2026) 156-159 https://doi.org/10.21741/9781644904459-31

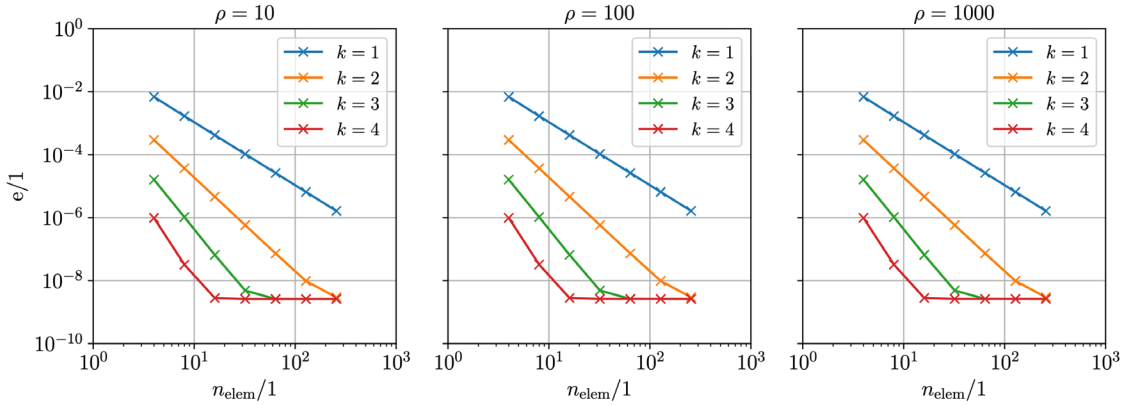

Figure 2: Arc-segment under out-of-plane force: rates of convergence for beam elements of orders $k = 1,\ldots,4$ and different values of slenderness; $\rho = 10$ (left), $\rho = 100$ (center), and $\rho = 1000$ (right).

The second example of a fork-like structure is meant to demonstrate that the proposed formulation can be applied to structures with kinks and branches, which are common in real-world problems. The fork is subjected to a pair of opposing out-of-plane forces applied at the tips of the fork's tines, see Fig. 3. First, we apply the force at one tine only (Fig. 3, center), before applying the opposing force.

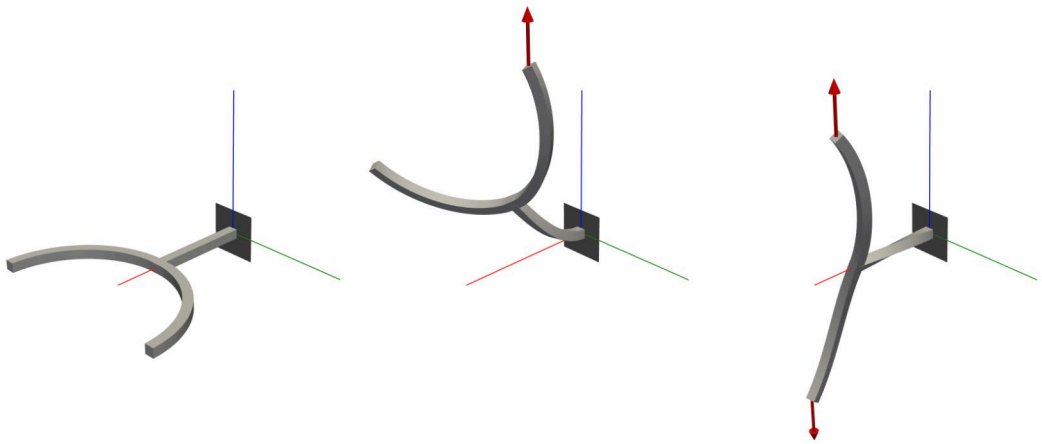

Figure 3: Fork structure subjected to a force couple: undeformed configuration (0; left), equilibrium configuration under a single force (1; center), and final configuration under a force couple (2; right). Red arrows indicate the forces acting in the respective configurations.

Table 1: Fork structure: components of the tip-displacement in configurations (1) and (2) for element orders $k = 1,\ldots,4$ obtained with three elements per segment (top) and ten elements per segment (bottom).

k	n_{elem}	$u_1^{(1)}/L$	$u_2^{(1)}/L$	$u_3^{(1)}/L$	$u_1^{(2)}/L$	$u_2^{(2)}/L$	$u_3^{(2)}/L$
1	9	−1.08435	−0.759430	1.98136	−0.599783	−0.731959	1.46555
2	9	−1.08857	−0.746239	1.97810	−0.598926	−0.727164	1.47968
3	9	−1.08861	−0.746318	1.97840	−0.598811	−0.727135	1.47997
4	9	−1.08861	−0.746307	1.97830	−0.598829	−0.727134	1.47986
1	30	−1.08821	−0.747378	1.97836	−0.598936	−0.727541	1.47857
2	30	−1.08861	−0.746306	1.97830	−0.598830	−0.727134	1.47986
3	30	−1.08861	−0.746307	1.97830	−0.598829	−0.727134	1.47986
4	30	−1.08861	−0.746307	1.97830	−0.598829	−0.727134	1.47986

Numerical values of the displacement vector at the tip in configurations (1) and (2) are listed in Table 1. As with the previous example, we study element orders $k = 1,\ldots,4$ and two levels of mesh refinement. The coarse mesh (upper half) uses three elements per segment, whereas ten elements are employed in the fine mesh (lower half). We can observe excellent results, with the tip-displacement being already converged for the coarse mesh when using fourth-order elements ($k = 4$). For the fine mesh, even linear elements $k = 1$ show relative errors in the displacements on a permille level.

Conclusions

We have proposed a new mixed method for geometrically exact beams, and, on this basis, we have developed a beam element that shows superior numerical properties. The moment vector has been added as independent field. A discontinuous interpolation of the rotations has proven central to our method. For the virtual work to be well-defined at element interfaces, the notion of a discrete curvature has been introduced. Hybridization allows conventional boundary conditions to be imposed in a straightforward way. Our beam element shows optimal rates of convergence irrespective of the polynomial order employed and the beam's slenderness.

References

[1] Reissner, E.: On one-dimensional finite-strain beam theory: The plane problem. Zeitschrift für angewandte Mathematik und Physik (ZAMP) (1972) https://doi.org/10.1007/BF01602645

[2] Antman, S.S.: The Theory of Rods. In: Truesdell, C. (ed.) Linear Theories of Elasticity and Thermoelasticity vol. VIa/2, pp. 641–703. Springer, Berlin Heidelberg (1973) https://doi.org/10.1007/978-3-662-39776-3_6

[3] Simo, J.C.: A finite strain beam formulation. The three-dimensional dynamic problem. Part I. Computer Methods in Applied Mechanics and Engineering 49(1), 55–70 (1985) https://doi.org/10.1016/0045-7825(85)90050-7

[4] Simo, J.C., Vu-Quoc, L.: A three-dimensional finite-strain rod model. part II: Computational aspects. Computer Methods in Applied Mechanics and Engineering 58(1), 79–116 (1986) https://doi.org/10.1016/0045-7825(86)90079-4

[5] Meier, C., Popp, A., Wall, W.A.: Geometrically Exact Finite Element Formulations for Slender Beams: Kirchhoff–Love Theory Versus Simo–Reissner Theory. Archives of Computational Methods in Engineering 26(1), 163–243 (2019) https://doi.org/10.1007/s11831-017-9232-5

[6] Humer, A., Steinbrecher, I., Pechstein, S.: Mixed Finite Elements for Geometrically Exact Beams using Discontinuous Rotations and Discrete Curvature. Acta Mechanica, (2026) https://doi.org/10.1007/s00707-026-04768-5

[7] Bathe, K.-J., Bolourchi, S.: Large displacement analysis of three-dimensional beam structures. International Journal for Numerical Methods in Engineering 14(7), 961–986 (1979) https://doi.org/10.1002/nme.1620140703

Materials Research Proceedings 73 (2026) 160-165 https://doi.org/10.21741/9781644904459-32

Fatigue Limit Evaluation of Hybrid Fibre Reinforced Polymer-Matrix Composites (PMC) Using Self-Heating Tests and Embedded Piezoelectric Transducers

Ones GAMMOUDI[1,2,a*], Walid HARIZI[1], Jamal NAJD[1], Enrico ZAPPINO[2], Erasmo CARRERA[2]

[1]Roberval (Mechanics, Energy and Electricity), Université de Technologie de Compiègne, France

[2]MUL2 Lab, Politecnico di Torino, Italy

[a]ones.gammoudi@utc.fr

Keywords: Hybrid PMC, Flax/Glass Fibres, Fatigue Limit, Self-Heating, SMART Composites, Piezoelectric transducers, Structural Health Monitoring

Abstract. Hybrid glass/flax fibre-reinforced polymer-matrix composites offer stiffness and damping, but conventional fatigue-limit assessment is costly and time-consuming. This study evaluates a rapid self-heating method combined with embedded polyvinylidene fluoride (PVDF) transducers. Five specimens manufactured by liquid resin infusion underwent tension-tension loading blocks at 5 Hz. Surface temperature and sensor capacitance were monitored throughout testing. All specimens failed during the eighth block, confirming repeatable behaviour. Both indicators increased gradually at low stresses and sharply as damage accumulated. Bilinear analysis produced consistent fatigue-limit estimates from thermal and electrical responses. Post-mortem microscopy revealed delamination, fibre breakage, and interfacial debonding. The results support self-heating as an efficient alternative to conventional S-N testing and demonstrate the potential of embedded PVDF sensors for in-situ fatigue-damage monitoring.

1. INTRODUCTION

Over the past few decades, Polymer-Matrix Composites (PMC) have established themselves as materials of choice across a wide range of structural applications, owing to their well-known strength-to-weight ratio, corrosion resistance, and passive vibration-damping capacity [1]. Hybrid fibre-reinforced composites have been shown to achieve improved mechanical properties, vibration damping, and sound absorption compared to single-fibre systems, making them attractive candidates for fatigue-critical designs. Yet, accurately determining their fatigue limit remains a prerequisite for any reliable structural application. The conventional approach relies on constructing S-N curves, which involve cycling a series of specimens at progressively higher stress levels until failure. While well established, this method is notoriously time-consuming and costly. As an alternative, the self-heating approach exploits the temperature rise generated by the internal dissipation mechanisms under cyclic loading to identify fatigue-related thresholds in a fraction of the time (≈1 day). However, despite its proven effectiveness on metals and monolithic PMC, this method remains insufficiently applied and studied for hybrid PMCs, where the anisotropic nature of the material and the complexity of its damage mechanisms complicate the interpretation of thermal signatures. The present work addresses this gap. The originality of this study lies in the application and adaptation of the self-heating methodology to hybrid Glass/Flax Fibre Reinforced Polymer composites, to establish a rapid and reliable experimental protocol for the estimation of their fatigue limit.

Content from this work may be used under the terms of the Creative Commons Attribution 3.0 license. Any further distribution of this work must maintain attribution to the author(s) and the title of the work, journal citation and DOI. Published under license by Materials Research Forum LLC.

Materials Research Proceedings 73 (2026) 160-165 https://doi.org/10.21741/9781644904459-32

2. MATERIALS AND EXPERIMENTAL METHODOLOGY

In this study, smart hybrid composite specimens were manufactured using the Liquid Resin Infusion (LRI) process. The integration of piezoelectric transducers directly within the laminate during manufacturing makes these specimens "smart" in the sense that it is possible to monitor their mechanical response under cyclic loading. The following subsections describe the manufacturing procedure, the sensor integration strategy, and the fatigue testing protocol.

2.1 Hybrid PMC Structure Manufacturing

The specimens were fabricated using glass and flax fibres as illustrated in **Figure 1**, combining the structural stiffness of glass fibre plies with the natural damping capacity of flax ones as a core layer. The reinforcing plies consist of four woven glass fibre fabrics on both outer faces, enclosing a flax fibre layer of two plies at the center, all consolidated within an unsaturated polyester resin matrix mixed with 1% methyl ethyl ketone peroxide (MEKP) hardener. During the manufacturing process (LRI), the dry fibrous plies are laid up on a glass table under vacuum, and the resin is drawn through the preform by the pressure differential of 0.6 bars until full impregnation is achieved, after which the assembly is left to cure at room temperature.

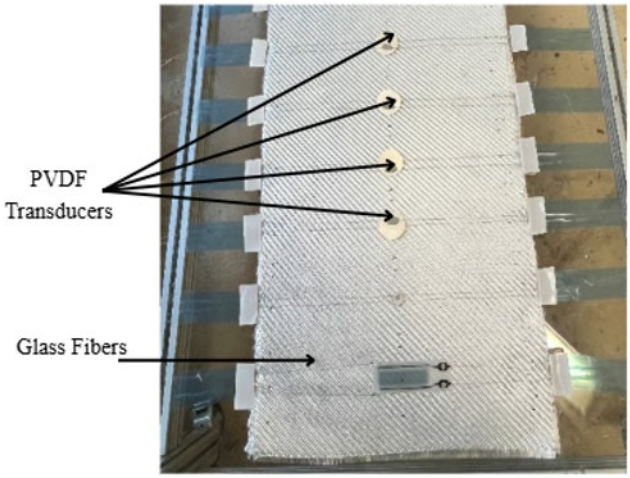

Figure 1: Transducers positioning.

2.2 Piezoelectric Transducers Integration

In order to monitor the mechanical response of the specimens during the fatigue loading, Polyvinylidene Fluoride (PVDF) piezoelectric transducers were embedded within the laminate during the manufacturing stage, prior to resin infusion. Each specimen incorporates two circular PVDF transducers of 25 mm in diameter, one positioned at the center of each glass/flax fibre interface, between the outer glass ply and the flax core on each face of the specimen.

The transducers were carefully aligned and fixed in position before positioning the vacuum bag, ensuring minimal disturbance to the fibre architecture. Their electrical connections (copper wires) were routed outside the vacuum bag and protected during infusion to allow real-time signal acquisition during the mechanical test.

2.3 Fatigue Testing Protocol

Fatigue tests were conducted under uniaxial tension-tension cyclic loading using a hydraulic MTS testing machine equipped with a load cell of 50 KN and operated at a crosshead speed of 2 mm/min for loading and unloading ramps. The self-heating test procedure consists of applying successive loading blocks of increasing magnitude to each specimen, where each block is maintained for a fixed number of cycles at a frequency of 5 Hz, sufficient to allow the surface temperature to reach a stabilized value. The temperature response was measured using thermocouples affixed to the surface of the specimen. Two additional thermocouples were added to the machine jaws to

Materials Research Proceedings 73 (2026) 160-165 https://doi.org/10.21741/9781644904459-32

compensate for room temperature changes and heating of the jaws. In parallel, the capacitance response of the specimen was continuously recorded throughout the test using embedded PVDF transducers.

The stabilized temperature at the end of each stress block is then plotted as a function of the applied stress amplitude. The Two Curves Method (TCM or Luong method) is used to obtain the fatigue limit [2], identified from the characteristic change in slope of this curve, which reflects the onset of significant internal damage accumulation within the material.

3. Results and Discussion

The self-heating tests were carried out on five hybrid Glass/Flax specimens under tension-tension cyclic loading. A consistent and reproducible behaviour was observed across all tested specimens: in each case, the failure occurred at the 8th loading block, indicating a high degree of repeatability in both the manufacturing process and the final rupture response of the PMC material.

3.1 Typical Thermal and Capacitance Responses

A representative evolution of the corrected temperature rise and the electrical capacitance of the embedded PVDF transducers as a function of the applied stress blocks is presented in **Figure 2**. Both signals exhibit a similar trend: at low stress amplitudes, the temperature and capacitance values increase gradually and remain relatively stable from one block to the next, reflecting a regime of limited internal dissipation. As the applied stress increases, a more pronounced and accelerating rise in both indicators is observed, consistent with the progressive accumulation of damage within the hybrid laminate. The final rupture, systematically occurring at the 8th block, is preceded by a sharp change in the temperature signal.

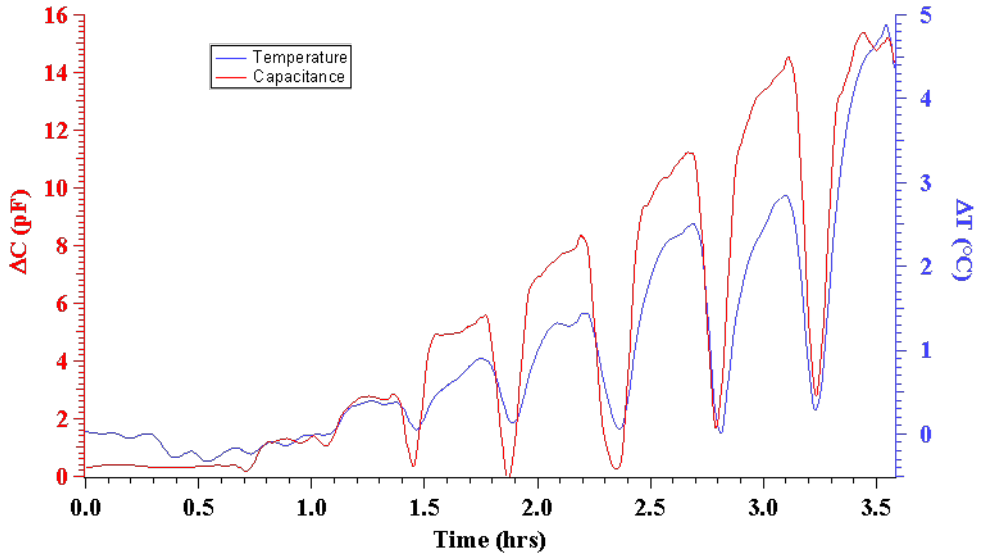

Figure 2: Typical capacitance and temperature variation responses during the self-heating tests conducted on the hybrid PMC.

3.2 Fatigue limit estimation

The stabilized temperature and capacitance values were extracted from the curves at the end of each stress block for all five specimens. The mean values were then calculated across the specimen population and plotted against the step loads.

The relatively narrow standard deviation bands observed across the five specimens further confirm the reproducibility of the experimental protocol and the reliability of the embedded sensor measurements.

Materials Research Proceedings 73 (2026) 160-165 https://doi.org/10.21741/9781644904459-32

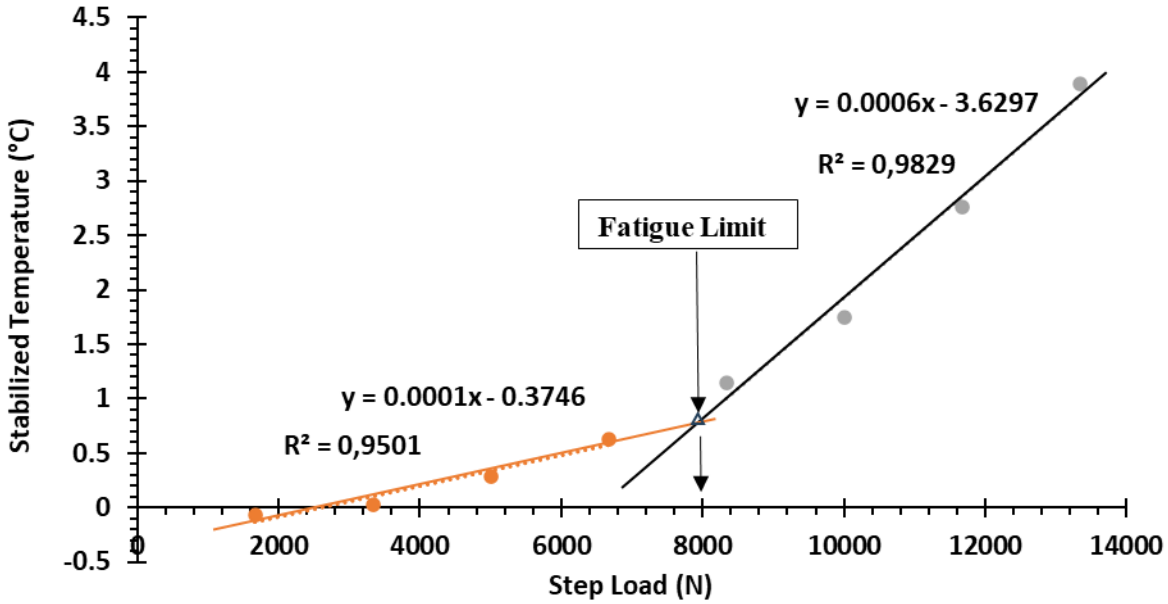

Figure 3:a) Typical average stabilized temperature recorded vs the maximum stresses applied during the self-heating test

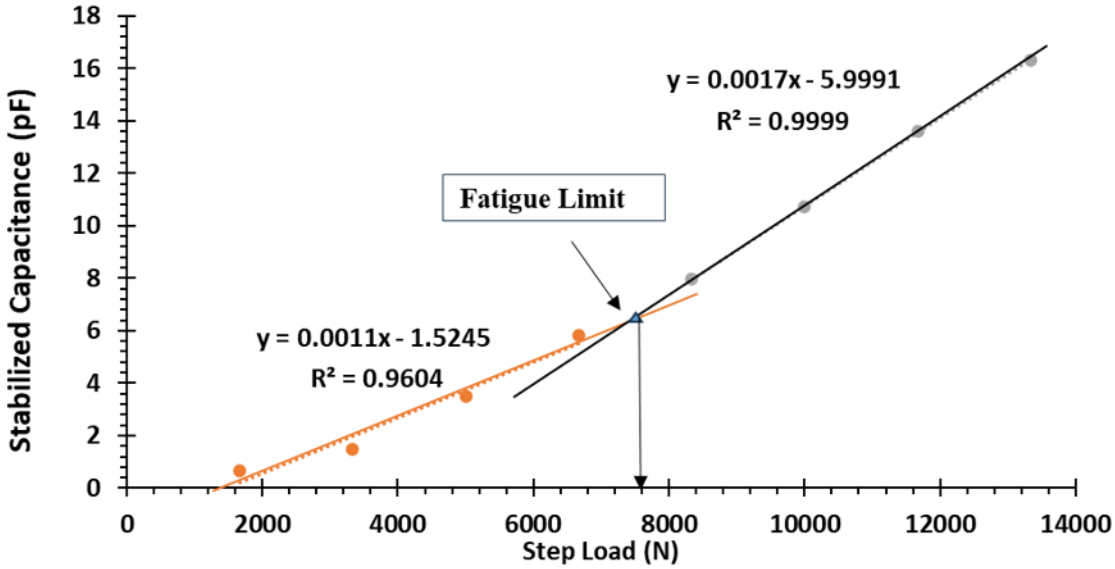

Figure 3:b) Average stabilized capacitance of the embedded PVDF transducers vs the maximum stresses applied during the test.

The fatigue limit of the hybrid PMC composite was determined from the mean response curves using the bilinear intersection method as shown in Figure 3. This change in slope reflects the onset of significant and irreversible damage mechanisms within the PMC material. The intersection between these two linear regimes (a first with a fairly low slope and a second more pronounced with a higher slope) provides a quick estimate of the fatigue limit of this PMC material.

Importantly, both indicators (stabilized temperature and electrical capacitance) yielded consistent and mutually corroborating fatigue limit values similar to [3]. This agreement between a thermal indicator and an electrical one is a notable finding of this study, as it reinforces the physical interpretation of the identified threshold and demonstrates that the embedded PVDF transducers can serve as a reliable in-situ characterization of hybrid PMC specimens.

Materials Research Proceedings 73 (2026) 160-165 https://doi.org/10.21741/9781644904459-32

The fatigue limit determined in this study is discussed in light of the material's hybrid architecture, and the implications of these results for the broader application of self-heating methods to similar composite systems are addressed in the concluding section.

4. Post-Mortem inspection

In complement of the fatigue limit obtained from the thermal and capacitive indicators, a post-mortem fractographic inspection as performed on the failed specimens using Scanning Electron Microscopy (SEM) in order to identify the underlying damage mechanisms. **Figure 4** presents representative micrographs of the fracture regions: delamination between plies (a), fibre breakage (b) and interfacial debonding (c).

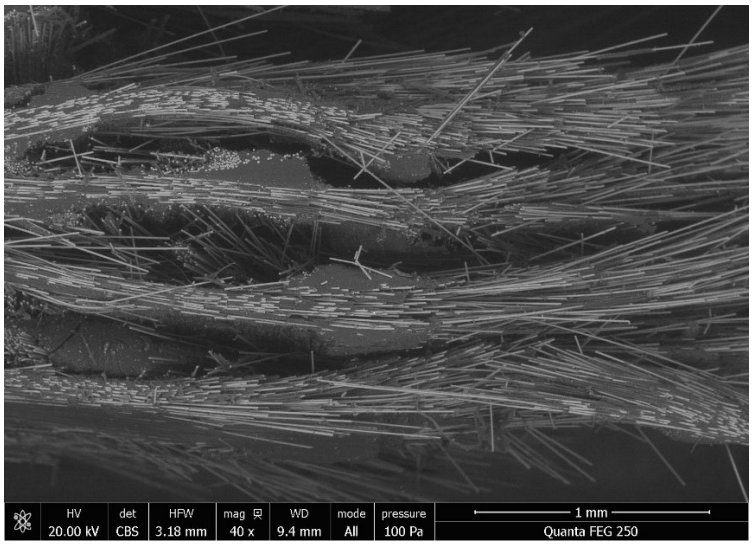

(a)

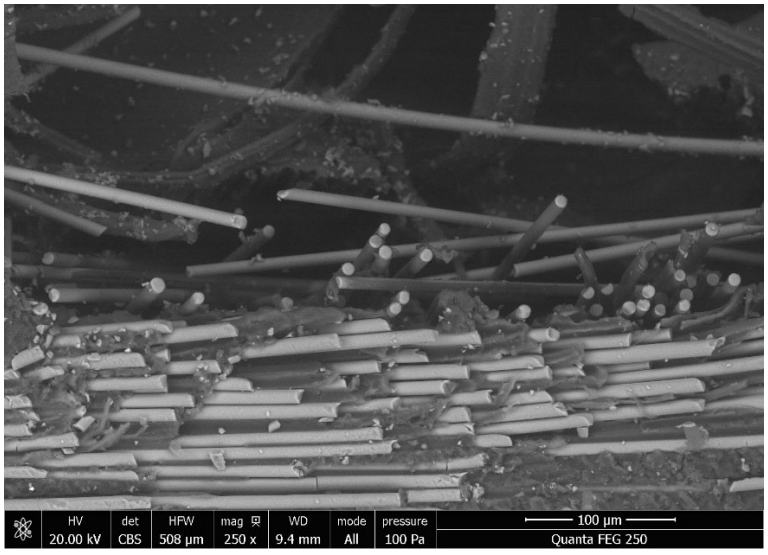

(b)

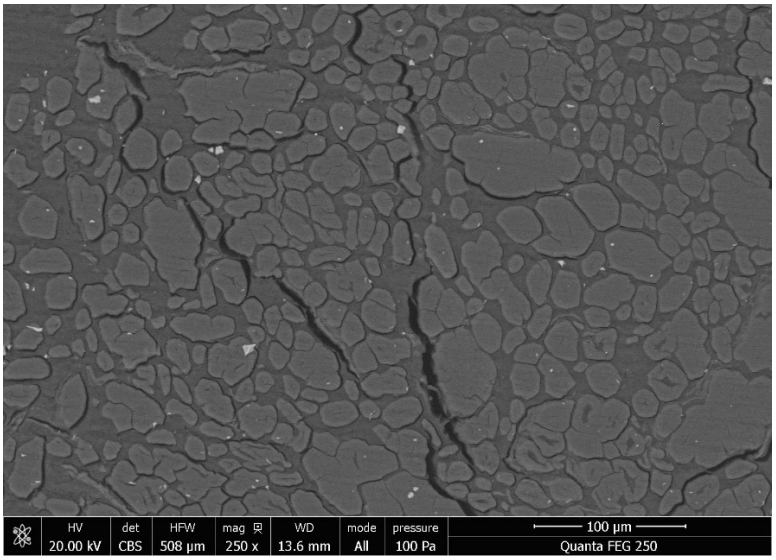

(c)

Figure 4: Damage mechanisms: a) delamination between plies, b) Fibre breakage, c) Interfacial debonding.

CONCLUSION

This study presents the fatigue characterization of flax/glass hybrid PMCs manufactured by LRI using a combined self-heating and embedded piezoelectric monitoring approach. The principal conclusions are:

- The self-heating approach successfully estimates the fatigue limit of the hybrid composite from SMART configurations under tension-tension cycling at 5 Hz, providing a rapid alternative to conventional S-N testing.
- Embedded piezopolymer transducers deliver a reliable in-situ capacitance indicator of fatigue damage that converges with the fatigue limit obtained by thermal signature.

Future work will extend the investigation to different fibre volume fractions, perform post-fatigue micro-tomographic damage analysis, and evaluate the long-term signal stability of the embedded transducers under extended cyclic loading.

ACKNOWLEDGEMENTS

The author would like to thank Région Hauts-de-France and Politecnico di Torino for funding this work as part of the doctoral thesis of Ones Gammoudi.

REFERENCES

[1] X. Tang et X. Yan, « A review on the damping properties of fiber reinforced polymer composites », J. Ind. Text., vol. 49, no 6, p. 693-721, janv. 2020. https://doi.org/10.1177/1528083718795914

[2] W. Wei, L. He, Y. Sun, et X. Yang, « A Review of Fatigue Limit Assessment Using the Thermography-Based Method », Metals, vol. 14, no 6, p. 640, mai 2024. https://doi.org/10.3390/met14060640

[3] J. Najd, W. Harizi, Z. Aboura, E. Zappino, et E. Carrera, « Rapid estimation of the fatigue limit of Smart Polymer-Matrix Composites (PMC) using the self-heating tests », Compos. Struct., vol. 282, p. 115039, févr. 2022. https://doi.org/10.1016/j.compstruct.2021.115039

Materials Research Proceedings 73 (2026) 166-169 https://doi.org/10.21741/9781644904459-33

Novel Glass Fibre Z-Pins to Improve the Delamination Bridging Performance of Laminated Composite Materials

Romain RUTAR[1,2,a*], Luiz KAWASHITA[1], Eduardo SANTANA DE VEGA[1], Christophe BOUVET[2,c*], Bruno CASTANIÉ[2], Stephen R HALLETT[1,b*]

[1]Bristol Composites Institute (BCI), University of Bristol, University Walk, Bristol BS8 1TR, UK

[2]Université de Toulouse, Institut Clément Ader, ISAE-SUPAERO/INSA/IMT Mines Albi/UPS/CNRS, Toulouse, France

[a]cl24784@bristol.ac.uk, [b]Stephen.Hallett@bristol.ac.uk, [c]christophe.bouvet@isae-supaero.fr

Keywords: Z-Pinning, Laminated Composite Materials, Through-Thickness Reinforcement, Glass Fibre

Abstract. Laminated composite stiffened panels are sensitive to impact-induced interlaminar damage, which can drastically diminish their strength. Z-pinning can help overcoming this issue by preventing delamination propagation. Among other, impact induces local mode II driven fracture, for which industry standard carbon fibre (CF) Z-pins perform poorly. This study exploits on the superior failure strain of S2-glass (GF) fibres to develop Z-pins that maintain effectiveness across a full spectrum of mode mixities. The 0.3mm diameter GF/epoxy pins are produced via in-house micro-pultrusion. To explore the impact of fibre diameter, two distinct configurations, 9µm and 14µm diameter fibres, are considered. These GF-based pins are then benchmarked against industry standard carbon fibre T300/BMI pins. Additionally, in order to separate the contributions of the fibre and that of the resin, T300/epoxy pins are manufactured through the same micro-pultrusion process. Z-pinned samples are loaded across the whole range of mode mixities using a miniature Arcan setup. S2-glass' superior compliance and failure strain delay the transition from Mode I pullout to mode II fibre rupture for GF pins compared to CF pins. Furthermore, in the event of GF pins rupture under mode II loading, a less brittle failure profile than the T300 pins is observed.

Introduction

Laminated composite materials are highly anisotropic, layered materials. Consequently, matrix cracking (inside the plies) and delamination (between the plies) can propagate through these preferential crack directions. This may occur in mode I (opening), mode II and mode III. This makes the material particularly sensitive to impact loading. Under such a loading scenario, localized shear induces matrix cracking, which then triggers delamination in mode I which subsequently propagates between the plies in mode II. The strength of the laminate is then substantially reduced especially under compression. It is therefore of paramount importance to mitigate this interlaminar damage. Regarding stiffened panels, the skin/stiffener interface may also be subject to debonding after impact in a scenario analogous to delamination. This may result in a premature collapse of the structure under subsequent loading. Therefore, such a damage must be prevented and/or stabilized.

In the literature, out-of plane reinforcement is presented as a technique to mitigate this damage, and numerous techniques can be noted. Stitching involves inserting a dry fibres tow orthogonally into a dry preform and securing it on the opposite surface using an additional tow, or the tow itself. Tufting has a similar principle, with the noteworthy difference that the tow is not secured on both sides of the laminate [1].

Content from this work may be used under the terms of the Creative Commons Attribution 3.0 license. Any further distribution of this work must maintain attribution to the author(s) and the title of the work, journal citation and DOI. Published under license by Materials Research Forum LLC.

Materials Research Proceedings 73 (2026) 166-169 https://doi.org/10.21741/9781644904459-33

Z-pinning is one of these out-of plane reinforcement techniques. Pre-cured composite cylindrical rods ("Z-pins" with a diameter generally comprised between 0.3 mm and 1 mm) are inserted through the thickness of an uncured laminate (the cross-section of an inserted pin can be seen in Figure 1a). When delamination opens the material, the pins are extracted from one side of the laminate. This process mainly dissipates frictional energy at the pin/laminate interface, which then increases the apparent fracture toughness of the material

Several ways of characterizing the mechanical behaviour of the pins can be found in the literature [2, 3]. Coupon-scale tests can be used for the characterization of industry standard carbon fibre pins. The double cantilever beam (DCB) setup can be used to study mode I (opening) crack propagation. This allows the achievement of a stable and significant crack propagation [4]. The Z-pins are pulled out during the crack propagation, which is a phenomenon called "bridging" and induces a large increase in the critical strain energy release rate (SERR). Three points end-notched flexure (3ENF) or an end-loaded split (ELS) can be considered to study mode II loading [5]. When the crack reaches a Z-pin, it first exhibits elastic deformation, then a partial pullout. Assuming that the pin is sufficiently long, the pin eventually fails at the delamination interface in shear failure and is no longer capable of withstanding any load. Such a failure profile is given in Figure 1b. This leads to a lesser performance compared to mode I due to the near absence of frictional pullout.

Novel material solutions were explored in the literature. Metallic pins show a good performance in mode II, however, exhibit a lesser performance in mode I. This is due to the weak interfacial bond between the pin and the laminate induced by the coefficient of thermal expansion mismatch and the smoother surface of the pin [6]. Fibres with an elevated failure strain have recently been considered to manufacture Z-pins [3]. While industry standard carbon fibre T300/BMI tend to fracture under elevated mode II loading (Figure 1b), polybenzoxazol (PBO) pins are able to get extracted across the whole range of mode-mixities (Figure 1c). These pins are able to accumulate a vast amount of matrix damage while little fibre damage can be noted, which largely improves the dissipated energy during the failure process.

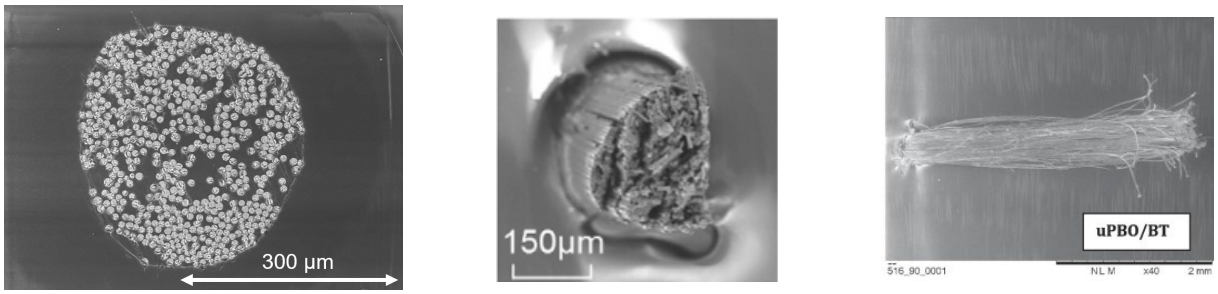

(a) (b) (c)

Figure 1 : (a) Z-pin inserted into a laminate cross-section; (b) CF/BMI industry standard pin after mid-range mode II loading [7]; (c) PBO Z-pin after mid-range mode II loading [3];

While these approaches are promising, their substandard ageing behaviour (galvanic corrosion, fibre degradation…) is cause for concern in the aerospace industry. A Z-pin material that performs well in any mode mixity with limited ageing concerns is yet to be found.

Methodology

In this work, novel Z-pins made of high failure strain S2-glass fibres and epoxy resin (GF) are manufactured via in-house micro-pultrusion and characterized. Two individual fibre diameters are available commercially and their effect is explored through the consideration of two configurations composed of fibres either 9µm or 14µm in diameter. These new configurations are compared to the industry standard T300/BMI pins. In order to rigorously separate the influence of the fibre and

Materials Research Proceedings 73 (2026) 166-169 https://doi.org/10.21741/9781644904459-33

that of the resin, a fourth T300/epoxy configuration is considered and manufactured via the same in-house micro-pultrusion process.

Different steps are necessary to manufacture the Z-pins and then fabricate Z-pinned laminates. The commercial dry glass fibre tow (supplied by AGY© and containing either 9 µm or 14 µm individual fibres) is guided through a splitter to reduce the tow to a size allowing the pultrusion of 0.28mm rods in diameter with approximately 60% fibre volume fraction. The dry fibres are guided into the micro-pultrusion setup using a series of rollers. They first go through a liquid resin bath, through a heated shaping die, then through a linear oven before being wound into a spool. The rods are then post-cured in an oven according to the manufacturer's guidelines. The insertion of the Z-pins cut from the rods into an uncured prepreg laminate involves the use of a specialized machine

Experimental Results

The specimen used to mechanically characterize the Z-pins is visible in Figure 2a. A low number of pins is embedded into a laminate separated at its mid-plane by a PTFE layer to only characterize the behaviour of the pins. Each half of the laminate is loaded across the whole range of mode mixities using a miniature Arcan setup.

It is found that S2-glass pins exhibit a transition from Mode I pullout to mode II fibre rupture around 70% mode II, which is a vast improvement compared to the 40% mode II of the industry standard T300/BMI pins.

In terms of energy, S2-glass 9µm/epoxy pins exhibit around a 4-fold increase in dissipated energy in mode II and 2-fold around 40% mode II compared to T300/BMI. The performances in mode I are comparable. Energy dissipation slightly decreases with fibre diameter, while the resin has a negligible influence

A systematic fractographic analysis is carried out to gain a finer understanding of the superior performance of the S2-glass pins. While their superior performance of S2-glass pins in pure mode II can be explained by a less brittle failure profile, the gain in energy dissipation for mid-range mode mixities can be explained by a difference in the failure mode. Indeed, around 60% mode II, T300/BMI pins are damaged at their root and eventually fail as visible in Figure 2b. On the contrary, while such damage also occurs for the S2-glass pins, they are still pulled out as visible in Figure 2c. This accumulation of substandard damage is essential to the superior behaviour of the S2-glass pins, since they allow a dramatic decrease in the bending stiffness of the pin. This subsequently allows to pin to sustain the higher rotations at the pin root present in elevated mode II loadings.

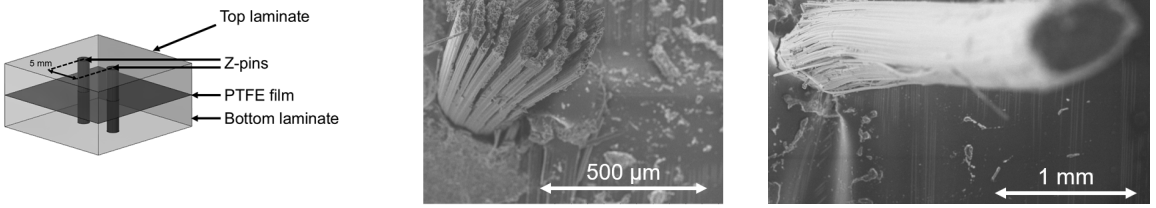

Figure 2: (a) double pin specimen loaded into a miniature Arcan setup; failure profiles under mid-range mode mixity loading (around 60% mode II) (b) CF/BMI pins; (c) S2-glass 9µm/epoxy pins

Conclusions

S2-glass Z-pins were developed and show a promising superior mechanical performance compared to the industry standard T300/BMI Z-pins. Also, it has little cause for concern regarding its aging behaviour (limited aging and no galvanic corrosion issues).

This superiority must then be verified at a scale more representative of a real load case, starting with the coupon scale.

Acknowledgment
The authors would like to thank EPSRC for providing part of the funding through the Doctoral Training Partnership grant, as well as the technical support team from the heavy and light laboratory at the University of Bristol.

References

[1] D. D. R. Cartié, G. Dell'Anno, E. Poulin, et I. K. Partridge, « 3D reinforcement of stiffener-to-skin T-joints by Z-pinning and tufting », *Engineering Fracture Mechanics*, vol. 73, nº 16, p. 2532-2540, nov. 2006. https://doi.org/10.1016/j.engfracmech.2006.06.012

[2] J. Toral Vazquez, B. Castanié, J.-J. Barrau, et N. Swiergiel, « Multi-level analysis of low-cost Z-pinned composite joints Part 1: Single Z-pin behaviour », *Composites Part A: Applied Science and Manufacturing*, vol. 42, nº 12, p. 2070-2081, déc. 2011. https://doi.org/10.1016/j.compositesa.2011.09.018

[3] E. Santana De Vega, G. Allegri, B. Zhang, I. Hamerton, et S. R. Hallett, « Pseudo-ductile behaviour of fibrous composite Z-pins », *Composites Part A: Applied Science and Manufacturing*, vol. 178, p. 108009, mars 2024. https://doi.org/10.1016/j.compositesa.2024.108009

[4] A. Knopp et G. Scharr, « Effect of z-pin surface treatment on delamination and debonding properties of z-pinned composite laminates », *J Mater Sci*, vol. 49, nº 4, p. 1674-1683, févr. 2014. https://doi.org/10.1007/s10853-013-7851-2

[5] F. Pegorin, K. Pingkarawat, S. Daynes, et A. P. Mouritz, « Influence of z-pin length on the delamination fracture toughness and fatigue resistance of pinned composites », *Composites Part B: Engineering*, vol. 78, p. 298-307, sept. 2015. https://doi.org/10.1016/j.compositesb.2015.03.093

[6] B. M'membe, M. Yasaee, S. R. Hallett, et I. K. Partridge, « Effective use of metallic Z-pins for composites' through-thickness reinforcement », *Composites Science and Technology*, vol. 175, p. 77-84, mai 2019. https://doi.org/10.1016/j.compscitech.2019.02.024

[7] M. Yasaee, L. Bigg, G. Mohamed, et S. R. Hallett, « Influence of Z-pin embedded length on the interlaminar traction response of multi-directional composite laminates », *Materials & Design*, vol. 115, p. 26-36, févr. 2017. https://doi.org/10.1016/j.matdes.2016.11.025

Materials Research Proceedings 73 (2026) 170-176 https://doi.org/10.21741/9781644904459-34

Development of ZnO Nanoparticle-Based Voltage Sensor using Copper Oxide Nanofluids via Large-Area Printing Technology

K.R.V. Subramanian*, Niranjan Murthy, Bharath V.

Dept. of Mechanical Engg, Ramaiah Institute of Technology, MSR Nagar, MSRIT Post, Bangalore 560054, India

Keywords: ZnO Nanoparticles, Copper Oxide (CuO) Nanofluid, UV-Visible Spectroscopy, Impedance Analysis, SEM, X-Cut Adhesion Test, Large Area Screen Printing, ZnO Voltage Sensor

Abstract. Zinc Oxide (ZnO) nanoparticles are inorganic metal oxides with remarkable Physical, Electronic Optical and Mechanical properties. ZnO nanoparticles also have excellent piezoelectric properties which makes them an appropriate candidate for a voltage sensor. This research explores the novel use of synthesized ZnO nanoparticles as voltage sensor, employing large-area printing technology. This innovative methodology has not been previously attempted, offering a new approach in the field of voltage sensing technology. The concept behind using ZnO nanoparticles as a voltage sensor involves the capillary action of CuO nanofluid flow, which subjects the ZnO nanoparticles to mechanical stress. This stress, due to the piezoelectric effect, results in the generation of voltage from the net charge produced. The co-precipitation method was utilized for the synthesis of ZnO nanoparticles and chemical reduction method was used for synthesis of copper oxide nanofluids. SEM images show the agglomerated architecture of the synthesized ZnO nanoparticles are more likely to have a uniform piezoelectric motion when subjected to external strain. The consistent scaled-up ZnO: Ethylene glycol ratio was utilized for large area printing observing uniform dispersion of 32.2 nm crystal-sized ZnO particles under pressure denoting an excellent packing density and fill factor. The research presents the use of printed ZnO nanoparticles as a voltage sensor with Copper oxide nanofluid flow, which resulted with an observed voltage of 0.9 mV due to unimpeded nanofluid flow and capillary action, and 0.45 mV was observed with pure capillary action of copper oxide nanofluids.

Introduction

Zinc oxide (ZnO) nanoparticles are nanoscale particles of zinc oxide, ZnO nanoparticles offer several advantages over bulk ZnO. They have a significantly larger surface area-to-volume ratio enhancing their reactivity, unique optical properties due to quantum confinement effects, superior antimicrobial activity, improved photo catalytic efficiency, and enhanced mechanical strength. ZnO nanoparticles can have various shapes, including spherical, rod-like, and flower-like structures, depending on the synthesis method and conditions. It has garnered significant attention due to its distinctive optical, semiconducting, and piezoelectric characteristics [1]. Among the array of piezoelectric materials, ZnO notably has a high mobility of 210 $cm^2V^{-1}s^{-1}$ [2]. The exploration of Zinc oxide (ZnO) nanoparticles is underway due to their intriguing potential properties, including a resistivity modifiable across the range of 10^{-3}–10^5 Ω cm, alongside their transparency within the visible spectrum and high reflectivity in the infrared region [3]. These characteristics position them as viable candidates for various applications, notably serving as infrared reflectors, thick film varistors, gas sensors, and piezoelectric films in surface acoustic wave devices [4]. ZnO stands as a pivotal metal oxide semiconductor within the group II-VI category, exhibiting a wide direct band gap [5]. It demonstrates n-type semiconducting behavior, aligning it with other extensively studied wide band gap semiconductors such as GaN and ZnS, which have witnessed heightened exploration in response to the escalating demand for solid-state

Content from this work may be used under the terms of the Creative Commons Attribution 3.0 license. Any further distribution of this work must maintain attribution to the author(s) and the title of the work, journal citation and DOI. Published under license by Materials Research Forum LLC.

Materials Research Proceedings 73 (2026) 170-176 https://doi.org/10.21741/9781644904459-34

light source sensors in the UV-visible spectral domains. ZnO's adaptability extends to its multi-functional properties, including semiconducting, magnetic, and piezoelectric attributes, making it attractive for a spectrum of electronics and optoelectronics applications [6]. Furthermore, ZnO seves as a transparent conductive oxide that can be used as a thin film for organic light emitting devices [7] which is characterized by high electrical conductivity, substantial binding energy of 60 m eV, elevated optical gain of 320 cm^{-1} at ambient temperature, cost-effectiveness, and non-toxicity [8]. These attributes position ZnO's potential applications spanning solar cells, light-emitting diodes, gas sensors [9], and anti-bacterial and cancer treatment techniques [10].

The generation of an electric charge on a material's surface in response to applied pressure is referred to as the piezoelectric effect. Materials that display this behavior are called piezoelectric materials [11]. ZnO exhibits the highest piezoelectric response (d33) among various tetrahedral semiconductors, positioning it as a superior candidate for electromechanical and communication device applications [12]. The hexagonal wurtzite structure of ZnO, characterized by its 6 mm symmetry, lacks a center of symmetry, making it an exemplary piezoelectric material. ZnO consists of alternating planes of tetrahedrally coordinated Zn^{2+} and O^{2-} ions, stacked sequentially along the c-axis [13]. Initially, the center of the negatively charged electron cloud coincides with the positively charged ionic center. The Zn-O bond distance is 1.983 Å along the c-axis and 1.973 Å in the other three directions of the tetrahedral arrangement of nearest neighbors. When external stress is applied along the c-crystallographic axis, the ZnO crystal experiences a displacement between these two centers, thus generating an electric dipole moment [14].

The researchers involved in this study aim to synthesize and characterize zinc oxide (ZnO) nanoparticles utilizing a diverse array of techniques. The researchers aim to demonstrate the effectiveness of large-area screen printing through adhesion tests and endeavor to represent the potential utility of ZnO nanoparticles as voltage sensors through evident outcomes of various characterization methodologies employed in this research.

Experimental section

Materials

Analytical-grade chemicals were utilized in this research. The synthesis of ZnO nanoparticles involved the use of Zinc Nitrate($Zn(NO3)_2$) sourced from Otto Chemie Pvt Ltd, Hexamine ($C_6H_{12}N_4$) sourced from Nice Chemicals Pvt Ltd, and Ammonium hydroxide(NH_4OH) which was sourced from Thomas Baker (Chemicals) Pvt Ltd. Adhesion and synergistic tests involved the utilization of Ethylene glycol($C_2H_4O_2$) which was sourced from Nice Chemicals Pvt Ltd and for precise cutting operations, a sharp razor blade served as the cutting tool, complemented by a hard metal straight edge as the cutting guide. A wide semi-transparent pressure-sensitive tape with a pre-determined adhesion strength was employed. To ensure stability and accuracy lab-grade adhesion glass served as the substrate for ZnO nanoparticles during X-cut Adhesion tests and Large Area Screen Printing. The acquisition of a Large-area screen printing machine was from Techdyne Industries, Coimbatore.

Preparation of ZnO nanoparticles

ZnO nanoparticles were synthesized via the Co-Precipitation method, to achieve this 5 mM Zinc Nitrate and 5 mM of HMTA(Hexa Methyl Tetra Amine) were subjected to dissolution in 100 ml of distilled water each, The precursor and surfactant were subjected to magnetic stirring for 60 minutes, during which 0.5M NH_4OH (ammonium hydroxide) was gradually added in a titration process. Filtration using Whatman filter paper was employed through water washing to separate the nanoparticles from the reaction mixture. The filtrated nanoparticles were then subjected to a carefully controlled thermal treatment process via a hot air oven at 90◦ C for 180 minutes.

Materials Research Proceedings 73 (2026) 170-176 https://doi.org/10.21741/9781644904459-34

Preparation of CuO nanofluid

Copper oxide (CuO) nanofluids were synthesized using a systematic chemical reduction method followed by purification and preparation steps. 3.02 grams of sodium borohydride was dissolved in 50 ml of distilled water, and 7.4907 grams of copper sulfate ($CuSO_4$) in 10 ml of distilled water. These solutions were titrated together for 30 minutes at 400 rpm and 37°C. Subsequently, the mixture underwent filtration using Whatman filter paper, followed by washing with a 1:1 mixture of distilled water and ethanol to ensure thorough purification. The filtered nanoparticles were dried in a hot air oven at 80°C for 5 hours. Post-drying, the particles were aged for 24 hours to achieve proper formation of copper oxide nanoparticles.

1.5% of the synthesized copper oxide nanoparticles were mixed with 15 ml of ethylene glycol and 0.1 grams of SLS. This nanofluid solution was stirred for 30 minutes at 600 rpm for uniform mixture of CuO nanoparticles in the CuO nanofluid.

Characterization

X-ray diffraction information of the ZnO in the 2θ range 10◦–80◦ was obtained using Bruker AXS D8 Advanced powder X-ray diffractometer with Cu Kα (λ = 1.5418 Å). The surface morphology of the samples underwent examination through scanning electron microscope (SEM) imaging using the Zeiss Ultra-55. This instrument is equipped with Gemini technology, incorporating a high-efficiency In-lens detector to achieve high-contrast topographic imaging. Additionally, it inherits features from the SUPRA 55, such as the angle-selective Backscattered Electron (EsB) detector. Image rendering and control operations were conducted using the SmartSEM software.

Results And Discussion

Following sections describe the detailed characterization which is used in the study with some discussions.

A. Powder X-Ray Diffraction (PXRD)

Powder X-ray diffraction (PXRD) was conducted to confirm the presence and determine the structure of ZnO nanoparticles. Samples were readied on zero-background SI plates, offering an unobstructed view, and set up following Bragg-Brentano geometry. Subsequently, analysis was conducted using a Bruker AXS D8 Advanced powder X-ray diffractometer, utilizing Cu Kα radiation (λ = 1.5418 Å). Intensity Peaks at different angles were obtained as represented in Fig. 1. Notably, Sharp Intensity peaks were observed at angles 31.742, 34.397, and 36.224 assigning to (100), (002), and (101) crystal planes which suggests the lattice of the synthesized ZnO nanoparticles are highly regular. The average crystalline size of the ZnO nanoparticles is estimated by the Debye Scherrer formula

$$D = K\lambda/(\beta cos\theta) \quad (1)$$

In equation (1), D corresponds to the crystal size (nm), λ is the wavelength of the X-ray source (1.5418 A^o), β is the full width at half the maximum diffraction peak (FWHM) in radians, K the Scherrer constant having a value of 0.9-1. The value of D obtained is about 28.38 nm. The diffraction peaks observed were in complete agreement with the Powder Diffraction File (PDF) no: 01-090-7518, insinuating the crystal system of the material is hexagonal, with a space group of P63mc (186). The calculated density is 5.662 g/cm^3, while the structural density is slightly higher at 5.6641 g/cm^3. The molecular weight of the compound is 81.38 g/mol. It exhibits non-centrosymmetric properties, making it suitable for pyroelectric and piezoelectric applications, including second harmonic generation. Its Wyckoff sequence is denoted by b2.

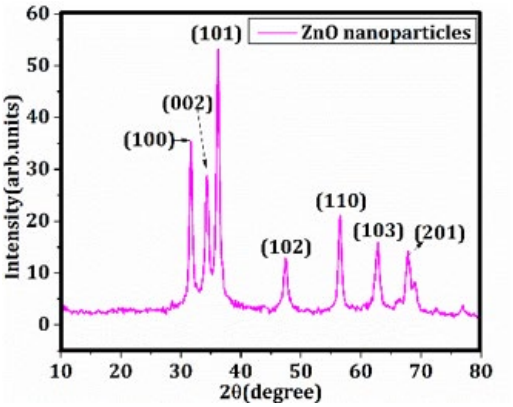

Fig. 1. PXRD of synthesized ZnO nanoparticles.

B. Scanning Electron Microscopy (SEM) And Electron Dispersive Spectroscopy (EDS)

The SEM images are displayed in Fig. 2(a), (b) at a magnification of 1, 00,000x and 50,000x. The SEM images at different magnifications reveal highly agglomerated nanoparticles with lesser nanoflakes, ZnO nanoparticles typically have high surface energy, which drives them to minimize their total surface area by aggregating. The weaker Vander waal forces between the ZnO nanoparticles also cause the neighboring nanoparticles to be attracted to each other leading to clustering. The coalesced nanoparticles have mean diameter of 32.2 nm whereas nanoflakes have widths less than 20 nm. Further, the elemental distribution was confirmed by the EDS elemental mapping technique shown in Fig.2(c). EDS captures the emission of X-rays at specific energies characteristic of elements present in a ZnO nanoparticles sample, thereby providing qualitative insights into the composition of synthesized ZnO nanoparticles, which exclusively consist of zinc (Zn) and oxygen (O) as represented in Fig.2 (d).

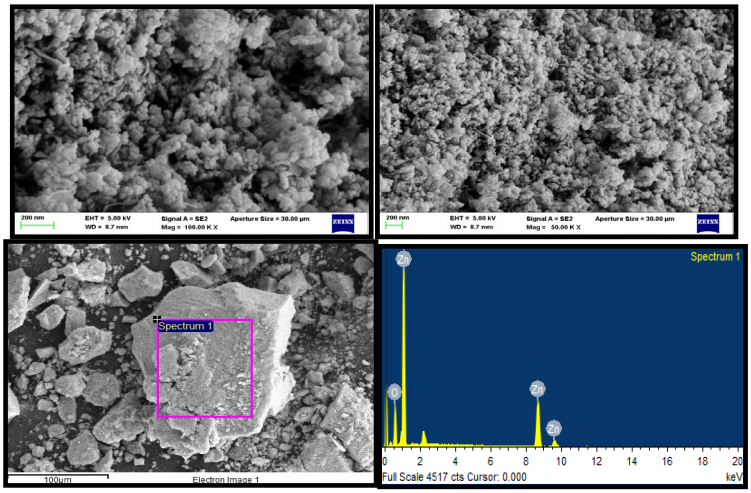

Fig. 2. (a)SEM of ZnO nanoparticles at 100000x magnification, (b) SEM of ZnO nanoparticles at 50000x magnification, (c)(d)EDS of ZnO nanoparticles.

C. Large-Area Printing and Sensor Test

Following the printing process, the printed glass substrate was subjected to a hot air oven, where it was exposed to a temperature of 80°C for 20 minutes. This thermal treatment was conducted to facilitate the curing and stabilization of the printed ZnO nanoparticle pattern on the glass substrate. The successful adhesion of the printed ZnO nanoparticles highlights the efficacy of the formulated paste in adhering to the substrate surface. The ZnO nanoparticles form a closely packed deposition, resulting in a uniform arrangement with high packing density. This uniformity ensures a

Materials Research Proceedings 73 (2026) 170-176 https://doi.org/10.21741/9781644904459-34

continuous and uniform conducting path throughout the printed layer, essential for reliable sensor performance. The high packing density and uniform deposition contribute to an increased fill factor, enhancing the sensor's sensitivity and response. Additionally, the closely packed nanoparticle arrangement enhances the sensitivity of the sensor, allowing it to detect even subtle changes in voltage levels showcasing the successful implementation of the large-area printing technique for the deposition of ZnO nanoparticles onto the substrate.

The experimental setup as depicted in Fig 3 (a) involved printed ZnO electrode positioned at 75° angle. A burette was used to dispense unimpeded copper oxide nanofluid onto the ZnO electrode, ensuring that the fluid directly contacted the bottom edge of the circular printed sensor. Following contact, capillary action and the Langmuir-Blodgett effect caused the nanofluid to rise against gravity, spreading from the bottom to the upper edge of the sensor. During the experiment, a voltmeter was used to measure the voltage output, which showed a reading of 0.9 mV. However, it was observed that the probes of the multimeter left dents on the ZnO sensor, these indentations may have caused open circuits, potentially reducing the sensing output voltage from the fluid flow.

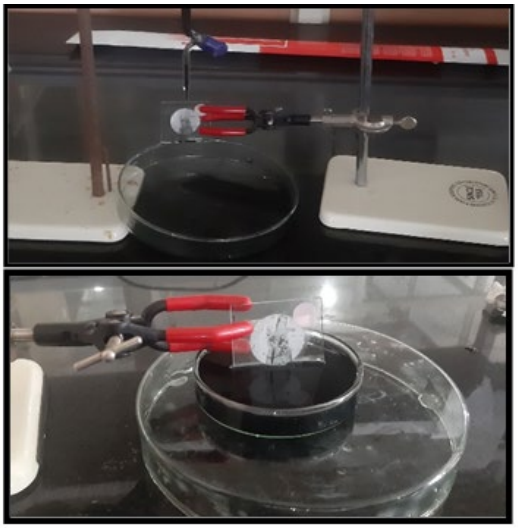

Fig.3. (a) ZnO Voltage Sensor Setup-1 (b) ZnO Voltage Sensor Setup-2

In Setup 2 as depicted in Fig 3 (b), the experiment was conducted without using the unimpeded nanofluid flow from a burette. Instead, the voltage generated solely by capillary action was measured. A petri dish filled with 75 ml of copper oxide nanofluids was used, and the printed glass electrode was dipped into the dish at an angle of 75 ^{o}, ensuring that the CuO nanofluid contacted the edge of the circular ZnO sensor. The setup was left undisturbed for about two hours to allow the nanofluids to rise due to capillary action. A voltage of 0.45 mV was measured. This voltage measurement reflects the influence of pure capillary action without the interference of unimpeded nanofluid flow.

Conclusion

Unlike nanoparticles, bulk forms of zinc oxide lack the surface characteristics and interactions needed for optimal adhesion and synergistic effects. This is because bulk materials have larger particle sizes and less surface area, making it harder to form strong bonds with substrates. ZnO is a prime candidate for voltage sensors due to its unique properties, such as high piezoelectric coefficients, wide band gap, and excellent semiconducting characteristics. These properties make ZnO well-suited for voltage sensing applications, where precise and sensitive detection of electrical signals is essential. The calculated piezoelectric coefficient is 45.6 pm/V, based on a Debye-Scherrer radius of 14.15 nm. SEM analysis shows an average ZnO nanoparticle radius of 16 nm, resulting in a d33 value of 35.65 pm/V. The observed d33 value of 35.65 pm/V as per the

morphological analysis of SEM suggests that the nanoparticles have a well-defined crystalline structure and are capable of efficiently converting mechanical energy into electrical energy, making them highly suitable for applications in piezoelectric sensors and devices. The proposed ZnO voltage sensor was successfully tested which gave 0.9 mV due to capillary action and unimpeded CuO nanofluid flow and 0.45 mV from pure capillary action of CuO nanofluid, the authors of this work are engaged in ongoing research on ZnO related voltage sensors and nanofluids.

Declaration of Competing Interest

The authors declare that they have no known competing financial interests or personal relationships that could have appeared to influence the work reported in this paper.

Declaration of Funding

This research was supported by Project Code No: TDP/DRISHTI CPS/L2M/SL/2023/0014, funded by the IIT Indore Drishti CPS Foundation. Their financial support is gratefully acknowledged.

References

[1] Z. W. Pan, Z. R. Dai, and Z. L. Wang, Nanobelts of semiconducting oxides, Science, 291, (2001) 1947-1949. https://doi.org/10.1126/science.1058120

[2] D. Wang et al., Piezoelectric polarization induced by dual piezoelectric materials ZnO nanosheets/MoS2 heterostructure for enhancing photoelectrochemical water splitting, Journal of Colloid and Interface Science, 653 (2024) 1166-1176. https://doi.org/10.1016/j.jcis.2023.09.157

[3] R. A. Zargar et al., Synthesis and characterization of screen printed ZnO films for solar cell applications, Optik, 126 (2015) 4171-4174. https://doi.org/10.1016/j.ijleo.2015.08.115

[4] B. Ismail, M. Abaab, and B. Rezig, Structural and electrical properties of ZnO films prepared by screen printing technique, Thin Solid Films, 383 (2001) 92-94. https://doi.org/10.1016/S0040-6090(00)01787-9

[5] V. K. Kapur, B. M. Basol, and E. S. Tseng, Low cost methods for the production of semiconductor films for CuInSe2/CdS solar cells, Solar Cells, 21 (1987) 65-72. https://doi.org/10.1016/0379-6787(87)90105-0

[6] S. Velumani, X. Mathew, and P. J. Sebastian, Structural and optical characterization of hot wall deposited CdSexTe1− x films, Solar Energy Materials and Solar Cells, 76 (2003) 359-368. https://doi.org/10.1016/S0927-0248(02)00288-X

[7] G. Manjunath, S. Pujari, D. R. Patil, and S. Mandal, A scalable screen-printed high performance ZnO-UV and gas sensor: Effect of solution combustion, Materials Science in Semiconductor Processing, 107 (2020) 104828. https://doi.org/10.1016/j.mssp.2019.104828

[8] M. M. Hassan, W. Khan, A. Azam, and A. H. Naqvi, Effect of size reduction on structural and optical properties of ZnO matrix due to successive doping of Fe ions, Journal of Luminescence, 145 (2014) 160-166. https://doi.org/10.1016/j.jlumin.2013.06.024

[9] Q. Qi et al., Properties of humidity sensing ZnO nanorods-base sensor fabricated by screen-printing, Sensors and Actuators B: Chemical, 133 (2008) 638-643. . https://doi.org/10.1016/j.snb.2008.03.035

[10] N. H. Nickel and E. Terukov, Eds., Zinc Oxide-A Material for Micro-and Optoelectronic Applications: Proceedings of the NATO Advanced Research Workshop on Zinc Oxide as a Material for Micro-and Optoelectronic Applications, held in St. Petersburg, Russia, from 23 to

25 June 2004, 194 (2005) Springer Science & Business Media. https://doi.org/10.1007/1-4020-3475-X

[11] A. Dal Corso, M. Posternak, R. Resta, and A. Baldereschi, Ab initio study of piezoelectricity and spontaneous polarization in ZnO, Physical Review B, 50 (1994) 10715. https://doi.org/10.1103/PhysRevB.50.10715

[12] S. Goel, N. Sinha, H. Yadav, and B. Kumar, On the prediction of external shape of ZnO nanocrystals, Physica E: Low-dimensional Systems and Nanostructures, 106 (2019) 291-297. https://doi.org/10.1016/j.physe.2018.08.014

[13] Z. L. Wang, Progress in piezotronics and piezo-phototronics, Advanced Materials, 24 (2012) 4632-4646.. https://doi.org/10.1002/adma.201104365

[14] K. Rekha, M. Nirmala, M. G. Nair, and A. Anukaliani, Structural, optical, photocatalytic and antibacterial activity of zinc oxide and manganese doped zinc oxide nanoparticles, Physica B: Condensed Matter, 405 (2010) 3180-3185.. https://doi.org/10.1016/j.physb.2010.04.042

Materials Research Proceedings 73 (2026) 177-182 https://doi.org/10.21741/9781644904459-35

Multi-Fidelity Reliability-Based Design Optimization of Advanced Composite Structures

Dario ZAMANI[1,a *], Alfonso PAGANI[1,b], Marco PETROLO[1,c] and Erasmo CARRERA[1,d]

[1]MUL2 Lab, Department of Mechanical and Aerospace Engineering, Politecnico di Torino, Corso Duca degli Abruzzi 24, 10129 Torino, Italy

[a]dario.zamani@polito.it, [b]alfonso.pagani@polito.it, [c]marco.petrolo@polito.it, [d]erasmo.carrera@polito.it

Keywords: Tow-Steered Composites, Reliability-Based Design Optimization, Multi-Fidelity Modeling, Carrera Unified Formulation, Gaussian Process Regression

Abstract. This paper presents a Multi-Fidelity Reliability-Based Design Optimization (MF-RBDO) strategy for Automated Fibre Placement (AFP) tow-steered composite structures. The framework combines manufacturing-aware fibre-path design, uncertainty propagation and multi-fidelity structural theories based on the Carrera Unified Formulation (CUF). The composite optimization framework is posed as a mixed-integer problem, where the number of plies is discrete and the tow-steering parameters are continuous. Deterministic AFP constraints on curvature, gaps and overlaps are enforced before the structural analysis, while stochastic variability in material properties, load, thickness and fibre angles is propagated through a multi-fidelity Gaussian Process Regression (GPR). Low-fidelity Equivalent-Single-Layer models provide inexpensive exploration, whereas high-fidelity Layerwise descriptions enrich the surrogate in regions where through-thickness stresses and failure indices are critical. A benchmark tow-steered plate shows that the reliability-based solutions require only a modest mass increase, but reduce the predicted failure indices and make the design less sensitive to manufacturing-signature variability.

Introduction

Automated Fibre Placement (AFP) enables variable-stiffness composite laminates by steering the tow direction inside each ply [1]. This design freedom can improve stiffness tailoring, stress redistribution and buckling response, but it also introduces a strong coupling between the nominal fibre path and the physical manufacturing signature of the part [2]. In tow-steered laminates, gaps, overlaps, local fibre-angle deviations and thickness variations can move the final structure away from the ideal design; therefore, optimized solutions must be robust to manufacturing defects and explicitly account for their effect on structural performance [3,4]. Reliability-based design optimization (RBDO) is well suited to this problem because it embeds uncertainty directly into the design constraints [5]. However, probabilistic assessment of composite failure requires repeated evaluations of stress fields, including transverse shear and out-of-plane normal stresses that are especially relevant for delamination. Full Layerwise (LW) Finite Element (FE) analyses are accurate but too expensive to be used repeatedly inside a stochastic optimization loop. The present work addresses this limitation by combining CUF structural models [6] with an adaptive multi-fidelity Gaussian Process Regression (MF-GPR) surrogate [7]. In this framework, the Carrera Unified Formulation (CUF) is used as a generator of structural-theory, enabling node-wise variation of model fidelity from efficient Equivalent Single-Layer (ESL) descriptions to refined LW kinematics. This allows ESL models to support efficient exploration of the design and uncertainty space, while LW models are selectively introduced in regions where accurate through-thickness stress fields are required. The remainder of the paper introduces the tow-steered design parameterization, AFP manufacturing constraints, CUF-based multi-fidelity modelling strategy

Content from this work may be used under the terms of the Creative Commons Attribution 3.0 license. Any further distribution of this work must maintain attribution to the author(s) and the title of the work, journal citation and DOI. Published under license by Materials Research Forum LLC.

Materials Research Proceedings 73 (2026) 177-182 https://doi.org/10.21741/9781644904459-35

and adaptive MF-GPR reliability assessment. The proposed framework is then evaluated on a benchmark tow-steered composite plate.

Methodology

Tow-steered design variables. The laminate is described by a mixed vector x containing the discrete number of plies N and the continuous steering parameters of each independent layer. For a symmetric stack, only the half-laminate is parameterized. In the *k*-th ply, the fibre angle follows the linear law

$$\theta^k(s) = T_0^k + \left(T_1^k - T_0^k\right) s/a, \quad s \in [0, a] \tag{1}$$

where T_0 and T_1 are the centre and edge fibre angles of the *k*-th ply, respectively, and a is the half-length along the steering direction. The full stacking sequence is obtained by mirroring the half-stack through the mid-plane. This representation keeps the design space compact while allowing layerwise tailoring of variable-stiffness laminates.

Manufacturing constraints. The AFP process is embedded through deterministic constraints based on the tangent vector v = [cos θ, sin θ]. The local tow curvature κ and divergence ψ are defined as

$$\kappa = \nabla \times v, \qquad \psi = \nabla \cdot v \tag{2}$$

Curvature controls the minimum steering radius, whereas divergence describes the tendency of adjacent tow paths to separate or converge. Positive divergence promotes gaps, while negative divergence promotes overlaps. The admissible design set is obtained by imposing $|\kappa| \leq \kappa_{max}$ and $\psi_{min} \leq \psi \leq \psi_{max}$, where the bounds are computed from AFP machine limits, allowable gap/overlap fractions and minimum cut/add lengths [8,9]. These checks are evaluated before the structural response, so infeasible fibre paths are discarded without expensive FE analyses. The complete MF-RBDO workflow is summarized in Fig. 1, where the manufacturing signature acts as an early feasibility filter before the CUF-based multi-fidelity reliability assessment is performed within the optimization loop.

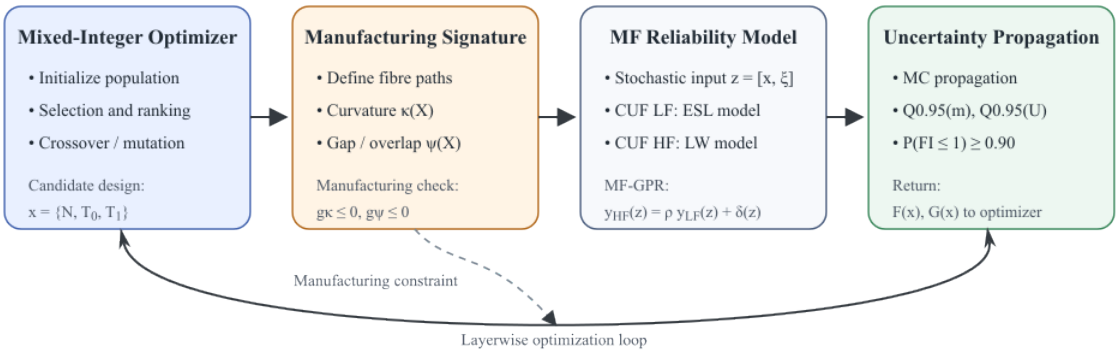

Figure 1. MF-RBDO architecture coupling AFP manufacturability filters, CUF low- and high-fidelity structural models, adaptive MF-GPR surrogate learning and probabilistic design optimization.

CUF multi-fidelity structural theories. The displacement field is expressed in CUF form as a through-thickness expansion multiplied by two-dimensional generalized unknowns [10]:

$$u(x, y, z) = F_\tau(z) u_\tau(x, y) \quad \tau = 1, \ldots, M \tag{3}$$

Materials Research Proceedings 73 (2026) 177-182 https://doi.org/10.21741/9781644904459-35

The symbol M represents the number of expansion terms, and $u_\tau(x, y)$ represents the vector containing the generalized displacements, with τ indicating summation. Changing the thickness functions F_τ generates different structural theories within the same FE assembly. Taylor expansions lead to ESL models, used here as low-fidelity analyses, while Lagrange expansions generate LW models that describe each ply independently and recover more accurate through-thickness stress fields. This hierarchy is the key enabler of the proposed multi-fidelity strategy, since the same formulation supplies both inexpensive global predictions and high-fidelity failure estimates.

Reliability-based optimization. For a random vector ξ collecting material, load, thickness, density and fibre-angle uncertainties, the robust optimization problem minimizes probabilistic mass and strain-energy measures while enforcing a target probability of safe condition:

$$\min_x \left[Q_{0.95}\big(m(x,\xi)\big), Q_{0.95}\big(U(x,\xi)\big)\right], \quad \text{subject to} \quad P(\mathrm{FI}(x,\xi) \le 1) \ge 0.90 \tag{4}$$

Failure Index (FI) is evaluated through three-dimensional Hashin criteria and a quadratic delamination index [11,12]. In the present study, the target probability of safety is 90%. The deterministic design optimization (DDO) and RBDO problems are solved with NSGA-II [13] which is suitable for mixed discrete-continuous design variables.

Multi-fidelity Gaussian-process surrogate. The high-fidelity response y_{HF} is represented through an autoregressive correction of the low-fidelity response y_{LF}:

$$y_{\mathrm{HF}}(z) = \rho\, y_{\mathrm{LF}}(z) + \delta(z), \qquad z = [x,\xi]^{\mathrm{T}} \tag{5}$$

where ρ is a correlation coefficient and δ is a discrepancy Gaussian Process (GP). For any candidate design, Monte Carlo samples of ξ are propagated through the surrogate rather than through repeated LW analyses. Adaptive enrichment adds high-fidelity CUF samples close to the failure boundary and in regions of large predictive uncertainty. In the numerical database used here, 70% of the training points are evaluated with the ESL model and 30% with the LW model, reducing the number of high-fidelity analyses while preserving accuracy in the failure quantities.

Numerical Results

The framework is assessed on a rectangular tow-steered composite plate representative of a wing-box skin panel. The plate has dimensions 0.508 m x 0.508 m and ply thickness 0.1905 mm. Simply supported boundary conditions are applied along the plate edges. The structure is subjected to a uniformly distributed transverse pressure of 1000 Pa and an in-plane edge load of 1000 N/m, respectively. A 10 x 10 Q9 in-plane mesh is used after convergence. The uncertainty model includes fibre-angle perturbations, load scaling, ply thickness, density, elastic constants and strength allowables (see [7]). The representative QI, DDO and RBDO solutions are summarized in Table 1, while the corresponding deterministic and reliability-based fibre paths are shown in Fig. 2.

Materials Research Proceedings 73 (2026) 177-182 https://doi.org/10.21741/9781644904459-35

Table 1. Comparison of Quasi-Isotropic (QI), Deterministic Design Optimization (DDO), and Reliability-Based Design Optimization (RBDO) representative solutions.

Case	N_{ply}	Mass [kg]	Strain energy [J]	Manufacturing indicators	Main reliability outcome
QI	3 / 4	0.195 / 0.260	22.12 / 9.65	–	Reference straight-fibre baseline
DDO	3 / 4	0.195 / 0.260	16.01 / 6.90	$\max \lvert\kappa\rvert / \kappa_{max} \leq 1.50/2.5$; $\max \lvert\psi\rvert / \psi_{max} \leq 0.76/2$	Lowest nominal compliance, but critical failure modes may be redistributed
RBDO	3 / 4	0.20 / 0.27	19.47 / 8.38	$\max \lvert\kappa\rvert / \kappa_{max} \leq 0.82/2.5$; $\max \lvert\psi\rvert / \psi_{max} \leq 0.44/2$	Slight mass increase, lower failure indices and improved robustness

As reported in Table 1, the deterministic optima achieve the lowest nominal strain energy, with reductions of about 38-40% with respect to the corresponding quasi-isotropic references. Nevertheless, the associated fibre paths in Fig. 2 show that deterministic steering tends to exploit more aggressive curvature and may transfer criticality from one failure mechanism to another. The reliability-based solutions are slightly heavier, by approximately 2-3%, and less compliant than the deterministic optima, but they remain more efficient than the quasi-isotropic baselines while reducing the severity of the manufacturing indicators.

The failure-index comparison confirms the benefit of the RBDO formulation. For the three-ply case, the RBDO design reduces fibre tension, fibre compression and matrix tension by about 62%, 69% and 72%, respectively, compared with the quasi-isotropic reference, while the delamination index decreases from 0.05 to 0.003. For the four-ply case, the robust design also lowers the fibre and matrix failure indices and keeps delamination at a low level. These trends indicate that reliability-based optimization does not merely shift the critical mode; instead, it improves the global failure margin across several mechanisms.

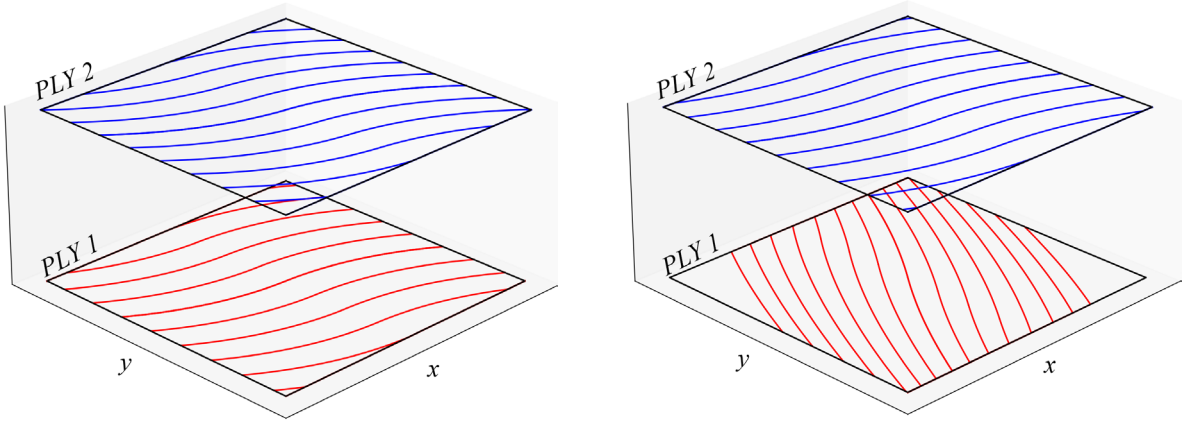

(a) DDO optimized fibre paths *(b) RBDO optimized fibre paths*

Figure 2. Comparison of representative optimal fibre paths for the tow-steered laminate.

The ESL and LW comparisons further justify the multi-fidelity framework. ESL-TE1 analyses are approximately 52-60% cheaper than LW-LD2 analyses for the representative configurations, but the largest discrepancies appear in delamination and through-thickness failure indices. The surrogate therefore uses ESL evaluations for inexpensive exploration and reserves LW evaluations for the response regions where layerwise accuracy is necessary.

As an additional structural check, the optimized plates are evaluated through linear buckling analysis. The corresponding first buckling mode shapes are reported in Fig. 3 for the QI, DDO,

Materials Research Proceedings 73 (2026) 177-182 https://doi.org/10.21741/9781644904459-35

and RBDO configurations. Tow steering substantially improves the first critical load of the deterministic designs. The robust designs exhibit a more complex behaviour, including mode switching, because the stiffness field is redistributed to satisfy reliability constraints rather than only to maximize nominal stiffness. This observation is important for future extensions in which buckling metrics are included directly in the RBDO formulation.

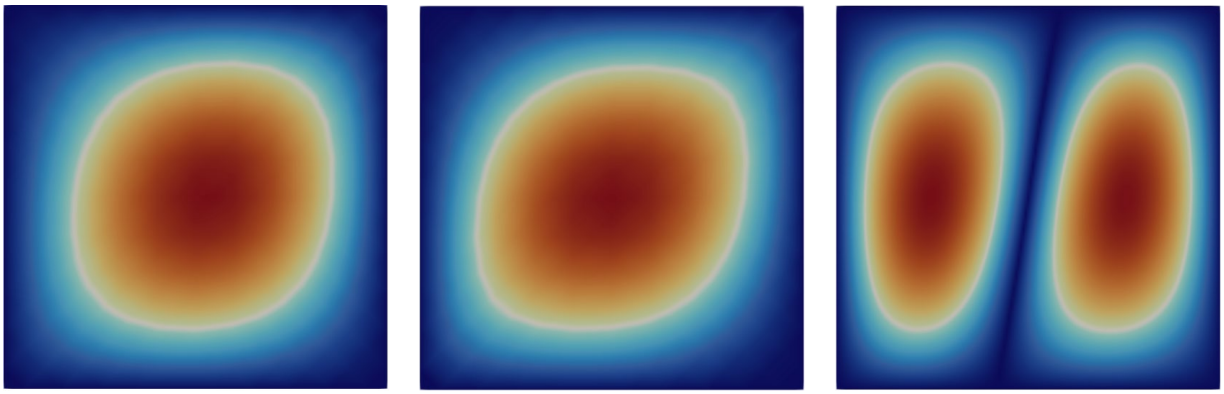

(a) QI *(b) DDO* *(c) RBDO*

Figure 3. First buckling mode shapes for the three-layer optimal designs: (a) reference QI laminate, (b) DDO solution, and (c) RBDO solution.

Conclusions

A MF-RBDO framework has been presented for tow-steered composite plates manufactured by AFP. The method combines mixed-integer fibre-path optimization, deterministic manufacturability signature, CUF-based ESL/LW structural theories and adaptive MF-GPR uncertainty propagation. The benchmark results show that reliability-based solutions require only a small mass penalty compared with deterministic optima, while providing lower failure indices and less severe manufacturing indicators. The multi-fidelity surrogate is essential because delamination and 3D failure metrics require layerwise accuracy, but a full high-fidelity stochastic optimization would be computationally prohibitive. Future work will extend the formulation to explicit gap/overlap FE modelling, more complex geometries and direct probabilistic buckling constraints.

Acknowledgment

The support of the Italian Ministry of University and Research through the program FARE-III Edition (project LOUD, No. R20EENHZEJ) is acknowledged.

References

[1] A. Brasington, C. Sacco, J. Halbritter, R. Wehbe, R. Harik, Automated fiber placement: a review of history, current technologies, and future paths forward, Composites Part C: Open Access 6 (2021). https://doi.org/10.1016/j.jcomc.2021.100182

[2] K. Fayazbakhsh, M. Arian Nik, D. Pasini, L. Lessard, Defect layer method to capture effect of gaps and overlaps in variable stiffness laminates made by automated fiber placement, Composite Structures 97 (2013). https://doi.org/10.1016/j.compstruct.2012.10.031

[3] A. Pagani, A.R. Sánchez-Majano, D. Zamani, M. Petrolo, E. Carrera, Fundamental frequency layer-wise optimization of tow-steered composites considering gaps and overlaps, Aerotecnica Missili e Spazio (2025). https://doi.org/10.1007/s42496-024-00212-w

[4] D. Zamani, A. Racionero Sánchez-Majano, A. Pagani, Mixed-integer, multi-objective layerwise optimization of variable-stiffness composites with gaps and overlaps, Struct. Multidisc. Optim. 68 (2025) 107. https://doi.org/10.1007/s00158-025-04043-6

[5] H. An, B.D. Youn, H.S. Kim, Reliability-based design optimization of laminated composite structures under delamination and material property uncertainties, International Journal of Mechanical Sciences 205 (2021). https://doi.org/10.1016/j.ijmecsci.2021.106561

[6] S. Scano, E. Carrera, M. Petrolo, Use of the 3D equilibrium equations in the free-edge analyses for laminated structures with the variable kinematics approach, Aerotecnica Missili e Spazio 103 (2024). https://doi.org/10.1007/s42496-023-00177-2

[7] D. Zamani, A. Pagani, M. Petrolo, E. Carrera, Multi-fidelity probabilistic failure onset analysis of composite structures under uncertainties, Computer Methods in Applied Mechanics and Engineering 454 (2026). https://doi.org/10.1016/j.cma.2026.118849

[8] T.R. Brooks, J.R.R.A. Martins, On manufacturing constraints for tow-steered composite design optimization, Composite Structures 204 (2018) 548-559. https://doi.org/10.1016/j.compstruct.2018.07.100

[9] C. Luo, F. Ferrari, J.K. Guest, Design optimization of advanced tow-steered composites with manufacturing constraints, Composites Part B: Engineering 284 (2024). https://doi.org/10.1016/j.compositesb.2024.111739

[10] E. Carrera, M. Cinefra, M. Petrolo, E. Zappino, Finite Element Analysis of Structures Through Unified Formulation, Wiley, Amsterdam, 2014. https://doi.org/10.1002/9781118536643

[11] Z. Hashin, Failure criteria for unidirectional fiber composites, Journal of Applied Mechanics 47 (1980) 329-334. https://doi.org/10.1115/1.3153664

[12] J.C. Brewer, P.A. Lagace, Quadratic stress criterion for initiation of delamination, Journal of Composite Materials 22 (1988) 1141-1155. https://doi.org/10.1177/002199838802201205

[13] K. Deb, A. Pratap, S. Agarwal, T. Meyarivan, A fast and elitist multiobjective genetic algorithm: NSGA-II, IEEE Transactions on Evolutionary Computation 6 (2002) 182-197. https://doi.org/10.1109/4235.996017

Materials Research Proceedings 73 (2026) 183-189 https://doi.org/10.21741/9781644904459-36

An Effective Methodology for Strength Prediction of Fusion-Welded Thermoplastic Composite Repairs

A. Viste[1,a], B. Castanié[1,b], L. Crouzeix[1,c], D. Espinassou[2,d], C. Briançon[2,e]

[1]Institut Clément Ader (ICA), CNRS UMR 5312, INSA, ISAE-Supaéro, INSA, IMT Mines Albi, UPS, Espace clément ader, 3 Rue Caroline Aigle, F-31400 Toulouse, France

[2]Cetim, 52 Avenue Félix Louat, 60300 Senlis, France

[a]viste@insa-toulouse.fr, [b]castanie@insa-toulouse.fr, [c]laurent.crouzeix@iut-tlse3.fr, [d]denis.espinassou@cetim.fr, [e]christophe.briancon@cetim.fr

Keywords: Repair, Welded Joints, Thermoplastic Composite

Abstract. Fracture mechanics-based approaches are often used to predict the strength of repairs to composite structures. While these approaches offer high accuracy and provide insight into fracture mechanisms before ultimate failure, they require significant computational resources, even for small structures. This makes them impractical for predicting the strength of industrial applications. This study therefore proposes a simplified model that accurately calculates stresses and strains on each component of a thermoplastic composite repair. Cohesive and shell elements are used with a specific formulation. The model is then compared to a reference model for a simple loading case and geometry similar to that of a composite repair. The results show that the simplified model can accurately calculate stresses and strains while significantly reducing computation time.

Introduction.

Future needs on more sustainable materials is driving development on thermoplastics composite materials, especially for aeronautical industry [1]. Thanks to the matrix's remelting capability, structures made from thermoplastic composite materials are easier to recycle and repair [2]. Fusion-welded thermoplastic joints are attracting growing interest, and characterization tests conducted on these joints are yielding excellent results [3], making thermoplastic fusion welded joints attractive for composite repair.

Repair of composite material is necessary due their vulnerability to impacts, causing defects such as matrix cracking, fiber breakage or delamination [4]. The load-bearing capacity and stiffness of the parts are reduced and must be effectively restored. For that, repairs with patch flush to the surface, with step or scarf geometry, are the lightest and most aerodynamic solution [5]. Conducting a repair must be done after defining key parameters such as bond length, shape and layup definition of the patch [6]. This requires strength prediction tools. These strength predictions methodologies are widely studied for bonded thermoset composite repairs [7]. However, few studies have proposed methodologies to predict strength of fusion welded joints [8], which mainly focus on process development of the fusion welding technique.

Finite element models are the most commonly used tool for composite materials due to their ability to easily model complex geometries, loading cases, and material laws. Advanced models are often developed for composite repairs analysis to predict strength but also failure behaviour. Cohesive zone modelling associated with continuum damage mechanisms is often seen in the literature [9], while virtual closure technique is less studied. Other authors proposed models that more computational effective, only for strength prediction.

These models are based on stress or strains criteria, used in the initial studies with linear elastic material laws for the composite and the adhesive [10]. Due to the stress concentrations associated with the linear elasticity approach and the stress allowable that is extracted directly from the

Content from this work may be used under the terms of the Creative Commons Attribution 3.0 license. Any further distribution of this work must maintain attribution to the author(s) and the title of the work, journal citation and DOI. Published under license by Materials Research Forum LLC.

Materials Research Proceedings 73 (2026) 183-189 https://doi.org/10.21741/9781644904459-36

characterization test, the maximum stress criterion used provides a poor correlation with the tests performed on the composite repairs. One common way to address stress concentrations is to apply critical distance theory [11], which consists of predicting the strength of the composite or the adhesive at a critical distance from the singularity, often called d_o. Odi and friend [12] applied this methodology on scarf repairs, with an empirical definition of the critical distance. The maximum deviation of 43.6% for experimental results. Even if these FEM models use simple elements such as solid elements, they are still computationally expensive for large-scale repairs. Cerisier [13] proposed a model using the same strength prediction methodology with shell elements for the composite and a dynamic definition of the critical distance d_o in order to be robust against changing geometries and external loading conditions. However, this model has not been fully validated thought experimental testing, and numerical issues can be observed when using coarse meshes.

Thus, the goal of this work is to propose an efficient model for predicting the strength of composite thermoplastic repairs.

Methodology.

The simplified model uses a combination of cohesive and shell elements to model the resin and composite of the welded interface, respectively. The cohesive elements are defined with a linear traction-separation law without degradation. The stiffness of these elements is defined based on previous work modelling composite bonded interfaces [14]. Compared to solid elements, cohesive elements do not experience hourglass problems, especially when the thickness-to-length ratio is low. The stiffness matrix is diagonal, which is explained by the fact that the thickness of the welded interface was under 70 µm.

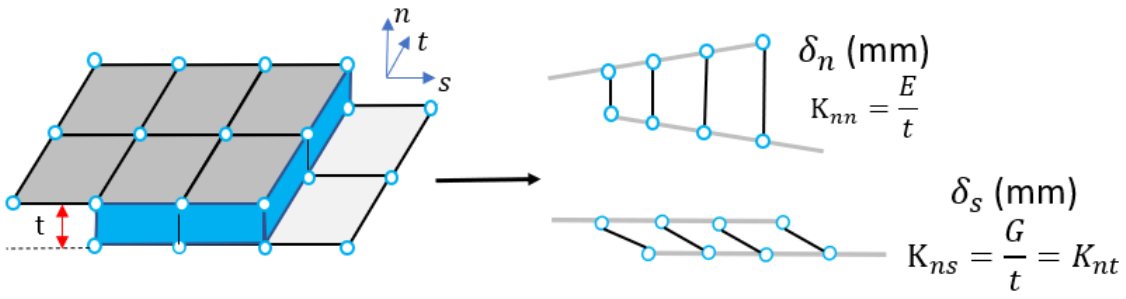

Fig. 1: Stiffness definition of cohesive elements for welded interface (stiffnesses in [N/mm])

$$\begin{Bmatrix} \sigma_{nn} \\ \tau_{ns} \\ \tau_{nt} \end{Bmatrix} = \begin{bmatrix} K_{nn} & 0 & 0 \\ 0 & K_{ss} & 0 \\ 0 & 0 & K_{tt} \end{bmatrix} \begin{Bmatrix} \delta_n \\ \delta_s \\ \delta_t \end{Bmatrix} \quad (1)$$

Transversal orthotropic assumption is made for the material law used to model composite material. A characterisation on the thermoplastic composite has been conducted, and some material properties were obtained based on common relationships [15] :

$$E_{22} = E_{33} \quad (2)$$

$$G_{12} = G_{13} \quad (3)$$

$$\nu_{12} = \nu_{13} \quad (4)$$

Materials Research Proceedings 73 (2026) 183-189 https://doi.org/10.21741/9781644904459-36

$$G_{23} = 0.4 \times G_{12} \tag{5}$$

$$\nu_{23} = 1.34 \times \nu_{12} \tag{6}$$

This law is associated with S4R shells elements, with enhanced hour glassing formulation and second order accuracy. To validate the proposed model, it is compared to a model composed of volumetric C3D8R elements with an enhanced hourglass formulation to model the composite and welded interfaces.

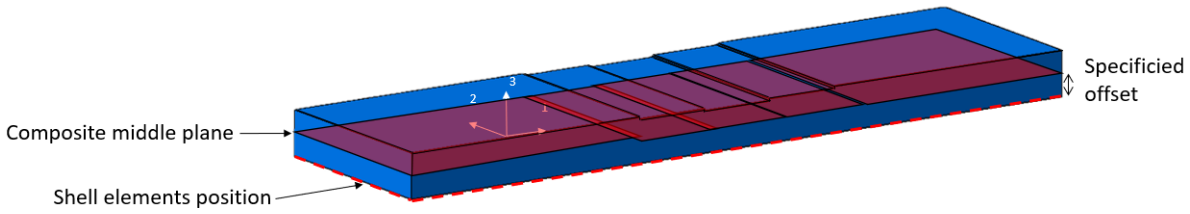

Fig. 2: Specified offset of the composite shell elements (example on a parent laminate)

The modelled geometry closely corresponds to the geometry of a repair, with three step lap patch of 10 mm welded length each. The purpose of the simulation is to validate the stiffness definition taken from Ridha et al [14]. Additionally, tie connections are established between composite and welded interface elements, also known as cohesive elements. These tie connections are designed to link the displacements of the master nodes to those of the secondary nodes. Due to the higher rigidity of the material, composite element nodes are always defined as master nodes. However, shell elements have degrees of freedom in rotation that need to be transformed into equivalent translations for the secondary nodes of cohesive elements, that can alter the precision of the results.

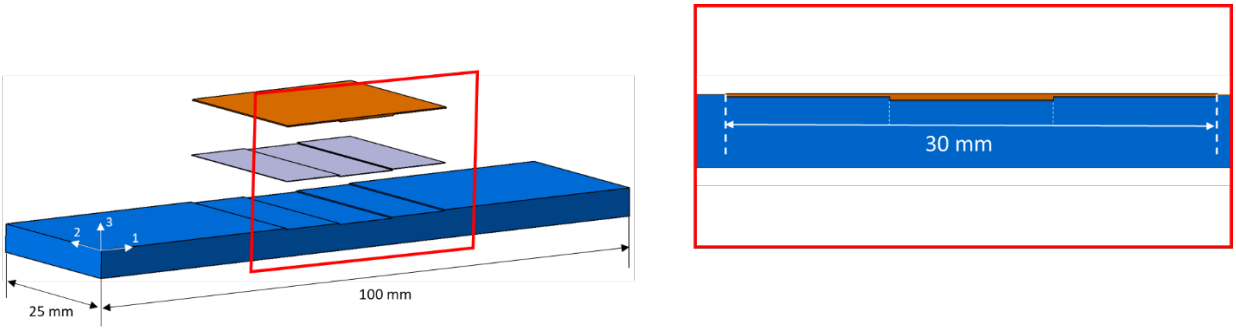

Fig. 3: Geometry for bending simulation (fusion welded patch (orange), welded interfaces (grey), parent laminate (blue))

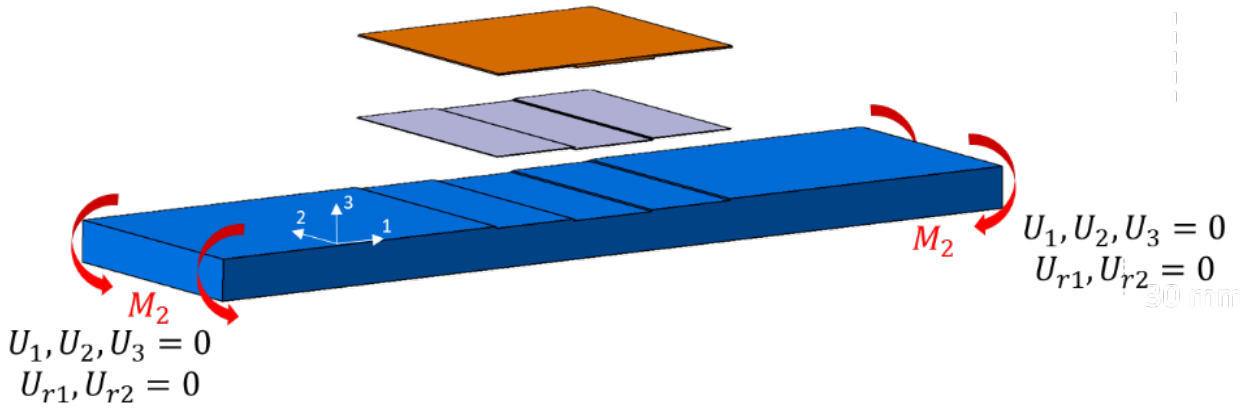

Fig. 4: Boundary conditions for bending simulation

Results

The following figure shows the peel and shear stress on the welded interface. All results are displayed at the integration points of the associated elements. The stress profiles are associated with the elements on the midplane of the specimen. The observations and conclusions drawn from the comparison are valuable for different areas of the welded interface. Only half of the welded interfaces are displayed in the figures below. The model made of solid elements is referenced as "Full Solid," and the proposed model is referenced as "Simplified Model."

Shear stress calculated near the egde of each welded interfaces show the biggest difference between the two different models (Fig. 5). However, the maximum and minimum shear stress calculated show acceptable differences. Difference on the calculated max shear stress is 13.4%, and the difference is negligeable for minimum shear stress.

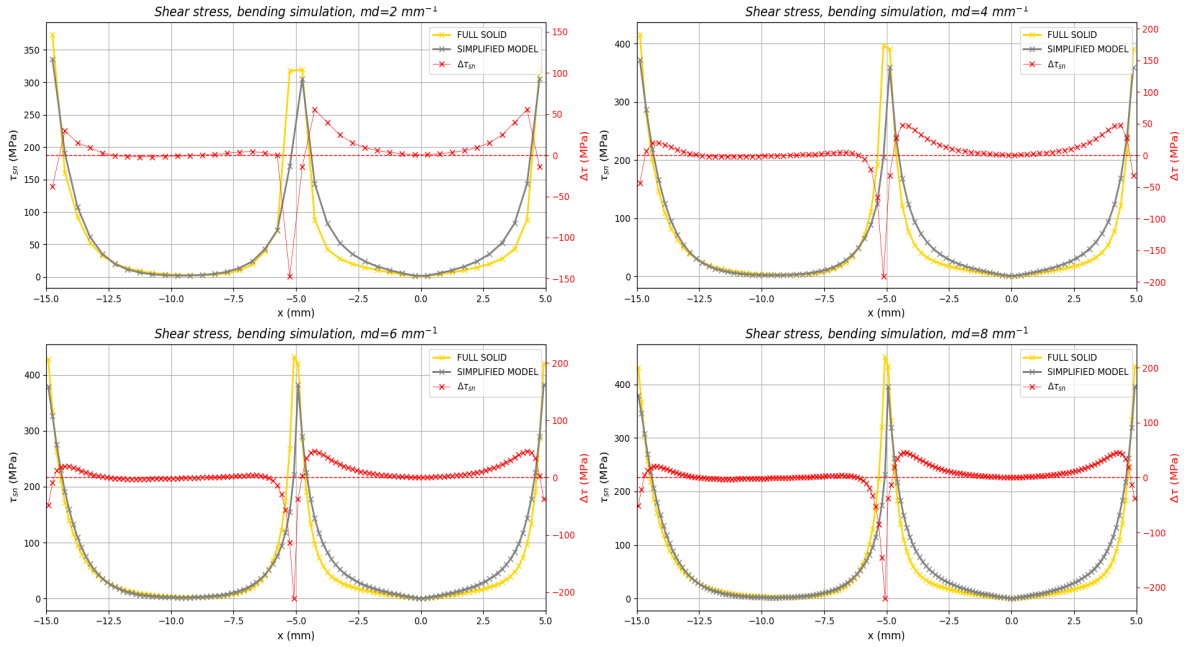

Fig. 5: Shear stress results and error between reference and simplified model

Hour glassing phenomenon can be seen on the peel stress calculated by the referenced model on coarse meshes (Fig. 6), showing that simplified model is able to accurately calculate stress for coarse mesh modelling.

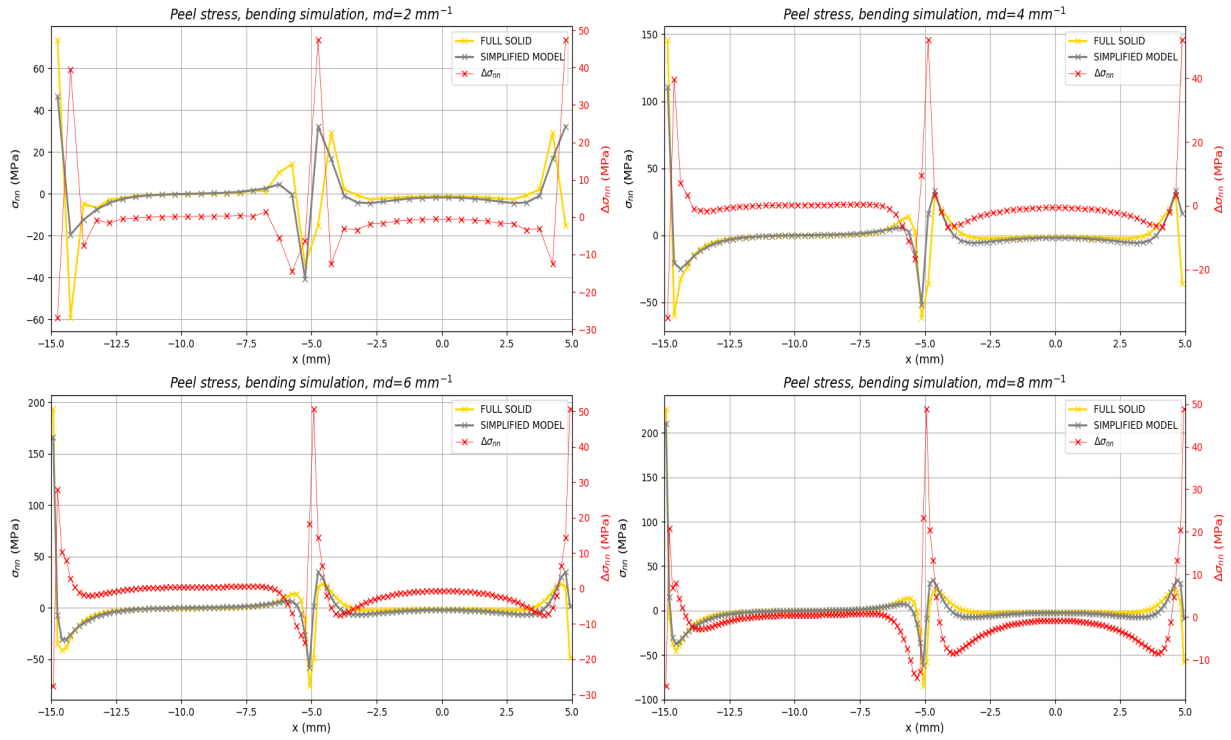

Fig. 6: Peel stress results and error between reference and simplified model

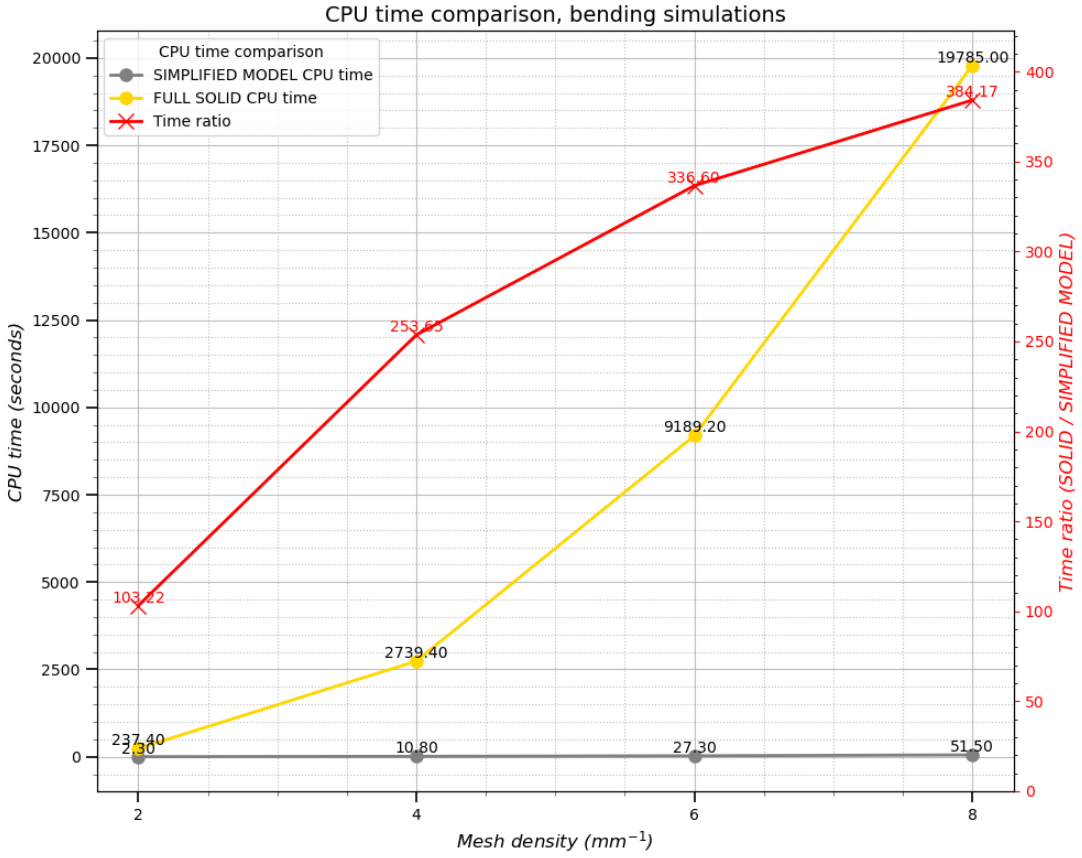

Fig. 7: CPU time according to mesh density for bending loading simulations, with time ratio between reference and simplified model

Discussion

Computational time of the simplified model has been drastically reduced compared to that of the reference model.

A comparison of different solutions for calculating stresses on bonded/welded interfaces in 3D space with complex geometries reveals that the proposed model strikes a great balance between accuracy and computational time. It shows better performance than user-developed elements [16] or semi-analytical models [17].

The mesh dependency on the calculated maximum and minimum stresses as can been seen on Fig. 5 and Fig. 6 show that calibrated allowables are necessary when using low mesh densities for predicting the strength of welded interfaces. Further work on this model involves proposing a methodology to calibrate mesh-independent allowables.

Conclusion

The proposed model is based on a combination of shell and cohesive elements. Comparing it to a reference model made of volumetric elements validates the stress and strain calculated by the proposed model. The computational time is drastically reduced, showing that this type of model is relevant for predicting the strength of large structures repaired with thermoplastic fusion-welded joints.

Acknowledgment

The authors thank the industrial partners, CETIM and Airbus Atlantic, for their support on this work.

References

[1] B. Castanie *et al.*, « Review of monolithic composite laminate and stiffened structures in aeronautic applications », *Compos. Part C Open Access*, vol. 17, p. 100585, juill. 2025. https://doi.org/10.1016/j.jcomc.2025.100585.

[2] J. P. Reis, M. de Moura, et S. Samborski, « Thermoplastic Composites and Their Promising Applications in Joining and Repair Composites Structures: A Review », *Materials*, vol. 13, nº 24, Art. nº 24, janv. 2020. https://doi.org/10.3390/ma13245832.

[3] B. H. A. H. Tijs, A. Turon, et C. Bisagni, « Characterization and analysis of conduction welded thermoplastic composite joints considering the influence of manufacturing », *Compos. Struct.*, vol. 348, p. 118505, nov. 2024. https://doi.org/10.1016/j.compstruct.2024.118505.

[4] M. O. W. Richardson et M. J. Wisheart, « Review of low-velocity impact properties of composite materials », *Compos. Part Appl. Sci. Manuf.*, vol. 27, nº 12, p. 1123-1131, 1996. https://doi.org/10.1016/1359-835X(96)00074-7.

[5] A. A. Baker et R. Jones, Éd., *Bonded Repair of Aircraft Structures*. Dordrecht: Springer Netherlands, 1988. doi: 10.1007/978-94-009-2752-0.

[6] H. Bendemra, P. Compston, et P. J. Crothers, « Optimisation study of tapered scarf and stepped-lap joints in composite repair patches », *Compos. Struct.*, vol. 130, p. 1-8, oct. 2015. https://doi.org/10.1016/j.compstruct.2015.04.016.

[7] J.-B. Orsatelli, E. Paroissien, F. Lachaud, et S. Schwartz, « Bonded flush repairs for aerospace composite structures: A review on modelling strategies and application to repairs optimization, reliability and durability », *Compos. Struct.*, vol. 304, p. 116338, janv. 2023. https://doi.org/10.1016/j.compstruct.2022.116338.

[8] B. H. A. H. Tijs, M. H. J. Doldersum, A. Turon, J. E. A. Waleson, et C. Bisagni, « Experimental and numerical evaluation of conduction welded thermoplastic composite joints »,

Compos. Struct., vol. 281, p. 114964, févr. 2022. https://doi.org/10.1016/j.compstruct.2021.114964.

[9] J.-B. Orsatelli, E. Paroissien, F. Lachaud, S. Schwartz, et N. Barrière, « Experimental and numerical multiscale testing of CFRP bonded stepped repairs », *Thin-Walled Struct.*, vol. 208, p. 112764, mars 2025. https://doi.org/10.1016/j.tws.2024.112764.

[10] F. Z. Hu et C. Soutis, « Strength prediction of patch-repaired CFRP laminates loaded in compression », *Compos. Sci. Technol.*, vol. 60, nº 7, p. 1103-1114, mai 2000. https://doi.org/10.1016/S0266-3538(00)00011-7.

[11] D. Taylor, « The theory of critical distances », *Eng. Fract. Mech.*, vol. 75, nº 7, p. 1696-1705, mai 2008. https://doi.org/10.1016/j.engfracmech.2007.04.007.

[12] R. A. Odi et C. M. Friend, « An improved 2D model for bonded composite joints », *Int. J. Adhes. Adhes.*, vol. 24, nº 5, p. 389-405, oct. 2004. https://doi.org/10.1016/j.ijadhadh.2001.06.001.

[13] A. Cerisier, « Prédiction du comportement d'une réparation structurale collée en escalier : application d'une méthodologie par évaluateurs technologiques », phd, Université de Toulouse, Université Toulouse III - Paul Sabatier, 2017. Consulté le: 19 août 2024. [En ligne]. Disponible sur: http://thesesups.ups-tlse.fr/3637/

[14] M. Ridha, V. B. C. Tan, et T. E. Tay, « Traction–separation laws for progressive failure of bonded scarf repair of composite panel », *Compos. Struct.*, vol. 93, nº 4, p. 1239-1245, mars 2011. https://doi.org/10.1016/j.compstruct.2010.10.015.

[15] T. Zaragkas, S. Psarras, G. Sotiriadis, et V. Kostopoulos, « Experimental and Numerical Study of Bearing Damage of a CF-LMPAEK Thermoplastic Composite », *J. Compos. Sci.*, vol. 8, nº 1, p. 35, janv. 2024. https://doi.org/10.3390/jcs8010035.

[16] M. Calì, S. Schwartz, F. Lachaud, S. Teixeira de Freitas, et E. Paroissien, « A high-order 2D-plate macro-element model for the analysis of bonded joints », 30 septembre 2025, *Social Science Research Network, Rochester, NY*: 5547001. doi: 10.2139/ssrn.5547001.

[17] L. F. M. Da Silva, P. J. C. Das Neves, R. D. Adams, A. Wang, et J. K. Spelt, « Analytical models of adhesively bonded joints—Part II: Comparative study », *Int. J. Adhes. Adhes.*, vol. 29, nº 3, p. 331-341, avr. 2009. https://doi.org/10.1016/j.ijadhadh.2008.06.007.

Materials Research Proceedings 73 (2026) 190-194 https://doi.org/10.21741/9781644904459-37

Evaluation of Best Theories using Neural Networks and Adaptive Sampling

Marco PETROLO[1,a *], Giulio CANDITA[1,b], Alfonso PAGANI[1,c], Erasmo CARRERA[1,d]

[1]MUL2 lab, Department of Mechanical and Aerospace Engineering, Politecnico di Torino, Italy

[a]marco.petrolo@polito.it, [b]giulio.candita@polito.it, [c]alfonso.pagani@polito.it, [d]erasmo.carrera@polito.it

Keywords: CUF, FEM, Structural Theories, Neural Networks, Adaptive Sampling

Abstract. This work presents an Adaptive Sampling-based surrogate framework for predicting the accuracy of higher-order beam theories generated within the Carrera Unified Formulation. The objective is to identify the minimal set of generalized displacement variables required to achieve a prescribed accuracy, thereby reducing the need for exhaustive high-fidelity structural analyses. Structural theories are built using Taylor-like polynomial expansions, and an Adaptive Sampling strategy based on an Extra Trees Regressor iteratively selects the most informative generalized variables by combining predicted error, uncertainty, and structural diversity. The selected dataset is then used to train a Neural Network to predict the average error in natural frequencies. The proposed strategy is evaluated using Best Theory Diagrams, which relate model accuracy to the number of degrees of freedom. Results show that Adaptive Sampling achieves accuracy comparable to, and in some cases better than, random sampling at the same sampling budget, while correctly identifying the most effective structural theories with fewer high-fidelity analyses. The framework, therefore, provides an efficient tool for data-driven selection of refined beam models.

Introduction

In structural mechanics, creating accurate reduced models is crucial to lowering the computational complexity of 3D analyses. Since they involve fewer degrees of freedom than full 3D models, 1D and 2D theories are frequently employed. However, their accuracy may vary significantly depending on the structural problem, geometry, material properties, and loading conditions. Classical theories such as the Euler–Bernoulli Beam Theory (EBBT) [1] and the Timoshenko Beam Theory (TBT) [2,3] often fail to capture complex behaviors, including material anisotropy, shear deformability, and warping effects. To overcome these limitations, higher-order theories (HOT) [4,5] have been developed to address more complex structural problems. The Carrera Unified Formulation (CUF) [6] provides a general and systematic framework for defining structural theories of any order. The Axiomatic/Asymptotic Method (AAM) [7,8] can be applied to identify the most influential generalized unknowns and to construct efficient reduced theories for a given problem. Through AAM, the Best Theory Diagrams (BTD) [7,8] can be generated, which require evaluating a large number of candidate theories, resulting in high computational costs. In recent years, Machine Learning (ML) techniques [9,10], and in particular Neural Networks (NN), have attracted increasing attention in structural mechanics and finite element analysis due to their predictive capabilities and reduced computational time. The present paper trains an NN to predict the influence of each generalized variable and to identify the best theories that achieve the highest accuracy for a given number of degrees of freedom. In previous works [11,12], the theories included in the training set were randomly selected. In the present work, the selection uses the Adaptive Sampling [13-15] strategy to identify the most informative and meaningful generalized variables for training the NN. During the selection process, an Extra Trees

Content from this work may be used under the terms of the Creative Commons Attribution 3.0 license. Any further distribution of this work must maintain attribution to the author(s) and the title of the work, journal citation and DOI. Published under license by Materials Research Forum LLC.

Materials Research Proceedings 73 (2026) 190-194 https://doi.org/10.21741/9781644904459-37

surrogate model is iteratively updated and used to guide sampling based on quality, uncertainty, and diversity criteria.

CUF and FEM Formulations

The reference system adopted for beam structures is shown in Fig. 1. Here, the x-z plane lies on the cross-section Ω. More details about the theoretical formulations are available in [6].

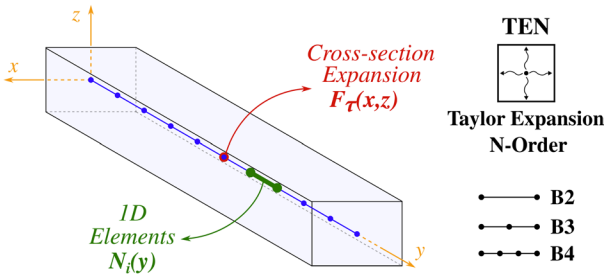

Figure 1: Reference Coordinate System for Beam Models

The displacement field for beams can be expressed as:

$$\boldsymbol{u}(x,y,z) = N_i F_\tau(x,z)\boldsymbol{u}_{\tau i} \tag{1}$$

Where F_τ is the expansion function; τ=1,…, M, and M is the number of expansion terms. N_i is the shape function; $i = 1, \ldots, N_n$, where N_n is the number of FE nodes. $\boldsymbol{u}_{\tau i}$ is the vector of the nodal unknowns. For 1D theories, the expansion function F_τ acts on the cross-section x-z, while the shape function is along the beam axis. For a complete fourth-order beam theory, the displacement field is:

$$\begin{aligned} u_x &= u_{x_1} + xu_{x_2} + zu_{x_3} + x^2u_{x_4} + xzu_{x_5} + z^2u_{x_6} + \cdots + xz^3u_{x_{14}} + z^4u_{x_{15}} \\ u_y &= u_{y_1} + xu_{y_2} + zu_{y_3} + x^2u_{y_4} + xzu_{y_5} + z^2u_{y_6} + \cdots + xz^3u_{y_{14}} + z^4u_{y_{15}} \\ u_z &= u_{z_1} + xu_{z_2} + zu_{z_3} + x^2u_{z_4} + xzu_{z_5} + z^2u_{z_6} + \cdots + xz^3u_{z_{14}} + z^4u_{z_{15}} \end{aligned} \tag{2}$$

Modal shapes and natural frequencies (ω_n) can be obtained by solving the eigenvalue problem:

$$(\boldsymbol{K} - \omega_n^2\boldsymbol{M})\boldsymbol{U} = 0 \tag{3}$$

Neural Networks and Adaptive Sampling

This work aims to train an NN to estimate the accuracy of a structural theory. NN has one input vector, each representing a structural beam theory, which is encoded as a sequence of 0s and 1s, where 1 represents an active generalized variable, e.g.,

$$u_x = u_{x_1} + xu_{x_2} + x^2u_{x_4} + z^2u_{x_6} + x^3u_{x_7} + z^4u_{x_{15}} = [1\ 1\ 0\ 1\ 0\ 1\ 0\ 0\ 0\ 0\ 0\ 1] \tag{4}$$

The resulting arrays are fed into a NN, where the labels are the average relative errors of the first 10 natural frequencies computed for each beam theory with respect to the reference complete fourth-order theory shown in Eq. (2), e.g.,

$$u_x = u_{x_1} + xu_{x_2} + x^2u_{x_4} + z^2u_{x_6} + x^3u_{x_7} + z^4u_{x_{15}} \rightarrow \%E_{AVG} = 3.26\% \tag{5}$$

The trained NN predicts the error of a beam theory for that structural case, taking as inputs the vectors of the structural theories. In previous works [11,12], the training input samples were randomly selected. In contrast, here they are selected using a multi-criteria Adaptive Sampling [13

Materials Research Proceedings 73 (2026) 190-194 https://doi.org/10.21741/9781644904459-37

15] algorithm to train the NN with the most informative and meaningful samples, as shown in Fig. 2.

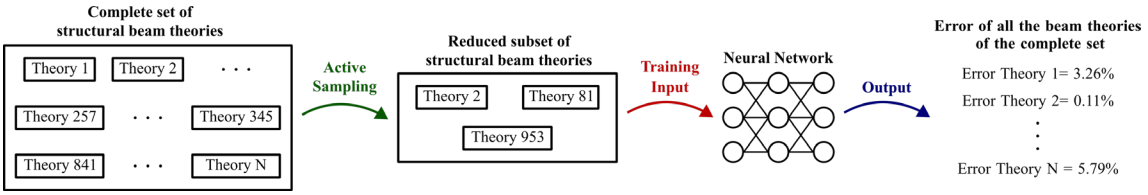

Figure 2: Workflow of the Adaptive Sampling and NN

The adaptive sampling algorithm starts from a small initial set of beam theories and progressively enriches it by selecting new candidates from the complete set. At each step, an Extra Trees surrogate model is trained on the currently selected theories to approximate the relationship between the beam theories and their errors. The trained surrogate is then used to predict the error of the unselected candidate theories. These predictions define a quality contribution, while the variability among the individual trees' predictions provides an estimate of uncertainty. A diversity contribution is also introduced to promote candidates differing from the already selected theories. The final acquisition score is computed as a weighted combination of quality ($\alpha Q(x)$), uncertainty ($\beta U(x)$), and diversity terms ($\gamma D(x)$). The acquisition function is the following:

$$f(x) = \alpha Q(x) + \beta U(x) + \gamma D(x) \tag{6}$$

The theory with the highest score is added to the selected set, and the Extra Trees surrogate is retrained on the enriched dataset. The procedure is repeated until the number of theories requested in the reduced subset is reached, and the resulting set is then used to train the NN.

Numerical Results

The results provided hereafter refer to a single structural beam case. The beam is clamped-free, with a length L of 5m. The material properties are: E=69 GPa, ν=0.33, ρ=2700 kg/m3. The cross section of the beam is shown in Fig. 3. The BTD computed by FEM, NN with random sampling, and NN with adaptive sampling are shown in Fig. 4, while Tables 1, 2, and 3 report the best theories and their accuracies, from AAM using FEM, and the two NN, respectively. In Table 1, the solid black triangle indicates that the generalized variable is active, and the empty one indicates the opposite. A solid blue triangle in Table 2 indicates that the NN predicted the presence of an inactive term in the reference AAM table; an empty blue triangle indicates the opposite. The same applies to the red triangles in Table 3.

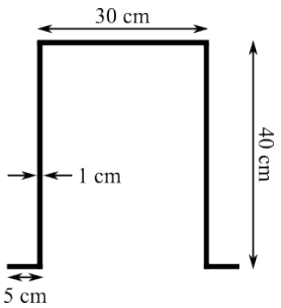

Figure 3: Omega cross-section and its dimensions

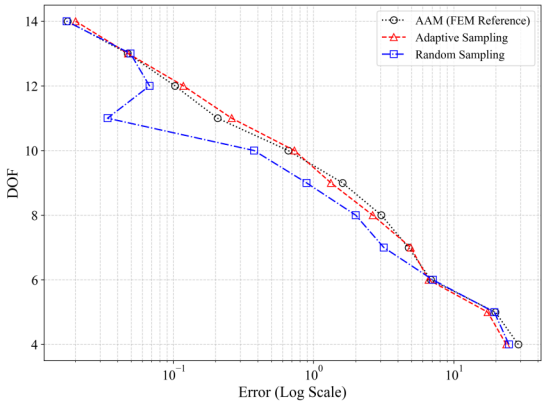

Figure 4: Best Theory Diagram computed by AAM, NN with Random Sampling, and NN with Adaptive Sampling

DOF	x^2	xz	z^2	x^3	x^2z	xz^2	z^3	x^4	x^3z	x^2z^2	xz^3	z^4	$\%E_{AVG}$
14	▲	▲	▲	▲	▲	▲	▲	▲	▲	△	▲	▲	1.757E-02
13	▲	▲	▲	▲	▲	▲	▲	▲	▲	△	▲	△	4.720E-02
12	▲	▲	▲	▲	▲	▲	▲	△	▲	△	▲	△	1.027E-01
11	▲	▲	▲	▲	△	▲	▲	△	▲	△	▲	△	2.064E-01
10	▲	▲	▲	▲	△	▲	△	△	▲	△	▲	△	6.602E-01
9	▲	▲	▲	▲	△	△	△	△	▲	△	▲	△	1.608E+00
8	▲	▲	▲	▲	△	△	△	△	▲	△	△	△	3.046E+00
7	△	▲	▲	▲	△	△	△	△	▲	△	△	△	4.755E+00
6	△	▲	△	▲	△	△	△	△	▲	△	△	△	6.876E+00
5	△	▲	△	▲	△	△	△	△	△	△	△	△	1.983E+01
4	△	△	△	▲	△	△	△	△	△	△	△	△	2.889E+01

Table 1: Best theories of the omega beam computed by AAM (FEM Reference)

DOF	x^2	xz	z^2	x^3	x^2z	xz^2	z^3	x^4	x^3z	x^2z^2	xz^3	z^4	$\%E_{AVG}$
14	▲	▲	▲	▲	▲	▲	▲	▲	▲	△	▲	▲	1.728E-02
13	▲	▲	▲	▲	▲	▲	▲	▲	▲	△	▲	△	4.940E-02
12	▲	▲	▲	▲	△	▲	△	▲	▲	△	▲	▲	6.752E-02
11	△	▲	▲	▲	△	▲	▲	▲	▲	△	▲	△	3.387E-02
10	△	▲	▲	▲	△	▲	△	▲	▲	△	▲	△	3.764E-01
9	△	▲	△	▲	△	▲	△	△	▲	△	▲	▲	8.909E-01
8	△	▲	△	▲	△	▲	△	△	▲	△	▲	△	1.998E+00
7	△	▲	△	▲	△	▲	△	△	▲	△	△	△	3.172E+00
6	△	▲	△	▲	△	△	△	△	▲	△	△	△	7.095E+00
5	△	△	△	▲	△	△	△	△	▲	△	△	△	1.949E+01
4	△	△	△	▲	△	△	△	△	△	△	△	△	2.478E+01

Table 2: Best theories of the omega beam predicted by NN trained with Random Sampling

DOF	x^2	xz	z^2	x^3	x^2z	xz^2	z^3	x^4	x^3z	x^2z^2	xz^3	z^4	$\%E_{AVG}$
14	▲	▲	▲	▲	▲	▲	▲	▲	▲	△	▲	▲	2.009E-02
13	▲	▲	▲	▲	▲	▲	▲	▲	▲	△	▲	△	4.752E-02
12	▲	▲	▲	▲	▲	▲	▲	△	▲	△	▲	△	1.179E-01
11	▲	▲	▲	▲	△	▲	▲	△	▲	△	▲	△	2.605E-01
10	▲	▲	▲	▲	△	▲	△	△	▲	△	▲	△	7.305E-01
9	△	▲	▲	▲	△	△	△	▲	▲	△	▲	△	1.330E+00
8	△	▲	△	▲	△	△	△	▲	▲	△	▲	△	2.642E+00
7	▲	▲	△	▲	△	△	△	△	▲	△	△	△	4.941E+00
6	△	▲	△	▲	△	△	△	△	▲	△	△	△	6.628E+00
5	△	△	△	▲	△	△	△	△	▲	△	△	△	1.747E+01
4	△	△	△	▲	△	△	△	△	△	△	△	△	2.371E+01

Table 3: Best theories of the omega beam predicted by NN trained with Adaptive Sampling

Conclusions

This paper presents an improved methodology, compared with previous works, for estimating the accuracy of a beam theory and its generalized variables for a given problem. The proposed methodology uses an NN to correlate structural theories with their error and an Adaptive Sampling algorithm to select the most informative generalized variables for training the NN. The results show that the NN trained with Adaptive Sampling predicts both the error and the generalized variables of the best theories more accurately than the NN trained with random sampling. Compared with random sampling, the error prediction of the NN trained with Adaptive Sampling improves, and the NN can predict the exact formulation of the best theories with greater precision. For instance, in Table 2, the NN trained with random sampling correctly predicts 56 terms out of 66, while this number increases to 61 terms out of 66 for the NN trained with Adaptive sampling. The results are problem-dependent, since the error and the number of correctly predicted terms vary with the structural beam case. Nevertheless, a general improvement is achieved with only a minor increase in the computational cost of the Adaptive sampling algorithm.

Acknowledgment
This publication is part of the project PNRR-NGEU which has received funding from the MUR–DM117/2023.

References

[1] Euler L. De curvis elasticis. Lausanne and Geneva: Bousquet, 1744.

[2] Timoshenko S.P. On the transverse vibrations of bars of uniform cross-section. The London, Edinburgh, and Dublin Philosophical Magazine and Journal of Science, 43(253):125-131, 1922. https://doi.org/10.1080/14786442208633855

[3] Timoshenko S.P. On the correction for shear of the differential equation for transverse vibrations of prismatic bars. The London, Edinburgh, and Dublin Philosophical Magazine and Journal of Science, 41(245):744-746, 1921. https://doi.org/10.1080/14786442108636264

[4] Carrera E., Petrolo M., On the effectiveness of higher-order terms in refined beam theories. Journal of Applied Mechanics, 78(2):021013, 11 2010. https://doi.org/10.1115/1.4002207

[5] Carrera E., Pagani A., Petrolo M., Zappino E., Recent developments on refined theories for beams with applications. Mechanical Engineering Reviews, 2(2):14-00298-14-00298, 2015. https://doi.org/10.1299/mer.14-00298

[6] Carrera E., Cinefra M., Petrolo M., Zappino E., Finite element analysis of structures through unified formulation. John Wiley & Sons, 2014. https://doi.org/10.1002/9781118536643

[7] Petrolo M., Carrera E., Best theory diagrams for multilayered structures via shell finite elements. Advanced Modeling and Simulation in Engineering Sciences, 2019. https://doi.org/10.1186/s40323-019-0129-8

[8] Petrolo M., Iannotti, P., Best Theory Diagrams for Laminated Composite Shells Based on Failure Indexes. Aerotec. Missili Spaz. 102, 199-218, 2023. https://doi.org/10.1007/s42496-023-00158-5

[9] Kudela J., Matousek R., Recent advances and applications of surrogate models for finite element method computations: a review: J. Kudela, R. Matousek. Soft Computing, 26(24), pp.13709-13733, 2022. https://doi.org/10.1007/s00500-022-07362-8

[10] Cunha B.Z, Droz C., Zine A.M., Foulard S., Ichchou M., A review of machine learning methods applied to structural dynamics and vibroacoustic. Mechanical Systems and Signal Processing, 200, p.110535, 2023. https://doi.org/10.1016/j.ymssp.2023.110535

[11] Petrolo M., Pagani A., Carrera E., Candita G., Iannotti P., Mapping beam cross-section features to higher-order generalized variables using machine learning. Thin-Walled Structures, Volume 218, Part C, 2026. https://doi.org/10.1016/j.tws.2025.114108

[12] Petrolo M., Pagani A., Candita G., Iannotti P., Carrera E., Assessment of multi-fidelity structural theories for dynamic analyses using machine learning. In Proceedings of the ASME 2025 Aerospace Structures, Structural Dynamics, and Materials Conference SSDM2025, Houston, 2025. https://doi.org/10.1115/SSDM2025-152306

[13] Settles, B. Active learning literature survey, 2009

[14] Liu H., Ong Y.S., Cai J., A survey of adaptive sampling for global metamodeling in support of simulation-based complex engineering design: H. Liu et al. Structural and Multidisciplinary Optimization, 57(1), pp.393-416, 2018. https://doi.org/10.1007/s00158-017-1739-8

[15] Ghazi Y., Alhazmi N., Tezaur R. and Farhat C., Training a neural-network-based surrogate model for aerodynamic optimisation using a Gaussian process. International Journal of Computational Fluid Dynamics, 36(7), pp.538-554, 2022. https://doi.org/10.1080/10618562.2022.2138863

Materials Research Proceedings 73 (2026) 195-199 https://doi.org/10.21741/9781644904459-38

Effect of Geometric Parameters on the Failure Index of Composite Deployable Booms

Riccardo AUGELLO[1,a*], Erasmo CARRERA[1,2,b], Francesco LATINI[3,c], Marco PETROLO[1,d]

[1]MUL2 lab, Politecnico di Torino, Italy

[2]College of Eng, PMU, SA

[3]Agenzia Spaziale Italiana, Via del Politecnico snc – 00133 Roma, Italy

[a]riccardo.augello@polito.it, [b]erasmo.carrera@polito.it, [c]francesco.latini@asi.it, [d]marco.petrolo@polito.it

Keywords: Deployable Composite Booms, Geometric Parameters, Failure Index, Carrera Unified Formulation, Nonlinear Structural Analysis

Abstract. This study investigates how geometric parameters (particularly the length) influence the failure index of thin-walled composite deployable booms. The analysis is performed using a 1D refined finite-element model based on the Finite Element Method (FEM) and the Carrera Unified Formulation (CUF). In this model, the 3D displacement field is expanded across the cross-section with quadratic Lagrange polynomials (L9) and along the boom axis with cubic (B4) finite elements. Hashin's failure criteria are used at each equilibrium state to compute Failure Index (FI), assuming a pristine linear-elastic material. Numerical results show that longer booms achieve larger tip rotations before activating FI, and that the first failure mode is consistently matrix compression (MC). The findings confirm that increasing boom length significantly alters the moment–rotation response, maximum achievable rotation, and damage initiation pattern, underlining the critical role of geometry. A progressive damage model is recommended for future work to capture post-initiation behavior.

Introduction

Lightweight deployable composite booms are key enabling components for space structures (antennas, solar arrays, telescopes, etc.) because they deliver high stiffness-to-mass ratio and can be stowed compactly. Common designs include tape-spring elements and TRAC (triangular rollable and collapsible) booms. However, their extreme slenderness and material anisotropy pose challenges: classical 3D finite-element models are accurate but computationally expensive for such thin-walled beams. Refined one-dimensional models using the Carrera Unified Formulation (CUF) [1,2] have proven effective for composite structures [3,4]. CUF allows arbitrary-order expansions of the displacement field across the cross-section, enabling high-order 1D elements that capture 3D stress states. For example, a global/local CUF approach for deployable booms achieved accurate local stress fields with reduced cost [5].

Geometric design parameters strongly affect the mechanical response of composite beams. Prior studies [5] highlight that variations in thickness, length, or cross-sectional shape significantly change load transmission and failure behavior in composite components. In the context of deployable booms, boom length and boundary conditions markedly influence bending stiffness and failure onset [6]. Here, the effect of length on the Failure Index (FI) of booms under bending is examined. The failure index is computed using the three-dimensional Hashin failure criteria for composites, and the influence of geometric variations on the point at which the FI exceeds 1 is identified. The adopted refined 1D CUF model provides a balance between accuracy and efficiency.

Content from this work may be used under the terms of the Creative Commons Attribution 3.0 license. Any further distribution of this work must maintain attribution to the author(s) and the title of the work, journal citation and DOI. Published under license by Materials Research Forum LLC.

Materials Research Proceedings 73 (2026) 195-199 https://doi.org/10.21741/9781644904459-38

Methodology

According to the CUF, the 3D displacement field can be expressed in the following unified form:

$$\boldsymbol{u}(x,y,z) = F_\tau(x,z)\boldsymbol{u}_\tau(y), \tau = 1,2,\ldots,M$$

where $\boldsymbol{u}$ is the displacement vector, whose components are defined with respect to the global reference system (x,y,z). The functions $F_\tau(x,z)$ are the cross-sectional expansion functions defined over the in-plane coordinates (x,z), τ is the summation index, and M is the number of terms adopted in the cross-sectional displacement expansion. In the present work, quadratic Lagrange polynomials (L9) are used to approximate the kinematic field over the cross-section.

The displacement field along the beam axis is discretized by means of the Finite Element Method (FEM). Accordingly, the generalized displacement vector $\boldsymbol{u}_\tau(y)$ can be interpolated along the beam axis as:

$$\boldsymbol{u}(x,y,z) = N_i(y)F_\tau(x,z)\boldsymbol{u}_{\tau i}, i = 1,2,\ldots,N_n$$

where $N_i(y)$ is the i-th one-dimensional shape function, i is the summation index, N_n is the number of finite-element nodes per element, whereas $\boldsymbol{u}_{\tau i}$ is the vector of nodal unknowns associated with the cross-sectional expansion term F_τ.

The stress $\boldsymbol{\sigma}$ components are given in vectorial form as follows.

$$\boldsymbol{\sigma} = \{\sigma_{xx}\ \sigma_{yy}\ \sigma_{zz}\ \sigma_{yz}\ \sigma_{xz}\ \sigma_{xy}\}^T$$

To assess material failure, the 3D Hashin failure criterion [7] is adopted. This criterion allows the identification of the dominant failure mode at the ply level on the basis of the local stress state. Four different failure indices are considered, namely Fiber Tension (FT), Fiber Compression (FC), Matrix Tension (MT), and Matrix Compression (MC):

FT: $\left(\frac{\sigma_{11}}{X_T}\right)^2 + \frac{\sigma_{12}^2+\sigma_{13}^2}{S_{12}^2} \geq 1$

FC: $\left(\frac{\sigma_{11}}{X_C}\right)^2 \geq 1$

MT: $\frac{(\sigma_{22}+\sigma_{23})^2}{Y_T^2} + \frac{\sigma_{23}^2-\sigma_{22}\sigma_{33}}{S_{23}^2} + \frac{\sigma_{12}^2+\sigma_{13}^2}{S_{12}^2} \geq 1$

MC: $\left[\left(\frac{Y_C}{2S_{23}}\right)-1\right]\left(\frac{\sigma_{22}+\sigma_{33}}{Y_C}\right) + \frac{(\sigma_{22}+\sigma_{13})^2}{4S_{23}^2} + \frac{\sigma_{23}^2-\sigma_{22}\sigma_{33}}{S_{23}^2} + \frac{\sigma_{12}^2+\sigma_{13}^2}{S_{12}^2} \geq 1$

where X represents the material strength in the fiber direction, and Y represents that of the transverse direction, with the subscripts T and C denoting tensile and compressive loading, respectively. S_{ij} denotes the material shear strengths.

Numerical Results

The first numerical result regards the tape spring of Fig. 1, with t = 80 μm, r = 11.25 mm, and α = 90°.

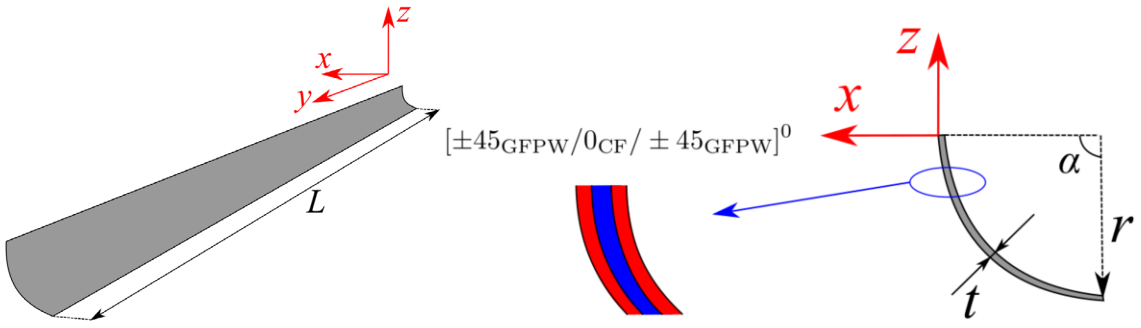

Figure 1 – Considered tape spring.

Materials Research Proceedings 73 (2026) 195-199 https://doi.org/10.21741/9781644904459-38

The structure is simply supported at its edges and subjected to opposite moments to induce bending. Figure 1 shows the nonlinear static curves considering various lengths of the deployable.

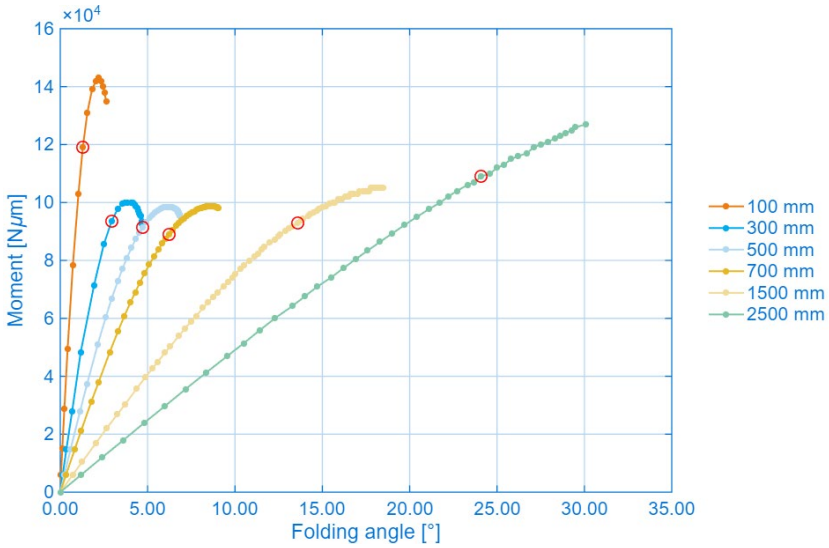

Figure 2 – Nonlinear curves varying the length of the analyzed tape spring. Circles indicate the point of first FI > 1.

Several considerations can be made:

- The longer the structure, the higher are the reached angle before any failure occurs;
- The peak moment is around 145 Nmm for the 100 mm-long TAPE deployable boom. It then decreases as the boom length increases, reaching about 100 Nmm for lengths between 300 and 700 mm. For longer booms, the peak moment increases again, almost reaching the same value as the 100 mm case in the 2500 mm case.

In Fig. 2, red circles correspond to the first FI greater than 1. In all cases, the first active failure mode is MC (Matrix Compression). Figure 3 shows the deformed configuration of 1500 and 2500 mm tape springs in correspondence of MC > 1.

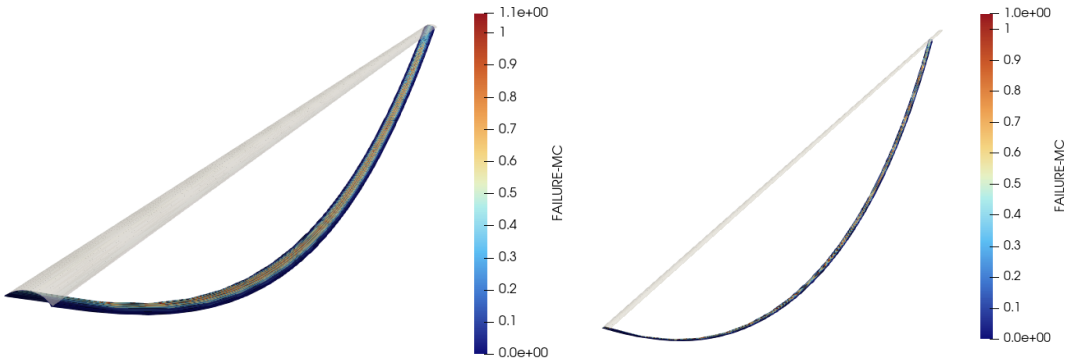

Figure 3 – Deformed configuration of MC > 1 for the tape spring study case. 1500mm left, 2500mm right.

The second study case is about the TRAC boom. The geometry of the cross-section is reported in Fig. 4, and w=8mm, r=12.7mm, θ= 90°, t = 0.08mm. The stacking sequence is the same as for the tape spring.

Materials Research Proceedings 73 (2026) 195-199 https://doi.org/10.21741/9781644904459-38

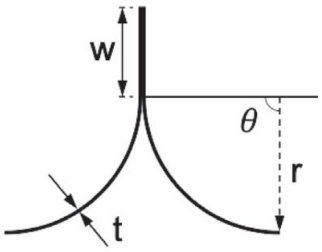

Figure 4 – Geometry of the cross-section of the TRAC.

The boundary and loading conditions are the same as in the previous analysis and the results are reported in Fig. 5, along with circles indicating the first FI > 0.

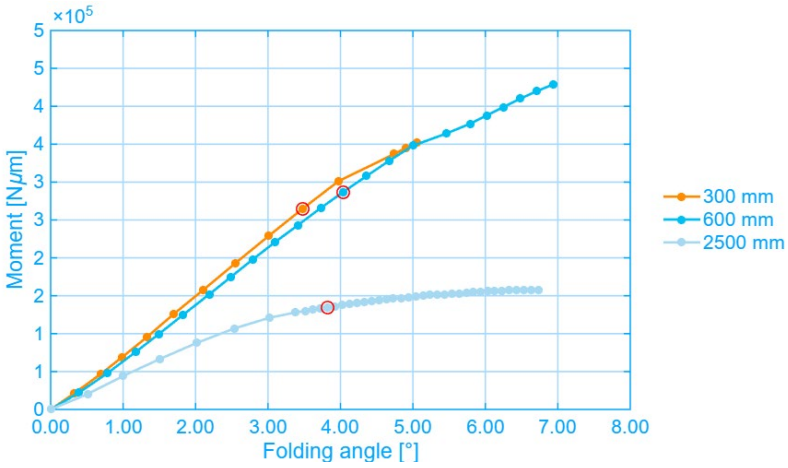

Figure 5 – Nonlinear curves varying the length of the analyzed TRAC. Circles indicate the point of first FI > 1.

Clearly, similar values for 300 and 500-mm-cases arise and convergence is met and the curves align with those available in the literature [8]. As the previous cases, the first FI to exceed the value of 1 is MC.

Finally, Fig. 6 reports deformed the failing deformed configurations. The 2500 m buckles.

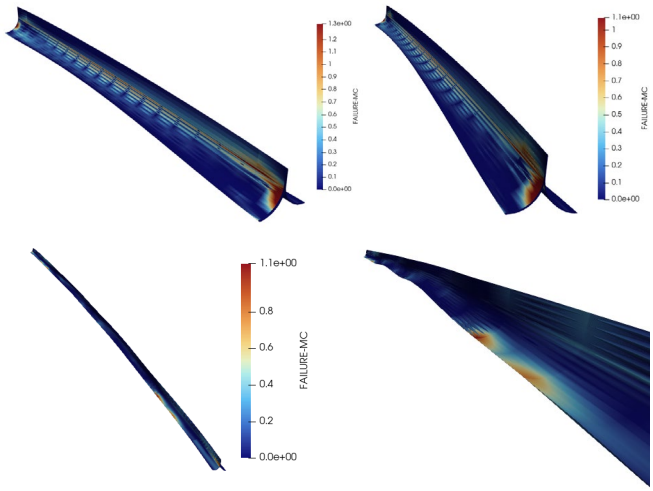

Figure 6 – Deformed configuration of MC > 1 for the TRAC study case. 300mm top left, 500mm top right and 2500mm bottom.

Conclusions

This parametric study highlights the significant role of geometry in deployable composite boom response. Boom length strongly influences the load–deflection behavior and failure onset. Longer booms exhibit greater flexibility and delay the onset of failure under the same end moments. Across all cases, matrix-compression was the first failure mode. The results confirm that careful geometric design (length, cross-section) is crucial for ensuring structural integrity of deployable booms. The CUF-based 1D modelling strategy proved effective for capturing these effects. Future work will implement progressive damage models to simulate post-initiation behavior under even larger loads.

Acknowledgments

This study was carried out within the DISPCOMP funded by the Italian Space Agency, ASI, under contract n. 2024-38.I.0.

References

[1] E. Carrera, G. Augello, and R. Augello, Implementation of Beam-Type Finite Elements Based on Carrera Unified Formulation. Cham, Switzerland: Springer, 2026. https://doi.org/10.1007/978-3-031-95856-4

[2] E. Carrera, M. Cinefra, M. Petrolo, and E. Zappino, Finite Element Analysis of Structures Through Unified Formulation. Hoboken, NJ, USA: Wiley, 2014. https://doi.org/10.1002/9781118536643

[3] I. Kaleel, M. Petrolo, and E. Carrera, "Elastoplastic and progressive failure analysis of fiber-reinforced composites via an efficient nonlinear microscale model," Aerotecnica Missili & Spazio, vol. 97, no. 2, pp. 103–110, 2018. https://doi.org/10.1007/BF03405805

[4] D. Scano, E. Carrera, and M. Petrolo, "Use of the 3D equilibrium equations in the free-edge analyses for laminated structures with the variable kinematics approach," Aerotecnica Missili & Spazio, vol. 103, pp. 179–195, 2024. https://doi.org/10.1007/s42496-023-00177-2

[5] R. Augello, A. Pagani, E. Carrera, and D. A. Iannotta, "Stress and failure onset analysis of thin composite deployables by global/local approach," AIAA Journal, vol. 60, no. 10, pp. 5954–5966, 2022. https://doi.org/10.2514/1.J061899

[6] A. Pagani, R. Augello, and E. Carrera, "Numerical simulation of deployable ultra-thin composite shell structures for space applications and comparison with experiments," Mechanics of Advanced Materials and Structures, vol. 30, no. 8, pp. 1591–1603, 2023. https://doi.org/10.1080/15376494.2022.2037173

[7] Z. Hashin, "Failure criteria for unidirectional fiber composites," Journal of Applied Mechanics, vol. 47, no. 2, pp. 329–334, 1980. https://doi.org/10.1115/1.3153664

[8] C. Leclerc and S. Pellegrino, "Nonlinear elastic buckling of ultra-thin coilable booms," International Journal of Solids and Structures, vol. 203, pp. 46–56, 2020. https://doi.org/10.1016/j.ijsolstr.2020.06.042

Materials Research Proceedings 73 (2026) 200-205 https://doi.org/10.21741/9781644904459-39

Mode Change and Evolution of Thin Deployable Space Structures in Small and Large Displacement Regimes

Erasmo CARRERA[2,a*], Riccardo AUGELLO[2,b], Andrea SERINO[1,2,c]

[1]University in Trento, Italy

[2] mul[2] lab, Politecnico di Torino, Italy

[a]erasmo.carrera@polito.it, [b]riccardo.augello@polito.it, [c]andrea.serino@polito.it

Keywords: Deployable Space Structures, Geometric Non-Linearities, Modes Change, Carrera Unified Formulation (CUF)

Abstract. Predicting the dynamic response of thin-walled deployable space structures, such as tape springs, remains a major challenge due to severe geometric nonlinearities. Classical 1D beam models miss essential cross-sectional morphing. Consequently, analyzing these architectures typically requires the use of computationally expensive 3D solid elements. To overcome this limitation, this study employs the 1D Carrera Unified Formulation (CUF) to investigate the modal evolution of a tape spring subjected to large axial tensile loads. By solving the generalized eigenvalue problem around distinct equilibrium states, the pre-stress field is explicitly incorporated via the geometric stiffness matrix ($\boldsymbol{K}_{\sigma}$). Comparing linear and non-linear analyses reveals that a linear assumption yields an unmitigated stress-stiffening effect, causing unrealistic frequency spikes and chaotic modal shifts. The non-linear analysis, however, successfully captures cross-section deformation, which significantly mitigates artificial stiffening and stabilizes modal evolution. These findings highlight that combining high-fidelity non-linear equilibrium analysis with advanced modal tracking (MAC) is essential to correctly interpret these complex structural dynamics.

Introduction

Deployable space structures are essential for modern space missions due to their high packaging efficiency and minimal mass [1], physically transforming from highly compact stowed envelopes into large-scale operational systems. However, during orbital deployment and operation, these ultra-thin members are subjected to severe dynamic environments. Predicting their response is inherently complex due to the simultaneous presence of large global deflections and local instabilities. Recent findings [2] highlight that high periodic forces near resonant frequencies can trigger local flange buckling; this localized instability drastically alters the structural signature and overall dynamic behavior. Since ground testing of such highly flexible structures is severely limited by gravity sagging and suspension effects, high-fidelity numerical simulation becomes an indispensable design tool. In this context, standard commercial Finite Element Method (FEM) software packages utilizing classical 1D beam elements (e.g., Euler-Bernoulli or Timoshenko) exhibit critical limitations. As demonstrated by Pagani and Carrera [3], these theories fail to capture essential cross-sectional deformations such as in-plane stretching and warping, which are massive in thin-walled space architectures. By neglecting these terms, classical models provide an incomplete description of the six-component stress tensor. Since the geometric stiffness matrix $\boldsymbol{K}_{\boldsymbol{\sigma}}$ explicitly maps the internal pre-stress state, any approximation in the stress field directly leads to inaccurate predictions of natural frequencies and mode shapes under load. Indeed, previous studies [4] show that geometric nonlinearities in post-buckling regimes can shift natural frequencies by over 100%, severely altering mode shapes. Failing to track this evolution leads to undetected mode veering and crossing phenomena. Moving beyond classical approximations, this work utilizes the

Content from this work may be used under the terms of the Creative Commons Attribution 3.0 license. Any further distribution of this work must maintain attribution to the author(s) and the title of the work, journal citation and DOI. Published under license by Materials Research Forum LLC.

Materials Research Proceedings 73 (2026) 200-205 https://doi.org/10.21741/9781644904459-39

Carrera Unified Formulation (CUF), a framework extensively validated for the nonlinear analysis of metallic and composite structures [5]. By comparing linear and non-linear equilibrium paths, the study traces how cross-sectional morphing and internal pre-stress accumulation fundamentally reshape the dynamic signature of the structure.

Methodology

Structural modeling relies on the 1D Carrera Unified Formulation (CUF) [5] implemented via the mul2 code. To accurately capture the complex kinematics of the tape spring, Lagrange Expansion (LE) polynomials are employed, providing 3D-like accuracy while overcoming the shear-locking issues typical of classical theories. The numerical procedure investigates the modal evolution using a two-tiered approach. The first approach evaluates the dynamic behavior assuming a linear geometric response. The internal pre-stress state is scaled through an incremental load factor $\boldsymbol{\lambda}$, varying in symmetrical steps from 0 (undeformed state) to 1 (target elongation). The generalized eigenvalue problem is solved using a linearized stiffness matrix:

$$\det(\boldsymbol{K}_0 + \lambda \boldsymbol{K}_\sigma - \omega^2 \boldsymbol{M}) = 0 \text{ , with } \boldsymbol{K_t}(\lambda) = \boldsymbol{K_0} + \lambda \boldsymbol{K}_\sigma$$

where K_0 is the linear elastic stiffness and $\boldsymbol{K}_\sigma$ is the geometric stiffness matrix.

To account for the large displacements and rotations typical under operating conditions of these thin-walled structures, a total Lagrangian approach is subsequently adopted. Following the framework established by Pagani and Carrera [3], the geometrically nonlinear equilibrium path is traced using a Newton-Raphson scheme coupled with an arc-length method [6]. Unlike the linear model, the generalized eigenvalue problem is solved using the exact tangent stiffness matrix $\boldsymbol{K}_t$:

$$\det(\boldsymbol{K}_t - \omega^2 \boldsymbol{M}) = 0, with\ \boldsymbol{K}_t = \boldsymbol{K}_0 + \boldsymbol{K}_{NL} + \boldsymbol{K}_\sigma$$

where $\boldsymbol{K_{NL}}$ represents the nonlinear contribution arising from large displacements (incorporating first and second-order variations) [3]. Thanks to the CUF framework to analyse the kinematics, these matrices rigorously map the evolving 3D pre-stress field and cross-sectional flattening at each discrete load step.

To distinguish between mode crossing and mode veering during the non-linear equilibrium path [4], tracking solely the frequency eigenvalues is insufficient. Therefore, the Modal Assurance Criterion (MAC) [7], is employed to correlate the extracted eigenvectors Φ across consecutive load increments (i.e., adjacent equilibrium states) [4] - [8]. A MAC value approaching 1 confirms the correct tracking of the physical mode shape despite frequency shifts. Conversely, sudden drops in the diagonal MAC values pinpoint energy redistributions, identifying the exact load levels where structural coupling and mode veering occur.

Numerical Results.

The tape spring is 1 meter long and subjected to clamped-free (cantilever) boundary conditions. The structure is manufactured with a symmetric composite layup sequence defined as $\left[\pm 45^{\circ GFPW}/0^{\circ CF}/\pm 45^{\circ GFPW}\right]$. In this specific arrangement, CF denotes a thin ply reinforced with unidirectional carbon fibers, while GFPW refers to a plain weave glass fiber scrim. The specific physical and mechanical properties of the constituent laminae, essential for the accurate computation of the laminate stiffness, are summarized in Table 1.

Table 1. ***Composite material properties***

Material	E_1, E_2 *[GPa]*	G_{12} *[GPa]*	ν_{12}	ρ $[kg/m^3]$	***t*** *[mm]*
CF	128, 6.5	7.6	0.35	1550	0.030
GFPW	23.8, 23.8	3.3	0.17	1100	0.025

Materials Research Proceedings 73 (2026) 200-205 https://doi.org/10.21741/9781644904459-39

To discretize the computational domain, the longitudinal axis is meshed with 10 four-node cubic beam elements (B4), while the cross-sectional kinematics are modeled using nine-node Lagrange polynomial expansions (L9). The dynamic signature of the tape spring is investigated under a pure tension state induced by applying a uniform pressure to the free-end cross-section; the load is incrementally scaled until the structure reaches a 20% longitudinal elongation. Although this extreme deformation level may exceed the physical elastic threshold of the composite material, it is intentionally selected as a severe computational benchmark to assess the massive geometric non-linearities and pre-stress accumulation.

Consistent with the previously outlined procedure, the equilibrium states along the non-linear path are analyzed at the same discrete elongation intervals used for the linear case. For these configurations, the free vibrations are evaluated by solving the eigenvalue problem formulated with the updated exact tangent stiffness matrix $\boldsymbol{K}_t$. Figure 1 illustrates both the linear and non-linear equilibrium paths, tracking the axial displacement (u_y) at the tip cross-section alongside the 3D structural deformation at representative load steps.

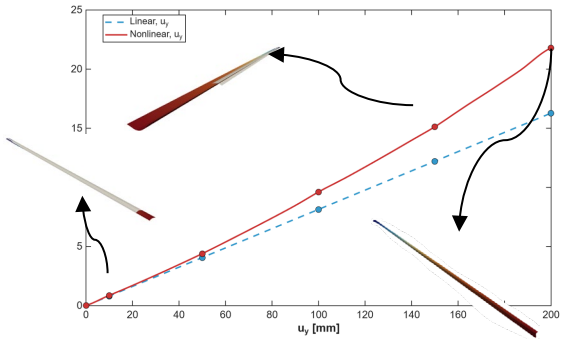

Figure 1. Nonlinear and linear equilibrium path.

Assuming a linear geometric response, the frequency tracking (Figure 3) reveals a pronounced, mode-dependent stiffening behavior under axial elongation. From a computational standpoint, this behavior is governed by the geometric stiffness matrix ($\boldsymbol{K}_\sigma$), whose contribution becomes increasingly dominant as the axial stress-stiffening induced by the applied tensile load increases. As a result, the natural frequencies exhibit an overall monotonic increase. Notably, the MAC analysis (Figure 4) successfully captures complex dynamic interactions that would otherwise be lost. A severe mode crossing involves the initial 3rd mode, which is highly sensitive to the $\boldsymbol{K}_\sigma$ contribution. It exhibits a steep stiffening gradient, abruptly crossing the 4th mode around $u_y = 1$ mm. Subsequently, its frequency decreases in the displacement range between $u_y = 150$ mm and 200 mm. However, this trend should not be regarded as a physical response. As discussed previously, the linear formulation evaluates the tangent stiffness matrix by assuming that the geometric stiffness matrix is linearly proportional to the applied load. Under this assumption, an increase in load necessarily leads to an increase in tangent stiffness and consequently, in the natural frequencies. Globally, fundamental modes, despite minor frequency fluctuations, experience consistent spatial alterations mainly due to the torsional modes behavior (Figure 2).

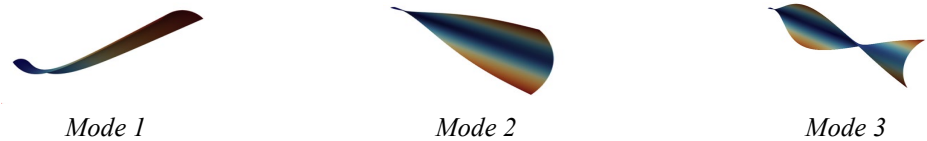

Mode 1 *Mode 2* *Mode 3*



Mode 4 *Mode 5*

Materials Research Proceedings 73 (2026) 200-205 https://doi.org/10.21741/9781644904459-39

Figure 2. The first fifth mode shapes (linear analysis).

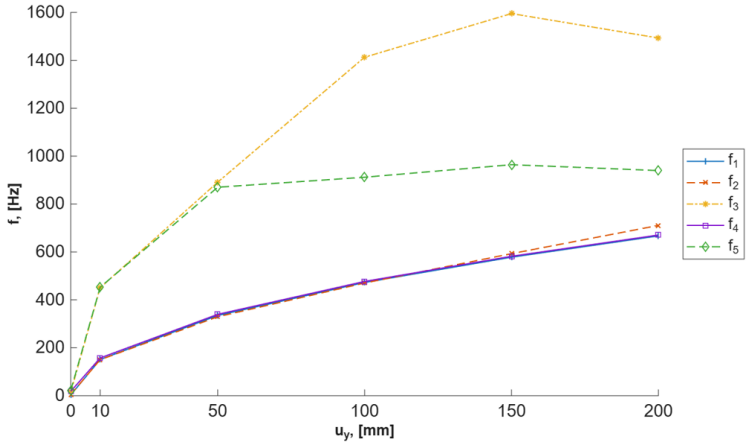

Figure 3. Natural frequencies vs. tape spring elongation (linear regime). Evolution of the natural frequencies as the tape elongation increases from the initial undeformed configuration up to 20% strain relative to the initial state.

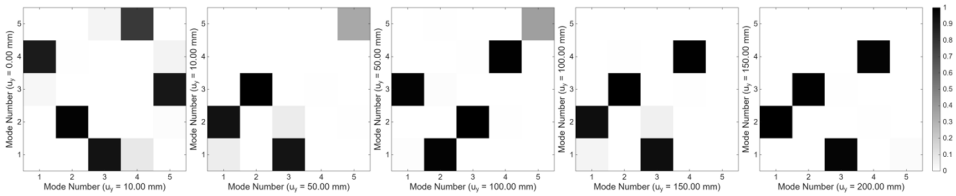

Figure 4. MAC matrices used to evaluate the modal correspondence across the six loading steps of the linear equilibrium path, associated with structural elongations ranging from 0% to 20% of the initial length.

To fully capture the actual dynamic behavior of the tape spring, the frequency tracking is subsequently performed along the non-linear equilibrium path, considering the same elongation steps (up to 20% of the initial length). The corresponding natural frequencies and MAC matrices are reported in Figure 5 and Figure 6, respectively. Comparing the linear and non-linear results reveals fundamental differences driven by the cross-sectional morphing of the tape spring. In the non-linear analysis, the axial elongation induces a progressive alteration of the cross-section [9]. This geometric shape adaptation drastically reduces the principal moments of inertia, providing a softening effect that counteracts the stress-stiffening [4] observed in the linear assumption. As a direct consequence, the severe and unrealistic frequency spikes observed in the linear analysis (e.g., the former 3rd mode) are significantly mitigated. Instead, the non-linear tracking highlights new, complex modal interactions. Notably, a drop in the 3rd mode is observed around $u_y = 100$ mm, indicating a severe loss of stiffness due to the cross-section alteration, see Figure 7b. Furthermore, the MAC matrices successfully capture a new distinct mode crossing between $mode\ \ 1$ and $mode\ \ 4$ occurring between $u_y = 150$ mm and 200 mm, see Figure 7a. As the cross section changes its shape, the stiffness drops, causing the two fundamental spatial shapes to swap their frequency order. A closer inspection of the MAC matrices (Figure 6) alongside the frequency tracking (Figure 5) reveals that, unlike the linear scenario, the mode shapes preserve their spatial identity more consistently over the initial elongation steps.

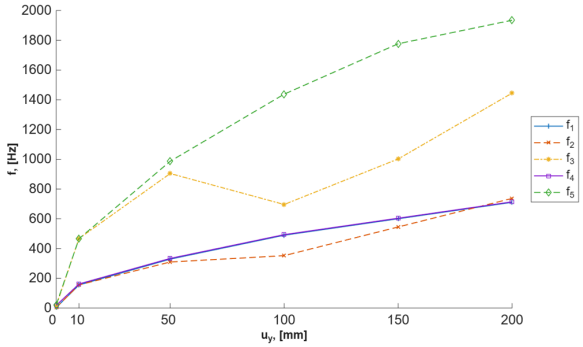

Figure 5. Natural frequencies vs. tape spring elongation (non-linear regime). Evolution of the natural frequencies as the tape elongation increases from the initial undeformed configuration up to 20% strain relative to the initial state.

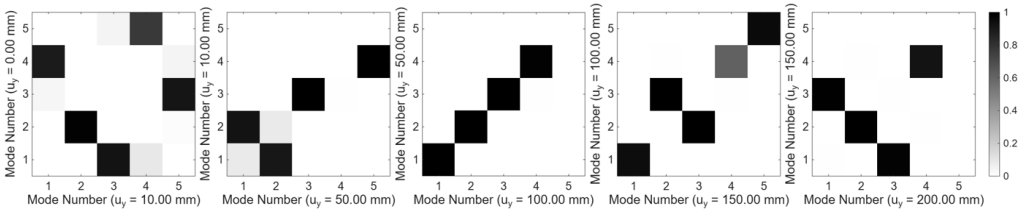

Figure 6. MAC matrices used to evaluate the modal correspondence across the six loading steps of the nonlinear equilibrium path, associated with structural elongations ranging from 0% to 20% of the initial length.

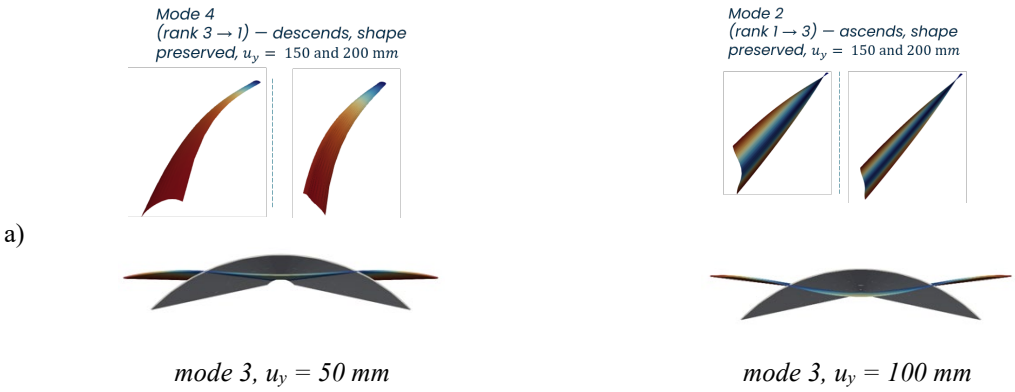

Figure 7. Relevant mode shapes from the non-linear analysis highlighting the effects of cross-sectional morphing: (a) spatial shape exchange between Mode 1 and Mode 4; (b) progressive cross-section alteration of Mode 3, responsible for the localized drop in stiffness. For improved visual clarity, the deformed structure is represented using a color gradient, in contrast to the undeformed configuration shown in grey.

Conclusions

This paper investigated the complex non-linear dynamic behavior of tape spring structures subjected to large axial displacements. The study highlighted the critical influence of geometric non-linearities and cross-sectional morphing on the evolution of the structural natural frequencies and mode shapes.

Methodologically, the adopted total Lagrangian formulation, coupled with Green-Lagrange strains and the CUF, provided a highly accurate description of the non-linear states. This aspect proved to be of fundamental importance for the correct evaluation of the tangent stiffness matrix, which directly governs the extraction of the load-dependent eigenfrequencies and eigenmodes.

Moreover, the 1D CUF successfully captured complex 3D-like deformations, circumventing the need for computationally prohibitive 3D solid elements in standard commercial software.

The comparison between the linear and nonlinear equilibrium paths revealed that the linear formulation is physically inadequate for open thin-walled structures undergoing large displacements. The linear analysis predicts an unbounded stress-stiffening effect, leading to spurious modal interactions and unrealistically high natural frequencies. In contrast, the non-linear model explicitly captures the geometric adaptation of the cross-section, leading to a more coherent modal evolution and suppressing the excessive artificial stiffening.

References

[1] S. Pellegrino, "Deployable structures in engineering," in Deployable structures, Springer, 2001, pp. 1-35. https://doi.org/10.1007/978-3-7091-2584-7_1

[2] R. Augello and S. Pellegrino, "Vibration Damping of Thin-Shell Deployable Structures Through Local Buckling," in AIAA SCITECH 2025 Forum, 2025. https://doi.org/10.2514/6.2025-0693

[3] A. Pagani and E. Carrera, "Unified formulation of geometrically nonlinear refined beam theories," vol. 25, no. 1, pp. 15-31, 2018. https://doi.org/10.1080/15376494.2016.1232458

[4] A. Pagani, R. Augello and E. Carrera, "Frequency and mode change in the large deflection and post-buckling of compact and thin-walled beams," vol. 432, pp. 88-104, 2018. https://doi.org/10.1016/j.jsv.2018.06.024

[5] E. Carrera, G. Giunta and M. Petrolo, Beam structures: classical and advanced theories, John Wiley & Sons, 2011. https://doi.org/10.1002/9781119978565

[6] E. Carrera, "A study on arc-length-type methods and their operation failures illustrated by a simple model," vol. 50, no. 2, pp. 217-229, 1994. https://doi.org/10.1016/0045-7949(94)90297-6

[7] R. J. Allemang, R. W. Rost and D. L. Brown, "Dual input estimation of frequency response functions for automotive structures," 1982. https://doi.org/10.4271/820193

[8] F. Franzoni, R. Degenhardt, J. Albus and M. A. Arbelo, "Vibration correlation technique for predicting the buckling load of imperfection-sensitive isotropic cylindrical shells: An analytical and numerical verification," vol. 140, pp. 236-247, 2019. https://doi.org/10.1016/j.tws.2019.03.041

[9] K. A. Seffen and S. Pellegrino, "Deployment dynamics of tape springs," vol. 455, no. 1983, pp. 1003-1048, 1999. https://doi.org/10.1098/rspa.1999.0347

Materials Research Proceedings 73 (2026) 206-210 https://doi.org/10.21741/9781644904459-40

Numerical Simulation of the Water-Air-Abrasive Mixture within a Cutting Head for Water Jet Machining

Amene ALLAL[1,2,a *], Pascal FEDE[2,b *], Laurent CROUZEIX[1,c] and Patrick GILLES[1,d]

[1]Institut Clément Ader, 3 Rue Caroline Aigle, 31400, France

[2]Institut Mécanique des Fluides de Toulouse, 2 Allée du Pr Camille Soula, 31400, France

[a]amene.allal@utoulouse.fr, [b]pascal.fede@imft.fr, [c]laurent.crouzeix@iut-tlse3.fr, [d]gilles@insa-toulouse.fr

Keywords: Abrasive Water Jet, Computational Fluid Dynamics, Three-Phase Mixing, Machining

Abstract. Abrasive waterjet machining is an unconventional process for blind machining and is in full expansion. Its concentrated action limits both the heating of the machined zone and the forces exerted on the workpiece, allowing the reduction of deformation of thin and hard metal plates during machining. Previous studies identified the process parameters that must be controlled to meet quality requirements. However, they also highlighted the limits of experimental approaches. In this work, numerical simulations have been performed to better understand the jet dynamics, which is difficult to access experimentally because it is composed of three phases: the air (gas), the water (liquid) and the abrasive particles (solid). In the numerical model, the three phases are represented with an Euler-Euler approach and their inter-play interactions are accounted for. The main parameters of the study are the water pressure and the abrasive flow rate. The represented domain corresponds to a Paser 4 ™ head from the nozzle to the outlet of the focusing tube. The three-dimensional mesh is composed of approximately 700 000 tetrahedral and hexahedral cells. The analysis focuses on the particle concentration and their velocities. This approach allows a deeper understanding of the mixing occurring in the upper part of the cutting head and enables a fine characterization of the abrasive jet at the outlet of the focusing tube. The particle volume fraction and velocity components are evaluated at different cross-sections of the cutting head. The results show the presence of air recirculation in the mixing chamber, which affect the particle trajectories, and consequently their distribution at the outlet of the focusing tube.

Introduction

The use of hard metals such as the titanium alloy Ti-6Al-4V in the aeronautics sector is of great importance given their application in turbojet engines. This combination of metals creates a material with significant properties, such as high fatigue resistance and resistance to highly aggressive environments. However these properties make it extremely difficult to machine using conventional processes. This is why the transition to non-conventional machining methods is essential such as abrasive waterjet machining. The advantage of mixing water with abrasive and air lies in the low cutting forces involved, as well as the absence of a heat-affected zone [1]. However depending on the operating conditions, the three-phase flow behaves differently and therefore directly affects the depth of milling. The aim of this study is to predict and understand the flow within the Paser 4 ™ cutting head in order to better predict the jet at its outlet. Given the limitations of experimental studies [2], [3] numerical simulations have been carried out in the past to predict the behavior of the abrasive waterjet inside or outside the machine. Such predictions could subsequently lead to the prediction of material removal, but these simulations don't take into consideration the full physics of the jet [4], The following study takes into account the entire

Content from this work may be used under the terms of the Creative Commons Attribution 3.0 license. Any further distribution of this work must maintain attribution to the author(s) and the title of the work, journal citation and DOI. Published under license by Materials Research Forum LLC.

Materials Research Proceedings 73 (2026) 206-210 https://doi.org/10.21741/9781644904459-40

domain as well as the mutual interaction between the three phases. The details of the geometry are presented in Table 1, the geometry and the mesh are presented by Figure 1.

Table 1: Geometric characteristics of the cutting head Paser 4 ™.

Parameter	Value
Water inlet diameter [mm]	0.94
Mixing chamber diameter [mm]	7.5
Focalization tube diameter [mm]	1.02
Abrasive inlet diameter [mm]	4
Mixing chamber length [mm]	18.5
Focalization tube length [mm]	101.6
Abrasive inlet angle [°]	45
Convergent angle [°]	25

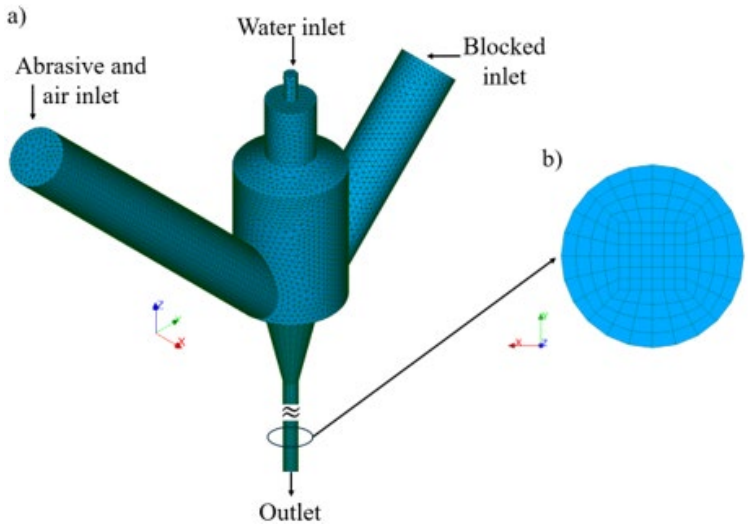

Figure 1: Mesh of the cutting head Paser 4 ™, a) isometric view, b) bottom view of the O-grid mesh.

Modelling

The simulation was carried out by using neptune_cfd, the software is based on an Euler-Euler approach. For this type of approach, the continuity and momentum equations are governed for each phase (water, air and particles). For the three phases, turbulence is taken into account using the $k-\varepsilon$ model for water and air. For the particulate phase, a closure model derived from the kinetic theory of granular flows is employed. The water–air phases are coupled using the GLIM model [5], while the particles are coupled through interphase transfer terms, due to the large particle-to-fluid density ratio only the drag force will be taken in consideration for momentum exchange [6]. The mesh generated contains nearly 700 000 cells, a hexahedral mesh is used for the focusing tube and the converging section, as well as a tetrahedral mesh for the mixing chamber shown by Figure 1. In practice the first orifice of the cutting head has a diameter of 0.33 mm which at an inlet water pressure of 13.5 MPa corresponds to a flow velocity of 164 m/s. To prevent prohibitively small time steps, the computational domain is modelled starting from the second orifice, with a diameter of 0.94 mm. The continuity equation is then applied to derive the corresponding inlet velocity of 20 m/s, which serves as the inlet boundary condition for the water,

Materials Research Proceedings 73 (2026) 206-210 https://doi.org/10.21741/9781644904459-40

the density of water, air and particles is respectively equal to $1000\ kg/m^3$, $1.2\ kg/m^3$ and $4000\ kg/m^3$, and the dynamic viscosity of water and air is respectively equal to $0.001\ Pa \cdot s$ and $1.85 \times 10^{-5}\ Pa \cdot s$, the abrasive is 80 Mesh garnet with a flow rate of 5 g/s, a coefficient of compaction of 0.64 and restitution coefficient of 0.9.

Numerical results

Figure 2 present the evolution of the mass flow rate of the three phases over the course of a numerical simulation spanning approximately 0.045 seconds. For each phase the inlet condition is imposed at a constant value throughout the simulation, reflecting stable and controlled boundary conditions. Regarding water whose flow rates are on the order of $10^{-2}\ kg/s$, the outlet oscillates around a negative value of approximately $-1.5 \times 10^{-2}\ kg/s$ after an initial transient phase, the negative sign convention simply indicating an outgoing flux, the inlet outlet balance remains consistent and confirms mass conservation. Air whose flow rate is three orders of magnitude lower $10^{-5}\ kg/s$, exhibits notable oscillations at the outlet throughout the simulation, suggesting that this minority gaseous phase, likely entrained air does not reach a fully established regime over the simulated duration, which may be attributed to interfacial instabilities between water and air. Finally the behavior of the abrasive particles is particularly revealing, their outlet flow rate remains zero for approximately 0.03 seconds, then drops sharply to $-4.5 \times 10^{-3}\ kg/s$, this delay corresponding to the transit time of the particles through the computational domain, that is the time required for them to travel from the inlet to the outlet across the entire geometry. This simulation thus likely describes the transient behavior of an abrasive waterjet, with a fully established regime for the liquid phase, but still developing for the gas and solid phases.

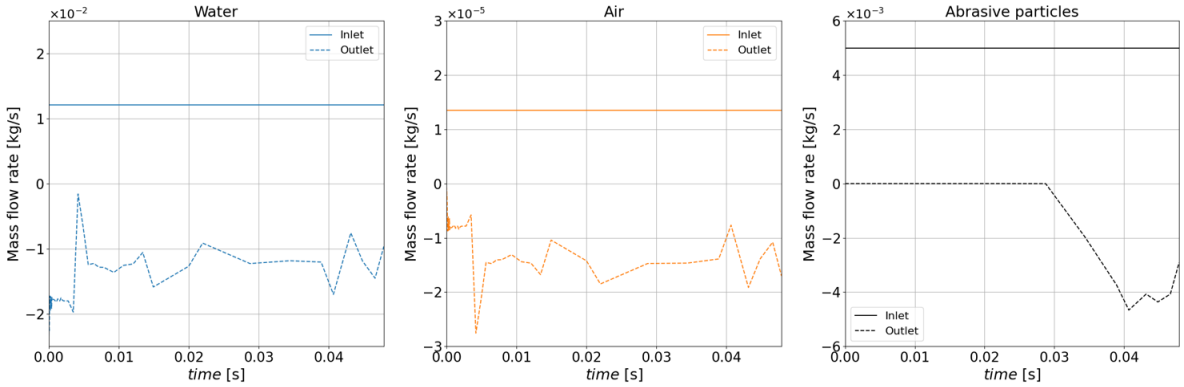

Figure 2: Mass flow rate of each phase.

The data are extracted at the outlet of the focusing tube. the volume fraction visualizations from the bottom for water and abrasive particles reveal a significant evolution of the phase distribution between t = 0.01 s and t = 0.04 s.

Materials Research Proceedings 73 (2026) 206-210 https://doi.org/10.21741/9781644904459-40

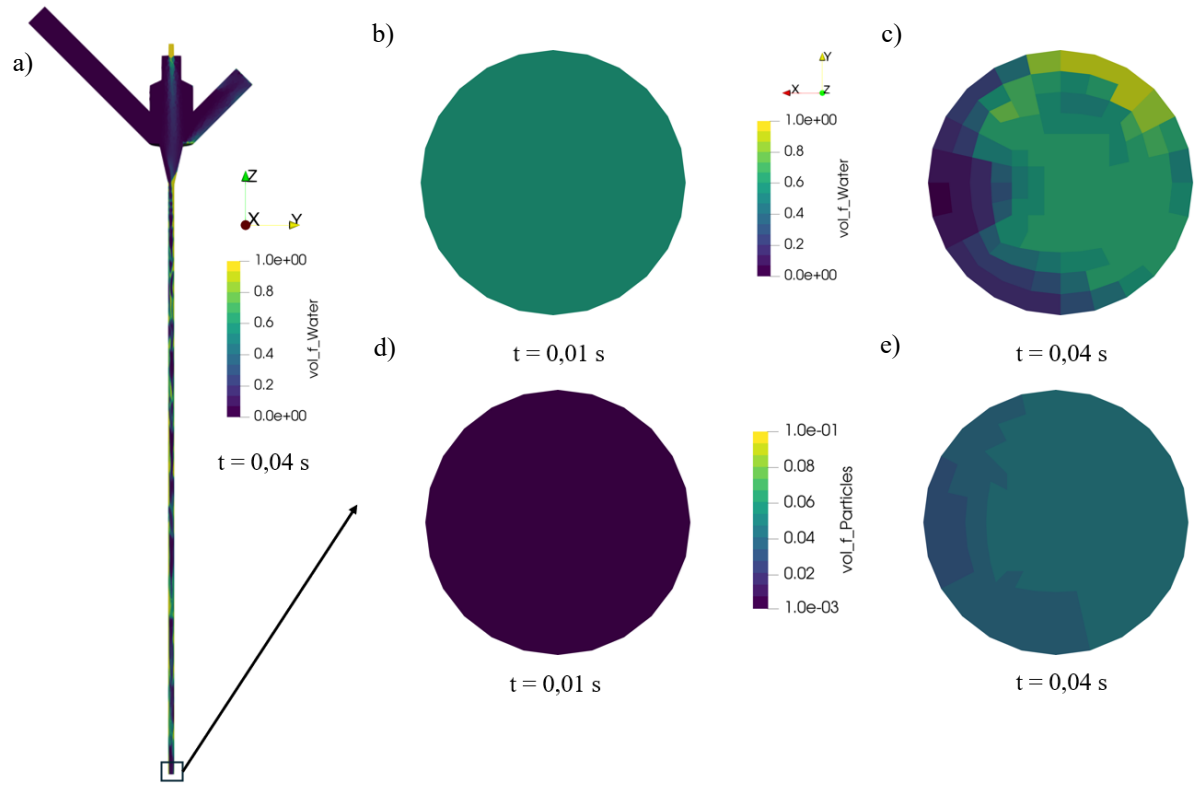

Figure 3: Volume fractions of water and abrasive particles at the outlet at two different time steps, a) water volume fraction at t = 0.04 s (ZY view), b) water volume fraction at t = 0.01 s, c) water volume fraction at t = 0.04 s, d) abrasive particle volume fraction at t = 0.01 s, and e) abrasive particle volume fraction at t = 0.04 s.

At t = 0.01 s, the water volume fraction shown by Figure 3 is nearly uniform across the entire circular cross-section, displaying a value close to 0.4 indicating that water occupies the nozzle exit section in a relatively homogeneous manner with no particular spatial organization. Simultaneously, the volume fraction of abrasive particles is extremely low and perfectly uniform across the entire section, remaining close to the minimum value of 10^{-3}, confirming that the particles have not yet reached this cross-section at that time, which is consistent with the transit time observed on the mass flow rate curves. At t = 0.04 s the situation evolves considerably the water distribution becomes strongly heterogeneous, with water-rich zones at the upper periphery and water-depleted zones on the sides and periphery, reflecting an annular or asymmetric organization of the jet at the nozzle exit. Regarding the particles, their volume fraction has noticeably increased and also exhibits a non-uniform distribution across the section, with higher concentrations in certain areas mainly in areas where there is more water, indicating that the particle front has reached the nozzle exit and that the particles are redistributing under the effect of the hydrodynamic forces exerted by the water jet. This temporal evolution highlights the strongly transient and unsteady nature of the three-phase flow within the focusing nozzle, with a progressive structuring of the jet that organizes spatially between 0.01 s and 0.04 s.

Conclusions

The Euler-Euler simulation demonstrates its feasibility for modeling the three-phase flow within an abrasive waterjet cutting head, correctly reproducing particle transit time, and the spatial organization of the phases. However the simulated duration of 0.045 s proves insufficient to reach a fully established regime. Looking ahead, a parametric study focusing on operating conditions would allow the influence of these parameters on the quality and coherence of the jet at the nozzle

exit to be assessed. Furthermore by adding an external fluid region at the nozzle outlet would enable the simulation of the abrasive jet behavior in the surrounding medium, allowing analysis of its dispersion, coherence, and interactions with the ambient air, thus paving the way for a complete characterization of the free jet.

References

[1] Y. W. Seo, M. Ramulu, et D. Kim, « Machinability of titanium alloy (Ti'6Al'4V) by abrasive waterjets », *Proceedings of the Institution of Mechanical Engineers, Part B: Journal of Engineering Manufacture*, vol. 217, nº 12, p. 1709-1721, déc. 2003. https://doi.org/10.1243/095440503772680631

[2] V. H. Bui, P. Gilles, T. Sultan, G. Cohen, et W. Rubio, « A new cutting depth model with rapid calibration in abrasive water jet machining of titanium alloy », *Int J Adv Manuf Technol*, vol. 93, nº 5, p. 1499-1512, nov. 2017. https://doi.org/10.1007/s00170-017-0581-x

[3] T. Sultan, P. Gilles, G. Cohen, F. Cenac, et W. Rubio, « Modeling incision profile in AWJM of Titanium alloys Ti6Al4V », *Mechanics & Industry*, vol. 17, nº 4, p. 403, 2016. https://doi.org/10.1051/meca/2015102

[4] T. N. D. Kumar et D. S. Srinivasu, « Integration of CFD simulated abrasive waterjet flow dynamics with the material removal model for kerf geometry prediction in overlapped erosion on Ti-6Al-4V alloy », *Simulation Modelling Practice and Theory*, vol. 127, p. 102788, sept. 2023. https://doi.org/10.1016/j.simpat.2023.102788

[5] S. Mer, O. Praud, H. Neau, N. Merigoux, J. Magnaudet, et V. Roig, « The emptying of a bottle as a test case for assessing interfacial momentum exchange models for Euler–Euler simulations of multi-scale gas-liquid flows », *International Journal of Multiphase Flow*, vol. 106, p. 109-124, sept. 2018. https://doi.org/10.1016/j.ijmultiphaseflow.2018.05.002

[6] A. Gobin, H. Neau, O. Simonin, J. Llinas, V. Reiling, et J. Sélo, « Fluid dynamic numerical simulation of a gas phase polymerization reactor », *Numerical Methods in Fluids*, vol. 43, nº 10-11, p. 1199-1220, déc. 2003. https://doi.org/10.1002/fld.542

Materials Research Proceedings 73 (2026) 211-216 https://doi.org/10.21741/9781644904459-41

Dynamic Mechanical Analysis of Mechanical Anomalies at Spin-State Transitions in Powder Samples

Maryam NASIMSOBHAN[1,a], Nagham MAWASSY[1,b], Baptiste MARTIN[1,c], Ruben TURO-CORTES[2,d], Carlos BARTUAL-MURGUI[3,e], José Antonio REAL[2,f], Malcolm HALCROW[4,g], Gábor MOLNÁR[1,h], Azzedine BOUSSEKSOU[1,i *]

[1]University of Toulouse, CNRS, LCC, 205 route de Narbonne, 31077 Toulouse, France

[2]Departamento de Quimica Inorganica, Instituto de Ciencia Molecular (ICMol), Universidad de Valencia, Catedratico José Beltran 2, 46980, Paterna, Spain

[3]Departamento de Quımica Fısica, Universitat de Valencia, Burjassot, 46100, Spain

[4]School of Chemistry, University of Leeds, Leeds LS2 9JT, U.K.

[a]maryam.sobhan70@gmail.com, [b]nagham.mawassy@gmail.com, [c]baptiste.martin@lcc-toulouse.fr, [d]ruben.turocortes@imdea.org, [e]Carlos.Bartual@uv.es, [f]Jose.A.Real@uv.es, [g]M.A.Halcrow@leeds.ac.uk, [h]gabor.molnar@lcc-toulouse.fr, [i]azzedine.bousseksou@lcc-toulouse.fr

Keywords: Spin-Crossover, Anelasticity, Dynamic Mechanical Analysis, Powder Samples

Abstract. Using dynamical mechanical analysis (DMA) in conjunction with a metal pocket, we study mechanical anomalies displayed by powder samples of spin-crossover complexes. In each sample, we reveal elastic softening and associated mechanical damping at the spin transition temperature. The DMA results align well with calorimetric measurements and appear even more sensitive to detect the spin-state changes both at first-order and continuous transformations. Overall, this work highlights the interest of DMA for the investigation of mechanical signatures of phase transitions in powder samples.

Introduction

Conventional dynamic mechanical analysis uses freestanding, solid specimens with appropriate geometric shapes (stripes, disks, fibers, etc.), allowing their mechanical fixture as well as the use of accurate form factors when calculating elastic moduli. It is less recognized that DMA is also a relevant technique to characterize powder samples. Notably, due to it is high sensitivity to changes in viscoelastic properties, DMA is widely used to determine glass-transition temperatures (T_g) in polymers. During the glass transition, the storage modulus (E') decreases, while the loss modulus (E'') and the damping factor ($\tan\delta = E''/E'$) generally display a peak, allowing the transition temperature to be identified with high sensitivity. Compared to differential scanning calorimetry (DSC), where T_g is detected through a subtle change in heat flow, DMA directly probes the mechanical response of the material and can therefore reveal relaxation phenomena that may be weak or difficult to detect by calorimetry [1]. To leverage this sensitivity for the investigation of powder samples, metallic pockets can be used to confine the powder during DMA measurements [1-5]. For example, Pinheiro and Mano demonstrated that metallic pockets allow the investigation of the glass-transition dynamics of materials that are difficult to test in compact solid form [1]. Metal pockets have also been applied to study conjugated polymer powders, where DMA enabled the detection of α and β-relaxations and the determination of T_g from peaks in the damping factor [2]. Similarly, DMA using a powder pocket has been employed to extract the Arrhenius parameters (e.g. energy barriers), associated with relaxation phenomena in polymers, through the frequency dependence of the loss tangent peaks [3]. Furthermore, powder DMA was successfully employed

Content from this work may be used under the terms of the Creative Commons Attribution 3.0 license. Any further distribution of this work must maintain attribution to the author(s) and the title of the work, journal citation and DOI. Published under license by Materials Research Forum LLC.

Materials Research Proceedings 73 (2026) 211-216 https://doi.org/10.21741/9781644904459-41

to detect the presence of small amounts of amorphous phases in crystalline powder samples [4], and even the quantification of the amorphous content could be achieved in certain cases [5]. Overall, these studies demonstrate that DMA combined with a powder pocket is a relevant approach for probing thermo-mechanical properties of powder materials. Powder DMA can provide transition temperatures comparable to those obtained by DSC, while also detecting additional weak transitions, which are not seen by the DSC apparatus. On the other hand, the measured absolute modulus is strongly influenced by the metallic pocket, meaning that the method is suitable for identifying transition temperatures, but it cannot be readily used for quantitative modulus determination. Recently, some of us also used the metal pocket DMA technique to detect elastic softening and mechanical damping during first-order phase transitions, associated with electronic spin-state changes in powder samples [6]. These studies appear relevant in the context of using these micro/nano-crystalline powders for the development of smart composites, with applications in mechanical transducer devices [7]. The objective of the present work is to enlarge the scope of our previous investigation for the thermomechanical characterization of powder samples of spin-crossover (SCO) materials. In particular, this study aims to determine whether the spin transition can be detected both for discontinuous (first-order) and continuous spin-state changes. We aim also to assess mechanical spectroscopy signatures of the spin transition and determine the sensitivity of the method in diluted samples.

Methodology

To characterize the powder materials using the DMA, a dedicated rectangular, stainless steel powder sample holder was used, as shown in Fig. 1. The powder (ca. 50 mg) was placed in the pocket, which confines the material and allows its mechanical response to be recorded. The filled powder holder was then mounted in the DMA oven using a dual-cantilever clamp, as illustrated in Fig. 1a, and it was oscillated perpendicular to its base plate by the middle clamp. Using this experimental configuration, different DMA tests were performed on several SCO powder samples. All measurements were carried out using a DMA-850 apparatus (TA Instruments) at heating/cooling rates of 3 °C/min, in displacement modulation mode with 20 µm oscillation amplitude and 1 Hz frequency (except otherwise mentioned).

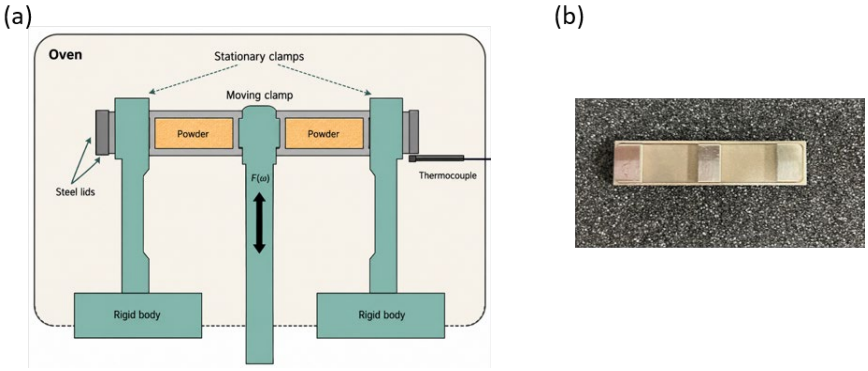

Fig. 1. (a) Scheme of the DMA setup using a dual cantilever clamp with a powder sample holder. (b) Photograph of the metallic pocket.

Results and discussion

The first investigated compound, the SCO powder $[Fe(HB(1,2,4\text{-triazol-1-yl})_3)_2]$ (sample 1) is known to display an abrupt, first-order transition near 60 °C with a small hysteresis [8], as shown in the DSC thermogram in Fig. 2a. This sample can be considered similar to the two SCO compounds investigated in our previous work [6], in that all these compounds exhibit discontinuous, first-order spin transitions above room temperature (with more or less large thermal hysteresis). Fig. 2b displays the storage and loss moduli, recorded between -75 °C and +125 °C for the metal pocket of sample 1 over a complete heating-cooling cycle. The spin transition of the

Materials Research Proceedings 73 (2026) 211-216 https://doi.org/10.21741/9781644904459-41

powder material is accompanied by clear mechanical anomalies, characterized by a softening of the storage modulus and enhanced mechanical dissipation, evidenced by a peak in the loss modulus. (N.B. One shall note that the hysteresis appears larger in the DMA measurements in comparison with the DSC curve, but this is just a technical burden, due to the slow sample thermalization, resulting in a temperature lag between the sample and the sensor reading.) The observed mechanical behavior is consistent with previous observations on SCO powders [6] and particulate composites [9], showing that, at the spin transition point, the elastic modulus reaches a minimum while the mechanical damping simultaneously exhibits a maximum.

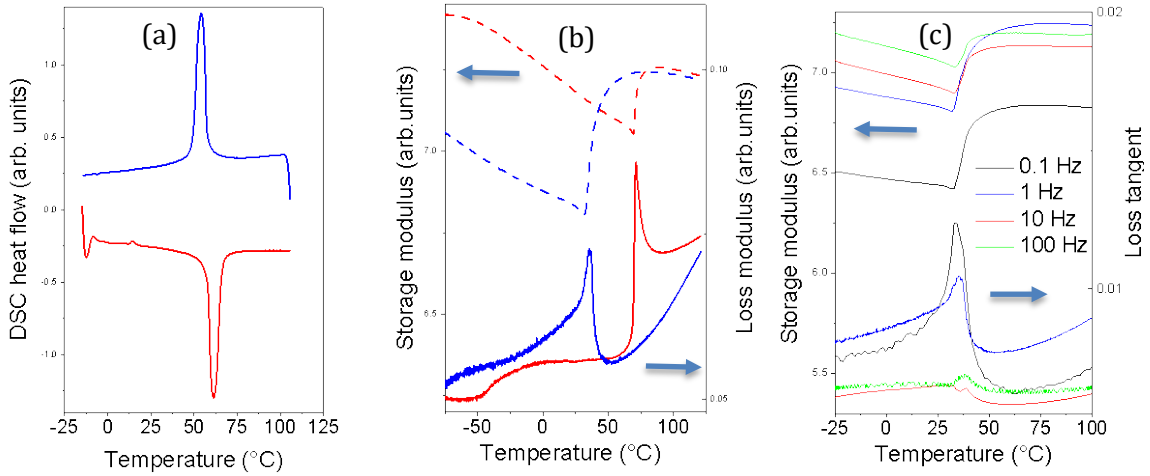

Fig. 2. Measurements on the powder sample 1: (a) DSC thermogram on heating (red) and cooling (blue). (b-c) DMA data: (b) Storage and loss moduli for heating (red) and cooling (blue), 1 Hz. (c) Storage modulus and loss tangent recorded at different frequencies in the cooling mode.

Previous mechanical spectroscopy studies of SCO-polymer composite materials revealed that the internal friction related to the anomalous mechanical events at the spin transition can be deconvoluted into two main contributions [10]. On one hand side, there is the so-called 'transitory contribution', which appears only when the material transforms, i.e. only on heating or cooling. Because first-order transitions proceed via slow nucleation and growth, the associated damping becomes negligible at sufficiently high frequencies where the transformation cannot track the mechanical oscillation. In contrast, the isothermal contribution reveals a mechanistically distinct relaxation channel that is essentially frequency-independent, and dominates the elastic softening. This second 'isothermal contribution' has been attributed to the coupling between molecular scale spin-sate relaxations and the mechanical strain. Since the spin-state relaxation induces a volume change, the material appears softer than expected from its intrinsic elastic properties. It appears therefore highly relevant to investigate the frequency dependence of the mechanical behavior of the sample near the SCO temperature. This is nicely illustrated in the powder DMA experiments conducted for sample 1 at selected frequencies (0.1, 1, 10 and 100 Hz). As shown in Fig. 2b, for a frequency of 0.1 Hz, the loss tangent shows the largest peak. When increasing the frequency, this internal friction peak progressively decreases, and at 10 Hz it becomes barely detectable. This indicates that the transitory contribution becomes less and less pronounced, whereas the small isothermal contribution remains present even at 100 Hz. On the other hand, the magnitude of the elastic softening associated with the SCO phenomenon shows only a weak frequency dependence. One can notice also that, contrary to the glass transition in polymers, the temperature at which the modulus relaxation occurs is essentially frequency independent. This is a characteristic feature of mechanical relaxations associated with phase transition phenomena [11]. Overall, these DMA

Materials Research Proceedings 73 (2026) 211-216 https://doi.org/10.21741/9781644904459-41

results acquired for the powder sample show the same tendencies than those obtained on freestanding polymer composite films, using conventional DMA techniques [9].

The example in Fig. 2 refers to the detection of a discontinuous, first-order spin transition. It appeared thus interesting for us to examine if the powder DMA method is applicable for the detection of continuous SCO phenomena as well. To investigate this question powder DMA measurements were performed on the SCO powder sample 2: $\{Fe(AnPy)_2[Ag(CN)_2]_2\}\cdot NO_2bz$ (AnPy = 4-anthracenepyridine, NO_2bz = nitrobenzene). A very interesting feature of this sample is that it exhibits a multi-step spin transition with three distinct SCO events: on cooling, the first two transformations (corresponding to ca. 25-25 % spin state conversion) are continuous, whereas the third transformation (with ca. 50 % conversion) occurs in a discontinuous manner [12]. These three steps can be clearly seen in the DSC thermograms of the powder (Fig. 3a). The DMA measurement shown in Figure 3b reveals a similar picture. (N.B. Only the cooling mode is shown because the heating curve is comparable.) The lowest temperature (first-order) transition is characterized by a sharp and intense loss modulus peak and an associated storage modulus softening. The two other transition steps appear less intense and broader, but can be perfectly resolved in the loss modulus behavior. Interestingly, the integrated area of the low- and the high-temperature loss peaks are comparable, indicating a possible quantitative link with the SCO phenomenon, which will require further investigations.

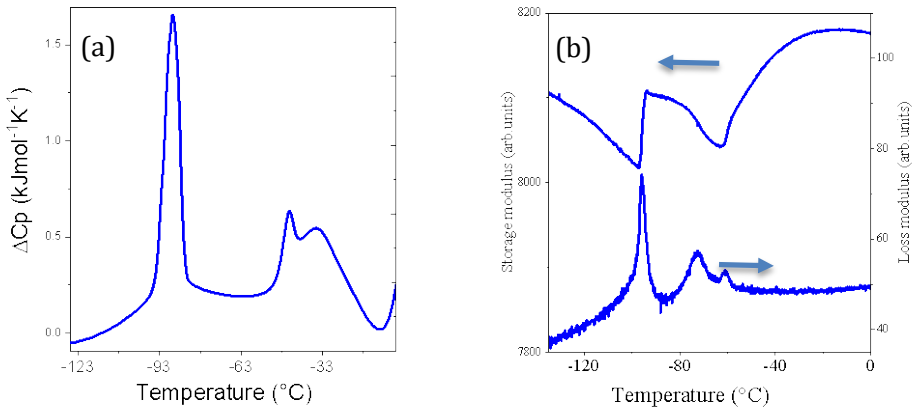

Fig. 3. Measurements on the powder sample 2: (a) DSC thermogram on cooling. (b) Storage and loss moduli obtained from powder DMA in the cooling mode.

The powder sample 3 for the DMA measurements was synthesized in three different compositions, each based on the general formula $[M(bpp)_2][BF_4]_2$ (bpp = 2,6-bis{pyrazol-1-yl}pyridine), but with different M = Fe + Ru mixtures. The samples included the pure Fe compound $[Fe(bpp)_2][BF_4]_2$ and two mixed Fe/Ru compounds, $[Fe_{0.67}Ru_{0.33}(bpp)_2][BF_4]_2$ and $[Fe_{0.49}Ru_{0.51}(bpp)_2][BF_4]_2$, denoted as samples $3_{100\%Fe}$, $3_{67\%Fe}$ and $3_{49\%Fe}$, respectively. The Ru replaces the Fe ion and affords for an isostructural crystal lattice, but the Ru ion being spin crossover inactive, it results in the extinction of the SCO properties [13]. This effect is clearly seen in the DSC thermograms of the samples in Fig. 4, showing less and less intense peaks with increasing Ru content. For the highest dilution ($3_{49\%Fe}$), the enthalpy change associated with the SCO phenomenon could not be detected by calorimetry. The powder DMA measurements in Fig. 4 show similar trends in that the mechanical anomalies associated with the spin transition, namely softening and dissipation, are less and less marked. Nevertheless, for each sample, including the most diluted $3_{49\%Fe}$, the softening of the storage modulus remains clearly observable. Interestingly, in the diluted samples the loss peaks appear faintly. Instead, a step in the loss modulus can be depicted at the transition, the losses being more important in the low temperature phase.

Materials Research Proceedings 73 (2026) 211-216 https://doi.org/10.21741/9781644904459-41

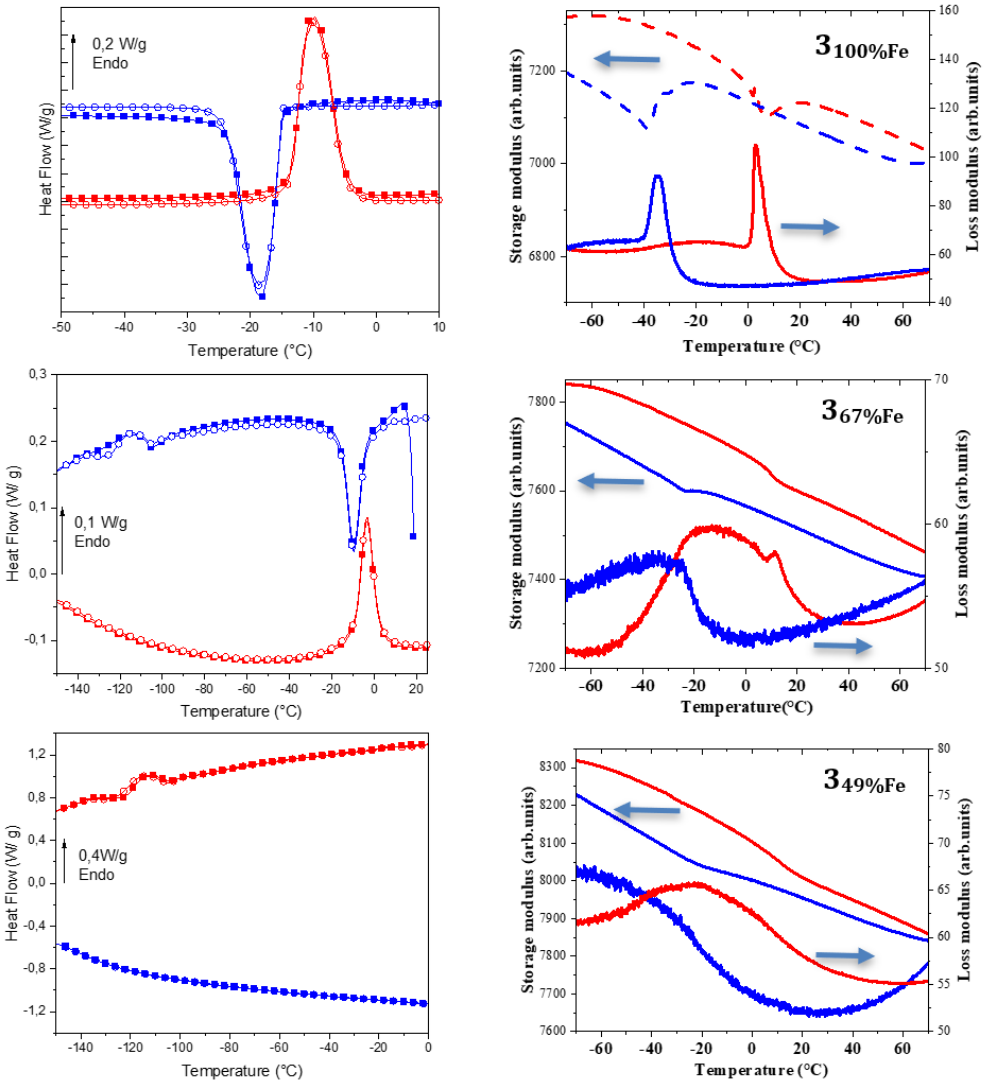

Fig. 4. Measurements on the powder samples $3_{100\%Fe}$ (top panel) $3_{67\%Fe}$ (middle panel) and $3_{49\%Fe}$ (bottom panel): (left) DSC thermograms on heating (red) and cooling (blue), (right) Storage and loss moduli obtained from powder DMA on heating (red) and cooling (blue).

Conclusions

DMA was used to characterize the spin transition in powder samples of spin crossover complexes through the associated mechanical anomalies, which comprise the softening of the storage modulus and enhanced damping. Both continuous and discontinuous transitions could be detected by DMA, even for diluted samples. DMA provided also some mechanistic insights through the frequency dependent behavior of the viscoelastic properties. Overall, these results demonstrate that DMA combined with a powder pocket is a promising approach for detecting and analyzing mechanical anomalies accompanying spin state changes in powder samples.

Acknowledgment

This work has received funding from the European Research Council (ERC) under the European Union's Horizon 2020 research and innovation program (Grant Agreement No.101019522).

References

[1] A. Pinheiro, J. F. Mano, Study of the glass transition on viscous-forming and powder materials using dynamic mechanical analysis, Polym. Test. 28 (2009) 89-95. https://doi.org/10.1016/j.polymertesting.2008.11.008

[2] M. Xiao, et al., Linking glass-transition behavior to photophysical and charge transport properties of high-mobility conjugated polymers, Adv. Funct. Mater. 31 (2021) 2007359. https://doi.org/10.1002/adfm.202007359

[3] D. Mahlin, J. Wood, N. Hawkins, J. Mahey, P. G. Royall, A novel powder sample holder for the determination of glass transition temperatures by DMA, Int. J. Pharmaceut. 371 (2009) 120-125. https://doi.org/10.1016/j.ijpharm.2008.12.039

[4] P. G. Royall, C. Huang, S. J. Tang, J. Duncan, G. Van-de-Velde, M. B. Brown, The development of DMA for the detection of amorphous content in pharmaceutical powdered materials, Int. J. Pharmaceut. 301 (2005) 181-191. https://doi.org/10.1016/j.ijpharm.2005.05.015

[5] S. Clas, K. Lalonde, K. Khougaz, C. R. Dalton, R. Bilbeisi, Detection of a minor amorphous phase in crystalline etoricoxib by dynamic mechanical analysis: Comparison with raman spectroscopy and modulated differential scanning calorimetry, J. Pharm. Sci. 101 (2011) 101, 558-565. https://doi.org/10.1002/jps.22774

[6] D. Paliwoda, et al., Elastic Properties of the Iron(II)–Triazole Spin Crossover Complexes [Fe(Htrz)2trz]BF4 and [Fe(NH2trz)3]SO4, Cryst. Growth Des. 23 (2023) 1903-1914. https://doi.org/10.1021/acs.cgd.2c01396

[7] M. Piedrahita-Bello, et al., Colossal expansion and fast motion in spin-crossover@ polymer actuators, Mater. Horiz. 8 (2021) 3055-3062. https://doi.org/10.1039/d1mh00966d

[8] S. Rat, K. Ridier, L. Vendier, G. Molnár, L. Salmon, A. Bousseksou, Solvatomorphism and structural-spin crossover property relationship in bis[hydrotris(1,2,4-triazol-1-yl)borate]iron(ii), CrystEngComm 19 (2017) 3271-3280. https://doi.org/10.1039/c7ce00741h

[9] S. E. Alavi, et al., Dynamical mechanical analysis and micromechanics simulations of spin-crossover@ polymer particulate composites: toward soft actuator devices, Chem. Mater. 35 (2023) 3276-3289. https://doi.org/10.1021/acs.chemmater.3c00293

[10] M. Nasimsobhan, Investigation of the mechanical properties of molecular spin crossover materials: towards a new family of artificial muscles, PhD Thesis, Université de Toulouse, France, 2026. https://utheme.utoulouse.fr/s/fr/item/46733

[11] A. S. Nowick, B. S. Berry, Anelastic Relaxation in Crystalline Solids, Academic Press, New York, London, 1972. https://doi.org/10.1002/pol.1973.130110713

[12] R. Turo-Cortés, M. Meneses-Sánchez, T. Delgado, C. Bartual-Murgui, M. C. Munoz, J. A. Real, Coexistence of luminescence and spin-crossover in 2D iron(ii) Hofmann clathrates modulated through guest encapsulation, J. Mater. Chem. C 10 (2022) 10686-10698. https://doi.org/10.1039/d2tc02039d

[13] P. Ghosh, et al., The effect of inert dopant ions on spin-crossover materials is not simply controlled by chemical pressure, J. Mater. Chem. C 11 (2023) 12570-12582. https://doi.org/10.1039/d3tc02683c

Materials Research Proceedings 73 (2026) 217-222 https://doi.org/10.21741/9781644904459-42

Buckling and Post-Buckling of Multi-Material Metastructure Panels

Riccardo AUGELLO[1,a*], Erasmo CARRERA[1,2,b]

[1]MUL2 lab, Politecnico di Torino, Italy

[2]College of Eng, PMU, SA

[a]riccardo.augello@polito.it, [b]erasmo.carrera@polito.it

Abstract. This paper investigates the buckling and post-buckling response of multi-material metastructure panels. The main objective is to clarify how the local allocation of materials with different stiffness properties affects the global stability of the panel, the critical buckling load, the dominant instability modes, and the nonlinear equilibrium path. The panel is modeled as a heterogeneous metastructured assembly in which different regions or groups of unit cells are assigned different constituent materials. This modeling strategy allows the influence of material contrasts on load redistribution, stiffness degradation, and deformation localization in the post-critical regime to be systematically assessed. The numerical formulation is based on the Carrera Unified Formulation (CUF), which provides a hierarchical and flexible framework for the refined modeling of complex structural systems. Thanks to its variable-kinematics capabilities, CUF enables accurate descriptions of both global panel deformation and local effects induced by the metastructure topology, while reducing the computational effort with respect to full three-dimensional finite element models. The results aim to provide insight into the role of multi-material distributions in governing the stability response of metastructure panels and to support the development of lightweight architected structures with tailored buckling and post-buckling performance.

Introduction

Mechanical metamaterials and metastructures are engineered systems whose effective properties are primarily governed by their internal architecture rather than by the properties of the base material alone. Through a suitable design of the unit cell, its periodic repetition, and the connectivity among structural members, these systems can exhibit mechanical responses that are difficult to achieve with conventional homogeneous materials [1–3]. For this reason, metastructured panels are receiving growing attention in aerospace, mechanical, and civil engineering applications, where lightweight design, high stiffness-to-weight ratio, and tailored deformation mechanisms are key requirements.

One of the most relevant features of metastructures is the possibility of tuning their global response by modifying the geometry and topology of the underlying unit cell. In panel-like configurations, this aspect is particularly important because the structural behavior is the result of an interaction between global panel deformation and local cell-level mechanisms. As a consequence, the same material can lead to significantly different stiffness, strength, and stability properties depending on the architecture adopted. This feature makes metastructures promising candidates for the design of advanced lightweight panels, but it also introduces additional complexity in their mechanical analysis.

Stability is a critical issue in the design of thin and lightweight panels. Under compressive, shear, bending, or combined loading conditions, such structures may undergo buckling, and their load-carrying capability after the critical point strongly depends on the post-buckling path. In conventional panels, the buckling response is mainly governed by geometry, thickness, boundary conditions, and material properties. In metastructure panels, however, the instability behavior is also affected by the periodic architecture and by the local deformation modes of the unit cells.

Content from this work may be used under the terms of the Creative Commons Attribution 3.0 license. Any further distribution of this work must maintain attribution to the author(s) and the title of the work, journal citation and DOI. Published under license by Materials Research Forum LLC.

Materials Research Proceedings 73 (2026) 217-222 https://doi.org/10.21741/9781644904459-42

Local cell rotations, bending of slender members, deformation localization, and load redistribution may all contribute to the onset of instability and to the subsequent nonlinear response.

An additional design variable is introduced when different materials are assigned to different regions of the same metastructure. In this case, the panel is no longer characterized by a uniform distribution of stiffness and mass, but by a heterogeneous material layout. The use of stiffer or more compliant materials in selected domains may alter the position at which instability first develops, modify the critical buckling mode, and influence the stiffness degradation occurring in the post-critical regime. For example, stiffer regions may be used to reinforce highly stressed parts of the panel and delay buckling, whereas more compliant regions may guide the deformation toward prescribed and potentially more favorable patterns. Therefore, the combined design of topology and material distribution opens new possibilities for tailoring the stability response of metastructured panels.

Despite this potential, the buckling and post-buckling behavior of multi-material metastructure panels remains a challenging problem. The numerical model must be able to capture both the global response of the panel and the local effects associated with the unit-cell geometry and material heterogeneity. Standard three-dimensional finite element models can provide accurate results, but they often require a large number of degrees of freedom, especially when complex architectures, several material domains, and nonlinear post-buckling analyses are considered. On the other hand, classical beam, plate, and shell theories may not be sufficiently refined to describe local deformation mechanisms and three-dimensional stress states in complex metastructures.

The Carrera Unified Formulation (CUF) represents an effective framework for this class of problems [4,5]. CUF allows the development of refined structural models through hierarchical expansions of the displacement field. Different orders of approximation can be adopted within the same formulation, making it possible to move from classical low-order models to higher-order and component-wise descriptions. This feature is particularly useful for metastructures, where local cell-level effects and global structural behavior must be represented consistently. CUF has already been successfully applied to the analysis of complex structures and metamaterial-like systems, showing its capability to capture refined kinematics and nonlinear effects with reduced computational effort compared with full three-dimensional models [6-9].

In this work, CUF is employed to investigate the buckling and post-buckling response of multi-material metastructure panels. The panel is modeled as a heterogeneous assembly composed of different material regions, and several layouts are considered in order to evaluate the influence of local stiffness variations on the critical load, instability modes, and nonlinear equilibrium path. The main aim is to assess whether a proper allocation of materials can improve the stability performance of the panel, delay the onset of buckling, or promote more controlled post-critical deformation mechanisms. The results are expected to provide preliminary design guidelines for the development of advanced lightweight metastructure panels in which both geometry and material distribution are exploited as design variables.

Methodology

The approach used in this frame is based on the 1D mathematical representation of metamaterial structures. With this approach, which is possible thanks CUF, problems involving complex geometries can be simply represented using a single beam element. The three-dimensional displacement field of a 1D beam structure can be written in vector notation as given in the following

$$\boldsymbol{u}(x,y,z) = \{u_x u_y u_z\}^T$$

where x, y, and z are the coordinates of a Cartesian reference system. CUF together with the Finite Element Method (FEM) enables the representation of the 3D displacement field according to the

$$\boldsymbol{u}(x,y,z) = N_i(y)F_\tau(x,z)\boldsymbol{u}_{\tau i}, i = 1,2,\ldots,N_n\ \tau = 1,2,\ldots,M$$

Materials Research Proceedings 73 (2026) 217-222 https://doi.org/10.21741/9781644904459-42

where N_i is the i-th shape function in the y direction and $F_\tau(x,z)$ are the cross-section expansion functions in x and z directions; M is the number of the terms used in the expansion, N is the number of the nodes on the beam axis and $\boldsymbol{u}_{\tau i}$ is the vector of the nodal unknowns.

CUF allows for more efficient modeling of thin-walled structures. Indeed, traditional FE analysis software offers several modeling options, among which 3D, two-dimensional (2D), and 1D FEs. 3D modeling provides the most accurate results, but it is computationally demanding. Achieving careful through-thickness analysis requires at least three to four solid elements [32], resulting in a high number of degrees of freedom. Although 2D finite elements may appear suitable for thin structures, these cannot adequately capture through-thickness strain and stress, which are critical for design considerations. Finally, 1D finite elements present similar limitations in modeling capabilities.

Considering a generic metastructure as the one shown in Fig. 1(a), In this framework, exploiting CUF capabilities, the entire structure is described by 1D beam elements whose axis is aligned with the width direction, departing from the conventional beam idealisation tied to the longest structural dimension. This is shown in Fig. 1(b).

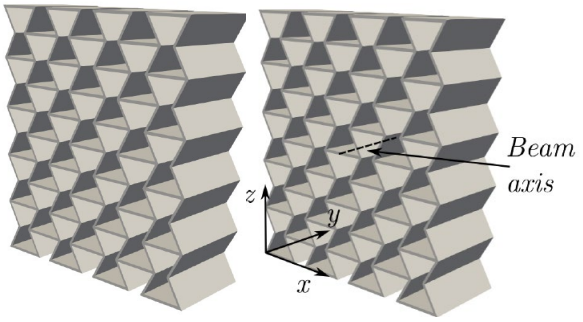

Fig. 1 - CUF model of a generic metastructure.

The cross-sections of the metamaterial is discretized using high-order Lagrange polynomials; this discretization ensures detailed representation of geometry and its mechanical behaviour. To maintain displacement continuity between the components, shared Lagrange points are defined at their interfaces. The precise alignment of shared Lagrange points eliminates spurious discontinuities, enabling an accurate description of the coupling between the components.

The procedure starts with the resolution of a static geometrical nonlinear problem, solved by means of Newton- Raphson method based on the arc-length approach. An increasing load introducing large displacements is considered to assess this nonlinear problem. Then, the tangential stiffness matrix $\boldsymbol{K}_T$ is introduced, assessed as the stiffness matrix of the structure around its equilibrium states in different points of the nonlinear curve load-displacement.

Numerical results

The numerical investigation concerns a honeycomb metastructure panel subjected to a compressive loading condition. The panel is clamped at one edge, while a uniform pressure is applied at the opposite edge in order to induce a global axial compression of the structure. The geometry of the considered metastructure is shown in Fig. 2. The panel has a total length of 868 mm, a width of 470 mm, and an overall height of 120 mm. The upper and lower skins have a thickness of 3 mm and are connected by an internal honeycomb core composed of hexagonal cells. This configuration is representative of lightweight sandwich-like metastructures in which the global response is governed by the interaction between the external skins and the internal cellular architecture.

Materials Research Proceedings 73 (2026) 217-222 https://doi.org/10.21741/9781644904459-42

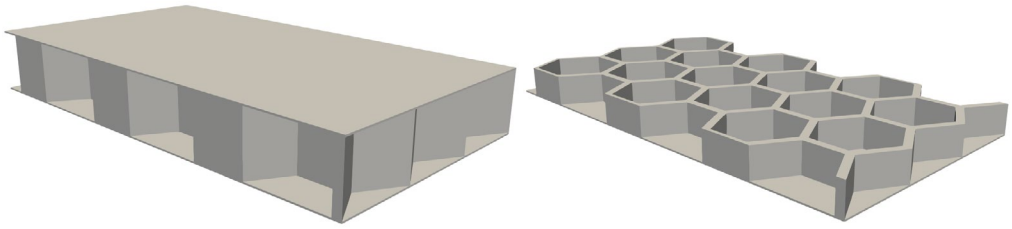

Fig. 2 – Considered honeycomb metastructure.

The first configuration analyzed is a homogeneous reference panel entirely made of aluminium. This case is used as a baseline in order to assess the nonlinear response of the honeycomb metastructure without any local material reinforcement. The use of aluminium leads to a relatively uniform distribution of stiffness throughout the panel. Consequently, the deformation is mainly controlled by the geometry of the honeycomb core and by the bending and membrane response of the external skins. In this configuration, the cellular architecture plays the dominant role in determining the global compressive stiffness and the post-buckling shape. A second configuration is then considered in order to evaluate the effect of a local material modification. In this case, two selected honeycomb cells are assigned the mechanical properties of steel, while the remaining part of the structure is kept in aluminum. The reinforced cells are highlighted in Fig. 3.

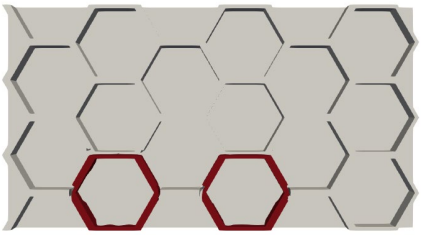

Fig. 3 – Considered honeycomb metastructure with steel cells

This configuration introduces a localized stiffness contrast inside the honeycomb core. As a result, the panel is no longer characterized by a uniform mechanical response, but by a heterogeneous distribution of stiffness. The nonlinear equilibrium curves obtained for the two configurations are reported in Fig. 4. The curves describe the relationship between the applied compressive load and the axial displacement of the loaded edge. The comparison clearly shows that the multi-material configuration has a different post-buckling response with respect to the homogeneous aluminium panel. In the initial part of the curve, the panel with steel cells exhibits a steeper response. This indicates that the insertion of the steel cells increases the effective axial stiffness of the metastructure. Therefore, for the same applied load, the reinforced configuration undergoes a smaller axial displacement than the fully aluminium panel.

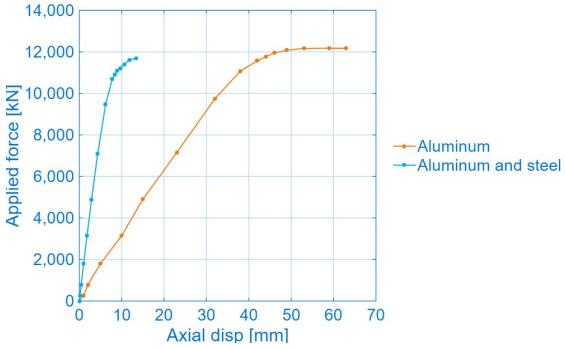

Fig. 4 – Nonlinear post-buckling curves of metastructures with constant material (blue) and with steel celss (red).

Materials Research Proceedings 73 (2026) 217-222 https://doi.org/10.21741/9781644904459-42

This effect is particularly evident along the ascending branch of the equilibrium path. The reinforced panel reaches high load levels with a much smaller axial displacement. This behavior confirms that the local stiffening of selected cells is able to redistribute the load inside the honeycomb architecture and to reduce the global compliance of the structure. The steel cells act as stiff inclusions embedded in the aluminium cellular network. Their presence constrains part of the deformation of the surrounding cells and modifies the way in which the load is transmitted from the loaded edge to the clamped region. The comparison between the two curves also highlights the importance of the post-buckling regime for this class of structures. The response cannot be described only in terms of the initial stiffness or of the first instability point. After the onset of nonlinear effects, the deformation evolves through a combination of skin bending, local cell distortion, and interaction between adjacent honeycomb walls. For this reason, the ability to follow the complete equilibrium path is essential. The arc-length strategy adopted in the present CUF-based formulation allows the nonlinear response to be tracked even when stiffness degradation and large displacement effects become significant.

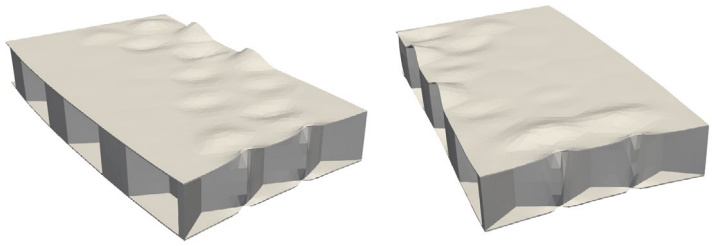

Fig. 5 – Deformation of metastructure with constant material (left) and with steel cells (rigth).

The deformed shapes of the two configurations are shown in Fig. 5. The figure confirms that the introduction of steel cells affects not only the load-displacement curve, but also the spatial distribution of the deformation. In the homogeneous aluminium case, the deformation pattern is more spread over the panel surface. The external skin exhibits a sequence of local out-of-plane undulations associated with the deformation of the underlying honeycomb core. These undulations are distributed over a relatively wide portion of the panel, suggesting that several cells participate in the post-buckling mechanism. In the multi-material configuration, the deformation pattern is altered by the presence of the steel cells. The steel inclusions locally constrain the honeycomb deformation and modify the development of the instability pattern. This confirms that the material layout can be used to guide the post-buckling response and to influence the regions in which deformation localization occurs. A more detailed view of the skin deformation is provided in Fig. 6. The deformation of the skins is particularly relevant because the skins contribute significantly to the global load-carrying capacity of the panel. The figure shows that the out-of-plane displacement of the skins is not independent from the cellular core, but is strongly coupled with the deformation of the internal honeycomb walls.



Fig. 6 – Deformation of the skins of the metastructure.

The skin deformation also confirms the need for a refined numerical model. Classical low-order beam, plate, or shell models may not be sufficient to capture the local deformation mechanisms generated by the honeycomb architecture and by the material heterogeneity. In contrast, the CUF-based approach used in this work allows the three-dimensional displacement field to be represented through enriched cross-sectional expansions.

Conclusions

This work investigated the buckling and post-buckling response of a honeycomb metastructure panel using a CUF-based numerical formulation. Two configurations were compared: a homogeneous aluminium panel and a multi-material panel in which selected cells were assigned steel properties.

The results show that the local introduction of steel cells significantly affects the nonlinear equilibrium path and the deformation pattern of the structure. The reinforced configuration exhibits a stiffer response and reaches high load levels with lower axial displacements than the fully aluminium panel. Moreover, the presence of stiffer cells modifies the post-buckling deformation, influencing both the honeycomb core and the external skins.

These preliminary results confirm that material distribution can be used as an effective design parameter to tailor the stability response of metastructured panels. Future work will focus on additional material layouts, different loading conditions, and further validation against refined three-dimensional finite element models.

References

[1] R. Liu, C. Ji, Z. Zhao, and T. Zhou, "Metamaterials: reshape and rethink," Engineering, vol. 1, no. 2, pp. 179-184, 2015. https://doi.org/10.15302/J-ENG-2015036

[2] J. U. Surjadi, L. Gao, H. Du, X. Li, X. Xiong, N. X. Fang, and Y. Lu, "Mechanical metamaterials and their engineering applications," Advanced Engineering Materials, vol. 21, no. 3, 1800864, 2019. https://doi.org/10.1002/adem.201800864

[3] E. Barchiesi, M. Spagnuolo, and L. Placidi, "Mechanical metamaterials: a state of the art," Mathematics and Mechanics of Solids, vol. 24, no. 1, pp. 212-234, 2019. https://doi.org/10.1177/1081286517735695

[4] E. Carrera, M. Cinefra, M. Petrolo, and E. Zappino, Finite Element Analysis of Structures through Unified Formulation. West Sussex, United Kingdom: John Wiley & Sons, 2014. https://doi.org/10.1002/9781118536643

[5] E. Carrera, G. Augello, and R. Augello, Implementation of Beam-Type Finite Elements Based on Carrera Unified Formulation. Cham, Switzerland: Springer, 2026. DOI: 10.1007/978-3-031-95856-4. https://doi.org/10.1007/978-3-031-95856-4

[6] M. Cinefra, A. G. de Miguel, M. Filippi, C. Houriet, A. Pagani, and E. Carrera, "Homogenization and free-vibration analysis of elastic metamaterial plates by Carrera Unified Formulation finite elements," Mechanics of Advanced Materials and Structures, vol. 28, no. 5, pp. 476-485, 2021. https://doi.org/10.1080/15376494.2019.1578005

[7] R. Augello and E. Carrera, "Nonlinear dynamics and bandgap evolution of thin-walled metamaterial-like structures," Journal of Sound and Vibration, vol. 578, 118329, 2024. https://doi.org/10.1016/j.jsv.2024.118329

[8] Xu, X., Carrera, E., Yang, H., Daneshkhah, E. and Augello, R., 2022. Evaluation of stiffeners effects on buckling and post-buckling of laminated panels. Aerospace Science and Technology, 123, p.107431. https://doi.org/10.1016/j.ast.2022.107431

[9] Carrera, E., Pagani, A., Augello, R. and Mul Group, 2021. Large deflection and post-buckling of thin-walled structures by finite elements with node-dependent kinematics: E. Carrera et al. Acta Mechanica, 232(2), pp.591-617. https://doi.org/10.1007/s00707-020-02857-7

Materials Research Proceedings 73 (2026) 223-228 https://doi.org/10.21741/9781644904459-43

Investigating the Dynamic Behavior of FGM Structures using the Carrera Unified Formulation

Munise Didem DEMİRBAS[1,a *], Riccardo AUGELLO[2,b] and Erasmo CARRERA[3,c]

[1]Department of Mechanical Engineering, Erciyes University, Kayseri 38039, Turkey

[2]Mul2 Group, Department of Mechanical and Aerospace Engineering, Politecnico di Torino, Italy

[a]mddemirbas@erciyes.edu.tr, [b]riccardo.augello@polito.it, [c]erasmo.carrera@polito.it

Keywords: CUF, Mechanics, Dynamic Behavior, Linear Dynamic Analysis, FG Box Beam

Abstract. This study investigates the dynamic behavior of aviation-grade functionally graded material (FGM) thin-walled structures under load using the linear Carrera Unified Formulation (CUF) [1]. The governing equations are derived from virtual displacements and solved using the Navier method. Refined beam models, with polynomial and non-polynomial cross-sectional functions, evaluate displacement, strain, and stress fields. Numerical analyses assess transverse loading effects on FG beams, considering material gradation and refined kinematics.

Introduction

Functionally graded materials (FGMs) have continuously varying constituent phases and mechanical properties, which enable tailored structural responses and improved thermal-stress distribution, strength, fatigue performance, and integrity [1-3]. These characteristics make FGMs attractive for high-performance aerospace and aviation structures that require low weight and high mechanical performance.

Thin-walled elements provide favorable stiffness-to-weight ratios and may benefit from material gradation. Their response depends on material distribution, structural theory, cross-sectional geometry, displacement approximation, and loading, which together determine behavior. Under sufficiently large loads, geometric nonlinearities may also become important. Refined formulations are therefore useful for describing their mechanical and dynamic behavior.

Thin-walled elements provide favorable stiffness-to-weight ratios and can benefit from material gradation. Their response depends on material distribution, structural theory, cross-sectional geometry, displacement approximation, and loading. Under sufficiently large loads, geometric nonlinearities may also become important; therefore, refined formulations are useful for describing their mechanical and dynamic behavior.

The Carrera Unified Formulation (CUF) provides a unified framework for expressing structural theories through suitable expansion functions [4-7]. It enables the study of different approximation orders, polynomial or non-polynomial functions, material distributions, and structural configurations within the same formulation, making it particularly suitable for FG structures.

Unified finite beam element

Preliminaries. Consider a beam of length L with cross-sectional domain Ω on the xz-plane and longitudinal axis along y, where the displacement field is defined in global coordinates.

$$u = \{u_x \;\; u_y \;\; u_z\}^T \tag{1}$$

The strain ε and stress σ tensors are expressed as:

$$\varepsilon = \{\varepsilon_{xx} \;\; \varepsilon_{yy} \;\; \varepsilon_{zz} \;\; \varepsilon_{xz} \;\; \varepsilon_{yz} \;\; \varepsilon_{xy}\}^T \tag{2}$$

Content from this work may be used under the terms of the Creative Commons Attribution 3.0 license. Any further distribution of this work must maintain attribution to the author(s) and the title of the work, journal citation and DOI. Published under license by Materials Research Forum LLC.

Materials Research Proceedings 73 (2026) 223-228 https://doi.org/10.21741/9781644904459-43

and stress tensors are expressed, respectively, as:

$$\sigma = \{\sigma_{xx} \ \sigma_{yy} \ \sigma_{zz} \ \sigma_{xz} \ \sigma_{yz} \ \sigma_{xy}\}^T \tag{3}$$

The beam materials are assumed linear elastic, and the constitutive relation follows Hooke's law:

$$\sigma = C\varepsilon \tag{4}$$

where C is a material matrix; its open form [8] and its examination with finite elements can be found in Refs [9,10]. The geometric relations are described using the Green–Lagrange nonlinear strain components. Accordingly, the strain–displacement relations can be written as follows:

$$\varepsilon = \varepsilon_l + \varepsilon_{nl} = (b_l + b_{nl})u \tag{5}$$

where b_l and b_{nl} are linear and nonlinear differential operators. See Ref. [11] for details on these operators.

Carrera Unified Formulation. Within the CUF framework, the three-dimensional displacement field u(x, y, z) is expressed as a generalized expansion in terms of the primary variables. For one-dimensional beam theories, the expression can be written as follows:

$$u(x, y, z) = F_s(x, z)u_s(y) \qquad s = 1,2, \dots, M \tag{6}$$

where $\mathbf{F_s}$ are functions of the cross-sectional coordinates x and z, and $\mathbf{u_s}$ represents the vector of generalized displacements defined along the beam axis. M denotes the number of terms considered in the expansion, while the repeated subscript s implies summation over the adopted terms. The selection of the functions F_s determines the class of the one-dimensional CUF model to be employed. In this work, nine-point polynomial functions (L9) over the xz cross-section are used to accurately capture refined structural kinematics. The resulting displacement field for a single L9 element is given by [12,13]:

$$\begin{aligned} u_x &= F_1u_{x1} + F_2u_{x2} + F_3u_{x3} + F_4u_{x4} + F_5u_{x5} + F_6u_{x6} + F_7u_{x7} + F_8u_{x8} + F_9u_{x9} \\ u_y &= F_1u_{y1} + F_2u_{y2} + F_3u_{y3} + F_4u_{y4} + F_5u_{y5} + F_6u_{y6} + F_7u_{y7} + F_8u_{y8} + F_9u_{y9} \\ u_z &= F_1u_{z1} + F_2u_{z2} + F_3u_{z3} + F_4u_{z4} + F_5u_{z5} + F_6u_{z6} + F_7u_{z7} + F_8u_{z8} + F_9u_{z9} \end{aligned} \tag{7}$$

where $u_{x1},\dots,u_{z9}$ are the displacement variables of the problem. They represent the translational displacement components of each of the nine points of the L9 element. For further details on Lagrange Expansion (LE) models utilized in this paper, interested readers can refer to [14].

Finite element formulation

Discretizing along the y-axis via FEM, the generalized displacement vector $\mathbf{u_s}(y)$ is approximated as:

$$u_s(y) = N_j(y)q_{sj}, \quad j = 1,2, \dots, p+1 \tag{8}$$

where N_j is the j-th shape function of order p (with summation implied over j), and q_{sj} is the nodal parameter vector, defined as:

$$q_{sj} = [q_{u_x sj} \ \ q_{u_y sj} \ \ q_{uzsj}]^T \tag{9}$$

Materials Research Proceedings 73 (2026) 223-228 https://doi.org/10.21741/9781644904459-43

Explicit expressions for N_j are omitted for brevity [9]. Notably, the cross-sectional polynomial selection in LE kinematics is independent of the axial finite element interpolation. Here, classical 4-node beam elements (B4) providing cubic interpolation along the y-direction are employed.

Functionally Graded Beam

The FG beam is analyzed for various compositional gradient exponents. Fig. 1 shows the beam geometry, the CUF-based Lagrange Expansion (LE) cross-sectional discretization, and the axial four-node (B4) beam element discretization (ten B4 elements along the length).

The FG beam is an isotropic material graded continuously between ceramic and metal phases. The ceramic volume fraction follows the power-law distribution of Ref. [14]:

$$V_c(z) = (\frac{z}{h} + \frac{1}{2})^n \tag{10}$$

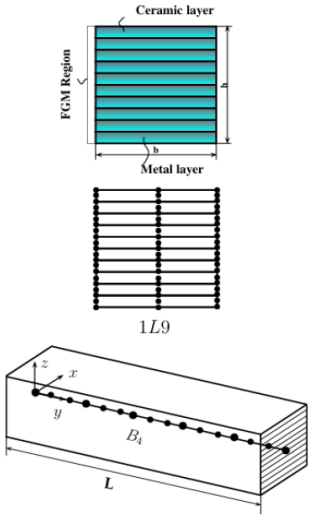

Fig. 1. For the FG beam, from top to bottom: the material layer distribution, the cross-sectional representation based on the Lagrange Expansion, and the discretization of the beam using B4 elements.

For the volume fraction of the metal phase (m), the following relation is used:

$$V_m(z) = 1 - V_c(z) \tag{11}$$

Here, n denotes the compositional gradient exponent in the z-direction, and h denotes the beam thickness (Fig. 1). The temperature-independent effective mechanical properties of the FGM are computed using the Mori–Tanaka scheme [15], which yields the effective bulk modulus as:

$$K(z) = K_m + \frac{V_c(K_c - K_m)}{1+(1-V_c)\frac{3(K_c-K_m)}{3K_m+4G_m}} \tag{12}$$

Table 2: Physical and mechanical properties of ceramic and metal materials [16].

Material	K [GPa]	G [GPa]	ρ [kg/m³]	E [GPa]	ν
Ti-6Al-4V	96.78	44	4429	114.63	0.3026
ZrO_2	72.92	54	5680	129.95	0.203

The overall shear modulus G is expressed as

$$G(z) = G_m + \frac{V_c(G_c - G_m)}{1+(1-V_c)\frac{G_c-G_m}{G_m+f_1}} \tag{13}$$

Materials Research Proceedings 73 (2026) 223-228 https://doi.org/10.21741/9781644904459-43

where f_1 is given by

$$f_1 = \frac{G_m(9K_m+8G_m)}{6(K_m+2G_m)} \qquad (14)$$

The overall modulus of elasticity is

$$E(z) = \frac{9KG}{3K+G} \qquad (15)$$

The overall Poisson's ratio is written as

$$E(z) = \frac{9KG}{3K+G} \qquad (16)$$

Using the linear rule of mixtures, the density is given as

$$\rho(z) = \rho_c V_c + \rho_m V_m \qquad (17)$$

The FG beam geometry is shown in Fig. 3(a), where L/h = 10 and b = h. The Young's moduli of the top and bottom layers of the FG beam are taken as 379.69 and 69.62 GPa, respectively. The metallic and ceramic constituents of the beam are Ti-6Al-4V and ZrO_2, respectively. The mechanical properties of the ceramic and metallic constituents are given in Table 2.

Fig. 2 shows the ceramic volume fraction distributions across the FG beam for various gradient exponents n. The cross-section is ceramic-rich for n = 0.1, metal-rich for n = 10.0, and linear for n = 1, with top and bottom surfaces being 100% ceramic and 100% metal, respectively. Subsequent analyses are conducted using n = 1.

Fig. 3 illustrates the linear vibration behavior of the FG beam across load cases P_i and vibration modes f_j, highlighting the evolution of natural frequencies and mode shapes with increasing load. For mode f_1, natural frequencies remain nearly constant under lower loads (P_1–P_4), demonstrating that global stiffness is largely preserved under small transverse loading.

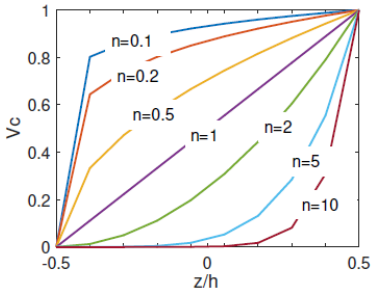

Fig. 2. Distributions of the ceramic volume fraction for different compositional gradient exponents in the FG beam.

Increasing the load level causes noticeable variations in natural frequencies because the beam's deformation state and effective structural stiffness change. Higher vibration modes (f3–f10) exhibit more complex shapes with additional nodal points along the length and show greater sensitivity to load variations, leading to more pronounced frequency shifts.

The results indicate that transverse load levels noticeably alter the linear dynamic response, natural frequencies, and mode shapes of FG beams by changing the effective stiffness. Therefore, consider load-level effects when evaluating the dynamic behavior of functionally graded structures.

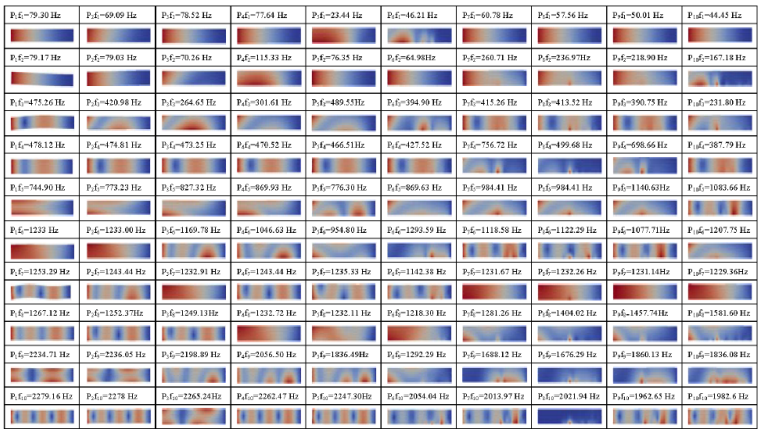

Fig. 3. Linear vibration behavior of the FG beam under various load cases Pi, where Pifj denotes the natural frequency of the jj-th vibration mode at load level Pi (L = 1.0 m).

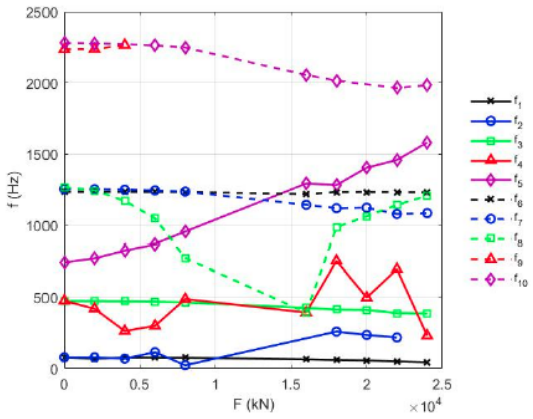

Fig. 4. Variation of the natural frequencies of the FG beam under different transverse load levels, grouped according to vibration modes exhibiting similar dynamic characteristics.

Figure 4 shows the natural-frequency variation with transverse load. The modes are grouped according to similar trends. Lower vibration modes (f_1 and f_2) remain relatively low and stable as load increases because of their global bending nature, showing minimal sensitivity to load-induced stiffness variations. Intermediate modes (f_3 and f_4) fluctuate more noticeably; notably, f_3 decreases before partially recovering, reflecting a non-uniform loading effect on effective stiffness. Higher-order modes (f_5–f_{10}) show diverse trends—some increasing (such as f_5) and others decreasing—confirming that transverse loads significantly alter specific higher-order modal stiffnesses. Overall, Fig. 4 shows that lower modes remain largely insensitive, whereas higher modes are strongly affected by transverse loading.

Using the Carrera Unified Formulation, the linear dynamic response of FG beams was systematically evaluated under varying transverse loads. The results confirm that transverse load levels noticeably modify natural frequencies and vibration modes, with higher-order kinematics showing greater load sensitivity. This demonstrates the CUF-based beam formulation's ability to accurately capture the dynamic behavior of functionally graded structures while accounting for material gradation and refined cross-sectional kinematics.

Acknowledgements
The authors gratefully acknowledge TÜBİTAK support under the 2224-A International Scientific Events Participation Support Program and Erciyes University BAP support under Project No. FUI-2024-13879.

References

[1] M. Naebe, K. Shirvanimoghaddam, Functionally graded materials: A review of fabrication and properties, Applied Materials Today 5 (2016) 223–245. https://doi.org/10.1016/j.apmt.2016.10.001
[2] J.N. Reddy, E. Ruocco, J.A. Loya, A.M.A. Neves, Theories and analysis of functionally graded beams, Applied Sciences 11 (2021) 7159. https://doi.org/10.3390/app11157159.
[3] J. Xu, C. Feng, Z. Ni, Z. Hang, J. Zhang, Numerical analysis on nonlinear dynamics of functionally graded graphene nanoplatelet-reinforced multiphase porous composite beam with DQ and IHB methods, Mechanics of Advanced Materials and Structures (2025). https://doi.org/10.1080/15376494.2025.2477227
[4] E. Carrera, M. Cinefra, M. Petrolo, E. Zappino, Finite Element Analysis of Structures through Unified Formulation, John Wiley & Sons, 2014. https://doi.org/10.1002/9781118536643
[5] E. Carrera, M. Maiarú, M. Petrolo, Component-wise analysis of laminated anisotropic composites, International Journal of Solids and Structures 49 (2012) 1839–1851. https://doi.org/10.1016/j.ijsolstr.2012.03.025
[6] E. Carrera, A. Pagani, Free vibration analysis of civil engineering structures by component-wise models, Journal of Sound and Vibration 333 (2014) 4597–4620. https://doi.org/10.1016/j.jsv.2014.04.063
[7] X. Liu, A. Pagani, E. Carrera, X. Liu, Free vibration analysis of composite beams and laminated reinforced panels by refined dynamic stiffness method and CUF-based component-wise theory, Composite Structures 337 (2024) 118058. https://doi.org/10.1016/j.compstruct.2024.118058
[8] E. Carrera, G. Giunta, M. Petrolo, Beam Structures: Classical and Advanced Theories, John Wiley & Sons, 2010. https://doi.org/10.1002/9781119978565
[9] K.J. Bathe, Finite Element Procedures, Prentice Hall, Upper Saddle River, 1996.
[10] T.J.R. Hughes, The Finite Element Method: Linear Static and Dynamic Finite Element Analysis, Courier Corporation, North Chelmsford, 2012.
[11] A. Pagani, E. Carrera, Unified formulation of geometrically nonlinear refined beam theories, Mechanics of Advanced Materials and Structures 25 (2018) 15–31. https://doi.org/10.1080/15376494.2016.1232458
[12] Carrera E, Petrolo M. Refined beam elements with only displacement variables and plate/shell capabilities. Meccanica 2012;47(3):537–556. https://doi.org/10.1007/s11012-011-9466-5
[13] A. Pagani, R. Augello, E. Carrera, Frequency and mode change in the large deflection and post-buckling of compact and thin-walled beams, Journal of Sound and Vibration 2018;432:88–104. https://doi.org/10.1016/j.jsv.2018.06.024
[14] M. Nemat-Alla, Reduction of thermal stresses by developing two-dimensional functionally graded material, International Journal of Solids and Structures 40 (2003) 7339–7356. https://doi.org/10.1016/j.ijsolstr.2003.08.017
[15] T. Mori, K. Tanaka, Average stress in matrix and average elastic energy of materials with misfitting inclusions, Acta Metallurgica 21 (1973) 571–574. https://doi.org/10.1016/0001-6160(73)90064-3
[16] MatWeb, Materials Information Resource [Online], 2016. Available: http://www.matweb.com.

Materials Research Proceedings 73 (2026) 229-234 https://doi.org/10.21741/9781644904459-44

Tailoring Interfacial Strategies to Enhance Mechanical Properties of Bi-Layered LSR-Based Polymer Composite Radiation Shields

Pramod A.C.[1], Ambika M.R.[1*], Subramanian K.R.V.[2], Niranjan Murthy[2], Roopa S.[3], Nagaiah N.[4], Sherry Shajan Kuttukaran[1]

[1]Department of Physics, MS Ramaiah Institute of Technology, Bengaluru-560 054, India

[2]Department of Mechanical Engineering, MS Ramaiah Institute of Technology, Bengaluru-560 054, India

[3]Department of Polymer Science and Technology, Sri Jayachamarajendra College of Engineering, Mysuru-570 006, India

[4]Department of Physics, Jnana Bharathi Campus, Bangalore University, Bengaluru-560 056, India

*ambikamr@msrit.edu

Keywords: Bi-Layer Composite, Interfacial Adhesion, Gamma Radiation Shielding, Tensile Properties, Surface Engineering

Abstract. This study presents the fabrication and evaluation of bi-layered Liquid Silicone Rubber (LSR) composites by incorporating Tungsten trioxide (WO_3) and Antimony (Sb) as fillers, with a particular focus on how interfacial surface treatment affects the mechanical integrity of the bilayer. Two sets of three composite formulations (WOSB1, WOSB2, and WOSB3) were prepared at progressively higher filler loadings, one set with and the other without mechanical surface treatment at the inter-layer interface. The highest-loading formulation, WOSB3, achieved an overall composite density of 2.318 ± 0.069 g cm^{-3} and proved to be the best-performing of the three. Untreated bi-layer specimens delaminated prematurely at the interface during tensile testing (ASTM D412), showing a characteristic stepwise load drop on the stress-strain curve. For WOSB3, the treatment elevated tensile strength from 0.811 ± 0.03 MPa to 1.398 ± 0.05 MPa and elongation at break from 129 ± 4% to 172 ± 5%. Radiation attenuation measurements for 80 keV gamma rays yielded a Mass Attenuation Coefficient (MAC) of 2.884 ± 0.105 $cm^2\ g^{-1}$ for WOSB3, surpassing the MAC of conventional lead (2.312 $cm^2\ g^{-1}$) at the same energy.

1. Introduction

The increasing use of ionizing radiation in medical imaging, therapeutic radiation treatments, nuclear energy production, and non-destructive testing (NDT) has increased the need for effective radiation shielding materials with high attenuation efficiency, durability, and worker safety [1,2]. Conventional radiological personal protective equipment (PPE), including aprons, thyroid shields, and gonadal shields, is composed of lead-based materials due to their ability to absorb effectively and scatter gamma rays due to their high atomic number (Z=82) and density (ρ=11.35 g cm^{-3}) [3]. Nevertheless, the well-known toxic effects of lead exposure as a neurotoxic and environmental pollutant have led to increased international pressure for eliminating its usage within the manufacture of medical products, and the European RoHS (Restriction of Hazardous Substances) directives prohibit its use in many categories of equipment [4].

One important aspect to consider about the production of elastomeric multi-layered composites is the quality of the interface layer that separates the two distinct layers. In the absence of conscious surface preparation of the interface, the result would be adhesive delamination, which could potentially become the failure mechanism that makes the structural integrity of the clothing less reliable when repeatedly used throughout its lifetime [5]. Mechanical interlocking due to abrasion

Content from this work may be used under the terms of the Creative Commons Attribution 3.0 license. Any further distribution of this work must maintain attribution to the author(s) and the title of the work, journal citation and DOI. Published under license by Materials Research Forum LLC.

Materials Research Proceedings 73 (2026) 229-234 https://doi.org/10.21741/9781644904459-44

with sandpaper has even been proven to be an effective method to improve bonding through increased interfacial area and mechanical interlocking [6].

In the present study, three bilayered LSR composite formulations (WOSB1, WOSB2, WOSB3) with systematically increasing WO_3 and Sb filler loadings were fabricated both with and without P120-grade silicon carbide abrasion treatment at the inter-layer interface. The materials were evaluated through bulk density measurement, tensile testing (ASTM D412), and narrow-beam gamma-ray transmission measurements at 80, 356, and 662 keV energy to assess the mass attenuation coefficient. By demonstrating that a simple, low-cost abrasion treatment transforms the failure mode from adhesive delamination to cohesive bulk fracture, this study establishes a practical, scalable fabrication protocol for high-performance, lead-free, bi-layered LSR radiation shields suited to next-generation wearable PPE in diagnostic radiology and interventional medicine.

2. Materials and Methods

2.1 Materials

LSR (base elastomer) was used as the polymer matrix in this study. Tungsten trioxide (WO_3) and Antimony (Sb) powders were procured from commercial suppliers and used as received without further purification. P120-grade silicon carbide sandpaper was employed for interfacial surface preparation.

2.2 Composite Formulation

Three composite formulations were fabricated with increasing filler loadings while maintaining a constant LSR base loading of 100 parts per hundred rubber (phr) in all cases. The formulations are designated as WOSB1, WOSB2, and WOSB3. Full formulation details and measured densities are given in Table 1. The increase in Sb loading from WOSB1 to WOSB3 and WO_3 loading was kept constant for both layers for each formulation, to isolate the effect of the Sb gradient on the density profile.

Table 1. Formulation details and measured bulk density of WOSB bi-layered composites.

Sample	Layer	LSR (phr)	Sb (phr)	WO_3 (phr)	Density (g cm^{-3})
WOSB1	Layer 1	100	25	25	1.623 ± 0.041
	Layer 2	100	50	25	
WOSB2	Layer 1	100	50	50	2.057 ± 0.053
	Layer 2	100	100	50	
WOSB3	Layer 1	100	75	75	2.318 ± 0.069
	Layer 2	100	150	75	

2.3 Fabrication Process

The fillers were dispersed in LSR by sonication followed by vacuum degassing. Bilayered composites were fabricated by sequential casting. For treated specimens, Layer 1 was fabricated in accordance with the aforementioned procedure. For specimens designated for surface treatment, the cured first-layer surface was carefully abraded using P120 silicon carbide paper with strokes in both directions for about 2 minutes. Further, the surface was wiped using Isopropyl Alcohol (IPA) for cleaning and dried within 5 minutes before the second layer casting. The composite post-cure cycle (80 °C, 6 h, vacuum) completed the process. Untreated specimens followed the same procedure, without the abrasion and IPA cleaning steps.

Materials Research Proceedings 73 (2026) 229-234 https://doi.org/10.21741/9781644904459-44

2.4 Characterization Techniques

Tensile tests were conducted according to the procedure specified in ASTM D412-16, using Type C dumbbell-shaped specimens (with gauge length equal to 33 mm) on a Universal Testing Machine (UTM) equipped with a 50 kN load cell at a crosshead speed of 500 mm min^{-1} [7]. The mass attenuation coefficients were estimated by employing the narrow-beam transmission method. Gamma photon detection was carried out using a NaI (Tl) scintillation detector (resolution ~7.5% at 662 keV) with a multi-channel analyser (MCA). Ba-133 (80 keV, 356 keV) and Cs-137 (662 keV) gamma- ray sources were used in this measurement [8].

3. Results and Discussion

3.1 Mechanical Properties: Effect of Interfacial Treatment

3.1.1. Failure Mode Analysis: Stepwise versus Continuous Fracture

The effect of interfacial surface treatment on the tensile failure behaviour of the bi-layered composites is illustrated in Figures 1-3. Untreated specimens exhibited a characteristic stepwise load–displacement response with multiple peaks, indicating progressive interfacial delamination [Figure 2]. In contrast, specimens treated with P120 silicon carbide abrasion showed smooth single-peak curves and failed through cohesive fracture [Figure 3], demonstrating improved interlayer bonding. The enhanced performance is attributed to the mechanical interlocking created by surface roughening, which strengthened the adhesion between the two layers [9,10]. As a result, the failure mode shifted from adhesive delamination to cohesive bulk fracture, confirming the effectiveness of the interfacial treatment [11].

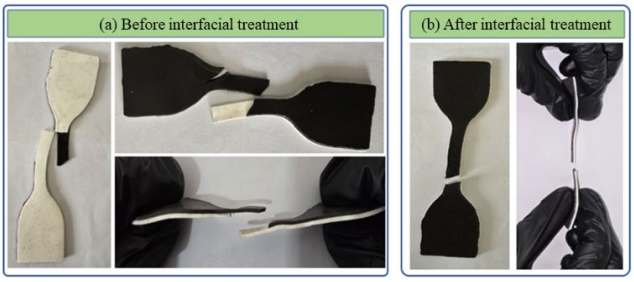

Figure 1. Images of samples before and after interfacial treatment

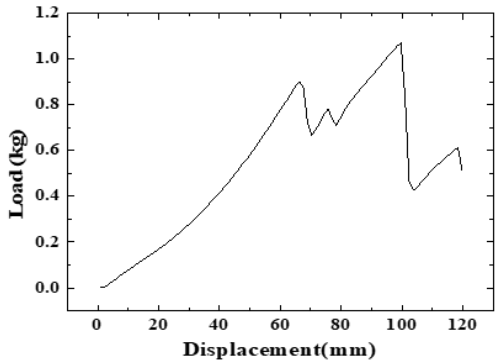

Figure 2. Load v/s displacement graph of the untreated samples.

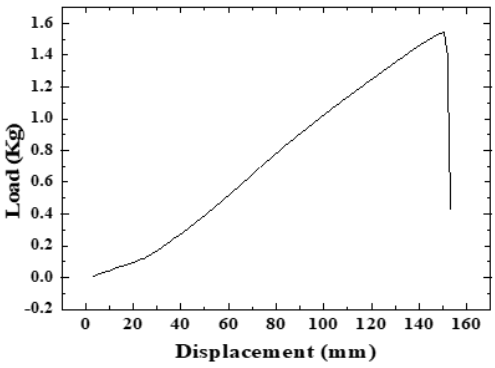

Figure 3. Load v/s displacement graph of the treated samples.

3.1.2. Tensile Strength and Elongation at Break

Tensile strength and elongation at break for all formulations are shown in Figures 4 and 5. Surface treatment improved both properties across all composites. Tensile strength increased from 1.446 to

Materials Research Proceedings 73 (2026) 229-234 https://doi.org/10.21741/9781644904459-44

1.591 MPa for WOSB1, from 1.234 to 1.412 MPa for WOSB2, and from 0.811 to 1.398 MPa for WOSB3. Similarly, elongation at break increased from 220.78% to 244.70%, from 161.28% to 192.72%, and from 129.28% to 172.08%, respectively, for the said samples. The most significant improvement was observed for WOSB3, indicating that interfacial surface treatment effectively enhanced the bonding between the two layers, even at the highest filler loading. As the filler content increased, tensile strength gradually decreased (WOSB1 > WOSB2 > WOSB3), which is consistent with the behaviour of highly filled rubber composites, where the reduced polymer matrix and increased filler–matrix interactions limit efficient stress transfer [12,13].

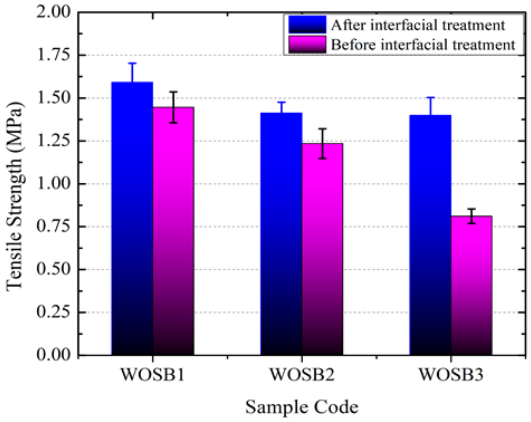

Figure 4. Tensile Strength of the treated and untreated samples

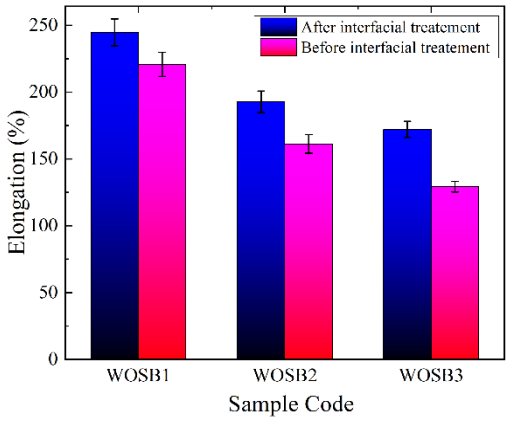

Figure 5. Percentage of elongation of the treated and untreated samples

3.2 Radiation Attenuation Performance

The measured mass attenuation coefficients for all three formulations at three photon energies are illustrated in Figure 6. At 80 keV within the diagnostic X-ray range, the MAC values increased progressively from WOSB1 (1.33 ± 0.04 cm^2g^{-1}) through WOSB2 (2.15 ± 0.07 cm^2g^{-1}) to WOSB3 (2.884 ± 0.105 cm^2g^{-1}). The MAC value of WOSB3 at 80 keV exceeds that of lead (2.312 cm^2g^{-1}), a practically important result, given that lead is the conventional benchmark for radiation shielding performance. This advantage at diagnostic energies follows the Z/E energy dependence of the photoelectric cross-section; the combined contribution of WO_3 and Sb atoms becomes disproportionately large as photon energy decreases toward 80 keV, and at sufficiently high filler loadings, the composite photoelectric cross-section per unit mass can exceed that of lead, thus enhancing the probability of absorption of the gamma photons. Additionally, interfacial treatment had little influence on the radiation shielding performance of the composites. As shown in Figure 6, the MAC values of the treated and untreated composites were very similar at all investigated photon

energies. Although WOSB3 exhibited a slight increase in MAC at 80 keV after interfacial treatment, the difference was small, while WOSB1 and WOSB2 showed no noticeable change. Similarly, the MAC values at 356 and 662 keV remained essentially unchanged after treatment for all formulations. These results indicate that interfacial treatment has a minimal effect on the intrinsic radiation attenuation capability of the composites, as the MAC is primarily governed by the type, concentration, and density of the high-Z fillers and also the interfacial bonding between the fillers and the polymer matrix. Thus, the interfacial strategy used for fabricating the layered composites and the measured outstanding low-energy attenuation in a mechanically robust, Pb-free elastomer are the key findings of this study.

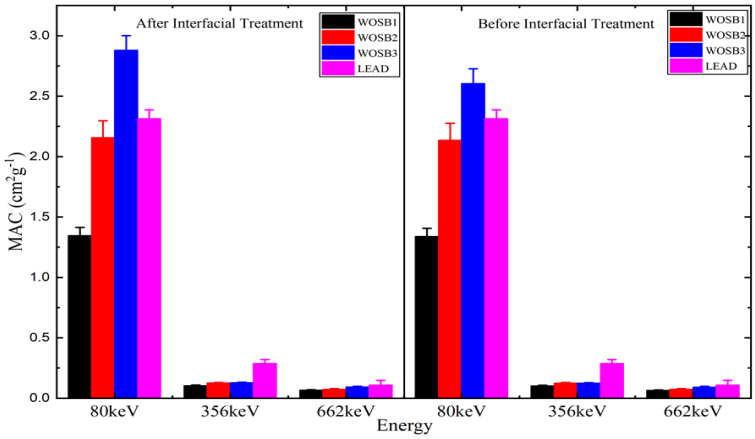

Figure 6. Variation of MAC of the treated and untreated samples with respect to the gamma photon energy

Conclusion

The current investigation has revealed that adopting a straightforward P120 sandpaper abrading technique on the interfacial region of bilayered LSR/WO_3/Sb composites, has changed the failure mechanism from adhesive delamination to bulk cohesive failure, thus revealing the entire mechanical performance of such bilayered materials. Bilayered samples without any surface treatment had their failure occur prematurely, resulting in a characteristic stepwise curve of stress-strain response. Abraded bilayered samples exhibited cohesive fracturing in a single event, suggesting proper inter-layer binding. This effect was most pronounced in the sample formulation with the highest filler loading level (WOSB3), showing an increase in tensile strength (0.811 to 1.398 MPa) and elongation at break (from 129% to 172%). WOSB3 achieved a MAC of 2.884 ± 0.105 $cm^2\ g^{-1}$ at 80 keV, surpassing that of elemental lead (2.312 $cm^2\ g^{-1}$) at the same energy. The fact that interfacial treatment and filler loading act as largely independent variables gives composite designers considerable flexibility when tuning the mechanical and shielding performance of LSR bi-layered shields for specific clinical or industrial uses.

Acknowledgment

The author gratefully acknowledges the financial support provided by the Department of Atomic Energy, Board of Research in Nuclear Sciences (DAE-BRNS), Government of India, under the research project entitled “Radiative protective qualities of wearable, nontoxic & layered polymer composites with multifillers”. (Sanction No. 51/14/11/2024-BRNS, dated 16.12.2024).

References

[1] Podgorsak, E. B. (2016). Radiation Physics for medical physicists. In Graduate texts in physics. https://doi.org/10.1007/978-3-319-25382-4

[2] International Commission on Radiological Protection (ICRP), “The 2007 Recommendations of the International Commission on Radiological Protection,” ICRP Publication 103, Ann. ICRP, vol. 37, nos. 2–4, 2007.

[3] Nambiar, S., & Yeow, J. T. W. (2012b). Polymer-Composite materials for radiation protection. ACS Applied Materials & Interfaces, 4(11), 5717–5726. https://doi.org/10.1021/am300783d

[4] Safari, A., Rafie, P., Taeb, S., Najafi, M., & Mortazavi, S. M. J. (2024). Development of Lead-Free Materials for Radiation shielding in Medical Settings: A review. Journal of Biomedical Physics and Engineering, 14(3), 229–244. https://doi.org/10.31661/jbpe.v0i0.2404-1742

[5] Kuttukaran, S. S., Ambika, M. R., Siddaraju, C., Nagaiah, N., Srilakshmi, B. P., Reddy, Y. H., Goel, P., Kimothi, S., Ganguly, D., Chattopadhyay, S., & Roopa, S. (2025). Fabrication and investigation of a novel bi-layered, silicone rubber-based composite as a promising radiation shield. Journal of Radioanalytical and Nuclear Chemistry, 334(10), 7459–7471. https://doi.org/10.1007/s10967-025-10216-w

[6] Comyn, J. (1997). Polymer science dictionary 2nd edition. International Journal of Adhesion and Adhesives, 17(4), 381. https://doi.org/10.1016/s0143-7496(97)00015-8

[7] ASTM D412-16, Standard Test Methods for Vulcanized Rubber and Thermoplastic Elastomers—Tension. West Conshohocken, PA, USA: ASTM International, 2016.

[8] Srilakshmi, B. P., Reddy, A. J., Ambika, M. R., Kuttukaran, S. S., Reddy, Y. H., Nagaiah, N., Deepika, D. N., & Prashantha, K. (2025). Exploration of the gamma-ray shielding capabilities of tungsten oxide and chromium-infused silicone rubber composites. Radiation Physics and Chemistry, 232, 112661. https://doi.org/10.1016/j.radphyschem.2025.112661

[9] Connolly, J. V. (1984). Structural adhesive joints in engineering. Robert D. Adams and william C. Wake. Elsevier applied science publishers, london. 1984. 309pp. Illustrated. £35.00. The Aeronautical Journal, 88(877), 329–329. https://doi.org/10.1017/s0001924000020777

[10] Park, H., & Lee, S. H. (2021). Review on Interfacial bonding mechanism of functional polymer coating on Glass in Atomistic Modeling Perspective. Polymers, 13(14), 2244. https://doi.org/10.3390/polym13142244

[11] Awaja, F., Gilbert, M., Kelly, G., Fox, B., & Pigram, P. J. (2009). Adhesion of polymers. Progress in Polymer Science, 34(9), 948–968. https://doi.org/10.1016/j.progpolymsci.2009.04.007

[12] Guth, E. (1945). Theory of filler reinforcement. Journal of Applied Physics, 16(1), 20–25. https://doi.org/10.1063/1.1707495

[13] Smith, W. R. (1967). Reinforcement of elastomers. Gerard Kraus, Ed. Interscience, New York, 1965. xv + 611. Journal of Applied Polymer Science, 11(10), 2079–2079. https://doi.org/10.1002/app.1967.070111026

Materials Research Proceedings 73 (2026) 235-238 https://doi.org/10.21741/9781644904459-45

Lamb Wave Propagation in Damaged Sandwich Structures using High Order Finite Plate Elements

Myka ABAQUIN[1,a*], Alfonso PAGANI[1,b], Matteo FILIPPI[1,c]

[1]mul2 lab, Politecnico di Torino, DIMEAS, Turin, Italy

[a]myka.abaquin@polito.it, [b]alfonso.pagani@polito.it, [c]matteo.filippi@polito.it

Keywords: Carrera Unified Formulation, Structural Health Monitoring, Homogenized Honeycomb Sandwich, Lamb Wave Propagation

Abstract. A major concern with the use of honeycomb-core sandwich structures in aerospace applications is the phenomenon of debonding at the skin-core interface, which can significantly compromise structural integrity. While these composite assemblies offer superior mechanical properties, the numerical simulation of wave-damage interaction presents a formidable challenge. The multi-scale nature of the honeycomb geometry, combined with the high-frequency excitation required to resolve debond regions, typically demands extremely fine discretisation, making conventional 3D simulations of wave-damage interaction computationally demanding. This paper proposes an efficient modelling framework utilising the Carrera Unified Formulation (CUF) to address these constraints for debond damage analysis. The following study examines the efficacy of this homogenised layer-wise model in capturing Lamb wave propagation and interaction with debonded regions in sandwich components. Results demonstrate that the combination of high-order CUF kinematics and core homogenisation provides a robust balance between local damage sensitivity and global resource efficiency. This approach maintains high fidelity in predicting wave-front distortions while achieving a substantial reduction in degrees of freedom and runtime compared to full-scale 3D models. The study demonstrates a scalable solution for the rapid development and validation of damage detection algorithms in complex aeronautical structures.

Introduction

Honeycomb sandwich structures are increasingly deployed in modern aerospace and aeronautical applications due to their exceptional stiffness-to-weight ratio and energy absorption characteristics. Despite these superior mechanical properties, a persistent threat to the structural integrity of these assemblies is the onset of facesheet-core debonding. The detection of debond at an early stage is therefore of critical importance for the safe operation of components, motivating the development of reliable structural health monitoring (SHM) techniques based on guided Lamb waves.

Lamb waves exhibit remarkable sensitivity to localized changes in thickness and boundaries, enabling them to travel long distances with minimal attenuation and scatter significantly when interacting with internal flaws. However, the physical problem of modeling wave-damage interaction in honeycomb panels remains a significant computational challenge. The intricate, multi-scale geometry of the hexagonal core cells demands an excessively high mesh density when traditional three-dimensional finite element approaches are applied. This issue is worsened by the high frequencies required to resolve micro-scale debond regions, making conventional 3D analyses restrictively expensive in terms of runtime and computational memory.

To mitigate these limitations, this paper investigates an efficient modeling approach for the detection of facesheet-core debond damage in aluminium sandwich plates. High-order CUF plate elements are employed together with a layer-wise kinematic description across the facesheet and homogenized core layers.

Content from this work may be used under the terms of the Creative Commons Attribution 3.0 license. Any further distribution of this work must maintain attribution to the author(s) and the title of the work, journal citation and DOI. Published under license by Materials Research Forum LLC.

Materials Research Proceedings 73 (2026) 235-238 https://doi.org/10.21741/9781644904459-45

Methodology

The Carrera Unified Formulation [1] expresses the three-dimensional displacement field as a generic expansion in the thickness coordinate z:

$$\boldsymbol{u}(x,y,z) = F_\tau(z)\boldsymbol{u}_\tau(x,y), \quad \tau = 1,2,\dots,M \tag{1}$$

, where $\boldsymbol{u}_\tau$ are generalized displacement unknowns defined on the plate mid-surface, $F_\tau(z)$ are thickness assumption functions whose class and order constitute the structural theory and M is the total number of expansion terms. The Einstein summation convention is adopted over the repeated index τ. The choice of F_τ entirely determines the kinematic assumptions of the model. This separation between the in-plane finite element discretization and the through-thickness expansion is the defining feature of CUF.

In-plane discretization employs Lagrangian shape functions $N_i(x,y)$, so that the full displacement field within an element is written as:

$$\boldsymbol{u}(x,y,z) = N_i(x,y)F_\tau(z)\boldsymbol{u}_{\tau i} \tag{2}$$

, where i is the finite element node index and $\boldsymbol{u}_{\tau i}$ is the vector of nodal unknowns. Higher-order in-plane elements are adopted here due to their superior convergence in wave propagation problems.

For sandwich structures, the difference in stiffness between the facesheets and the core produces steep gradients in the transverse stress and strain fields that classical equivalent single layer (ESL) theories cannot accurately represent. A layer-wise approach is therefore adopted, where independent thickness expansions are defined for each physical layer with displacement continuity enforced at the interfaces. This allows each layer to develop its own kinematic state while maintaining a fully compatible displacement field across the cross-section. This study utilizes the hierarchical Legendre expansion model [2]. For a 2D plate, the kinematics of a single layer are expressed as:

$$u_x = F_\tau(z)u_\tau(x,y) \tag{3}$$

$$u_y = F_\tau(z)u_\tau(x,y) \tag{4}$$

$$u_z = F_\tau(z)u_\tau(x,y) \tag{5}$$

, where $F_\tau(z)$ is the one-dimensional complete Legendre polynomial set of the selected order. The use of hierarchical polynomials means that the expansion order can be increased by appending higher-degree terms without modifying lower-order contributions. This property makes HLE models particularly efficient, since the expansion order can be tuned independently in each layer to match the local accuracy requirements. The debond between the upper facesheet and the core is introduced by releasing the displacement compatibility conditions at the corresponding interface, which means the nodal degrees of freedom of the adjacent layers are left unmerged over the debond region while full compatibility is retained elsewhere.

The governing equations for the wave propagation problem are derived from the principle of virtual displacements. Substituting the CUF displacement field and the constitutive relations $\boldsymbol{\sigma} = \widetilde{\boldsymbol{C}}\varepsilon$, $\varepsilon = \boldsymbol{D}\boldsymbol{u}$ where $\boldsymbol{D}$ is the geometrical differential operator and $\widetilde{\boldsymbol{C}}$ is the material stiffness matrix. The principle of virtual displacements yields the discretised equations of motion in terms of the fundamental nuclei of the mass and stiffness matrices:

Materials Research Proceedings 73 (2026) 235-238 https://doi.org/10.21741/9781644904459-45

$$\delta \boldsymbol{u}_{sj}^{T} \boldsymbol{M}^{ij\tau s} \ddot{\boldsymbol{u}}_{\tau i} + \delta \boldsymbol{u}_{sj}^{T} \boldsymbol{K}^{ij\tau s} \boldsymbol{u}_{\tau i} = \boldsymbol{u}_{sj}^{T} \boldsymbol{P}^{sj} \tag{6}$$

, where $\boldsymbol{K}^{ij\tau s}$ and $\boldsymbol{M}^{ij\tau s}$ are the fundamental nuclei of the stiffness and mass matrices respectively, and $\boldsymbol{P}$ is the external force vector. For the 2D plate model the nuclei are defined as:

$$\boldsymbol{M}^{ij\tau s} = \int_h \int_\Omega F_s N_j (\rho \boldsymbol{I}_3) F_\tau N_i \, d\Omega \, dz \tag{7}$$

$$\boldsymbol{K}^{ij\tau s} = \int_h \int_\Omega \left(\boldsymbol{D} F_s N_j\right)^T \tilde{\boldsymbol{C}} \boldsymbol{D} F_\tau N_i \, d\Omega \, dz \tag{8}$$

$$\boldsymbol{P}^{sj} = \int_\Omega F_s N_j P \, d\Omega \tag{9}$$

, where the volume integrals are split into the in-plane domain Ω and the thickness domain h. Assembling the nuclei over all node pairs (i, j) and the expansion indices (τ, s) yields the global system:

$$\boldsymbol{M}\ddot{\boldsymbol{U}} + \boldsymbol{K}\boldsymbol{U} = \boldsymbol{P}(t) \tag{10}$$

The structure is excited by a sine-burst force [3] of the form:

$$F = F_0 \sin(\omega t) \sin\left(\frac{\omega t}{2n}\right) \tag{11}$$

applied transversely at one edge of the plate. This modulated tone-burst simultaneously excites the symmetric and anti-symmetric Lamb wave modes.

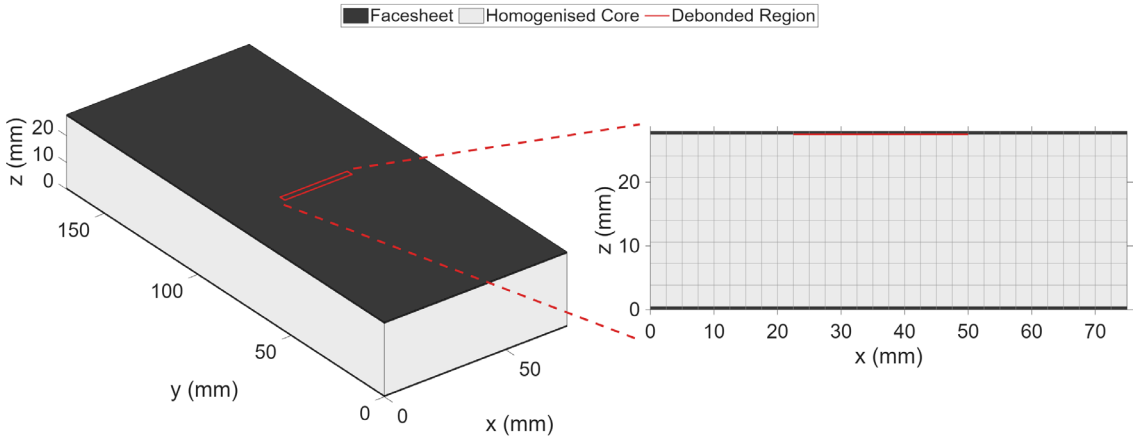

Figure 1: Model of sandwich plate with delamination damage

Numerical Results

The structure presented by Carrera et al. [4] is considered in this study. A wave packet consisting of 2 cycles with a central frequency of 100 kHz is excited on the top surface of the plate. The plate is discretised into 30 x 68 quadratic plate elements, resulting in 1176657 DOFs altogether.

Materials Research Proceedings 73 (2026) 235-238 https://doi.org/10.21741/9781644904459-45

Table 1: Material properties of the homogenized core

E_x[MPa]	E_y[MPa]	E_z[MPa]	G_{xy}[MPa]	G_{xz}[MPa]	G_{yz}[MPa]	ν_{xy}	ν_{xz}	ν_{yz}	ρ[kg/m^3]
1650	101	19.1	691	1280	5760	0.25	$1.7\text{x}10^{-3}$	$2.8\text{x}10^{-3}$	738

The debonded region between the upper facesheet and core is highlighted in Figure 1. Figure 2 shows the signals recorded by the virtual sensor in both the pristine and damaged structure. Prominent amplitude change and phase shift can be observed between the curves exhibiting clear damage detection.

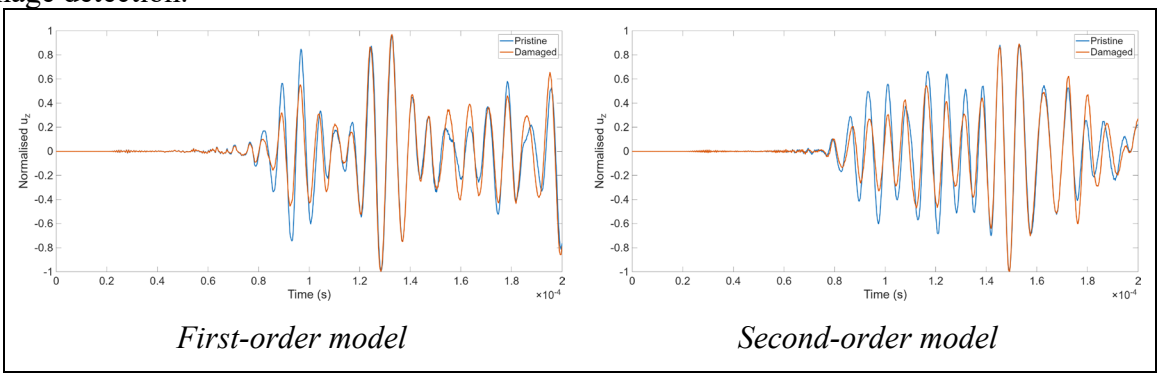

Figure 2: Normalised out-of-plane displacement response of pristine and damaged plate

Conclusions

This work demonstrates the efficacy of a higher-order CUF layer-wise plate model combined with core homogenization for simulating Lamb wave propagation and interaction with facesheet-core debond damage in aluminium sandwich plates. While the time of arrival, a key parameter for damage detection in SHM systems, is identical in the first-order model, the second-order model captures a difference of 0.4 microseconds. This variance highlights the necessity for higher-order models in wave propagation simulations. Future work will investigate optimal sensor placement based on these findings.

Acknowledgment

This research has been carried out within the ASSESS Project – Automated Online Monitoring of Smart Composite Structures – funded by the Marie Sklodowska-Curie actions grant agreement no. 101168031.

References

[1] E. Carrera, M. Cinefra, M. Petrolo, E. Zappino. Finite element analysis of structures through unified formulation. John Wiley & Sons Ltd, 2014. https://doi.org/10.1002/9781118536643

[2] A.G. De Miguel, E. Carrera, A. Pagani, Simulation of Lamb waves via refined FE models with SHM applications, AIAA Scitech Forum, San Diego (2019)

[3] F. Nicassio, M. Cinefra, G. Scarselli, M. Filippi, A. Pagani, E. Carrera, Carrera unified formulation (CUF) for the analysis of disbonds in single lap joints (SLJ), Nondestructive Characterization and Monitoring of Advanced Materials, Aerospace, Civil Infrastructure, and Transportation XVI, Long Beach (2022.) https://doi.org/10.1117/12.2616542

[4] E. Carrera, K. Abu Salem, R. Augello, Free vibration analysis of sandwich plates by component-wise approach, Thin-Walled Structures (2026). https://doi.org/10.1016/j.tws.2025.114062

Materials Research Proceedings 73 (2026) 239-244 https://doi.org/10.21741/9781644904459-46

Advances in Design and Fabrication of Fiber-Reinforced Polymer Composite Bottles for Aerospace Applications

Girish V Kulkarni[1,a], Prakrathi S.[1,b *], Bijayalakshmi Das[1,c]

[1]Dept. of Mechanical Engineering, Ramaiah Institute of Technology, Bangalore, India

[a]gvkulkarni@msrit.edu, [b]krathi.s@gmail.com, [c]bijayalakshmi@msrit.edu

Keywords: FRP Bottle, Classical Lamination Theory, Tsai-Wu First Ply Failure, Aerospace

Abstract. The increasing demand for lightweight and high-performance pressure vessels in aerospace applications has prompted a shift from conventional metallic cylinders to fiber-reinforced polymer (FRP) composites. This study explores the design, development, and fabrication of FRP bottles, emphasizing the use of high-modulus, high-strength materials such as E-Glass, carbon, and Kevlar fibers, alongside epoxy resins as the matrix. The project employs Classical Lamination Theory and the Tsai-Wu first ply failure criterion to evaluate the structural integrity and safety factors of the composite bottles. Findings reveal that carbon fiber reinforcement yields the lowest weight for specified pressure and volume, while the optimal winding angle of 54-55 degrees minimizes thickness and enhances performance. Experimental validation indicates that the E-glass composite bottle requires increased thickness to meet internal pressure requirements, suggesting potential for further optimization. This research contributes to the advancement of composite materials in aerospace applications, highlighting their advantages in weight reduction, corrosion resistance, and design flexibility.

Introduction

Composite pressure vessels are important storage devices in the renewable energy sector for storing compressed natural gas (CNG) [1]. Fuel containers used in commercial and aerospace applications in the world today are manufactured from conventional monolithic materials. These metallic cylinders range from small bottles of a few centimeters in diameter to large storage tanks, which are heavy, reliable in service, and relatively low-cost. With the advancements in new technology, the need for lighter cylinders with lower losses is gaining importance, thereby resulting in the development and use of composite cylinders made of various reinforcements such as glass, carbon, or aramid fibres, with metallic or non-metallic liners.

The composite cylinders are used for a variety of applications such as traditional aerospace vessels for missiles, spacecrafts and ground support equipment function; fire extinguisher equipment cylinders, life support breathing tanks containing air or oxygen for firemen, rescue workers, miners, aircraft and undersea vehicle crew and passengers medical compressed gas cylinders, automate tanks for compressed natural gases (cars, buses, trucks, etc), industrial compressed gas cylinders, mobile refueling CNG stations, transportation of the CNG and cryogenic tanks[2-4].

Fibre-reinforced polymer composites (FRP) are a type of fibre-reinforced composite (FRC) in which the fibres (reinforcements) are dispersed in the polymer matrix that binds them together and facilitate stress transfer between the reinforcement[5-6]. Glass and carbon are the most used reinforcement fibres in composite pressure vessels[7]. Epoxies are polymeric resins exhibiting excellent dimensional stability, fatigue resistance, adhesion to reinforcements, high-temperature resistance, and low shrinkage [8-11]. In addition to low cost, the high strength-to-weight ratio makes the polymer matrix composite an ideal material for various engineering applications. Of the different fabrication techniques of PMC, filament winding (FW) emerges as an efficient, cost-effective method for fabricating axisymmetric products[12]. The foregoing paragraph emphasizes

Content from this work may be used under the terms of the Creative Commons Attribution 3.0 license. Any further distribution of this work must maintain attribution to the author(s) and the title of the work, journal citation and DOI. Published under license by Materials Research Forum LLC.

Materials Research Proceedings 73 (2026) 239-244 https://doi.org/10.21741/9781644904459-46

the need to replace the existing heavy, high-pressure gas cylinders made from steel with lightweight materials, such as polymeric composites.

Materials and Methodology

The present work concerns the design and development of FRP gas bottle to store inert gas at high pressure. A multidirectional laminate is made by stacking many laminae of 0.125 mm thick at different orientation angles and at a particular distance from the midplane in the laminate, depending on the loading conditions. The laminate code is used to designate the stacking sequence of the lamina. The program is coded in C, making use of stress and failure analysis for a general multidirectional laminate applying the first ply failure proposed by Tsai-Wu. The FRP composite pressure vessel is designed using the classical lamination theory. The pressure on the walls of the gas bottle is calculated from the pressure acting internally and the internal diameter of the gas bottle. The unit load acting on the elements of the cylindrical shell along the axial and the hoop direction is then calculated. The bottle is assumed to be cylindrically orthotropic. Of the different types of architecture available, the cross-ply $[0_m / 90_n]s$, angle ply $[\pm\theta]_{ns}$, and $[90_m/\pm\theta_n]_s$ laminates have been considered for the present investigation. In $[0_m / 90_n]s$ laminates, the choice of m & n for the optimum weight has been reached by trying different values of m & n around the initial guesses until the sum (m + n) is minimized. $[\pm\theta]_{ns}$ and $[90_m/\pm\theta_n]$ laminate involve only one variable θ for optimization. The safety factors are computed for the basic laminate for three different materials and the unit thickness h_0= 6t. The weight of the bottle is computed from the density and volume using the equation

$$Weight = 2\pi rl\rho t \quad (1)$$

Where p =pressure, r= radius of the pressure vessel, l = length of the glass bottle, ρ = Density of the material used, t is the thickness of the laminate. The stiffness matrix, laminate stress, and safety factor are obtained using the program.

The glass bottles are fabricated using a three-axis filament winding machine. 2 bottles are fabricated, one with an aluminum liner and E-glass fiber reinforcement, and the other with a polypropylene liner and carbon as the reinforcement. 10 creels were employed to carry out the winding at $\pm$54°. After preliminary checks of fiber tension and winding angle, the winding was completed in 2 hours. The bottle was then cured in the oven at 120°C for about 2 hours, and an additional layer of 2 mm was added to protect the bottle against damage during handling. The cured bottle was taken out and cooled to room temperature. The irregularities were removed using the Emery paper.

The dimensions of the bottles are checked along with visual examination for any defects such as air pockets, misalignment, dry patches, etc. The bottle is subjected to internal pressures of 125, 199, and 375 bars in steps. Strain measurements are carried out at 3 pressures using foil-type rosette gauges, mounted at different locations on the bottle as shown in Fig.1.

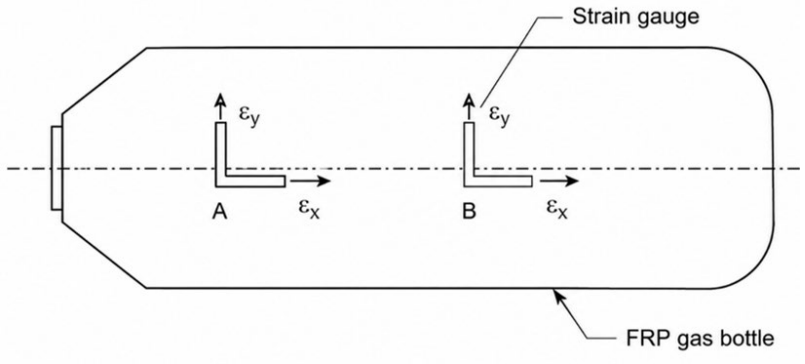

Fig.1. Strain gauge location on the FRP glass bottle

Materials Research Proceedings 73 (2026) 239-244 https://doi.org/10.21741/9781644904459-46

Results and discussion

The output of the developed program and the comparison with the published results [13] are presented in Table 1.

Table1: Comparison of the program results with published results

Properties	Computer Program Results			Published Results		
Laminate Strains × 10^{-3}	ε_x^0	ε_y^0	ε_{xy}^0	ε_x^0	ε_y^0	ε_{xy}^0
	1.622	0.692	1.845	1.62	0.69	1.85
Safety Factor of Each Ply	0°	90°	45°	0°	90°	45°
	2.424165	1.928621	1.784678	2.42	1.93	1.79
On-axis Strain of i-th Ply	$\varepsilon_1 \times 10^{-3}$	$\varepsilon_2 \times 10^{-3}$	$\varepsilon_{12} \times 10^{-3}$	$\varepsilon_1 \times 10^{-3}$	$\varepsilon_2 \times 10^{-3}$	$\varepsilon_{12} \times 10^{-3}$
for θ = 0°	1.622	0.6924	-1.845	1.62	0.69	-1.85
for θ = 90°	0.692	1.622	1.845	0.69	1.62	1.85
for θ = 45°	0.234	2.080	-0.93	0.24	2.08	-0.93
On-axis Stress of the i-th Ply	σ_1 (MPa)	σ_2 (MPa)	σ_{12} (MPa)	σ_1 (MPa)	σ_2 (MPa)	σ_{12} (MPa)
for θ = 0°	296.99	11.86	-13.23	297	12	-13
for θ = 90°	130.59	18.79	13.23	131	19	13
for θ = 45°	48.67	22.20	-6.68	49	22	-7
Off-axis Ply Stress	σ_x (MPa)	σ_y (MPa)	σ_{xy} (MPa)	σ_x (MPa)	σ_y (MPa)	σ_{xy} (MPa)
for θ = 0°	296.99	11.86	-13.23	297	12	-13
for θ = 90°	18.792	130.59	-13.23	19	131	-13
for θ = 45°	42.10	28.76	13.23	42	29	13

The result shows the accuracy of the programme. The gas bottle designs were carried out using 3 different architectures along with 3 different reinforcements. Process optimization for the layout has been carried out by using the program. The allowable laminate thickness is determined and plotted against the lamination angle. It was found that the optimum angle θ corresponding to the minimum thickness of the fiber considered lies in the range between 54° to 55° has shown in Fig.2. The weight of the bottle, computed from the density and the volume, is represented in Table2.

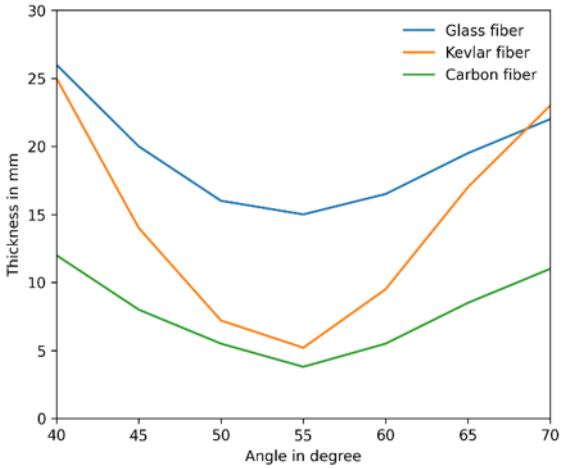

Fig.2. Effect of lamination angle on allowable thickness in a pressure vessel

Materials Research Proceedings 73 (2026) 239-244 https://doi.org/10.21741/9781644904459-46

Table 2: Comparison of Weight for the different fibres

Material	Lay-Up	Weight [kg]	Safety Factor at Working Pressure
E-glass/Epoxy	[±54]30s	6.679	3.089989
	$[90_{40}/\pm54_{20}]s$	8.906	3.015241
	$[O_{27}/90_{54}]s$	9.017	3.109375
Carbon/Epoxy	[±54]7s	1.191	2.783114
	$[90_8/\pm54_8]s$	2.042	2.795794
	$[O_6/90_{12}]s$	1.531	3.204707
Kevlar/Epoxy	[±54]9s	1.337	3.217912
	$[90_{13}/\pm54_{13}]s$	2.898	2.981206
	$[O_7/90_{14}]s$	1.56	3.048108

Strains measured at location B are shown in Table 3 and Table 4. The values of strain in the axial and hoop directions have been plotted against the internal pressure. It is observed that the measured hoop strains are lower than the calculated values, and hence the failure of fiber in the hoop direction is ruled out.

At proof pressure of 199 bar, the micro strain developed is 1810 against 1516. This indicates the failure of the bottle in the axial direction, which is confirmed by the leak observed during the test. Therefore, the bottle should be wound with more number of layers of the E glass fiber.

In the case of the carbon epoxy bottle, the experimental values of strains are less than the calculated values at any specified pressure. This indicates that the bottle is safe until a pressure of 130 bar. It is also confirmed by the fact that no leak was observed during the testing.

Table3: Strain and Safety Factor for Polypropylene-Lined Carbon/Epoxy Composite Bottle $[\mathbf{90_8/\pm54_{10}}]_s$

Pressure [bar]	Strain [μm/m]	Predicted	Experimental	Factor of Safety	Remarks
100	ε_x	845.77	789	6.991	No leak
	ε_y	463.46	455		
130	ε_x	1099.50	924	5.37	No leak
	ε_y	602.505	577		
375	ε_x	3171.646	Test could not be conducted due to lack of facility	1.8644	—
	ε_y	1737.995			

Materials Research Proceedings 73 (2026) 239-244 https://doi.org/10.21741/9781644904459-46

Table 4: Strain and Safety Factor for Aluminium-Lined E-glass/Epoxy Composite Bottle $[\pm 54_{20}]_s$

Pressure [bar]	Strain [µm/m]	Predicted	Experimental	Factor of Safety	Remarks
Working, 125	ε_x	952.4165	1010	2.059991	No failure
	ε_y	3361.489	2150		
Proof, 199	ε_x	1516.247	1810	1.293965	Leakage observed after 10 min
	ε_y	5351.490	3920		
Burst, 375	ε_x	2857.247	Could not be measured; test terminated at 199 bar	0.686639	Nil
	ε_y	952.4165			

Conclusions

Carbon fibre reinforced polymer (CFRP) gas bottles exhibited the lowest weight among the E-glass, carbon, and aramid reinforced composite designs for the same pressure and storage volume requirements. Carbon/epoxy composite bottles fabricated using a high-temperature-grade epoxy resin required a relatively low wall thickness ranging from 3.1 mm to 6.1 mm, depending on the laminate configuration. Among the laminate architectures investigated, the angle-ply layup ([±54°]) resulted in the minimum bottle weight while satisfying the structural design requirements. Fibre winding angles in the range of 54°–55° provided the most efficient load-carrying capability, leading to the minimum required laminate thickness irrespective of the fibre type. The E-glass composite bottle with a 10 mm wall thickness was found to be inadequate for meeting the specified internal pressure requirements. To satisfy the pressure design criteria, the E-glass composite bottle thickness had to be increased to approximately 15 mm through the addition of extra ±54° winding layers. The study demonstrates that carbon fibre reinforced composite pressure vessels offer superior structural efficiency and significant weight savings compared with E-glass and aramid counterparts. The lightweight characteristics of CFRP pressure vessels make them highly suitable for aerospace applications, where weight reduction directly contributes to improved payload capacity, flight endurance, and mission performance.

References

[1] Y. Regassa, J. Gari, and H. G. Lemu, “Composite overwrapped pressure vessel design optimization using numerical method,” J. Compos. Sci., vol. 6, no. 8, p. 229, Aug. 2022. https://doi.org/10.3390/jcs6080229

[2] J. Smith, A. Doe, and L. Brown, “Lightweight composite materials: Innovations and applications in aerospace engineering,” J. Aerosp. Mater., vol. 45, no. 3, pp. 123–134, 2021.

[3] R. Johnson and K. Lee, “Performance evaluation of fiber reinforced polymer composites in high-stress environments,” Int. J. Compos. Struct., vol. 102, no. 4, pp. 567–580, 2022.

[4] S. Alam, G. R. Yandek, R. C. Lee, and J. M. Mabry, “Design and development of a filament wound composite overwrapped pressure vessel,” Compos. Part C: Open Access, vol. 2, p. 100045, Jun. 2020. https://doi.org/10.1016/j.jcomc.2020.100045

[5] A. K. Hamzat, M. S. Murad, I. A. Adediran, E. Asmatulu, and R. Asmatulu, “Fiber-reinforced composites for aerospace, energy, and marine applications: An insight into failure mechanisms under chemical, thermal, oxidative, and mechanical load conditions,” Adv. Compos. Hybrid Mater., vol. 8, no. 1, 2025,Doi:10.1007/s42114-024-01192-y

[6] A. R. Bunsell, Fundamentals of Fibre Reinforced Composite Materials. Bristol, UK: IOP Publishing, 2017.

[7] A. C. Reddy, “Design and finite element analysis of E-glass fiber reinforced epoxy composite air bottle,” Int. J. Eng. Res., vol. 6, no. 8, pp. 157–165, 2015

[8] A. C. Reddy, “Evaluation of curing process for carbon-epoxy composites by mechanical characterization for re-entry vehicle structure,” Int. J. Sci. Res., vol. 4, no. 4, pp. 65–70, Apr. 2015. [Online]. Available: https://www.ijsr.net/archive/v4i4/SUB153699.pdf

[9] A. C. Reddy, “Evaluation of curing process for Kevlar 49-epoxy composites by mechanical characterization designed for brake liners,” Int. J. Sci. Res., vol. 4, no. 4, pp. 471–476, 2015.

[10] M. S. Srinivasa Rao and A. C. Reddy, “Two-dimensional theoretical modeling of anisotropic wear in carbon/epoxy FRP composites: Comparison with experimental data,” Int. J. Trends Eng. Technol., vol. 6, no. 1, pp. 47–57, 2011. [Online]. Available: http://jntuhceh.ac.in/web/tutorials/faculty/793_I-16.pdf

[11] G. Suresh et al., “Experimental analysis of compressive behavior of E-Glass fiber reinforced IPN (vinyl ester/polyurethane) composite pipes,” IOP Conf. Ser.: Mater. Sci. Eng., vol. 988, no. 1, p. 012011, 2020. https://doi.org/10.1088/1757-899X/988/1/012011

[12] G. Suresh and L. S. Jayakumari, “Analyzing the mechanical behavior of E-glass fibre-reinforced interpenetrating polymer network composite pipe,” J. Compos. Mater., vol. 50, no. 22, pp. 3053–3061, 2016. https://doi.org/10.1177/0021998315615408

[13] S. W. Tsai and J. M. Patterson, “Integrated micro-mechanics of composite materials,” in Reference Book for Composite Technology, vol. 2, S. M. Lee, Ed. Lancaster, PA, USA: Technomic Publishing Co., Inc., 1989.

Materials Research Proceedings 73 (2026) 245-248 https://doi.org/10.21741/9781644904459-47

Numerical Analysis of Composite Shells with Curved Fibers via Curvilinear 2|3D Finite Elements

Piero CHIAIA[1,a *], Maria CINEFRA[2,b]

[1]Department of Mechanics, Mathematics and Management, Politecnico di Bari, Via Edoardo Orabona, 4, 70126, Bari, Italy

[a]piero.chiaia@poliba.it, [b]maria.cinefra@poliba.it

Keywords: Curved Shells, Curvilinear Models, Finite Element Models, Composites

Abstract. In this work, a finite element model for the analysis of curved panel with variable thickness and arbitrary curvature made of composite materials is proposed. Higher-order shell models are derived in a general non-orthogonal coordinate system, recovering the Cartesian description of the physical quantities via a consistent transformation law. The Carrera Unified Formulation (CUF) framework is adopted in the derivation of 2|3D shell models, embedding a Lagrange-type theory of structures within the finite element interpolation of the reference mid-surface, enhancing the three-dimensional geometrical modeling capabilities of the present approach. This strategy is here extended for the first time to the analysis of composite, laminated structures by modeling curved path fibers by means of the local covariant reference frame by which the element is defined, validating the model against 3D solutions obtained via commercial software.

Introduction

The increasing demand for lightweight, high-performance structures in aerospace and mechanical engineering has driven the development of advanced composite manufacturing techniques such as Automatic Fiber Placement (AFP), to obtain structures with improved efficiency and reducing material waste. In this context, Variable Angle Tow (VAT) structures allow fiber orientations to vary spatially within the laminate, tailoring stiffness and enhancing mechanical performance [1]. For this reason, the development of advanced numerical tools is essential to accurately model complex geometries, manufacturing-induced fiber paths, and the resulting anisotropic material behavior of advanced composite structures. Conventional beam, plate, and shell finite element formulations, due to simplified geometrical assumptions, are inadequate for structures with variable thickness, curvature, anisotropy, or tailored fiber orientations [2,3]. To address these limitations, novel 2|3D shell finite elements based on Carrera Unified Formulation (CUF) have been proposed in a generic non-orthogonal reference frame [4], and now extended to the analysis curved composite panels with variable thickness and curvilinear fiber paths. Using the Principle of Virtual Displacements and the concept of Fundamental Nuclei (FN), CUF enables to derive any shell theory in a covariant framework, while Node-Dependent Kinematics (NDK) allows local enrichment without significantly increasing computational cost [5]. In the already established model, the curved fiber path will be modeled through adaptive meshes and an isoparametric formulation that ensure consistent interpolation of geometry, displacement fields, and fiber orientations along local covariant frames. The proposed approach integrates composites with spatially varying fiber orientations, allowing arbitrary reinforcement paths, curvature and thickness variations, again within the element definition by considering the element formulation in curvilinear coordinates. The resulting finite element model provides an efficient and robust tool for simulating and optimizing next-generation lightweight composite structures.

Content from this work may be used under the terms of the Creative Commons Attribution 3.0 license. Any further distribution of this work must maintain attribution to the author(s) and the title of the work, journal citation and DOI. Published under license by Materials Research Forum LLC.

Materials Research Proceedings 73 (2026) 245-248 https://doi.org/10.21741/9781644904459-47

Methodology

The proposed modeling strategy is defined within the CUF approach, my merging in a 3D-sense the finite element approximation of the reference mid-surface with the Lagrange-type theory-of-structure approximation along the thickness direction. In this sense, complex shell configurations can be accurately described within a unified three-dimensional framework based on higher-order theories. In addition, the isoparametric approach is exploited to compute all geometrical quantities required, straightforwardly computed from the discretized expression of the geometrical description of the shell [8]. The expression of the displacement field and:

$$\boldsymbol{u}(\alpha^1,\alpha^2,\alpha^3) = F_\tau^i(\alpha^3)N_i(\alpha^1,\alpha^2)\boldsymbol{u}_{\tau i} = L_{\tau i}(\alpha^1,\alpha^2,\alpha^3)\boldsymbol{u}_{\tau i} \quad \tau = 1,..,\mathrm{M}^i, \quad \mathrm{i} = 1,..,\mathrm{N_n} \tag{1}$$

$$\boldsymbol{X}(\alpha^1,\alpha^2,\alpha^3) = L_{\tau i}(\alpha^1,\alpha^2,\alpha^3)\boldsymbol{X}_{\tau i} \tag{2}$$

where $\boldsymbol{M^i}$ is the related to the order of the node-wise structural theory considered, $\boldsymbol{F_\tau^i(z)}$ is the set of the through-the-thickness expansion functions, representing the theory of structure approximation, $\boldsymbol{N_i(x,y)}$ is the set of 2D shape functions of the discrete $\boldsymbol{N_n}$ finite nodes along the reference mid-surface, and finally $\boldsymbol{u_{\tau i}}$ is the vector of generalized displacements. In the present work, the set of 1D Lagrange's polynomials will be adopted in the z-direction [4].

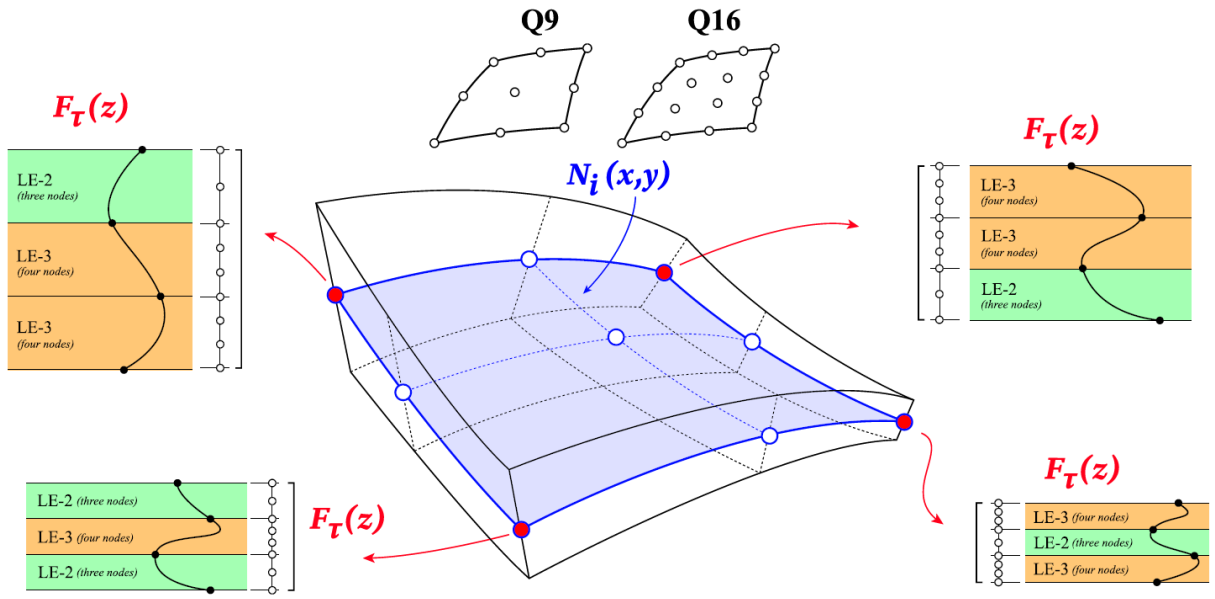

Figure 1: Curvilinear shell model with node-dependent through-the-thickness kinematics, including curvature and thickness variation.

In this way, starting from the Principle of Virtual Displacements, the governing equations are re the FN (Fundamental Nuclei) of the linear stiffness matrix and external force vector can be derived, obtaining the matrix form of the governing equation.

$$\delta\mathcal{L}_{int} = \delta\hat{\boldsymbol{u}}_{sj}^T\left[\int_\Omega \boldsymbol{B}_{curv}^{sj\,T}\boldsymbol{J}_{c2c}\boldsymbol{C}\,(\alpha^1,\alpha^2)\boldsymbol{J}_{c2c}\boldsymbol{B}_{curv}^{\tau i}\,|\boldsymbol{J}|dV\right]\hat{\boldsymbol{u}}_{\tau i} = \delta\hat{\boldsymbol{u}}_{sj}^T\boldsymbol{K}^{\tau sij}\hat{\boldsymbol{u}}_{\tau i} \tag{3}$$

$$\delta\mathcal{L}_{ext} = \delta\hat{\boldsymbol{u}}_{sj}^T\left[\int_\Sigma L_{sj}(\alpha^1,\alpha^2,\alpha^3)\,\boldsymbol{f}\,|\boldsymbol{J}_\Sigma|dV\right] = \delta\hat{\boldsymbol{u}}_{sj}^T\boldsymbol{P}^{sj} \tag{4}$$

where $\boldsymbol{B_{curv}^{\tau i}}$ and $\boldsymbol{B_{curv}^{sj}}$ are the algebraic matrices of derivative operators applied to shape functions in curvilinear coordinates, $\boldsymbol{J_{c2c}}$ is the transformation matrix from covariant and Cartesian reference frame, $|\boldsymbol{J}|$ and $|\boldsymbol{J_\Sigma}|$ are respectively the Jacobian from curvilinear and natural reference frames, $\boldsymbol{\delta\hat{u}_{sj}}$

Materials Research Proceedings 73 (2026) 245-248 https://doi.org/10.21741/9781644904459-47

are the Cartesian components of the virtual displacements and finally $\hat{\boldsymbol{u}}_{\tau i}$ are the Cartesian components of the final, unknown, displacement field. The quantities $\boldsymbol{K}^{\tau sij}$ and $\boldsymbol{P}^{sj}$ are the FN of the stiffness matrix and external force vector, independent of the chosen FE implementation models, allowing for a flexible implementation of any arbitrary shell model. More details about the derivation can be found in [4].

Methodology

The proposed case study deals with the analysis of a curved panel made of carbon fiber reinforced polymer (CFRP), whose elastic constants are given by $\boldsymbol{E_1 = 132.38}$ GPa, $\boldsymbol{E_2 = E_3 = 10.76}$ GPa, $\boldsymbol{\nu_{12} = \nu_{13} = \nu_{23} = 0.22}$, $\boldsymbol{G_{12} = G_{13} = G_{23} = 5.65}$ GPa. The curved panel have dimensions $\boldsymbol{L = 5}$ m, $\boldsymbol{a = 2}$ m, $\boldsymbol{z_0 = -3}$ m, and constant thickness $\boldsymbol{h = 0.05}$ m and it is considered clamped at one end. The mesh adopted is constructed in such a way the local $\boldsymbol{g_1}$ direction provide automatically the fiber direction, following the panel curvature. The graphical representation of geometrical features and boundary conditions is provided in Fig. 2.

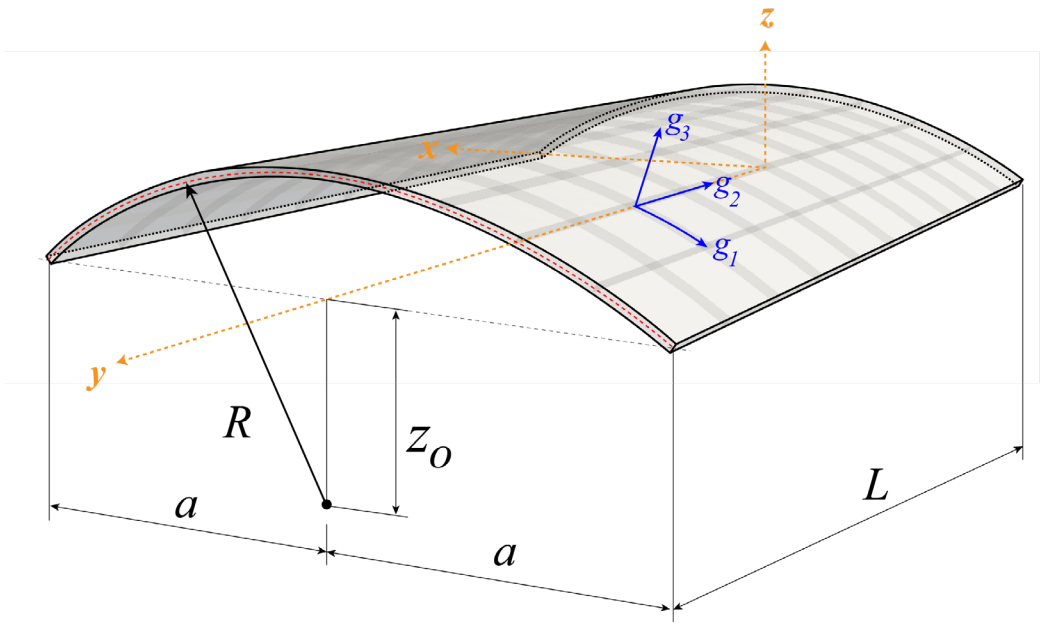

Figure 1 – Curved composite panel: geometrical features and boundary conditions.

A comparison with respect to reference 3D solution computed with ABAQUS, comparing the first five natural frequencies of the panel, comparing also the computational costs in terms of total number of degrees of freedom (DOFs) involved during the simulation. The comparison between 2|3D elements and 3D ABAQUS hexahedral models is provided in Table 1.

Table 1- Curved composite panel: convergence analysis on natural frequencies [Hz]. Comparison between 2|3D CUF curvilinear models and 3D elasticity solutions. In brackets, the percentage difference the proposed solutions.

	Quadratic Q9			**Cubic Q16**			**ABAQUS**
Mode	**10x10**	**15x15**	**20x20**	**10x10**	**15x15**	**20x20**	**C3D20**
1	$9.99^{(1.64\%)}$	$9.88^{(0.50\%)}$	$9.85^{(0.17\%)}$	$9.84^{(0.07\%)}$	$9.83^{(0.05\%)}$	$9.82^{(0.10\%)}$	9.83
2	$11.42^{(3.42\%)}$	$11.14^{(0.87\%)}$	$11.08^{(0.30\%)}$	$11.05^{(0.06\%)}$	$11.04^{(0.04\%)}$	$11.04^{(0.08\%)}$	11.05
3	$26.89^{(0.61\%)}$	$26.78^{(0.19\%)}$	$26.75^{(0.07\%)}$	$26.74^{(0.05\%)}$	$26.72^{(0.03\%)}$	$26.71^{(0.06\%)}$	26.73
4	$30.23^{(5.41\%)}$	$29.07^{(1.35\%)}$	$28.81^{(0.46\%)}$	$28.68^{(0.01\%)}$	$28.66^{(0.07\%)}$	$28.65^{(0.09\%)}$	28.68
5	$33.40^{(5.04\%)}$	$32.28^{(1.50\%)}$	$31.97^{(0.54\%)}$	$31.86^{(0.18\%)}$	$31.78^{(0.08\%)}$	$31.75^{(0.18\%)}$	31.80
DOFs	3969	8649	15129	8649	19044	33489	27408

Conclusions

The analyses confirm the effectiveness of the present modeling strategy when shell panel with curved fibers (oriented along the tangential direction) is effective in computing accurate results also in the case of coarse meshed with reduced computational costs, thanks to the adoption of higher-order models. Additionally, thanks to the incorporated geometrical approximation by means of the 3D-like shape functions, the geometrical description of the model is straightforwardly embedded within the element definition.

Acknowledgment

P. Chiaia and M. Cinefra acknowledge support by the Space It Up! project funded by the Italian Space Agency, ASI, and the Ministry of University and Research, MUR, under contract CUP n. D93C23001190006.

References

[1] Kim B.C. and Potter P. and Weaver P.M. “Continuous tow shearing for manufacturing variable angle tow composites”. Composites Part A: Applied Science and Manufacturing, Vol. 43, pp. 1347-1356, 2012. https://doi.org/10.1016/j.compositesa.2012.02.024.

[2] Reddy J. N. “A Simple Higher-Order Theory for Laminated Composite Plates”. Journal of Applied Mechanics, Vol. 51, n.4. pp. 1347-1356, 2012. https://doi.org/10.1016/j.compositesa.2012.02.024.

[3] Reddy J. N and Liu C.F. “A higher-order shear deformation theory of laminated elastic shells”. International Journal of Engineering Science, Vol 23, n.3, pp. 319-330, 1985. https://doi.org/10.1016/0020-7225(85)90051-5.

[4] Chiaia P., Cinefra M. and Carrera E.. “Curvilinear 2|3D finite elements for the analysis of shells with arbitrary curvature and variable thickness”. Computers & Structures, Vol 317, 107911, 2025. https://doi.org/10.1016/j.compstruc.2025.107911.

[5] Li G., Carrera E., Cinefra M., de Miguel A.G., Pagani A. and Zappino E. “An adaptable refinement approach for shell finite element models based on node-dependent kinematics”. Composite Structures, Vol. 210, pp. 1-19, 2019. https://doi.org/10.1016/j.compstruct.2018.10.111.

Materials Research Proceedings 73 (2026) 249-252 https://doi.org/10.21741/9781644904459-48

Impact of Blades Icing on Wind Turbine Aeroelastic Fragility

Carmelo Rosario Vindigni[1,a] , Giuseppe Mantegna[1,b], Antonio Esposito[1,c], Calogero Orlando[1,d], Andrea Alaimo[1,e], Djamel Rezgui[2,f], Raffaele De Risi[2,g]

[1]Kore University of Enna, Department of Engineering and Architecture, 94100, Enna, Italy

[2]University of Bristol, Queen's Building, University Walk, Bristol, BS8 1TR, UK

[a]carmelorosario.vindigni@unikore.it, [b]giuseppe.mantegna@unikore.it, [c]antonio.esposito@unikore.it, [d]calogero.orlando@unikore.it, [e]andrea.alaimo@unikore.it, [f]djamel.rezgui@bristol.ac.uk, [g]raffaele.derisi@bristol.ac.uk

Keywords: Wind Turbine, Aeroelastic Fragility Analysis, Blades Icing

Abstract. This work presents an aeroelastic fragility-based framework to assess the impact of ice accretion on the risk of blade-to-tower strike in wind turbines operating in cold environments. A reduced-order aeroelastic model is developed, combining an Euler–Bernoulli beam finite element structural formulation with BEMT aerodynamics, including dynamic inflow effects. Ice accretion shape and effects are computed using Ansys Fluent and is then modeled as a modification of aerodynamic coefficients and mass distribution, altering load and deformation patterns. Turbulent wind fields are generated using a Kaimal spectrum with spatial coherence to capture realistic stochastic excitation. Fragility analysis is then performed by comparing blade tip displacement with tower clearance, deriving probabilistic failure curves. Results show that icing increases blade deflections and variability, leading to a higher probability of tower strike under nominal operating conditions. The study allows the definition of optimized activation strategies for de-icing systems, based on the predicted blade-to-tower strike risk under ice accretion over time, thereby reducing unnecessary energy consumption and improving the overall efficiency of wind farm operation.

Introduction

Wind energy development is progressively expanding into cold and high-altitude regions, where low temperatures, high humidity, and in-cloud or precipitation supercooled droplets expose wind turbine blades to severe ice accretion phenomena. While these sites are attractive because of favorable wind resources and higher air density, icing remains one of the main threats to turbine efficiency, reliability, and safety. Ice accumulation modifies blade geometry and surface roughness, degrades aerodynamic performance, increases structural loading, and may trigger abnormal vibrations, premature shutdowns, and ice-throw hazards [1].

The aerodynamic effects of icing are already well known. Ice accretion generally reduces lift, increases drag, and promotes earlier flow separation, with direct consequences for rotor power and thrust [2]. For the NREL 5 MW reference turbine, which is the case study selected in this work, previous numerical studies showed that icing can shift the rated operating condition toward higher wind speeds and produce substantial power losses, while the severity of the degradation depends strongly on temperature, liquid water content, droplet size, and radial blade position [3]. These effects are particularly critical in the outer blade region, where the relative velocity is highest and where a significant portion of the turbine power is generated.

Beyond aerodynamic penalties, icing also affects the structural and aeroelastic response of the rotor. The added ice mass modifies blade inertia and natural frequencies, while the altered pressure distribution changes the dynamic loading and may reduce aeroelastic damping [4].

Although the literature has addressed icing formation, power losses, detection systems, and anti-/de-icing technologies, most studies have focused on performance degradation or component

Content from this work may be used under the terms of the Creative Commons Attribution 3.0 license. Any further distribution of this work must maintain attribution to the author(s) and the title of the work, journal citation and DOI. Published under license by Materials Research Forum LLC.

Materials Research Proceedings 73 (2026) 249-252 https://doi.org/10.21741/9781644904459-48

loads rather than on the probabilistic assessment of blade-to-tower strike risk. This motivates the present work, whose aim is to investigate how ice accretion modifies the aeroelastic behavior of wind turbine blades and how these changes may increase the blade-to-tower strike risk.

Methodology

The methodology integrates a reduced-order aeroelastic model, a stochastic wind description, and a fragility-based risk assessment procedure.

The structural behavior of the blade is modeled using an equivalent beam finite element formulation based on Euler–Bernoulli theory. This approach allows capturing the dominant bending and torsional dynamics of the blade while maintaining computational efficiency, which is essential for large-scale parametric analyses. The formulation includes gravitational effects and centrifugal stiffening due to rotor rotation, enabling a realistic representation of the blade response under operational conditions. The model is reduced through modal projection, retaining the most significant vibration modes based on mass participation criteria to obtain a reduced-order system suitable for time-domain simulations that reads as

$$\mathbf{m_j}\ddot{\overline{\Delta}} + \mathbf{c_j}\dot{\overline{\Delta}} + \mathbf{k_j}\overline{\Delta} = \mathbf{f_j} \quad (1)$$

being $\overline{\Delta}$ the modal displacements vector, $\mathbf{m_j}$ the modal mass, $\mathbf{c_j}$ the modal damping, $\mathbf{k_j}$ the modal stiffness, and $\mathbf{f_j}$ the modal force vector. The finite element matrices definition can be found in [5].

The aerodynamic loading is computed using Blade Element Momentum Theory (BEMT), which provides distributed aerodynamic forces along the blade span by combining momentum theory with sectional airfoil characteristics. The formulation accounts for tip-loss corrections and induced velocity effects, and it is coupled with a dynamic inflow model to capture unsteady aerodynamic phenomena. The aeroelastic coupling is achieved by updating the aerodynamic loads based on the instantaneous deformed configuration of the blade, thus accounting for the interaction between structural deformation and aerodynamic forces [6]. A stochastic wind model is adopted to represent realistic operating conditions. The turbulent wind field is generated according to IEC 61400 guidelines using a Kaimal spectrum-based formulation that describes the energy distribution across frequencies and incorporates turbulence intensity and spatial coherence across the rotor disk.

The aeroelastic response is evaluated in the time domain by solving the reduced system of equations under turbulent wind excitation, using turbulence intensity recorded by the offshore measuring platform FIN01 [7]. A fragility analysis framework is then employed to obtain the probabilistic curves of blade-to-tower strike. In this context, the blade tip displacement is treated as the demand parameter D, while the blade–tower clearance represents the structural capacity C.

Numerical CFD analyses of ice accretion were carried out following a two-step procedure. All the analyses were conducted using the commercial software ANSYS FENSAP-ICE, a fully three-dimensional finite-element CFD suite specifically developed for icing simulations. At first, the aerodynamic field around the clean airfoil was computed to establish a reference baseline. The reference section lies at 59 m from the turbine hub. A multi-shot glaze ice accretion strategy was employed to simulate progressive ice growth over multiple discrete time intervals, such that the geometry is sequentially updated at each shot to account for the evolving ice shape. This approach allows for a more physically accurate representation of the ice accretion process compared to single-shot methods, as it captures the time-dependent redistribution of the impingement zone and the associated thermodynamic changes. Specifically, two-hour accretion shots were simulated up to a total ice accretion time of 24 hours. Following each accretion shot, the updated iced profiles were re-meshed using a structured multi-block approach and subsequently imported into ANSYS Fluent for aerodynamic performance evaluation. Reynolds-Averaged Navier–Stokes simulations were performed over a range of angles of attack in order to systematically assess the aerodynamic

Materials Research Proceedings 73 (2026) 249-252 https://doi.org/10.21741/9781644904459-48

performance degradation induced by surface roughness. In particular, the analysis quantified the changes of the aerodynamic coefficients. The $k-\omega$ SST turbulence model was adopted for the flow-field calculations, and the rough-wall boundary condition was defined by means of a surface roughness distribution interpolated from the roughness files generated by FENSAP-ICE. The obtained ice shapes were validated against those reported in [3] where the same 24-hour ice accretion scenario was studied.

Results

In the considered atmospheric conditions [3], a 4 hours ice accretion moves the operating point of the wind turbine, corresponding to 12.1 rpm rotational speed, to a higher incoming wind velocity, increasing from 11.4 m/s to 12.8 m/s. This shift results in a corresponding increase in the overall aerodynamic thrust acting on the rotor disk. Figure 3 shows the aeroelastic response of the blade in terms of tip deflection for a turbulence intensity of 15%, comparing clean and iced operating conditions. It can be observed that the maximum deflection increases from 5.56 m to 6.01 m, indicating a higher oscillation amplitude due to the combined effects of modified aerodynamic loads and changes in the inertial properties of the iced blade sections. These results highlight the need of assessing the impact of ice accretion on blade-to-tower strike fragility, as icing conditions can significantly increase the operative loads, reduce aerodynamic damping, and introduce imbalance on the blade.

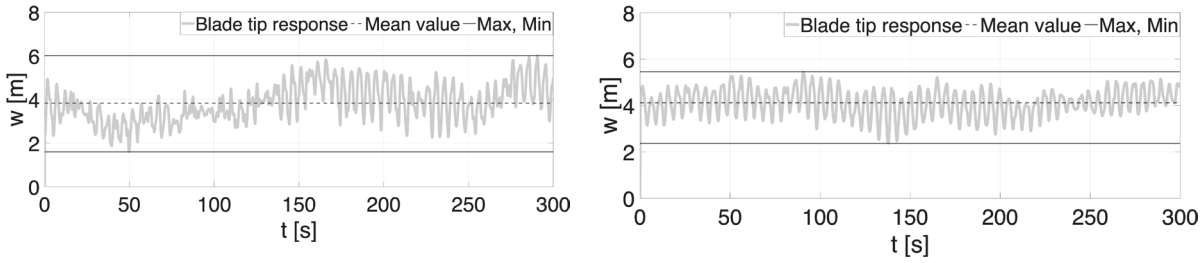

a) Iced (4 hours accretion) - $V_{mean} = 12.8\ m/s$

b) Clean - $V_{mean} = 11.4\ m/s$

Figure 3 – Blade tip deflection at the rated operating points

By analyzing the shift in turbine operating conditions associated with different ice accretion times and performing numerical aeroelastic simulations to evaluate the corresponding blade tip displacements in turbulent wind, the fragility curve in Figure 4 is derived. Although ice accretion leads to a consistent increase in blade tip excursions relative to the available clearance, the associated rise in blade-to-tower strike risk remains limited within the time interval considered. The obtained fragility curve suggests that de-icing systems may be activated at later stages of ice accretion without significantly compromising wind farm operational safety, thereby reducing unnecessary energy consumption.

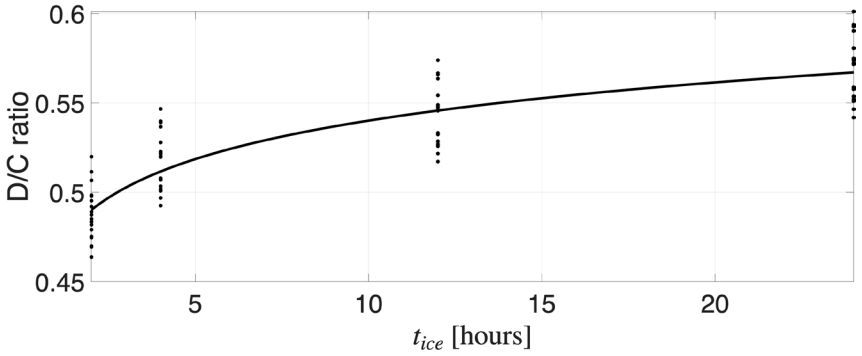

Figure 4 – Fragility curve for icing

References

[1] Z. Zhang, H. Zhang, X. Zhang, Q. Hu, and X. Jiang, "A Review of Wind Turbine Icing and Anti/De-Icing Technologies," *Energies (Basel).*, vol. 17, no. 12, p. 2805, Jun. 2024. https://doi.org/10.3390/en17122805

[2] B. Öztürk and E. Koçak, "An Investigation of Atmospheric Icing Effects on Wind Turbine Blade Aerodynamics and Power Output: A Case Study of the NREL 5 MW Turbine," *Applied Sciences*, vol. 16, no. 6, p. 2991, Mar. 2026. https://doi.org/10.3390/app16062991

[3] M. Etemaddar, M. O. L. Hansen, and T. Moan, "Wind turbine aerodynamic response under atmospheric icing conditions," *Wind Energy*, vol. 17, no. 2, pp. 241–265, Feb. 2014. https://doi.org/10.1002/we.1573

[4] S. Gantasala, N. Tabatabaei, M. Cervantes, and J.-O. Aidanpää, "Numerical Investigation of the Aeroelastic Behavior of a Wind Turbine with Iced Blades," *Energies (Basel).*, vol. 12, no. 12, p. 2422, Jun. 2019. https://doi.org/10.3390/en12122422

[5] C. R. Vindigni, G. Mantegna, C. Orlando, and A. Alaimo, "Simple adaptive wing-aileron flutter suppression system," *J. Sound Vib.*, vol. 570, 2024. https://doi.org/10.1016/j.jsv.2023.118151

[6] M. Hansen, *Aerodynamics of wind turbines*. Taylor and Francis, 2015.

[7] M. Türk and S. Emeis, "The dependence of offshore turbulence intensity on wind speed," *Journal of Wind Engineering and Industrial Aerodynamics*, vol. 98, no. 8–9, pp. 466–471, Aug. 2010. https://doi.org/10.1016/j.jweia.2010.02.005

Materials Research Proceedings 73 (2026) 253-261 https://doi.org/10.21741/9781644904459-49

Effect of Cumulative Impact Energy on Damage Accumulation in Glass–Carbon Hybrid Composite Laminates

Shilpa R.S.[1,a], Jyothilakshmi R.[2,b], Mohandas K.N.[2,c]

[1]Research Scholar, Department of Mechanical Engineering, M. S. Ramaiah Institute of Technology, Bangalore-54, India

[2]Faculty, Department of Mechanical Engineering, M. S. Ramaiah Institute of Technology, Bangalore-54, India

[a]shilpars1519@gmail.com, [b]jyothirswamy@gmail.com, [c]mohandaskn@msrit.edu

Keywords: Cumulative Impact, Absorbed Energy, Low Velocity Impacts, Delamination, Modelling Analysis

Abstract. Glass–carbon hybrid composite laminates offer an excellent balance of stiffness, strength, and impact resistance, making them suitable for structural and aerospace applications. This study investigates the influence of impact energy distribution on damage accumulation in 12-layer glass–carbon hybrid laminates with different layering sequences like [G_2 C_4 C_4 G_2], [C_2 G_4 G_4 C_2], [G_4 C_2 C_2 G_4], [C_4 G_2 G_2 C_4] subjected to low-velocity impact loading. Cumulative impact loading includes 8 J, 8 J + 16 J, 12 J + 12 J, and 16 J + 8 J, along with a single impact of 24 J. The analysing parameters such as force–time, displacement–time, and absorbed energy–time responses were evaluated to understand deformation and damage progression. Results reveal that both the sequence and magnitude of impact energies significantly influence damage development and energy absorption. The single 24 J impact caused severe delamination, while cumulative impacts exhibited varied damage patterns governed by the order of energy application. Additionally, an Artificial Neural Network (ANN) model was developed to predict impact response parameters, demonstrating high accuracy in capturing complex damage trends and enhancing the reliability of impact behaviour assessment. Overall, the hybrid laminates demonstrated improved damage tolerance and progressive failure behaviour u`nder sequential impact conditions.

Introduction

The growing demand for lightweight and high-strength materials has stimulated extensive research into advanced composite systems. Composite materials consist of multiple constituent phases with distinct physical and chemical attributes that work together to produce superior overall performance. This synergistic combination enables the development of materials possessing characteristics beyond those of the individual constituents. As a result, composites have become increasingly important in engineering applications such as aerospace structures, automotive components, marine vessels, construction materials, and sports equipment due to their favourable mechanical properties and durability [1]

Cumulative impact events can progressively degrade the mechanical properties of composite laminates through the accumulation of internal damage. With each impact, existing defects may enlarge, increasing the extent of matrix cracking, delamination, and fibre failure. Impact loading is generally categorized as either low-velocity or high-velocity, depending on the impact speed[2]. In the case of FRP composites, studies on repeated low-velocity impacts have mainly examined damage propagation mechanisms and changes in structural response. Factors such as impact energy, impactor characteristics, laminate thickness, material constituents, and stacking sequence play a significant role in determining impact performance[3]. Research has indicated that damage caused by repeated impacts may differ considerably from that generated by a single impact of

Content from this work may be used under the terms of the Creative Commons Attribution 3.0 license. Any further distribution of this work must maintain attribution to the author(s) and the title of the work, journal citation and DOI. Published under license by Materials Research Forum LLC.

Materials Research Proceedings 73 (2026) 253-261 https://doi.org/10.21741/9781644904459-49

equivalent total energy. When impacts occur repeatedly at the same location, damage tends to accumulate rapidly due to stress concentration and the progressive weakening of the affected region. Consequently, several predictive models have been proposed to characterize and forecast damage development under repeated impact conditions.[4]

Although significant progress has been made in understanding impact behaviour in composite materials, the failure response of FRP laminates subjected to repeated low-velocity impacts has not yet been fully established owing to the combined effects of several governing parameters. Accordingly, this study focuses on assessing the cumulative damage development in GFRP laminates under different impact conditions.

Experimental Procedure

MATERIALS

In the present investigation, bidirectional woven glass–carbon hybrid composite laminates with fibres oriented along the 0°/90° directions were selected and subjected to low-velocity impact loading. By combining glass and carbon fibres, the hybrid laminates achieve a balanced combination of stiffness, damage tolerance, and economic viability.

Earlier studies have shown that optimized glass–carbon hybrid laminates absorb more impact energy and sustain less damage than monolithic carbon composites [5]. In the present work, laminates were fabricated by sequentially stacking woven fibre plies and impregnating each layer with LY556 epoxy resin and HY951 hardener mixed in a 10:1 ratio. The characteristics of the constituent fibres are presented in Table 1.

Table 1: Material Characteristics and specifications

Characteristic	Carbon fibre	Glass fibres
Areal Weight (g/m^2)	200	200
Standard Width (mm)	1000 ± 10 mm	1000 ± 10 mm
Dry Fabric Thickness (mm)	0.2±0.05 mm	0.2±0.05 mm
Density (g/cm$^{3)}$	1.8 min.	2.63 min.
Filament Diameter (µm)	7 nominal	13 nominal
Tensile Strength (MPa)	4000 min.	3750 min.
Tensile Modulus (GPa)	240 min.	70 min.
Elongation (%)	1.8 max.	4.8 max.
Sizing	Epoxy Compatible	Epoxy Compatible

FABRICATION PROCESS

A vacuum bagging technique was adopted for the fabrication of the composite laminates Both glass fibre and carbon fibre reinforced epoxy laminates were fabricated under controlled processing conditions to obtain consistent quality and minimize manufacturing defects

The laminates were manufactured with varying ply counts in accordance with ASTM D7136 specifications for low-velocity impact testing. Accordingly, bidirectional glass and carbon fibre laminates comprising 12 layers were produced. The corresponding stacking sequences and ply sequence thickness, mass and the percentage composition of the fabricated laminates are presented in Figure 1 and Table 2.

Materials Research Proceedings 73 (2026) 253-261 https://doi.org/10.21741/9781644904459-49

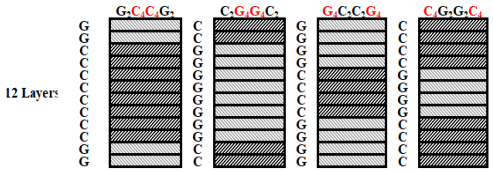

Fig 1: Stacking Sequence with four conditions G – glass fibres and C- caron fibres

Table 2: Layering configurations of hybrid glass and carbon composite laminates

Configuration	ply Count	sequence	Thickness (mm)	Mass (g)	Carbon (%)	glass (%)
A12	12	$G_2C_4C_4G_2$	2.42	9	7	33
B12	12	$C_2G_4G_4C_2$	2.42	9	33	67
C12	12	$G_4C_2C_2G_4$	2.42	0.8	33	67
D12	12	$C_4G_2G_2C_4$	2.42	60.8	67	33

DROP WEIGHT IMPACT TESTING

Table 3: Specifications of drop weight testing machine

Drop Weight Impact Testing Machine	
Description	Parameters
Drop Height	0.2 m–1.5 m
Weight of Tup	4 kg–30 kg
Impactor Type	Hemispherical (ϕ12.7
Velocity	1.98–5.42 m/sec
Impact Energy	8 J–441 J
Machine Weight	650 kg
Test Area	ASTM D7136
Compressed Air	4 BAR
Anti-rebound	YES
DAC System	NI 6210
oftware System	Impact Soft



Fig 2: Drop Weight Testing machine

Fig 2 shows the Instrumented Drop Weight Testing Machine, manufactured by SS Instruments, Bangalore, was utilized for impact testing, as illustrated in the machine's specifications are outlined

Materials Research Proceedings 73 (2026) 253-261 https://doi.org/10.21741/9781644904459-49

in Table 3. The testing apparatus included a 12.7 mm diameter hemispherical striker, attached to a tup weighing 4 kg and the height of fall of the impactor is been set as 198mm as per the setting of the drop weight testing machine.[6]

This study investigates the influence of impact energy distribution on damage accumulation in 12-layer glass–carbon hybrid laminates with different layering sequences like [G_2 C_4 C_4 G_2], [C_2 G_4 G_4 C_2], [G_4 C_2 C_2 G_4], [C_4 G_2 G_2 C_4] subjected to low-velocity impact loading. Cumulative impact loading includes 8 J, 8 J + 16 J, 12 J + 12 J, and 16 J + 8 J, along with a single impact of 24 J.

Results and Discussions

ANALYSIS OF PEAK FORCE

Table 4: Values of Peak Force

Laminate Configuration	Impact Energies						
	8 J	8 J + 16 J	12 J	12 J + 12 J	16 J	16 J + 8 J	24 J
$C_2G_4G_4C_2$	2.48	1.115	2.59	1.04	2.7	1.035	2.76
$G_2C_4C_4G_2$	2.88	2.645	3.69	2.44	3.5	2.07	3.59
$C_4G_2G_2C_4$	3.09	2.545	3.12	2.54	3.1	2.205	3.64
$G_4C_2C_2G_4$	2.3	1.47	2.74	1.14	2.3	1.035	2.79

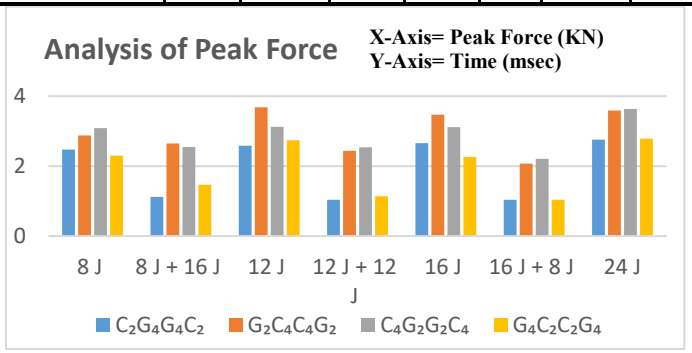

Fig 3: Distribution of peak force of laminate configurations

Table 4 and fig 3 presents the peak force values obtained for the four glass–carbon hybrid laminates subjected to single and cumulative impact loading.

Under single-impact conditions, the laminates exhibited higher peak forces than under cumulative impacts, indicating that the initial impact caused internal damage that reduced the residual stiffness of the laminates during subsequent impacts. For example, the [C_2G_4 G_4 C_2] laminate recorded a peak force of 2.755 kN under a single 24 J impact, whereas after sequential loading (8 J + 16 J) the peak force dropped to 1.115 kN, representing a reduction of approximately 60%. Similarly, the [G_4C_2 C_2 G_4] laminate showed a decrease from 2.785 kN under 24 J to 1.035–1.470 kN under cumulative loading conditions, indicating substantial stiffness degradation due to progressive matrix cracking and delamination.[7]

Among the laminates investigated, [G_2C_4 C_4 G_2] and [C_4G_2 G_2 C_4] exhibited higher peak force values, reaching 3.685 kN and 3.635 kN, respectively, suggesting that increasing the carbon fibre content enhances laminate stiffness and load-bearing capability. These laminates also retained relatively higher peak forces after repeated impacts, indicating improved resistance to damage propagation. In contrast, the glass-dominant laminates, [C_2G_4 G_4 C_2] and [G_4C_2 C_2 G_4] experienced

Materials Research Proceedings 73 (2026) 253-261 https://doi.org/10.21741/9781644904459-49

larger reductions in peak force following sequential impacts, implying greater energy dissipation through matrix cracking, fibre fracture, and delamination.

The sequence of impact energies also affected the response. For all laminates, the peak forces recorded during 8 J + 16 J, 12 J + 12 J, and 16 J + 8 J loading were lower than those observed under single impacts. This behaviour confirms that damage accumulation depends not only on the total impact energy but also on the order in which the energy is applied. The lower peak forces observed after the first impact indicate progressive degradation of structural integrity and the development of damage mechanisms before the subsequent impact event.[8] [9]

ANALYSIS OF MAXIMUM DISPLACEMENT

Table 4: Values of Maximum Displacement configurations

Laminate Configuration	Impact Energies						
	8 J	8 J + 16 J	12 J	12 J + 12 J	16 J	16 J + 8 J	24J
$C_2G_4G_4C_2$	5.89	7.183	9.09	7.17	8.7	8.701	9.26
$G_2C_4C_4G_2$	5.08	1.394	6.4	10	8.2	6.894	12.6
$C_4G_2G_2C_4$	4.9	9.829	6.16	8.39	8	6.888	12.9
$G_4C_2C_2G_4$	6.63	8.24	9.08	7.19	15	14.81	10.7

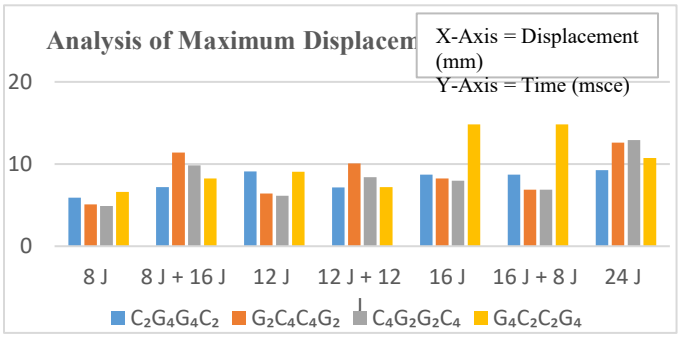

Fig 4: : Distribution of Max Displacement of laminate

Table 4 and Fig 4 shows that the maximum displacement results demonstrate that both stacking sequence and impact energy distribution significantly affect the deformation characteristics of the glass–carbon hybrid laminates. The displacement generally increased under cumulative impact conditions, indicating progressive stiffness degradation and damage accumulation. The [C_4G_2 G_2 C_4] laminate exhibited the highest displacement under a single 24 J impact (12.904 mm), whereas [$C_2G_4G_4C_2$] showed the lowest value (9.259 mm), indicating superior resistance to deformation. The differences observed between the 8 J + 16 J, 12 J + 12 J, and 16 J + 8 J loading sequences confirm that the order of energy application influences damage evolution. The significant increase in displacement after the second impact suggests the formation of matrix cracks, delamination, and reduced residual stiffness, thereby demonstrating progressive failure behaviour and confirming that cumulative impacts produce varying damage patterns governed by the impact sequence.[10]

Materials Research Proceedings 73 (2026) 253-261 https://doi.org/10.21741/9781644904459-49

ANALYSIS OF ABSORBED ENERGY

Table 5: Values of Absorbed Energy

Laminate Configuration	Impact Energies						
	8 J	8 J + 16 J	12 J	12 J + 12 J	16 J	16 J + 8 J	24 J
$C_2G_4G_4C_2$	7.76	3.683	11.7	3.61	12	11.71	13.2
$G_2C_4C_4G_2$	7.76	15.511	11.7	11.7	16	7.763	23.3
$C_4G_2G_2C_4$	7.76	15.569	11.7	11.7	16	7.762	23.2
$G_4C_2C_2G_4$	7.76	5.063	11.7	3.87	14	11.71	14.2

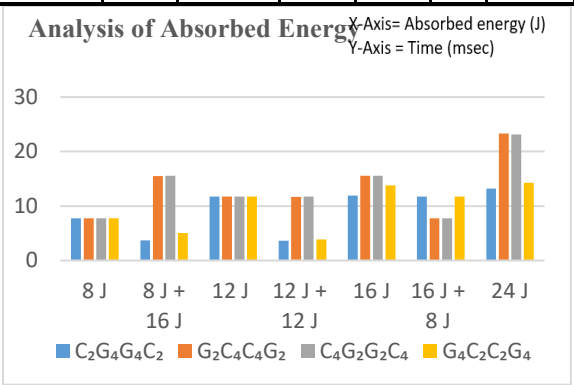

Fig 5:Distribution of Absorbed Energy of laminate configurations

The absorbed energy results reveal that both laminate architecture and impact energy distribution significantly influence the damage accumulation behaviour of glass–carbon hybrid laminates. Under single-impact conditions, the absorbed energy increased with increasing impact energy, indicating greater dissipation of impact energy through matrix cracking, delamination, and fibre fracture.[11]

Among the laminates investigated, $G_2C_4C_4G_2$ and $C_4G_2G_2C_4$ exhibited the highest energy absorption under a single 24 J impact, with values of 23.300 J and 23.165 J, respectively. These values indicate extensive internal damage and enhanced energy dissipation mechanisms due to the higher carbon content. In contrast, $C_2G_4G_4C_2$ absorbed only 13.225 J, suggesting a larger proportion of elastic rebound energy and better retention of structural integrity.

The influence of impact sequence is clearly observed in the cumulative impact conditions. For example, $G_2C_4C_4G_2$ absorbed 15.511 J during the 8 J + 16 J sequence, whereas only 7.763 J was absorbed during the 16 J + 8 J sequence, despite the same total impact energy. Similarly, $C_4G_2G_2C_4$ showed absorbed energies of 15.569 J and 7.762 J for the 8 J + 16 J and 16 J + 8 J sequences, respectively. This demonstrates that the order of energy application governs the extent of damage accumulation and residual energy dissipation capability.

The $C_2G_4G_4C_2$ and $G_4C_2C_2G_4$ laminates showed comparatively lower absorbed energies under cumulative loading, particularly during the 8 J + 16 J and 12 J + 12 J sequences. The reduced absorbed energy after the second impact indicates a decrease in residual stiffness caused by matrix cracking and delamination initiated during the first impact. Consequently, subsequent impacts resulted in lower energy dissipation and more pronounced damage progression.[12] Refer table 5 and fig 5.

Materials Research Proceedings 73 (2026) 253-261 https://doi.org/10.21741/9781644904459-49

These findings are consistent with the abstract and highlight the importance of stacking sequence and impact energy distribution in governing the damage accumulation behaviour of hybrid composite laminates.[13]

ARTIFICIAL NEURAL NETWORK MODELLING

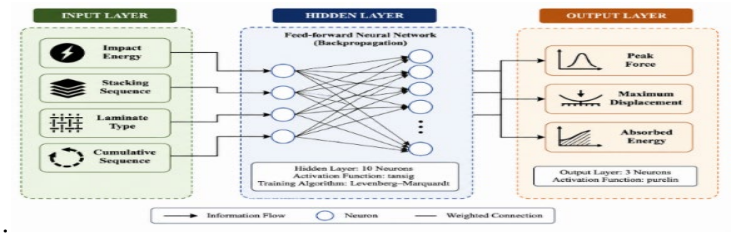

Fig : Schematic representation of ANN Model.

An Artificial Neural Network (ANN) model was developed to predict the impact response of glass–carbon hybrid composite laminates subjected to cumulative low-velocity impact loading. The ANN approach was employed owing to its capability to capture complex nonlinear relationships between input variables and output responses. The model was designed to establish correlations between laminate architecture, impact energy sequence, and the resulting mechanical response parameters, thereby providing an efficient predictive tool for assessing impact behaviour without extensive experimental testing.[14]

The input parameters considered for the network included laminate configuration, impact energy sequence, and cumulative impact energy, whereas the output parameters comprised peak force, maximum displacement, and absorbed energy. The complete dataset was randomly divided into training, validation, and testing subsets in the ratio of 70%, 15%, and 15%, respectively.[15]

A feed-forward backpropagation neural network consisting of an input layer, a hidden layer, and an output layer was adopted. The hidden layer contained an optimum number of neurons determined through trial-and-error analysis to minimize prediction errors and avoid overfitting. The tangent sigmoid transfer function (tansig) was employed in the hidden layer, while a linear transfer function (purelin) was used in the output layer. The network weights and biases were updated using the Levenberg–Marquardt backpropagation algorithm due to its rapid convergence and high prediction accuracy for nonlinear engineering problems.[16]

A high correlation coefficient and low prediction error indicated that the developed model successfully captured the nonlinear interaction between impact energy distribution, stacking sequence, and damage accumulation behaviour. The results demonstrated that ANN can effectively predict the impact response of glass–carbon hybrid laminates under cumulative loading conditions and may serve as a reliable tool for optimizing laminate configurations and reducing experimental efforts.[17]

Conclusions

The present study investigated the effect of cumulative impact energy on damage accumulation in glass–carbon hybrid composite laminates subjected to low-velocity impact loading. Four hybrid stacking sequences, namely [G_2 C $_4$ C $_4$ G_2], [C_2 G_4 G_4 C_2], [G_4 C_2 C_2 G_4], [C_4 G_2 G_2 C_4], were evaluated under different impact energy distributions (8 J + 16 J, 12 J + 12 J, 16 J + 8 J) and compared with a single 24 J impact. Based on the experimental observations and ANN predictions, the following conclusions can be drawn:

The impact response of glass–carbon hybrid laminates was strongly influenced by both stacking sequence and impact energy distribution. Although the total cumulative energy remained constant, different energy sequences produced distinct damage patterns and mechanical responses, demonstrating that the order of impact application governs the evolution of damage.

Peak force values under cumulative impacts were lower than those observed under single impacts, indicating progressive degradation of laminate stiffness due to matrix cracking, interlaminar delamination, and fibre fracture initiated during the first impact. Carbon-rich laminates, exhibited higher peak forces, indicating superior load-bearing capability and higher structural stiffness.

Maximum displacement increased significantly under repeated impacts, confirming progressive damage accumulation and reduction in residual stiffness.

The absorbed energy results revealed that carbon-rich laminates exhibited superior energy dissipation capability. The variation in absorbed energy between the 8 J + 16 J and 16 J + 8 J sequences further confirmed that damage accumulation is highly dependent on the order of energy application.

An Artificial Neural Network (ANN) model based on a feed-forward backpropagation architecture was successfully developed to predict peak force, maximum displacement, and absorbed energy under cumulative impact loading conditions. The combined experimental and ANN analyses confirmed that cumulative impact loading induces progressive damage accumulation, and the extent of degradation depends not only on the total impact energy but also on the sequence of energy application. The proposed methodology can therefore be utilized for the design and optimization of hybrid composite structures used in aerospace, automotive, and protective engineering applications.

References

[1] M. O. W. Richardson and M. J. Wisheart, “Review of low-velocity impact properties of composite materials,” *Compos. Part A Appl. Sci. Manuf.*, vol. 27, no. 12, pp. 1123–1131, Jan. 1996. https://doi.org/10.1016/1359-835X(96)00074-7.

[2] J. Zhou, P. Wen, and S. Wang, “Numerical investigation on the repeated low-velocity impact behavior of composite laminates,” *Compos. B Eng.*, vol. 185, p. 107771, Mar. 2020. https://doi.org/10.1016/J.COMPOSITESB.2020.107771.

[3] M. Rezasefat, A. A. X. da Silva, S. C. Amico, M. Giglio, and A. Manes, “Repeated impact behaviour of inter-ply hybrid aramid/S2-glass epoxy laminates,” *Thin-Walled Structures*, vol. 186, May 2023. https://doi.org/10.1016/j.tws.2023.110680.

[4] R. Basavanna, S. Raja, and K. , “Low Velocity Impact Response on GFRP and GF-SMP Panels in Structural and High Frequency Bands,” *Advances in Aerospace Science and Technology*, vol. 05, no. 02, pp. 58–70, 2020. https://doi.org/10.4236/aast.2020.52004.

[5] J. Summerscales and D. Short, “Carbon fibre and glass fibre hybrid reinforced plastics,” *Composites*, vol. 9, no. 3, pp. 157–166, Jul. 1978. https://doi.org/10.1016/0010-4361(78)90341-5.

[6] L. Sunith Babu *et al.*, “Effect of laminate thickness on low-velocity impact of GFRP/epoxy composites,” *Mater. Today Proc.*, Aug. 2023. https://doi.org/10.1016/j.matpr.2023.08.229.

[7] S. Mutsuddy, D. Cai, M. H. Hossain, and X. Wang, “Repeated Low-Velocity Impact Properties of Hybrid Woven Composite Laminates,” *Materials*, vol. 18, no. 20, Oct. 2025. https://doi.org/10.3390/ma18204774.

[8] K. G. Pranesh *et al.*, “Influence of Nanosilica on Mechanical Performance in Woven Carbon/Kevlar/Epoxy Hybrid Composites,” *Journal of Engineering (United Kingdom)*, vol. 2024, no. 1, 2024. https://doi.org/10.1155/je/2646317.

[9] C. Dong, “Carbon and glass fibre-reinforced hybrid composites in flexure,” *Hybrid Advances*, vol. 10, p. 100471, Sep. 2025. https://doi.org/10.1016/j.hybadv.2025.100471.

[10] C. Zhang, Y. Rao, Z. Li, and W. Li, "Low-velocity impact behavior of interlayer/intralayer hybrid composites based on carbon and glass non-crimp fabric," *Materials*, vol. 11, no. 12, Dec. 2018. https://doi.org/10.3390/ma11122472.

[11] N. Rajesh Mathivanan, S. Babu, and B. S. Sridhar, "Cumulative Damage Analysis of GFRP Laminates with Different 1 Impact Scenarios."

[12] Y. Fang, D. Sheng, Z. Lin, and P. Fei, "Study of Low-Velocity Impact Behavior of Hybrid Fiber-Reinforced Metal Laminates," *Polymers (Basel).*, vol. 16, no. 2, Jan. 2024. https://doi.org/10.3390/polym16020173.

[13] D. Chen, Q. Luo, M. Meng, and G. Sun, "Low velocity impact behavior of interlayer hybrid composite laminates with carbon/glass/basalt fibres," *Compos. B Eng.*, vol. 176, Nov. 2019. https://doi.org/10.1016/j.compositesb.2019.107191.

[14] M. H. Malik and A. F. M. Arif, "ANN prediction model for composite plates against low velocity impact loads using finite element analysis," *Compos. Struct.*, vol. 101, pp. 290–300, Jul. 2013. https://doi.org/10.1016/J.COMPSTRUCT.2013.02.020.

[15] N. R. Mathivanan and C. Mouli, "Modeling the low-velocity impact characteristics of woven glass epoxy composite laminates using artificial neural networks," *Journal of the Mechanical Behaviour of Materials*, vol. 21, no. 3–4, pp. 69–80, Dec. 2012. https://doi.org/10.1515/jmbm-2011-0026.

[16] V. S. Hiremath, S. Patil, D. M. Reddy, R. R. Mutra, B. Patil, and N. Poornima, "An ANN approach to predicting the impact parameters of GFRP composites under low-velocity impact," *International Journal on Interactive Design and Manufacturing*, vol. 18, no. 2, pp. 709–720, Mar. 2024. https://doi.org/10.1007/s12008-023-01668-z.

[17] B. Yang, K. Fu, J. Lee, and Y. Li, "Artificial Neural Network (ANN)-Based Residual Strength Prediction of Carbon Fibre Reinforced Composites (CFRCs) After Impact," *Applied Composite Materials*, vol. 28, no. 3, pp. 809–833, Jun. 2021. https://doi.org/10.1007/s10443-021-09891-1.

Materials Research Proceedings 73 (2026) 262-265 https://doi.org/10.21741/9781644904459-50

Hierarchical Anisotropic-Order Finite Elements for the Analysis of Incompressible Materials

Piero CHIAIA[1,a *], Alexander HUMER[2,b] and Alfonso PAGANI[3,c]

[1]Department of Mechanics, Mathematics and Management, Politecnico di Bari, Via Edoardo Orabona, 4, 70126, Bari, Italy

[2]Institute of Technical Mechanics, Johannes Kepler University Linz, Altenberger Str. 69, Linz, 4040, Austria

[3]MUL2 Lab, Department of Mechanical and Aerospace Engineering, Politecnico di Torino, Corso Duca degli Abruzzi 24, 10129, Torino, Italy

[a]piero.chiaia@poliba.it, [b]alexander.humer@jku.at, [c]alfonso.pagani@polito.it

Keywords: Incompressible Materials, Hyperelasticity, Higher Order, Mixed Formulation, Finite Elements

Abstract. In this paper, a new anisotropic-order element (AOE) formulation for the analysis of incompressible and nearly incompressible material behavior is proposed. Novel element technologies are proposed to formulate mixed displacement–pressure finite elements, with distinct polynomial orders for variables in different directions. This element technology is established within the context of higher-order models developed under the Carrera Unified Formulation (CUF) framework, the mathematical framework exploited for AOE. The consistency and the robustness of this new approach are demonstrated through a representative example of a cantilever beam in the pure incompressible condition, analyzing the influence of the polynomial order of approximation on the global structural response.

Introduction

Standard displacement-based finite element formulations have been demonstrated to be inefficient for the finite-strain analysis of pure incompressible or nearly incompressible materials, as they suffer from volumetric locking, leading to an artificially stiff response, particularly when low-order elements are used [1]. To overcome these limitations, mixed/hybrid displacement–pressure formulations have been proposed, as they mitigate locking by introducing an independent pressure field variable, still introducing additional complexities related to stability requirements, identified by the inf-sup (Ladyzhenskaya–Babuška–Brezzi) condition [2]. This work proposes a novel anisotropic-order element (AOE) formulation, where different variables can adopt different polynomial orders in different directions, allowing for new hybrid element technologies for incompressible materials, including unconventional displacement–pressure combinations that fall outside the already established LBB-compliant pairs, like the Taylor-Hood element [3], still satisfying the LBB condition. The approach is investigated through nonlinear analyses of soft materials, focusing on the stability, accuracy, and potential instabilities of these new element technologies. This formulation is implemented within the Carrera Unified Formulation (CUF), which provides a mathematical basis for defining anisotropic-order interpolations and extending it to hybrid formulations [4]. The influence of AOE and non-standard interpolation combinations on the static response of an incompressible cantilever beam is presented in the following, comparing results obtained with higher-order, hybrid 1D CUF models with those obtained within the open-source finite element framework Netgen/NGSolve [5].

Content from this work may be used under the terms of the Creative Commons Attribution 3.0 license. Any further distribution of this work must maintain attribution to the author(s) and the title of the work, journal citation and DOI. Published under license by Materials Research Forum LLC.

Materials Research Proceedings 73 (2026) 262-265 https://doi.org/10.21741/9781644904459-50

Methodology

In the context of hyperelasticity, the governing equations are written by means of variational principles in a Total Lagrangian setting, where the incompressibility condition is enforced through an additional constraint equation (in a weak sense) by means of the independent variable provided by the hydrostatic pressure:

$$\begin{cases} \int_{\Omega_0} \boldsymbol{S}(\boldsymbol{u},p) : \delta\boldsymbol{E}\, dV = \int_{\Omega_0} \boldsymbol{f}\cdot\delta\boldsymbol{u}\, dV + \int_{\partial\Omega_0} \boldsymbol{t}\cdot\delta\boldsymbol{u} \\ \int_{\Omega} (J(\boldsymbol{u})-1)\delta p = 0 \end{cases} \quad (1)$$

where $\boldsymbol{S}(\boldsymbol{u},\boldsymbol{p})$ is the second Piola-Kirchhoff stress tensor evaluated in a decoupled sense, $\boldsymbol{\delta E}$ is the virtual variation of the full Green-Lagrange strain tensor, $\boldsymbol{f}$ is the vector of external loads, t is the vector of traction boundary conditions applied at the boundary surfaces, $\boldsymbol{\delta p}$ is the virtual variation of the independent hydrostatic pressure, and finally $(\boldsymbol{J(u)-1})$ is the incompressibility constraint. This set of equations is further manipulated to obtain the finite element matrices (tangent stiffness matrix, internal and residual force vector) imposing a beam-type finite element formulation, where independent polynomial expansion along the axis and cross-section directions are exploited by means of the CUF approach:

$$\boldsymbol{u}(x,y,z) = F_{\tau_u}^{(u)}(x,z) N_{i_u}^{(u)}(y)\boldsymbol{u}_{\tau_u i_u}, \qquad i_u = 1,\dots,N_n^u, \quad \tau_u = 1,\dots,M^u \quad (2)$$

$$p(x,y,z) = F_{\tau_p}^{(p)}(x,z) N_{i_p}^{(p)}(y) p_{\tau_p i_p}, \qquad i_p = 1,\dots,N_n^p, \quad \tau_u = 1,\dots,M^p \quad (3)$$

where $\boldsymbol{N_n}$ and $\boldsymbol{M}$ represents the total number of nodes adopted along the beam axis and expansion terms along the beam cross-section, for each independent variable discretized by the generalized unknowns $\boldsymbol{u_{\tau_u i_u}}$ and $\boldsymbol{p_{\tau_p i_p}}$. In this sense, introducing the independent sets of beam axis discretization $\left(\boldsymbol{N_{i_u}^{(u)}}, \boldsymbol{N_{i_p}^{(p)}}\right)$, as well as the independent sets of the theory-of-structure approximation along the beam cross-section $\left(\boldsymbol{F_{\tau_u}^{(u)}}, \boldsymbol{F_{\tau_p}^{(p)}}\right)$, novel element technologies can be straightforwardly implemented in a formal mathematical setting independent of the specific finite element space considered. From now on, using this hierarchical and recursive approach based on index expansion, a generic anisotropic-order element (AOE) will be used to generalize the concept of independent polynomial approximations.

Numerical results

In this proposed study, the capabilities of the present hybrid approach are assessed in the case of a rectangular cantilever beam with length L = 3000 mm, height h = 100 mm and lateral side w = 200 mm. An incompressible Neo-Hookean material is considered, whose material constant is given by μ=80 MPa. The beam is clamped at one end and subjected to a uniform pressure in the downward direction p = -p_0 k at the top surface. A graphical representation of the considered case study and the element technology adopted is depicted in Fig. 1.

Materials Research Proceedings 73 (2026) 262-265 https://doi.org/10.21741/9781644904459-50

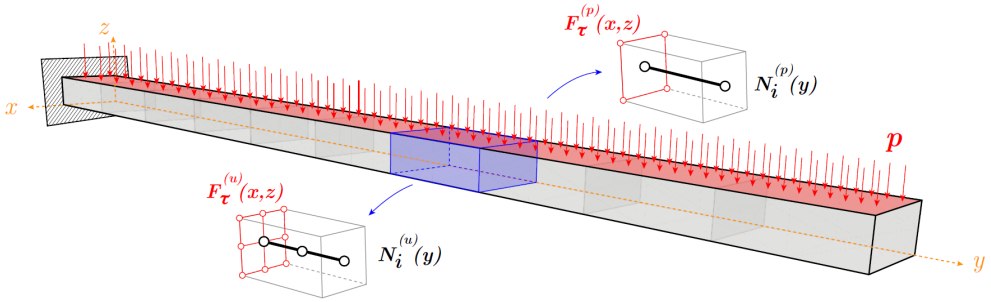

Figure 1 - Cantilever rectangular beam under pressure load: geomtrical features, boundary conditions considered and element technology involved

A detailed convergence analysis of this new element technology has been conducted to investigate the capabilities of this modeling approach, testing in particular different AOE with new polynomial pairs. Table 1 shows the comparison between the results obtained via 1D CUF models and 3D NGSolve models, where a new AOE is considered in the proposed element technologies, including cubic, quadratic and linear models within the same element as reported in the table. The total number of degrees of freedom (DOFs), in terms of displacement and pressure variables, is also reported. A perfect superposition of both quantities across models and applied pressure is found.

Table 1 - Cantilever rectangular beam under pressure load, AOE: comparison between 1D CUF and NGSolve results. Computation of the transverse displacement $\boldsymbol{u_z(w,L,h)}$ [mm] at the tip free end. Relative percentage difference reported in brackets.

		$p = 0.004\ Pa$		$p = 0.01\ Pa$		$p = 0.016\ Pa$		
Displacement	**Pressure**	**1D CUF**	**3D NGSolve**	**1D CUF**	**3D NGSolve**	**1D CUF**	**3D NGSolve**	**DOFs**
$10B4 + 1\times 1L9$	$10B3 + 1\times 1L4$	$-1585.547^{(0.002\%)}$	-1585.511	$-2354.850^{(0.000\%)}$	-2354.854	$-2578.530^{(0.000\%)}$	-2578.534	1107
$10B4 + 2\times 1L9$	$10B3 + 2\times 1L4$	$-1586.414^{(0.002\%)}$	-1586.376	$-2355.259^{(0.000\%)}$	-2355.258	$-2578.764^{(0.000\%)}$	-2578.762	1929
$10B4 + 3\times 1L9$	$10B3 + 3\times 1L4$	$-1586.833^{(0.002\%)}$	-1586.795	$-2355.623^{(0.000\%)}$	-2355.622	$-2579.078^{(0.000\%)}$	-2579.076	2751
$15B4 + 1\times 1L9$	$15B3 + 1\times 1L4$	$-1586.046^{(0.002\%)}$	-1586.009	$-2355.491^{(0.000\%)}$	-2355.491	$-2579.232^{(0.000\%)}$	-2579.231	1632
$15B4 + 2\times 1L9$	$15B3 + 2\times 1L4$	$-1587.074^{(0.002\%)}$	-1587.035	$-2356.033^{(0.000\%)}$	-2356.03	$-2579.576^{(0.000\%)}$	-2579.572	2844
$15B4 + 3\times 1L9$	$15B3 + 3\times 1L4$	$-1587.516^{(0.002\%)}$	-1587.477	$-2356.415^{(0.000\%)}$	-2356.413	$-2579.907^{(0.000\%)}$	-2579.902	4056

An accuracy study is also carried out, now considering the mean value of the transverse displacement computed along the free cross-section as the reference value. Considering instead the classical Taylor-Hood pair, Fig. 2 (left) shows the evolution of relative errors as the number of elements along the axis is increased from n_{axis}= 2 to 32 in powers of two, taking as reference value one obtained from a reference solution given by fourth-order (displacement) and third-order (pressure) interpolations. Figure 2 (right), instead, shows the effects of the cross-section discretization n_{cs} when the total number of elements along the axis is considered fixed at n_{axis}= 2, 4, 8, 16 and 32. The respective abscissae show the number of DOFs required by the simulation. Particularly, in the proposed case study, the results obtained with Lagrange-type finite elements implemented in the CUF formalism are perfectly matched by the solution obtained with higher-order Legendre polynomials implemented in the Netgen/NGSolve code.

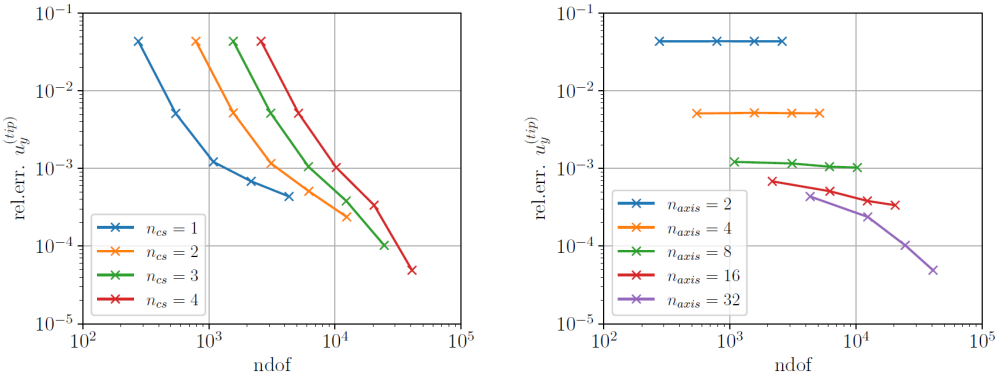

Figure 2 - Cantilever rectangular beam under pressure load: dependency of the relative error in the tip deflection on the axial (left) and cross-section discretization (right), respectively.

Conclusions

The analyses confirm the effectiveness of the present implementation of anisotropic-order element (AOE) for the nonlinear modeling of incompressible and nearly compressible materials and structures. The proposed approach, based on a flexible, recursive definition of primary variable expansion within the Carrera Unified Formulation (CUF) framework, provides a robust and reliable tool for generating new mixed-element technologies. The results demonstrate reliable predictions of displacement values, even under large displacements and rotations.

Acknowledgment

P. Chiaia acknowledge support by the Space It Up! project funded by the Italian Space Agency, ASI, and the Ministry of University and Research, MUR, under contract CUP n. D93C23001190006.

References

[1] Elguedj T., Bazilevs Y., Calo V.M. and Hughes T.J.R.. “B and F projection methods for nearly incompressible linear and non-linear elasticity and plasticity using higher-order NURBS elements”. Computer Methods in Applied Mechanics and Engineering, Vol. 197, n. 33, pp. 2732-2762, 2008. https://doi.org/10.1016/j.cma.2008.01.012

[2] Zienkiewicz O.C., Qu S., Taylor R.L. and Nakazawa S. “The patch test for mixed formulations”. International Journal for Numerical Methods in Engineering, Vol. 23, n. 10, pp. 1873-1883, 1986. https://doi.org/10.1002/nme.1620231007

[3] Taylor C.M. and Hood P. “A numerical solution of the Navier-Stokes equations using the finite element technique”, Computers & Fluids, Vol. 1, n. 1, pp. 73-100, 1973. https://doi.org/10.1016/0045-7930(73)90027-3

[4] Chiaia P., Pagani A. and Carrera E. “Large strain and 3D stress analysis of laminated fiber-reinforced soft material structures with high order beam finite elements”. Computers & Structures, Vol 313, 107735, 2025. https://doi.org/10.1016/j.compstruc.2025.107735

[5] Netgen/NGSolve, high performance multiphysics finite element software: https://ngsolve.org

Materials Research Proceedings 73 (2026) 266-269 https://doi.org/10.21741/9781644904459-51

Comparative Analysis of FGM Euler - Bernoulli and Timoshenko - Ehrenfest Beam Theories for Bending Response of Sea Ice

Giacomo STIRPE[1,a*] and Mikko SUOMINEN[1,b]

[1]Department of Energy and Mechanical Engineering, Aalto University, Finland

[a]giacomo.stirpe@aalto.fi, [b]mikko.suominen@aalto.fi

Keywords: FGM, Sea Ice, Analytical Solutions, Flexural Stress

Abstract. In the definition of design properties, such as flexural strength, sea ice beams are loaded in test scenarios like cantilever and three-point bending. Selecting the correct theory to estimate the flexural stresses based on the force measurements and displacements is of crucial importance to compute accurate values. The present paper explores the differences in predictions of displacements and stresses for two functionally graded material (FGM) ice beam models based on the Euler - Bernoulli and Timoshenko - Ehrenfest theories. The estimates of each theory, for a case study based on common elastic and thermal properties of sea ice, are compared against a 3D Finite Element Method (FEM) model to consider the best modelling approach for testing. The closed-form solution for the two theories will be presented for an in-situ test scenario, where the effects of buoyancy, gravity, and thermal loadings are considered. It is known that, as the Euler - Bernoulli theory ignores shear deformations, it introduces errors for thick and short beams or when complex loading scenarios are present. This work analyses the displacements and stress predictions of FGM beams in the context of sea ice test and determines possible errors due to neglecting of shear deformation effects in Euler - Bernoulli theory, offering possibilities to introduce Timoshenko - Ehrenfest beam-based models to lower these errors in sea ice beams response modelling.

Introduction

Understanding the bending response of sea ice is fundamental to define the flexural strength of sea ice, which although not being a material property offers important information to the design of offshore structures and vessels operating in ice-infested waters. Currently, the flexural strength of sea ice is extracted from tests, as cantilever and three-point bending, using methods based on the homogeneous Euler – Bernoulli beam theory to interpretate the obtained force measurements [1, 2]. The models present simplifying assumptions on the homogeneity and elastic behaviour of sea ice, furthermore they disregard external loading effects as buoyancy, gravity and thermal gradients.

Nonetheless, it is known that mechanical properties of sea ice vary throughout its thickness and they are dependent upon different factors as temperature, salinity, density, and porosity [3]. Functionally Graded Material (FGM) based beam theories can be used to model these variations through thickness representing the variation of properties in the macroscopic continuum description offering a good trade-off between accuracy and computational efficiency [4, 5, 6, 7].

The present work highlights the differences in predictions of flexural stresses for Euler – Bernoulli and Timoshenko – Ehrenfest based FGM sea ice beam models and aims to showcase a preferred modelling approach when compared with an equivalent FEM 3D model of the beam. The work focuses on the cantilever test setup used for in-situ ice samples, which are exposed to gravity, buoyancy, and thermal gradients.

Methods

The monodimensional beam models are solved analytically following the methodology of Stirpe et al. [8] where the closed-form solution for von Kármán nonlinear FGM Euler – Bernoulli based

Content from this work may be used under the terms of the Creative Commons Attribution 3.0 license. Any further distribution of this work must maintain attribution to the author(s) and the title of the work, journal citation and DOI. Published under license by Materials Research Forum LLC.

Materials Research Proceedings 73 (2026) 266-269 https://doi.org/10.21741/9781644904459-51

sea ice beam models were derived, as an example the displacement fields for a thermally loaded cantilever beam are reported in Eq. 1.

$$\begin{cases} w(x) = \frac{x^2\left(3A_{xx}M_{T,xx} - 3B_{xx}N_{T,xx} + A_{xx}F(-3L+x)\right)}{6\left(B_{xx}^2 - A_{xx}D_{xx}\right)} \\ u(x) = -\frac{1}{2}\int \left(\frac{dw(x)}{dx}\right)^2 dx + \frac{B_{xx}}{A_{xx}}\frac{dw(x)}{dx} + \frac{N_{T,xx}}{A_x}x \end{cases} \quad \textbf{(1)}$$

A similar set of solution is hereby derived for FGM Timoshenko – Ehrenfest beam model and then applied to a test ice beam of which the dimensions and properties are reported in Table 1 and Table 2.

Table 1: Dimensions and Point Load of Ice Beam

	Length [mm]	Width [mm]	Thickness [mm]	Point Load [N]
Test Beam	740	120	71	113

Table 2: Thermo-elastic properties of Ice Beam

	Bottom Value	M Ratio	n Exponent
T	-1.8 [°C]	5	1
α_T	$2 \cdot 10^{-5}$ $[K^{-1}]$	3	0.6
E	$1.67 \cdot 10^{9}$ $[Pa]$	2.63	0.5

Timoshenko – Ehrenfest (TE) FGM. The FGM based Timoshenko – Ehrenfest beam theory model is based on the equilibrium Eq. 2 from Reddy [6].

$$\begin{cases} -\frac{\partial}{\partial x}\left\{A_{xx}\left[\frac{\partial u}{\partial x} + \frac{1}{2}\left(\frac{\partial w}{\partial x}\right)^2\right] + B_{xx}\frac{\partial \phi_x}{\partial x} - N_{xx}^T\right\} = 0 \\ -\frac{\partial}{\partial x}\left[S_{xz}\left(\phi_x + \frac{\partial w}{\partial x}\right)\right] - \frac{\partial}{\partial x}\left\{A_{xx}\frac{\partial w}{\partial x}\left[\frac{\partial u}{\partial x} + \frac{1}{2}\left(\frac{\partial w}{\partial x}\right)^2\right] + B_{xx}\frac{\partial w}{\partial x}\left(\frac{\partial \phi_x}{\partial x}\right) - \frac{\partial w}{\partial x}N_{xx}^T\right\} + c_f w - q = 0 \\ -\frac{\partial}{\partial x}\left\{B_{xx}\left[\frac{\partial u}{\partial x} + \frac{1}{2}\left(\frac{\partial w}{\partial x}\right)^2\right] + D_{xx}\frac{\partial \phi_x}{\partial x} - M_{xx}^T\right\} + S_{xz}\left(\phi_x + \frac{\partial w}{\partial x}\right) = 0 \end{cases} \quad \textbf{(2)}$$

These are then solved according to the cantilever test boundary conditions to obtain the displacement and stress fields. For beams with slenderness ratio of less than 15 the combined action of buoyancy and gravity can be effectively disregarded without reducing accuracy of the solution as shown in [8]. Considering this simplification, we can write the displacement fields in Eq. 3.

$$\begin{cases} w(x) = -\frac{\alpha F}{6}x^3 + \frac{\alpha \mathcal{K}}{2}x^2 + \frac{F}{S_{xz}}x \\ \phi(x) = \frac{\alpha F}{2}x^2 - \alpha \mathcal{K}x \\ u(x) = -\frac{\beta F}{2}x^2 + \frac{B_{xx}(FL - M_{xx}^T) + D_{xx}N_{xx}^T}{\Delta}x - \frac{1}{2}\int \left(\frac{dw(x)}{dx}\right)^2 dx \end{cases} \quad \textbf{(3)}$$

Where:

$$\Delta = A_{xx} \cdot D_{xx} - {B_{xx}}^2 \qquad \mathcal{K} = FL - {M_{xx}}^T + B_{xx} \cdot {N_{xx}}^T / A_{xx}$$
$$\alpha = A_{xx}/\Delta \qquad \beta = B_{xx}/\Delta$$

Materials Research Proceedings 73 (2026) 266-269 https://doi.org/10.21741/9781644904459-51

Furthermore, it is worth stating that closed-form solution that retain buoyancy and gravity effects for the FGM Timoshenko – Ehrenfest beam exists but the associated algebraic formulation is lengthy and therefore the focus is restricted to this simplified case.

FEM Model. A 3D FEM model has been developed using the commercial finite element code ABAQUS to compare the response of the 1D beam models with a high-fidelity three-dimensional reference solution. The results of the 3D simulation are then sampled at the mid-width and mid-height axis line to extract reasonable values for comparisons; at the same time the stress distribution of the finite element simulation shows discontinuity due to few numbers of through thickness elements. Furthermore, Poisson's ratio of the material has been set to zero to exclude effects of lateral strain on the result and allow direct comparison with the beam theories.

Results

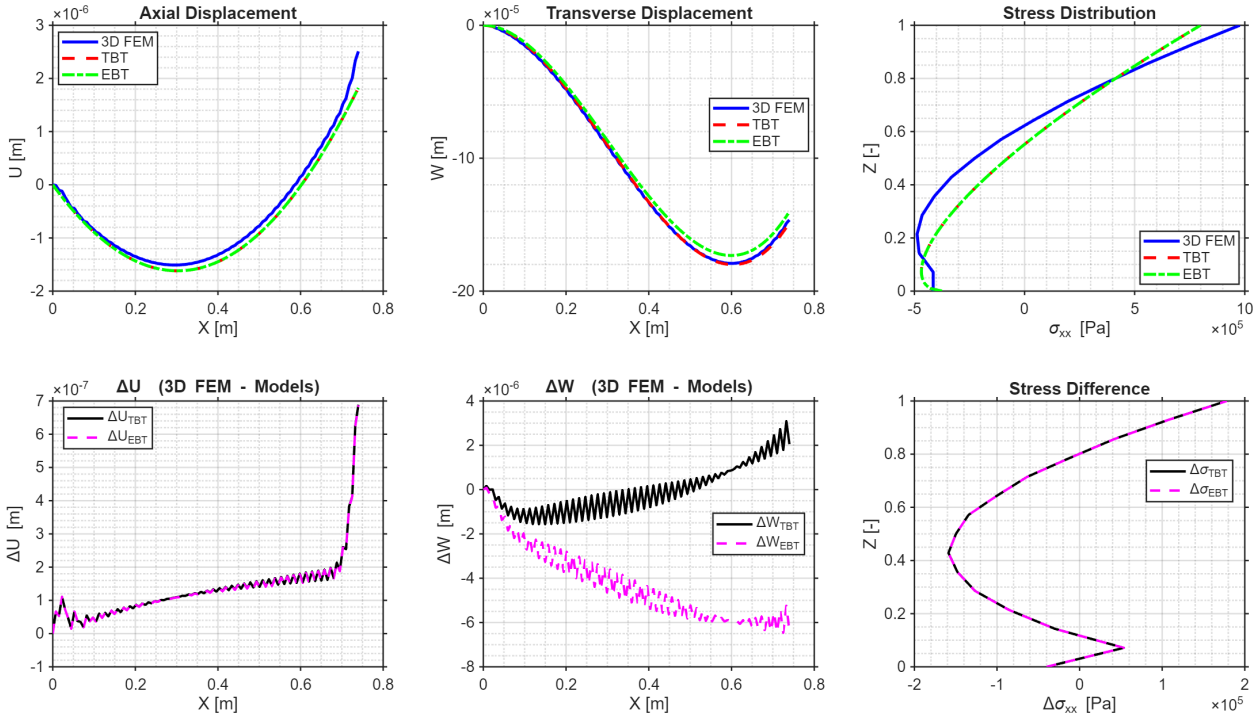

Fig.1: Comparison of 1D Models and 3D FEM in the Cantilever test scenario

The comparison results, as shown in Fig.1, highlight a good correspondence of the displacements and axial stress distributions between the 3D simulations and the 1D models. The figure highlights how the FGM Timoshenko – Ehrenfest based formulation better represents the transverse displacement of the ice beam when compared with the FGM Euler – Bernoulli based one, while it shows similar predictions for both 1D theories when looking at the axial displacement and axial stress distributions. The smooth ramp at the tip value in the axial displacement can be explained due to the tip loading being applied on the top face and not through the neutral axis in the 3D model. This means the resultant force acts above the neutral axis, creating a small local tip moment that the 1D theories ignore. This local moment produces an extra axial displacement at the tip via the FGM coupling term, which is why the axial displacement diverges while the transverse one is less affected.

The differences in the axial stress distributions are likely caused by reduced number of through thickness elements and the differences in load application, as the loading is applied as a distributed pressure over a small area at the tip of the beam in the 3D model against a point load in the 1D assumptions. The axial stresses are sampled away from the wall to avoid further errors due to boundary condition effects in the 3D model.

Conclusion

From the comparison shown, it is possible to highlight how the FGM Timoshenko – Ehrenfest based model better tracks the displacement fields of the ice beam when compared against the FGM Euler – Bernoulli one. Nonetheless, the axial stress prediction for both models remains very close to each other, suggesting that for beams of dimensions commonly used in in-situ ice testing the flexural stress distribution would be similar in both theories thus showing that switching to FGM Timoshenko – Ehrenfest based models would increase accuracy only in the prediction of the displacement fields of the ice beams, unless less slender beams would be tested.

Closed form solutions for more complex cases than the ones presented exist and consequently can be used to analytically solve the displacement and stress fields of beams under complex loading scenarios in a computationally cheap solution. This gives a possibility to extend the application's realm beyond sea ice modelling to other natural and engineered FGM materials, such as timber or composites in marine, offshore, and aeronautical structures.

References

[1] G. W. Timco, "On the test methods for model ice," *Cold Reg. Sci. Technol.*, vol. 4, no. 3, pp. 269–274, Jul. 1981. https://doi.org/10.1016/0165-232X(81)90009-4

[2] G. W. Timco and W. F. Weeks, "A review of the engineering properties of sea ice," *Cold Reg. Sci. Technol.*, vol. 60, no. 2, pp. 107–129, Feb. 2010. https://doi.org/10.1016/j.coldregions.2009.10.003

[3] S. Løset, K. Shkhinek, O. Gudmestad, and K. Høyland, *Actions from ice on arctic offshore and coastal structures*. Krasnodar, St.Petersburg, 2006.

[4] Y. Li *et al.*, "A Review on Functionally Graded Materials and Structures via Additive Manufacturing: From Multi-Scale Design to Versatile Functional Properties," *Adv. Mater. Technol.*, vol. 5, no. 6, p. 1900981, 2020. https://doi.org/10.1002/admt.201900981

[5] A. Pragya and T. K. Ghosh, "Soft Functionally Gradient Materials and Structures – Natural and Manmade: A Review," *Adv. Mater.*, vol. 35, no. 49, p. 2300912, 2023. https://doi.org/10.1002/adma.202300912

[6] J. N. Reddy, *Theories and Analyses of Beams and Axisymmetric Circular Plates*. Boca Raton: CRC Press, 2022. doi: 10.1201/9781003240846

[7] J. N. Reddy, "Analysis of functionally graded plates," *Int. J. Numer. Methods Eng.*, vol. 47, no. 1–3, pp. 663–684, 2000. https://doi.org/10.1002/(SICI)1097-0207(20000110/30)47:1/3<663::AID-NME787>3.0.CO;2-8

[8] G. Stirpe, T. Gustafsson, H. Jawaid, F. Mancini, J. Romanoff, and M. Suominen, "Modelling flexural stress of sea ice using functionally graded material beam theories," *Eur. J. Mech. - ASolids*, vol. 121, p. 106287, Jan. 2027. https://doi.org/10.1016/j.euromechsol.2026.106287

Materials Research Proceedings 73 (2026) 270-273 https://doi.org/10.21741/9781644904459-52

Deep Learning Prediction of Crack Propagation in Ductile Materials using Surface Displacements Fields

Lahouari BENABOU[1,a *]

[1]LISV, Université de Versailles Saint-Quentin-en-Yvelines, Paris Saclay, France

[a]lahouari.benabou@uvsq.fr

Keywords: Deep Learning, Crack Propagation, CNN, LSTM

Abstract. This study presents a deep learning framework for predicting incremental crack propagation in ductile materials using only surface displacement measurements. A synthetic dataset is generated via the eXtended Finite Element Method (XFEM), enabling the simulation of diverse crack paths under various mixed-mode loading conditions on an Arcan specimen made of aluminum alloy 6061-T6. From each simulation, sequences of displacement fields (u_x,u_y) are extracted over a regular grid within the region of interest, together with the corresponding crack-path maps, to form the training dataset. Three convolutional-recurrent architectures are developed in Python using the Keras library to capture the spatiotemporal features of crack growth. Model 1 (CNN-BiLSTM) processes displacement fields through a single branch. Model 2 (Dual-Branch CNN-BiLSTM) incorporates an explicit damage branch fed with the current crack-path map (downsampled via MaxPooling2D). Model 3 (ConvLSTM) employs native spatiotemporal convolution. All models regress the next crack tip position, enabling iterative full-path prediction from displacement sequences alone. Comparative evaluation on unseen mixed-mode cases demonstrates the potential of the proposed approach for non-intrusive fracture assessment.

Introduction

Fracture is a complex physical process that can lead to catastrophic structural failure. Accurate prediction of crack initiation and propagation is therefore essential for assessing structural integrity. In brittle materials, cracks propagate rapidly with minimal energy dissipation, while in ductile materials, significant plastic deformation precedes failure, resulting in slower crack growth.

In classical fracture mechanics, Irwin [1] introduced the stress intensity factor and energy release rate concepts within linear elastic fracture mechanics (LEFM). To account for plasticity, Dugdale [2] later proposed plastic zone models. Although computational fracture mechanics based on the finite element method (FEM) is now widely used, traditional FEM requires remeshing or predefined crack paths, making it computationally expensive for complex crack trajectories.

In recent years, artificial intelligence and deep learning have shown strong potential in materials science. Several studies have applied physics-informed neural networks (PINNs), graph convolutional networks combined with RNNs, and CNN-LSTM architectures to forecast crack evolution [3-6]. Building on these advances, the present work develops three deep learning models to predict incremental crack advance directly from sequences of surface displacement fields, offering a fast and non-intrusive alternative to classical numerical methods.

Dataset generation

The eXtended Finite Element Method (XFEM) is used to simulate crack initiation and propagation under arbitrary mixed-mode loading. Based on the partition of unity, XFEM enriches the displacement field with discontinuous and singular functions to represent cracks [7]. Damage is modeled using a traction-separation law. Crack initiation occurs when the maximum principal stress reaches a critical value, and the crack direction is determined perpendicular to this stress. A

Content from this work may be used under the terms of the Creative Commons Attribution 3.0 license. Any further distribution of this work must maintain attribution to the author(s) and the title of the work, journal citation and DOI. Published under license by Materials Research Forum LLC.

Materials Research Proceedings 73 (2026) 270-273 https://doi.org/10.21741/9781644904459-52

linear softening law governed by the material fracture energy is adopted, assuming mode-independent behavior for simplicity.

The material investigated is aluminum alloy 6061-T6, which exhibits ductile behavior described by the Ramberg-Osgood law. An Arcan specimen with an initial crack length of 5 mm is used to generate mixed-mode I/II loading conditions by varying the loading angle β. The specimen is modeled with 4-node plane strain elements under displacement-controlled loading (Fig. 1). Multiple XFEM simulations produce 200 distinct fracture experiments with varying crack paths under different mixed-mode ratios. These simulations constitute the synthetic dataset for training the deep learning models.

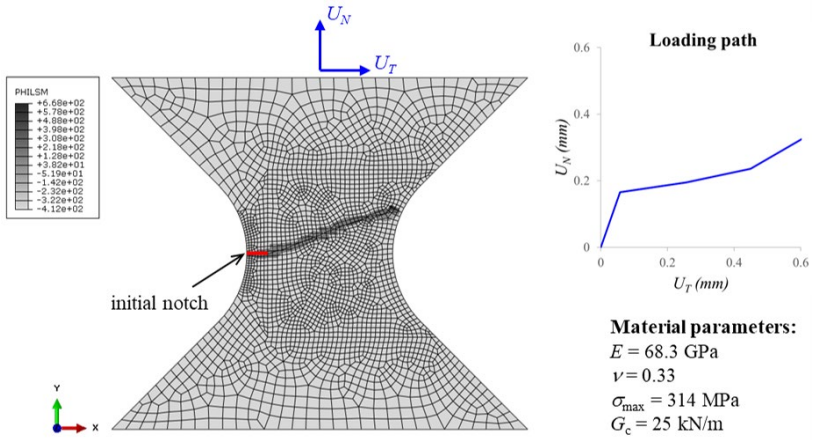

Figure 1: XFEM simulation of crack propagation under mixed-mode I/II loading.

Deep Learning Models

Crack propagation is a spatiotemporal phenomenon: displacement fields evolve both spatially (particularly near the crack tip) and temporally (loading history). This justifies the combination of Convolutional Neural Networks (CNNs) for spatial feature extraction and Long Short-Term Memory (LSTM) networks for temporal modeling.

CNN layers extract spatial features such as the displacement distribution around the crack tip and over the deformed surface. LSTM layers capture temporal dependencies across consecutive time steps. A many-to-one architecture is used: given a sequence of input fields, the model predicts the next crack increment. Because the CNN must be applied independently to each time step, the TimeDistributed wrapper in Keras is employed. Input data at each time step is a tensor of shape (W × H × C), where W and H are the height and width of the region of data collection, and C is the number of channels (C = 2 since displacement fields u_x and u_y are measured over the surface). Three models are proposed:

- Model 1 (CNN-BiLSTM): Single-branch architecture using TimeDistributed Conv2D layers followed by LSTM or BiLSTM (several variants were systematically tested to evaluate the impact of key design choices on prediction accuracy).
- Model 2 (Dual-Branch CNN-BiLSTM): Two parallel branches; one for displacement fields and one for the current crack-path progression at the same timesteps. Features from both branches are concatenated before the final prediction.
- Model 3 (ConvLSTM): Native spatiotemporal model using ConvLSTM2D, offering a compact single-stream alternative.

The dataset consists of 200 XFEM fracture experiments. 90% are used for training and 10% for validation. Inputs are standardized (zero mean, unit standard deviation) and outputs normalized to [0, 1] using training statistics only. Models are trained with the Adam optimizer (learning rate 0.001) and Mean Squared Error (MSE) loss using backpropagation through time. Batch sizes vary according to the duration of each fracture experiment.

Materials Research Proceedings 73 (2026) 270-273 https://doi.org/10.21741/9781644904459-52

Results and Discussion

The influence of key hyperparameters was first investigated on the baseline CNN-LSTM architecture (Model 1). Figure 2 shows the effect of the input sequence length (number of timesteps) using the basic structure, denoted as variant M1-A: CONV2D + AVERAGEPOOLING2D + FLATTEN + LSTM. Increasing the input sequence length from 3 to 7 timesteps progressively reduces the MSE. With 3 timesteps, the model achieves an MSE of 3.04E-04. This value decreases to 1.95E-04 with 5 timesteps and further reduces to 1.68E-04 when using 7 timesteps, confirming that longer temporal context improves prediction accuracy.

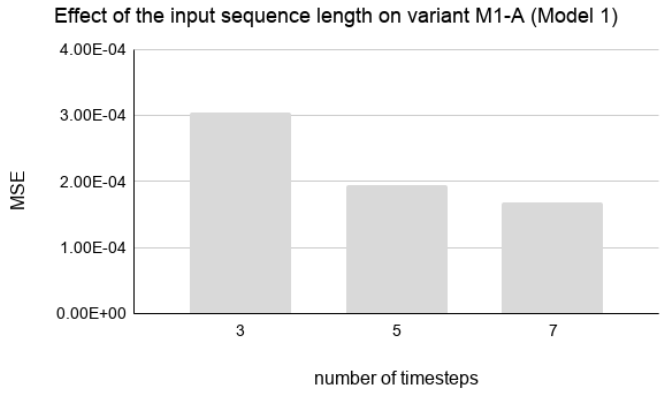

Figure 2: Validation MSE as a function of the number of input timesteps for the preliminary CNN-BiLSTM variant (M1-A).

Table 1 presents an ablation study to evaluate the impact of different layer configurations on Model 1. The best performance is achieved by configuration M1-D which incorporates a BiLSTM layer and is denoted as CNN-BiLSTM for simplicity. Adding a second Conv2D layer (M1-E) slightly degrades performance, suggesting that excessive depth may lead to overfitting on this relatively small dataset. The introduction of Bidirectional LSTM and moderate dropout proves particularly beneficial.

Table 1: Comparison of different CNN-LSTM configurations for Model 1.

Layer configuration	Validation MSE
M1-A: CONV2D + AVERAGEPOOLING2D + FLATTEN + LSTM	3.04E-04
M1-B: CONV2D + MAXPOOLING2D + FLATTEN + LSTM	2.50E-04
M1-C: CONV2D + MAXPOOLING2D + FLATTEN + BI-LSTM	2.18E-04
M1-D: CONV2D + MAXPOOLING2D + FLATTEN + BI-LSTM + DROPOUT	2.28E-04
M1-E: CONV2D + MAXPOOLING2D + CONV2D + FLATTEN + BI-LSTM + DROPOUT	2.86E-04

Figure 3 presents the predicted crack paths according to the 3 models against the ground truth. Overall, all three models are able to reproduce the general trend of crack propagation. However, noticeable differences appear in prediction accuracy. Model 1 (CNN-BiLSTM) and Model 3 (ConvLSTM) show good agreement with the ground truth across most cases, with particularly stable and accurate predictions in cases 1, 2, and 5. Model 3 tends to produce smoother trajectories, while Model 1 captures sharp changes reasonably well. In contrast, Model 2 (Dual-Branch CNN-BiLSTM) exhibits larger deviations from the ground truth in several cases (especially visible in cases 1, 3, and 5). Despite the explicit inclusion of crack-path information, the dual-branch architecture appears more sensitive to the resolution mismatch and downsampling process, leading to less accurate incremental predictions in some mixed-mode scenarios. This suggests that late fusion of the damage branch may introduce noise or misalignment that outweighs its theoretical advantage on the current coarse grid.

These results highlight that a well-tuned single-branch CNN-BiLSTM (M1-D) and the ConvLSTM model offer the best balance between accuracy and robustness for incremental crack path prediction using only displacement fields. The ConvLSTM model, in particular, benefits from its native spatiotemporal processing, making it an efficient candidate for real-time applications.

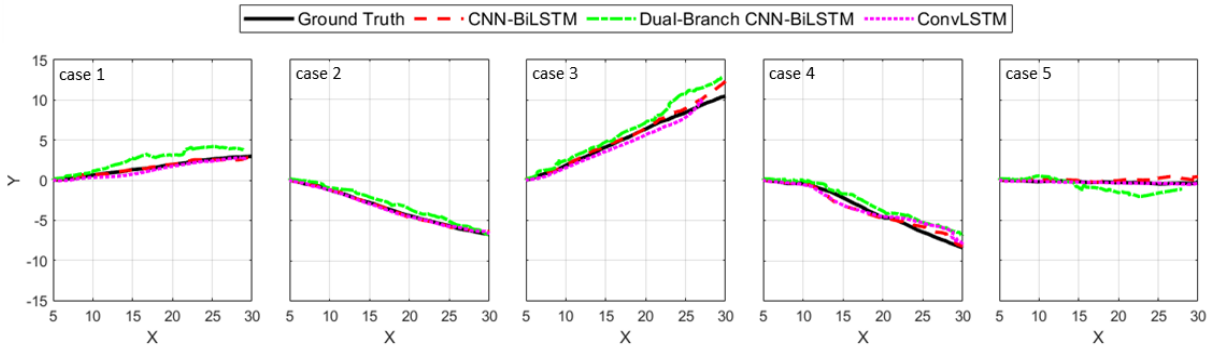

Figure 3: Predicted crack paths obtained with the three proposed models compared to XFEM ground truth.

Conclusions

This study demonstrates the feasibility of using deep learning models to predict incremental crack propagation in ductile aluminum alloy 6061-T6 from sequences of surface displacement fields only. Three main architectures were developed and compared. Systematic hyperparameter investigations on Model 1 (CNN-BiLSTM) revealed that bidirectional LSTM combined with max pooling and moderate dropout yields the best performance. Comparative evaluation on unseen mixed-mode crack paths showed that both Model 1 (CNN-BiLSTM) and Model 3 (ConvLSTM) provide accurate and robust predictions, while the dual-branch architecture (Model 2) exhibited higher sensitivity to input alignment on the current coarse grid.

References

[1] G.R. Irwin, Onset of fast crack propagation in high strength steel and aluminum alloys, Sagamore Research Conference Proceedings 2 (1956), 289-305. https://doi.org/10.21236/AD0099305

[2] D.S. Dugdale, Yielding in steel sheets containing slits, Journal of the Mechanics and Physics of Solids 8 (1960) 100-104. https://doi.org/10.1016/0022-5096(60)90013-2

[3] M. Schwarzer, B. Rogan, Y. Ruan, et al., Learning to fail: Predicting fracture evolution in brittle material models using recurrent graph convolutional neural networks, Computational Materials Science 162 (2019) 322-332. https://doi.org/10.1016/j.commatsci.2019.02.046

[4] S. Goswami, C. Anitescu, S. Chakraborty, T. Rabczuk, Transfer learning enhanced physics informed neural networks for phase-field modeling of fracture, Theoretical and Applied Fracture Mechanics 106 (2020) 102447. https://doi.org/10.1016/j.tafmec.2019.102447

[5] Y.C. Hsu, C.H. Yu, M.J. Buehler, Using deep learning to predict fracture patterns in crystalline solids, Matter 3 (2020) 197-211. https://doi.org/10.1016/j.matt.2020.04.019

[6] Y. Wang, D. Oyen, W. Guo, et al., StressNet - Deep learning to predict stress with fracture propagation in brittle materials, Materials Degradation 5 (2021). https://doi.org/10.1038/s41529-021-00151-y

[7] N. Moës, J. Dolbow, T. Belytschko, A finite element method for crack growth without remeshing, International journal for Numerical Methods in Engineering 46 (1999), 131-150. https://doi.org/10.1002/(SICI)1097-0207(19990910)46:1<131::AID-NME726>3.0.CO;2-J

Materials Research Proceedings 73 (2026) 274-279 https://doi.org/10.21741/9781644904459-53

Dynamic Stiffness Method and CUF-based Component-Wise Theories Applied to Free Vibration Analysis of Composite, Thin-Walled, and Viscoelastic Sandwich Structures

Xiao LIU[1], Alfonso PAGANI[2], Erasmo CARRERA[2], Xiang LIU[3]*

[1]College of Mechanical and Vehicle Engineering, Changsha University of Science and Technology, Changsha, China

[2]MUL2 Lab, Department of Mechanical and Aerospace Engineering, Politecnico di Torino, Torino, Italy

[3]Key Laboratory of Traffic Safety on Track, Ministry of Education, School of Traffic & Transportation Engineering, Central South University, Changsha, China

Keywords: Carrera Unified Formulation, Dynamic Stiffness Method, Damped Dynamic Stiffness, Component-Wise Approach, Composite Structures, Free Vibration

Abstract. This paper presents a unified CUF(LE)–DSM/DDSM framework for free vibration analysis of composite, thin-walled, and viscoelastic sandwich structures. Higher-order three-dimensional displacement fields are expanded using Lagrange polynomials, enabling layer-wise and component-wise modeling of heterogeneous cross-sections. Intrinsic composite damping and frequency-dependent viscoelastic behavior are introduced through complex constitutive properties. The governing equations are derived through the principle of virtual displacements and solved analytically to construct frequency-domain dynamic stiffness matrices. The Wittrick–Williams algorithm is used for undamped systems, while its extension combined with the homotopy perturbation method extracts complex eigenvalues of damped systems. Comparisons with three-dimensional finite element solutions demonstrate high accuracy with substantially fewer degrees of freedom, providing an efficient framework for broadband vibration analysis and damping-oriented design.

1. Introduction

Beam and reduced-order structural models are widely used because they provide efficient representations of slender structures at much lower computational cost than full three-dimensional models. Classical Euler–Bernoulli and Timoshenko theories [1-3] are effective for slender homogeneous beams, but may become inadequate for thin-walled, laminated, stiffened, and locally deformable cross-sections [4-6]. Refined structural models are therefore required to capture higher-order kinematics and heterogeneous material behavior.

The Carrera Unified Formulation (CUF) provides a systematic framework for constructing structural theories of arbitrary order [7-9]. In one-dimensional CUF models, the three-dimensional displacement field is expanded over the cross-section using suitable functions. Lagrange expansions (LE) are particularly convenient for complex and heterogeneous sections because the unknowns are physical translational displacements that can be assigned locally [10-11]. Consequently, layer-wise (LW) and component-wise (CW) descriptions allow solid regions, thin-walled parts, composite layers, stiffeners, and damping layers to be modeled within the same framework.

Most CUF models are solved by the finite element method, whose cost increases with mesh refinement, whereas available Navier-type analytical solutions are generally restricted to particular boundary conditions [12-14]. The dynamic stiffness method (DSM) provides an efficient alternative by deriving the frequency-dependent stiffness matrix from the closed-form solution of

Content from this work may be used under the terms of the Creative Commons Attribution 3.0 license. Any further distribution of this work must maintain attribution to the author(s) and the title of the work, journal citation and DOI. Published under license by Materials Research Forum LLC.

Materials Research Proceedings 73 (2026) 274-279 https://doi.org/10.21741/9781644904459-53

the governing equations [15-16]. Combined with the Wittrick–Williams (WW) algorithm [17], it enables reliable broadband natural-frequency extraction without conventional axial element refinement. For damped composites and viscoelastic structures, complex constitutive properties lead to non-Hermitian dynamic stiffness matrices; the DSM is therefore extended to the damped dynamic stiffness method (DDSM) and combined with a homotopy-based complex eigensolution strategy. The present CUF(LE)–DSM/DDSM framework thus treats undamped and damped structures with different geometries, materials, and boundary conditions in a consistent manner.

2. Unified CUF(LE)–DSM/DDSM Formulation

2.1 CUF(LE) kinematics and component-wise modeling

Consider a beam-like structure of length L with the longitudinal axis along *y* and cross-section Ω in the *xz*-plane. The displacement vector is

$$\mathbf{u}(x,y,z) = \{u_x,\ u_y,\ u_z\}^{\mathrm{T}} \qquad (1)$$

Within CUF, the three-dimensional displacement field is written in the unified form

$$\mathbf{u}^{k}(x,y,z)=F_\tau(x,z)\ u^{k}_\tau(y)\ ,\ \tau=1,\ldots,M \qquad (2)$$

where F_τ denotes the cross-sectional expansion functions, u_τ contains the generalized displacement variables along the beam axis, and M is the number of expansion terms.For laminated composites, each layer is introduced through its transformed material properties. The same kinematic formulation is retained for damped systems by using complex-valued constitutive parameters: intrinsic composite damping is represented through complex elastic and shear moduli, while frequency-dependent complex properties are adopted for viscoelastic layers. Thus, intrinsic and viscoelastic damping are described without changing the CUF(LE) cross-sectional assembly.

Lagrange polynomials are adopted as cross-sectional expansion functions. Bilinear L4, cubic L9, and fourth-order L16 approximations can be selected according to the required refinement. Their unknowns correspond directly to translational displacements at Lagrange points, so the kinematics can be refined by increasing either the polynomial order or the number of local subdomains.

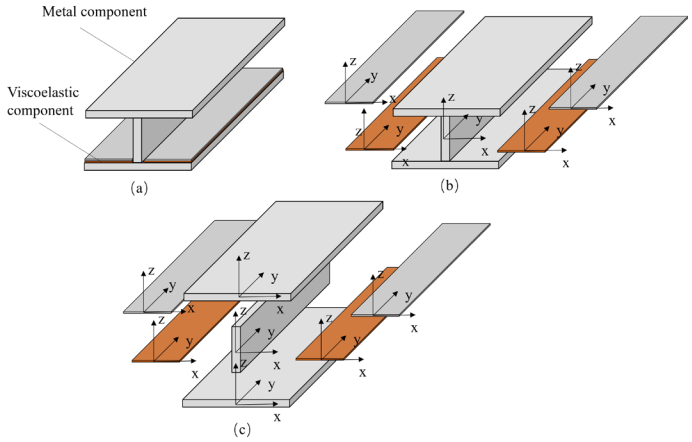

Fig. 1. Unified CUF(LE) modeling of representative complex cross-sectional structures.

This feature is particularly suitable for LW and CW modeling (Fig. 1). Individual structural regions are assigned their own material properties and kinematics and are assembled through common Lagrange nodes, naturally enforcing interface compatibility. Solid, thin-walled, composite, stiffened, and viscoelastic components can therefore be represented within a single cross-sectional framework.

Materials Research Proceedings 73 (2026) 274-279 https://doi.org/10.21741/9781644904459-53

2.2 Governing equations and dynamic stiffness formulation

The governing equations are derived through the Principle of Virtual Displacements (PVD),

$$\delta L_{\text{int}}=\int_v \delta\varepsilon^T\sigma \mathrm{d}V=-\delta L_{\text{ine}} \quad (3)$$

where L_{int} stands for the strain energy and L_{ine} is the work done by the inertial loadings. δ stands for the usual virtual variation operator. Substitution of the CUF displacement approximation into the PVD and integration over the cross-section lead to the CUF fundamental nuclei. Eq. (3) becomes

$$\delta L_{int} = \int_L \delta\mathbf{u}_\tau^T \mathbf{Y}^{\tau s}\mathbf{u}_s\, dy + \left[\delta\mathbf{u}_\tau^T \mathbf{\Pi}^{\tau s}\mathbf{u}_s\right]_{y=0}^{y=L} \quad (4)$$

where $\mathbf{Y}^{\tau s}$ is the linear differential stiffness matrix and $\mathbf{\Pi}^{\tau s}$ is the matrix of natural boundary conditions. For the sake of brevity, these matrices are not given here but they can be found in [13].

The virtual variation of the inertial work is given by

$$\delta L_{ine} = \int_L \delta u_\tau \int_\Omega \rho F_\tau F_s d\Omega \ddot{u}_s dy = \int_L \delta u_\tau \mathbf{M}^{\tau s}\ddot{u}_s dy \quad (5)$$

where ρ denotes the material density and double over dots stand for the second derivative with respect to time (t). $\mathbf{M}^{\tau s}$ is the 3×3 fundamental, diagonal nucleus of the mass matrix, whose components can be found in [13].

Assuming harmonic motion reduces the problem to a system of ordinary differential equations with constant coefficients along the beam axis, which is solved analytically. Collecting the integration constants in **Q** gives the nodal displacement and force amplitudes as $\bar{\mathbf{U}} = \mathbf{AQ}$ and $\bar{\mathbf{P}} = \mathbf{RQ}$; elimination of **Q** yields

$$\bar{\mathbf{P}}=\mathbf{K}(\omega)\bar{\mathbf{U}},\ \mathbf{K}(\omega)=\mathbf{RA}^{-1} \quad (6)$$

Eq. (6) defines the frequency-dependent dynamic stiffness matrix. Real constitutive properties give the conventional DSM, whereas complex and/or frequency-dependent properties produce the DDSM. For the adopted CUF kinematics, the frequency-domain solution is analytical, and the element matrices are assembled in the same manner as conventional stiffness matrices.

2.3 Real and complex eigensolution

For undamped structures, the WW algorithm solves the transcendental eigenvalue problem through reliable mode counting, ensuring that no natural frequencies are missed. For damped systems, the dynamic stiffness matrix is complex and generally non-Hermitian; the undamped WW eigensolutions are therefore used as initial estimates for a homotopy perturbation procedure combined with inverse iteration. This strategy efficiently extracts the corresponding complex eigenvalues and eigenvectors within the same analytical framework.

3 Numerical Results

The CW formulation is assessed through the free vibration analysis of a damped laminated reinforced panel with five stiffeners. Its geometry and CUF(LE) cross-sectional discretization are shown in Fig. 2. Two representative cross-sections, A–A and C–C, are discretized independently to account for the local geometry induced by the stiffeners and are assembled through common nodal interfaces. The notation 25L9 & 33L9, for example, denotes 25 L9 elements at A–A and 33 L9 elements at C–C. The main geometric dimensions are a = b = 0.15 m, t = 0.05 m, and $h_1 = h_2 =$ 0.05 m.

Materials Research Proceedings 73 (2026) 274-279 https://doi.org/10.21741/9781644904459-53

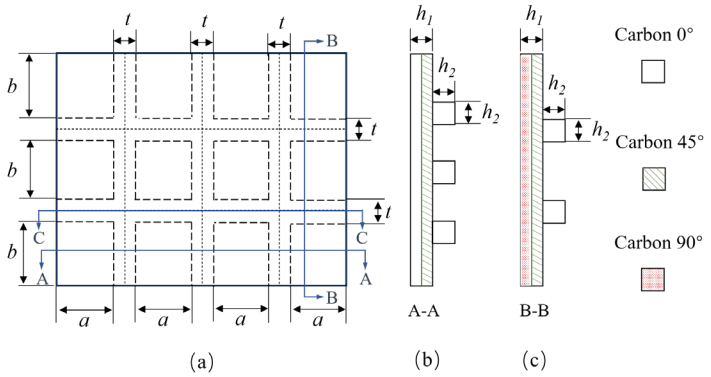

Fig. 2. Geometry and LE modeling of the eccentrically stiffened panel with five stiffeners: (a) top view; (b) A–A cross-section; (c) B–B cross-section.

The plate consists of two equal-thickness composite layers [45°/90°], while the stiffeners use a [0°] lamination with the same orthotropic material properties. The loss factors of the stiffener, middle, and bottom layers are $\eta_1 = 0.20$, $\eta_2 = 0.16$, and $\eta_3 = 0.12$, respectively.

Table 1. The first five complex frequencies (Hz) and modal damping ratios of the SFSF damped laminated reinforced panel.

Model	DOFs	Frequency (Hz)					Modal damping ratio (%)				
		First	Second	Third	Fourth	Fifth	First	Second	Third	Fourth	Fifth
3D FEM coarse	22707	160.12	165.71	278.82	400.36	406.64	8.09	7.91	7.98	7.76	7.82
3D FEM finer	169903	159.49	164.48	277.21	397.55	403.11	8.09	7.91	7.98	7.75	7.81
76L4 & 105L4	1892	163.28	168.77	283.72	411.51	417.73	8.12	7.93	8.01	7.78	7.83
25L9 & 33L9	2064	162.47	167.92	282.31	408.62	413.38	8.12	7.93	8.01	7.78	7.83
76L9 & 105L9	6548	159.45	164.51	277.46	398.12	404.54	8.11	7.92	7.99	7.76	7.82

Table 1 compares the first five complex frequencies and modal damping ratios under SFSF boundary conditions with ABAQUS C3D20 reference models. The refined 76L9 & 105L9 model gives the closest agreement with the finer 3D FEM solution, while using only 6,548 DOFs compared with 169,903 DOFs. The higher-order L9 discretization provides sufficient cross-sectional kinematic richness to capture local bending, torsional, and shell-like deformation induced by the stiffeners. The modal damping ratios are also reproduced accurately, confirming that the CW CUF(LE)-DDSM formulation retains three-dimensional accuracy with a substantially smaller computational model.

Conclusions

1. Lagrange-based CUF models provide a flexible higher-order representation of the three-dimensional displacement field. Their LW and CW capabilities enable solid regions, thin-walled members, composite layers, stiffeners, and damping layers to be treated within the same cross-sectional modeling framework.
2. The dynamic stiffness formulation provides an exact frequency-domain solution for the adopted CUF kinematics and avoids conventional element refinement along the structural axis. Combined with the WW algorithm, accurate broadband natural-frequency extraction can therefore be achieved with relatively few generalized degrees of freedom.
3. By introducing complex constitutive properties, the conventional CUF(LE)-DSM formulation is naturally extended to CUF(LE)-DDSM. The hybrid WW and homotopy perturbation strategy enables the corresponding complex eigenvalues and mode shapes to be extracted efficiently.
4. Comparisons with three-dimensional finite element models demonstrate that the proposed method can reproduce flexural, torsional, coupled, and shell-like vibration modes with substantially reduced computational size. The formulation also captures the influence of heterogeneous material loss factors on modal damping characteristics.

Acknowledgment

The authors appreciate the supports from the National Natural Science Funds for Distinguished Young Scholar (52325211), National Natural Science Foundation of China (52372348, 52172399) which made this research possible.

References

[1] L. Euler. De curvis elasticis. Lausanne and Geneva: Bousquet, 1744.

[2] S.P. Timoshenko. On the correction for shear of the differential equation for transverse vibrations of prismatic bars. Philosophical Magazine, 41(245):744-746, 1921. https://doi.org/10.1080/14786442108636264

[3] S.P. Timoshenko. On the transverse vibrations of bars of uniform cross section. Philosophical Magazine, 43(1):125-131, 1992. https://doi.org/10.1080/14786442208633855

[4] K. Kapania and S. Raciti. Recent advances in analysis of laminated beams and plates. Part I - Sheareffects and buckling. AIAA Journal, 27(7):923-935, 1989. https://doi.org/10.2514/3.10202

[5] K. Kapania and S. Raciti. Recent Advances in Analysis of Laminated Beams and Plates, Part II:Vibrations and Wave Propagation. AIAA Journal, 27(7):935-946, 1989. https://doi.org/10.2514/3.59909

[6] E. Carrera, A. Pagani, M. Petrolo, and E. Zappino. Recent developments on refined theories for beams with applications. Mechanical Engineering Reviews, 2(2), 2015. https://doi.org/10.1299/mer.14-00298

[7] E. Carrera, G. Giunta, and M. Petrolo. Beam Structures. John Wiley & Sons, 2011. https://doi.org/10.1002/9781119978565

[8] E. Carrera and M. Petrolo. Refined beam elements with only displacement variables and plate/shell capabilities. Meccanica, 47(3):537-556, 2012. https://doi.org/10.1007/s11012-011-9466-5

[9] E. Carrera, M. Cinefra, E. Zappino, and M. Petrolo. Finite Element Analysis of Structures through Unified Formulation. John Wiley & Sons, 2014. https://doi.org/10.1002/9781118536643

[10] E. Carrera and M. Petrolo. Refined beam elements with only displacement variables and plate/shell capabilities. Meccanica, 47(3):537-556, 2012. https://doi.org/10.1007/s11012-011-9466-5

[11] E. Carrera and M. Petrolo. Refined one-dimensional formulations for laminated structure analysis. AIAA Journal, 50(1):176-189, 2012. https://doi.org/10.2514/1.J051219

[12] G. Giunta, F. Biscani, S. Belouettar, A. J.M. Ferreira, and E. Carrera. Free vibration analysis of composite beams via refined theories. Composites Part B: Engineering, 44(1):540-552, 2013. https://doi.org/10.1016/j.compositesb.2012.03.005

[13] A. Pagani, E. Carrera, J. R. Banerjee, P. H. Cabral, G. Caprio, and A. Prado. Free vibration analysis of composite plates by higher-order 1D dynamic stiffness elements and experiments. Composite Structures, 118:654-663, 2014. https://doi.org/10.1016/j.compstruct.2014.08.020

[14] Y. Yan, A. Pagani, and E. Carrera. Exact solutions for free vibration analysis of laminated, box and sandwich beams by refined layer-wise theory. Composite Structures, 175:28-45, 2017. https://doi.org/10.1016/j.compstruct.2017.05.003

[15] J. R. Banerjee and A. Ananthapuvirajah. Coupled axial-bending dynamic stiffness matrix for beam elements. Computers and Structures, 215:1-9, 2019. https://doi.org/10.1016/j.compstruc.2019.01.007

[16] J. R. Banerjee. Dynamic stiffness formulation and its application for a combined beam and a two degree-of-freedom system. Journal of Vibration and Acoustics, Transactions of the ASME, 125(3):351-358, 2003. https://doi.org/10.1115/1.1569943

[17] WH. Wittrick and FW. Williams. A general algorithm for computing natural frequencies of elastic structures. Quarterly Journal of Mechanics and Applied Mathematics, 24(3):263-284, 1971. https://doi.org/10.1093/qjmam/24.3.263

Materials Research Proceedings 73 (2026) 280-283 https://doi.org/10.21741/9781644904459-54

Design of Sandwich Panels for Lightweight Vibroacoustic Performance

Nuno R. COSTA[1,a], José F. AGUILAR MADEIRA[2,b], Aurélio ARAÚJO[1,c], Girolamo DI CARA[3,d], Michele D'OTTAVIO[3,e], Olivier POLIT[3,f]

[1]IDMEC, Instituto Superior Técnico, Universidade de Lisboa, Lisboa, Portugal

[2]IDMEC, ISEL, Instituto Politécnico de Lisboa, Lisboa, Portugal

[3]LEME, Université Paris Nanterre, Ville d'Avray, France

[a]nuno.r.costa@tecnico.ulisboa.pt, [b]aguilarmadeira@tecnico.ulisboa.pt, [c]aurelio.araujo@tecnico.ulisboa.pt, [d]dicarag@parisnanterre.fr, [e]mdottavi@parisnanterre.fr, [f]opolit@parisnanterre.fr

Keywords: Vibroacoustics, Direct MultiSearch, Sublaminate Formulation, Multilayered Plates, Ritz Method

Abstract. This work introduces a unified framework for the multi-objective optimisation of lightweight sandwich panels, integrating the Sublaminate Generalised Unified Formulation with the Direct MultiSearch algorithm. Structural responses are predicted using the Sublaminate Generalised Unified–Ritz approach, while radiated sound power is evaluated through a directly coupled Rayleigh-based method that enables accurate and computationally efficient vibroacoustic assessment across a wide range of panel configurations. The optimisation space spans six candidate materials—including metals, composites, cores, and viscoelastic layers—together with ply thicknesses, fibre orientations, and symmetry constraints, with Hashin criteria ensuring structural integrity. The resulting Pareto sets reveal a clear trade-off between mass and vibroacoustic performance: lightweight carbon-fibre-reinforced plastic panels exhibit strong radiation at resonance, whereas heavier, well-damped metallic and hybrid solutions achieve markedly lower sound power levels. Overall, the proposed Sublaminate Generalised Unified Formulation–Direct MultiSearch framework provides a robust and extensible foundation for physics-informed optimisation of lightweight vibroacoustic structures.

Introduction

The development of high-performance lightweight structural systems is a primary objective in aerospace and automotive engineering, where mass reduction directly correlates with improved fuel efficiency and reduced environmental impact. In aerospace applications, marginal weight reductions can lead to substantial savings in fuel consumption and greenhouse gas emissions over the lifecycle of an aircraft. Similarly, in the automotive sector, reducing vehicle weight enhances fuel economy and general performance while maintaining safety and durability standards. Achieving these targets requires the integration of advanced materials and robust multi-objective optimisation strategies to navigate the trade-offs between conflicting requirements, such as structural stiffness and acoustic insulation or strength and cost.

Among contemporary structural solutions, sandwich panels provide a high stiffness-to-weight ratio and multifunctional adaptability. These panels, typically comprising stiff outer skins and a lightweight core, can be tailored through strategic material selection and layering strategies.

The present work advances the state of the art by introducing a unified framework for the broadband vibroacoustic optimisation of hybrid panels. Unlike previous studies by some of the authors—which focused on active control or specific damping configurations — this research integrates refined through thickness structural kinematics with broadband radiation-based acoustic

Content from this work may be used under the terms of the Creative Commons Attribution 3.0 license. Any further distribution of this work must maintain attribution to the author(s) and the title of the work, journal citation and DOI. Published under license by Materials Research Forum LLC.

Materials Research Proceedings 73 (2026) 280-283 https://doi.org/10.21741/9781644904459-54

metrics. The specific contributions are: (i) Unified computational framework: The SGUF coupled with the Ritz method is integrated for the first time with the DMS algorithm for multi-objective optimization; (ii) Broadband vibroacoustic objective: A scalar objective function based on the arc length of the radiated sound power spectrum is proposed to capture frequency dependent behaviour across the entire band of interest; (iii) Comprehensive design study: The methodology is demonstrated on a design space comprising six material families (steel, aluminium, CFRP, GFRP, honeycomb, viscoelastic) with Hashin failure constraints.

Unlike most existing vibroacoustic optimisation studies, which rely on finite elements or surrogate-based approaches, the present framework integrates refined SGUF structural modelling with broadband acoustic metrics within a deterministic derivative-free multiobjective optimisation setting. Insert introduction content here.

Methodology

In this work, a multi-objective optimisation strategy based on the Direct MultiSearch (DMS) algorithm, originally proposed by Custódio et al. [1], is employed. The DMS algorithm belongs to the broader class of direct search methods, which have been extensively studied due to their robustness and suitability for derivative-free optimisation in both single and multiobjective contexts. These approaches are particularly effective when objective functions are expensive to evaluate, lack analytical gradients, or are treated as black boxes, as is common in vibroacoustic simulations using the SGUF framework.

The Sublaminate Generalised Unified Formulation (SGUF) is a versatile and computationally efficient framework for modelling layered composite structures, allowing the seamless integration of various materials, geometries, and boundary conditions within a single unified approach [2, 3]. The proposed optimisation framework is developed under the following modelling assumptions:

(i) The structural response is linear, assuming small deformations and harmonic steady-state excitation; (ii) Material behavior is linear elastic for metallic and composite layers. Viscoelastic layers are modelled using a frequency-dependent complex modulus based on a discrete Prony-series (generalized Maxwell) representation; (iii) Perfect bonding is assumed between all layers, with no interfacial slip or delamination; (iv) The plate is assumed to be flat, with no geometric nonlinearities or initial imperfections; (v) Structural boundary conditions are simply supported along all edges; (vi) Acoustic radiation is computed using the Rayleigh integral, assuming the plate is mounted in an infinite rigid baffle and radiates into a semi-infinite fluid domain; (vii) A one-way vibroacoustic coupling is considered: the structural vibration field generates acoustic radiation, but the radiated acoustic pressure does not feed back into the structural response.

The sandwich panel optimisation problem is formulated as a constrained multi-objective problem, where the design vector includes material indices, fibre orientation angles, and layer thicknesses. Each candidate panel configuration is evaluated with respect to mass and acoustic objectives. To assess structural integrity the stress-based Hashin failure criterion is applied to evaluate the failure indices of each individual ply.

Numerical Results

A sandwich plate is considered, with in-plane dimensions of 300mm × 200mm. For the present optimisation framework, each sandwich panel is defined physically as a stack of six plies drawn from the material palette. These plies may correspond to stiff skins (steel, aluminium, CFRP, GFRP) or to weak/thick core layers (honeycomb or viscoelastic). The physical arrangement is described by the material type, ply thickness, and fibre orientation, together with a global symmetry condition. This definition reflects how a real panel would be manufactured: thin and stiff face-sheets enclosing one or more core plies, with optional damping interlayers.

The boundary conditions for all simulations correspond to simply supported edges, ensuring comparability with previous studies and simplifying modal analysis. The loading is a uniform

impulsive pressure applied to the bottom surface of the plate at t=0. The displacements and velocities are calculated through the plate's response at the top surface. The DMS optimisation was executed until the termination criterion was satisfied, requiring a total of 4048 objective function evaluations. The final nondominated set comprises 123 distinct configurations spanning the mass vibroacoustic trade-off (Figure 1). The well-distributed nature of the Pareto front and the consistent satisfaction of the Hashin failure constraints across all solutions provide empirical evidence of the robustness and practical convergence of the optimisation process. Also in Figure 1 is the representation of the sound power level versus frequency for the selected sandwich panel configurations.

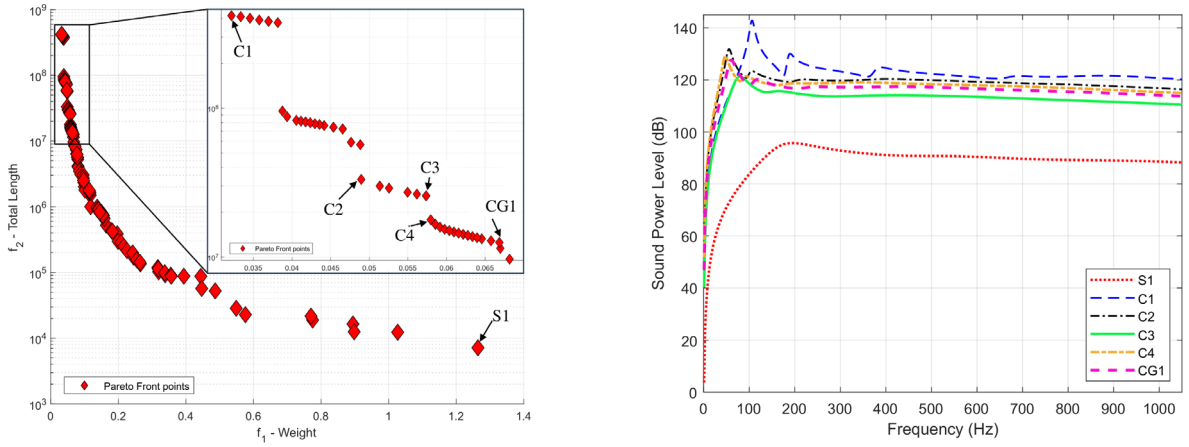

Figure 1 – Pareto Front with analysed plate configurations highlighted (left) and sound power level of the selected sandwich panel configurations.

Conclusions

The results demonstrate that the combined SGUF–DMS approach enables high-fidelity predictions of both structural and acoustic responses across a wide variety of sandwich panel configurations. The Pareto fronts obtained clearly illustrate the fundamental trade-off between minimising mass and enhancing sound insulation, allowing for the identification of optimal compromise solutions suitable for diverse engineering applications. Detailed comparison of selected designs confirms the effectiveness of including viscoelastic layers and thicker cores to achieve substantial reductions in radiated sound power, with all resulting configurations meeting the imposed failure criteria for composite and metallic layers.

The methodology established in this work provides a comprehensive foundation for future research on multi-functional composite structures, including the integration of additional objectives, more advanced biocomposite systems, or manufacturing constraints. Such developments will be critical for advancing the design of next-generation lightweight, sustainable, and acoustically efficient components for aerospace, automotive, and related industries.

Acknowledgment

The authors acknowledge Fundação para a Ciência e a Tecnologia (FCT) for its financial support via LAETA (project https://doi.org/10.54499/UID/50022/2025).

References

[1] A. Custódio, J. Madeira, A. Vaz, L. Vicente, Direct multisearch for multiobjective optimization, SIAM Journal on Optimization 21 (2011) 1109–1140. https://doi.org/10.1137/10079731X

[2] M. D'Ottavio, A Sublaminate Generalized Unified Formulation for the analysis of composite structures and its application to sandwich plates bending, Composite Structures 142 (2016) 187–199. https://doi.org/10.1016/j.compstruct.2016.01.087

[3] R. Vescovini, L. Dozio, Analysis of monolithic and sandwich panels subjected to non-uniform thickness-wise boundary conditions, Curved and Layered Structures 5 (2018) 232–232. https://doi.org/10.1515/cls-2018-0017

Materials Research Proceedings 73 (2026) 284-289 https://doi.org/10.21741/9781644904459-55

Dynamic Stiffness Method for Free Vibration of Beams and Frameworks with Cutouts

J. Ranjan BANERJEE[1,a *] and David KENNEDY[2,b]

[1]School of Science and Technology, City St. George's, University of London, Northampton Square, London EC1V 0HB, United Kingdom

[2]School of Engineering, Cardiff University, Queen's Buildings, The Parade, Cardiff CF24 3AA, United Kingdom

[a]j.r.banerjee@citystgeorges.ac.uk, [b]kennedydcf64@aol.com

Keywords: Dynamic Stiffness, Free Vibration, Beams, Cutouts, Wittrick-Williams Algorithm

Abstract. The free vibration behaviour of beams and frames with rectangular cutouts is investigated by the dynamic stiffness method. Essentially, the beam is split into three components, of which the middle one is the cutout portion. The dynamic stiffness matrix of the beam is assembled from those of the three parts using symbolic computation, and is related to the degrees of freedom at the end nodes by partial Gauss elimination. The Wittrick-Williams algorithm is applied to analyse the in-plane and out-of-plane free vibration characteristics. Representative results are presented with important conclusions drawn.

Introduction

Cutouts occur frequently in engineering structures to provide accessibility, inspection and weight reduction. While finite element analysis of structures with cutouts can provide approximate results, there is a scarcity of analytical methods based on closed form solutions due to difficulties arising principally from geometric discontinuities. Free vibration analysis of beams with cutouts has been reported by relatively few investigators [1-4]. Research in this area is important because the effects of cutouts on the free vibration behaviour of structures do not follow a predictable trend since the reductions of mass and stiffness due to cutouts usually have opposite effects on the natural frequencies. In this paper, attention is focused on free vibration of beams with rectangular cross-sections and with rectangular cutouts by using an exact dynamic stiffness method.

Theory

Fig. 1 shows a beam of rectangular cross-section with length L, width b and thickness h. A rectangular cutout commences at a distance L_1 from the left-hand end and has length L_0 and width b_0 as shown. Essentially the beam has three components of which the middle one is the cutout portion. The dynamic stiffness matrices of the three components are obtained using Bernoulli-Euler beam theory [5], and are assembled into the dynamic stiffness matrix of the complete beam. Note that the node numbering in Fig. 1(b) necessitates a standard rotation transformation [6] for the left-hand component. Symbolic algebra [7] is used to perform partial Gaussian elimination on he degrees of freedoms for nodes 1 and 2, to formulate the forc-displacement relationship for the end nodes of the beam in the form of the dynamic stiffness matrix [8]. Next, free vibration analysis for motion in both the XY (i.e., out-of-plane) and XZ planes (i.e., in-plane) is performed using the Wittrick-Williams algorithm [9]. Because the Bernoulli-Euler assumption is most suited for beams with a high slenderness ratio b/h, the illustrative examples which follow focus on out-of-plane free vibration (i.e. in the XY-plane). Advanced theories [10-12] can be applied to beams with a lower slenderness ratio.

Content from this work may be used under the terms of the Creative Commons Attribution 3.0 license. Any further distribution of this work must maintain attribution to the author(s) and the title of the work, journal citation and DOI. Published under license by Materials Research Forum LLC.

Materials Research Proceedings 73 (2026) 284-289 https://doi.org/10.21741/9781644904459-55

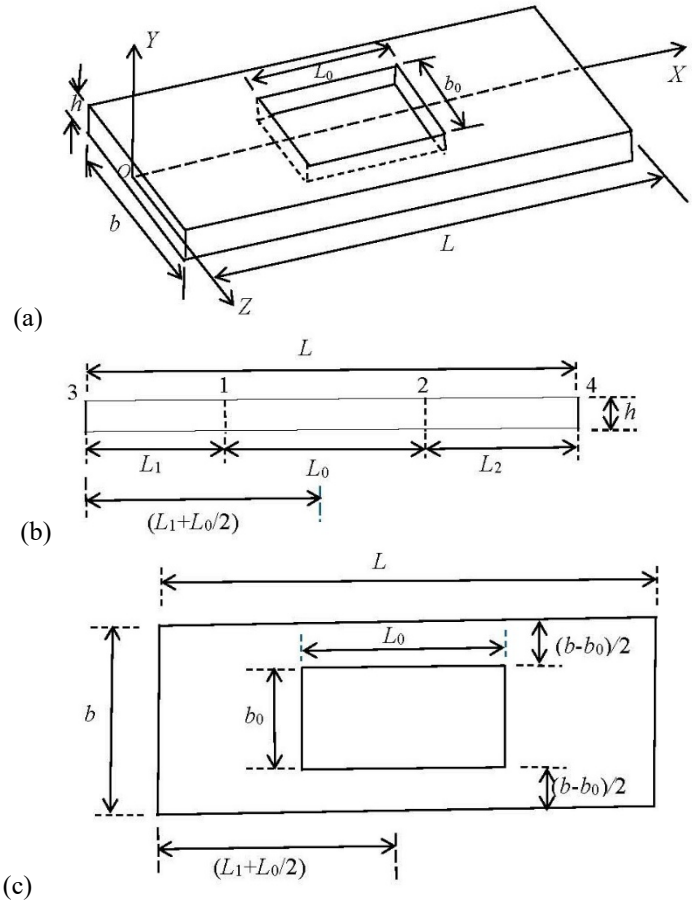

Fig. 1. A beam with a rectangular cross-section and with a rectangular cutout. Isometric view. (b) View on the XY plane. (c) View on the XZ plane

Results and Discussion

The theory of this paper was validated against two- and three-dimensional COMSOL finite element models [13]. Referring to Fig. 1, the beam analysed had L=1m, L_0=0.2m, L_1=L_2=0.4m, b=0.1m, b_0=0.04m and h=0.01m. The beam material is steel with Young's modulus E=210 GPa and density ρ = 7850 kg/m^3. Table 1 shows the first five natural frequencies ω_i for vibration of the beam in the XY plane, for Clamped-Free (C-F), Simple support-Simple support (S-S) and Clamped-Clamped (C-C) boundary conditions. The maximum discrepancy with the COMSOL results is less than 2%. Representative mode shapes are shown for cantilever (C-F) boundary conditions in Fig. 2 and broadly agree with those from COMSOL.

The next sets of results were obtained in terms of the non-dimensional parameters $\eta_1 = L_0/L$, $\eta_2 = b_0/b$ and $\eta_3 = (L_1 + L_0/2)/L$, respectively representing the relative length, width and location of the cutout.

Fig. 3 illustrates the effects of varying each of these parameters in turn, showing the natural frequencies ω_i^c of the beam with a cutout relative to those of an intact beam ω_i^u. Fig. 3(a) shows no appreciable changes in the natural frequencies. The minor fluctuations in the natural frequencies with the cutout length do not follow any pattern and appear to be independent of the order of the natural frequencies. Fig. 3(b) shows that increasing the cutout width slightly reduces the natural frequencies, except for the fourth natural frequency which increases slightly as the width is increased. Fig. 3(c) indicates that the fundamental natural frequency increases with η_3, i.e. when the cutout is further away from the built-in end. However, the other four natural frequencies diminish with η_3, with some fluctuations in the amount of decrease. This can be

Materials Research Proceedings 73 (2026) 284-289 https://doi.org/10.21741/9781644904459-55

attributed to disproportionate effects of the reductions in the mass and stiffness of the beam due to the cutout.

Table 1. Natural frequencies of a beam with a rectangular cutout using the present theory and COMSOL [13] for out-of-plane free vibration in the XY plane (see Fig. 1).

Freq. No (i)	Natural frequency ω_i [rad/s]								
	Boundary conditions								
	C-F			S-S			C-C		
	Present theory	COMSOL		Present theory	COMSOL		Present theory	COMSOL	
		Solid element	Plate element		Solid element	Plate element		Solid element	Plate element
1	51.793	51.934	51.914	143.43	141.89	141.88	346.74	346.67	349.23
2	324.25	323.76	323.62	586.38	583.81	583.78	916.60	920.98	920.17
3	914.77	913.65	913.20	1331.9	1331.4	1331.3	1813.9	1831.6	1830.0
4	1817.9	1827.0	1826.1	2334.9	2314.5	2314.1	2955.0	2948.8	2945.9
5	2956.0	2938.5	2936.8	3715.6	3729.1	3728.3	4491.3	4525.7	4521.0

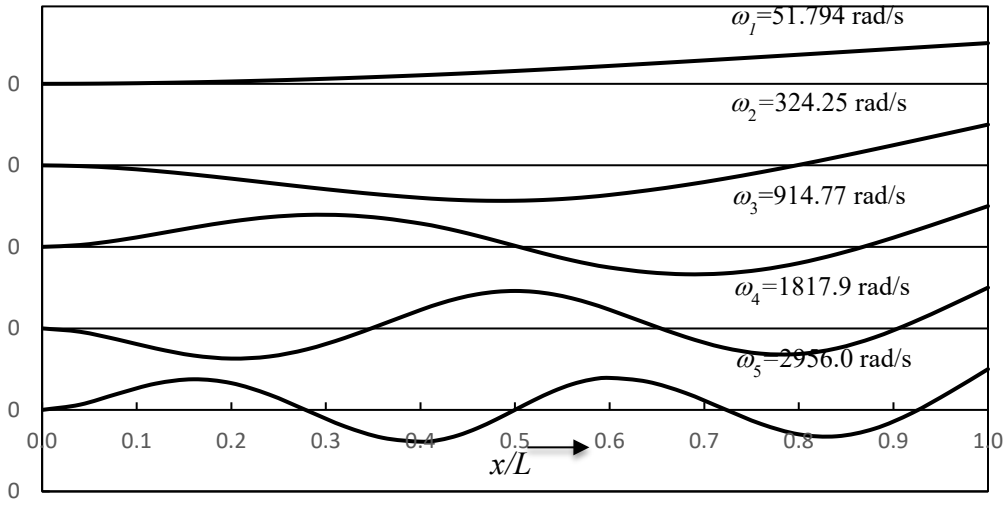

Fig. 2. Mode shapes of a cantilever beam with a rectangular cutout using present theory.

Representative results for in-plane free vibration in the *XZ*-plane are shown in Table 2. The results showed complete agreement with the space frame computer program BUNVIS-RG [14] for which the cutout was represented by an equivalent stepped beam analogy.

The final set of results was obtained for the portal frame shown in Fig. 4. Each member has length L = 1m, width b = 0.10m and thickness h = 0.01m. The vertical members are uniform, but the horizontal member has a central rectangular cutout with dimensions L_0 = 0.2m, $L_1 = L_2$ = 0.4m and b_0 = 0.04m. The material properties are Young's modulus E=210 GPa and density ρ = 7850 kg/m^3. The first ten natural frequencies of the frame for free vibration in the *XY* and *XZ* planes are shown in Table 3 alongside the corresponding results when there was no cutout. The cutout generally increases the natural frequencies, with a greater effect on out-of-plane free vibration. This is expected because the reduction in the bending stiffness due to the cutout follows a cubic variation with b_0 as opposed to the linear variation for in-plane free vibration.

Materials Research Proceedings 73 (2026) 284-289 https://doi.org/10.21741/9781644904459-55

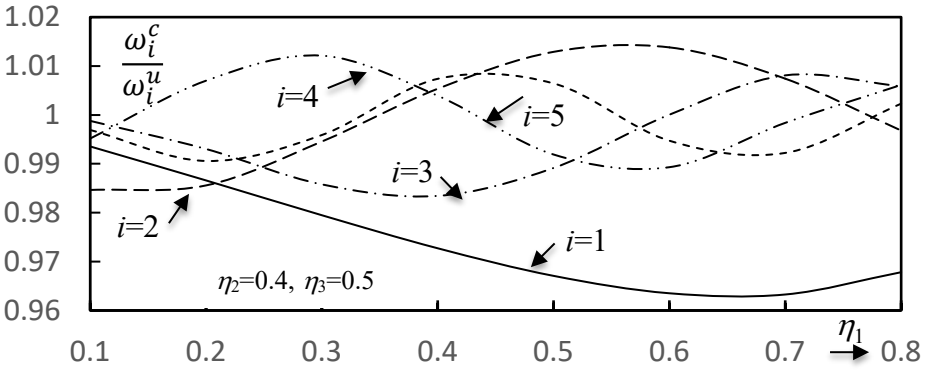

(a)

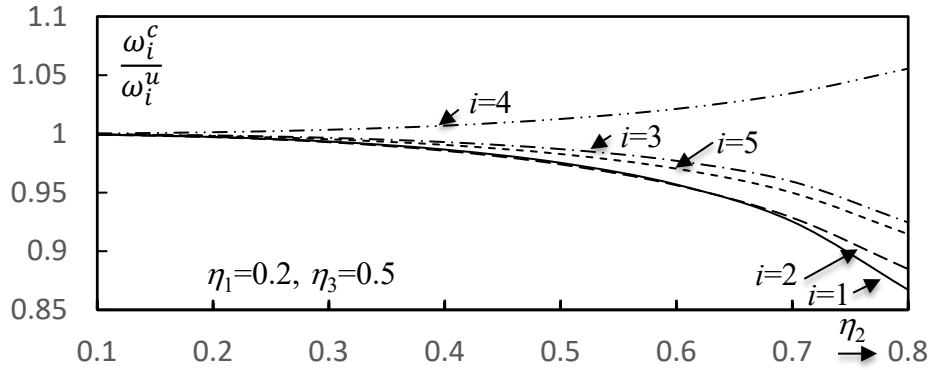

(b)

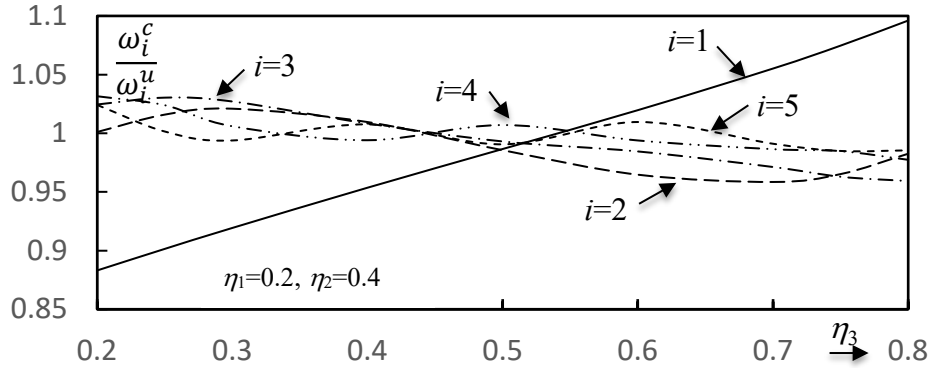

(c)

Fig. 3. Variation of natural frequencies of a beam with C-F boundary condition freely vibrating in the XY plane with: (a) length (η_1); (b) width (η_2); and (c) location (η_3) of cutout.

Table 2. Natural frequencies of a beam with a rectangular cutout using the present theory for in-plane free vibration in the XZ-plane (see Fig. 1).

Frequency Number (i)	Natural frequencies ω_i (rad/s)		
	Boundary conditions		
	C-F	S-S	C-C
1	533.540	1852.64	3680.70
2	3540.93	5943.11	9333.07
3	7928.51	14168.5	17603.9
4	9327.33	17603.9	19191.4
5	19212.7	24220.7	29920.1

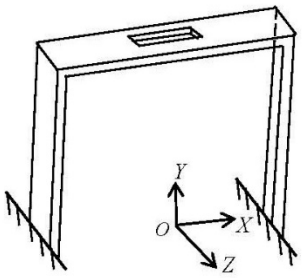

Fig. 4. A portal frame with a rectangular cutout on its horizonal member

Table 3. Natural frequencies of a portal frame with and without a cutout in its central member

Frequency Number (i)	Natural frequencies ω_i (rad/s)			
	Free vibration in XY plane		Free vibration in XZ plane	
	With cutout	Without cutout	With cutout	Without cutout
1	49.0239	47.8459	489.404	477.370
2	189.363	188.812	1945.55	1853.04
3	309.764	308.002	3094.36	3072.81
4	338.204	333.932	3302.57	3210.75
5	672.589	674.442	5798.85	5774.21
6	824.808	823.858	7405.92	7382.24
7	954.122	952.987	7898.44	7898.58
8	1449.47	1446.19	8015.08	7992.29
9	1709.96	1708.21	10202.7	10131.1
10	1804.07	1801.43	12583.6	13378.2

Conclusions

The dynamic stiffness matrix of a beam with a rectangular cross-section and with a rectangular cutout is developed by the application of symbolic computation. The Wittrick-Williams algorithm is used to compute the natural frequencies and mode shapes of beams with cutouts for different boundary conditions. Results are validated against the finite element program COMSOL and the space frame program BUNVIS-RG. An illustrative example of a portal frame comprising a member with cutout is also given. For these problems the cutouts have little effect on the free vibration characteristics, probably because the loss of stiffness due to the cutout is compensated by the loss of structural mass. The investigation is expected to pave the way for further research on the effects of cutouts on the free vibration of complex structures.

Acknowledgement

The authors thank Xueyi Zhao of Central South University, China for obtaining COMSOL results.

References

[1] K.H. Almitani, A. Abdelrahman, M.A. Eltaher, On forced and free vibrations of cutout squared beams, Steel Compos. Struct. 32 (2014) 643-655. https://doi.org/10.12989/scs.2019.32.5.643

[2] E. Demir, A study on natural frequencies and damping ratios of composite beams with holes, Steel Compos. Struct. 21 (2016) 1211-1226. http://dx.doi.org/10.12989/scs.2016.21.6.1211

[3] H. Mousavi, M. Azhari,·M.M. Saadatpour, S. Sarrami-Foroushani, Application of improved element-free Galerkin combining with finite strip method for buckling analysis of channel-section beams with openings, Eng. with Comput. 38 (2022) 739–755. https://doi.org/10.1007/s00366-020-01087-8

[4] U. Kafkas, On the free vibration of a perforated Rayleigh beam with deformable ends, Eng. Sci. Tech. Int. J. 56 (2024) 101787. https://doi.org/10.1016/j.jestch.2024.101787

[5] F.W. Williams, W.P. Howson, Compact computation of natural frequencies and buckling loads for plane frames, Int. J. Numer. Meth. Eng. 11 (1977) 1067-1081. https://doi.org/10.1002/nme.1620110704

[6] K.J. Bathe, Finite Element Procedures in Engineering Analysis, Prentice-Hall, Englewood Cliffs, 1982.

[7] J. Fitch, Solving algebraic problems with REDUCE, J. Symb. Comput. 1 (1985) 211-227. https://doi.org/10.1016/S0747-7171(85)80015-8

[8] J.R. Banerjee, D. Kennedy, Dynamic stiffness method for free vibration of beams and frameworks with cutouts, Mech. Adv. Mater. Struct. 33 (2026) 2699288. https://doi.org/10.1080/15376494.2006.2699288

[9] W.H. Wittrick, F.W. Williams, A general algorithm for computing natural frequencies of elastic structures, Quart. J. Mech. Appl. Math. 24 (1971) 263-284. http://dx.doi.org/10.1093/qjmam/24.3.263

[10] J.R. Banerjee, D. Kennedy, I. Elishakoff, Further insights into the Timoshenko–Ehrenfest beam theory, J. Vib. Acous. 144 (2022) 061011. https://doi.org/10.1115/1.4055974

[11] V.Z. Vlasov, Thin-Walled Elastic Beams, 2nd edition, National Science Foundation, Washington D.C., 1961.

[12] E. Carrera, G. Giunta, Refined beam theories based on a unified formulation, Int, J. Appl. Mech. 2 (2010) 117-143. https://doi.org/10.1142/S1758825110000500

[13] COMSOL Multiphysics Reference Manual, Version 6.4, COMSOL AB, Stockholm. www.comsol.com

[14] M.S. Anderson, F.W. Williams, J.R. Banerjee, B.J. Durling, C.L. Herstorm, D. Kennedy, D.B. Warnaar, User manual for BUNVIS-RG: an exact buckling and vibration program for lattice structures, with repetitive geometry and substructuring options. NASA Technical Memorandum 87669, 1986.

Materials Research Proceedings 73 (2026) 290-293 https://doi.org/10.21741/9781644904459-56

Shell Finite Elements with Arbitrary Fields Along the Thickness by using RMVT

Erasmo CARRERA[1,a], and Daniele SCANO[1,b *]

[1]Full Mul2 Lab, DIMEAS, Politecnico di Torino, Corso Duca degli Abruzzi 24, Torino, Italy

[a]erasmo.carrera@polito.it, [b]daniele.scano@polito.it

Keywords: Shell Models, Composite Structures, Refined Kinematic, RMVT, Refined Stress Analysis, Lagrange Polynomials

Abstract. Enhanced two-dimensional finite elements based on the Reissner Mixed Variational Theorem are introduced in this paper. In this formulation, the three displacements and the three out-of-plane stresses constitute the unknowns of the mechanical problem. The development is carried out within the Carrera Unified Formulation, which permits the selection of the desired theory. The proposed approach allows for the independent selection of models for each of the six generalized variables, employing both Taylor and Lagrange expansions. Lagrange-based functions are used for the finite element discretization. Validation of the method is performed for the bending of a laminated composite shell by comparison with literature results and highly refined benchmark solutions. The findings indicate that optimal results can be achieved through careful selection of the employed model.

Introduction

This work develops advanced two-dimensional finite elements for the analysis of composite laminated shell structures under mechanical loading. Composite materials are lighter than isotropic alternatives, and their mechanical behavior can be tailored through lamination. However, their inherent anisotropy introduces complex phenomena, including layerwise shear continuity, the characteristic zig-zag displacement pattern (often referred to as the C_z^0 requirements [1]), and strong coupling between in-plane and out-of-plane strains. To model these complex responses accurately, highly refined structural theories are required. One effective strategy is to employ the Reissner Mixed Variational Theorem (RMVT) [2], a variational principle that treats out-of-plane stress components as independent unknowns alongside displacements. While RMVT generally delivers more accurate stress predictions compared to the Principle of Virtual Displacements (PVD), it involves six unknowns per node, which leads to a higher computational cost. Nevertheless, the improved accuracy in stress evaluation often justifies the additional expense, particularly in thick or highly heterogeneous laminates.

This work adopts an enhanced version of the Carrera Unified Formulation (CUF) to develop a flexible structural modeling framework that allows the most suitable shell theory to be selected for each problem. A consistent formulation is developed, enabling users to choose theories with a desired level of accuracy. To strike a balance between accuracy and computational efficiency, the formulation integrates both Equivalent Single Layer (ESL) and Layer-Wise (LW) approaches, supporting Lagrange- and Taylor-based thickness expansions within a unified mathematical setting. In previous work by Carrera and Scano [3], this method was applied within the PVD framework, yielding interesting results for stress calculations. The aim of the present paper is to extend that work by demonstrating the potential of introducing out-of-plane stresses as independent unknowns through the RMVT. In particular, the paper investigates how the additional degrees of freedom can be exploited to capture interlaminar stress continuity more accurately and to reduce the computational cost associated with highly refined layer-wise models. Numerical benchmarks are presented to compare the performance of the proposed mixed formulation against

Content from this work may be used under the terms of the Creative Commons Attribution 3.0 license. Any further distribution of this work must maintain attribution to the author(s) and the title of the work, journal citation and DOI. Published under license by Materials Research Forum LLC.

Materials Research Proceedings 73 (2026) 290-293 https://doi.org/10.21741/9781644904459-56

traditional displacement-based approaches, highlighting the trade-offs between accuracy, model complexity, and computational effort.

Methodology

In the CUF framework, it is possible to express the three displacements and three shear stresses as:

$$\begin{aligned}
u_\alpha^k(\alpha,\beta,z) &= N_i(\alpha,\beta)F_{u_\alpha\tau}^k(z)q_{\alpha_{\tau i}}^k \quad \text{with } \tau = 1,\dots,M_{u_\alpha}; i = 1,\dots,N_n \\
u_\beta^k(\alpha,\beta,z) &= N_i(\alpha,\beta)F_{u_\beta\tau}^k(z)q_{\beta_{\tau i}}^k \quad \text{with } \tau = 1,\dots,M_{u_\beta}; i = 1,\dots,N_n \\
u_z^k(\alpha,\beta,z) &= N_i(\alpha,\beta)F_{u_z\tau}^k(z)q_{z_{\tau i}}^k \quad \text{with } \tau = 1,\dots,M_{u_z}; i = 1,\dots,N_n \\
\sigma_{\alpha z}^k(\alpha,\beta,z) &= N_i(\alpha,\beta)F_{\sigma_{\alpha z}\tau}^k(z)q_{\alpha z_{\tau i}}^k \quad \text{with } \tau = 1,\dots,M_{\sigma_{\alpha z}}; i = 1,\dots,N_n \\
\sigma_{\beta z}^k(\alpha,\beta,z) &= N_i(\alpha,\beta)F_{\sigma_{\beta z}\tau}^k(z)q_{\beta z_{\tau i}}^k \quad \text{with } \tau = 1,\dots,M_{\sigma_{\beta z}}; i = 1,\dots,N_n \\
\sigma_{zz}^k(\alpha,\beta,z) &= N_i(\alpha,\beta)F_{\sigma_{zz}\tau}^k(z)q_{zz_{\tau i}}^k \quad \text{with } \tau = 1,\dots,M_{\sigma_{zz}}; i = 1,\dots,N_n
\end{aligned} \tag{1}$$

where $F_{u_\alpha\tau}^k$, $F_{u_\beta\tau}^k$, $F_{u_z\tau}^k$, $F_{\sigma_{\alpha z}\tau}^k$, $F_{\sigma_{\beta z}\tau}^k$, and $F_{\sigma_{zz}\tau}^k$, denote the expansion functions associated with the generalized displacements $q_{\alpha_{\tau i}}^k$, $q_{\beta_{\tau i}}^k$, $q_{z_{\tau i}}^k$, $q_{\alpha z_{\tau i}}^k$, $q_{\beta z_{\tau i}}^k$, and $q_{zz_{\tau i}}^k$, respectively. The superscript k indicates the mathematical domain along the thickness. The index τ indicates summation, while M_{u_α}, M_{u_β}, M_{u_z}, $M_{\sigma_{\alpha z}}$, $M_{\sigma_{\beta z}}$, and $M_{\sigma_{zz}}$ represent the number of expansion terms for each displacement component. Moreover, N_i denotes the shape functions, with the repeated subscript i implying summation, and N_n the number of shape functions per element. Nine-node Lagrange-based elements are adopted for the present results.

By applying the Reissner Mixed Variational Theorem, the weak form of the equilibrium equations can be derived, which leads directly to the finite element stiffness matrix formulation. Further details on this derivation can be found in reference [2]. As a result, the following six governing equations may be written as follows

$$\begin{aligned}
&\delta q_{\alpha_{sj}}^k: K_{u_\alpha u_\alpha s\tau ji}^k q_{\alpha_{\tau i}}^k + K_{u_\alpha u_\beta s\tau ji}^k q_{\beta_{\tau i}}^k + K_{u_\alpha u_z s\tau ji}^k q_{z_{\tau i}}^k + K_{u_\alpha \sigma_{\alpha z} s\tau ji}^k q_{\alpha z_{\tau i}}^k + K_{u_\alpha \sigma_{\beta z} s\tau ji}^k q_{\beta z_{\tau i}}^k + K_{u_\alpha \sigma_{zz} s\tau ji}^k q_{zz_{\tau i}}^k = P_{u_\alpha sj}^k \\
&\delta q_{\beta_{sj}}^k: K_{u_\beta u_\alpha s\tau ji}^k q_{\alpha_{\tau i}}^k + K_{u_\beta u_\beta s\tau ji}^k q_{y_{\tau i}}^k + K_{u_\beta u_z s\tau ji}^k q_{z_{\tau i}}^k + K_{u_\beta \sigma_{\alpha z} s\tau ji}^k q_{\alpha z_{\tau i}}^k + K_{u_\beta \sigma_{\beta z} s\tau ji}^k q_{\beta z_{\tau i}}^k + K_{u_\beta \sigma_{zz} s\tau ji}^k q_{zz_{\tau i}}^k = P_{u_\beta sj}^k \\
&\delta q_{z_{sj}}^k: K_{u_z u_\alpha s\tau ji}^k q_{\alpha_{\tau i}}^k + K_{u_z u_\beta s\tau ji}^k q_{y_{\tau i}}^k + K_{u_z u_z s\tau ji}^k q_{z_{\tau i}}^k + K_{u_z \sigma_{\alpha z} s\tau ji}^k q_{\alpha z_{\tau i}}^k + K_{u_z \sigma_{\beta z} s\tau ji}^k q_{\beta z_{\tau i}}^k + K_{u_z \sigma_{zz} s\tau ji}^k q_{zz_{\tau i}}^k = P_{u_z sj}^k \\
&\delta q_{\alpha z_{sj}}^k: K_{\sigma_{\alpha z} u_\alpha s\tau ji}^k q_{\alpha_{\tau i}}^k + K_{\sigma_{\alpha z} u_\beta s\tau ji}^k q_{y_{\tau i}}^k + K_{\sigma_{\alpha z} u_z s\tau ji}^k q_{z_{\tau i}}^k + K_{\sigma_{\alpha z} \sigma_{\alpha z} s\tau ji}^k q_{xz_{\tau i}}^k + K_{\sigma_{\alpha z} \sigma_{\beta z} s\tau ji}^k q_{yz_{\tau i}}^k + K_{\sigma_{\alpha z} \sigma_{zz} s\tau ji}^k q_{zz_{\tau i}}^k = 0 \\
&\delta q_{\beta z_{sj}}^k: K_{\sigma_{\beta z} u_\alpha s\tau ji}^k q_{\alpha_{\tau i}}^k + K_{\sigma_{\beta z} u_\beta s\tau ji}^k q_{y_{\tau i}}^k + K_{\sigma_{\beta z} u_z s\tau ji}^k q_{z_{\tau i}}^k + K_{\sigma_{\beta z} \sigma_{\alpha z} s\tau ji}^k q_{xz_{\tau i}}^k + K_{\sigma_{\beta z} \sigma_{\beta z} s\tau ji}^k q_{yz_{\tau i}}^k + K_{\sigma_{\beta z} \sigma_{zz} s\tau ji}^k q_{zz_{\tau i}}^k = 0 \\
&\delta q_{zz_{sj}}^k: K_{\sigma_{zz} u_\alpha s\tau ji}^k q_{\alpha_{\tau i}}^k + K_{\sigma_{zz} u_\beta s\tau ji}^k q_{y_{\tau i}}^k + K_{\sigma_{zz} u_z s\tau ji}^k q_{z_{\tau i}}^k + K_{\sigma_{zz} \sigma_{\alpha z} s\tau ji}^k q_{xz_{\tau i}}^k + K_{\sigma_{zz} \sigma_{\beta z} s\tau ji}^k q_{yz_{\tau i}}^k + K_{\sigma_{zz} \sigma_{zz} s\tau ji}^k q_{zz_{\tau i}}^k = 0
\end{aligned} \tag{2}$$

This work introduces a novel formulation of the Fundamental Nucleus (FN). The key innovation lies in treating the FN components $K_{mls\tau ji}^k$ and P_{msj}^k as scalar quantities rather than the conventional 6×6 matrix representation [1]. The explicit expressions of $K_{mls\tau ji}^k$ and P_{msj}^k are not presented in this work for brevity. Assembly of the contributions from all generalized components, finite element nodes, and elements leads to the following global system: $\mathbf{KU} = \mathbf{P}$.

Numerical Results

The paper compares the present models with the results from the open literature [5]. Figure 1 presents the geometric details of a simply-supported composite shell. The curvature ratio is defined as $R_\beta/b = \pi/3$. A thick structure is considered with $R_\beta/h = 4$. The axial length a is taken as unitary. The shell features a three-layered stacking sequence given by $[0^\circ/90^\circ/0^\circ]$. The composite material is orthotropic, with the following elastic properties: $E_L/E_T = 25, E_T/E_z = 1, \nu_{LT} = \nu_{Tz} = \nu_{Lz} = 0.25, G_{LT}/E_T = G_{Lz}/E_T = 0.5, G_{Tz}/E_T = 0.2$. Here, the subscript L denotes the fiber

Materials Research Proceedings 73 (2026) 290-293 https://doi.org/10.21741/9781644904459-56

direction, while T and z denote the transverse and thickness directions, respectively. The shell is simply supported at its straight edges.

A sinusoidal pressure load is applied on the top surface of the shell and is expressed as $p = P_z \sin(\pi\beta/b)$, where P_z is the pressure amplitude. The following dimensionless quantities are adopted. The transverse displacement is normalized as $\bar{u}_z = 10E_T u_z/[P_z h(R_\beta/h)^4]$. The circumferential normal stress is defined as $\bar{\sigma}_{\beta\beta} = \sigma_{\beta\beta}/[P_z(R_\beta/h)^2]$. The transverse shear stress is given by $\bar{\sigma}_{\beta z} = \sigma_{\beta z}/[P_z(R_\beta/h)]$.

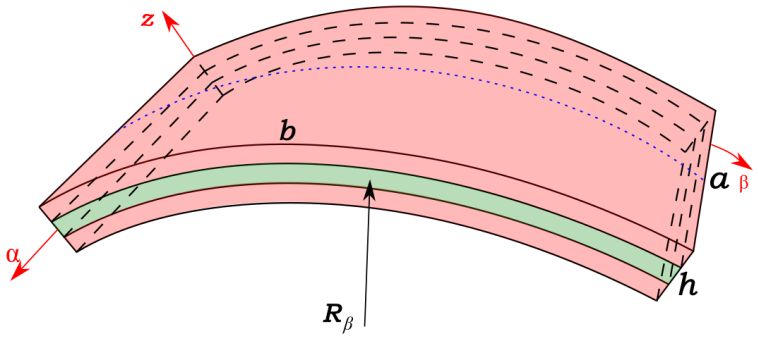

Figure 1: Properties of the three-layer composite shell. The study case is taken from [5].

In Table 1, a comparison is made between the present models and the analytical solution from reference [5]. In addition to the RMVT models, a refined PVD model is presented that employs two Lagrange CUF elements. For the RMVT models, one Lagrange expansion is used for each material layer. Regarding notation, in Lagrange expansions, the number indicates the number of Lagrangian points, while in Taylor expansions, the polynomial order is indicated. On the mid-surface, fifteen Q9 Lagrange finite elements are adopted. For each model, the table reports the transverse displacements, the in-plane and shear stresses, and the number of Degrees of Freedom (DOF).

Table 1: Models used for the three-layered shell and relative results.

Model	$\bar{u}_z^{\mathrm{a}}$	$\bar{\sigma}_{\beta\beta}^{\mathrm{b}}$	$\bar{\sigma}_{\beta z}^{c}$	DOF
Exact[5]	0.457	1.367	0.476	–
$\mathrm{PVD}_{\mathrm{2LE4-2LE4-2LE4}}$	0.458	1.372	0.477	5301
$\mathrm{RMVT}^{\mathrm{LE4-LE4-LE4}}_{\mathrm{LE4-LE4-LE4}}$	0.458	1.376	0.476	5508
$\mathrm{RMVT}^{\mathrm{0-LE4-TE2}}_{\mathrm{0-LE4-TE2}}$	0.458	1.376	0.476	2418
$\mathrm{RMVT}^{\mathrm{0-LE4-TE2}}_{\mathrm{0-TE6-TE2}}$	0.457	1.240	0.445	2139

(a): Computed at $[a/2, b/2, h/2]$; (b): Computed at $[a/2, b/2, h/2]$;
(c): Computed at $[a/2, 0, 0]$.

Figures 2a and 2b illustrate the trends for the in-plane (at $[a/2, b/2, z]$) and shear stresses (at $[a/2, 0, z]$) along the thickness, respectively.

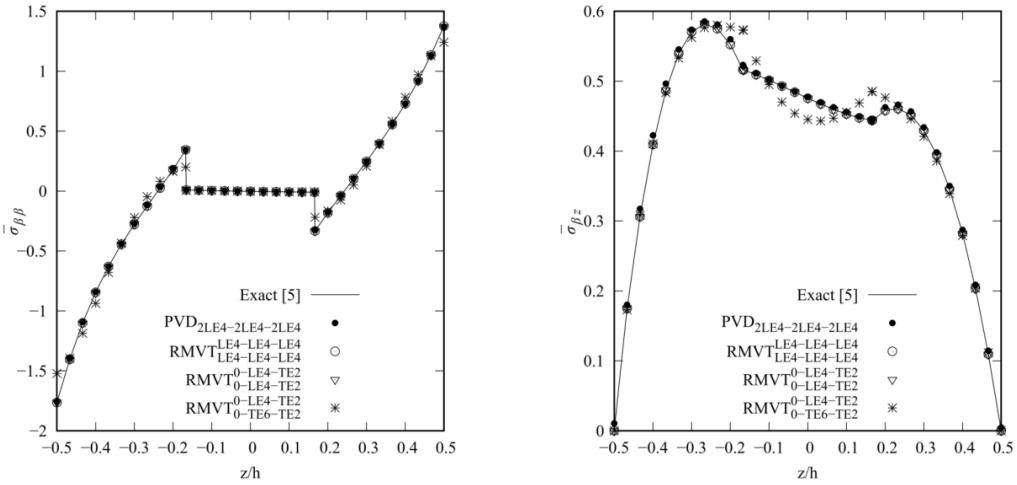

Figure 2: In-plane and shear stresses along $\mathbf{z}$ *of the three-layered shell.*

The previous analysis shows that the CUF models successfully replicate the analytical results. Furthermore, the displacement component u_α and the shear stress component $\sigma_{\alpha z}$ can be completely neglected. It is also observed that both u_z and σ_{zz} may be adequately approximated using a second-order Taylor model. For these reasons, the $\mathrm{RMVT}^{0-LE4-TE2}_{0-LE4-TE2}$ model proves to be the most convenient. The model $\mathrm{RMVT}^{0-LE4-TE2}_{0-TE6-TE2}$ is also noteworthy.

Conclusions

This work presents an enhanced formulation for the analysis of two-dimensional structures based on the Carrera Unified Formulation (CUF). By rethinking the conventional CUF approach and restructuring the assembly of finite element matrices, the proposed method introduces greater flexibility. Its core novelty lies in allowing distinct expansions for each displacement and stress variable, using both Taylor- and Legendre-based expansions. The present paper demonstrates that the proposed method can effectively combine different types of expansions and polynomial orders, thereby enabling a substantial reduction in degrees of freedom through judicious selection of expansions for each generalized displacement. It is also shown that, under certain conditions, Taylor expansions may be employed for the assumed stresses. Directions for future work include extending this formulation to nonlinear and multifield analyses.

References

[1] E. Carrera, M. Cinefra, M. Petrolo, E. Zappino, Finite Element Analysis of Structures Through Unified Formulation, Wiley, Amsterdam, 2014. https://doi.org/10.1002/9781118536643

[2] E. Carrera, Theories and Finite Elements for Multilayered Plates and Shells: A Unified compact formulation with numerical assessment and benchmarking, Arch. Comput. Methods Eng. 10 (2003) 215–296. https://doi.org/10.1007/BF02736224

[3] E. Carrera, D. Scano, Composite shell finite elements with arbitrary displacement fields along the thickness, Mech. Adv. Mater. Struct. 32 (2025) 1–21. https://doi.org/10.1007/s00419-022-02210-5

[4] K.J. Bathe, Finite Element Procedure, Prentice hall, Upper Saddle River, New Jersey, USA, 1996.

[5] J.G. Ren, Exact solutions for laminated cylindrical shells in cylindrical bending, Compos. Sci. Technol. 29 (1987) 169–187. https://doi.org/10.1016/0266-3538(87)90069-8

Materials Research Proceedings 73 (2026) 294-297 https://doi.org/10.21741/9781644904459-57

Dynamic Analysis of Bolted Rotor Systems using CUF-Based Beam Models and Interface Friction Modelling

Rodolfo AZZARA[1,a *], Yulian JIANG[2,b], Matteo FILIPPI[1,c], Chaofeng LI[2,3] and Erasmo CARRERA[1,d]

[1]Department of Mechanical Engineering and Aerospace Engineering, Politecnico di Torino, Corso Duca degli Abruzzi 24, 10129, Turin, Italy

[2]School of Mechanical Engineering and Automation, Northeastern University, Shenyang 110819, China

[3]Key Laboratory of Vibration and Control of Aero-Propulsion System Ministry of Education, Northeastern University Shenyang, 110819, China

[a]rodolfo.azzara@polito.it, [b]yljiangneu@foxmail.com, [c]matteo.filippi@polito.it, [d]erasmo.carrera@polito.it

Keywords: CUF, FEM, Higher-Order Beam Models, Rotordynamics, Bolted Joints, Stick-Slip

Abstract. Bolted joints are widely employed in high load rotor systems such as aero-engines, where frictional stick-slip at the interfaces significantly influences the system's dynamic response. These nonlinear effects cannot be captured adequately by conventional linearized stiffness models. To address this limitation, a high fidelity structural model of bolted rotor systems is developed using the Carrera Unified Formulation (CUF). CUF provides a procedure for automatically and hierarchically obtaining lower- and higher-order one-dimensional beam models. The linearized equations of motion include the Coriolis and initial stress contributions. A frictional contact model is integrated to capture the time varying stick-slip behavior at bolted interfaces. The proposed CUF-based methodology with bolted-interface friction modelling provides an effective tool for analyzing bolted rotor systems and offers valuable insights for the design of bolted joints in rotating machinery.

Introduction

Rotating systems are key components in high-performance applications such as aircraft engines, gas turbines, and power transmission systems. The demand for lightweight designs and higher operating speeds has led to increasingly complex rotor assemblies, typically composed of shafts, disks, and drums connected through bolted [1]. Although essential for modularity and manufacturability, these joints introduce structural discontinuities and nonlinear effects that strongly influence the overall dynamic behaviour of the system. From a dynamics standpoint, bolted interfaces exhibit complex mechanical behaviour governed by contact interactions, friction, preload-dependent stiffness, and possible interface slip. Under operating conditions, especially at high rotational speeds, the interaction between unbalance forces and friction can cause transitions between sticking, slipping, and separation. These phenomena generate nonlinear and time-varying responses, affecting vibration levels, frequency content, and system stability. Despite their importance, many traditional modelling approaches simplify bolted joints as linear stiffness elements or lumped parameters. While computationally efficient, such assumptions neglect key nonlinear effects like hysteresis, energy dissipation, and higher harmonic generation, potentially resulting in inaccurate predictions, particularly in modern high-speed rotors. To address these limitations, several studies have developed advanced finite element (FE) models to better capture the behaviour of bolted rotor assemblies, see for example Refs [2,3,4].

Content from this work may be used under the terms of the Creative Commons Attribution 3.0 license. Any further distribution of this work must maintain attribution to the author(s) and the title of the work, journal citation and DOI. Published under license by Materials Research Forum LLC.

Materials Research Proceedings 73 (2026) 294-297 https://doi.org/10.21741/9781644904459-57

In this context, this study proposes high-fidelity one-dimensional (1D) models as an efficient alternative to classical beam theories and full solid FE models. Refined 1D formulations based on higher-order kinematics allow improved representation of shear deformation, rotary inertia, and cross-sectional warping, while maintaining significantly lower computational costs. The approach is based on the Carrera Unified Formulation (CUF) [5] enabling advanced modelling of rotating bolted structures through the use of Lagrange polynomials. The interface coupling between different bodies is enabled through Lagrange multipliers. The governing equations include rotational effects such as Coriolis forces and spin softening [6] and the transient response is computed using an implicit time integration scheme.

Rotordynamic equation in CUF form and friction modelling

The basic theory needed for study the dynamic response of rotating structure is detailed in [6]. Nonetheless, to maintain the self-contained nature of this work, some essential equations are included below. According to the CUF and FEM, the 3D displacement field for a generic beam model is expressed as:

$$\boldsymbol{u}(x,y,z;t) = F_\tau(x,z)N_i(y)\boldsymbol{q}_{\tau i} \quad \tau = 1, \ldots, \mathrm{M} \quad i = 1, \ldots, N_n \tag{1}$$

in which F_τ stands for the expansion functions, N_i denotes the shape functions, $\boldsymbol{q}_{\tau i}$ represents the unknown nodal variables, M represents the order of the expansion, N_n is the number of nodes per element, t indicates time, and the repeated indexes stand for summation.

To account for local dissipation mechanisms arising at contact interfaces, the structural formulation is enriched with a frictional constraint enforced through Lagrange multipliers and governed by a Jenkins-type model [7]. Let u_t denote the relative tangential displacements at the interface and f_t the corresponding tangential forces. The Jenkins law is expressed as:

$$f_t = k_{Jenk}(u_t - u_t^P), \tag{2}$$

where u_t^P is the plastic (sliding) component of the displacement and k_{Jenk} denotes the stiffness of the bolted connection. Stick-slip transitions are governed by the conditions:

$$STICK \quad |f_t| \leq \mu F_N \rightarrow f_t = f_t,\ u_t^P = 0, \quad SLIP \quad |f_t| > \mu F_N \rightarrow f_t = \mu F_N sign(u_t) \tag{3}$$

with μ the friction coefficient and F_N the normal reaction force. During stick, the response is purely elastic, whereas once the Coulomb bound is reached the force saturates at $F_{MAX} = \pm\mu F_N$, producing the characteristic hysteretic loop associated with energy dissipation. The interface kinematics are enforced through Lagrange multipliers acting along the local normal direction. To introduce these constraints in the CUF domain, the following expressions are used:

$$\Pi = \lambda^{\mathrm{T}}(\boldsymbol{u}^1(x_k,y_k,z_k) - \boldsymbol{u}^2(x_k,y_k,z_k))\lambda^{\mathrm{T}}\boldsymbol{B}\boldsymbol{q} \tag{4}$$

where B represents the matrix containing the Lagrange multipliers. The normal force is obtained as follows: $F_N = \lambda + F_{preload}$. By introducing the principle of virtual work and after simple mathematics operations, the resulting equations of motion for the rotating structure, including gyroscopic and centrifugal effects, read:

$$\boldsymbol{M}\ddot{\boldsymbol{q}}(t) + \boldsymbol{D}\dot{\boldsymbol{q}}(t) + \Omega\boldsymbol{G}\dot{\boldsymbol{q}}(t) + \left(\boldsymbol{K}_s + \Omega^2\boldsymbol{K}_\Omega + \dot{\Omega}\boldsymbol{K}_{\dot{\Omega}}\right)q(t) = \Omega^2\boldsymbol{F}_\Omega(t) + \dot{\Omega}\boldsymbol{F}_{\dot{\Omega}}(t) + F_{fric} \tag{5}$$

in which $\boldsymbol{M}$, $\boldsymbol{D}$, $\boldsymbol{G}$, $\boldsymbol{K}_s$, $\boldsymbol{K}_\Omega$, $\boldsymbol{K}_{\dot{\Omega}}$, $\boldsymbol{F}_\Omega$ and $\boldsymbol{F}_{\dot{\Omega}}$ indicate the assembled finite element arrays of the final FE model, F_{fric} is the assembled friction force vector, and Ω stands for the rotational speed.

Materials Research Proceedings 73 (2026) 294-297 https://doi.org/10.21741/9781644904459-57

Numerical examples

For the representative purpose, a clamped-clamped non-rotating bolted rotor model is considered, illustrated in Fig. 1. The material properties are the following: E = 210 GPa, ν = 0.3, and ρ= 7850 kg/m^3.

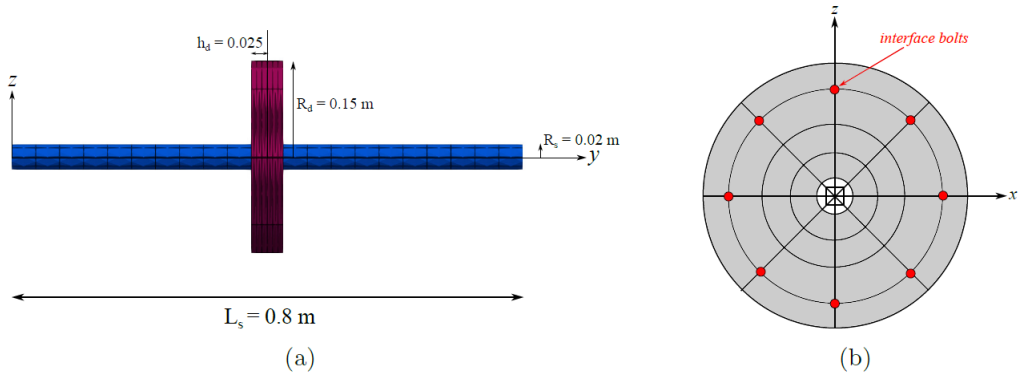

Figure 1. (a) Geometry of the bolted rotor model; (b) Interface contact model of the bolt connection.

Table 1 provides the natural frequencies at standstill, using the following mesh discretization: 10 B4 (for-node beam element) for each shaft and 3 B4 for each disk along the longitudinal axis and using 12 LE9 (nine-node Lagrange element) and 44 LE9 for the cross-section of the shaft and disk, respectively. Then, the dynamic response of the bolted rotor assembly is evaluated under a sinusoidal excitation with angular frequency ω = 2094 rad/s and an initial force amplitude of 43865 N applied simultaneously along the x- and z-directions. A pre-load of 100 N and a friction coefficient of 0.3 are assumed. Rayleigh damping is included in the analysis using the following parameters: α = 36.3 and $\beta = 3.28\times10^{-5}$.

Table 1. Natural frequencies of the bolted rotor system. Comparison between CUF 1D and ANSYS model.

Mode number	CUF	ANSYS	Error	Mode shape
1	96.53	96.22	0.32	
2	292.67	291.85	0.28	
3	1233.20	1243.10	-0.80	

Figure 2 shows the time domain response over a selected interval and the corresponding hysteresis loop at one of the interface bolts, respectively, considering $k_{Jenk} = 1.0\times10^8$.

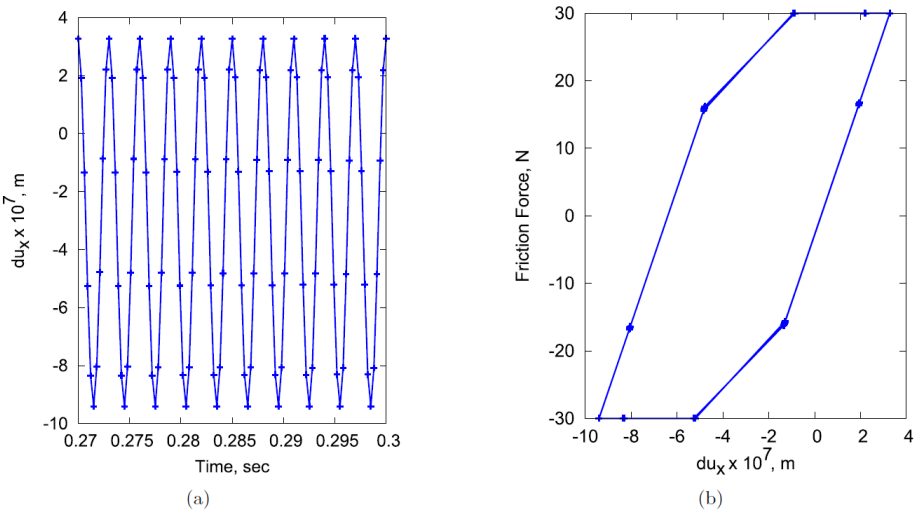

Figure 2. (a) Time domain response; (b) Hysteresis curve.

Conclusions

This study presented preliminary results on the dynamic response of bolted rotor systems modelled through one-dimensional finite elements and an interface friction formulation based on the Jenkins model. The displacement field of each element was interpolated using Lagrange expansions, while the mechanical coupling across the joint was enforced via Lagrange multipliers. Numerical simulations demonstrated the accuracy and robustness of the proposed strategy in automatically incorporating bolted-joint friction within a rotordynamic framework formulated using the Carrera Unified Formulation (CUF).

References

[1] Nguyen-Hoang M., and Becker W., 2020. Tension failure analysis for bolted joints using a closed-form stress solution. Composite Structures, 238, 111931. https://doi.org/10.1016/j.compstruct.2020.111931

[2] Yang, T., Ma, H., Qin, Z., Guan, H., and Xiong, Q., 2022. Coupling vibration characteristics of the shaft-disk-drum rotor system with bolted joints. Mechanical Systems and Signal Processing, 169, 108747. https://doi.org/10.1016/j.ymssp.2021.108747

[3] Sharos, P.A., and McCarthy, C.T., 2020. Novel finite element for near real-time design decisions in multi-fastener composite bolted joints under various loading rates. Composite Structures, 240, 112005. https://doi.org/10.1016/j.compstruct.2020.112005

[4] Wu, B., Wang, T., Xu, C., and Xu, B., 2010. Finite element analysis of behavior of bolted flange connections under bending loading. Applied Mechanics and Materials, 26, 1168-1171. https://doi.org/10.4028/www.scientific.net/AMM.26-28.1168

[5] Carrera, E., Cinefra, M., Petrolo, M., and Zappino, E., 2014. Finite element analysis of structures through unified formulation. John Wiley & Sons. https://doi.org/10.1002/9781118536643

[6] Azzara, R., Filippi, M., and Carrera, E., 2024. Geometrically nonlinear transient analyses of rotating structures through high-fidelity models. Composite Structures, 343, 118265. https://doi.org/10.1016/j.compstruct.2024.118265

[7] Jiang, Y., Zhao, Y., Cao, H., Li, C., and Zhou, J., 2025. Dynamic modeling of a shaft-disk system considering bolted interface friction. International Journal of Mechanical Sciences, 297, 110332. https://doi.org/10.1016/j.ijmecsci.2025.110332

Materials Research Proceedings 73 (2026) 298-301 https://doi.org/10.21741/9781644904459-58

Numerical Modeling of a Bistable Composite Piezoelectric Energy Harvester with Four-Corner Simply Supported Boundary Conditions

Danish BASHIR[1,2,a*], P.M. ANILKUMAR[2,b], S. SCHEFFLER[2,c], A. HALDAR[3,4,d], B.N. RAO[1,e], and R. ROLFES[2,f]

[1]Structural Engineering Laboratory, Department of Civil Engineering, Indian Institute of Technology Madras, 600 036 Chennai, India

[2]Institute of Structural Analysis, Leibniz Universität Hannover, Appelstraße 9A, 30167 Hannover, Germany

[3]Department of Civil Engineering, Indian Institute of Technology (BHU), 221005 Varanasi, India

[4]Department of Engineering Structures, Delft University of Technology, Stevinweg 1, 2628 CN Delft, the Netherlands

[a]ce21d402@smail.iitm.ac.in, [b]a.nair@isd.uni-hannover.de, [c]s.scheffler@isd.uni-hannover.de, [d]ayan.civ@itbhu.ac.in, [e]bnrao@iitm.ac.in, [f]r.rolfes@isd.uni-hannover.de

Keywords: Bistable Laminates, Piezoelectric, Finite Elements, Nonlinear Dynamics

Abstract. Bistable piezoelectric energy harvesters are attractive for harvesting energy from ambient vibrations because their large-amplitude cross-well motion can generate higher electrical output over a broader operating range than conventional linear harvesters. Among the available host structures, bistable composite laminates are particularly promising because they possess two stable equilibrium configurations and can transition between them under external excitation, thereby generating large strains and rich nonlinear dynamics that are well suited for energy conversion. In this work, a high-fidelity electromechanical finite element (FE) framework is developed in ABAQUS for a four corner simply supported (FCSS) bistable composite laminate energy harvester bonded with a Macro Fiber Composite (MFC) patch. The framework is used to predict the nonlinear dynamic response of the harvester and the corresponding open-circuit voltage under external harmonic excitation. To further evaluate the energy harvesting capability in terms of usable electrical output, the predicted open-circuit voltage is subsequently supplied as input to an electronic circuit simulation framework developed in LTspice, through which the corresponding power-harvesting performance is determined. The proposed combined FE–electronic circuit framework provides an integrated and robust approach for predicting both the structural dynamics and electrical power output of the FCSS bistable laminate–MFC energy harvester. The proposed framework provides an integrated basis for design assessment, performance evaluation, and parametric optimization of bistable piezoelectric energy-harvesting systems.

Introduction

Nonlinear piezoelectric energy harvesting systems have attracted considerable attention because of their ability to harvest ambient vibrational energy over a broad frequency range. Among various nonlinear concepts, bistable laminates are particularly attractive as host structures for energy harvesting applications. These laminates possess two stable equilibrium configurations and can undergo continuous snap-through transitions under external vibrations, thereby generating large strains [1]. When piezoelectric Macro Fiber Composites (MFCs) are bonded to their surfaces, these strains are converted into electrical energy through the piezoelectric effect. Bistable composite laminate-based energy harvesters have been investigated under various boundary conditions, laminate layups, and excitation scenarios. Among these, laminates with four-corner simply

Content from this work may be used under the terms of the Creative Commons Attribution 3.0 license. Any further distribution of this work must maintain attribution to the author(s) and the title of the work, journal citation and DOI. Published under license by Materials Research Forum LLC.

Materials Research Proceedings 73 (2026) 298-301 https://doi.org/10.21741/9781644904459-58

supported (FCSS) boundary conditions are of particular interest, as they can be mounted on vibrating host structures in multiple units, making them promising candidates for harvesting significant levels of ambient vibrational energy. Arrieta et al. [2] developed an energy harvester based on a center-fixed, square bistable composite laminate with MFCs. Wu et al. [3] investigated the nonlinear dynamic snap-through behavior of FCSS bistable laminates using theoretical and numerical frameworks, supported by experimental validation. Guo et al. [4] then examined the snap-through behavior and nonlinear oscillations of FCSS bistable composite laminates under foundation excitations using theoretical, numerical, and experimental approaches. Guo et al. [5] further explored the energy harvesting capabilities of bistable piezoelectric composite laminates under FCSS boundary conditions. Despite these studies, the development of an integrated numerical framework for predicting both the open-circuit voltage and power-harvesting capability of FCSS bistable energy harvesters under base excitation remains an ongoing research challenge. In this work, a numerical modeling approach is developed to predict the open-circuit voltage and power-harvesting capability of the FCSS energy harvester under base excitation.

Methodology

The configuration investigated in the present study is an FCSS bistable energy harvester, as shown in Fig. 1(a). The host vibrating structure consists of a 150 × 150 mm square bistable composite laminate with a [0/90] stacking sequence, as shown in Fig. 1(b), and a total thickness of 0.180 mm. A centrally bonded MFC M8557 P2 patch is attached to the laminate, and the material properties of both the laminate and MFC are taken from [6]. The simulation frameworks used in this study are briefly described in the subsequent subsections.

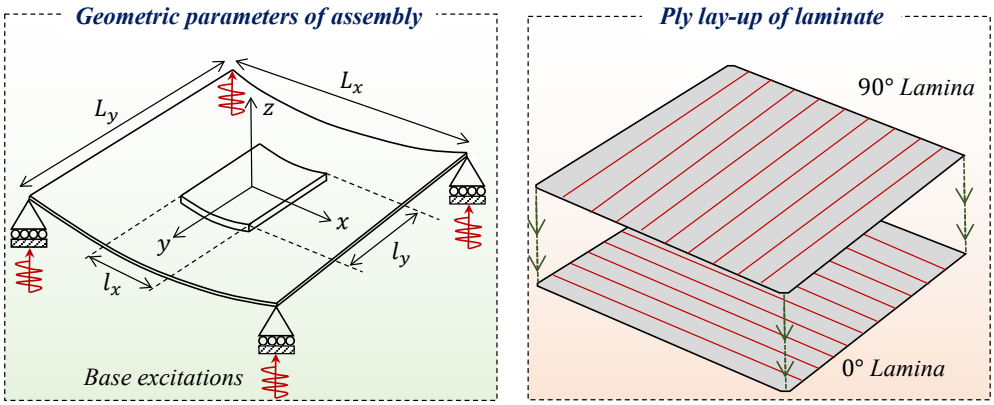

(a) (b)

***Fig 1**. Representation of (a) FCSS bistable energy harvester, (b) laminate stacking sequence*

FE framework: To determine the open-circuit voltage output of FCSS energy harvester a fully nonlinear FE model is developed in ABAQUS. The laminate is discretized using 4-noded quadrilateral shell elements (S4R), and the MFC patch is modeled using 3D piezoelectric solid elements (C3D20RE). The MFC is bonded to the laminate through a TIE constraint, while the top and bottom electrode nodes are constrained using EQUATION constraints, with the bottom electrode grounded. Geometric nonlinearity is included throughout the analysis using NLGEOM, and a curing temperature of 180 °C is applied to the entire laminate. The dynamic characteristics of the two stable shapes are extracted using the embedded LANCOZS eigen solver. Thereafter, a displacement-controlled excitation is applied at the four corners to obtain the voltage response of the FCSS harvester in different dynamic regimes.

Electronic simulations: After obtaining the open-circuit voltage from the FE framework, the energy harvesting performance of the FCSS bistable harvester is evaluated in LTspice. As shown in Fig 2, the harvester is represented by a voltage source defined by the peak open-circuit voltage

Materials Research Proceedings 73 (2026) 298-301 https://doi.org/10.21741/9781644904459-58

V_{peak} (from ABAQUS), forcing frequency ω, phase angle φ, and internal capacitance C_p (C_p = 548 nF) . This source charges a larger capacitor C_m (C_m= 10 µF in all electronic simulations) from 0 V to 5 V through a full-wave rectifier, corresponding to 125 μJ of harvested energy. The charging time of C_m obtained from the LTspice simulations is then used to determine the average power output of the harvester.

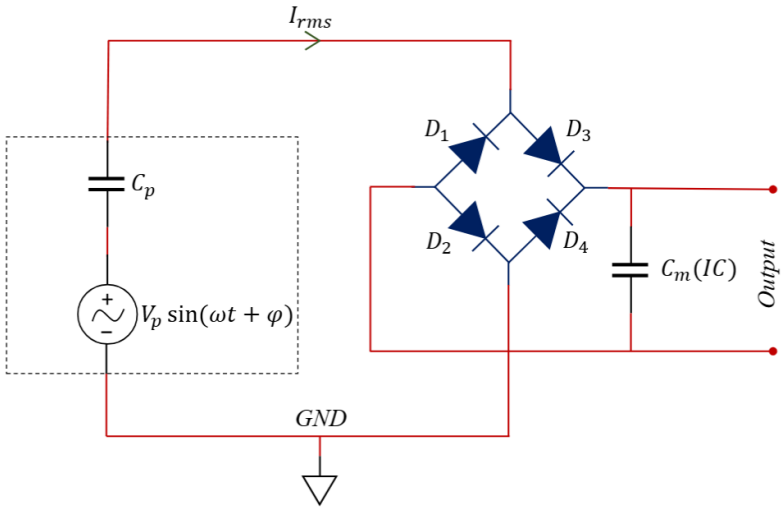

***Fig 2**. Schematic showing the circuit diagram of energy harvesting system*

Numerical Resuls

Using the LANCOZS solver and free-vibration analysis, the natural frequencies of the two stable shapes of the FCSS energy harvester were determined as 33.18 Hz and 34.14 Hz. A forcing frequency of 20 Hz, sufficiently below both natural frequencies, was selected, and the excitation amplitude was increased from 2 mm until cross-well oscillations occurred. As shown in Fig. 3(a), the harvester produced a peak open-circuit voltage of 5.43 V under single-well vibrations. When the excitation amplitude was increased to 7 mm, the harvester exhibited cross-well oscillations, continuously transitioning between the two stable states and generating much larger strains and voltage output. In this regime, a peak open-circuit voltage of 53.02 V was obtained, as shown in Fig. 3(b), confirming the effectiveness of cross-well oscillations for energy harvesting.

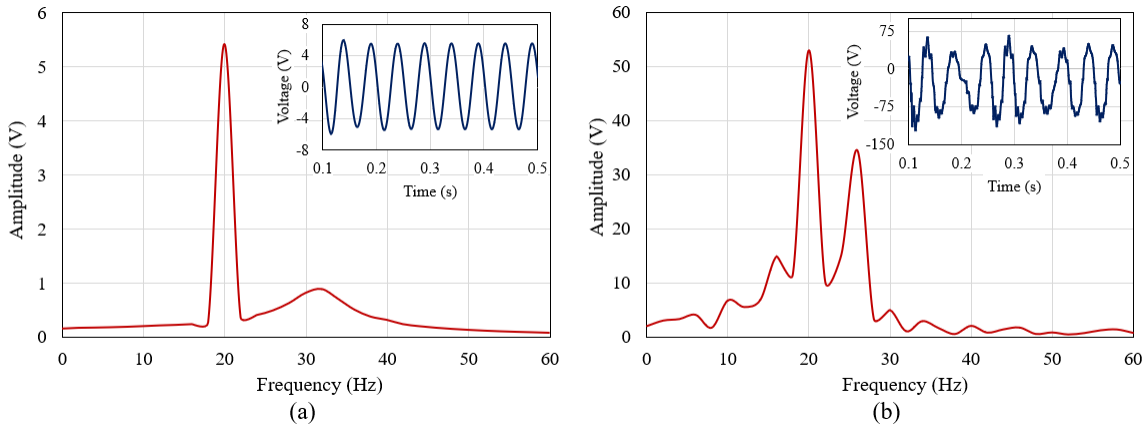

***Fig 3**. Predicted open-circuit voltage of the FCSS energy harvester at 20 Hz: (a) single-well oscillation, 2 mm; (b) cross-well oscillation, 7 mm*

The predicted output power of the energy harvester under the two dynamic regimes was calculated using LTSpice and is summarized in Table 1. The results clearly show that the FCSS energy harvester produces substantially higher output power during cross-well oscillations than

during single-well oscillations, confirming that cross-well oscillations constitute the most favorable dynamic regime for energy harvesting.

***Table 1**: Predicted average output power of the FCSS energy harvester in two dynamic regimes*

Dynamic regime	V_{peak} (V)	V_{rms} (V)	I_{rms} (mA)	Time (ms)	Power (μW)
Single-well	5.43	3.84	0.264	1423.06	87.84
Cross well	53.02	37.49	2.582	145.76	857.57

Conclusions

In this study, an efficient numerical framework was developed for evaluating the power-harvesting performance of the FCSS energy harvester. The framework comprises a fully nonlinear FE model implemented in ABAQUS to predict the natural vibration characteristics and open-circuit output voltage of the FCSS bistable energy harvester, followed by LTSpice-based electronic simulations to assess its power-harvesting capability. The results of the amplitude sweep at constant frequency confirm that cross-well motion is the most favorable dynamic regime for enhanced power harvesting. Overall, the proposed numerical framework provides a robust basis for future parametric investigations and design optimization studies.

Acknowledgment

The first author would like to acknowledge the German Academic Exchange Service: Deutscher Akademischer Austauschdienst - DAAD, and Prime Minister's Research Fellowship, India during the course of this research.

References

[1] Bashir, D., et al., A review of the dynamic behavior of thermally induced bistable configurations of unsymmetrical composite laminates and their applications, Arch. Comput. Methods Eng. 32 (2025) 1635–1677. https://doi.org/10.1007/s11831-024-10192-6

[2] Arrieta, A.F., et al., A piezoelectric bistable plate for nonlinear broadband energy harvesting, Appl. Phys. Lett. 97 (2010). https://doi.org/10.1063/1.3487780

[3] Wu, M.Q., Zhang, W., Chronopoulos, D., Nonlinear vibrations and dynamic snap-through behaviors of four-corner simply supported bistable asymmetric laminated composite square shell, Mech. Syst. Signal Process. 173 (2022) 109023. https://doi.org/10.1016/j.ymssp.2022.109023

[4] Guo, X.T., Zhang, W., Zhang, Y.F., Snap-through and nonlinear oscillations of bistable asymmetric FCSS composite laminated square plate subjected to excitation: Theoretical, numerical and experimental researches, Thin-Walled Struct. 179 (2022) 109669. https://doi.org/10.1016/j.tws.2022.109669

[5] Guo, X.T., et al., Nonlinear snap-through vibrations and energy harvesting for bistable piezoelectric composite laminated plate supported at four corners, Thin-Walled Struct. 210 (2025) 112991. https://doi.org/10.1016/j.tws.2025.112991

[6] Bashir, D., Anilkumar, P.M., Rao, B.N., Exploring the potential energy landscape of square bistable laminates bonded with piezoelectric macro fiber composites, Compos. Struct. 369 (2025) 119239. https://doi.org/10.1016/j.compstruct.2025.119239

Materials Research Proceedings 73 (2026) 302-306 https://doi.org/10.21741/9781644904459-59

Damage Localization Beyond Modal Curvature Methods

Giada FARACO[1,a], Andrea Vincenzo DE NUNZIO[1,b], Nicola Ivan GIANNOCCARO[1,c] and Arcangelo MESSINA[1,d *]

[1]University of Salento, Department of Innovation Engineering, Lecce, Italy

[a]giada.faraco@unisalento.it, [b]andreavincenzo.denunzio@unisalento.it, [c]ivan.giannoccaro@unisalento.it, [d]arcangelo.messina@unisalento.it

Keywords: Damage Detection, Damage Localization, Mode Shapes, Mode Shapes Derivatives

Abstract. Structural health monitoring and damage localization using non-destructive techniques have long been key research topics, aimed at detecting defects that may evolve into critical failures if left unnoticed. In this context, reference-free approaches are particularly important, since information about the undamaged state is often unavailable. Among the various techniques, vibration-based methods, and particularly the analysis of mode shapes, have been widely investigated. The curvature method, based on the second derivative of mode shapes, has attracted significant attention, proving to be one of the most reliable and established techniques for identifying localized stiffness reductions associated with damage without requiring baseline data. However, the use of second- or higher-order derivatives poses notable challenges when dealing with experimental data, as these operations tend to amplify measurement noise and complicate the estimation process. To overcome these limitations, the authors have proposed an extension of traditional curvature-based methods by introducing a novel damage indicator based on the first derivative of mode shapes, combined with appropriate filtering techniques. The aim of this manuscript is to provide an experimental validation of this previously developed approach, showing how it simplifies the computational procedure while preserving, and in some cases enhancing, the accuracy of damage detection and localization. As in conventional curvature-based methods, damage is identified through the presence of localized peaks in the derived indicators. The effectiveness of the proposed approach is demonstrated numerically, through a case study of a stepped beam with a circular cross-section.

Introduction

Structural Health Monitoring (SHM) has assumed growing importance due to its critical role in ensuring structural integrity and life safety. Among the great range of different technical and scientific approaches, the present work focuses on vibration-based methods, and in particular on the processing of mode shapes for the identification of damaged locations. In this context, the state of the art has been strongly shaped by the analysis of modal curvature [1]. This method has attracted substantial attention from the scientific community, also owing to its simplicity and the fact that it does not require baseline information on the undamaged structure. Damage can be identified by detecting peaks in the derivatives of static or dynamic mode shapes. For this, several authors have investigated the effectiveness of the second derivative (curvature) [2–5]. Other contributions showed that damage may also be detected through peaks in wavelet transforms [6–9]. Recently, curvature-based methods have been experimentally validated, compared, and applied to a wide range of structural configurations [10–13].

The aim of this manuscript is to investigate under which conditions the first derivative can replace, or complement, the second derivative in identifying damaged locations. This is particularly relevant because the estimation of first derivatives is generally less demanding than that of higher-order derivatives, especially when experimental data are contaminated by noise. So,

Content from this work may be used under the terms of the Creative Commons Attribution 3.0 license. Any further distribution of this work must maintain attribution to the author(s) and the title of the work, journal citation and DOI. Published under license by Materials Research Forum LLC.

Materials Research Proceedings 73 (2026) 302-306 https://doi.org/10.21741/9781644904459-59

a numerical validation of the previously proposed approach is here given, showing that it can simplify the computational procedure while preserving the accuracy of damage localization, depending on the structural configuration and on the mode shape under analysis.

Methodology

The proposed methodology [14,15] is derived with reference to a beam with circular cross-section under the assumptions of classical beam theory.

Considering the constitutive equations of the beam (assumed to be isotropic and homogeneous) the following two equations can be derived as written at a given instant of time:

$$\boldsymbol{\chi(x)} = \frac{\boldsymbol{M_b(x)}}{\boldsymbol{EJ}} \tag{1}$$

$$\boldsymbol{\theta_{,x}(x)} = \frac{\boldsymbol{M_t(x)}}{\boldsymbol{GJ_o}} \tag{2}$$

where $\boldsymbol{M_b}$is the bending moment and M_t the torque; $\boldsymbol{E}$ is Young's modulus while G represents the shear modulus; $\boldsymbol{J}$, and $\boldsymbol{J}_0$, are the geometric moment of inertia of the beam's cross-section. So, according to the curvature method [1], a localized reduction in flexural stiffness ($\boldsymbol{EJ}$) produces an abrupt variation in curvature $\boldsymbol{\chi(x)}$ (Eq. 1), which appears as a peak at the damaged section. However, analogously, as highlighted from Eq. 2, a localized reduction in torsional stiffness (*GJo*), in presence of a continuous torque, would also cause a change in the first derivative of the rotation angle $\boldsymbol{\theta}$*(x)*. Since rotational sensors are rarely available in practical applications, torsional mode shapes are reconstructed from the transverse displacement field $\boldsymbol{w(x)}$ measured through biaxial accelerometers, exploiting its proportional relationship with the torsional rotation angle $\boldsymbol{\theta(x)}$ ($\boldsymbol{w(x)} = \boldsymbol{R\theta(x)}$).

$$\boldsymbol{w_{,x}(x)} = \frac{\boldsymbol{M_t(x)}}{\boldsymbol{RGJ_o}} \tag{3}$$

Eqs. 1 and 3 show that damage localization can be achieved not only through the second derivative, but also through the first derivative. While curvature-based approaches are suitable for bending-dominated modes, first-derivative analysis is more appropriate for torsional modes. In structures exhibiting coupled flexural–torsional behaviour, both indicators should be considered jointly. The first and second derivatives were estimated through differentiator filters based on Lanczos convolution operators.

Numerical Results

The analysed case study considers a homogeneous and isotropic stepped beam with circular cross-section, clamped at one end and free at the other, with a total length of 600 mm. Under these assumptions, bending and torsional vibrations are naturally decoupled, thus enabling the independent analysis of the corresponding mode shapes. Damage was introduced by imposing a localized 30% reduction in the cross-sectional radius over a 2 mm-long region within the intermediate segment of the beam, resulting in a local reduction of both flexural and torsional stiffness.

Materials Research Proceedings 73 (2026) 302-306 https://doi.org/10.21741/9781644904459-59

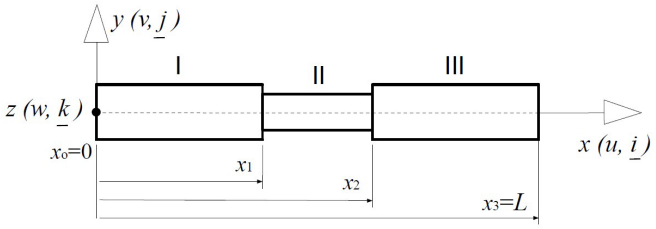

Figure 1. Stepped beam under investigation

The structural dynamics were modelled according to classical beam theory. Bending and torsional mode shapes were obtained by solving the governing differential equations through the transfer matrix method combined with the exponential matrix formulation [16]. The solution procedure requires the use of appropriate continuity and boundary conditions at the interfaces between beam segments, as well as at the clamped and free ends of the structure.

$$\boldsymbol{G\theta(x;t)_{,xx} = \rho\theta(x;t)_{,tt}} \tag{4}$$

$$\boldsymbol{EJy(x;t)_{,xxxx} + \rho Ay(x;t)_{,tt} = 0} \tag{5}$$

Mode shapes associated with the damaged configuration were sampled at 300 equally spaced points and contaminated with Gaussian noise in order to reproduce realistic experimental conditions. Two scenarios were considered: noise-free data and noisy data with a signal-to-noise ratio equal to 50 dB. The obtained numerical results were then used to compare the effectiveness of first- and second-derivative indicators in localizing structural damage through the occurrence of localized peaks in the processed mode shapes. In particular, Fig. 2 shows the results related to the damage localization based on the torsional mode shapes. Damage was located between 320 mm and 322 mm.

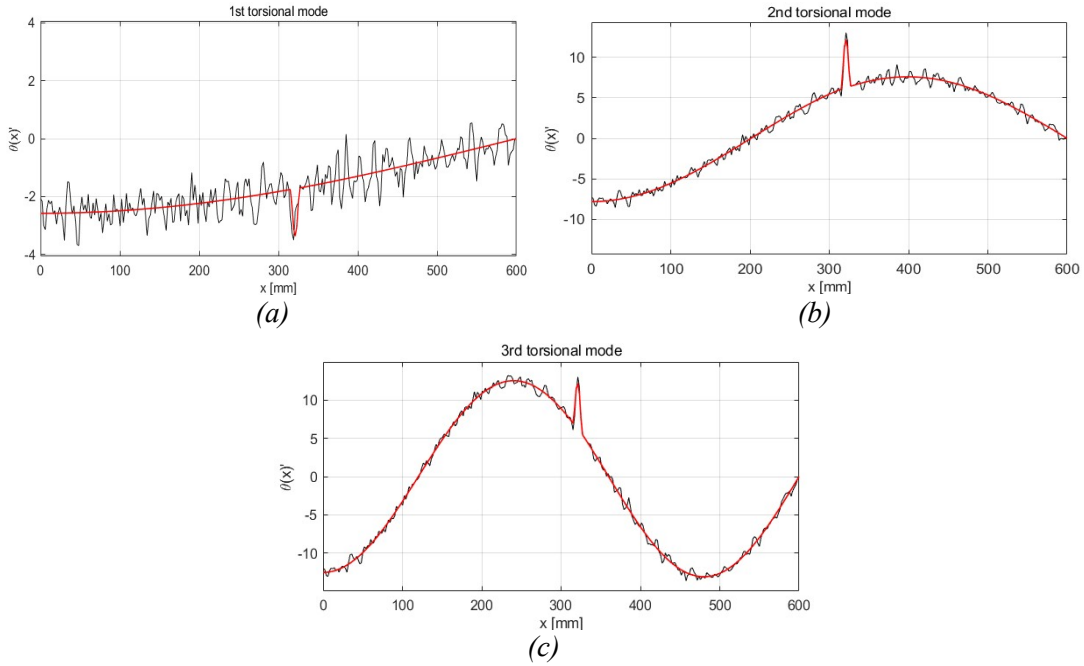

Figure 2. Damage localization results on the first three torsional mode shapes (first (a), second (b), third (c)) contaminated by noise (SNR= ∞ in red, SNR=50 in black)

Conclusions

This work presents an extension of the traditional curvature-based approach for structural damage localization using only vibration measurements, without requiring baseline information from the undamaged structure. The proposed methodology is based on the use of the first derivative of mode shapes characterized by significant torsional components. The results demonstrate that the proposed approach is highly effective in both detecting and accurately localizing structural damage, so, it represents a valid alternative to the classical curvature method and, under certain conditions, may even provide superior performance. The methodology has been validated through numerical investigations, also considering the presence of measurement noise. As seen, the first derivative exhibits low sensitivity to noise amplification, which represents a major advantage when dealing with experimental datasets. Finally, preliminary experimental investigations conducted on real structures have also confirmed the effectiveness of the first-derivative-based approach compared with the traditional curvature method. Further experimental validation and extension of these findings will be addressed in future research activities.

References

[1] A.K. Pandey, M. Biswas, M.M. Samman, Damage detection from changes in curvature mode shapes, J. Sound Vib. 145 (1991) 321–332. https://doi.org/10.1016/0022-460X(91)90595-B

[2] C.P. Ratcliffe, Damage detection using a modified Laplacian operator on mode shape data, J. Sound Vib. 204 (1997) 505–517. https://doi.org/10.1006/jsvi.1997.0961

[3] R.P.C. Sampaio, N.M.M. Maia, J.M.M. Silva, Damage detection using the frequency-response-function curvature method, J. Sound Vib. 226 (1999) 1029–1042. https://doi.org/10.1006/jsvi.1999.2340

[4] A. Gentile A, A. Messina, Detection of crack by only measured mode shapes in damaged conditions, in: The Cromwell Press Ltd., University of Wales Swansea, 2002.

[5] E. Parloo, P. Guillaume, M. Van Overmeire, Damage assessment using mode shape sensitivities, Mech. Syst. Signal Process. 17 (2003) 499–518. https://doi.org/10.1006/mssp.2001.1429

[6] Q. Wang, X. Deng, Damage detection with spatial wavelets, Int. J. Solids Struct. 36 (1999) 3443–3468. https://doi.org/10.1016/S0020-7683(98)00152-8

[7] S.-T. Quek, Q. Wang, L. Zhang, K.-K. Ang, Sensitivity analysis of crack detection in beams by wavelet technique, Int. J. Mech. Sci. 43 (2001) 2899–2910. https://doi.org/10.1016/S0020-7403(01)00064-9

[8] J.-C. Hong, Y.Y. Kim, H.C. Lee, Y.W. Lee, Damage detection using the Lipschitz exponent estimated by the wavelet transform: applications to vibration modes of a beam, Int. J. Solids Struct. 39 (2002) 1803–1816. https://doi.org/10.1016/S0020-7683(01)00279-7

[9] A. Gentile, A. Messina, On the continuous wavelet transforms applied to discrete vibrational data for detecting open cracks in damaged beams, Int. J. Solids Struct. 40 (2003) 295–315. https://doi.org/10.1016/S0020-7683(02)00548-6

[10] S. Rucevskis, M. Wesolowski, Identification of Damage in a Beam Structure by Using Mode Shape Curvature Squares, Shock Vib. 17 (2010) 601–610. https://doi.org/10.1155/2010/729627

[11] Yazdanpanah, O., Seyedpoor, S.M., Bengar, H. Akbarzadeh, A new damage detection indicator for beams based on mode shape data, Struct. Eng. Mech. 53 (2015) 725–744. https://doi.org/10.12989/SEM.2015.53.4.725

[12] D. Dessi, G. Camerlengo, Damage identification techniques via modal curvature analysis: Overview and comparison, Mech. Syst. Signal Process. 52–53 (2015) 181–205. https://doi.org/10.1016/j.ymssp.2014.05.031

[13] M.C. Porcu, D.M. Patteri, S. Melis, F. Aymerich, Effectiveness of the FRF curvature technique for structural health monitoring, Constr. Build. Mater. 226 (2019) 173–187. https://doi.org/10.1016/j.conbuildmat.2019.07.123

[14] G. Faraco, A.V. De Nunzio, N.I. Giannoccaro, A. Messina, A Non-destructive Approach for Damage Localization in Civil or Mechanical Structures Without Reference Model, in: E. Caetano, Á. Cunha (Eds.), Exp. Vib. Anal. Civ. Eng. Struct., Springer Nature Switzerland, Cham, 2025: pp. 671–680. https://doi.org/10.1007/978-3-031-96110-6_65

[15] G. Faraco, A.V.D. Nunzio, N.I. Giannoccaro, A. Messina, Experimental Validation on a Real-World Truss Structure of a Damage Localization Method Based on Mode Shape Derivatives, Struct. Durab. Health Monit. 0 (2025) 1–10. https://doi.org/10.32604/sdhm.2025.075327

[16] W.E. Boyce, R.C. DiPrima, Elementary differential equations and boundary value problems, Jonh Wily & Sons, New York, NY, 1997.

Materials Research Proceedings 73 (2026) 307-310 https://doi.org/10.21741/9781644904459-60

Beam Finite Elements with Arbitrary Shape Functions

Erasmo CARRERA[1,a], and Daniele SCANO[1,b *]

[1]Full Mul2 Lab, DIMEAS, Politecnico di Torino, Corso Duca degli Abruzzi 24, Torino, Italy

[a]erasmo.carrera@polito.it, [b]daniele.scano@polito.it

Keywords: Beam models, Composite Structures, Refined kinematic, Lagrange polynomials, Carrera Unified Formulation

Abstract. This paper presents advanced one-dimensional finite elements for the analysis of composite laminated beams. A key novelty of the proposed approach lies in the ability to independently select shape functions for each of the three displacement variables, using different Lagrange-based functions. The formulation is developed within the framework of the Carrera Unified Formulation, which decomposes the three-dimensional displacement field into in-plane and cross-sectional components. Lagrange expansions are adopted to characterize the cross-section, although other polynomial choices are also possible. The method is validated against literature results for a bending problem. The findings demonstrate that it is possible to tune the computational cost while achieving results identical to those obtained with classical approaches.

Introduction

The formulation of beam theories remains a fundamental topic in structural engineering. Despite substantial advances in computational mechanics and the continual increase in computing power, beam models continue to be widely used due to their inherent simplicity. As a result, they find application across a broad range of engineering problems.

The present work adopts the Carrera Unified Formulation (CUF) [1], a versatile framework for generating beam, plate, and shell theories. Within this approach, one can conveniently select both the expansion functions over the beam cross-section and the shape functions along its axis. Moreover, this formulation is fully compatible with the Finite Element Method (FEM).

Finite elements are known to be susceptible to numerical issues when modeling thin structures. In bending-dominated problems, this manifests as artificial stiffening of the element, a phenomenon known as shear locking. Caused by an excessive increase in the shear stiffness component, shear locking is a well-documented limitation of standard finite element formulations [2].

This work pursues three concurrent objectives: (a) improving computational efficiency by reducing the system's degrees of freedom, (b) implementing strategies to resolve FEM locking issues, and (c) maintaining accurate predictions of displacements and out-of-plane stresses.

To achieve these goals, the CUF has been reformulated to allow the use of different shape functions for each displacement component. Additionally, the proposed approach enables the adoption of distinct structural theories for individual displacements [3]. However, for the sake of brevity, this capability is not explicitly shown in the results but is described in the theoretical formulation.

Methodology

The stress tensor, $\boldsymbol{\sigma}^k$, and the strain tensor, $\boldsymbol{\epsilon}^k$, can be conveniently expressed as:

$$\boldsymbol{\sigma}^k = \left\{\sigma_{xx}^k\ \sigma_{yy}^k\ \sigma_{zz}^k\ \sigma_{yz}^k\ \sigma_{xz}^k\ \sigma_{xy}^k\right\}^T, \quad \boldsymbol{\epsilon}^k = \left\{\epsilon_{xx}^k\ \epsilon_{yy}^k\ \epsilon_{zz}^k\ \epsilon_{yz}^k\ \epsilon_{xz}^k\ \epsilon_{xy}^k\right\}^T \tag{1}$$

The geometric relationships between strains and displacements are defined as:

Content from this work may be used under the terms of the Creative Commons Attribution 3.0 license. Any further distribution of this work must maintain attribution to the author(s) and the title of the work, journal citation and DOI. Published under license by Materials Research Forum LLC.

Materials Research Proceedings 73 (2026) 307-310 https://doi.org/10.21741/9781644904459-60

$$\boldsymbol{\epsilon}^k = \mathbf{D}\mathbf{u}^k \tag{2}$$

where $\mathbf{D}$ is the matrix of differential operators, valid under the assumption of small displacements and small rotations [1]. For linear elastic orthotropic materials, the constitutive relation is given by

$$\boldsymbol{\sigma}^k = \mathbf{C}^k\boldsymbol{\epsilon}^k \tag{3}$$

where $\mathbf{C}^k$ denotes the matrix of material coefficients (see [4] for details).

Furthermore, the three-dimensional displacement field may be expressed mathematically as follows:

$$\begin{aligned} u_x^k(x,y,z) &= N_{u_x i}(y)F_{u_x\tau}^k(x,z)q_{x_{\tau i}}^k,\ \ \tau = 1,\dots,M_{u_x}; i = 1,\dots,N_{nu_x} \\ u_y^k(x,y,z) &= N_{u_y i}(y)F_{u_y\tau}^k(x,z)q_{y_{\tau i}}^k,\ \ \tau = 1,\dots,M_{u_y}; i = 1,\dots,N_{nu_y} \\ u_z^k(x,y,z) &= N_{u_z i}(y)F_{u_z\tau}^k(x,z)q_{z_{\tau i}}^k,\ \ \tau = 1,\dots,M_{u_z}; i = 1,\dots,N_{nu_z} \end{aligned} \tag{4}$$

where $F_{u_x\tau}^k$, $F_{u_y\tau}^k$, and $F_{u_z\tau}^k$ denote the expansion functions associated with the generalized displacements $q_{x_{\tau i}}^k$, $q_{y_{\tau i}}^k$, and $q_{z_{\tau i}}^k$, respectively. The index τ indicates summation, while M_{u_x}, M_{u_y}, and M_{u_z} represent the number of expansion terms for each displacement component. Moreover, $N_{u_x i}$, $N_{u_y i}$, and $N_{u_z i}$ denote the different shape functions for the displacement fields, with the repeated subscript i implying summation. N_{nu_x}, N_{nu_y}, and N_{nu_z} are the number of shape functions per element and displacement component. In this case, Lagrange polynomials are used [4]. In the case of the virtual system, the indices i and τ are replaced by j and s, respectively.

By applying the Principle of Virtual Displacements, the weak form of the equilibrium equations is obtained, leading to the finite element stiffness matrix formulation:

$$\begin{aligned} &\delta L_{int} = \delta L_{ext} = \\ &\int_{Vk}\left(\delta\epsilon_{xx}^k\sigma_{xx}^k + \delta\epsilon_{yy}^k\sigma_{yy}^k + \delta\epsilon_{zz}^k\sigma_{zz}^k + \delta\epsilon_{yz}^k\sigma_{yz}^k + \delta\epsilon_{xz}^k\sigma_{xz}^k + \delta\epsilon_{zz}^k\sigma_{zz}^k\right)\mathrm{d}V^k = \\ &\delta u_x^k P_{u_x}^k + \delta u_y^k P_{u_y}^k + \delta u_z^k P_{u_z}^k \end{aligned} \tag{5}$$

It is possible to obtain three governing equations for each virtual displacement:

$$\begin{aligned} \delta q_{x_{sj}}^k &: K_{u_x u_x s\tau ji}^k q_{x_{\tau i}}^k + K_{u_x u_y s\tau ji}^k q_{y_{\tau i}}^k + K_{u_x u_z s\tau ji}^k q_{z_{\tau i}}^k = P_{u_x sj}^k \\ \delta q_{y_{sj}}^k &: K_{u_y u_x s\tau ji}^k q_{x_{\tau i}}^k + K_{u_y u_y s\tau ji}^k q_{y_{\tau i}}^k + K_{u_y u_z s\tau ji}^k q_{z_{\tau i}}^k = P_{u_y sj}^k \\ \delta q_{z_{sj}}^k &: K_{u_z u_x s\tau ji}^k q_{x_{\tau i}}^k + K_{u_z u_y s\tau ji}^k q_{y_{\tau i}}^k + K_{u_z u_z s\tau ji}^k q_{z_{\tau i}}^k = P_{u_z sj}^k \end{aligned} \tag{6}$$

The fundamental nuclei for the load vector are expressed in the following equations.

$$\begin{aligned} P_{u_x sj}^k &= N_j F_{u_x\tau}^k P_{u_x}^k \\ P_{u_y sj}^k &= N_j F_{u_y\tau}^k P_{u_y}^k \\ P_{u_z sj}^k &= N_j F_{u_z\tau}^k P_{u_z}^k \end{aligned} \tag{7}$$

A novel formulation of the Fundamental Nucleus (FN) is employed in this work, marking a significant departure from standard CUF implementations. The principal innovation consists of treating the FN components $K_{u_m u_l s\tau ji}^k$ and $P_{u_m sj}^k$ as individual scalar quantities, in contrast to the conventional 3×3 matrix representation [1]. Explicit expressions for $K_{u_m u_l s\tau ji}^k$ are omitted for

Materials Research Proceedings 73 (2026) 307-310 https://doi.org/10.21741/9781644904459-60

brevity. The assembly process, which aggregates contributions from all displacement components, finite element nodes, and elements, yields the following global system: $\mathbf{KU} = \mathbf{P}$.

Numerical Results

The paper compares the present models with the results from the open literature [5]. Figure 1 presents the geometric details of the cantilevered two-layered composite beam. The beam has length $L = 2$ m, width $b = 0.2$ m, and height $h = 0.1$ m. The material properties are: $E_L/E_T = 25$, $E_T/E_3 = 1$, $\nu_{LT} = \nu_{T3} = \nu_{L3} = 0.25$, $G_{LT}/E_T = 0.5$, and $G_{L3}/E_T = G_{T3}/E_T = 0.2$. A constant downward pressure of 1000 Pa is applied to the top surface.

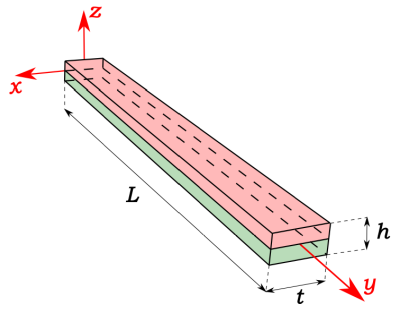

Figure 1: Two-layered composite beam. The study case is taken from [5].

Table 1 presents the characteristics of the Unified Formulation models, including the adopted shape functions for the three displacement components, the number of Degrees of Freedom (DOF), and the corresponding DOF reduction. For all models, transverse displacements and shear stresses are computed. Regarding the mesh, seven beam elements are used as in the reference. Sixteen-node Lagrange-based expansions are used in the cross-section for each layer across all models.

Table 1: Models used for the two-layered beam and relative results.

Shape functions	$-u_z^{\mathrm{a}} \times 10^3$[m]	$\sigma_{yz}^{\mathrm{b}} \times 10^3$[m]	DOF	DOF Reduction [%]
B4-B4-B4	5.263	22.99	1848	–[c]
B3-B3-B3	5.256	21.20	1260	31.81
B4-B4-B2	4.111	19.26	1456	21.21
B4-B4-B3	5.257	21.20	1652	10.60
B2-B2-B4	5.226	22.92	1064	42.42
B2-B3-B4	5.262	23.05	1260	31.81

(a): Computed at $[0, L, h/2]$; (b): Computed at $[0, L/2, -h/4]$;
(c): Taken as the reference solution [5].

Shear stresses along the thickness are studied, as displayed in Fig. 2.

The analysis reveals that it is necessary to use higher-order shape functions for the displacement component u_z. It is possible to obtain a great reduction in terms of computational time if the models B2-B2-B2 and B2-B3-B4 are adopted.

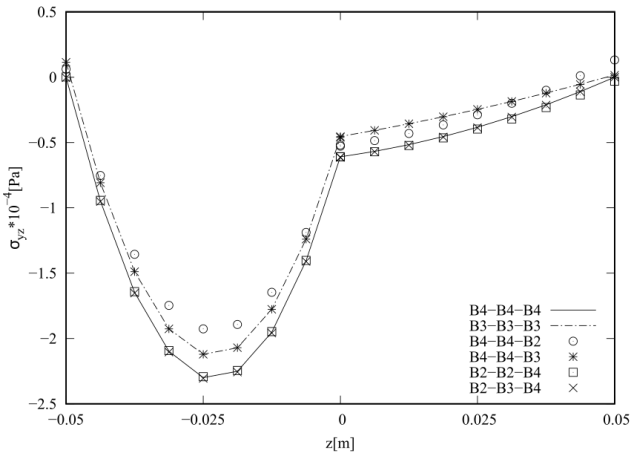

Figure 2: Shear stresses along $\boldsymbol{z}$ *of the composite laminate along* $[\boldsymbol{0}, \boldsymbol{L/2}, \boldsymbol{z}]$.

Conclusions

This work introduces an enhanced method for the analysis of one-dimensional structures within the Carrera Unified Formulation (CUF). The proposed method is derived by reformulating the traditional CUF approach and reorganizing the assembly of the finite element matrices. The resulting framework leverages the ability to employ different shape functions for each displacement component. The paper demonstrates that the method effectively combines various types of expansions and polynomial orders, enabling a significant reduction in degrees of freedom through the judicious selection of shape functions per component. In particular, the shear stresses may be evaluated with great precision. Future work will focus on extending the approach to dynamic analyses and to the solid formulation. Moreover, the proposed method will be employed in conjunction with the capability to adopt different expansions in a single model [3], a concept that was theoretically illustrated in the Methodology section.

References

[1] E. Carrera, M. Cinefra, M. Petrolo, E. Zappino, Finite Element Analysis of Structures Through Unified Formulation, Wiley, Amsterdam, 2014. https://doi.org/10.1002/9781118536643

[2] J.N. Reddy, On locking-free shear deformable beam finite elements, Comput. Methods Appl. Mech. Eng. 149 (1997) 113–132. https://doi.org/10.1016/S0045-7825(97)00075-3

[3] E. Carrera, D. Scano, Nonlinear composite beam finite elements with arbitrary cross-sectional displacement fields. Compos. Struct. 377 (2026) 119883. https://doi.org/10.1016/j.compstruct.2025.119883

[4] K.J. Bathe, Finite Element Procedure, Prentice hall, Upper Saddle River, New Jersey, USA, 1996.

[5] E. Carrera, R. Augello, D. Scano, Multilayered beam, plate and shell theories with interlaminar variables and Lagrange polynomials, Memorie dell'Accademia delle Scienze di Torino. (2022) 99–134.

Materials Research Proceedings 73 (2026) 311-314 https://doi.org/10.21741/9781644904459-61

Economical and Global Warming Potential Evaluation of Thermoplastic Pultruded Materials

Léo SUDRIÈS[1,a*], Joël SERRA[1], Wiyao AZOTI[1,b], Bruno CASTANIÉ[1,c]

[1]Université de Toulouse, Institut Clément Ader, UMR CNRS 5312, INSA/UPS/ISAE-SUPAERO/IMT-Mines Albi, Toulouse, France

[a]sudries@insa-toulouse.fr, [b]azoti@insa-toulouse.fr, [c]castanie@insa-toulouse.fr

Keywords: Railways Tracks, Pultruded Composite, Eco-Design, Cost/Performance Ratio

Abstract. With the aim of decarbonize railway transport, a solution of lightweight railways tracks with composites materials is investigated. Using thermoplastics PA6 (from caprolactam), Elium® (acrylic-based) resin and thermoset epoxy resin with carbon, glass, basalt and flax fibers, seven fibre/matrix combinations have been studied. In order to objectively compare a new composite solution, an estimation of the economic cost as well as the carbon cost using a cradle-to-gate approach on raw materials with the Global Warming Potential (GWP) criterion was carried out and compared to the traditional steel solution. A ratio between ecological impact and mechanical performance has been established in order to determine the best composite combination for eco-design. Configurations involving basalt fibres offer the best ecological cost/performance ratio. Configurations with carbon fibres achieves the best mechanical properties but are not competitive in terms of carbon cost/performance ratio. Therefore, basalt fibres open up new possibilities for designing and sizing the next generation of composite railways.

Introduction

Decarbonising human and freight transportation are one of the keys to reducing carbon emissions. In France, transport accounted for 30% of CO_2 emissions in 2021 [1] . Therefore, it is essential to transform and evolve rail transport. Bearing this in mind, a project to develop new low-carbon railway infrastructure using composite materials is currently underway. The design of a composite structure depends on several factors, including its shape, the materials used, and the manufacturing method employed [2]. Pultrusion was chosen for this project because the geometry of the rails is particularly well-suited to this manufacturing method, and because it enables continuous production with consistent geometry at a lower cost for large-scale manufacturing [3]. Designing a composite structure requires an understanding of the mechanical properties of the materials under consideration [4]. Thus, mechanical characterisation was conducted to determine the stiffness and strength of several material configurations [5]. The resins studied are Arkema's recyclable Elium® resin and PA6 resin, which is obtained by in-situ polymerisation of ε-caprolactam [6]. For comparison, the study also considered a thermosetting epoxy resin. Synthetic fibers such as carbon, glass and basalt, as well as natural flax fiber, were studied in combination with the aforementioned resins. In order to design low-carbon, accessible rail systems, it is useful to estimate and compare the economic and environmental costs of each configuration with those of a conventional steel rail system. Life cycle assessment (LCA) enables the environmental impact of a product to be assessed over its entire life cycle [7]. In this study, a cradle-to-gate approach is used with the global warming potential (GWP) as the sole criterion to allow for a simple comparison of CO_2 equivalent emissions.

Content from this work may be used under the terms of the Creative Commons Attribution 3.0 license. Any further distribution of this work must maintain attribution to the author(s) and the title of the work, journal citation and DOI. Published under license by Materials Research Forum LLC.

Materials Research Proceedings 73 (2026) 311-314 https://doi.org/10.21741/9781644904459-61

Materials and methods

A total of seven combinations were studied, as shown in Table 1.

Table 1. Composite configurations studied [5]

Configurations	Resin	Resin references	Fibres	Fibre references
C-1	Elium®	C195 E	Carbon	SIGRAFIL® C T50-4.0/240
C-2	Elium®	C195 E	Glass	PULSTRAND® 4100
C-3	Elium®	C195 E	Basalt	BASALTEX® 2400tex
C-4	Elium®	C195 E	Flax	LINCORE® 2400tex
C-5	PA6	ε-caprolactame	Glass	JM STARROV® 086
C-6	PA6	ε-caprolactame	Carbon	SIGRAFIL® C T50 4.0/240
C-7	Epoxy	LITESTONE 3400E/3102H	Basalt	BASALTEX® 2400tex

The mechanical properties were determined by conducting tensile and compressive tests in the longitudinal, transverse and off-axis directions. Preliminary rail dimensioning calculations suggest that stress is low in the fibre direction. However, significant compressive stress is observed in the transverse direction. Therefore, only the transverse properties will be examined here. The results obtained during the characterization campaign are presented in Table 2.

Table 2. Mechanical properties of composite configurations studied in transversal direction [5]

Resin		**Elium®**	**Elium®**	**Elium®**	**Elium®**	**PA6**	**PA6**	**Epoxy**
Fibres		**Carbon**	**Glass**	**Basalt**	**Flax**	**Glass**	**Carbon**	**Basalt**
Transversal tensile	Et^t [GPa]	7.8	8.5	12.0	2.2	8.0	6.3	14.6
	σ_t^t [MPa]	26	9	15	6	32	43	42
	ν_{tz}	0,38	0,39	0,42	0,46	0,64	0,58	0,40
Transversal compression	Et^c [GPa]	9.7	15.0	17.8	2.8	11.3	7.1	17.2
	σ_t^c [MPa]	115	110	98	34	107	123	137

This study shows that the mechanical properties of composites made with Elium® resin are affected by the type of fibers used due to poor impregnation and the presence of voids linked to the pultrusion process. For each configuration, carbon and financial costs were estimate based on literature data as shown in Table 3.

Table 3. Estimate global warming potential and estimate cost for all material [5]

Materials	Average [kg CO_2eq/kg]	Estimate price [€/kg]
Steel	2.2	*0.8*
Epoxy resin	6.8	*10.0*
Elium® resin	4.3	*10.0*
PA6 resin	8.8	*5.0*
Carbon fibres	34.0	*20.0*
Glass fibres	1.9	*1.5*
Basalt fibres	0.5	*4.0*
Flax fibres	0.9	*4.0*

Materials Research Proceedings 73 (2026) 311-314 https://doi.org/10.21741/9781644904459-61

A comparison of economic and environmental costs will be provided for each configuration. These results will then be evaluated in relation to mechanical performance in the transverse direction, in order to determine the cost-performance ratio and identify the most advantageous fibre-matrix combination for the eco-design.

Results and discussion

In order to make the most accurate comparison possible between the various configurations and the standard steel rail, calculations were performed considering the fiber and resin volume fractions determined for each configuration [5]. Preliminary design results show that the composite solution has a mass of 15 kg per meter, compared to 50 kg per meter for a conventional steel rail. Taking all this information into account, Fig. 1 presents a carbon and economic cost analysis for all configurations as well as those of the standard steel rail.

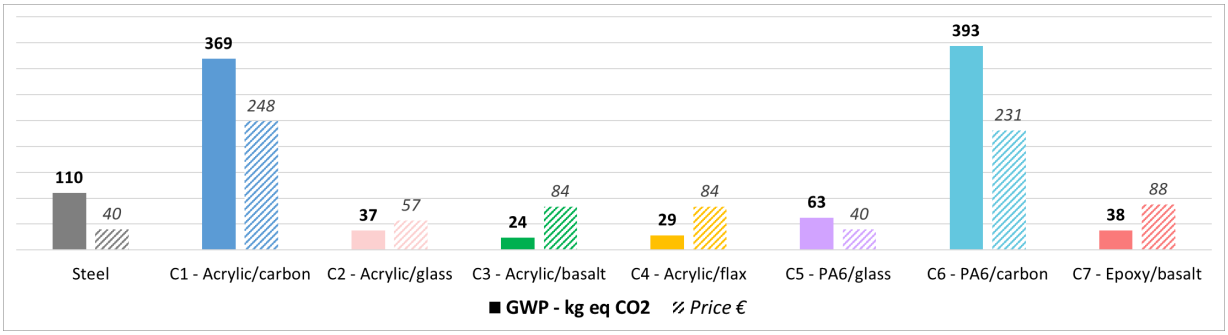

Figure 1. GWP and economic cost of raw materials for 1 meter of rail

According to these results, all configurations without carbon fibers appear to be more advantageous than the conventional steel solution. Solutions incorporating basalt fibers appear to be the most promising option for achieving CO_2 emission reduction targets. From an economic point of view, solution C5 (PA6/glass) appears to be equivalent to the steel solution.

In order to make an objective comparison and select the most suitable configuration for manufacturing a low-carbon composite rail, a cost-performance ratio is calculated. For each configuration, the GWP value shown in Fig. 1 is divided by the transverse tensile and compressive strength. The results presented in Fig. 2 therefore correspond to the carbon cost per 1 MPa of transverse strength for each configuration.

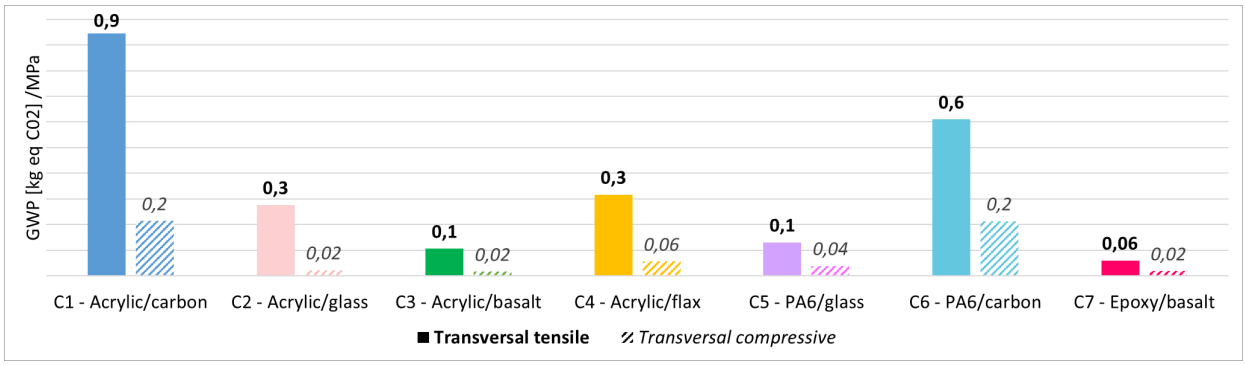

Figure 2. GWP in [kg Co2 eq] for 1 MPa of each configuration for transversal tensile and compressive test

These results demonstrate the favorable cost-performance ratio of configurations containing basalt fibers. The PA6/glass configuration comes second. While configurations with carbon fibers have a significantly better mechanical performance than other configurations, they remain highly disadvantageous in terms of the cost-performance ratio.

Conclusions and perspectives

In order to select the best configuration for designing an innovative low-carbon rail, a cost-performance ratio was established based on mechanical characterization data for several composite configurations with Elium®, PA6 and epoxy resins with carbon, glass, basalt and flax fibers. Despite their superior mechanical performance, configurations using carbon fibers demonstrate the difficulty of achieving a favorable cost-performance ratio. In contrast, basalt fibers yield an attractive ratio when combined with Elium® resin. The epoxy/basalt configuration achieves the best results in terms of performance, economic cost and environmental impact when using a cradle-to-gate approach. However, a comprehensive life cycle analysis of each material is necessary to definitively determine the optimal material configuration for this type of design.

Acknowledgment

The authors would like to thank the INFRAlight team's project as well as ADEME for their funding.

References

[1] Statistical Data and Studies Department (SDSD). Key Transportation Statistics – 2023 Edition [Internet]. 2023. Available from: https://www.statistiques.developpement-durable.gouv.fr/chiffres-cles-des-transports-edition-2023

[2] F. Neveu, B. Castanié, and P. Olivier, "The GAP methodology: A new way to design composite structures," *Materials & Design*, vol. 172, p. 107755, Jun. 2019. https://doi.org/10.1016/j.matdes.2019.107755.

[3] K. Minchenkov, A. Vedernikov, A. Safonov, and I. Akhatov, "Thermoplastic Pultrusion: A Review," *Polymers*, vol. 13, no. 2, p. 180, Jan. 2021. https://doi.org/10.3390/polym13020180.

[4] F. Tucci and A. Vedernikov, "Design Criteria for Pultruded Structural Elements," in *Reference Module in Materials Science and Materials Engineering*, vol. 3, 2021, pp. 51–68. doi: 10.1016/B978-0-12-819724-0.00086-0.

[5] Sudriès L, Diboune I, Cloos A, De Almeida O, Serra J, Azoti W *et al.*, "Selection of pultruded composite materials for new, low-carbon emission, lightweight railways tracks, with a focus on mechanics, economics and sustainability," *Materials & Design*, vol. 261, p. 115401, Dec. 2025. https://doi.org/10.1016/j.matdes.2025.115401.

[6] C. Vicard, O. De Almeida, A. Cantarel, and G. Bernhart, "Experimental study of polymerization and crystallization kinetics of polyamide 6 obtained by anionic ring opening polymerization of ε-caprolactam," *Polymer*, vol. 132, pp. 88–97, Dec. 2017. https://doi.org/10.1016/j.polymer.2017.10.039.

[7] G. Finnveden and J. Potting, "Life Cycle Assessment," in *Encyclopedia of Toxicology (Third Edition)*, P. Wexler, Ed., Oxford: Academic Press, 2014, pp. 74–77. doi: 10.1016/B978-0-12-386454-3.00627-8.

Materials Research Proceedings 73 (2026) 315-320 https://doi.org/10.21741/9781644904459-62

Interfacial Management via Dynamic Pore-Formation for High-Energy-Density Grid-Scale Aqueous Zn–MnO_2 Storage

J.V. Alamelu*, K.R.V. Subramanian, Sharath Ramesh, Gaurav Manoj Bhangale, K.S. Vignesh, and Mohamed Tanveer M.

Ramaiah Institute of Technology, Bengaluru – 560054, Karnataka, India

jvalamelu@msrit.edu

Keywords: Zn-MnO_2 Battery, Aqueous Zinc-Ion Battery, DFN Model, Dynamic Porosity, Effective Electron Transfer, Mn Dissolution, Grid-Scale Storage

Abstract. Aqueous zinc–manganese dioxide ($Zn\text{-}MnO_2$) batteries are compelling candidates for safe, low-cost grid-scale energy storage. Practical performance is persistently limited by progressive Mn dissolution and surface passivation, confining utilisation to the one-electron Mn^{4+}/Mn^{3+} regime. This paper develops and evaluates a dynamic pore-forming trilayer cathode comprising a graphene conductive interlayer, a sacrificial $MnCl_2$/MnOOH mixed interlayer, and an outer MnO_2 active layer. A physics-based Doyle–Fuller–Newman (DFN) continuum model incorporating multi-phase OCP blending, dissolution-driven porosity evolution, and a surface-passivation sub-model is formulated with all parameters derived from peer-reviewed literature without empirical fitting. The trilayer delivers approximately twofold higher specific capacity across 0.1–20 A g^{-1} (309.8 vs. 140.8 mAh g^{-1} at 5 A g^{-1}). The effective electron-transfer number n_{eff} exceeds unity at low-to-moderate rates (up to 1.21 at 0.1 A g^{-1}), approaching unity at 20 A g^{-1}, representing upper bounds under unit Mn^{2+} capture efficiency. Charge-transfer resistance is reduced 3.5× and ohmic resistance 8.1×. Ragone analysis confirms 270–391 Wh kg^{-1} (trilayer) vs. 133–209 Wh kg^{-1} (pure MnO_2) across three power decades.

Introduction

The global imperative to integrate large-scale intermittent renewable generation has placed electrochemical energy storage at the centre of energy-transition research [1]. Lithium-ion batteries face well-documented constraints at grid scale: supply-chain risk, flammable organic electrolytes, and costly recycling [2]. Aqueous $Zn\text{-}MnO_2$ systems have been specifically identified as promising grid-scale candidates [3,4], with their scientific challenges comprehensively reviewed [5,6]. Among candidate chemistries, zinc offers a favourable redox potential, while MnO_2 offers a theoretical two-electron capacity of 616 mAh g^{-1} across its β, δ, and γ polymorphs [7]. Realising this potential is nonetheless difficult: practical cathodes are limited by two coupled degradation mechanisms reviewed by Shin et al. [8]. The first is Mn^{3+} disproportionation that irreversibly depletes the active solid [9–11]. The second is the accumulation of insoluble discharge products at the solid–electrolyte interface, which raises charge-transfer resistance [12]. Together, these mechanisms confine practical operation to the one-electron regime. A further complexity is the H^+/Zn^{2+} co-insertion mechanism, in which the first discharge plateau is predominantly governed by proton intercalation, remaining polymorph- and rate-dependent and debated; the present model adopts a single-ion DFN framework as an acknowledged simplification [13-15]. Existing mitigation strategies—cationic doping [16], nanostructuring [17,18], and electrolyte additives [19]—each address one aspect of this problem, but none provide a concerted architectural response. Against this backdrop, the present work proposes a dynamic pore-forming trilayer cathode, distinguished from the recent single-phase DFN model by its multilayer architecture and dissolution-driven porosity sub-model.

Content from this work may be used under the terms of the Creative Commons Attribution 3.0 license. Any further distribution of this work must maintain attribution to the author(s) and the title of the work, journal citation and DOI. Published under license by Materials Research Forum LLC.

Materials Research Proceedings 73 (2026) 315-320 https://doi.org/10.21741/9781644904459-62

Physical Configuration And Assumptions

A. Electrode Stack Geometry

The trilayer cathode is deposited on a copper current collector: (i) graphene interlayer minimising ohmic contact resistance, (ii) sacrificial $MnCl_2$/MnOOH middle layer providing a Mn^{2+} reservoir and porosity-generating agent, and (iii) outer MnO_2 active layer. Baseline mass loadings: m_{MnO_2} = 4.0 mg, m_{mid} = 1.95 mg, m_{gr} = 0.05 mg; total = 6.0 mg, A = 8×10^{-4} m^2. Layer thickness follows $L_i = \frac{m_i}{\rho_i \varepsilon_{s,i} A}$, where the solid occupies fraction $\varepsilon_{s,i}$ of the total layer volume $L_i A$ and the complementary void fraction $\varepsilon_e = 1 - \varepsilon_s$ constitutes the electrolyte-accessible pore space. The composite electron-delivery capacity is in Eq.1

$$n_e = N_{MnO_2} \cdot 1 + N_{MnOOH} \cdot 1 + N_{MnCl_2} \cdot 2 \quad (1)$$

where the factor of 2 for $MnCl_2$ reflects the two-electron oxidation $Mn^{2+} \rightarrow Mn^{4+}$.

B. Model Assumptions and Governing Equations

The assumptions bound the model scope are isothermal at 298.15 K, neglecting Joule heating above 10 A g^{-1}; single-ion (Zn^{2+}) insertion, omitting H^+/Zn^{2+} co-insertion — known to underpredict the pure MnO_2 baseline but not the comparative ratio; mean-field single-particle representation; Mn^{2+} capture efficiency, n_{eff} are upper bounds; uniform Bruggeman tortuosity (b = 1.8), including for the graphene layer; no side reactions; single discharge, no cycling degradation; and linear OCP blending with no phase-interaction thermodynamics. The governing equations follow the DFN formalism, solved numerically using PyBaMM.

A. Solid-Phase Diffusion

Ion intercalation in spherical particles of radius r_p follows Fick's second law in spherical coordinates as in Eq.2, $\frac{\partial c_s}{\partial t} = \frac{1}{r^2}\frac{\partial}{\partial r}\left(r^2 D_s \frac{\partial c_s}{\partial r}\right)$ (2)

A no-flux condition applies at r = 0; at $r = r_p$, flux matches $-D_s \frac{\partial c_s}{\partial r}\Big|_{r_p} = \frac{j_n}{F}$. Diffusivities $D_{s,MnO_2} = 10^{-13}$, $D_{s,MnOOH} = 3.3\times10^{-14}$, $D_{s,MnCl_2} = 5\times10^{-12}\ m^2\ s^{-1}$.

B. Electrolyte Transport

Ion transport through the porous electrolyte follows the Bruggeman correction [20] from $D_{eff} = D_e \cdot \varepsilon_e^b$, $\kappa_{eff} = \kappa \cdot \varepsilon_e^b$, $b = 1.8$. A porosity increases from 0.38 to 0.55 improves D_{eff} by $1.45^{1.8} \approx 1.95$.

C. Butler–Volmer Kinetics

Reaction kinetics at the interface follow Butler–Volmer theory. The net interfacial current density at overpotential as in Eq.3 with $\alpha_a = \alpha_c = 0.5$.

$$\eta = \phi_s - \phi_e - U_{eq}: j_n = j_0\left[\exp\left(\frac{\alpha_a F\eta}{RT}\right) - \exp\left(-\frac{\alpha_c F\eta}{RT}\right)\right] \quad (3)$$

The exchange current density is in Eq.4

$$j_0^i = F k_0^i \left(\frac{c_e}{c^0}\right)^{0.5}\left(\frac{c_s}{c_{s,max}}\right)^{0.5}\left(1 - \frac{c_s}{c_{s,max}}\right)^{0.5} \quad (4)$$

Prefactors follow from the linearised BV relation [21] at 0: $\eta \rightarrow 0$: $j_{0,cell} = \frac{RT}{F \cdot R_{ct,0}}$, $R_{ct,0} = 80\ \Omega$ [12], giving $k_0^{MnO_2} = 1.057\times10^{-6}$ m s^{-1}; $k_0^{MnOOH} = 1.8 \times k_0^{MnO_2}$ [8]; $k_0^{MnCl_2} = 20 \times k_0^{MnO_2}$ [3], reflecting $MnCl_2$'s high Mn^{2+} mobility. The composite $j_0^{comp} = \sum f_i \cdot j_0^i$ weights kinetics by electron-delivery fraction.

D. Composite Open-Circuit Potential

The MnO_2 OCP encodes a two-plateau structure via arctangent terms at θ = 0.46 and 0.78 [9,10], for the $Mn^{4+} \rightarrow Mn^{3+}$ and $Mn^{3+} \rightarrow Mn^{2+}$ transitions. Analogous expressions apply for MnOOH ($U_0 = 1.03$ V, $\theta = 0.51$) and $MnCl_2$ (0.95 V, $\theta = 0.58$). The composite $U_{eq}^{comp} = \sum_i f_i \cdot U_{eq}^i$ is a linear blending, reasonable when each phase occupies a distinct spatial subdomain. The governing equations above describe transport and kinetics for a fixed electrode structure; the trilayer's

distinguishing behaviour, however, comes from how that structure evolves during discharge and following two sub-models capture this evolution

Sub-Models: Porosity Evolution And Passivation

A. Dissolution-Driven Porosity Evolution

As $MnCl_2$ dissolves, The fractional pore volume from complete dissolution [22] in Eq.5

$$k_{\text{pore}} = \frac{m_{\text{MnCl}_2}}{\rho_{\text{MnCl}_2} \cdot L \cdot A} \quad (5)$$

The SOC-dependent effective porosity (SOC = $MnCl_2$-layer state of charge) (Eq.6)

$$\varepsilon_e^{\text{tri}}(\text{SOC}) = \min\left(0.38 + k_{\text{pore}}(1 - e^{-0.80 \cdot \text{SOC}}),\ 0.65\right) \quad (6)$$

The exponential form reflects fast initial dissolution, slowing as the reservoir depletes; the rate constant 0.80 matches $MnCl_2$ kinetics, and 0.65 is the percolation threshold.

B. Passivation Sub-Model

Insoluble discharge products (primarily $Zn_4SO_4(OH)_6 \cdot 5H_2O$) also accumulate at the interface, competing with the porosity gain above. The effective charge-transfer resistance (Eq.7)

$$R_{ct} = R_{ct}^0 \cdot \exp\left(-\beta(\varepsilon_e - 0.38)\right) \cdot \left(1 + \frac{\delta_{\max} \cdot \text{SOC}}{\delta_{\text{ref}}}\right) \quad (7)$$

where β = 3.5 [22], δ_{ref} = 2.0 nm. For pure MnO_2, $\delta_{\max}$ = 9.4 nm, giving a 5.7× R_{ct} increase above fresh value. For the trilayer, a Hill-type function suppresses film growth as in Eq.8, Eq.9:

$$f_{\text{supp}} = \frac{k_{\text{pore}}}{k_{\text{pore}} + 0.05} \quad (8)$$

ensuring $f_{supp} \rightarrow 0$ with no pores and $f_{\text{supp}} \rightarrow 1$ at large pore volume, entering Eq. (8) via a reduced film-growth ceiling,

$$\delta_{\text{max,tri}} = \delta_{\text{max,pure}} \cdot \left(1 - f_{\text{supp}}\right) \quad (9)$$

at baseline (k_{pore} = 0.148), $f_{\text{supp}} = 0.748$, giving $\delta_{\text{max,tri}} = 2.37$ nm; the half-saturation constant 0.05 is calibrated so the predicted 3.5× R_{ct} reduction matches fresh-to-end-of-discharge resistance. The porosity and passivation sub-models above jointly determine the cell's impedance response, which is developed analytically in the following section.

Electrochemical Impedance Model

All EIS spectra are analytically derived from DFN parameters at end-of-discharge, not from equivalent-circuit fitting. The ohmic resistance integrates electrolyte conductivity over cathode and separator (Eq.10)

$$R_s = \frac{\left[\frac{L}{2\kappa_{eff}} + \frac{L_{sep}}{\kappa_{sep}}\right]}{A} + \frac{R_c}{A} \quad (10)$$

The factor of 2 reflects the DFN distributed-current approximation (L/2 average path). The separator (30 μm, porosity 0.55, b=1.8) gives $\kappa_{\text{sep}} = \kappa \cdot 0.55^{1.8}$. Contact resistances: $R_c = 4.9 \times 10^{-5}\ \Omega\,\text{m}^2$ (pure), $2.1 \times 10^{-6}\ \Omega\,\text{m}^2$ (trilayer) [23], a 23× reduction from graphene. Warburg coefficient from Eq.11;

$$\sigma_w = \frac{RT}{n^2 F^2 A \cdot c_s^{\text{ref.}} \cdot \sqrt{2D_{s,\text{MnO}_2}}} \quad (11)$$

reflecting the diffusion-limited nature of low-frequency impedance. The complex impedance (Eq.12) with $Z_{\text{CPE}} = (Q(j\omega)^{\alpha})^{-1}$, α = 0.87 (trilayer), 0.82 (pure), quantifying surface heterogeneity is,

$$Z(\omega) = R_s + \frac{1}{\frac{1}{R_{ct}} + \frac{1}{Z_{CPE}}} + \frac{\sigma_w}{\sqrt{(j\omega)}} \quad (12)$$

Results And Discussion

A. Galvanostatic Discharge Performance

Table 1 summaries capacity, energy, and n_{eff} for both configurations. The trilayer delivers substantially higher capacity at every rate, with the improvement factor increasing at higher current; consistent with dynamic pore opening amplifying transport when pure MnO_2 is most

Materials Research Proceedings 73 (2026) 315-320 https://doi.org/10.21741/9781644904459-62

penalised by concentration polarisation. At high rates, pure MnO_2 suffers because its fixed porosity of 0.38 cannot accommodate the larger ion flux, unlike the trilayer, whose effective porosity evolves toward 0.55 as dissolution proceeds.

TABLE 1. PREDICTED PERFORMANCE — PURE MnO_2 vs. TRILAYER

Rate (A g^{-1})	Pure (mAh g^{-1})	Trilayer† (mAh g^{-1})	n_{eff} Pure	n_{eff} Tri†	Gain
0.1	165.3	333.2	0.60	1.21*	2.02×
1.0	157.4	329.1	0.57	1.20	2.09×
5.0	140.8	309.8	0.51	1.13	2.20×
10.0	133.2	290.2	0.49	1.06	2.18×
20.0	125.6	267.0	0.46	0.97	2.13×

* 1.213 is within theoretical max 1.252; partial reservoir utilisation at low rate.; † Upper bounds: unit Mn^{2+} capture efficiency assumed.

The pure MnO_2 baseline predicts 165 mAh g^{-1} at 0.1 A g^{-1}, below the ~285 mAh g^{-1} [9] for $\alpha - MnO_2$, reflecting the exclusion of H^+/Zn^{2+} co-insertion (Assumption 2); in experimental cells the first plateau near 1.25 V is predominantly associated with H^+ uptake, evidenced by pH evolution and XRD data [14]. Since both configurations share this systematic underprediction, the comparative capacity ratio is unaffected.

B. n_{eff} and Reservoir Mechanism

The trilayer achieves $n_{eff} > 1$ at rates up to 10 A g^{-1}, with a maximum value of 1.21 at 0.1 A g^{-1}, before declining to 0.972 at 20 A g^{-1}, attributed to transport limitations preventing complete reservoir utilisation. Pure $MnO_2 < 0.61$ at all discharge rates. $MnCl_2$ dissolves, releasing oxidised Mn^{2+} at the electrode surface via $Mn^{2+} \rightarrow MnOOH \rightarrow MnO_2$, with each step affording two electrons per dissolved $MnCl_2$.

C. Ragone Analysis

Trilayer: 270–391 Wh kg^{-1}; pure MnO_2: 133–209 Wh kg^{-1} (advantage 2.02–2.20×). The near-constant separation confirms a rate-independent architectural advantage. The thermodynamic voltage ceiling limits the advantage of the trilayer at low rates. The specific power spans 117–21,189 W kg^{-1}, confirming its viability across both energy-storage and moderate power demand applications.

D. Sensitivity Analysis

To identify which architectural choices matter most, four parameters were varied about the baseline at 5 A g^{-1}. Increasing the middle-layer mass m_{mid} from 1.0 to 2.5 mg raises capacity from 301.6 to 311.6 mAh g^{-1} (avg. 6.7 mAh mg^{-1}, diminishing from 10.6 to 3.3 mAh mg^{-1}; n_{eff} 1.053→1.156); the returns diminish because, beyond a point, sacrificing primary active material outweighs the reservoir gain it buys. Increasing the outer MnO_2 mass m_{MnO_2} from 3 to 6 mg has the opposite effect, lowering capacity from 317.8 to 297.8 mAh g^{-1} (n_{eff} 1.186→1.052), since a larger MnO_2 mass dilutes the sacrificial fraction. Composition matters more than either mass: raising the MnOOH fraction x_{MnOOH} from 0 to 1 drops capacity from 309.8 to 241.1 mAh g^{-1} (n_{eff} 1.128→0.792), because MnOOH neither dissolves nor contributes to the reservoir, confirming pure $MnCl_2$ as the optimal choice. Particle radius, by contrast, is nearly irrelevant: capacity varies by less than 0.3% over 300–900 nm, since the characteristic solid-diffusion time $\frac{r_p^2}{D_s} \approx \frac{(700\text{ nm})^2}{10^{-13}} \approx 4.9$ s is far shorter than the ~223 s discharge time at 5 A g^{-1}, leaving the electrolyte phase as the rate-limiting step regardless of particle size.

E. Electrochemical Impedance

TABLE 2. PHYSICS-DERIVED EIS PARAMETERS (SOC = 1.0)

Config.	R_s (Ω)	R_{ct} (Ω)	σ_w (Ω $s^{0.5}$)
Pure MnO_2	0.067	456.0	0.01318
Trilayer	0.008	131.3	0.01420
Ratio	**8.1×**	**3.5×**	**0.93×**

Analytically derived from DFN model parameters; not from circuit fitting (tabulated in Table 2). The 8.1× R_s reduction reflects two contributions: the graphene interlayer cuts contact resistance ~23× via high in-plane conductivity and work-function matching, while higher porosity improves eff by $\left(\frac{0.55}{0.38}\right)^{1.8} \approx 1.95$ via Eq. (3). The shared 30 μm separator contributes a fixed offset to R_s, and the ratio is smaller than the ~23× contact-resistance ratio. The 3.5× R_{ct} reduction arises from passivation suppression—pure MnO_2 accumulates δ_{max} = 9.4 nm, giving a 5.7× increase above fresh value, which the trilayer limits through continuous pore opening. The Warburg coefficient is marginally higher for the trilayer (+7.7%) and practically insignificant next to the R_s /R_{ct} reductions since $\sigma_w \ll R_{ct}$ throughout.

Conclusions

A dynamic pore-forming trilayer cathode for aqueous Zn-MnO_2 batteries was evaluated via a physics-based DFN model with parameters drawn from peer-reviewed literature. It delivers ~2× the specific capacity of pure MnO_2 across 0.1–20 A g^{-1}, with n_{eff} >1 up to 10 A g^{-1} (max. 1.21 at 0.1 A g^{-1}; 0.972 at 20 A g^{-1}), confirming the Mn^{2+} reservoir mechanism under upper-bound capture efficiency. R_s and R_{ct} are reduced 8.1× and 3.5× respectively, yielding a 270–391 Wh kg^{-1} Ragone advantage over 133–209 Wh kg^{-1} for pure MnO_2. Pure $MnCl_2$ is the optimal sacrificial composition; particle radius is negligible (<0.3% over 300–900 nm) while middle-layer composition and mass dominate sensitivity, with $MnOOH$ fraction alone shifting capacity by ~22%. Placing the sacrificial layer adjacent to MnO_2 minimises Mn^{2+} diffusion distance, while the graphene interlayer—only 0.05 mg, <1% of total mass—delivers most of the R_s reduction Future work will extend the model to two-carrier H^+/Zn^{2+} insertion, zinc-anode effects, and multi-cycle degradation, alongside experimental validation of n_{eff} >1 and Mn^{2+} capture efficiency.

References

[1] B. Dunn, H. Kamath, J.-M. Tarascon, Electrical energy storage for the grid: a battery of choices, Science 334 (2011) 928-935. https://doi.org/10.1126/science.1212741

[2] G. Fang, J. Zhou, A. Pan, S. Liang, Recent advances in aqueous zinc-ion batteries, ACS Energy Lett. 3 (2018) 2480-2501. https://doi.org/10.1021/acsenergylett.8b01426

[3] Y. Liu et al., Manganese dioxide cathode materials for aqueous zinc ion battery: Development, challenges and strategies, EnergyChem 7 (2025) 100152. https://doi.org/10.1016/j.enchem.2025.100152

[4] E.D. Spoerke et al., Driving Zn-MnO_2 grid-scale batteries: A roadmap to cost-effective energy storage, MRS Energy Sustain. 9 (2022) 13-28. https://doi.org/10.1557/s43581-021-00018-4

[5] S.W.D. Gourley, R. Brown, B.D. Adams, D. Higgins, Zinc-ion batteries for stationary energy storage, Joule 7 (2023) 1415-1436. https://doi.org/10.1016/j.joule.2023.06.007

[6] L.E. Blanc, D. Kundu, L.F. Nazar, Scientific challenges for the implementation of Zn-ion batteries, Joule 4 (2020) 771-799. https://doi.org/10.1016/j.joule.2020.03.002

[7] H. Pan et al., Reversible aqueous zinc/manganese oxide energy storage from conversion reactions, Nat. Energy 1 (2016) 16039. https://doi.org/10.1038/nenergy.2016.39

[8] J. Shin et al., A review on mechanistic understanding of MnO_2 in aqueous electrolyte for electrical energy storage systems, Int. Mater. Rev. 65 (2020) 356-387. https://doi.org/10.1080/09506608.2019.1653520

[9] M.H. Alfaruqi et al., Electrochemically induced structural transformation in a γ-MnO_2 cathode of a high capacity zinc-ion battery system, Chem. Mater. 27 (2015) 3609-3620. https://doi.org/10.1021/cm504717p

[10] N. Zhang et al., Rechargeable aqueous zinc-manganese dioxide batteries with high energy and power densities, Nat. Commun. 8 (2017) 405. https://doi.org/10.1038/s41467-017-00467-x

[11] C. Xu, B. Li, H. Du, F. Kang, Energetic zinc ion chemistry: the rechargeable zinc ion battery, Angew. Chem. Int. Ed. 51 (2012) 933-935. https://doi.org/10.1002/anie.201106307

[12] P. Ragupathy, H.N. Vasan, N. Munichandraiah, Synthesis and characterization of nano MnO_2 by the soft chemical route, J. Electrochem. Soc. 155 (2008) A34-A40. https://doi.org/10.1149/1.2800163

[13] J.C. Bernard et al., Physics-based continuum modeling for an aqueous rechargeable Zn/MnO_2 battery, J. Electrochem. Soc. 171 (2024) 050502. https://doi.org/10.1149/1945-7111/ad3f55

[14] L. Wu et al., Unraveling the charge storage mechanism of β-MnO_2 in aqueous zinc electrolytes, ACS Energy Lett. 9 (2024) 5801-5809. https://doi.org/10.1021/acsenergylett.4c02559

[15] L. Meng et al., Rechargeable Zn-MnO_2 batteries: progress, challenges, rational design, and perspectives, ChemElectroChem 11 (2024) e202300495. https://doi.org/10.1002/celc.202300495

[16] B. Lee et al., Elucidating the intercalation mechanism of zinc ions into α-MnO_2 for rechargeable zinc batteries, Chem. Commun. 51 (2015) 9265-9268. https://doi.org/10.1039/C5CC02585K

[17] J. Liu et al., Progress in aqueous rechargeable batteries, Green Energy Environ. 3 (2018) 20-41. https://doi.org/10.1016/j.gee.2017.10.001

[18] J. Huang et al., Polyaniline-intercalated manganese dioxide nanolayers as a high-performance cathode material for an aqueous zinc-ion battery, Nat. Commun. 9 (2018) 2906. https://doi.org/10.1038/s41467-018-04949-4

[19] J. Zheng et al., Electrolyte additives toward practical aqueous zinc-ion batteries: recent advances and future challenges, ACS Energy Lett. 5 (2020) 2454-2465.

[20] B. Tjaden et al., On the origin and application of the Bruggeman correlation for analysing transport phenomena in electrochemical systems, Curr. Opin. Chem. Eng. 12 (2016) 44-51. https://doi.org/10.1016/j.coche.2016.02.006

[21] V. Srinivasan, J. Newman, Discharge model for the lithium iron-phosphate electrode, J. Electrochem. Soc. 151 (2004) A1530-A1537. https://doi.org/10.1149/1.1785013

[22] P.M. Biesheuvel, M.Z. Bazant, Nonlinear dynamics of capacitive charging and desalination by porous electrodes, Phys. Rev. E 81 (2010) 031502. https://doi.org/10.1103/PhysRevE.81.031502

[23] K.-E. Byun et al., Graphene for true ohmic contact at metal-semiconductor junctions, Nano Lett. 13 (2013) 4001-4005. https://doi.org/10.1021/nl402367y

Keyword Index

Abrasive Water Jet 206
Absorbed Energy 253
Acoustic Hologram 78
Acoustic Metamaterial 78
Adaptive Sampling 190
Additive Manufacturing 91, 95, 114
Adhesive Joints 105
Aeroelastic Fragility Analysis 249
Aerospace 239
Alloy 718 51
Amplitude-Phase Coupling Modulation 78
Analytical Solutions 266
Anelasticity 211
Anisotropy 66
Aqueous Zinc-Ion Battery 315

Band Structure 18
Beam models 307
Beam 118
Beams 284
Bi-Layer Composite 229
Biocomposites 91
Bistable Laminates 298
Blades Icing 249
Bolted Joints 294
Boundary Condition Nonlinearities 31
Buckling 217

Carrera Unified Formulation (CUF) 7, 31, 62, 85, 124, 147, 177, 195, 200, 217, 235, 274, 307
CFRP Composites 23
Classical Lamination Theory 239
CNN 270
Component-Wise Approach 274
Component-Wise Modelling 7
Composite Deployable Booms 195
Composite Materials 27, 105
Composite Pressure Vessel 100
Composite Railway 47
Composite Structures 274, 290, 307
Composite 118, 245
Compression 37
Compressive Failure 23
Computational Fluid Dynamics 206
Computational Study 18
Concrete Deterioration 56
Continuous Carbon Fiber Composites 95
Copper Oxide (CuO) Nanofluid 170
Cost/Performance Ratio 311
Crack Propagation 270
Creep 51
CUF 109, 190, 223, 294
Cumulative Impact 253
Curved Panels 85
Curved Shells 245
Curvilinear Models 245
Cutouts 284

Damage Detection 302
Damage Localization 302
Damped Dynamic Stiffness 274
Deep Learning 270
Delamination 253
Delta Phase 51
Deployable Composite Booms 195
Deployable Space Structures 200
Design of Thin Walls 72
DFN Model 315
Digital Image Correlation 1, 37
Direct MultiSearch 280
Discrete Curvature 156
Distributed Fiber Optic Strain Sensing 56
Doped ZnO 18

Ductile Damage 151
Dynamic Behavior 223
Dynamic Mechanical Analysis 211
Dynamic Porosity 315
Dynamic Response 13
Dynamic Stiffness Method 124, 274
Dynamic Stiffness 284

Eco-Design 311
Effective Electron Transfer 315
Elastic Constants 18
Electromechanical Coupling Response 124
Element-Free Galerkin Method 136
Embedded Fiber Optic Cable 56
Energy Absorption 43

Failure Index 195
Fatigue Crack Propagation 62
Fatigue Limit 160
FEM 190, 294
FG Box Beam 223
FGM 266
Finite Element Analysis 37
Finite Element Model 47, 245
Finite Element 56, 156, 262, 298
Finite-Strain 151
Flax/Glass Fibres 160
Flexural Stress 266
Fracture Toughness 130
Free Vibration 7, 274, 284
Frequency Response Function 118
Friction 31
FRP Bottle 239

Gamma Radiation Shielding 229
Gaussian Process Regression 177
Geometric Non-Linearities 200
Geometric Parameters 195
Geometrically Exact Beams 156
Glass Fibre 166
Grid-Scale Storage 315

Heat Treatment 51
Hierarchical Legendre Expansion 147
Higher Order 262
Higher-Order Beam Models 147, 294
High-Order Interpolation 156
High-Order Refined Elements 62
Homogenized Honeycomb Sandwich 235
Honeycomb Metastructures 85
Hot Isostatic Pressing 51
Hybrid PMC 160
Hydrogen Tank Optimization 100
Hygrothermal Ageing 105
Hyperelasticity 262
Hysteretic Maxwell Model 142

Impedance Analysis 170
Incompressible Materials 262
In-situ Consolidation 1
Interfacial Adhesion 229
Interlaminar Shear Strength 1
Isogeometric Analysis 56

Jenkins 31

Kink-Band 23

Lagrange Polynomials 290, 307
Lamb Wave Propagation 235
Laminated Composite Materials 166
Large Area Screen Printing 170
Laser Powder Bed Fusion 51
Laser-assisted Automated Fibre Placement 1

Lattice Structures 114
Layer-Substrate 66
Length Scale Parameter 13
Linear Dynamic Analysis 223
Lithium-Ion Battery 151
Low Velocity Impacts 109, 253
Low-Energy Impact 43
Low-Velocity 43
LPBF Process Simulation 72
LSTM 270

Machine Learning 72, 95
Machining 206
Magneto-Electro-Elasticity 66
Mechanics 223
Metamaterials 7
Metastructure Panels 217
Micromechanics 23
Mixed Formulation 156, 262
Mn Dissolution 315
Mobility 43
Mode Shapes Derivatives 302
Mode Shapes 302
Modeling 56
Modelling Analysis 253
Modes Change 200
Modified Couple Stress Theory 13
Multi-Fidelity Modeling 177
Multi-Material Metastructures 217
Multilayered Plates 280
Multiscale Fem Modelling 27

Natural Fibres 91
Neural Networks 190
Nickel-Based Superalloy 51
Nonlinear Analysis 147
Nonlinear Dynamics 298
Nonlinear Finite Element Analysis 217
Nonlinear Structural Analysis 195
Nonlocal Elasticity 136

Optics 18

Para-Aramid Fabric 130
Peridynamics 62
Phase Field Method 56
Phase Holographic Imaging 78
Physics-constrained 95
Piezoelectric Laminated Beams 124
Piezoelectric Transducers 160
Piezoelectric 298
Plasma Treatment 130
Post-Buckling 217
Powder Samples 211
P-refinement 147
Process Parameters 72, 91
Proper Generalized Decomposition 118
Pull-Out Energy 130
Pultruded Composite 311
Pultrusion 47

Railways Tracks 311
Refined Kinematic 290, 307
Refined Sinus Model 118
Refined Stress Analysis 290
Reliability-Based Design Optimization 177
Repair 183
Ritz Method 280
RMVT 290
Rotordynamics 294

Sandwich Structure 7, 27
Sandwich 37, 118
Sea Ice 266
Self-Heating 160

SEM 170
Shear Wrinkling 37
Shell Models 290
Silicon Anode 151
Simplified Models 114
SMART Composites 160
Space-Frequency Separation 118
Spin-Crossover 211
Static Analysis 85
Static Response 13
Stay Cable Vibration Control 142
Stick-Slip 294
Stiffened Panels 109
Strain-Driven Model 136
Stress Distribution 105
Structural Health Monitoring 160, 235
Structural Theories 190
Sublaminate Formulation 280
Surface Engineering 229
Surrogate Modeling 95
Sustainable Aviation 100

Tensile Properties 229
Thermo-Mechanical Behaviour 91
Thermoplastic Composites 1, 183
Thermoplastic 47
Three-Phase Mixing 206
Three-Point Bending 37
Through-Thickness Reinforcement 166
Tow-Steered Composites 177
Tsai-Wu First Ply Failure 239

UV-Visible Spectroscopy 170

Vibroacoustics 280
Vickers Hardness 51
Viscoelasticity 66
Viscous Damper 142
Vitrimer Composites 27
Welded Joints 183
Wind Turbine 249
Wittrick-Williams Algorithm 124, 284
Wood 43
Wrinkling 37

X-Cut Adhesion Test 170
XRD Spectra 18

Zn-MnO_2 Battery 315
ZnO Nanoparticles 170
ZnO Voltage Sensor 170
Z-Pinning 166

e